frontiers | Research Topics

Angiogenesis and tumor metastasis

Edited by
Guisheng Song, Julia Kzhyshkowska, Michal Amit Rahat and Qiangzhe Zhang

Published in
Frontiers in Oncology
Frontiers in Cell and Developmental Biology

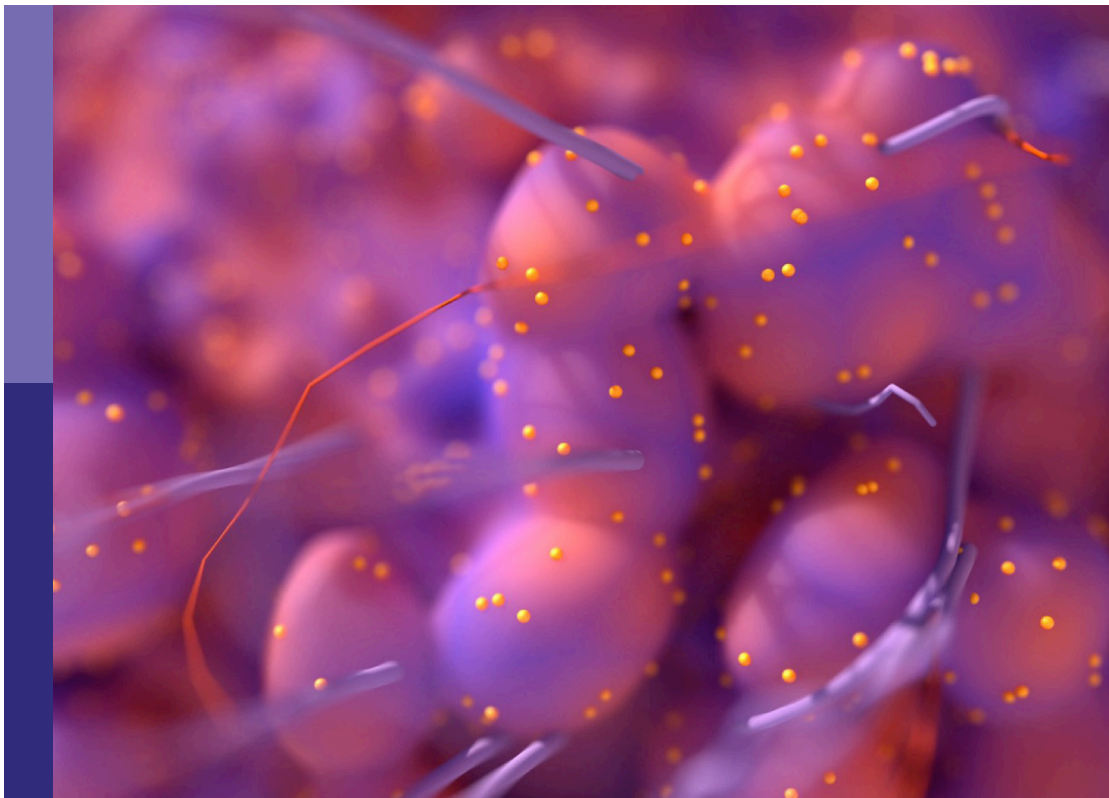

ISSN 1664-8714
ISBN 978-2-83251-508-2
DOI 10.3389/978-2-83251-508-2

About Frontiers

Frontiers is more than just an open access publisher of scholarly articles: it is a pioneering approach to the world of academia, radically improving the way scholarly research is managed. The grand vision of Frontiers is a world where all people have an equal opportunity to seek, share and generate knowledge. Frontiers provides immediate and permanent online open access to all its publications, but this alone is not enough to realize our grand goals.

Frontiers journal series

The Frontiers journal series is a multi-tier and interdisciplinary set of open-access, online journals, promising a paradigm shift from the current review, selection and dissemination processes in academic publishing. All Frontiers journals are driven by researchers for researchers; therefore, they constitute a service to the scholarly community. At the same time, the *Frontiers journal series* operates on a revolutionary invention, the tiered publishing system, initially addressing specific communities of scholars, and gradually climbing up to broader public understanding, thus serving the interests of the lay society, too.

Dedication to quality

Each Frontiers article is a landmark of the highest quality, thanks to genuinely collaborative interactions between authors and review editors, who include some of the world's best academicians. Research must be certified by peers before entering a stream of knowledge that may eventually reach the public - and shape society; therefore, Frontiers only applies the most rigorous and unbiased reviews. Frontiers revolutionizes research publishing by freely delivering the most outstanding research, evaluated with no bias from both the academic and social point of view. By applying the most advanced information technologies, Frontiers is catapulting scholarly publishing into a new generation.

What are Frontiers Research Topics?

Frontiers Research Topics are very popular trademarks of the *Frontiers journals series*: they are collections of at least ten articles, all centered on a particular subject. With their unique mix of varied contributions from Original Research to Review Articles, Frontiers Research Topics unify the most influential researchers, the latest key findings and historical advances in a hot research area.

Find out more on how to host your own Frontiers Research Topic or contribute to one as an author by contacting the Frontiers editorial office: frontiersin.org/about/contact

Angiogenesis and tumor metastasis

Topic editors

Guisheng Song — University of Minnesota, United States
Julia Kzhyshkowska — Heidelberg University, Germany
Michal Amit Rahat — Department of Immunology, Ruth and Bruce Rappaport Faculty of Medicine, Technion-Israel Institute of Technology, Israel
Qiangzhe Zhang — Nankai University, China

Citation

Song, G., Kzhyshkowska, J., Rahat, M. A., Zhang, Q., eds. (2023). *Angiogenesis and tumor metastasis*. Lausanne: Frontiers Media SA. doi: 10.3389/978-2-83251-508-2

Table of contents

frontiers | Frontiers in Oncology

TYPE Editorial
PUBLISHED 17 January 2023
DOI 10.3389/fonc.2022.1129736

OPEN ACCESS

EDITED AND REVIEWED BY
Robson Q. Monteiro,
Federal University of Rio de Janeiro, Brazil

*CORRESPONDENCE
Qiang-Zhe Zhang
zhangqiangzhe@nankai.edu.cn

SPECIALTY SECTION
This article was submitted to Molecular and Cellular Oncology, a section of the journal Frontiers in Oncology

RECEIVED 22 December 2022
ACCEPTED 28 December 2022
PUBLISHED 17 January 2023

CITATION
Zhang Q-Z, Zhu Y-P, Rahat MA and Kzhyshkowska J (2023) Editorial: Angiogenesis and tumor metastasis.
Front. Oncol. 12:1129736.
doi: 10.3389/fonc.2022.1129736

Editorial: Angiogenesis and tumor metastasis

Qiang-Zhe Zhang[1]*, Yi-Pan Zhu[1], Michal A. Rahat[2] and Julia Kzhyshkowska[3,4,5]

[1]State Key Laboratory of Medicinal Chemical Biology and College of Pharmacy, Tianjin Key Laboratory of Molecular Drug Research, Nankai University, Tianjin, China, [2]Immunotherapy Laboratory, Carmel Medical Center, and the Ruth and Bruce Rappaport Faculty of Medicine, Technion-Israel Institute of Technology, Haifa, Israel, [3]Institute of Transfusion Medicine and Immunology, Mannheim Institue for Innate Immunosciences (MI3), Medical Faculty Mannheim, Heidelberg University, Mannheim, Germany, [4]German Red Cross Blood Service Baden-Württemberg – Hessen, Mannheim, Germany, [5]Laboratory for Translational Cellular and Molecular Biomedicine, Tomsk State University, Tomsk, Russia

KEYWORDS

tumor metastasis, angiogenesis, EndoMT, EMT, biomarker

Editorial on the Research Topic
Angiogenesis and tumor metastasis

Angiogenesis, the process of forming new blood vessels from existing vasculature, allows the delivery of oxygen and nutrients to the tumor and supports its progression. Therefore, this necessary process has been recognized as one of the hallmarks of cancer (1). However, its role in promoting and sustaining metastasis is not yet fully elucidated. In cancer, the balance between pro- and anti-angiogenic factors is disrupted in favor of the former, leading to the activation of the "angiogenic switch." Cytokines such as VEGF and its inhibitor TNFSF15 that are secreted from the cells within the tumor microenvironment (TME) participate in the regulation of angiogenesis (2). Different molecules, namely protein factors, exosomes, and non-coding RNAs, can mediate the effect on different cells within the TME and activate signaling pathways that are involved in the process of angiogenesis (3). The resulting new blood vessels are usually leaky and permeable, and they promote the infiltration of immune cells and the progression of the tumor. On the other hand, they can also provide a pathway for the metastatic tumor cells to escape from the primary tumor and reach the circulation, thus supporting metastasis.

The term "metastasis" refers to the migration of cancer cells from their primary site to other organs in the body. This process requires that the metastatic cells become invasive through intravasation into a lymphatic or blood vessel, survive in the circulation, and then extravasate into the distant organ (4). These migratory and invasive properties require that the epithelial-to-mesenchymal transition (EMT) process be activated. This allows the metastatic cancer cells to disseminate and enter blood vessels recently formed by angiogenesis. Once the cancer cell is lodged in the new environment, it must undergo the opposite process of mesenchymal-to-epithelial transition (MET) in order to reacquire its ability to proliferate and colonize the distant sites, which is necessary to form a metastatic, secondary tumor in the distant organ (5). Another important transition of cells' states is the endothelial-to-mesenchymal transition (EndoMT), which contributes to both metastatic extravasation and intravasation. During EndoMT, vasculature endothelial cells (ECs) lose their endothelial cell-cell junctions, allowing the transendothelial migration of metastatic cells. Once metastatic colonization has been achieved, further steps are needed to start a new

round of angiogenesis to nourish the new tumor. This Research Topic provides an updated overview of new regulatory mechanisms and potential targets in tumor angiogenesis and metastasis.

Two papers suggest new mechanisms involved in inducing angiogenesis. Gao et al. found that STAT6, which is activated by IL-13, can bind to the neuropilin-1 (NRP1) promoter and increase NRP1 expression in ECs, thus promoting tumor angiogenesis. STAT6 inhibitor (AS1517499) and STAT6 siRNA could suppress tumor angiogenesis and growth in tumor xenograft models, suggesting that STAT6 may be a potential target for anti-angiogenesis therapy. Park et al. demonstrated that radiation stimulated angiogenesis in Glioblastoma multiforme (GBM) *via* the growth/differentiation factor-15 (GDF15), which in turn fosters the crosstalk between ECs and GBM cells. The radiation-induced secretion of GDF15 from ECs activated the VEGFA promoter in glioma cells through the pMAPK1/SP1 signaling pathway, consequently promoting angiogenesis in GBM. Silencing GDF15 ameliorated radiation-induced VEGFA upregulation in glioma cells and increased the angiogenic activity of ECs. Therefore, GDF15 is a potential target for radiation-induced angiogenesis in GBM patients receiving radio-chemotherapy.

Increased migration and invasion of tumor cells are necessary for tumor metastasis. Xue et al. found that mesenchymal stem cell-transformed cancer-associated fibroblasts (MTCAFs) secreted more ICAM-1 that could bind the LFA-1 receptors in colon cancer cells, activate Akt and STAT3 signaling, and promote the migration, invasion, and metastasis of the colon cancer cells, both *in vitro* and in xenograft tumor models. Tyumentseva et al. revealed that the chemotherapeutic agent dacarbazine changed the transcriptomic profiling of melanoma cells and affected primarily genes related to movement, migration, invasion, and adhesion pathways. Specifically, the upregulation of plexin A2 (PLXNA2) reduced the migratory and invasive capabilities of melanoma cells, establishing PLXNA2 as a new marker for the invasion and migration of melanoma cells.

Bai et al. reviewed how tumor-derived exosomes (TDEs) promote tumor metastasis by reshaping the TME and the distant metastatic niche. By delivering non-coding RNAs and proteins to tumor cells, TDEs promote the EMT program and activate ECM-degrading proteases to enhance tumor cell migration. TDEs can promote angiogenesis by activating macrophages and ECs. Intravasating tumor cells are protected by the layer of TDEs and by the ability of TDEs to suppress circulating NK, T, and B cells. When extravasating, TDEs prepare the pre-metastatic niche, and their integrins determine organotropism. In brain metastasis, Geng et al. demonstrated that exosomes derived from highly metastatic non-small cell lung cancer (NSCLC) cells are internalized in brain microvascular ECs and release the lncRNA LINC01356 that targets junctional proteins such as claudin-5, N-cadherin, Occludin, and ZO-1. This leads to the disruption of the blood-brain barrier (BBB) and promotes brain metastasis in lung cancer.

Presented next are three papers that describe a new mechanism of osteosarcoma metastasis. Lee et al. implicated CXCL1, which enhances the expression and nuclear translocation of NF-kB through the CXCR2/FAK/PI3K/AKT pathway, resulting in the upregulation of VCAM-1. This cascade enhances the migration, invasion, and metastatic ability of osteosarcoma cells to the lung. Shao et al. found that tetraspanin-9 (Tspan9) can promote EMT and lung metastasis of osteosarcoma cells and also interact with integrin β1 and enhance the FAK-RAS-ERK1/2 signaling cascade in osteosarcoma cells. The finding that the downregulation of Tspan9 could inhibit lung metastasis in a mouse model of osteosarcoma suggests that Tspan9 may be used as a new therapeutic target in osteosarcoma. Interestingly, Kuriyama et al. reported that the pigment epithelium-derived factor (PEDF) increased osteosarcoma cells' extravasation to the kidneys and lungs by triggering MET and inhibiting EndoMT through the PEDF-laminin receptor axis. Collectively, these three studies highlight new mechanisms of osteosarcoma metastasis and organotropism.

The search for useful and reliable biomarkers to determine prognosis and the response to immunotherapy in cancer patients is ongoing. Wang et al. implemented bioinformatics analyses to determine a risk score based on the identification of 31 key, differentially expressed angiogenesis-related genes (DE-ARG) in GBM patients. This signature proved to be effective in predicting the survival rate and the response to immunotherapy and useful in providing a personalized program for GBM patients. Similarly, Li et al. identified an angiogenesis score based on a pan-cancer analysis across 33 human cancer types. Higher values of the score were correlated with infiltration of macrophages and inducible Tregs, and patients with lower score values had a favorable prognosis and better responses to immunotherapy. Dong et al. identified another potential biomarker, the macrophage-related secreted phosphoprotein 1 (SPP1), for early lymph node metastasis in lung adenocarcinoma. LncRNA AC037441, which was negatively associated with SPP1 and infiltrating macrophages, was also implicated in the regulation of early lymph node metastasis. Jiang et al. constructed a scoring model based on the expression of 4 RNA-binding proteins to predict the risk for peritoneal metastasis in gastric cancer. The model could excellently predict TNM stage and prognosis, and the generated nomograms could help in making clinical decisions. Collectively, these studies suggest that data mining could accelerate the evolution of cancer therapy in the era of big data.

Myeloid-derived cells are key components of TME. Stefanescu et al. found that TGFβ/TGFβR2 signaling in myeloid cells could differently regulate metastasis in tissue-specific ways, depending on the specific TME. TGFβ signaling in myeloid-derived cells promoted lung metastasis of Lewis lung carcinoma cells by suppressing the activity of CD8+ T cells, while the same signaling pathway increased liver metastasis of colon cancer cells by enhancing M2-monocytic polarization. An interesting case of pancreatic solid pseudopapillary neoplasm (SPN) with peritoneal and hepatic metastasis is illustrated by Wang et al. The identification of the mutation variants in the PTEN and CTNNB1 genes was used to stabilize the disease with the targeted drugs sunitinib and everolimus. This report demonstrates how molecular studies can help explain the mechanism of SPN occurrence and contribute to the decision-making process for precision treatments.

Collectively, this series of articles highlights the importance of angiogenesis in tumor metastasis, sheds light on new mechanisms that promote metastasis, and suggests new therapeutic targets to decrease angiogenesis and the metastatic cascade in the treatment of cancer.

Author contributions

All authors listed have made a substantial, direct, and intellectual contribution to the work and approved it for publication.

Funding

National Natural Science Foundation of China (No. 82073233). Israel Science Foundation (ISF) grant number 2607/20.

Acknowledgments

We wish to express our sincere appreciation to all the authors and reviewers for their active participation in this Research Topic and their insightful comments.

Conflict of interest

The authors declare that the research was conducted in the absence of any commercial or financial relationships that could be construed as a potential conflict of interest.

Publisher's note

References

1. Hanahan D. Hallmarks of cancer: New dimensions. *Cancer Discovery* (2022) 12:31–46. doi: 10.1158/2159-8290.CD-21-1059

2. Yang GL, Li LY. Counterbalance: Modulation of VEGF/VEGFR activities by TNFSF15. *Signal transduction targeted Ther* (2018) 3:21. doi: 10.1038/s41392-018-0023-8

3. Pulkkinen HH, Kiema M, Lappalainen JP, Toropainen A, Beter M, Tirronen A, et al. BMP6/TAZ-hippo signaling modulates angiogenesis and endothelial cell response to VEGF. *Angiogenesis* (2021) 24:129–44. doi: 10.1007/s10456-020-09748-4

4. Lin Y, Xu J, Lan H. Tumor-associated macrophages in tumor metastasis: Biological roles and clinical therapeutic applications. *J Hematol Oncol* (2019) 12:76. doi: 10.1186/s13045-019-0760-3

5. Bakir B, Chiarella AM, Pitarresi JR, Rustgi AK. EMT, MET, plasticity, and tumor metastasis. *Trends Cell Biol* (2020) 30:764–76. doi: 10.1016/j.tcb.2020.07.003

frontiers in Cell and Developmental Biology

ORIGINAL RESEARCH
published: 27 September 2021
doi: 10.3389/fcell.2021.739358

Macrophage-Related SPP1 as a Potential Biomarker for Early Lymph Node Metastasis in Lung Adenocarcinoma

Bo Dong[1†], Chunli Wu[1†], Lan Huang[2] and Yu Qi[1*]*

[1] Department of Thoracic Surgery, The First Affiliated Hospital of Zhengzhou University, Zhengzhou, China, [2] Biotherapy Center, The First Affiliated Hospital of Zhengzhou University, Zhengzhou, China

OPEN ACCESS

Edited by:
Yongbin Chen,
Kunming Institute of Zoology, Chinese Academy of Sciences (CAS), China

Reviewed by:
Xiaofeng Zheng,
Zhejiang University, China
Qingling Zhang,
Guangdong Academy of Medical Sciences, China
Yi Li,
Kunming General Hospital of Chengdu Military Command, China

***Correspondence:**
Lan Huang
Lanhuang@zzu.edu.cn
Yu Qi
Qiyu@zzu.edu.cn

[†] These authors have contributed equally to this work and share first authorship

Specialty section:
This article was submitted to Molecular and Cellular Oncology, a section of the journal Frontiers in Cell and Developmental Biology

Received: 10 July 2021
Accepted: 06 September 2021
Published: 27 September 2021

Citation:
Dong B, Wu C, Huang L and Qi Y (2021) Macrophage-Related SPP1 as a Potential Biomarker for Early Lymph Node Metastasis in Lung Adenocarcinoma. Front. Cell Dev. Biol. 9:739358. doi: 10.3389/fcell.2021.739358

Lymph node metastasis is a major factor that affects prognosis in patients with lung adenocarcinoma (LUAD). In some cases, lymph node metastasis has already occurred when the primary tumors are still small (i.e., early T stages), however, relevant studies on early lymph node metastasis are limited, and effective biomarkers remain lacking. This study aimed to explore new molecular biomarker for early lymph node metastasis in LUAD using transcriptome sequencing and experimental validation. Here, we performed transcriptome sequencing on tissues from 16 matched patients with Stage-T1 LUAD (eight cases of lymph node metastasis and eight cases of non-metastasis), and verified the transcriptome profiles in TCGA, GSE68465, and GSE43580 cohorts. With the bioinformatics analysis, we identified a higher abundance of M0 macrophages in the metastatic group using the CIBERSORT algorithm and immunohistochemistry (IHC) analysis and the enrichment of the epithelial–mesenchymal transition (EMT) pathway was identified in patients with higher M0 infiltration levels. Subsequently, the EMT hallmark gene *SPP1*, encoding secreted phosphoprotein 1 (SPP1), was identified to be significantly correlated with macrophage infiltration and M2 polarization, and was determined to be a key risk indicator for early lymph node metastasis. Notably, SPP1 in the blood, as detected by enzyme-linked immunosorbent assay (ELISA) showed a superior predictive capability for early lymph node metastasis [area under the curve (AUC) = 0.74]. Furthermore, a long non-coding RNA (lncRNA, AC037441), negatively correlated with SPP1 and macrophage infiltration, had also been identified and validated to be involved in the regulation of early lymph node metastasis. In conclusion, we revealed the potential role of macrophages in lymph node metastasis and identified the macrophage-related gene *SPP1* as a potential biomarker for early lymph node metastasis in LUAD.

Keywords: lung adenocarcinoma, early lymph node metastasis, SPP1, macrophage, M2 polarization, epithelial-mesenchymal transition (EMT)

INTRODUCTION

Lung cancer is the most common form (11.6%) of malignant tumors worldwide (Bray et al., 2018; Ramos-Paradas et al., 2021). With advances in imaging technology and increased awareness of physical examinations, an increasing number of patients have been diagnosed with early-stage lung cancer. Lung adenocarcinoma (LUAD) represents a major form of lung cancer. Some LUAD

patients experience lymph node metastasis or pathologically indistinguishable micrometastasis when the primary tumors are still small (that is, an early T-stage in the TNM staging system for lung cancer) (Martinez-Zayas et al., 2021), which seriously affects long-term survival (Allemani et al., 2018). The underlying mechanisms of early-stage metastasis require comprehensive exploration to identify effective biomarkers and optimize personalized cancer treatments.

The dynamic tumor immune microenvironment (TIME) plays a vital role in tumor proliferation, invasion, angiogenesis, and even immune escape (Altorki et al., 2019; Sautès-Fridman et al., 2019; Fane and Weeraratna, 2020). Studies exploring early lung cancer have shown that immunoediting is relatively common (Zhang et al., 2019b), and the immune system can induce a variety of routes resulting in immune evasion (Rosenthal et al., 2019). Single-cell analysis revealed that myeloid cell subsets might impair the anti-tumor immunity of T cells in early-stage LUAD (Lavin et al., 2017). In addition, the role of TIME in lymph node metastasis has been explored in breast cancer (Gu et al., 2019). Therefore, the relevant molecular mechanisms associated with early lymph node metastasis may be further elucidated in LUAD through the TIME analysis.

Macrophages differentiate from mononuclear phagocytic lineage cells, which reside in almost all tissues and participate in the immune response and homeostasis maintenance (Gentek et al., 2014). Macrophages can participate in tumorigenesis and progression (Qian and Pollard, 2010; Cassetta and Pollard, 2018; Wu et al., 2020). Deng et al. (2010) found that the abundant expression of tumor necrosis factor α (TNFα) and interleukin-6 (IL-6) by macrophages can create a favorable inflammatory environment for the occurrence of colonic adenocarcinomas. Moreover, macrophages play a considerable role in the acquisition of the epithelial– mesenchymal transition (EMT) hallmarks observed in gastric cancer tissues (Guan et al., 2021), pancreatic duct epithelial cells (Otto et al., 2021), and tracheal epithelial cells (Li et al., 2021), and EMT signatures plays a vital role in tumor metastasis (Lu and Kang, 2019). Macrophages are heterogeneous cell clusters with intricate functions and forms. The CIBERSORT algorithm can elucidate the gene expression characteristics of three macrophage subtypes: unpolarized M0 macrophages and polarized M1 (pro-inflammatory) and M2 (anti-inflammatory) macrophages (Newman et al., 2015). Higher M0 infiltration is closely related to unfavorable overall survival (OS) in LUAD patients (Yi et al., 2021; Zheng et al., 2021). However, the role of macrophages in early lymph node metastasis has not been elucidated.

Secreted phosphoprotein 1 (SPP1), a hallmark gene of the EMT process, can participate in extracellular matrix (ECM)-receptor interactions and the focal adhesion response pathway to regulate tumor metastasis and invasion. SPP1 is significantly associated with adverse survival outcomes in various cancers (Wei et al., 2020; He et al., 2021; Wang et al., 2021). Notably, higher SPP1 expression levels are related to a higher N stage in LUAD patients (Guo et al., 2020), although the underlying mechanism has not yet been studied fully. To explore the clinical phenomenon in which some LUAD patients develop lymph node metastasis at a very early T-stage, we revealed the crucial roles played by macrophages in lymph node metastasis and identified macrophage-related SPP1 as a potential biomarker for early metastasis in lung cancer.

MATERIALS AND METHODS

Raw Data

To eliminate the influences of confounding factors (age, sex, and differentiation grade) on early lymph node metastasis, we selected eight patients with lymph node metastasis and matched eight patients without metastasis from the biobank of Stage-T1 LUAD. Transcriptome sequencing was performed on the tumor tissues and adjacent normal lung tissues from these 16 patients (one case of normal tissue was missing). RNA sequencing (RNA-seq) data and corresponding clinical information can be found in the supplementary materials. Furthermore, the transcriptome profiles of Stage-T1 LUAD patients from external validation cohorts were obtained from The Cancer Genome Atlas (TCGA) database (34 cases with lymph node metastasis, 131 cases without metastasis), the GSE68465 dataset (35 cases with lymph node metastasis, 114 cases without metastasis), and the GSE43580 dataset (11 cases of lymph node metastasis, 9 cases of no metastasis). The study protocol was approved by the institutional Ethics Committee of First Affiliated Hospital of Zhengzhou University (No. 2019-KY-255). Written informed consent was obtained from all study participants.

Bioinformatics Analysis

The relative proportion of 22 immune cells were determined for Stage-T1 LUAD and adjacent lung samples using the CIBERSORT algorithm[1]. The algorithm of random sampling consisted of 1,000 permutations. Only samples with a p-value < 0.05 were included for subsequent analysis.

The weighted gene co-expression network analysis (WGCNA) package (Langfelder and Horvath, 2008) was used to construct scale-free networks and identify gene sets related to lymph node metastasis and macrophage infiltration (the minimum number of genes was set to 15, the mRNA scale-free network was formed when the soft threshold β was set to 10, and the long non-coding RNA (lncRNA) network was constructed when $\beta = 8$). Subsequently, hub RNAs in the modules were identified using Cystoscope software version 3.7.1.

Enrichment Analysis of Biological Processes and Underlying Pathways

Gene Set Enrichment Analysis (GSEA) was conducted for on the hallmark gene sets of Molecular Signature Database (MSigDB) to explore the potential regulatory mechanisms associated with lymph node metastasis and M0 infiltration. GSEA analysis was performed using the software GESA version 4.01 (Subramanian et al., 2005), and gene sets related to EMT and inflammatory response (IR) hallmarks were also obtained from MSigDB.

Gene ontology (GO) and Kyoto Encyclopedia of Genes and Genomes (KEGG) enrichment analyses were performed using

[1]https://cibersort.stanford.edu/

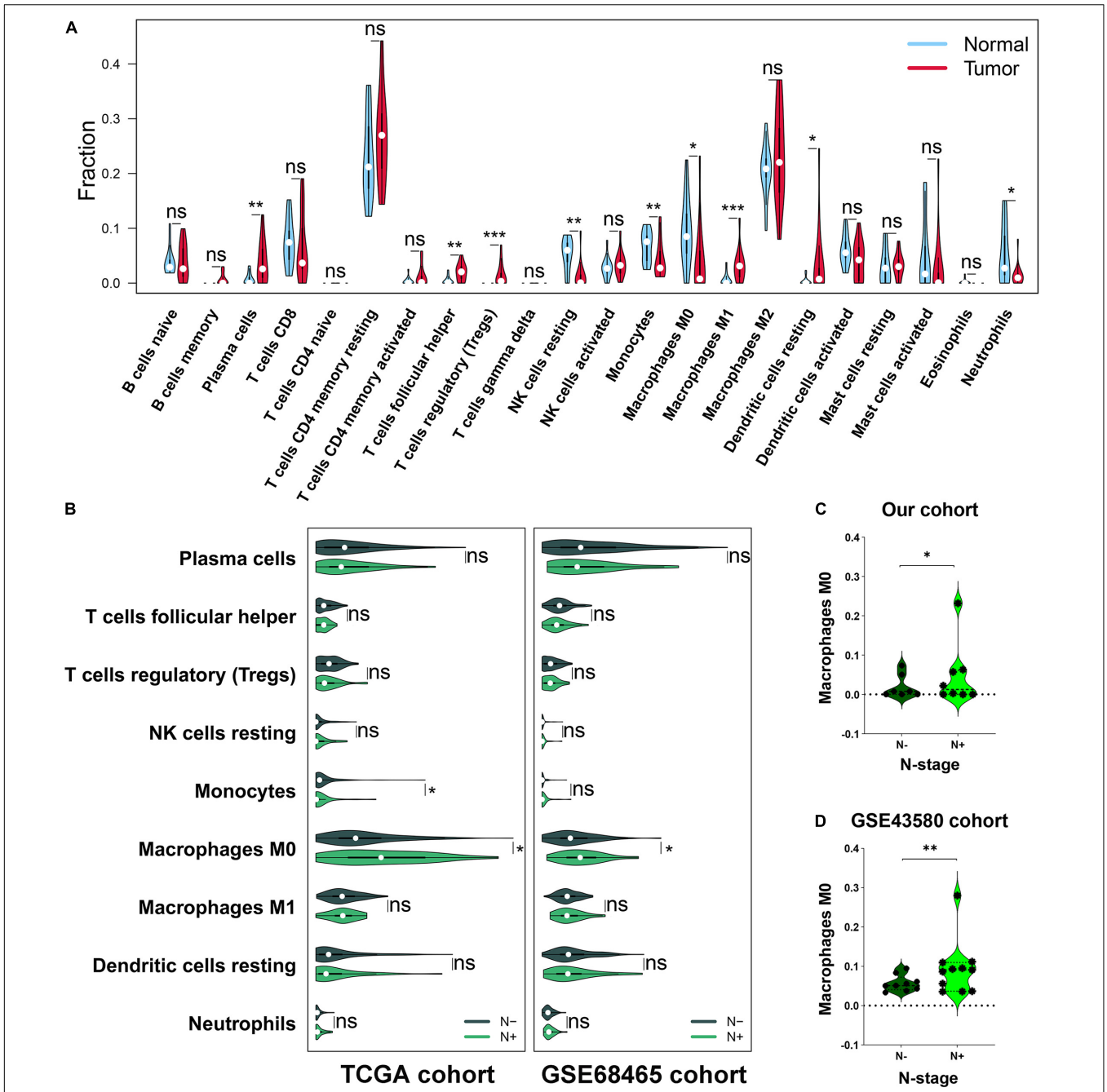

FIGURE 1 | Analysis of the immune cell infiltration abundance in Stage-T1 lung adenocarcinoma (LUAD). **(A)** Comparison of the infiltration levels of 22 immune cells in tumor tissues versus adjacent lung tissues. **(B)** Comparison of the infiltration abundance of nine immune cell types in the lymph node metastasis group versus the non-metastasis group of TCGA and GSE68465 cohorts. In our cohort **(C)** and the GSE43580 cohort **(D)**, a higher M0 infiltration was associated with early lymph node metastasis. ns, not significant, $^{*}p < 0.05$, $^{**}p < 0.01$, and $^{***}p < 0.001$. TCGA, The Cancer Genome Atlas.

the clusterProfiler and enrichplot packages. Only terms for which both the *p*-value and q-value < 0.05 were considered significantly enriched.

Enzyme-Linked Immunosorbent Assay

The plasma SPP1 levels in Stage-T1 LUAD patients were assayed using a commercial enzyme-linked immunosorbent assay (ELISA) kit (ELH-OPN-1; R&D company, United States). The 25-fold diluted plasma samples were directly transferred to a 96-well plate coated with an antibody specific for human SPP1 and assayed according to the manufacturer's instructions. The absorbance value was recorded at 450 nm in a microtest plate spectrophotometer with the correction wavelength set at 540 nm. SPP1 levels were quantified

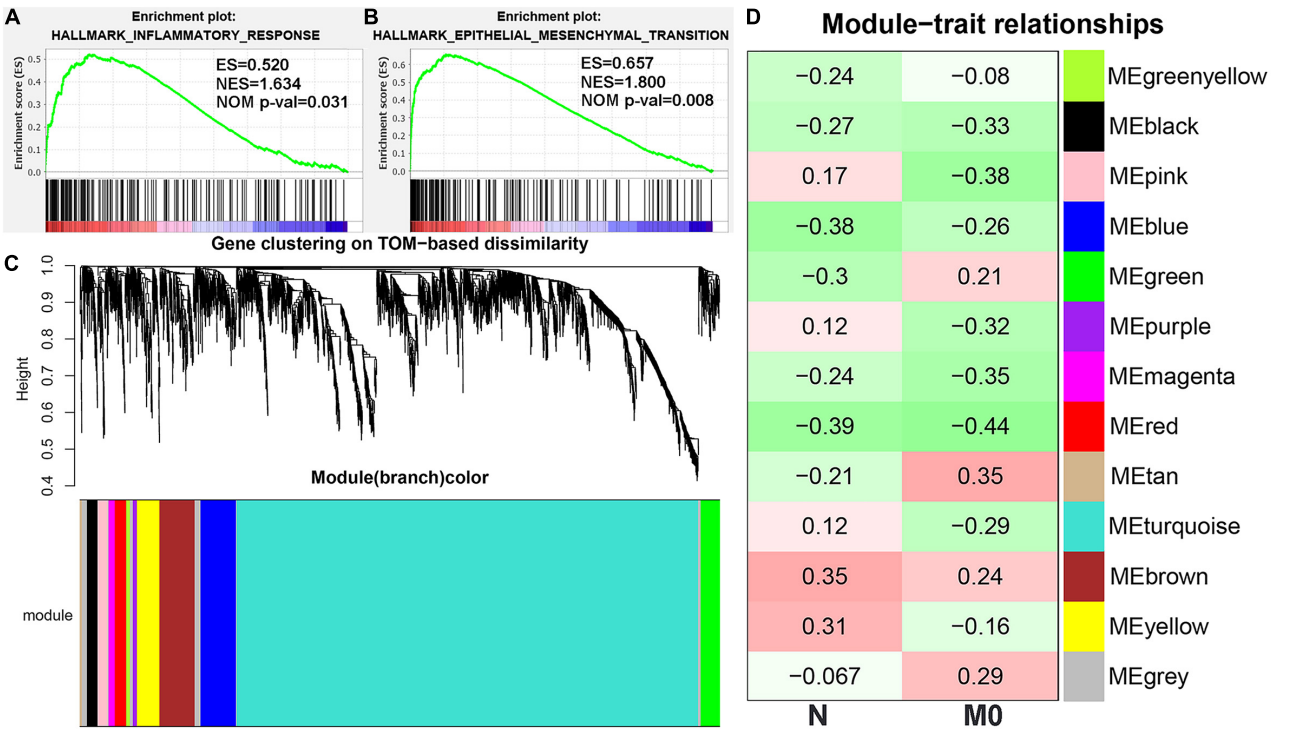

FIGURE 2 | Identification of mRNA modules associated with lymph node metastasis and M0 infiltration. Gene set enrichment analysis (GSEA) suggested that early lymph node metastasis was related to the inflammatory response (IR) pathway **(A)**, and the epithelial–mesenchymal transition (EMT) pathway were significantly enriched in the M0 high-infiltration group **(B)**. **(C)** The scale-free mRNA network was clustered into 13 modules by average hierarchical clustering and dynamic tree clipping. **(D)** The correlation heatmap was used to describe the relationship between 13 genesets and N stage, M0 infiltration. ES, enrichment score. NES, normalized ES. NOM *p*-val, normalized *p*-value. TOM, topological overlap matrix.

using a calibration curve based on a human osteopontin standard. Both standards and samples were evaluated in duplicate, and the results were adopted only when the inter-assay variations were within the range provided by the manufacturer.

Quantitative Reverse Transcriptase-Polymerase Chain Reaction

Total RNA was extracted from 25 other tumor samples (12 cases of lymph node metastasis, 13 cases of non-metastasis) in the biobank of Stage-T1 LUAD using NcmZol Reagent (M5100; NCM Biotech, China), according to the manufacturer's protocol, and cDNA was synthesized using the Reverse Transcription Kit (R2020; US Everbright® Inc., China). For quantitative reverse transcriptase-polymerase chain reaction (qRT-PCR) analysis, PCR was performed using a reaction mixture containing a cDNA template, primers, and a Universal SYBR Green qPCR SuperMix (S2024; US Everbright® Inc.) in a Step One Plus Real-Time PCR System (Thermo Fisher Scientific). The primers for SPP1 were 5′-ACAGCCAGGACTCCATTGAC-3′ and 5′-GGGGACAACTGGAGTGAAAA-3′, and the primers for the lncRNA (AC037441) were 5′-TCACTGAGCAGGGTTCACAC-3′, and 5′-TCTTCACTGGCCTCCAAAAT-3′.

Immunohistochemical

Immunohistochemical (IHC) staining was performed in paraffin-embedded continuous tissue sections. Tissue sections were dewaxed and rehydrated with xylene and gradient alcohol washes, and antigen retrieval was then performed at 121°C for 1 min using pH 6.0 citrate buffer. Subsequently, sections were blocked with hydrogen peroxide for 20 min at room temperature and incubated with primary antibodies against CD68 (1:200; GB14043, Service bio, China), CD163 (1:500; GB113152, Service bio), inducible nitric oxide synthase (iNOS; 1:1,000; GB11119, Service bio), interleukin (IL)-1β (1:800; GB11113, Service bio), and SPP1 (1:100; A1499; Abcam, United Kingdom) overnight at 4°C. After incubation with the secondary antibody at room temperature for 1 h, immunostaining with DAB and counterstaining of the slide with hematoxylin, the entire stained sections were scanned and analyzed in a panoramic view. After scanning the entire sections with a tissue scanner, the Seville image analysis system was used to identify and calculate the total tissue area, the stained tissue area, and the staining intensity score (0 = no color; 1 = faint yellow; 2 = light brown; and 3 = dark brown) and the percentage of various staining intensity cells under the panoramic view. CD68 antibody was used as a marker for macrophages; iNOS-positive cells and IL-1β-positive cells were regarded as M1 macrophages; and CD163−positive

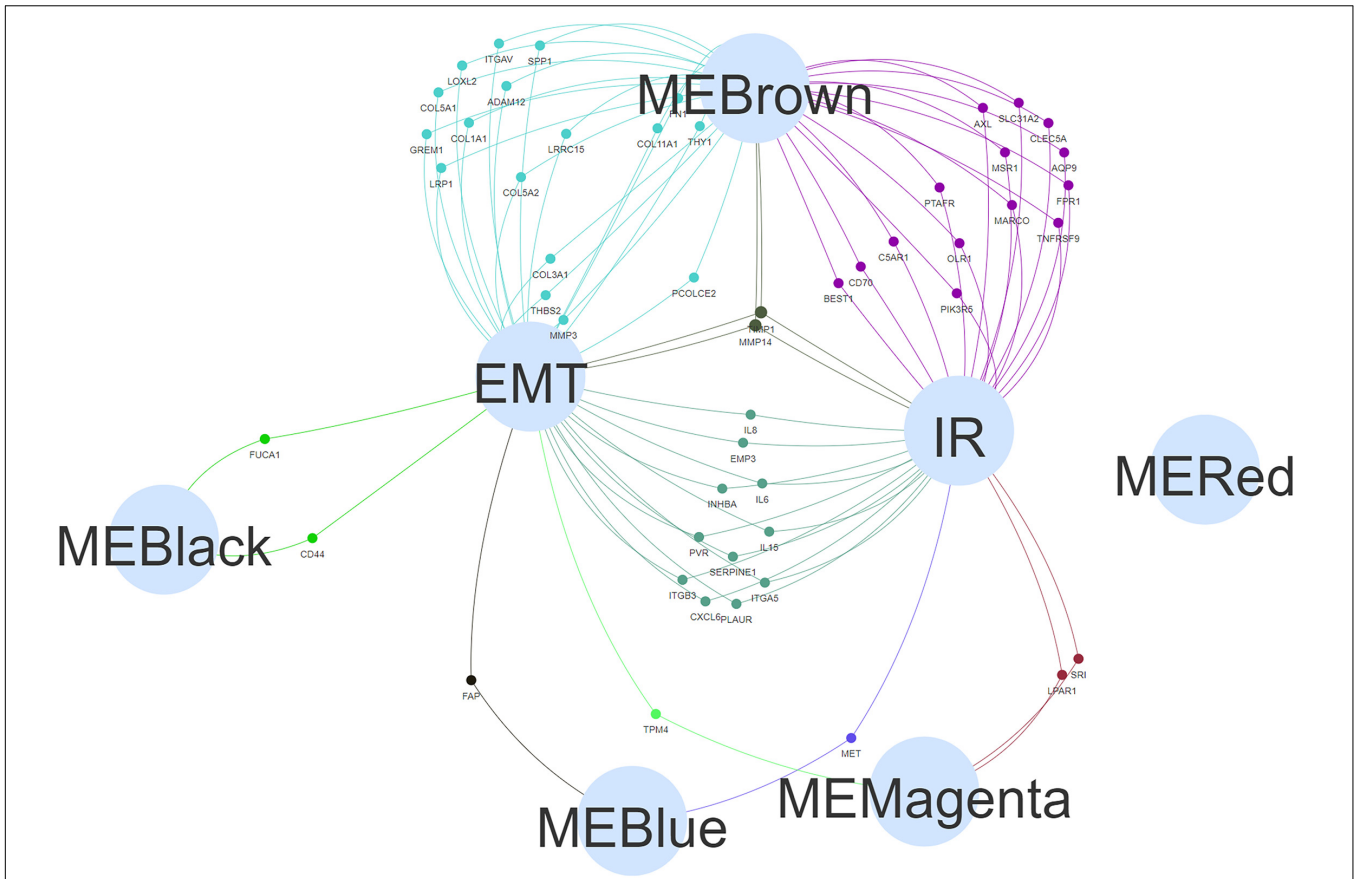

FIGURE 3 | The Venn diagram showing the intersection of five module genesets ("MEBrown," "MEBlack," "MERed," "MEBlue," and "MEMagenta") and hallmark genesets [epithelial–mesenchymal transition (EMT) and inflammatory response (IR)].

cells were regarded as M2 macrophages. In addition, the immunohistochemical staining of CD68/CD163/iNOS/IL-1β was quantified by measuring the positive area ratio (stained tissue area/total tissue area). SPP1 was quantified with a histochemistry score (H-score) to examine differences between samples from the early lymph node metastasis and non-metastasis groups [H-Score = Σ (percentage of staining intensity cells × staining intensity)].

Statistical Analysis

Statistical analyses were performed using R 4.0.3, GraphPad Prism 9.0, and SPSS 22.0. The expression levels of SPP1 and macrophage-related markers were compared between groups by an unpaired *t*-test. Survival analysis was performed using "survival" and "survminer" R packages. The Kaplan–Meier method was used to generate survival curves, and the log-rank test was used to determine significant differences in survival. The median values of SPP1 expression, M0 and M2 infiltration levels were set as the cut-off point for grouping. The correlation between SPP1 expression level and the abundance of immune cell infiltration was analyzed by Pearson's correlation test. The predictive performance of SPP1 detected in tissues and plasma for predicting early lymph node metastasis was evaluated using receiver operator characteristic (ROC) curves. $p < 0.05$ was considered significant.

RESULTS

M0 Macrophages Present a High Infiltration Level in Lung Adenocarcinoma Patients With Early Lymph Node Metastasis

First, based on the analysis of infiltration abundance among immune cells in the 16 cases of Stage-T1 LUAD tissues and the 15 cases of paired normal adjacent tissues, nine immune cell subtypes were found to have distinct infiltration levels (**Figure 1A**). The infiltration of plasma cells ($p < 0.01$), follicular helper T cells (FTH; $p < 0.01$), regulatory T cells (Tregs; $p < 0.001$), M1 macrophages ($p < 0.001$), and resting dendritic cells ($p < 0.05$) in tumor tissues was higher than that in normal lung tissues, whereas resting natural killer cells ($p < 0.01$), monocytes ($p < 0.01$), M0 macrophages ($p < 0.05$), and neutrophils ($p < 0.05$) had lower infiltration levels. These results suggested that the TIME presented a wide range of variability in early LUAD.

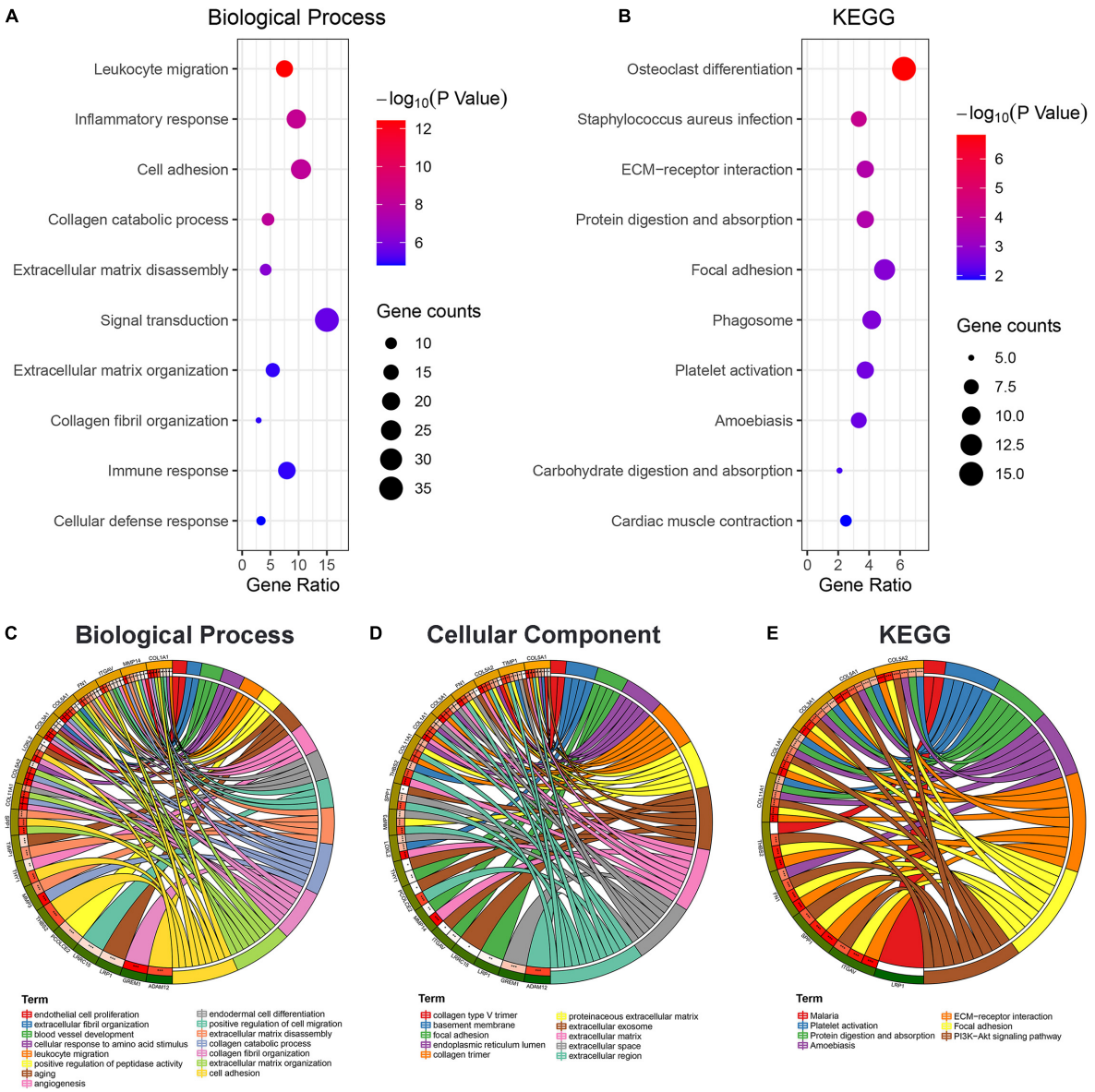

FIGURE 4 | Gene ontology (GO) and Kyoto Encyclopedia of Genes and Genomes (KEGG) enrichment analysis. The bubble diagram displayed the biological function **(A)** and KEGG **(B)** enrichment analysis results of the brown module genes. Biological function **(C)**, cellular component **(D)**, and KEGG **(E)** enrichment analysis was performed on 19 epithelial–mesenchymal transition (EMT)-related genes in the brown module, and the chord diagram was used to show the enriched GO/KEGG terms and statistical differences. $^{*}p < 0.05$, $^{**}p < 0.01$, and $^{***}p < 0.001$.

To identify the TIME characteristics associated with early lymph node metastasis in LUAD, the infiltration abundances of the nine immune cell subtypes were further analyzed in a TCGA cohort (n = 165) and a GSE68465 cohort (n = 149). M0 macrophages identified as highly infiltrated in the metastatic group (**Figure 1B**, $p < 0.05$), which was further validated in our cohort (n = 16, $p < 0.05$, **Figure 1C**) and the GSE43580 cohort (n = 20, $p < 0.01$, **Figure 1D**). Through the joint analysis of four independent cohorts, we demonstrated a correlation between M0 infiltration and early lymph node metastasis in LUAD.

Gene Set Enrichment Analysis and the Weighted Gene Co-expression Network Analysis Algorithm Identified Gene Sets Related to Lymph Node Metastasis and M0 Infiltration

To further explore the underlying mechanisms of M0 infiltration and early lymph node metastasis, GSEA was performed in our cohort, indicating that IR hallmarks were associated with early lymph node metastasis (**Figure 2A**), and the EMT pathway was significantly enriched in the M0 high-infiltration group

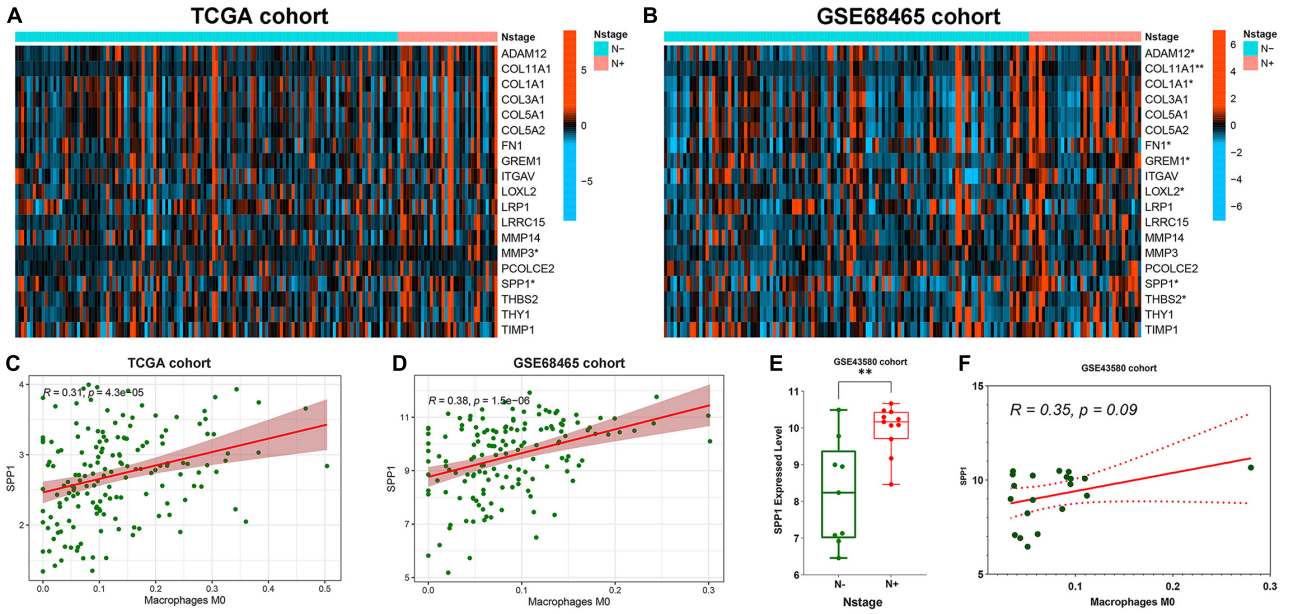

FIGURE 5 | Correlation analysis of secreted phosphoprotein 1 (SPP1) with early lymph node metastasis and macrophage infiltration in Stage-T1 lung adenocarcinoma (LUAD) patients from three external cohorts (TCGA, GSE68465 and GSE43580 cohorts). **(A)** SPP1 and matrix metalloprotease 3 (MMP3) were associated with N stages in the TCGA cohort. **(B)** thrombospondin 2 (THBS2), SPP1, lysyl oxidase like 2 (LOXL2), gremlin 1 (GREM1), fibronectin 1 (FN1), collagen type I alpha 1 chain (COL1A1), COL11A1, and ADAM metallopeptidase domain 12 (ADAM12) were associated with N stages in the GSE68465 cohort. TCGA cohort **(C)** and GSE68465 cohort **(D)** analysis verified that SPP1 was significantly positively correlated with M0 infiltration. In the GSE43580 cohort, SPP1 was highly expressed in the lymph node metastasis group **(E)**, and the correlation between SPP1 and M0 was also investigated **(F)**. $^{*}p < 0.05$, $^{**}p < 0.01$.

(**Figure 2B**). Moreover, the WGCNA algorithm was applied to construct an mRNA scale-free network, which resulted in the definition of 13 modules by average hierarchical clustering and dynamic tree clipping (**Figure 2C**). The black, blue, magenta, and red modules were negatively correlated with N stages and M0 infiltration, whereas the brown module showed a consistent positive correlation (**Figure 2D**).

Finally, a Venn diagram was constructed to investigate the intersections among the genes in the five modules and the genes identified as EMT and IR hallmarks (the hallmark gene sets were obtained from MSigDB). Compared with other modules, the brown module had more intersections with EMT and IR hallmarks and was selected for further analysis (**Figure 3**).

The Enrichment Analysis of the Selected Gene Suggests Cell Adhesion Plays a Key Role in Early Lymph Node Metastasis

The biological processes associated with genes in the brown module were primarily mapped to signal transduction, cell adhesion, inflammation, and immune response (**Figure 4A**). The KEGG enrichment analysis indicated the significant enrichment of focal adhesion and ECM-receptor interactions (**Figure 4B**). In addition, to further elucidate the potential regulatory mechanisms associated with the EMT during early lymph node metastasis, 19 EMT-related genes in the brown module were specifically selected for enrichment analysis. The results suggested that these 19 genes were primarily associated with cell adhesion and extracellular matrix organization (**Figure 4C**) and were enriched in the extracellular region (**Figure 4D**) and the phosphoinositide 3-kinase (PI3K)-AKT signaling pathway (**Figure 4E**). These clues indicated that the changes in cell adhesion might be key factors in early lymph node metastasis.

The Epithelial–Mesenchymal Transition Hallmark Gene Secreted Phosphoprotein 1 Is Associated With Early Lymph Node Metastasis and M0 Infiltration as Validated by Three External Cohorts

The association of 19 EMT-related genes with lymph node metastasis and M0 infiltration was further analyzed in three external cohorts. First, SPP1 was identified through the expression level analysis of 19 genes comparing the lymph node metastasis group with the non-metastatic group in both TCGA ($p < 0.05$, **Figure 5A**) and GSE68465 cohorts ($p < 0.05$, **Figure 5B**). Subsequently, the correlation between SPP1 expression and M0 infiltration was further verified in TCGA cases ($r = 0.31$, $p < 0.001$, **Figure 5C**) and the GSE68465 cohort ($r = 0.38$, $p < 0.001$, **Figure 5D**). In the GSE43580 cohort, SPP1 was highly expressed in the lymph node metastasis group ($p < 0.01$, **Figure 5E**), and the correlation between SPP1 and M0 was also analyzed ($r = 0.35$, $p = 0.09$, **Figure 5F**). Our results suggested that macrophage-related SPP1 expression may be a crucial risk indicator for early lymph node metastasis in LUAD.

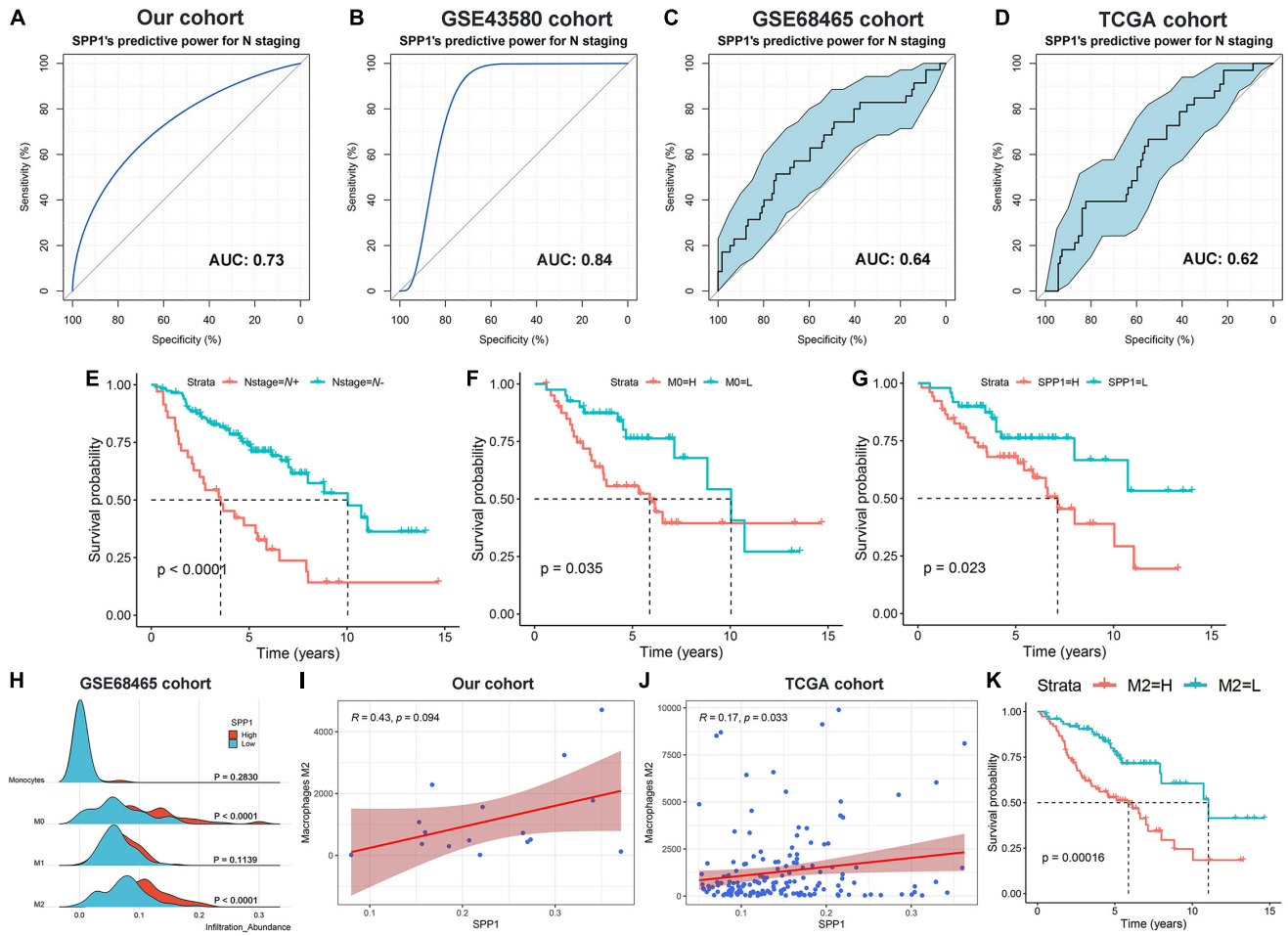

FIGURE 6 | Analysis of SPP1 for the prediction of lymph node metastasis and influence on the long-term survival of Stage-T1 LUAD patients. The receiver operating curve (ROC) and area under the curve (AUC) were used to evaluate the predictive power of SPP1 for early lymph node metastasis in our cohort [**(A)** n = 16], GSE43580 cohort [**(B)** n = 20], GSE68465 cohort [**(C)** n = 149] and TCGA cohort [**(D)** n = 165]. Kaplan–Meier curves of overall survival for patients with distinct N stages **(E),** M0 infiltration **(F),** and SPP1 expression **(G)**. **(H)** Multipeaked mountain map displaying the infiltration abundance divergence among the monophagocytic system (Monocytes, M0, M1, and M2) across groups with different levels of SPP1 expression in GSE68465 cohort. The correlation analysis of M2 infiltration and SPP1 expression in our cohort **(I)** and TCGA cohort **(J)**. **(K)** Kaplan–Meier curve to evaluate the influence of M2 infiltration on the OS in patients with Stage-T1 LUAD.

Secreted Phosphoprotein 1 Could Predicts Early Lymph Node Metastasis and Affects Prognosis in Stage-T1 Lung Adenocarcinoma Patients, Which May Be Related to the M2 Polarization

The predictive efficiency of SPP1 for early lymph node metastasis was evaluated in four cohorts. In our patient cohort (n = 16, **Figure 6A**) and the GSE43580 cohort (n = 20, **Figure 6B**), the area under the ROC curve (AUC) values were 0.73 and 0.84, respectively. The AUCs for the GSE68465 (n = 149, **Figure 6C**) and TCGA cohorts (n = 165, **Figure 6D**) were 0.64 (95% CI: 0.53–0.75) and 0.62 (95% CI: 0.52–0.72), respectively. In addition, using the survival data for the GSE68465 cohort, we demonstrated that early lymph node metastasis (p < 0.001, **Figure 6E**), higher M0 infiltration (p = 0.035, **Figure 6F**), and higher SPP1 expression (p = 0.023, **Figure 6G**) were significantly associated with the poor prognosis among patients with Stage-T1 LUAD.

The correlation between SPP1 and the monophagocytic system was systematically explored in early LUAD. In the GSE68465 cohort, the M0 and M2 infiltration abundances were significantly increased in the SPP1 high expression group (p < 0.001), whereas differences in monocyte (p = 0.283) and M1 infiltration (p = 0.114) were not significant between groups (**Figure 6H**). The correlation between SPP1 expression and M2 infiltration was verified using data from the cohorts from TCGA (r = 0.17, p = 0.033, **Figure 6I**) and our patients (r = 0.43, p = 0.094, **Figure 6J**). Patients with higher M2 infiltration had a shorter OS (p < 0.001, **Figure 6K**). Therefore, we speculated that SPP1 might induce the M2 polarization of macrophages in Stage-T1 LUAD, which could be closely related to the long-term survival of patients.

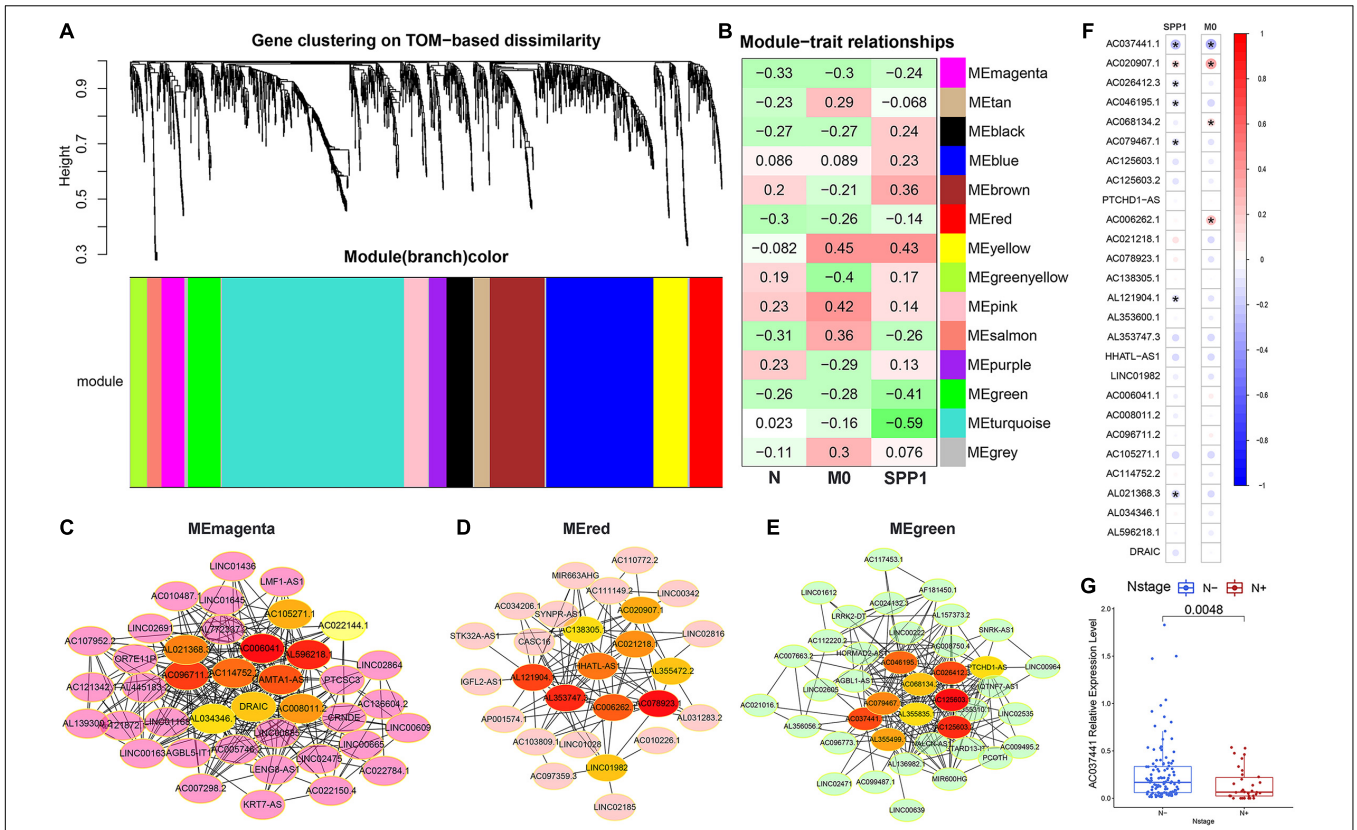

FIGURE 7 | Identification of long non-coding RNAs (lncRNAs) associated with early lymph node metastasis, SPP1 expression, and M0 infiltration. **(A)** Hierarchical clustering analysis was performed to determine the lncRNA co-expression modules represented by different colors. **(B)** The heatmap was used to demonstrate the correlation between the modules and lymph node metastasis, SPP1 expression, and M0 infiltration. **(C–E)** The top 10 hub lncRNAs and their first-level nodes of 3 key modules ("MEmagenta," "MEred," and "MEgreen") were identified through the maximal clique centrality (MCC) algorithm (the color of the hub nodes represented the hub level, red is the highest, and followed by orange). **(F)** The correlation analysis of 30 hub lncRNAs with SPP1 expression and M0 infiltration is based on TCGA dataset. **(G)** Expression level analysis of lncRNA (AC037441) between the lymph node metastasis group and the non-metastatic group in TCGA cohort. *$p < 0.05$.

The lncRNA AC037441 Is Associated With Early Lymph Node Metastasis, M0 Infiltration, and Secreted Phosphoprotein 1 Expression

To explore the potential lncRNA/SPP1-macrophage axis associated with early lymph node metastasis, the WGCNA algorithm was used to construct an lncRNA co-expression network based on our cohort. Thirteen modules were identified by subsequent hierarchical clustering and dynamic tree clipping (**Figure 7A**), among which the magenta, red and green modules showed consistent negative correlations with early lymph node metastasis, M0 infiltration, and SPP1 expression (**Figure 7B**). The maximal clique centrality (MCC) algorithm was used to determine hub lncRNAs for three modules (**Figures 7C–E**). In addition, further verification using TCGA cohort data identified that the hub lncRNA (AC037441) was significantly negatively correlated with SPP1 ($r = -0.27$, $p < 0.05$) and M0 infiltration ($R = -0.31$, $p < 0.05$; **Figure 7F**), and the expression level of AC037441 in the early lymph node metastasis group was significantly lower than that in the non-metastatic group ($p = 0.005$, **Figure 7G**). The analysis of the two cohorts revealed a potential RNA-immune cell axis (lncRNA AC037441/SPP1-macrophage) associated with early lymph node metastasis. However, further cell biological validation remains necessary.

Macrophage-Related Secreted Phosphoprotein 1Is a Biomarker for Early Lymph Node Metastasis, Validated in Tissue and Plasma Samples From Stage-T1 Lung Adenocarcinoma Patients

Following the bioinformatics analysis, the findings were verified using tissue and plasma samples from Stage-T1 LUAD patients. The qRT-PCR assay was performed on 25 cases of tumor tissues (12 cases of lymph node metastasis, 13 cases of non-metastasis), we confirmed the significantly increased expression of SPP1 (**Figure 8A**, $p < 0.05$) and the significantly decreased expression of lncRNA (AC037441) (**Figure 8B**, $p < 0.05$) in the lymph node metastasis group. The IHC analysis of 12 tumor samples (six cases of lymph node metastasis and six cases of non-metastasis) and nine paracancerous samples showed that SPP1 had lower H-scores in tumor tissues (**Figures 8C,D**, $p < 0.05$), and the H-score of the lymph node metastatic group was significantly

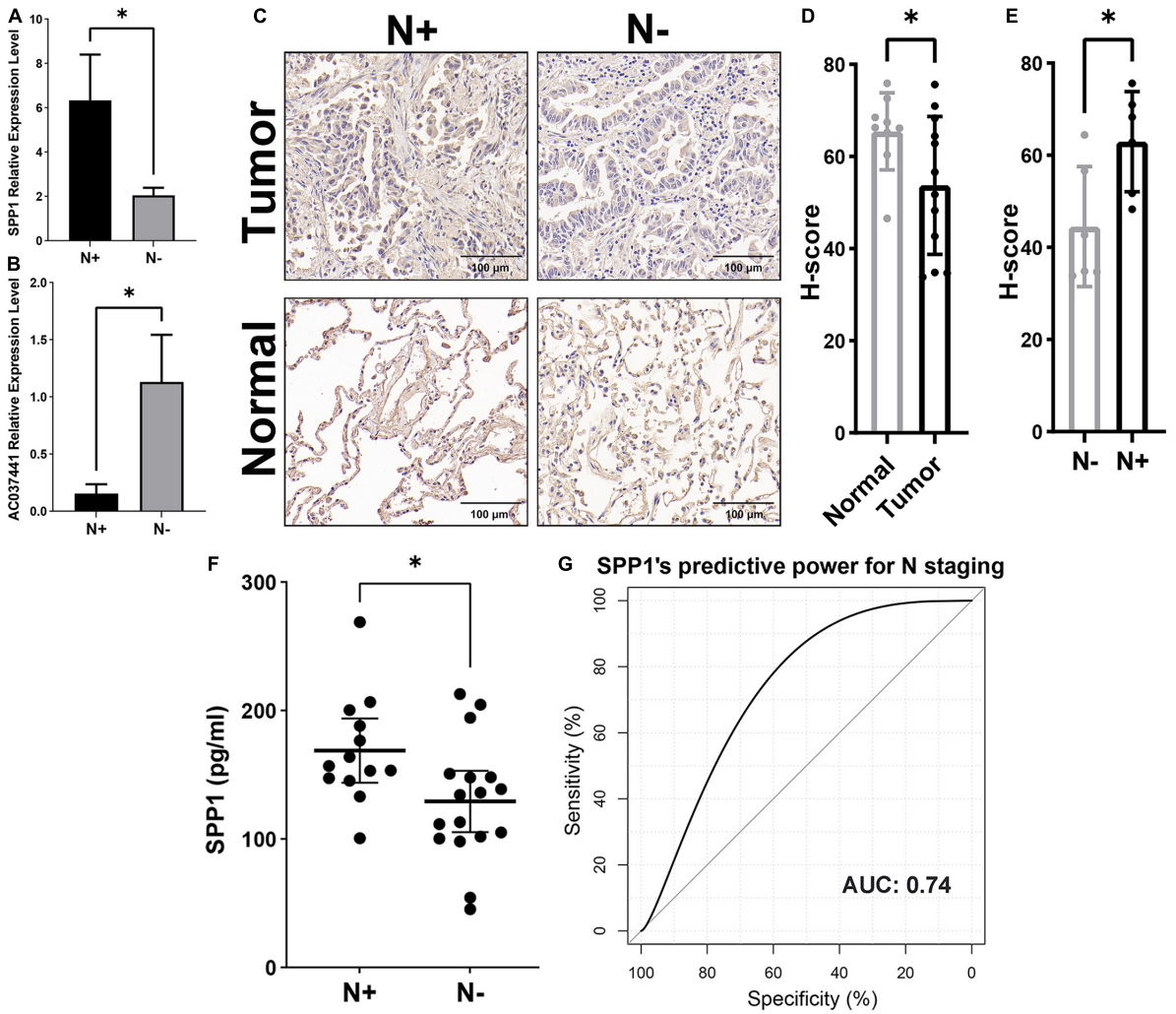

FIGURE 8 | Validation of SPP1 as a potential biomarker for early lymph node metastasis by quantitative reverse transcriptase-polymerase chain reaction (qRT-PCR), immunohistochemical (IHC), and enzyme-linked immunosorbent assay (ELISA) assays. The expression levels of SPP1 **(A)** and lncRNA (AC037441) **(B)** in tumor samples were compared by qRT-PCR in the lymph node metastasis group versus the non-metastatic group. **(C)** The representative IHC figures of SPP1 in Stage-T1 LUAD patients with and without lymph node metastasis. **(D)** The H-scores of SPP1 in tumor tissues (n = 12) were lower than that of adjacent normal tissues (n = 9). **(E)** The tumor sample scores distinction of SPP1 in the lymph node metastatic versus non-metastatic groups. **(F)** Comparison of the SPP1 concentration in the plasma of Stage-T1 LUAD patients between patients with lymph node metastasis and those without metastasis. **(G)** The receiver operating curve (ROC) and area under the curve (AUC) were used to evaluate the predictive efficiency of plasma SPP1 concentrations for early lymph node metastasis. *$p < 0.05$.

higher than that of the non-metastatic group (**Figures 8C,E**, $p < 0.05$). The SPP1 concentration in plasma was quantified by ELISA, which showed SPP1 concentrations in patients with lymph node metastasis were significantly higher than in the non-metastatic group (**Figure 8F**, $p < 0.05$), Moreover, the ROC curve showed that the plasma SPP1 level had good efficiency for predicting early lymph node metastasis (AUC = 0.74, **Figure 8G**).

Finally, the correlations between macrophages and lymph node metastasis and SPP1 expression were validated through the IHC analysis of tumor samples. The results showed that the positive area of macrophage marker (CD68) staining significantly increased in the lymph node metastasis group compared with the non-metastatic groups ($p < 0.05$), whereas the staining for M2 (CD163) and M1 markers (IL-1β and iNOS) showed no significant differences ($P > 0.05$; **Figure 9A**). In addition, the H-score of SPP1 was significantly positively correlated with the positive areas of CD68 staining ($r = 0.70$, $p = 0.016$) and CD163 staining ($r = 0.68$, $p = 0.021$); however, no significant correlation was observed for the positive areas of IL-1β staining ($r = 0.57$, $p = 0.070$) and iNOS staining ($r = 0.06$, $p = 0.851$; **Figure 9B**).

DISCUSSION

The TIME can regulate the growth and metastasis of lung cancer by promoting inflammation, angiogenesis, and immune modulation (Altorki et al., 2019; Bonanno et al., 2019; Rosenthal et al., 2019). In this study, we found that the infiltration of

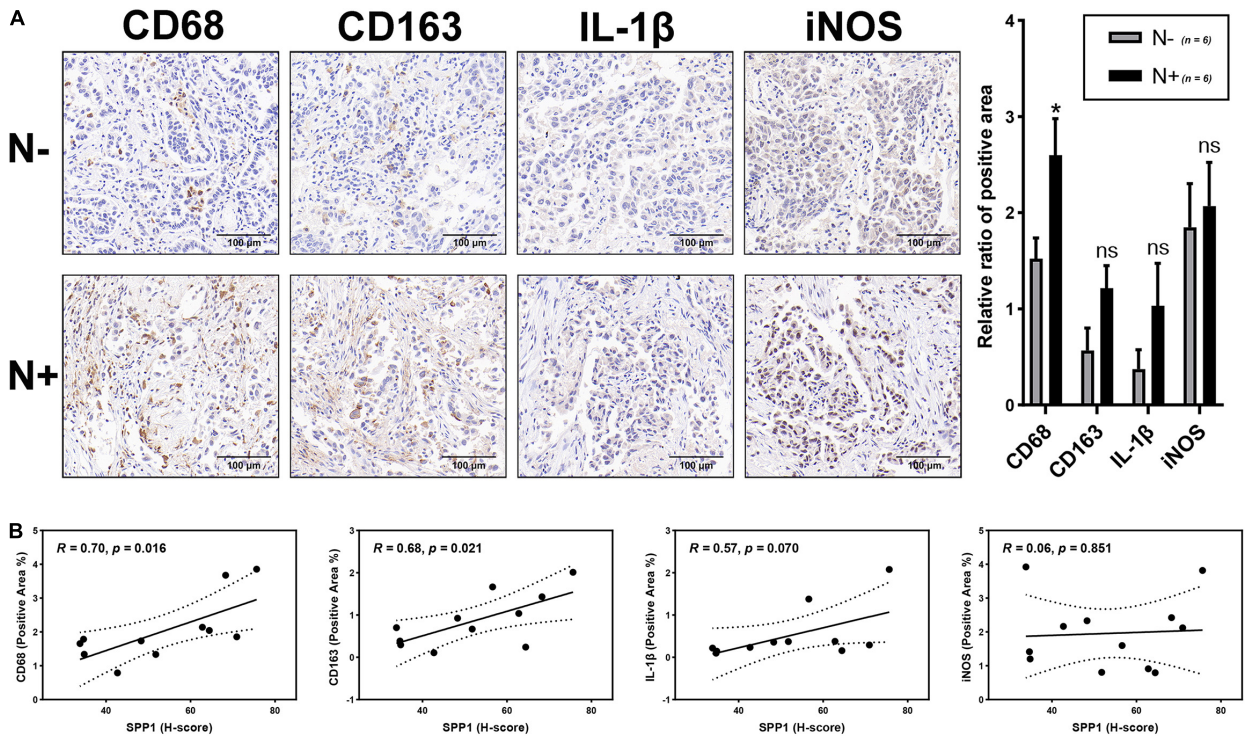

FIGURE 9 | Correlation analysis of macrophages with lymph node metastasis and SPP1 expression. **(A)** The representative figures of macrophage markers (CD68, CD163, IL-1β, and iNOS) staining in Stage-T1 LUAD samples and the comparison of positive area ratio in the lymph node metastatic and non-metastatic groups. **(B)** The H-score of SPP1 was significantly positively correlated with the positive area ratio of CD68 ($R = 0.70$, $p = 0.016$) and CD163 ($R = 0.68$, $p = 0.021$), while the correlation with the positive area ratio of IL-1β ($R = 0.57$, $p = 0.070$) and iNOS ($R = 0.06$, $p = 0.851$) was not statistically significant.*$p < 0.05$.

plasma cells, FTH, Tregs, M1 macrophages, and resting dendritic cells in LUAD tissues were higher than those in normal lung tissues, whereas resting natural killer cells, monocytes, M0 macrophages, and neutrophils had lower infiltration levels. Our results further demonstrated the diverse TIME in LUAD. In addition, the correlation between the TIME and lymph node metastasis has been reported. Coffelt et al. (2015) demonstrated that γδ T cell and neutrophil infiltration play important roles in the lymph node metastasis of breast cancer. However, the TIME changes that occur during LUAD lymph node metastasis have not been studied. We revealed a significant correlation between macrophages and lymph node metastasis through bioinformatics analysis and experimental verification. The role of macrophages in tumor metastasis has aroused broad concern, studies have indicated that macrophages can promote the metastasis of colorectal cancer cells by secreting miRNA-containing exosomes (Li et al., 2019) or cytokines, including IL-10 and IL-17 (Lan et al., 2019).

Notably, some LUAD patients develop lymph node metastasis when the diameter of the primary tumor remains very small. Early lymph node metastasis significantly affects the long-term survival of patients (Liu et al., 2019; Zhang et al., 2019a), and our study verified that stage-T1 patients with lymph node metastasis have a shorter OS. (Takada et al., 2020) demonstrated that early lymph node metastasis in breast cancer is related to tumor-infiltrating lymphocytes, whereas no relevant research has been published on early lymph node metastasis of lung cancer. In our study, GSEA showed that the IR pathway was significantly enriched in the metastasis group. IR plays an important role in tumorigenesis, progression, and metastasis (Diakos et al., 2014; Crusz and Balkwill, 2015). Moreover, the IR can also be modulated by pro-inflammatory cytokines and chemokines secreted by activated immune cells (Deng et al., 2010; Ferrari et al., 2019).

The EMT process can endow tumor cells with aggressiveness and mobility, which can be regarded as a sign of cancer metastasis (Lu and Kang, 2019) and poor prognosis (Fazilaty et al., 2019). We found that the EMT pathway was significantly enriched in the Stage-T1 LUAD patients with higher macrophage infiltration abundance. Wei C. et al. (2019) revealed that macrophages could secrete IL-6 to regulate the EMT program of colorectal cancer cells. Studies have also shown that EMT-related gene SPP1 is a potent macrophage chemokine, and SPP1 blockade can impair the macrophage recruitment ability of tumors (Wei J. et al., 2019). In this study, SPP1 was identified based on the exploration of the EMT hallmarks and macrophage-related genes in multiple cohorts, and was validated as a potential biomarker for early lymph node metastasis based on the tissue and plasma samples. In addition, SPP1 was shown to be significantly related to M2 macrophage infiltration in early LUAD, which was significantly associated with poor prognosis. Zhu et al. (2019) demonstrated that the number of tumor-associated macrophages

and the expression level of M2 markers decreased significantly in tumor tissues from SPP1 knockout mice compared with those from the control group, and the effect of SPP1 on the M2 phenotype maintenance (Wei J. et al., 2019) and M2 polarization (Zhang et al., 2017) had also been proved in many studies. Furthermore, the inhibition of SPP1 protein activation can prevent lung cancer metastasis by inactivating integrin/CD44-associated signaling and rearranging the actin cytoskeleton (Chiou et al., 2019). However, the correlation between SPP1 and tumor lymph node metastasis has not yet been investigated.

It has been well documented that M2 macrophages promote tumor growth and metastasis (Tao et al., 2020). On the other hand, many studies indicated tumor cells stimulate naive M0 macrophages to differentiate into M2 macrophages (Liu et al., 2021). Macrophages are mainly M2 subtypes in tumor microenvironment, especially in advanced stage of tumors. However, the characteristics of macrophage subsets remains unclear during the early stage of tumor metastasis. Interestingly, we found high M0 infiltration in LUAD with early lymph node metastasis. Our results suggest that more recruitment of naive M0 macrophages and subsequent M2 polarization in LUAD are likely a key determinant for early lymph node metastasis. Finally, a potential lncRNA (AC037441)/SPP1-macrophage axis was identified through the application of the WGCNA algorithm and correlation analysis, which has not been previously reported. Moreover, a significant correlation between lncRNA (AC037441) and early lymph node metastasis was further confirmed experimentally.

Some limitations must be addressed in this study. First, although a multi-cohort analysis and related experimental validation were conducted, the number of patients with Stage-T1 LUAD was relatively small, and more samples remain necessary for further verification. In addition, the relationship between SPP1 and macrophage infiltration was primarily based on correlation studies, and additional biological experiments remain necessary to explore the detailed underlying mechanism.

In summary, a correlation between macrophages and early lymph node metastasis in Stage-T1 LUAD was identified through a multi-cohort analysis and experimental validation. Patients with high macrophage infiltration were showed to present the significant enrichment of EMT pathway, and SPP1, an EMT hallmark gene, was identified to be significantly associated with macrophage infiltration and lymph node metastasis. In addition, the predictive efficacy of SPP1 detection in plasma for early lymph node metastasis was evaluated. Our study explored a potential mechanism for early lymph node metastasis in LUAD and identified and verified SPP1 as a potential biomarker.

DATA AVAILABILITY STATEMENT

Transcript sequencing data and clinical information for the 31 patient samples analyzed in this study can be found in the **Supplementary Material**. In addition, publicly available datasets were analyzed in this study, which can be found at TCGA (https://www.cancer.gov/about-nci/organization/ccg/research/structural-genomics/tcga) and GEO omnibus (https://www.ncbi.nlm.nih.gov/geo/) (GSE68465 and GSE43580).

ETHICS STATEMENT

The studies involving human participants were reviewed and approved by the institutional Ethics Committee of First Affiliated Hospital of Zhengzhou University. The patients/participants provided their written informed consent to participate in this study.

AUTHOR CONTRIBUTIONS

YQ and LH: conceptualization, writing—review and editing, and funding acquisition. BD: methodology. BD and CW: formal analysis and writing—original draft preparation. CW: data curation. YQ: supervision and project administration. All authors contributed to the article and approved the submitted version.

FUNDING

This research was funded by the Joint Construction Project of the Henan Medical Science and Technology Project, China (Grant No. LHGJ20190301) and the National Natural Science Foundation of China (Grant No. 81773045).

ACKNOWLEDGMENTS

The authors would like to thank for the TCGA and GEO databases for the availability of the data.

SUPPLEMENTARY MATERIAL

The Supplementary Material for this article can be found online at: https://www.frontiersin.org/articles/10.3389/fcell.2021.739358/full#supplementary-material

REFERENCES

Allemani, C., Matsuda, T., Di Carlo, V., Harewood, R., Matz, M., Nikšić, M., et al. (2018). Global surveillance of trends in cancer survival 2000-14 (CONCORD-3): analysis of individual records for 37 513 025 patients diagnosed with one of 18 cancers from 322 population-based registries in 71 countries. *Lancet* 391, 1023–1075. doi: 10.1016/s0140-6736(17)33326-3

Altorki, N. K., Markowitz, G. J., Gao, D., Port, J. L., Saxena, A., Stiles, B., et al. (2019). The lung microenvironment: an important regulator of tumour growth and metastasis. *Nat. Rev. Cancer* 19, 9–31. doi: 10.1038/s41568-018-0081-9

Bonanno, L., Zulato, E., Pavan, A., Attili, I., Pasello, G., Conte, P., et al. (2019). LKB1 and tumor metabolism: the interplay of immune and angiogenic microenvironment in lung cancer. *Int. J. Mol. Sci.* 20:1874. doi: 10.3390/ijms20081874

Bray, F., Ferlay, J., Soerjomataram, I., Siegel, R. L., Torre, L. A., and Jemal, A. (2018). Global cancer statistics 2018: GLOBOCAN estimates of incidence and mortality worldwide for 36 cancers in 185 countries. *CA Cancer J. Clin.* 68, 394–424. doi: 10.3322/caac.21492

Cassetta, L., and Pollard, J. W. (2018). Targeting macrophages: therapeutic approaches in cancer. *Nat. Rev. Drug Discov.* 17, 887–904. doi: 10.1038/nrd.2018.169

Chiou, J., Chang, Y. C., Tsai, H. F., Lin, Y. F., Huang, M. S., Yang, C. J., et al. (2019). Follistatin-like protein 1 inhibits lung cancer metastasis by preventing proteolytic activation of Osteopontin. *Cancer Res.* 79, 6113–6125. doi: 10.1158/0008-5472.Can-19-0842

Coffelt, S. B., Kersten, K., Doornebal, C. W., Weiden, J., Vrijland, K., Hau, C. S., et al. (2015). IL-17-producing γδ T cells and neutrophils conspire to promote breast cancer metastasis. *Nature* 522, 345–348. doi: 10.1038/nature14282

Crusz, S. M., and Balkwill, F. R. (2015). Inflammation and cancer: advances and new agents. *Nat. Rev. Clin. Oncol.* 12, 584–596. doi: 10.1038/nrclinonc.2015.105

Deng, L., Zhou, J. F., Sellers, R. S., Li, J. F., Nguyen, A. V., Wang, Y., et al. (2010). A novel mouse model of inflammatory bowel disease links mammalian target of rapamycin-dependent hyperproliferation of colonic epithelium to inflammation-associated tumorigenesis. *Am. J. Pathol.* 176, 952–967. doi: 10.2353/ajpath.2010.090622

Diakos, C. I., Charles, K. A., McMillan, D. C., and Clarke, S. J. (2014). Cancer-related inflammation and treatment effectiveness. *Lancet Oncol.* 15, e493–e503. doi: 10.1016/s1470-2045(14)70263-3

Fane, M., and Weeraratna, A. T. (2020). How the ageing microenvironment influences tumour progression. *Nat. Rev. Cancer* 20, 89–106. doi: 10.1038/s41568-019-0222-9

Fazilaty, H., Rago, L., Kass Youssef, K., Ocaña, O. H., Garcia-Asencio, F., Arcas, A., et al. (2019). A gene regulatory network to control EMT programs in development and disease. *Nat. Commun.* 10:5115. doi: 10.1038/s41467-019-13091-8

Ferrari, S. M., Fallahi, P., Galdiero, M. R., Ruffilli, I., Elia, G., Ragusa, F., et al. (2019). Immune and inflammatory cells in thyroid cancer microenvironment. *Int. J. Mol. Sci.* 20:4413.

Gentek, R., Molawi, K., and Sieweke, M. H. (2014). Tissue macrophage identity and self-renewal. *Immunol. Rev.* 262, 56–73. doi: 10.1111/imr.12224

Gu, Y., Liu, Y., Fu, L., Zhai, L., Zhu, J., Han, Y., et al. (2019). Tumor-educated B cells selectively promote breast cancer lymph node metastasis by HSPA4-targeting IgG. *Nat. Med.* 25, 312–322. doi: 10.1038/s41591-018-0309-y

Guan, Y., Du, Y., Wang, G., Gou, H., Xue, Y., Xu, J., et al. (2021). Overexpression of PLXDC2 in stromal cell-associated M2 macrophages is related to EMT and the progression of gastric cancer. *Front. Cell Dev. Biol.* 9:673295. doi: 10.3389/fcell.2021.673295

Guo, Z., Huang, J., Wang, Y., Liu, X. P., Li, W., Yao, J., et al. (2020). Analysis of expression and its clinical significance of the secreted phosphoprotein 1 in lung Adenocarcinoma. *Front. Genet.* 11:547. doi: 10.3389/fgene.2020.00547

He, Y., Liu, R., Yang, M., Bi, W., Zhou, L., Zhang, S., et al. (2021). Identification of VWF as a novel biomarker in lung adenocarcinoma by comprehensive analysis. *Front. Oncol.* 11:639600. doi: 10.3389/fonc.2021.639600

Lan, J., Sun, L., Xu, F., Liu, L., Hu, F., Song, D., et al. (2019). M2 macrophage-derived exosomes promote cell migration and invasion in colon cancer. *Cancer Res.* 79, 146–158. doi: 10.1158/0008-5472.Can-18-0014

Langfelder, P., and Horvath, S. (2008). WGCNA: an R package for weighted correlation network analysis. *BMC Bioinformatics* 9:559. doi: 10.1186/1471-2105-9-559

Lavin, Y., Kobayashi, S., Leader, A., Amir, E. D., Elefant, N., Bigenwald, C., et al. (2017). Innate immune landscape in early lung adenocarcinoma by paired single-cell analyses. *Cell* 169, 750–765.e7. doi: 10.1016/j.cell.2017.04.014

Li, R., Zhou, R., Wang, H., Li, W., Pan, M., Yao, X., et al. (2019). Gut microbiota-stimulated cathepsin K secretion mediates TLR4-dependent M2 macrophage polarization and promotes tumor metastasis in colorectal cancer. *Cell Death Differ.* 26, 2447–2463. doi: 10.1038/s41418-019-0312-y

Li, X., Yang, N., Cheng, Q., Zhang, H., Liu, F., and Shang, Y. (2021). MiR-21-5p in macrophage-derived exosomes targets Smad7 to promote epithelial mesenchymal transition of airway epithelial cells. *J. Asthma Allergy* 14, 513–524. doi: 10.2147/jaa.S307165

Liu, J., Luo, R., Wang, J., Luan, X., Wu, D., Chen, H., et al. (2021). Tumor cell-derived exosomal miR-770 inhibits M2 macrophage polarization via targeting MAP3K1 to inhibit the invasion of non-small cell lung cancer cells. *Front. Cell Dev. Biol.* 9:679658. doi: 10.3389/fcell.2021.679658

Liu, Z., Liang, H., Lin, J., Cai, X., Pan, Z., Liu, J., et al. (2019). The incidence of lymph node metastasis in patients with different oncogenic driver mutations among T1 non-small-cell lung cancer. *Lung Cancer* 134, 218–224. doi: 10.1016/j.lungcan.2019.06.026

Lu, W., and Kang, Y. (2019). Epithelial-mesenchymal plasticity in cancer progression and metastasis. *Dev. Cell* 49, 361–374. doi: 10.1016/j.devcel.2019.04.010

Martinez-Zayas, G., Almeida, F. A., Yarmus, L., Steinfort, D., Lazarus, D. R., Simoff, M. J., et al. (2021). Predicting lymph node metastasis in non-small cell lung cancer: prospective external and temporal validation of the HAL and HOMER models. *Chest* 160, 1108–1120. doi: 10.1016/j.chest.2021.04.048

Newman, A. M., Liu, C. L., Green, M. R., Gentles, A. J., Feng, W., Xu, Y., et al. (2015). Robust enumeration of cell subsets from tissue expression profiles. *Nat. Methods* 12, 453–457. doi: 10.1038/nmeth.3337

Otto, L., Rahn, S., Daunke, T., Walter, F., Winter, E., Möller, J. L., et al. (2021). Initiation of pancreatic cancer: the interplay of hyperglycemia and macrophages promotes the acquisition of malignancy-associated properties in pancreatic ductal epithelial cells. *Int. J. Mol. Sci.* 22:5086. doi: 10.3390/ijms22105086

Qian, B. Z., and Pollard, J. W. (2010). Macrophage diversity enhances tumor progression and metastasis. *Cell* 141, 39–51. doi: 10.1016/j.cell.2010.03.014

Ramos-Paradas, J., Hernández-Prieto, S., Lora, D., Sanchez, E., Rosado, A., Caniego-Casas, T., et al. (2021). Tumor mutational burden assessment in non-small-cell lung cancer samples: results from the TMB(2) harmonization project comparing three NGS panels. *J. Immunother. Cancer* 9:e001904. doi: 10.1136/jitc-2020-001904

Rosenthal, R., Cadieux, E. L., Salgado, R., Bakir, M. A., Moore, D. A., Hiley, C. T., et al. (2019). Neoantigen-directed immune escape in lung cancer evolution. *Nature* 567, 479–485. doi: 10.1038/s41586-019-1032-7

Sautès-Fridman, C., Petitprez, F., Calderaro, J., and Fridman, W. H. (2019). Tertiary lymphoid structures in the era of cancer immunotherapy. *Nat. Rev. Cancer* 19, 307–325. doi: 10.1038/s41568-019-0144-6

Subramanian, A., Tamayo, P., Mootha, V. K., Mukherjee, S., Ebert, B. L., Gillette, M. A., et al. (2005). Gene set enrichment analysis: a knowledge-based approach for interpreting genome-wide expression profiles. *Proc. Natl. Acad. Sci. U. S. A.* 102, 15545–15550. doi: 10.1073/pnas.0506580102

Takada, K., Kashiwagi, S., Asano, Y., Goto, W., Kouhashi, R., Yabumoto, A., et al. (2020). Prediction of lymph node metastasis by tumor-infiltrating lymphocytes in T1 breast cancer. *BMC Cancer* 20:598. doi: 10.1186/s12885-020-07101-y

Tao, S., Chen, Q., Lin, C., and Dong, H. (2020). Linc00514 promotes breast cancer metastasis and M2 polarization of tumor-associated macrophages via Jagged1-mediated notch signaling pathway. *J. Exp. Clin. Cancer Res.* 39:191. doi: 10.1186/s13046-020-01676-x

Wang, X. J., Gao, J., Wang, Z., and Yu, Q. (2021). Identification of a potentially functional microRNA-mRNA regulatory network in lung adenocarcinoma using a bioinformatics analysis. *Front. Cell Dev. Biol.* 9:641840. doi: 10.3389/fcell.2021.641840

Wei, C., Yang, C., Wang, S., Shi, D., Zhang, C., Lin, X., et al. (2019). Crosstalk between cancer cells and tumor associated macrophages is required for mesenchymal circulating tumor cell-mediated colorectal cancer metastasis. *Mol. Cancer* 18:64. doi: 10.1186/s12943-019-0976-4

Wei, J., Marisetty, A., Schrand, B., Gabrusiewicz, K., Hashimoto, Y., Ott, M., et al. (2019). Osteopontin mediates glioblastoma-associated macrophage infiltration and is a potential therapeutic target. *J. Clin. Invest.* 129, 137–149. doi: 10.1172/jci121266

Wei, T., Bi, G., Bian, Y., Ruan, S., Yuan, G., Xie, H., et al. (2020). The significance of secreted phosphoprotein 1 in multiple human cancers. *Front. Mol. Biosci.* 7:565383. doi: 10.3389/fmolb.2020.565383

Wu, K., Lin, K., Li, X., Yuan, X., Xu, P., Ni, P., et al. (2020). Redefining tumor-associated macrophage subpopulations and functions in the tumor microenvironment. *Front. Immunol.* 11:1731. doi: 10.3389/fimmu.2020.01731

Yi, M., Li, A., Zhou, L., Chu, Q., Luo, S., and Wu, K. (2021). Immune signature-based risk stratification and prediction of immune checkpoint inhibitor's efficacy for lung adenocarcinoma. *Cancer Immunol. Immunother.* 70, 1705–1719. doi: 10.1007/s00262-020-02817-z

Zhang, C., Zhang, J., Xu, F. P., Wang, Y. G., Xie, Z., Su, J., et al. (2019b). Genomic landscape and immune microenvironment features of preinvasive and early invasive lung adenocarcinoma. *J. Thorac. Oncol.* 14, 1912–1923. doi: 10.1016/j.jtho.2019.07.031

Zhang, C., Pang, G., Ma, C., Wu, J., Wang, P., and Wang, K. (2019a). Preoperative risk assessment of lymph node metastasis in cT1 lung cancer: a retrospective study from Eastern China. *J. Immunol. Res.* 2019:6263249. doi: 10.1155/2019/6263249

Zhang, Y., Du, W., Chen, Z., and Xiang, C. (2017). Upregulation of PD-L1 by SPP1 mediates macrophage polarization and facilitates immune escape in lung adenocarcinoma. *Exp. Cell Res.* 359, 449–457. doi: 10.1016/j.yexcr.2017.08.028

Zheng, Y., Tian, H., Zhou, Z., Xiao, C., Liu, H., Liu, Y., et al. (2021). A novel immune-related prognostic model for response to immunotherapy and survival in patients with lung adenocarcinoma. *Front. Cell Dev. Biol.* 9:651406. doi: 10.3389/fcell.2021.651406

Zhu, Y., Yang, J., Xu, D., Gao, X. M., Zhang, Z., Hsu, J. L., et al. (2019). Disruption of tumour-associated macrophage trafficking by the osteopontin-induced colony-stimulating factor-1 signalling sensitises hepatocellular carcinoma to anti-PD-L1 blockade. *Gut* 68, 1653–1666. doi: 10.1136/gutjnl-2019-318419

Conflict of Interest: The authors declare that the research was conducted in the absence of any commercial or financial relationships that could be construed as a potential conflict of interest.

Publisher's Note: All claims expressed in this article are solely those of the authors and do not necessarily represent those of their affiliated organizations, or those of the publisher, the editors and the reviewers. Any product that may be evaluated in this article, or claim that may be made by its manufacturer, is not guaranteed or endorsed by the publisher.

frontiers in Oncology

CASE REPORT
published: 18 October 2021
doi: 10.3389/fonc.2021.729151

Case Report: Targeted Therapy for Metastatic Solid Pseudopapillary Neoplasm of the Pancreas With *CTNNB1* and *PTEN* Mutations

Xinbo Wang[1], Daojun Zhu[1], Wei Bao[2], Min Li[1], Sizhen Wang[1] and Rongxi Shen[1]*

[1] Research Institute of General Surgery, Jinling Hospital, Nanjing University Medical School, Nanjing, China, [2] Department of Clinical Pathology, Jinling Hospital, Nanjing University Medical School, Nanjing, China

Background: Solid pseudopapillary neoplasm (SPN) of the pancreas shows an indolent clinical behavior in cases undergoing surgical resection. The efficacy of combination therapy in the metastatic extrapancreatic SPN treatment remains largely unknown and a clinical challenge.

Case Presentation: We report a case of a metastatic pancreatic SPN in a 45-year-old woman who presented with an aggressive peritoneal dissemination and hepatic metastases and still showed an indolent clinical course with combination therapy with repeated surgery and targeted therapy. Although the follow-up effect remains to be seen, this is the first report of practical experience of the targeted agents sunitinib and everolimus in metastatic SPN tumors based on the mutation status of *PTEN* (c.379G>A; p.G127R) and *CTNNB1* (c.98C>G; p.S33C). To our knowledge, the *PTEN* variant identified in this case has not been previously reported in SPN.

Conclusion: Evidence on variant genetics indicates that future molecular studies may not only help to explain the mechanism of SPN occurrence and development but are also more likely to direct to future precision treatments.

Keywords: targeted therapy, solid pseudopapillary neoplasm (SPN), metastasis, everolimus, sunitinib, pancreas

OPEN ACCESS

Edited by:
Qiangzhe Zhang,
Nankai University, China

Reviewed by:
Anca Maria Cimpean,
Victor Babes University of Medicine and Pharmacy, Romania
Qiuyu Liu,
Henan Provincial People's Hospital, China

****Correspondence:***
Xinbo Wang
wxinbo2008@163.com

Specialty section:
This article was submitted to Molecular and Cellular Oncology, a section of the journal Frontiers in Oncology

Received: *22 June 2021*
Accepted: *04 October 2021*
Published: *18 October 2021*

Citation:
Wang X, Zhu D, Bao W, Li M, Wang S and Shen R (2021) Case Report: Targeted Therapy for Metastatic Solid Pseudopapillary Neoplasm of the Pancreas With CTNNB1 and PTEN Mutations. Front. Oncol. 11:729151. doi: 10.3389/fonc.2021.729151

INTRODUCTION

Solid pseudopapillary neoplasm (SPN) of the pancreas is a rare low-grade malignant neoplasm that usually occurs in young women. SPN has an indolent clinical behavior even for cases of large tumor size, and long-term prognosis following surgical resection is generally excellent for both localized and distant disease (1). Patients with SPN occasionally present with liver metastasis or invasion into adjacent organs, relapse immediately after surgery, or cannot undergo surgical resection (2). Combination therapy could help stave off this particularly refractory SPN that arises in response to aggressive surgery. An important support for multidisciplinary comprehensive treatment strategy may be rooted in recent research on cytogenetic analyses and specific molecular pathways of SPN (3, 4).

To the best of our knowledge, the therapeutic value of targeted therapy compared with surgery and adjuvant therapy, as well as their combination, has never been evaluated in patients with metastatic SPN of the pancreas. In this study, we first report a metastatic pancreatic SPN case that presented with refractory peritoneal dissemination and hepatic metastases and maintained stable disease by the targeted agents sunitinib and everolimus based on the mutation status of *PTEN* and *CTNNB1*.

CASE PRESENTATION

The patient was a 45-year-old woman who received a distal pancreatectomy with splenectomy for a huge mass, encapsulated solid mass with cystic components (measuring 100 × 70 mm) in the body and tail of the pancreas in the local hospital on March 10, 2010. The histologic examination established the presumptive diagnosis of a well differentiated pancreatic neuroendocrine tumor (pNET). Immunohistochemical analysis showed positive staining for synaptophysin (Syn) and negative for cytokeratin (CK), and chromogranin A (CgA). No adjuvant therapy was administered. Metastasectomy of the lesions (maximum size of 50 × 40 cm) in her pancreatic remnant and adjacent peritoneum was performed with lymph node dissection on March 3, 2014. The revised diagnosis was metastases of low-grade pNET accompanied with SPN immunophenotype. The specimen was positive for Syn, CD56, vimentin, progesterone receptor (PR), and β-catenin immunostaining, whereas negative for CgA. The second metastasectomy was performed to remove recurrent nodules of the left adrenal gland (maximum size of 20 × 15 cm) on January 8, 2015 (**Figure 1**).

During the next 10 months the patient suffered some additional metastatic recurrences (maximum size of 55 × 35 cm) in her left adrenal gland and peritoneum (**Figure 1A**) before her first visit to our hospital on November 17, 2015. The patient participated in a nation-wide clinical study, approved by our hospital's Ethics Committee, to evaluate the efficacy and safety of sunitinib in the treatment of metastatic pNET in January, 2016. Meanwhile, the pathological features of the tumors from the first three operations were carefully reviewed in the glass slides and paraffin blocks by our own pathologists. All of the tumors were composed of relatively monomorphic polyhedral cells with hyalinized fibrovascular cores. Neoplastic cells were discohesive with round to oval nuclei. Mitotic figures were rare. The growth pattern of the tumor was heterogeneous, with a combination of solid and pseudocystic structures in varying proportions, even in the primary tumor. Sparse vascular invasion was found in the primary tumor with Ki67 index <1%. Immunohistochemical analysis including CD-56, PR, CD10, E-cadherin, and β-catenin was re-performed in the primary and recurrent tumors. All of the tumors were immunopositive for β-catenin (nuclei), CD10, vimentin, PR and Syn and immunonegative for E-cadherin. According to recently published data, a particular dot-like paranuclei expression of CD99 appears to be highly unique for SPN, and this distinctive staining pattern was present in this case. Even in the primary tumor, CD99 expression was punctate and granular positive in the cytoplasm (3+). CD99 accompanied by β-catenin definitely established the diagnosis of SPN in the case (5). The patient was finally diagnosed with a metastatic pancreatic SPN with low-grade malignant potential. She rejected the reoperation for fear of harm from multiple surgeries. According to RECIST 1.1 (response evaluation criteria in solid tumors), the patient's abdominal metastatic tumors were in a stable state, and given that patients did not have any severe comorbidities while taking sunitinib, the patient continued targeted therapy during the following 2 years.

In the first quarter of 2018, the patient presented with some new metastatic lesions in the peritoneum, pelvis, and retroperitoneum, and the earlier lesions increased in size significantly (**Figure 1B**). To obtain the evolutionary features of the tumor immune phenotype, metastasectomy of the biggest peritoneal lesion (maximum size of 75 × 55 cm) was performed on April 18, 2018. The pathological analysis confirmed the metastatic nature of the SPN as capsular with very few capsular and vascular invasions (**Figure 2**). Grossly, the cross-section of the peritoneal metastatic tumor revealed a round, well demarcated mass measuring 75 × 50 mm that consisted of a mixed component containing focal hemorrhage. The tumor showed nested-to-diffuse growth of more poorly cohesive monomorphic cells with scattered nuclear atypia and

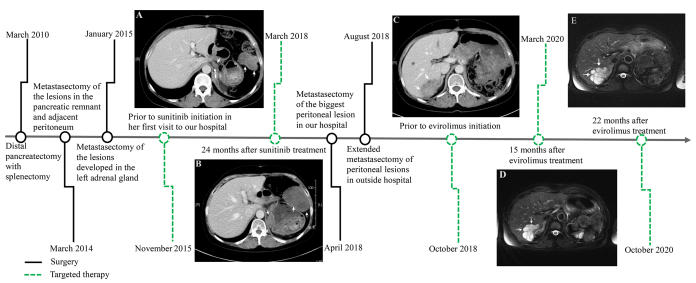

FIGURE 1 | Time axis of repeated surgery and targeted therapy for the metastatic pancreatic solid pseudopapillary neoplasm. Computed tomography scan showing multiple tumors in the peritoneum and retroperitoneum (white arrow) prior to sunitinib treatment after repeated surgery **(A)**. Tumors rapidly increased in size 24 months after sunitinib treatment **(B)**. There was a 52×36 mm, well-defined mass with heterogeneous contrast enhancement in the right lobe of the liver (white arrow) prior to evirolimus treatment after extended metastasectomy **(C)**, which maintained tumor volume stability 15 months **(D)** and 22 months **(E)** after evirolimus treatment.

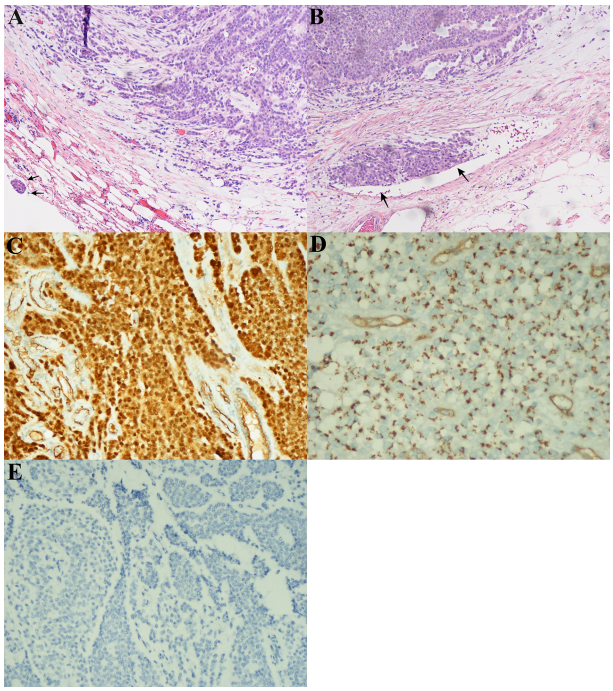

FIGURE 2 | Microscopic and immunohistochemical findings in peritoneal lesions of the metastatic solid-pseudopapillary neoplasms (SPN). **(A)**, The tumor had a heterogeneous growth with predominantly pseudopapillary pattern (hematoxylin-eosin, original magnification ×200). Note the capsular invasion (black arrow). **(B)**, Vascular invasion (black arrow). **(C)**, Nuclear positivity for β–catenin. **(D)**, Dot-like paranuclei positivity for CD99. **(E)**, Negative for chromogranin A (CgA) expression in immuonstaining.

fibrovascular stalks in which mitosis was sparse with the Ki-67 index 5-10%. The cytologic features also included characteristic myxoid clear material surrounding the papillae, the presence of cercariform cells and sparse mitotic figure. Regional cystic degeneration and haemorrhage were observed. Focal solid areas extended towards the surrounding fat tissue with prominent capsular and vascular invasion. No significant nuclear atypia, abundant necrosis, or high mitotic rate was found. The lesion showed typical immunohistochemical features for SPN, such as nuclear expression of β-catenin, paranuclei dot-like expression of CD-99, positive findings for CD10 (focal region, 3+), vimentin and PR. Interestingly, Syn was positive as always from the primary to the recurrent tumors. On the presumption of disseminated peritoneal metastasis, an extended metastasectomy was performed to remove the left kidney, left adrenal gland, partial diaphragm muscle, small liver nodules, several peritoneal nodules, and pelvic nodules in an outside hospital on August 21, 2018.

Two months postoperatively, the patient presented with a new metastatic lesion in the right hepatic lobe. She was admitted to our hospital again. Computed tomography (CT) scan revealed a well-defined hepatic encapsulated solid mass with cystic components but no calcification (maximum size of 52 × 36 cm, **Figure 1C**). Genomic DNA was isolated from formalin-fixed paraffin-embedded (FFPE) tissue for next-generation sequencing (NGS) by llumina Genome Analyzer. The patient was positive for *CTNNB1* c.98C>G (p.S33C), *ATM* c.5633C>T (p.S1878L), and *PTEN* c.379G>A (p.G127R) point mutations with a germline mutation in *FANCD2* c.888+1G>T. On December 28, 2018, the patient started treatment with everolimus for targeting *PTEN* mutations. Assessment of response was performed by means of computed tomography (CT) scan or magnetic resonance imaging (MRI), every 12 weeks of therapy, according to RECIST criteria 1.1. At present, the patient does not seem to have any serious discomfort except for grade 1 cutaneous vasculitis. She is well, and without any signs of disease progression. The serial follow-up magnetic resonance imaging examination on March 2020 (**Figure 1D**) and October 2020 (**Figure 1E**) showed that the patient's tumor had partially resolved and remained stable for more than 22 months after the targeted treatment of everolimus.

It was also noted that the tumor immune phenotype might have a certain degree of evolutionary characteristics over time (**Table 1**). In accordance with the immunohistochemical changes, we subdivided the lesions into early (first to third operations) and late (forth to fifth) lesions. In the early metastatic lesions, the tumors had almost no capsular or vascular invasion with weakly positive immunostaining of β-catenin (nuclei, +). The Ki-67 labeling index was also very low (<1%). In the late lesions, malignant histological features, such as peritumoral infiltration into the fat tissue (from the fourth lesion) and the organ, prominent capsular and vascular invasion were observed (**Figures 2A, B**). The specimen was strongly positive for immunostaining of β-catenin

TABLE 1 | Evolutionary characteristics of clinicopathological data of the tumor.

Operation No.	Recurrence interval (mo)	Site	Capsular invasion	vascular invasion	perineural invasion	β-catenin (nuclei)	Syn	paranuclei dot-like expression CD-99	PR	Ki-67 labeling index (%)
1■	0	Pancreas	N	Sparsely	N	+	+	+/-	Sparsely +	<1
2	48	Pancreas Peritoneum	N	Y	N	+	+	NE	NE	<1
3	58	Left adrenal gland	N	N	N	+	+	NE	+	3
4	97	Peritoneum Grater Omentum Retroperitoneum	Y	Y	N	+++	++ +	+++	+	5-10
5	101	Peritoneum Grater Omentum Left adrenal gland Retroperitoneum Pelvis Liver	Y	Y	N	++	+	+	+	15

■ *pathological performance amended by our own pathologist.*
NE, not evaluable; N, absent; Y, present; Syn, Synaptophysin; PR, progesterone receptor.
+, local expression; ++, moderate expression; +++, diffusively strong expression; +/-, sparse expression.

(nuclei, +++, **Figure 2C**). Furthermore, the average Ki-67 labeling index increased sharply (3%, 5–10%, and 15% in the third, fourth, and fifth metastatic lesions, respectively).

DISCUSSION

As there are no specific staging or grading systems for the malignancy of SPN, predicting its metastatic potential is difficult. The evolutionary characteristics of the tumor immune phenotype in this case might explain the aggressive behavior of this tumor. Consistent to our finding, Walter et al. (6) also found that the Ki-67 proliferation index was 2% in the primary tumor of SPN, 10% in ovarian lesions, and 20% in liver metastases. However, investigating the cause of the genetic variation of SPN may have enabled us to describe the metastatic potential molecular pathways involved in this disease (7). Compelling evidences now demonstrate that differences in the molecular pathology, of otherwise indistinguishable cancers, substantially impact the clinical characteristics of the disease (3). The somatic *ATM* gene mutation (c.5633C>T; p.S1878L) in this patient is a variant of unknown significance (VUS) in ClinVar (8) and thus ineligible for treatment. The germline FANCD2 mutation (c.888+1G>T) is also irrelevant, as the mutation that we found is not registered in common data bases such as LOVD3 (9) and thus it might be considered at best as a variant of undetermined significance. In fact, there are currently no US Food and Drug Administration- (FDA)-approved antitumor drugs or related drug-sensitivity studies for the *ATM* gene mutation and germline mutation in *FANCD2* identified in this patient. We focus on the other 2 significant mutations CTNNB1 (p.S33C) and PTEN (q.G127R).

Activating somatic mutations in the β-catenin gene (*CTNNB1* coding) on chromosome 3p occur in almost 100% of SPNs (10), where CTNNB1 mutations disrupt the phosphorylation and degradation of the β-catenin protein. All are missense mutations leading to loss of binding sites for glycogen synthase kinase-3beta (GSK-3b) phosphorylation, thereby interfering with degradation of the β-catenin protein (5). These mutations lead to cytoplasmic and nuclear accumulation of β-catenin in most SPNs. Deregulation of the pathway is closely linked to various aspects of human carcinogenesis such as cell viability, regulation of cell cycle, epithelial-mesenchymal transition, and maintenance of stemness. Consequently, a genetic program is switched on, leading to the uncontrolled growth, prolonged survival, and acquisition of mesenchymal phenotype (11, 12). A possible pathogenetic mechanism involving the interaction between β-catenin and the activation of cell proliferation machinery may also be hypothesized for SPN, although it needs to be better studied and clarified. By viewing the interconnections among each of the genes with variations in SPN specimens, *CTNNB1* was identified as the core portion in the network to regulate tumorigenesis (13). In addition, there is a growing body of evidence suggesting that Wnt/β-catenin signaling plays an essential role in the immune system. In metastatic melanoma, activation of the Wnt/β-catenin signaling pathway correlates with T cell exclusion (14). These reports suggested that activated Wnt signaling mediates cancer immune evasion and resistance to immunotherapies. Nevertheless, these studies could not identify recurrent genetic alterations in metastatic SPNs, which precluded us from identifying common drivers of SPN progression. Recent findings have also demonstrated that β-catenin, lymphoid enhancer-binding factor 1 (LEF1), androgen receptor (AR), and transcription factor E3 (TFE3), which are all expressed in SPNs, interact with each other by diverse pathways, so they are functionally closely interrelated (15). Using whole-exome sequencing and copy number variation analysis it has recently

been demonstrated that in metastatic SPNs, in addition to CTNNB1-activating mutations, inactivating mutations of epigenetic regulators (KDM6A, TET1, BAP1) are present in both primary and related metastases, suggesting a role of these genetic alterations in the metastatic dissemination of SPNs. Conversely, most copy number variations were not shared between primary and metastatic lesions from the same patients (4). All of these findings suggest a complex genetic background for SPNs. Future studies based on the molecular alterations of metastatic SPNs will be able to further unveil the pathologic and genetic enigma of metastatic SPN of the pancreas. There are no FDA-approved drugs available for *CTNNB1* mutations, except for a limited number of clinical trials in endometrial cancer. Slomovitz et al. (16) stated that recurrent endometrial cancer patients with *CTNNB1* mutations responded well to everolimus and letrozole. CTNNB1 mutations were also associated with longer progression-free survival (PFS) for advanced endometrial cancer on temsirolimus (17). The signaling relationship between Wnt and mTOR pathways remains an emergent area of study. There is no similar study on SPN disease.

The phosphoinositide 3-kinase (PI3K)-v akt murine thymoma viral oncogene homolog (AKT)-mechanistic target of rapamycin (mTOR) signaling cascade is one of the most important intracellular pathways that is frequently activated in diverse cancers (18). The first identified genetic mechanism of phosphoinositide 3-kinase (PI3K)-v-akt murine thymoma viral oncogene homolog (AKT)-mechanistic target of rapamycin (mTOR) signaling cascade was the loss of *PTEN* function by point mutation or deletion (19). In many types of tumors, the activation of the PI3K- AKT-mTOR pathway has been known as the relation to tumorigenesis, cancer progression and the acquired resistance to various anti-neoplastic agents. Although rare activating somatic mutations in the *PTEN* gene have been described, loss of *PTEN* expression is strongly associated with the presence of invasive carcinoma and poor survival in patients with intraductal papillary mucinous neoplasm of the pancreas (20). *PIK3CA/PTEN* genomic aberrations have been suggested to be strong predictors of everolimus sensitivity (21). The *PTEN* variant identified in this case has not been previously reported in SPN.

Based on the above, considering that our patient has a *CTNNB1* mutation and a non-functional *PTEN* product, it is reasonable to hypothesize that targeting mTOR may provide an effective strategy to regulate SPN tumorigenesis in this patient. This can also explain why she was partially relieved for more than 2 years from refractory metastatic SPNs after five surgeries. What confused us is that this patient actually had maintained stable conditions for nearly 27 months with the target agent sunitinib, a tyrosine kinase inhibitor (TKI) before her forth operation. After that, not only did the original metastases rapidly increase, but new peritoneal metastases appeared. Sunitinib, which has been used to suppress angiogenesis in cancer patients (22), has not been previously reported in patients with SPN. *In vitro* studies showed that inhibition of endogenous PTEN in cultured endothelial cells enhances vascular endothelial growth factor (VEGF) signaling (23). However, clinical reports describe cases in which, after administration of sunitinib, tumor relapse has occurred with severe growth and increased metastatic behavior (24). Treatment with sunitinib led to upregulation of vegfaa in wild-type zebrafish embryos and to a further upregulation of vegfaa expression in mutant embryos lacking *Pten* (25), which may result in hyperproliferation of endothelial cells, hence, explaining the tumor relapse after sunitinib treatment. The signaling relationship between Wnt and mTOR pathways remains an emergent area of study (26); however, this molecular relationship has not been explored in SPN disease. We speculate that combined treatment with a PI3K inhibitor and sunitinib suppresses hypervascularization without enhancing vegfaa expression, suggesting a new approach for therapeutic intervention in VEGFR-signaling-dependent tumors. Combination treatment with TKI and mTOR inhibitors has been evaluated in several phase I trials to date (27). Further investigation using other genomic candidates and new-generation mTOR inhibitors is also warranted in patients with treatment-refractory cancer (28). This study suggests that by targeting the Wnt/β-catenin and the PI3K-AKT-mTOR pathways, it is possible to understand if that would either kill more tumor cells or further delay SPN recurrence.

This case report was based on nonstandardized pathologic report of each institutional pathologic examination during the long time period. Therefore, there might be inconsistency in reporting immunohistochemical characters among different specimens in different hospitals, which can easily confuse the readers. We admit that, in the past, many pathologists and clinicians were unaware of pancreatic SPNs and had no interest at all in these rare pathologic conditions; as such, they just focused on the diagnosis rather than pathologic characterization and oncologic outcomes. However, all the pathological features of the tumors from the formalin-fixed paraffin-embedded (FFPE) tissue were carefully reviewed by our own pathologists. Furthermore, the focus of this case report is to suggest that evidence on variant genetics indicates that future molecular studies may not only help to explain the mechanism of SPN occurrence and development but are also more likely to direct to future precision treatments.

CONCLUSION

In conclusion, this case depicted the aggressive peritoneal dissemination and hepatic metastases of a metastatic pancreatic SPN that still showed an indolent clinical course when combination therapy with repeated surgery and targeted therapy were applied. Although the follow-up effect remains to be seen, this is the first report of practical experience of the targeted agents sunitinib and everolimus in metastatic SPN tumors based on the mutation status of *PTEN* and *CTNNB1*. Future molecular studies are required to provide more precision tools to guide preclinical and clinical therapeutic development and treatment in metastatic SPN.

DATA AVAILABILITY STATEMENT

The original contributions presented in the study are included in the article/supplementary material. Further inquiries can be directed to the corresponding author.

ETHICS STATEMENT

The studies involving human participants were reviewed and approved by Jinling Hospital, School of Medicine, Nanjing University. The patients/participants provided their written informed consent to participate in this study. Written informed consent was obtained from the individual(s) for the publication of any potentially identifiable images or data included in this article.

AUTHOR CONTRIBUTIONS

XW was involved in the identification, selection, and management of patient cases and wrote and revised the manuscript. DZ, ML, SW, and RS was involved in the management of patient cases. WB performed the histological images analysis and reviewed the manuscript. All authors contributed to the article and approved the submitted version.

REFERENCES

1. Marchegiani G, Andrianello S, Massignani M, Malleo G, Maggino L, Paiella S, et al. Solid Pseudopapillary Tumors of the Pancreas: Specific Pathological Features Predict the Likelihood of Postoperative Recurrence. *J Surg Oncol* (2016) 114(5):597–601. doi: 10.1002/jso.24380
2. Naar L, Spanomichou DA, Mastoraki A, Smyrniots V, Arkadopoulos N. Solid Pseudopapillary Neoplasms of the Pancreas: A Surgical and Genetic Enigma. *World J Surg* (2017) 41(7):1871–81. doi: 10.1007/s00268-017-3921-y
3. Guo M, Luo G, Jin K, Long J, Cheng H, Lu Y, et al. Somatic Genetic Variation in Solid Pseudopapillary Tumor of the Pancreas by Whole Exome Sequencing. *Int J Mol Sci* (2017) 18(1):81–92. doi: 10.3390/ijms18010081
4. Amato E, Mafficini A, Hirabayashi K, Lawlor RT, Fassan M, Vicentini C, et al. Molecular Alterations Associated With Metastases of Solid Pseudopapillary Neoplasms of the Pancreas. *J Pathol* (2019) 247(1):123–34. doi: 10.1002/path.5180
5. La Rosa S, Bongiovanni M. Pancreatic Solid Pseudopapillary Neoplasm: Key Pathologic and Genetic Features. *Arch Pathol Lab Med* (2020) 144(7):829–37. doi: 10.5858/arpa.2019-0473-RA
6. Walter T H-FJ, Hervieuc V, Adham M, Poncet G, Dumortier J, Lombard-Bohas C, et al. Primary Malignant Solid Pseudopapillary Tumors of the Gastroduodenal Area. *Clin Res Hepatol Gastroenterol* (2011) 35:227–33. doi: 10.1016/j.clinre.2011.01.004
7. Kang CM, Choi SH, Kim SC, Lee WJ, Choi DW, Kim SW. Predicting Recurrence of Pancreatic Solid Pseudopapillary Tumors After Surgical Resection: A Multicenter Analysis in Korea. *Ann Surg* (2014) 260(2):348–55. doi: 10.1097/SLA.0000000000000583
8. National Center for Biotechnology Information. *ClinVar; [Vcv000426534.11]*. Available at: https://www.ncbi.nlm.nih.gov/clinvar/variation/VCV000426534.11 (Accessed June 4, 2021).
9. Leiden Open Variation Database. *Global Variome Shared LOVD; [All Variants in the FANCD2 Gene]*. Available at: https://databases.lovd.nl/shared/variants/FANCD2?search_position_c_start=195&search_position_c_start_intron=0&search_position_c_end=195&search_position_c_end_intron=0&search_vot_clean_dna_change=%3D%22195G%3EC%22&search_transcriptid=00007723 (Accessed June 4, 2021).
10. Reid MD, Saka B, Balci S, Goldblum AS, Adsay NV. Molecular Genetics of Pancreatic Neoplasms and Their Morphologic Correlates: An Update on Recent Advances and Potential Diagnostic Applications. *Am J Clin Pathol* (2014) 141(2):168–80. doi: 10.1309/AJCP0FKDP7ENVKEV
11. Yamaguchi K, Nagatoishi S, Tsumoto K, Furukawa Y. Discovery of Chemical Probes That Suppress Wnt/β-Catenin Signaling Through High-Throughput Screening. *Cancer Sci* (2020) 111(3):783–94. doi: 10.1111/cas.14297
12. Tanaka Y, Kato K, Notohara K, Hojo H, Ijiri R, Miyake T, et al. Frequent Beta-Catenin Mutation and Cytoplasmic/Nuclear Accumulation in Pancreatic Solid-Pseudopapillary Neoplasm. *Cancer Res* (2001) 61(23):8401–4.
13. Wang J, Gerrard G, Poskitt B, Dawson K, Trivedi P, Foroni L, et al. Targeted Next Generation Sequencing of Pancreatic Solid Pseudopapillary Neoplasms Show Mutations in Wnt Signaling Pathway Genes. *Pathol Int* (2019) 69(4):193–201. doi: 10.1111/pin.12778
14. Spranger S, Bao R, Gajewski TF. Melanoma-Intrinsic Beta-Catenin Signalling Prevents Anti-Tumour Immunity. *Nature* (2015) 523(7559):231–5. doi: 10.1038/nature14404
15. Li P, Hu Y, Yi J, Li J, Yang J, Wang J. Identification of Potential Biomarkers to Differentially Diagnose Solid Pseudopapillary Tumors and Pancreatic Malignancies *via* a Gene Regulatory Network. *J Transl Med* (2015) 13:361. doi: 10.1186/s12967-015-0718-3
16. Slomovitz BM, Jiang Y, Yates MS, Soliman PT, Johnston T, Nowakowski M, et al. Phase II Study of Everolimus and Letrozole in Patients With Recurrent Endometrial Carcinoma. *J Clin Oncol* (2015) 33(8):930–6. doi: 10.1200/JCO.2014.58.3401
17. Myers AP, Filiaci VL, Zhang Y, Pearl M, Behbakht K, Makker V, et al. Tumor Mutational Analysis of GOG248, a Phase II Study of Temsirolimus or Temsirolimus and Alternating Megestrol Acetate and Tamoxifen for Advanced Endometrial Cancer (EC): An NRG Oncology/Gynecologic Oncology Group Study. *Gynecol Oncol* (2016) 141(1):43–8. doi: 10.1016/j.ygyno.2016.02.025
18. Engelman JA. Targeting PI3K Signalling in Cancer: Opportunities, Challenges and Limitations. *Nat Rev Cancer* (2009) 9(8):550–62. doi: 10.1038/nrc2664
19. Vivanco I, Sawyers CL. The Phosphatidylinositol 3-Kinase AKT Pathway in Human Cancer. *Nat Rev Cancer* (2002) 2(7):489–501. doi: 10.1038/nrc839
20. Garcia-Carracedo D, Turk AT, Fine SA, Akhavan N, Tweel BC, Parsons R, et al. Loss of *PTEN* Expression Is Associated With Poor Prognosis in Patients With Intraductal Papillary Mucinous Neoplasms of the Pancreas. *Clin Cancer Res* (2013) 19(24):6830–41. doi: 10.1158/1078-0432.CCR-13-0624
21. Burris 3HA. Overcoming Acquired Resistance to Anticancer Therapy: Focus on the PI3K/AKT/mTOR Pathway. *Cancer Chemother Pharmacol* (2013) 71(4):829–42. doi: 10.1007/s00280-012-2043-3
22. Roskoski RJr. Sunitinib: A VEGF and PDGF Receptor Protein Kinase and Angiogenesis Inhibitor. *Biochem Biophys Res Commun* (2007) 356(2):323–8. doi: 10.1016/j.bbrc.2007.02.156
23. Huang J, Kontos CD. PTEN Modulates Vascular Endothelial Growth Factor-Mediated Signaling and Angiogenic Effects. *J Biol Chem* (2002) 277:10760–6. doi: 10.1074/jbc.M110219200
24. Tonini G, Intagliata S, Cagli B, Segreto F, Perrone G, Muda O, et al. Recurrent Scrotal Hemangiomas During Treatment With Sunitinib. *J Clin Oncol* (2010) 28(35):e737–8. doi: 10.1200/JCO.2010.30.4865
25. Choorapoikayil S, Weijts B, Kers R, Bruin A, Hertog J. Loss of *Pten* Promotes Angiogenesis and Enhanced Vegfaa Expression in Zebrafish. *Dis Model Mech* (2013) 6(5):1159–66. doi: 10.1242/dmm.012377
26. Shimobayashi M, Hall MN. Making New Contacts: The mTOR Network in Metabolism and Signalling Crosstalk. *Nat Rev Mol Cell Biol* (2014) 15(3):155–62. doi: 10.1038/nrm3757
27. Rodrigues HV, Ke D, Lim J, Stephen B, Bellido J, Janku F, et al. Phase I Combination of Pazopanib and Everolimus in PIK3CA Mutation Positive/

PTEN Loss Patients With Advanced Solid Tumors Refractory to Standard Therapy. *Invest New Drugs* (2015) 33(3):700–9. doi: 10.1007/s10637-015-0238-2

28. Kim ST, Lee J, Park SH, Park JO, Park YS, Kang WK, et al. Prospective Phase II Trial of Everolimus in *PIK3CA* Amplification/Mutation and/or *PTEN* Loss Patients With Advanced Solid Tumors Refractory to Standard Therapy. *BMC Cancer* (2017) 17(1):211–6. doi: 10.1186/s12885-017-3196-6

Conflict of Interest: The authors declare that the research was conducted in the absence of any commercial or financial relationships that could be construed as a potential conflict of interest.

Publisher's Note: All claims expressed in this article are solely those of the authors and do not necessarily represent those of their affiliated organizations, or those of the publisher, the editors and the reviewers. Any product that may be evaluated in this article, or claim that may be made by its manufacturer, is not guaranteed or endorsed by the publisher.

frontiers in Oncology

ORIGINAL RESEARCH
published: 25 October 2021
doi: 10.3389/fonc.2021.735277

A Role of CXCL1 Drives Osteosarcoma Lung Metastasis *via* VCAM-1 Production

Chiang-Wen Lee[1,2,3†], *Yao-Chang Chiang*[1,2,3†], *Pei-An Yu*[1,4], *Kuo-Ti Peng*[1,5], *Miao-Ching Chi*[3,6,7], *Ming-Hsueh Lee*[6,8], *Mei-Ling Fang*[9,10], *Kuan-Han Lee*[11], *Lee-Fen Hsu*[6,8*] and *Ju-Fang Liu*[12,13*]

[1] Department of Orthopaedic Surgery, Chang Gung Memorial Hospital, Puzi, Taiwan, [2] Department of Nursing, Chang Gung University of Science and Technology, Puzi, Taiwan, [3] Division of Basic Medical Sciences, and Chronic Diseases and Health Promotion Research Center, Chang Gung University of Science and Technology, Puzi, Taiwan, [4] Sports Medicine Center, Chang Gung Memorial Hospital at Chia Yi, Chiayi, Taiwan, [5] College of Medicine, Chang Gung University, Taoyuan, Taiwan, [6] Department of Respiratory Care, Chang Gung University of Science and Technology, Puzi, Taiwan, [7] Division of Pulmonary and Critical Care Medicine, Chang Gung Memorial Hospital, Kaohsiung, Taiwan, [8] Division of Neurosurgery, Department of Surgery, Chang Gung Memorial Hospital, Chiayi, Taiwan, [9] Center for Environmental Toxin and Emerging-Contaminant Research, Cheng Shiu University, Kaohsiung, Taiwan, [10] Super Micro Research and Technology Center, Cheng Shiu University, Kaohsiung, Taiwan, [11] Department of Pharmacy, Chia Nan University of Pharmacy and Science, Tainan, Taiwan, [12] School of Oral Hygiene, College of Oral Medicine, Taipei Medical University, Taipei, Taiwan, [13] Department of Medical Research, China Medical University Hospital, China Medical University, Taichung, Taiwan

OPEN ACCESS

Edited by:
Guisheng Song,
University of Minnesota, United States

Reviewed by:
Stephen B. Keysar,
University of Colorado Anschutz Medical Campus, United States
Paula Rezende-Teixeira,
University of São Paulo, Brazil

***Correspondence:**
Ju-Fang Liu
jufangliu@tmu.edu.tw
Lee-Fen Hsu
lfhsu@mail.cgust.edu.tw

[†]These authors have contributed equally to this work

Specialty section:
This article was submitted to Molecular and Cellular Oncology, a section of the journal Frontiers in Oncology

Received: 02 July 2021
Accepted: 30 September 2021
Published: 25 October 2021

Citation:
Lee C-W, Chiang Y-C, Yu P-A, Peng K-T, Chi M-C, Lee M-H, Fang M-L, Lee K-H, Hsu L-F and Liu J-F (2021) A Role of CXCL1 Drives Osteosarcoma Lung Metastasis via VCAM-1 Production. Front. Oncol. 11:735277. doi: 10.3389/fonc.2021.735277

Osteosarcoma, a common aggressive and malignant cancer, appears in the musculoskeletal system among young adults. The major cause of mortality in osteosarcoma was the recurrence of lung metastases. However, the molecular mechanisms of metastasis involved in osteosarcomas remain unclear. Recently, CXCL1 and CXCR2 have been crucial indicators for lung metastasis in osteosarcoma by paracrine releases, suggesting the involvement of directing neutrophils into tumor microenvironment. In this study, overexpression of CXCL1 has a positive correlation with the migratory and invasive activities in osteosarcoma cell lines. Furthermore, the signaling pathway, CXCR2/FAK/PI3K/Akt, is activated through CXCL1 by promoting vascular cell adhesion molecule 1 (VCAM-1) *via* upregulation of nuclear factor-kappa B (NF-κB) expression and nuclear translocation. The *in vivo* animal model further demonstrated that CXCL1 serves as a critical promoter in osteosarcoma metastasis to the lung. The correlated expression of CXCL1 and VCAM-1 was observed in the immunohistochemistry staining from human osteosarcoma specimens. Our findings demonstrate the cascade mechanism regulating the network in lung metastasis osteosarcoma, therefore indicating that the CXCL1/CXCR2 pathway is a worthwhile candidate to further develop treatment schemas.

Keywords: osteosarcoma, metastasis, CXCL1, VCAM-1, migration

INTRODUCTION

Among all bone malignancy diagnoses with children and young adults, osteosarcoma is the most common primary and aggressive malignant neoplasm (1, 2). Surgical excision, neoadjuvant, and adjuvant chemotherapies are widely used to treat osteosarcoma for the preservation of limb functions and increase of the successful rate of treatment (3); in addition, less than 70% of patients remain alive after 3 years with no clinical metastasis at first diagnosis (4). Osteosarcoma has high potentials of invasion and metastasis; subsequently, osteosarcoma metastases in the lung are the main reason for mortality rate (5). Approximately one-third of the patients presenting with localized disease will relapse, and patients with metastases at diagnosis are nearly three-quarters; approximately 90% of relapses occur because of lung metastases (6). In order to prevent osteosarcoma lung metastasis, effective therapy is urgently required.

Chemokines are low-molecular-weight proteins that have diverse roles in human physiology including cellular development, migration, immune surveillance, inflammation, and various pathological conditions (7). Chemokines are critical for mediating leukocyte trafficking and positioning, stimulating endothelial cell migration, and activating signaling pathways (8). Moreover, chemokines also regulate progression, metastasis, apoptosis, and chemoresistance in cancer cells (9–12). The chemokine (C-X-C motif) ligand 1 (CXCL1) has been linked to the effects on inflammation, angiogenesis, tumorigenesis, and wound healing (13). CXCR2, receptor of CXCL1, is highly expressed on the surface of neutrophils (14) and is involved in progression in several kinds of cancer, such as lung, prostate, breast, colorectal, ovarian, and pancreatic cancer (15). CXCL1 could mediate several kinds of CXCR2-expressed cells, such as neutrophils, macrophages, osteoblasts, and fibroblasts, to regulate the tumor microenvironment (16–18). Besides, the positive correlation of CXCL1 levels depends on the size of tumor, stage of advancing, and depth of invasion while negative to survival rate of patients has been reported (19–21). CXCL1 secretion could enhance the invasion and metastasis of several types of cancer cells (22–25); in contrast, silencing or knockdown of CXCL1 could inhibit tumor growth in hepatocellular carcinoma (26) and colorectal cancer liver metastasis (27). These studies conspicuously indicate that CXCL1 is a crucial indicator in the progress of cancer invasion and metastasis. However, the role and related mechanisms of CXCL1 in osteosarcoma remain unclear.

Vascular cell adhesion molecule 1 (VCAM-1/CD106), an inducible surface glycoprotein, belongs to the immunoglobulin superfamily (28). VCAM-1 expressions influence numerous biological activities in normal conditions including the regulation of migration and invasion during the cancer metastasis (28). Overexpression of VCAM-1 could occur in the metastatic cancer cells and correlated with the stage of disease including tumor progression in osteosarcoma enhancing the connective tissue growth factor stimulation to promote migration and metastasis (9, 29, 30).

The current study showed that the CXCL1 could signal the CXCR2/focal adhesion kinase (FAK)/phosphatidylinositol-3-kinase (PI3K)/Akt/nuclear factor-kappa B (NF-κB) pathway to increase VCAM-1 expression and subsequently upregulate the metastasis ability of human osteosarcoma cells. The strategy to suppress the expression level of CXCL1 could effectively decrease the VCAM-1 expression, which has the beneficial response for inhibiting migration, invasion, and wound healing abilities in osteosarcoma. This finding strongly suggests that CXCL1/CXCR2 signals act as indicators in metastatic osteosarcoma and could be a therapeutic target for developing anticancer medicine with their unique characteristics.

MATERIALS AND METHODS

Materials

All chemical reagents were purchased from Sigma-Aldrich (St. Louis, MO, USA). The CXCL1, CXCR2, VCAM-1, p-FAK, FAK, p-p85α, p85α, p-Akt, Akt, p-IKKα/β, IKKα/β, p-IκBα, IκBα, p-p65, p65, and β-Actin specific anti-mouse and anti-rabbit IgG-conjugated horseradish peroxidase antibodies were purchased from GeneTex International Corporation (Hsinchu City, Taiwan). Recombinant human CXCL1 was purchased from PeproTech (Rocky Hill, NJ, USA). Short hairpin RNA (shRNA) plasmid for CXCR2 and VCAM-1 were obtained from the National RNAi Core Facility Platform (Taipei, Taiwan). All siRNAs were ON-TARGETplus siRNAs, obtained from Dharmacon Research (Lafayette, CO, USA). The NF-κB luciferase report plasmid, pSV-β-galactosidase vector, and luciferase assay kit were purchased from Promega (Madison, WI, USA).

Cell Culture

The normal osteoblast cell lines (hFOB1.19) and human osteosarcoma cell lines (MG63, U2OS, and HOS) were purchased from the American Type Cell Culture Collection (Manassas, VA, USA). The hFOB1.19 cells were cultured in DMEM/F12 medium, U2OS cells were cultured in McCoy's 5A medium, and MG63 and HOS cells were cultured in Eagle's minimum essential medium. All cell mediums were supplemented with 20 mM HEPES, 10% heat-inactivated fetal bovine serum, and 2 mM-glutamine. Cells were maintained at 37°C in a humidified atmosphere of 5% CO_2/95% air. Migration-prone MG63 cells were selected by their differential migration abilities as described previously (9).

Establishment of Migration-Prone Subclones From Osteosarcoma Cell Line

The MG63 (M10 and M20) migration-prone subclones were established by using Transwell inserts. MG63 osteosarcoma cells (1×10^6) suspended in 1 ml of serum-free medium were seeded in the upper chamber, while 1 ml of growth medium contained 10% FBS was loaded into the lower compartment. After 24 h, the cells that migrated across the Transwell insert to the bottom of plate were detached by trypsin and cultured as MG63 (M1).

The cells were cultured for 2 days for a second round of selection. The MG63 migration-prone subclone continued migration selection for 10 and 20 rounds to generate MG63 (M10) and MG63 (M20), respectively.

Immunoblotting Assay

Total cell lysates were collected by using RIPA lysis buffer for further immunoblotting assay. Afterward, equal amounts of the protein were separated by SDS-polyacrylamide gel electrophoresis and transferred to polyvinyl difluoride (PVDF) membranes. Blots were blocked with 5% nonfat milk for at room temperature for 1 h; moreover, blots were incubated for another 1 h with different primary antibodies at room temperature to measure the levels of the targets. The peroxidase conjugated secondary antibody (1:5,000) at room temperature for 1 h after three washes to clear residue of primary antibodies. The signals were detected on a charge-coupled device camera-based detection system (UVP Inc., Upland, CA, USA), and the ImageJ software (National Institutes of Health, USA) was used for quantifying. At least three independent immunoblotting datasets were collected from the experiments and a closer figure pattern was selected for presentation.

RNA Extraction and Quantitative Real-Time PCR

Total RNA was isolated from cells by using Total RNA preparation kits (easy-Blue Total RNA Extraction kit, iNtRON Biotechnology, Seongnam, Korea) following the manufacturer's protocol. The RNA was reverse transcribed to cDNA by reverse transcriptase (Invitrogen, Carlsbad, CA, USA). Quantitative real-time PCR (qPCR) was used to determine the mRNA levels of target genes by running on a StepOnePlus machine (Applied Biosystems, Foster City, CA, USA). The SYBR Green fluorescence probe system (KAPA Biosystems, Woburn, MA, USA) was used for determining the threshold cycle (C_T) of target genes. Primers of human VCAM-1 and glyceraldehyde 3-phosphate dehydrogenase (GAPDH) were purchased from Sigma-Aldrich. The expression levels of the target genes were normalized to GAPDH levels and the formula of level ratio = $2^{-\Delta\Delta Ct}$, where $\Delta\Delta Ct = (Ct_{target} - Ct_{GADPH})_{Sample} - (Ct_{target} - Ct_{GADPH})_{Control}$, was used for calculation. The data were represented with three independent experiments with triplicate of each sample.

Transwell Cell Migration Assay

The Transwell inserts (8-μm pore size; Costar, NY, USA) in 24-well dishes were used for cell migration assay. Cells (2×10^4 cell/well) were pretreated with the designated inhibitors for 90 min and then incubated for 24 h in the culture supernatants. The cells were seeded in the upper Transwell chamber, and 300 μl of medium was prepared into the lower chamber. Cells were fixed in 3.7% formaldehyde for 30 min and stained with 0.05% crystal violet for 60 min after 24-h incubation was finished. Each chamber was washed with PBS after removing upper side cells by cotton-tipped swabs. The cells located on the underside of the filter were examined and counted under a microscope. The data were collected from at least three independent experiments.

Immunofluorescence Microscopy

MG63 cells (5×10^3 cell/well) were seeded on glass coverslips and treated with designed conditions. Once PBS was rinsed, the cells on the slice were fixed in 3.7% paraformaldehyde at room temperature for 15 min. Then, cells were washed three times with PBS to remove the residual of the fixed solution and then 4% BSA was used for blocking with another 15 min. The cells were incubated with anti-human p65 (1:100) at room temperature for 1 h. The cells were further incubated with FITC-conjugated goat anti-rabbit IgG for 1 h after twice PBS washed. Leica TCS SP2 Spectral Confocal System was used for photographing the mounted cells.

Reporter Assay

Cells (2×10^5 cell/well) were co-transfected with NF-κB report plasmid and pSV-β-galactosidase vector for 24 h by using Lipofectamine 3000™ (Invitrogen). Cells were lysed with lysis buffer (100 μl) and harvested by centrifugation (13,200 rpm for 15 min) for further luciferase assay. The supernatants with 1:4 luciferase assay buffer were reacted. Activities of luciferase were measured by a microplate luminometer and normalized to β-galactosidase expression vector co-transfection efficiency.

Chromatin Immunoprecipitation Assay

Details of chromatin immunoprecipitation (ChIP) analysis were described previously (9). In brief, DNA samples were immunoprecipitated by the anti-p65 antibody. The immunoprecipitated DNA after phenol-chloroform purification was further amplified with PCR and separated by 1.5% agarose gel electrophoresis. The signals were visualized and photographed by ultraviolet illumination. The promoter region of the NF-κB region (−2167 and −1967) in the promoter region of human VCAM-1 was amplified with primers 5'-ACAGA GAGAGGAGCTTCAGCAGTGAGAGCA-3' and 5'-GTCT GTGCTTTATAAAGGGTCTTGTTGCAG-3'.

CXCL1 Knockdown in Osteosarcoma Cell Lines

The lentiviral expression system for CXCL1 knockdown was purchased from the National RNAi Core Facility (RNAi Core, Academia Sinica, Taiwan). The CXCL1 shRNA plasmid was selected to knock down gene expression. The osteosarcoma cell line MG63 was transfected with the CXCL1 shRNA plasmid. The cells were puromycin-selected and the surviving cells were used as stable gene-modified cell lines. MG63 cell lines that stably expressed luciferase were established before transfection with the CXCL1 shRNA vector or the control vector, and the *in vivo* orthotopic model was analyzed using the *In Vivo* Imaging Systems (IVIS, Xenogen, UK).

Orthotopic Animal Model and Imaging

Ethical approval was obtained for the use of the animals, and all experiments were performed in accordance with the Guidelines for Animal Care of the Institutional Animal Care and Use Committee of College of Medicine, National Taiwan University (Approval No: 20150357). CB17/SCID mice were purchased from Lasco Inc. (Taipei, Taiwan) weighing 20–30 g, and were acclimatized to a

room maintained at 25°C and 50% ± 10% humidity under a 12-h day–night cycle for at least 3 days before experimentation. Individual mice were anesthetized with isoflurane (1%–3%) and oxygen (100%) inhalation. The cortex of the tibial crest was penetrated using a 27-gauge needle, 10 µl containing 1×10^6 cells were injected. Four weeks after injection, the tumor growth and local metastasis were monitored using IVIS Imaging System. The mice were euthanized by CO_2 inhalation. The lung tissues were removed and fixed in 10% formalin for further analysis. The number of lung tumor nodules was counted under a dissecting microscope. The experiment was repeated twice.

Histological Analysis of Lung Metastases

All of the lungs resected from mice were fixed with 10% buffered formalin and embedded in paraffin. Thick sections of 7 µm were stained with hematoxylin and eosin by using histological analyses.

Immunohistochemistry Staining

Human osteosarcoma tissue arrays (consisting 11 cases of normal bone, 7 cases of stage I osteosarcoma, 49 cases of stage II osteosarcoma, and 7 cases of stage III osteosarcoma) were applied for investigating the expression level of CXCL1 and VCAM-1. The clinical specimens were rehydrated and incubated in 3% hydrogen peroxide to block endogenous peroxidase activity. The slices after antigen retrieval were incubated in 3% bovine serum albumin and then the primary mouse polyclonal anti-CXCL1 and VCAM-1 antibodies (1:100 dilution) at 4°C overnight. After thrice PBS washes, slides were incubated with biotin-labeled goat anti-mouse IgG secondary antibody (1:100 dilution) and signals were amplified with the ABC Kit (Vector Laboratories, Burlingame, CA, USA). Sections on slides were stained with the chromogen diaminobenzidine, washed, counterstained with Delafield's hematoxylin, dehydrated, and treated with xylene, and then the bound signals were mounted and photographed by microscope. Intensities of tumor cell staining were scored from 0 to 5, where 0 = no staining or unspecific staining, 1 = very weak (intensity), 2 = weak staining, 3 = moderate staining, 4 = strong staining, and 5 = very strong staining. A pathologist scored staining intensity in all samples.

Statistical Analysis

Data were expressed as mean ± standard deviation (SD). Student's *t*-test and one-way ANOVA, followed by post-hoc Fisher LSD multiple comparisons (multiple groups), were used. The coefficient of determination (r^2) was used to evaluate the performance of a linear regression model and for modeling the coefficient of signals. A p-value < 0.05 was considered significant.

RESULTS

CXCL1 Stimulates Migration, Wound Healing, and Invasion in Osteosarcoma Cells

CXCL1 has been integrated to migration and metastasis in various types of cancer cells (21, 25, 26). To select the suitable human osteosarcoma cell lines (MG-63, HOS, and U2OS) and to further investigate the role of CXCL1 on invasion and metastases, the migration ability was measured. As shown in **Figure 1A**, MG63 has a rapid cell migration ability compared to other osteosarcoma cell lines; furthermore, the CXCL1 expression levels were also consistent with the trend of migration ability (**Figures 1B, C**).

The previously established high-migration-prone sublines, MG-63 (M10) and MG-63 (M20) (31), were also used to test the correlation of CXCL1 expression and migratory activity. Results showed that migration-prone sublines, MG-63 (M20) and MG-63 (M10), had a better cell motility, CXCL1 mRNA, and protein expression than the original MG63 cell line (**Figures 1D–F**). These findings implied a relationship of CXCL1 expression and metastasis in osteosarcoma cells. Next, CXCL1 (1–10 ng/ml) was applied to investigate whether CXCL1 expression influences cell motility in these three osteosarcoma cell lines. Results suggested that a concentration-dependently facilitated migration, wound healing, and invasive abilities could be affected in all osteosarcoma cell lines (**Figures 1G–I**). Furthermore, the pCDNA3.1-conjugated CXCL1 plasmid was transfected into MG63 cells to evaluate the relationship of CXCL1 levels and cell migration. **Figures 1J, K** indicated that the CXCL1 mRNA and protein have enhanced the expression level and the increases of migratory ability were also observed (**Figure 1L**) after transfected with the pCDNA3.1-CXCL1 plasmid. According to these results, the expression of CXCL1 showed a positive regulation on the migratory, wound healing, and invasive abilities in osteosarcoma cells.

CXCL1 Stimulates VCAM-1 Expression in Osteosarcoma Cells

Cell adhesion molecules play critical roles during the extravasation step, a situation where cancer cells adhere to the vasculature endothelium of small capillaries and then migrate through the vasculature wall to generate metastatic foci of tumor metastasis (32), but few known in human osteosarcoma. Previous studies suggested that VCAM-1-dependent motility is an essential factor for tumor metastatic developments (33, 34). To investigate tumor metastatic developments, the role of VCAM-1 in CXCL1 upon osteosarcoma cell migration was examined. Results (**Figure 2A**) showed that CXCL1 (1–10 ng/ml) could increase the VCAM-1 expression in a dose-dependent manner in MG63 cell, but no effects on intercellular adhesion molecule-1 (ICAM-1). Furthermore, the mRNA and protein levels of VCAM-1 were upregulated after CXCL1 stimulation (**Figures 2B, C**). Cells with VCAM-1 shRNA transfection could suppress CXCL1-induced VCAM-1 protein expressions and migration in MG63 osteosarcoma cells (**Figure 2D**). These results indicated that CXCL1 facilitated VCAM-1-dependent cell migration in osteosarcoma.

CXCL1 Stimulates VCAM-1 Expression and Cell Migration *via* CXCR2 Receptor in Osteosarcoma Cells

The CXCR2 is a specific receptor for CXCL1 and is involved in CXCL1-mediated cancer progress (9, 15, 17). To further

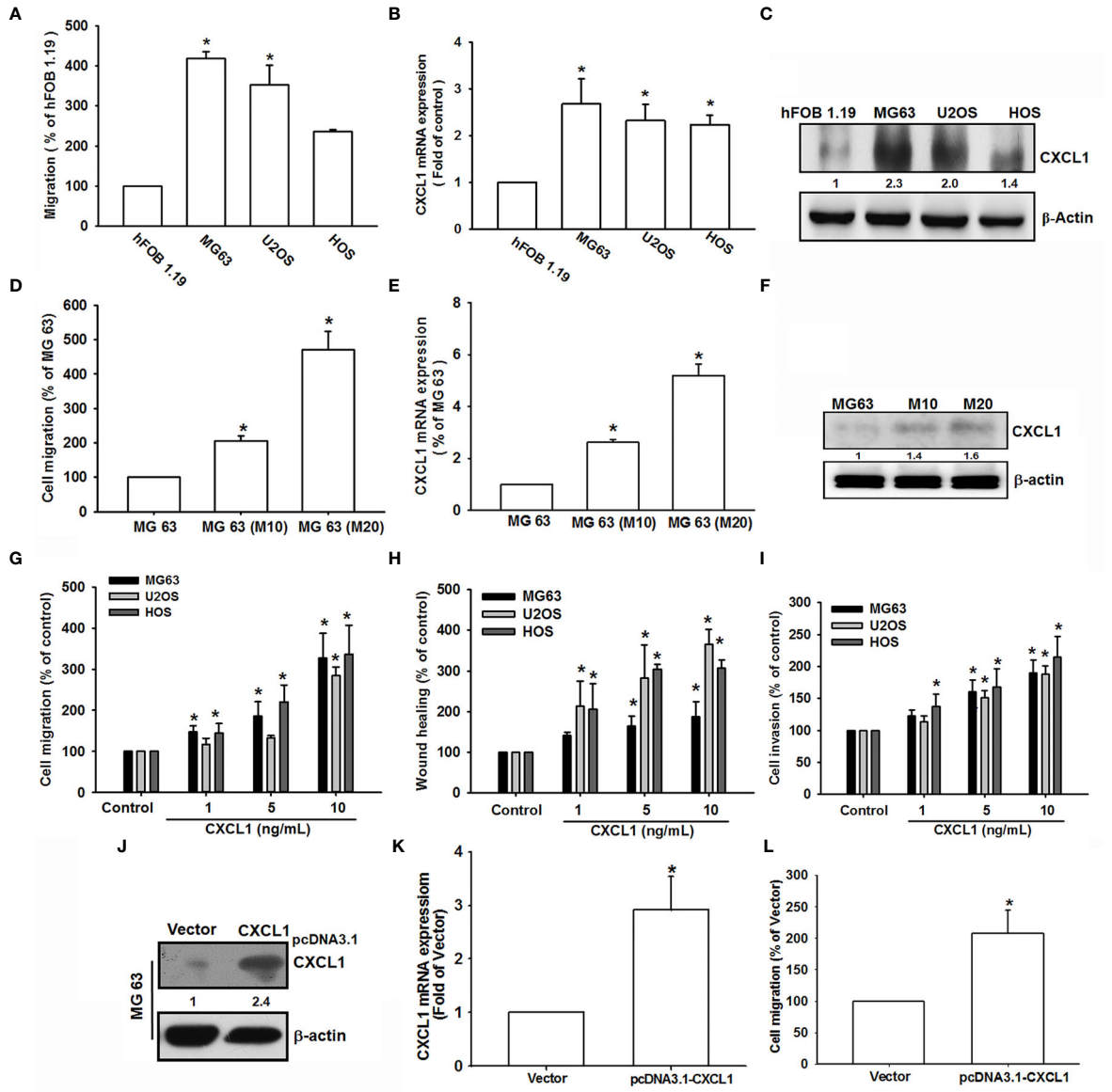

FIGURE 1 | CXCL1 increased migration, invasion, and wound healing in human osteosarcoma MG63, U2OS, and HOS cells. **(A)** The cell migration ability of the osteoblast cell line hFOB 1.19 and the osteosarcoma cell lines MG63, U2OS, and HOS was assessed using the Transwell assay. **(B, C)** Total mRNA and protein were collected from the indicated cell lines, and CXCL1 expression was detected using qPCR and Western blotting. **(D–F)** Migratory ability and CXCL1 expression of the indicated cells (MG63, M10, and M20) were examined by Transwell, qPCR, and immunoblotting assays. **(G–I)** Cells were incubated with CXCL1 (1–10 ng/ml) and the Transwell assay were used for detecting *in vitro* migratory, wound healing, and invasive activities after 18 h. **(J–L)** Cells were transfected with pcDNA3.1-conjugated CXCL1 plasmid and then CXCL1 mRNA, protein expression, and migratory potential were measured by immunoblotting, qPCR, and Transwell assays. Results were expressed as mean ± S.D. from at least three individual experiments. $^*p < 0.05$ compared with the control group of each experiment.

investigate whether CXCL1-induced VCAM-1 expression and cell migration are CXCR2-dependent mechanisms in osteosarcoma, the antagonist (SB225002), CXCR2 shRNA, and neutralizing antibody of CXCR2 were used for evaluation. As shown in **Figures 3A, B**, CXCR2 antagonist-SB225002 could significantly suppress CXCL1 (10 ng/ml)-induced cell migration and mRNA expression of VCAM-1. Similar results were observed in CXCR2 shRNA (**Figures 3C, D**) and CXCR2 neutralizing antibody (**Figures 3E, F**). These results demonstrated that CXCL1-mediated cell migration and VCAM-1 expression were upregulated by binding to the CXCR2 receptor.

The FAK/PI$_3$K/AKT/NF-κB Signaling Pathway Is Essential for CXCL1-Induced Increases in VCAM-1 Expression and Cell Migration

CXCL1/CXCR2-mediating signaling cascades, such as PI3K/Akt, mitogen-activated protein kinase (MAPK), and nuclear factor

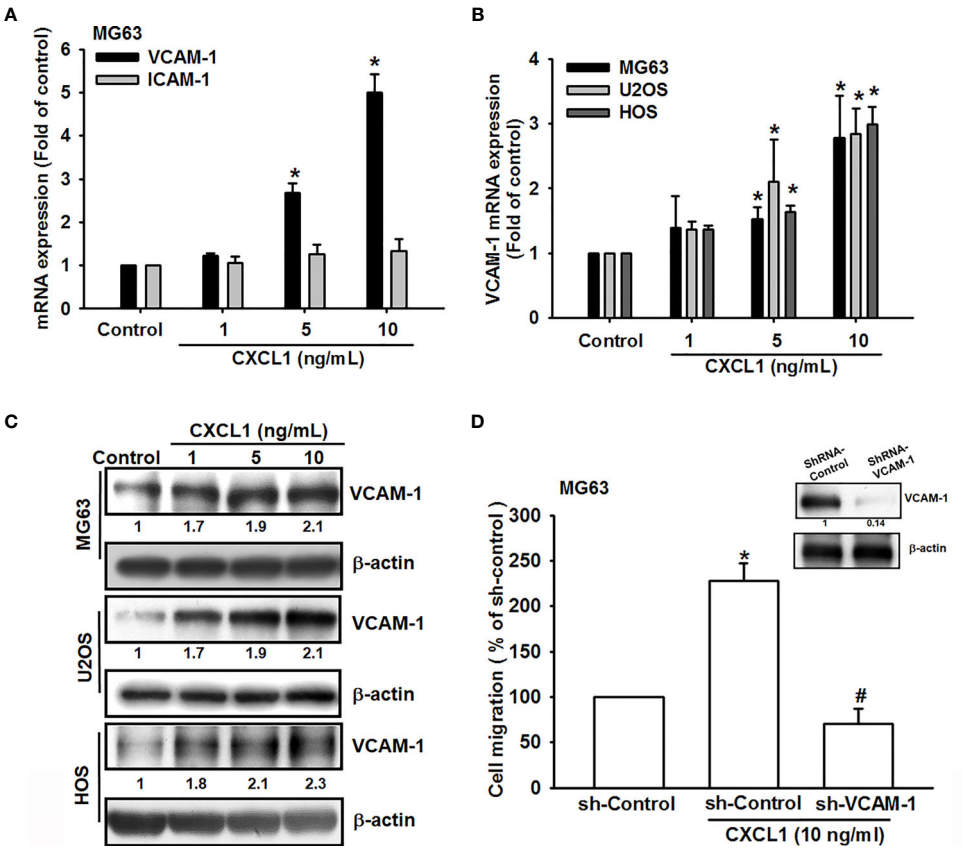

FIGURE 2 | CXCL1 promotes osteosarcoma migration by increasing VCAM-1 expression. **(A)** MG63 cells were stimulated with CXCL1 (1–10 ng/ml) and the mRNA levels of VCAM-1 and ICAM-1 were examined by real-time qPCR. **(B, C)** CXCL1 increased the VCAM-1 mRNA and protein expression in MG63, U2OS, and HOS human osteosarcoma cells. **(D)** VCAM-1 expression and migratory potential were examined by immunoblotting and Transwell assays in MG63 cells, which were transfected with VCAM-1 shRNA for 24 h and then stimulated with CXCL1 for another 24 h. The data were collected from at least three individual experiments and expressed as mean ± S.D. $^{*}p < 0.05$ as compared to the control group; $^{\#}p < 0.05$ compared with the CXCL1-treated shRNA-control group.

kappa-light-chain-enhancer of activated B cells (NF-κB), have been considered the regulatory signaling pathways for migration and invasion in several cancer cells (15, 35). Additionally, a previous study also suggested that CXCL8 is activated through the CXCR2 receptor to stimulate the downstream FAK, c-Src protein tyrosine kinase activity (36). To investigate the potential downstream signaling pathway by CXCL1 activation of CXCR2, the candidate signals of FAK/PI3K/Akt were screened by different inhibitors. Inhibitors of FAK (FAKi), PI3K (LY294002 and wortmannin), Akt (Akti), and NF-κB (TPCK and PDTC) were applied and showed a clear suppression pattern of CXCL1-triggered cell migration and VCAM-1 mRNA expression in MG63 osteosarcoma cells (**Figures 4A, B**). Furthermore, the phosphorylation of FAK, PI3K, Akt, and NF-κB were upregulated by CXCL1 treatment (**Figures 4C, D**). Dominant-negative mutants of several molecules in FAK/PI3K/Akt/NF-κB abolished CXCL1-promoted MG63 cell migration and VCAM-1 mRNA expression (**Figures 4E, F**). Moreover, CXCL1-enhanced VCAM-1 protein levels could be suppressed by pretreating respective pathway inhibitors (**Figures 4G–I**). These findings indicated that CXCL1-triggered cell migration and VCAM-1 expression were regulated through the FAK/PI3K/Akt/NF-κB pathway in osteosarcoma cells.

The NF-κB Signals Are Involved in CXCL1-Promoted Cell Migration and VCAM-1 Expression

NF-κB has been demonstrated as a crucial factor for cancer cell migration and invasion (33, 37, 38). The NF-κB luciferase promoter plasmid was used for evaluating the possibility of CXCL1-mediated CXCR2/FAK/PI3K/Akt pathway on NF-κB expression. As shown in **Figure 5A**, CXCL1 could enhance the luciferase activity of the NF-κB promoter as a reversed U pattern and the peak located at 10 ng/ml. CXCL1-induced NF-κB promoter luciferase activity could be suppressed by CXCR2/FAK/PI3K/Akt/NF-κB pathway inhibitors, dominant-negative mutants, and shRNA (**Figures 5B, C**). Expression level of phosphorylated p65 and nuclear translocation with FAK, PI3K, and Akt inhibitors pretreatment were measured to confirm the signaling transduction cascade. The inhibitors of FAK, PI3K, and Akt reversed CXCL1-induced p65 phosphorylation and nuclear translocation (**Figures 5D, E**). In addition, transcriptional

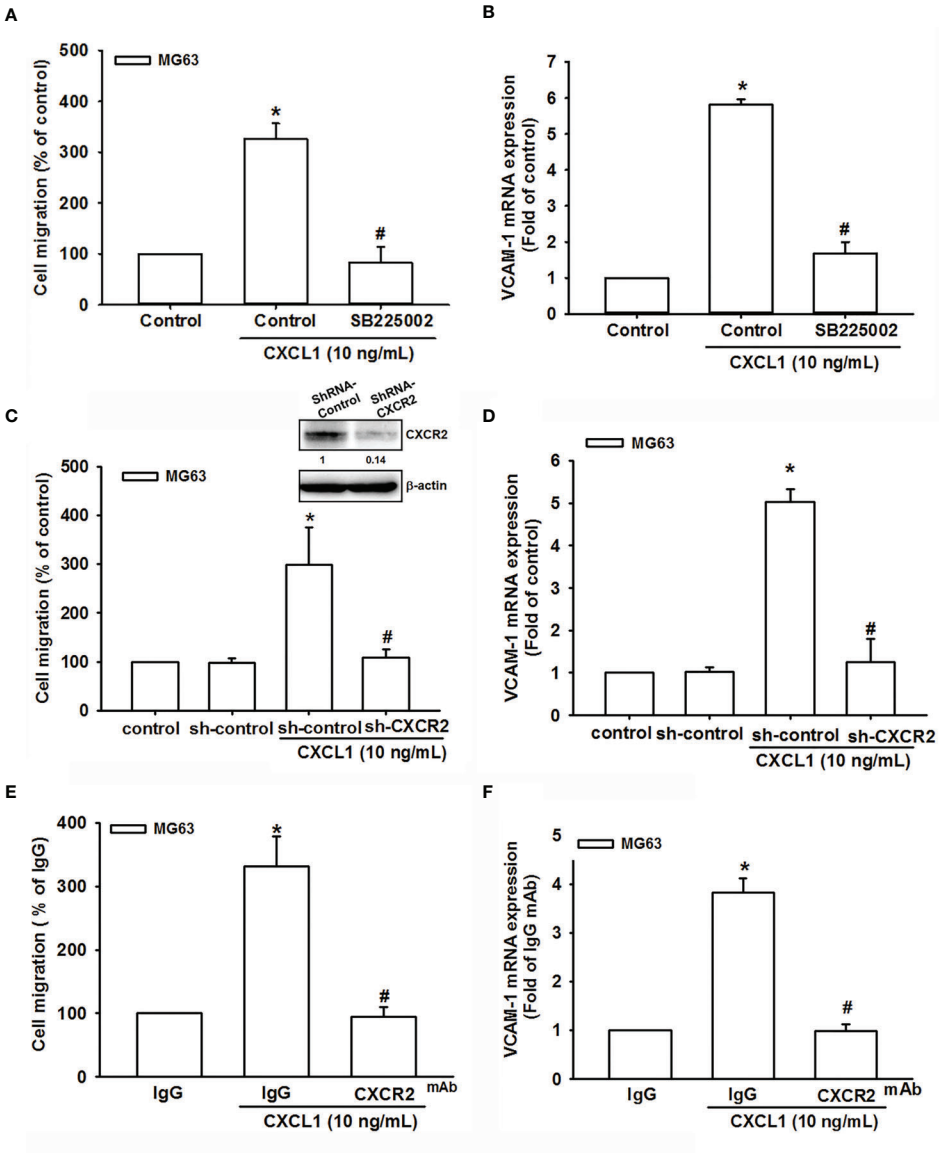

FIGURE 3 | The role of the CXCR2 receptor in CXCL1-mediated cell migration and VCAM-1 expression. **(A, B)** The CXCR2 antagonist, SB225002. **(C, D)** CXCR2-shRNA transfection. **(E, F)** CXCR2 neutralizing antibody reduced CXCL1-induced cell migration and VCAM-1 expression in MG63 cells. The data were collected from at least three individual experiments and expressed as mean ± S.D. $^{*}p < 0.05$ as compared to the control group; $^{\#}p < 0.05$ compared with the CXCL1-treated shRNA-control and IgG groups.

activation of NF-κB was further investigated whether it participates in CXCL1-promoted VCAM-1 expression. The chromatin immunoprecipitation (ChIP) assay was examined for evaluation and it was suggested that these pathway inhibitors could abolish the binding ability of CXCL1-induced p65 to the NF-κB binding element on the VCAM-1 promoter (**Figure 5F**). These results demonstrated that the CXCL1-driven CXCR2/FAK/PI3K/Akt pathway is involved in the regulation of NF-κB expression and nuclear translocation, and subsequently affected the expression of NF-κB-dependent VCAM-1.

Suppression of CXCL1 Expression in Osteosarcoma Reduces Metastatic Colonies Arising in Pulmonary Vasculature *In Vivo*

To confirm findings that CXCL1 is a positive regulator for osteosarcoma metastasis to the lung, an *in vivo* animal study was conducted. The transfection of CXCL1 shRNA could significantly reduce the CXCL1 protein, mRNA expression (**Figures 6A, B**), and cell migration ability of MG63 cells (**Figure 6C**).

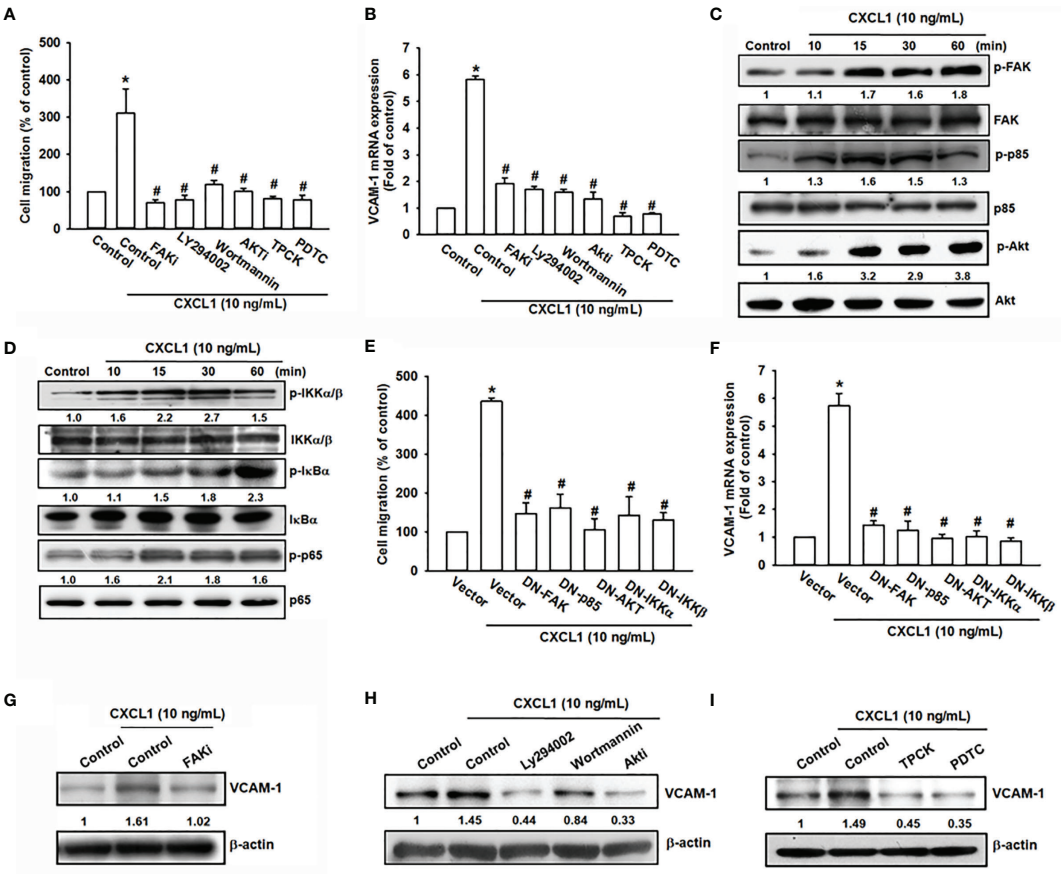

FIGURE 4 | The FAK, PI3K, Akt, and NF-κB pathways are involved in CXCL1-promoted migration and VCAM-1 expression in MG63 osteosarcoma cell. **(A, B)** CXCL1-increased cell migration and VCAM-1 mRNA expression could be reduced by pre-treated FAK inhibitor (2 μM), PI3K inhibitors LY294002 (5 μM) and wortmannin (2 μM), Akt inhibitor (5 μM), and NF-κB inhibitors TPCK (5 μM) and PDTC (1 μM) for 90 min. **(C)** Phosphorylated levels of FAK, P85, and Akt, and **(D)** phosphorylated levels of IKK, IκBα, and p65 were examined by immunoblotting assay in MG-63 cells with CXCL1 incubation for the indicated time intervals (0, 10, 15, 30, or 60 min). **(E, F)** Transfecting dominant-negative mutants of FAK, PI3K, Akt, and IKK for 24 h could suppress CXCL1 increased cell migration and VCAM-1 mRNA expression. **(G–I)** FAK, PI3K, Akt, and NF-κB inhibitors reduced CXCL1-induced VCAM-1 protein expressions. The data were collected from at least three individual experiments and expressed as mean ± S.D. $^{*}p < 0.05$ as compared to the control group; $^{\#}p < 0.05$ compared with the CXCL1-treated control or vector group.

An orthotopic mouse model was developed for osteosarcoma. MG63 cells were transduced with luciferase and clonally selected for orthotopic implantation and then orthotopically implanted into the right leg tibia. After 4 weeks, IVIS findings showed that the knockdown of CXCL1 reduced tumor metastasis to the lung (**Figure 6D**). Furthermore, the appearance, histochemistry, and number of metastasis nodules were significantly reduced in the lung specimens from sacrifice sh-CXCL1 mice as compared with their control group (**Figures 6E–G**). These results clearly suggested that the CXCL1 is a key regulator for osteosarcoma metastasis.

CXCL1 and VCAM-1 Levels Are Positively Correlated in Human Osteosarcoma Tissue

We next examined levels of CXCL1 and VCAM-1 expression in osteosarcoma specimens, to determine the prognostic relevance of CXCL1 and VCAM-1 in osteosarcoma progression. The IHC results revealed higher levels of CXCL1 and VCAM-1 expression in patients with a higher-grade osteosarcoma than in those with a lower-grade osteosarcoma; the levels of CXCL1 and VCAM-1 expression were reflected by the tumor stage (**Figures 7A–C**). These results illustrate how the levels of CXCL1 and VCAM-1 expression were significantly higher in higher-stage tumors than in lower-stage tumors. A positive correlation observed between the CXCL1 and VCAM-1 staining intensity of the human osteosarcoma tissue ($r^2 = 0.562$, **Figure 7D**) indicated that the levels of these proteins were associated with the progression of osteosarcoma.

DISCUSSION

Osteosarcoma is a common primary but aggressive with high metastatic potential cancer in the musculoskeletal system of

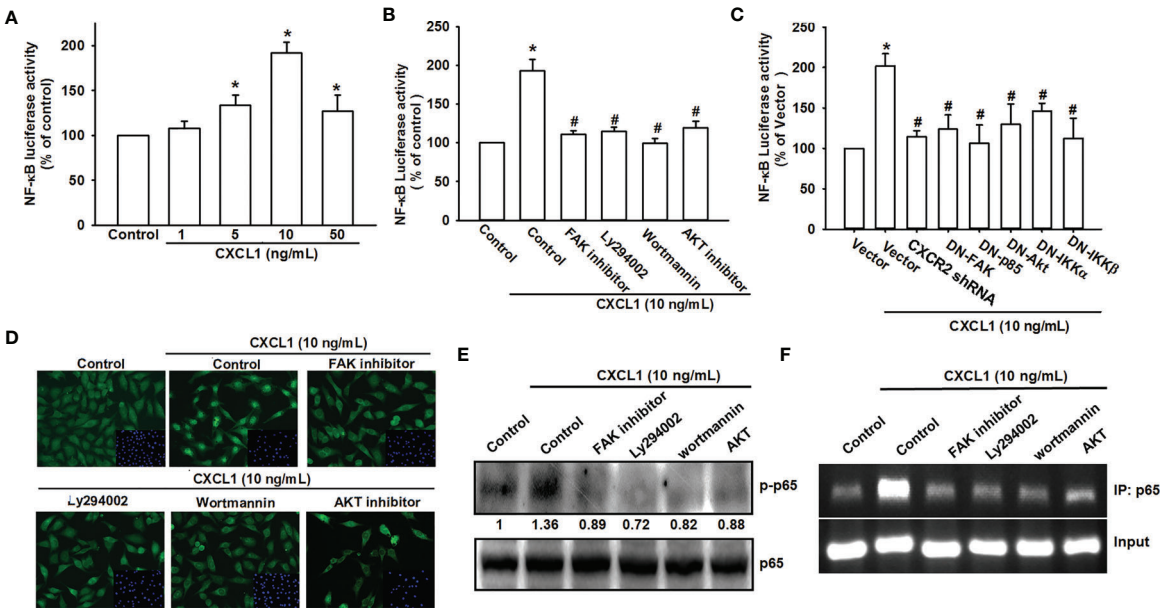

FIGURE 5 | NF-κB mediates the response of human osteosarcoma cells by CXCL1 stimulation. **(A)** The luciferase activity of NF-κB promoter plasmid was incubated with the indicated doses of CXCL1 for 24 h in MG63 cells. CXCL1 (1-50 ng/ml)-stimulated NF-κB luciferase activity was suppressed by **(B)** inhibitors of FAK, PI3K, and AKT and **(C)** dominant negative FAK, PI3K, AKT, IKK, or CXCR2 shRNA. **(D)** The anti-p65 and DAPI signals by pretreated several inhibitors and then CXCL1 (10 ng/ml)-stimulated, representative confocal microscopy images were shown. **(E)** CXCL1-induced p65 phosphorylation and **(F)** chromatin immunoprecipitation of anti-p65 in nuclear extracts of MG63 cells were measured with pretreated inhibitors. One percent of immunoprecipitated chromatin was assayed to verify equal loading (input). Results are expressed as the mean ± S.D. of triplicate samples. $^{*}p < 0.05$ as compared to the control group; $^{\#}p < 0.05$ compared with the CXCL1-treated control or vector group.

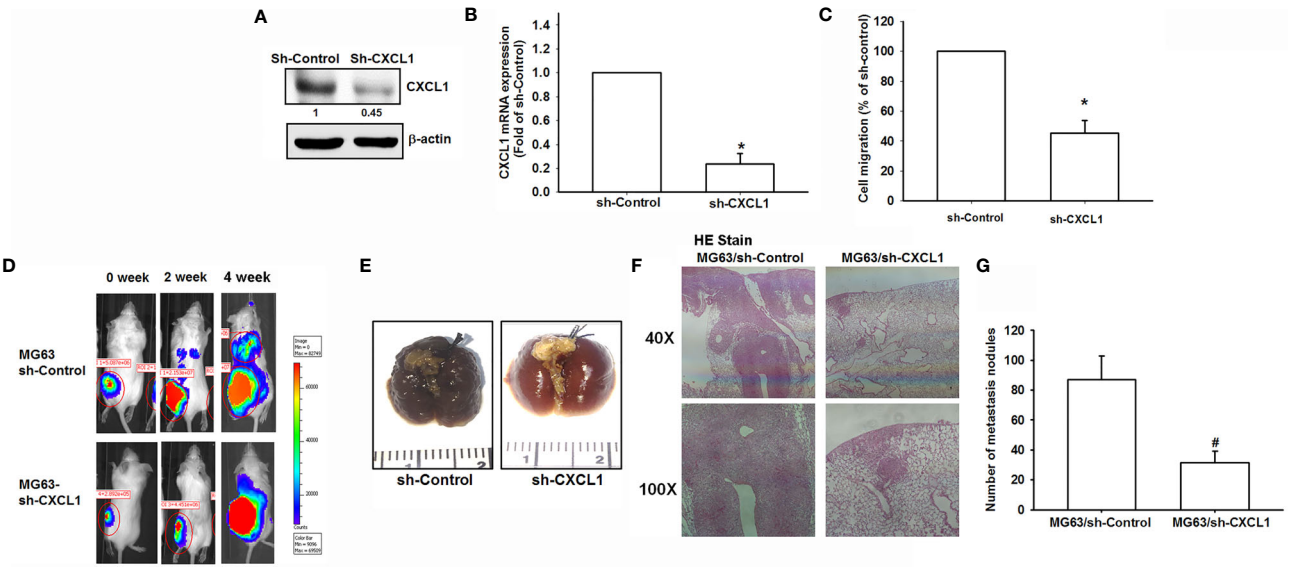

FIGURE 6 | The CXCL1/CXCR2 axis is required for osteosarcoma lung metastasis. **(A, B)** Protein and mRNA levels of CXCL1 and **(C)** cell migration ability of MG63 transfected with sh-CXCLI by immunoblotting, real-time qPCR, and Transwell assays in MG63 cells. **(D)** The mice were injected with MG63/control shRNA, or MG63/CXCL1 shRNA cells. Lung metastasis was monitored by bioluminescence imaging at the indicated time intervals. **(E–G)** The appearance of hematoxylin and eosin stain and numbers of metastasis nodules of lung specimens from sacrifice mice after 4 weeks of cell injection was shown. Results are expressed as the mean ± S.D. of triplicate samples. $^{*/\#}p < 0.05$ as compared to the shRNA-control group..

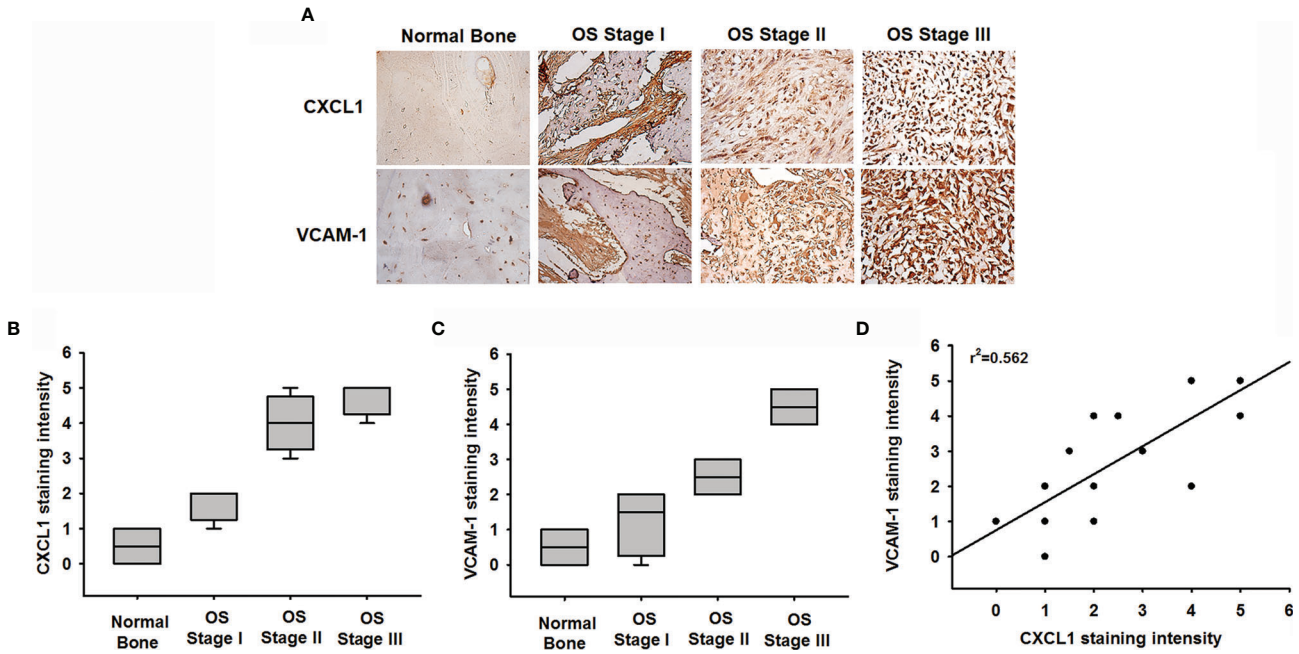

FIGURE 7 | Clinical significance of CXCL1 and VCAM-1 in osteosarcoma patient specimens. **(A)** CXCL1 and VCAM-1 expression levels in specimens were determined in a tumor tissue microarray by IHC staining. The stained specimens were photographed using an optical microscope. **(B, C)** IHC stain intensities were scored from 1 to 5 to quantify CXCL1 and VCAM-1 expression levels in different stages. **(D)** Correlation between CXCL1 and VCAM-1 expression in human osteosarcoma specimens. Results are shown as mean ± S.D.

childhood and adolescence (1, 2). The high chemoresistance development and lung metastasis propensities of osteosarcoma imply that developing an effective adjuvant therapy for inhibiting osteosarcoma metastasis is an important and urgent issue for treating osteosarcoma. Chemokines have pro-inflammatory functions and play various roles in regulations of cell activation, differentiation, adhesion, and trafficking in immune cells involved in reprogramming of somatic cells to pluripotent stem cells (39–41). Moreover, upregulations of chemokines to facilitate proliferation and manage apoptosis, survival, and metastasis in several types of cancer are observed (10, 33). Recently, evidence suggests that CXCL1 secreted from tumor through the paracrine or autocrine mechanisms attracted various inflammatory cells (10, 21, 32, 42) or stromal cells (43, 44) into the tumoral microenvironment promoting tumor growth and metastasis, such as bladder (16), lung (17), and liver metastasis colorectal cancer (42). CXCL1 could directly recruit circulatory CXCR2-expressing neutrophils and MDSCs into inflammatory sites, developing a supportive metastatic microenvironment as pre-metastatic niches (15–18, 21). A recent study suggested that CXCL1 secreted from human pulmonary artery endothelial cells played a homing role for osteosarcoma metastasis to the lung (9). In the current study, our *in vitro* and *in vivo* studies showed that CXCL1 directly facilitates cell migration and invasion abilities, and metastasis nodule formation to the lung in osteosarcoma. The result of the study firmly indicates that the CXCL1/CXCR2 is an essential axis for metastasis of osteosarcoma.

Overexpression of FAK mediating PI3K/Akt and MEK-extracellular signal-regulated kinase 1/2 (ERK1/2) signal transductions contributes to the antiapoptotic property for cancer survival (45). It is well known that the PI3K/Akt pathway is a critical regulatory signaling for almost all human cancers (46). PI3K is a heterodimer consisting of a catalytic subunit (p110) and an adaptor/regulatory subunit (p85) that could be activated by receptors with protein tyrosine kinase or G protein-coupled receptors and activated to its downstream Akt signals (47). The PI3K/Akt pathway has been approved and associated with cell-death regulation (such as suppression of Bad proapoptotic or caspase-9 induced apoptotic activities; inducing of NF-κB transcriptional activity), cell cycle progression, and cell growth (such as modulation of mTOR activity and inhibition of GSK3 catalytic activity) (47). Findings from Kinome profiling and genome-wide gene expression data showed a notable phenomenon in that most osteosarcoma cell lines existed with active Akt signals (48). This indicated that the PI3K/Akt-mediated pathways also play important roles in osteosarcoma. Moreover, serine/threonine kinases including the PI3K/Akt and MAPK signaling cascades have been suggested, which could be activated by CXCR2 receptor (36, 49). Integration of previous studies and our findings shows that dysregulation of CXCL1/CXCR2 and their downstream PI3K/Akt pathways is implicated in the metastasis progresses of osteosarcoma (invasion, migration, etc.) including several pathological progresses (tumorigenesis, proliferation, angiogenesis, and chemoresistance).

In this study, NF-κB expression and nuclear translocation could be raised by activating the PI3K/Akt pathway. NF-κB is an essential transcription factor that could bind the 5'-regulatory region of VCAM-1 promoting expression level of VCAM-1 (9, 50). According to the current results, all NF-κB inhibitors suppressed CXCL1-induced VCAM-1 mRNA, protein expressions, and migratory and invasive activities of MG63 cells, indicating that the activation of NF-κB is essential for these metastases' progress. Furthermore, CXCL1 facilitates NF-κB luciferase activity and enhances NF-κB p65 subunit to bind to the NF-κB binding site on the VCAM-1 promoter region. The CXCL1-increased activities of NF-κB upon VCAM-1 expression could be suppressed by inhibitors of CXCR2, FAK, PI3K, and Akt, indicating that these expressions are regulated by the CXCR2/FAK/PI3K/Akt pathway.

To establish the disseminated cancer cells that may finally cause metastases, the cancer cells were released by primary tumors into the circulation system at an early stage to adapt to new environmental stress, and transmigration of cells across endothelial capillary walls is the initial step (51). Transendothelial migration was the followed step, which occurred in monocytes or leukocytes that extravasate to the endothelial cell wall at inner blood vessels of the underlying tissues (52). VCAM-1 has been supported to associate with early leukocyte transmigration to the circulation system and into the extravasation to underlying tissues (52). Moreover, interactions of VCAM-1 with stroma are key factors for survival of metastatic cancer cells. A previous study has shown that lung metastatic breast cancer cells aberrantly expressed ICAM-1- and VCAM-1-promoted metastatic cells for survival in the parenchyma microenvironment of lung (53). Although ICAM-1 has also been shown to play roles during the initiation of the metastatic cascade driving tumor progression (54), this development seems to not involve the CXCL1-triggered metastatic cascade in osteosarcoma cells. Our results suggested that CXCL1 *via* the CXCR2/FAK/PI3K/Akt/NF-κB pathway enhanced VCAM-1 expression to assist the migratory and invasive activity in osteosarcoma cells. Evidence demonstrates that VCAM-1 advocated cascade relevance for tumorigenesis and metastasis and may be associated with the survival of osteosarcoma metastatic cells.

In conclusion, the current study demonstrates that chemokine CXCL1 plays a critical promotive factor *via* the CXCR2/FAK/PI3K/Akt pathway to upregulate the NF-κB expression and nuclear translocation, and further triggered the NF-κB-dependent VCAM-1 expression enhancing the migration, invasion, and homing abilities of osteosarcoma cells to the lung. Our investigation suggests that CXCL1/CXCR2, as a therapeutic candidate, can be targeted to further develop medicine to suppress or prevent the metastatic spread of osteosarcoma.

DATA AVAILABILITY STATEMENT

The raw data supporting the conclusions of this article will be made available by the authors, without undue reservation.

ETHICS STATEMENT

Ethical approval was obtained for the use of the animals, and all experiments were performed in accordance with the Guidelines for Animal Care of the Institutional Animal Care and Use Committee of College of Medicine, National Taiwan University (Approval No. 20150357).

AUTHOR CONTRIBUTIONS

J-FL, Y-CC, C-WL, and L-FH conceived and designed the experiments, which were performed by J-FL, L-FH, P-AY, M-CC, and K-TP. M-HL, M-LF, K-HL, and C-WL analyzed the data. C-WL, Y-CC, M-CC, K-TP, M-HL, and M-LF contributed reagents/materials/analysis tools. J-FL, L-FH, C-WL, and Y-CC wrote the paper. All authors contributed to the article and approved the submitted version.

FUNDING

This study was supported by grants from the Ministry of Science and Technology, Taiwan, R.O.C. (MOST 109-2320-B-255-004-MY3, MOST106-2314-B-038-099-MY3) and Taipei Medical University (TMU108-AE1-B47), and by Chang Gung Medical Research Program Foundation, grant number CMRPF6K0041, CMRPF6J0051, CMRPF6J0052 and CMRPF6K0021. Chang Gung University of Science and Technology (rants ZRRPF3K0111).

REFERENCES

1. Ottaviani G, Jaffe N. The Etiology of Osteosarcoma. *Cancer Treat Res* (2009) 152:15–32. doi: 10.1007/978-1-4419-0284-9_2
2. Arndt CA, Crist WM. Common Musculoskeletal Tumors of Childhood and Adolescence. *N Engl J Med* (1999) 341(5):342–52. doi: 10.1056/NEJM199907293410507
3. Fan TM, Roberts RD, Lizardo MM. Understanding and Modeling Metastasis Biology to Improve Therapeutic Strategies for Combating Osteosarcoma Progression. *Front Oncol* (2020) 10:13. doi: 10.3389/fonc.2020.00013
4. Isakoff MS, Bielack SS, Meltzer P, Gorlick R. Osteosarcoma: Current Treatment and a Collaborative Pathway to Success. *J Clin Oncol* (2015) 33 (27):3029–35. doi: 10.1200/JCO.2014.59.4895
5. Ando K, Mori K, Verrecchia F, Marc B, Redini F, Heymann D. Molecular Alterations Associated With Osteosarcoma Development. *Sarcoma* (2012) 2012:523432. doi: 10.1155/2012/523432
6. Briccoli A, Rocca M, Salone M, Guzzardella GA, Balladelli A, Bacci G. High Grade Osteosarcoma of the Extremities Metastatic to the Lung: Long-Term Results in 323 Patients Treated Combining Surgery and Chemotherapy, 1985-2005. *Surg Oncol* (2010) 19(4):193–9. doi: 10.1016/j.suronc.2009.05.002

7. Raman D, Sobolik-Delmaire T, Richmond A. Chemokines in Health and Disease. *Exp Cell Res* (2011) 317(5):575–89. doi: 10.1016/j.yexcr.2011.01.005
8. Sarvaiya PJ, Guo D, Ulasov I, Gabikian P, Lesniak MS. Chemokines in Tumor Progression and Metastasis. *Oncotarget* (2013) 4(12):2171–85. doi: 10.18632/oncotarget.1426
9. Chao CC, Lee CW, Chang TM, Chen PC, Liu JF. CXCL1/CXCR2 Paracrine Axis Contributes to Lung Metastasis in Osteosarcoma. *Cancers (Basel)* (2020) 12(2):459–75. doi: 10.3390/cancers12020459
10. Do HTT, Lee CH, Cho J. Chemokines and Their Receptors: Multifaceted Roles in Cancer Progression and Potential Value as Cancer Prognostic Markers. *Cancers (Basel)* (2020) 12(2):287–12. doi: 10.3390/cancers12020287
11. Lien MY, Tsai HC, Chang AC, Tsai MH, Hua CH, Wang SW, et al. Chemokine CCL4 Induces Vascular Endothelial Growth Factor C Expression and Lymphangiogenesis by miR-195-3p in Oral Squamous Cell Carcinoma. *Front Immunol* (2018) 9:412. doi: 10.3389/fimmu.2018.00412
12. Liu GT, Huang YL, Tzeng HE, Tsai CH, Wang SW, Tang CH. CCL5 Promotes Vascular Endothelial Growth Factor Expression and Induces Angiogenesis by Down-Regulating miR-199a in Human Chondrosarcoma Cells. *Cancer Lett* (2015) 357(2):476–87. doi: 10.1016/j.canlet.2014.11.015
13. Dhawan P, Richmond A. Role of CXCL1 in Tumorigenesis of Melanoma. *J Leukoc Biol* (2002) 72(1):9–18. doi: 10.1189/jlb.72.1.9
14. Eash KJ, Greenbaum AM, Gopalan PK, Link DC. CXCR2 and CXCR4 Antagonistically Regulate Neutrophil Trafficking From Murine Bone Marrow. *J Clin Invest* (2010) 120(7):2423–31. doi: 10.1172/JCI41649
15. Jaffer T, Ma D. The Emerging Role of Chemokine Receptor CXCR2 in Cancer Progression. *Trans Cancer Res* (2016) 5(Suppl 4):S616–28. doi: 10.21037/tcr.2016.10.06
16. Miyake M, Hori S, Morizawa Y, Tatsumi Y, Nakai Y, Anai S, et al. CXCL1-Mediated Interaction of Cancer Cells With Tumor-Associated Macrophages and Cancer-Associated Fibroblasts Promotes Tumor Progression in Human Bladder Cancer. *Neoplasia* (2016) 18(10):636–46. doi: 10.1016/j.neo.2016.08.002
17. Yuan M, Zhu H, Xu J, Zheng Y, Cao X, Liu Q. Tumor-Derived CXCL1 Promotes Lung Cancer Growth *via* Recruitment of Tumor-Associated Neutrophils. *J Immunol Res* (2016) 2016:6530410. doi: 10.1155/2016/6530410
18. Hardaway AL, Herroon MK, Rajagurubandara E, Podgorski I. Marrow Adipocyte-Derived CXCL1 and CXCL2 Contribute to Osteolysis in Metastatic Prostate Cancer. *Clin Exp Metastasis* (2015) 32(4):353–68. doi: 10.1007/s10585-015-9714-5
19. Ogata H, Sekikawa A, Yamagishi H, Ichikawa K, Tomita S, Imura J, et al. GROalpha Promotes Invasion of Colorectal Cancer Cells. *Oncol Rep* (2010) 24(6):1479–86. doi: 10.3892/or_00001008
20. Xiang Z, Jiang DP, Xia GG, Wei ZW, Chen W, He Y, et al. CXCL1 Expression Is Correlated With Snail Expression and Affects the Prognosis of Patients With Gastric Cancer. *Oncol Lett* (2015) 10(4):2458–64. doi: 10.3892/ol.2015.3614
21. Li L, Xu L, Yan J, Zhen ZJ, Ji Y, Liu CQ, et al. CXCR2-CXCL1 Axis Is Correlated With Neutrophil Infiltration and Predicts a Poor Prognosis in Hepatocellular Carcinoma. *J Exp Clin Cancer Res* (2015) 34:129. doi: 10.1186/s13046-015-0247-1
22. Acharyya S, Oskarsson T, Vanharanta S, Malladi S, Kim J, Morris PG, et al. A CXCL1 Paracrine Network Links Cancer Chemoresistance and Metastasis. *Cell* (2012) 150(1):165–78. doi: 10.1016/j.cell.2012.04.042
23. Xu J, Zhang C, He Y, Wu H, Wang Z, Song W, et al. Lymphatic Endothelial Cell-Secreted CXCL1 Stimulates Lymphangiogenesis and Metastasis of Gastric Cancer. *Int J Cancer* (2012) 130(4):787–97. doi: 10.1002/ijc.26035
24. Cheng WL, Wang CS, Huang YH, Tsai MM, Liang Y, Lin KH. Overexpression of CXCL1 and Its Receptor CXCR2 Promote Tumor Invasion in Gastric Cancer. *Ann Oncol* (2011) 22(10):2267–76. doi: 10.1093/annonc/mdq739
25. Kawanishi H, Matsui Y, Ito M, Watanabe J, Takahashi T, Nishizawa K, et al. Secreted CXCL1 Is a Potential Mediator and Marker of the Tumor Invasion of Bladder Cancer. *Clin Cancer Res* (2008) 14(9):2579–87. doi: 10.1158/1078-0432.CCR-07-1922
26. Han KQ, He XQ, Ma MY, Guo XD, Zhang XM, Chen J, et al. Targeted Silencing of CXCL1 by siRNA Inhibits Tumor Growth and Apoptosis in Hepatocellular Carcinoma. *Int J Oncol* (2015) 47(6):2131–40. doi: 10.3892/ijo.2015.3203
27. Bandapalli OR, Ehrmann F, Ehemann V, Gaida M, Macher-Goeppinger S, Wente M, et al. Down-Regulation of CXCL1 Inhibits Tumor Growth in Colorectal Liver Metastasis. *Cytokine* (2012) 57(1):46–53. doi: 10.1016/j.cyto.2011.10.019
28. Schlesinger M, Bendas G. Vascular Cell Adhesion Molecule-1 (VCAM-1)–an Increasing Insight Into Its Role in Tumorigenicity and Metastasis. *Int J Cancer* (2015) 136(11):2504–14. doi: 10.1002/ijc.28927
29. Kong DH, Kim YK, Kim MR, Jang JH, Lee S. Emerging Roles of Vascular Cell Adhesion Molecule-1 (VCAM-1) in Immunological Disorders and Cancer. *Int J Mol Sci* (2018) 19(4):1057–73. doi: 10.3390/ijms19041057
30. Wang LH, Tsai HC, Cheng YC, Lin CY, Huang YL, Tsai CH, et al. CTGF Promotes Osteosarcoma Angiogenesis by Regulating miR-543/Angiopoietin 2 Signaling. *Cancer Lett* (2017) 391:28–37. doi: 10.1016/j.canlet.2017.01.013
31. Hou CH, Lin FL, Hou SM, Liu JF. Cyr61 Promotes Epithelial-Mesenchymal Transition and Tumor Metastasis of Osteosarcoma by Raf-1/MEK/ERK/Elk-1/TWIST-1 Signaling Pathway. *Mol Cancer* (2014) 13:236. doi: 10.1186/1476-4598-13-236
32. Miles FL, Pruitt FL, van Golen KL, Cooper CR. Stepping Out of the Flow: Capillary Extravasation in Cancer Metastasis. *Clin Exp Metastasis* (2008) 25(4):305–24. doi: 10.1007/s10585-007-9098-2
33. Liu JF, Lee CW, Lin CY, Chao CC, Chang TM, Han CK, et al. CXCL13/CXCR5 Interaction Facilitates VCAM-1-Dependent Migration in Human Osteosarcoma. *Int J Mol Sci* (2020) 21(17):6095–108. doi: 10.3390/ijms21176095
34. Chang AC, Chen PC, Lin YF, Su CM, Liu JF, Lin TH, et al. Osteoblast-Secreted WISP-1 Promotes Adherence of Prostate Cancer Cells to Bone *via* the VCAM-1/Integrin Alpha4beta1 System. *Cancer Lett* (2018) 426:47–56. doi: 10.1016/j.canlet.2018.03.050
35. Yang G, Rosen DG, Liu G, Yang F, Guo X, Xiao X, et al. CXCR2 Promotes Ovarian Cancer Growth Through Dysregulated Cell Cycle, Diminished Apoptosis, and Enhanced Angiogenesis. *Clin Cancer Res* (2010) 16(15):3875–86. doi: 10.1158/1078-0432.CCR-10-0483
36. Cohen-Hillel E, Yron I, Meshel T, Soria G, Attal H, Ben-Baruch A. CXCL8-Induced FAK Phosphorylation *via* CXCR1 and CXCR2: Cytoskeleton- and Integrin-Related Mechanisms Converge With FAK Regulatory Pathways in a Receptor-Specific Manner. *Cytokine* (2006) 33(1):1–16. doi: 10.1016/j.cyto.2005.11.006
37. Liu JF, Lee CW, Tsai MH, Tang CH, Chen PC, Lin LW, et al. Thrombospondin 2 Promotes Tumor Metastasis by Inducing Matrix Metalloproteinase-13 Production in Lung Cancer Cells. *Biochem Pharmacol* (2018) 155:537–46. doi: 10.1016/j.bcp.2018.07.024
38. Tang CH, Tan TW, Fu WM, Yang RS. Involvement of Matrix Metalloproteinase-9 in Stromal Cell-Derived Factor-1/CXCR4 Pathway of Lung Cancer Metastasis. *Carcinogenesis* (2008) 29(1):35–43. doi: 10.1093/carcin/bgm220
39. Lee SJ, Kang KW, Kim JH, Lee BH, Jung JH, Park Y, et al. CXCR2 Ligands and mTOR Activation Enhance Reprogramming of Human Somatic Cells to Pluripotent Stem Cells. *Stem Cells Dev* (2020) 29(3):119–32. doi: 10.1089/scd.2019.0188
40. Mantovani A, Sica A, Sozzani S, Allavena P, Vecchi A, Locati M. The Chemokine System in Diverse Forms of Macrophage Activation and Polarization. *Trends Immunol* (2004) 25(12):677–86. doi: 10.1016/j.it.2004.09.015
41. Moser B, Willimann K. Chemokines: Role in Inflammation and Immune Surveillance. *Ann Rheum Dis* (2004) 63(Suppl 2):ii84–9. doi: 10.1136/ard.2004.028316
42. Wang D, Sun H, Wei J, Cen B, DuBois RN. CXCL1 Is Critical for Premetastatic Niche Formation and Metastasis in Colorectal Cancer. *Cancer Res* (2017) 77(13):3655–65. doi: 10.1158/0008-5472.CAN-16-3199
43. Kasashima H, Yashiro M, Nakamae H, Masuda G, Kinoshita H, Morisaki T, et al. Clinicopathologic Significance of the CXCL1-CXCR2 Axis in the Tumor Microenvironment of Gastric Carcinoma. *PloS One* (2017) 12(6):e0178635. doi: 10.1371/journal.pone.0178635
44. Zhang T, Tseng C, Zhang Y, Sirin O, Corn PG, Li-Ning-Tapia EM, et al. CXCL1 Mediates Obesity-Associated Adipose Stromal Cell Trafficking and Function in the Tumour Microenvironment. *Nat Commun* (2016) 7:11674. doi: 10.1038/ncomms11674
45. Tai YL, Chen LC, Shen TL. Emerging Roles of Focal Adhesion Kinase in Cancer. *BioMed Res Int* (2015) 2015:690690. doi: 10.1155/2015/690690

46. Porta C, Paglino C, Mosca A. Targeting PI3K/Akt/mTOR Signaling in Cancer. *Front Oncol* (2014) 4:64. doi: 10.3389/fonc.2014.00064
47. Fresno Vara JA, Casado E, de Castro J, Cejas P, Belda-Iniesta C, Gonzalez-Baron M. PI3K/Akt Signalling Pathway and Cancer. *Cancer Treat Rev* (2004) 30(2):193–204. doi: 10.1016/j.ctrv.2003.07.007
48. Kuijjer ML, van den Akker BE, Hilhorst R, Mommersteeg M, Buddingh EP, Serra M, et al. Kinome and mRNA Expression Profiling of High-Grade Osteosarcoma Cell Lines Implies Akt Signaling as Possible Target for Therapy. *BMC Med Genomics* (2014) 7:4. doi: 10.1186/1755-8794-7-4
49. Waugh DJ, Wilson C. The Interleukin-8 Pathway in Cancer. *Clin Cancer Res* (2008) 14(21):6735–41. doi: 10.1158/1078-0432.CCR-07-4843
50. Sharma R, Sharma R, Khaket TP, Dutta C, Chakraborty B, Mukherjee TK. Breast Cancer Metastasis: Putative Therapeutic Role of Vascular Cell Adhesion Molecule-1. *Cell Oncol (Dordr)* (2017) 40(3):199–208. doi: 10.1007/s13402-017-0324-x
51. Husemann Y, Geigl JB, Schubert F, Musiani P, Meyer M, Burghart E, et al. Systemic Spread Is an Early Step in Breast Cancer. *Cancer Cell* (2008) 13 (1):58–68. doi: 10.1016/j.ccr.2007.12.003
52. Muller WA. Mechanisms of Leukocyte Transendothelial Migration. *Annu Rev Pathol* (2011) 6:323–44. doi: 10.1146/annurev-pathol-011110-130224
53. Chen Q, Zhang XH, Massague J. Macrophage Binding to Receptor VCAM-1 Transmits Survival Signals in Breast Cancer Cells That Invade the Lungs. *Cancer Cell* (2011) 20(4):538–49. doi: 10.1016/j.ccr.2011.08.025
54. Benedicto A, Romayor I, Arteta B. Role of Liver ICAM-1 in Metastasis. *Oncol Lett* (2017) 14(4):3883–92. doi: 10.3892/ol.2017.6700

Conflict of Interest: The authors declare that the research was conducted in the absence of any commercial or financial relationships that could be construed as a potential conflict of interest.

frontiers in Oncology

ORIGINAL RESEARCH
published: 18 November 2021
doi: 10.3389/fonc.2021.765151

TGFβ Signaling in Myeloid Cells Promotes Lung and Liver Metastasis Through Different Mechanisms

Cristina Stefanescu[1], *Merel Van Gogh*[1], *Marko Roblek*[1,2], *Mathias Heikenwalder*[3] *and Lubor Borsig*[1,4*]

[1] Institute of Physiology, University of Zurich, Zurich, Switzerland, [2] Institute of Science and Technology (IST) Austria, Klosterneuburg, Austria, [3] Division of Chronic Inflammation and Cancer, German Cancer Research Center (DKFZ), Heidelberg, Germany, [4] Comprehensive Cancer Center Zurich, Zurich, Switzerland

TGFβ overexpression is commonly detected in cancer patients and correlates with poor prognosis and metastasis. Cancer progression is often associated with an enhanced recruitment of myeloid-derived cells to the tumor microenvironment. Here we show that functional TGFβ-signaling in myeloid cells is required for metastasis to the lungs and the liver. Myeloid-specific deletion of Tgfbr2 resulted in reduced spontaneous lung metastasis, which was associated with a reduction of proinflammatory cytokines in the metastatic microenvironment. Notably, $CD8^+$ T cell depletion in myeloid-specific *Tgfbr2*-deficient mice rescued lung metastasis. Myeloid-specific *Tgfbr2*-deficiency resulted in reduced liver metastasis with an almost complete absence of myeloid cells within metastatic foci. On contrary, an accumulation of Tgfβ-responsive myeloid cells was associated with an increased recruitment of monocytes and granulocytes and higher proinflammatory cytokine levels in control mice. Monocytic cells isolated from metastatic livers of *Tgfbr2*-deficient mice showed increased polarization towards the M1 phenotype, Tnfα and Il-1β expression, reduced levels of M2 markers and reduced production of chemokines responsible for myeloid-cell recruitment. No significant differences in Tgfβ levels were observed at metastatic sites of any model. These data demonstrate that Tgfβ signaling in monocytic myeloid cells suppresses $CD8^+$ T cell activity during lung metastasis, while these cells actively contribute to tumor growth during liver metastasis. Thus, myeloid cells modulate metastasis through different mechanisms in a tissue-specific manner.

Keywords: tumor microenvironment, metastasis, TGFβ, mouse model, lung, liver, myeloid cells

OPEN ACCESS

Edited by:
Guisheng Song,
University of Minnesota, United States

Reviewed by:
Eswari Dodagatta-Marri,
University of California, San Francisco, United States
Richa Shrivastava,
Birla Institute of Technology and Science, India

***Correspondence:**
Lubor Borsig
lborsig@access.uzh.ch

Specialty section:
This article was submitted to Molecular and Cellular Oncology, a section of the journal Frontiers in Oncology

Received: *26 August 2021*
Accepted: *01 November 2021*
Published: *18 November 2021*

Citation:
Stefanescu C, Van Gogh M, Roblek M, Heikenwalder M and Borsig L (2021) TGFβ Signaling in Myeloid Cells Promotes Lung and Liver Metastasis Through Different Mechanisms. Front. Oncol. 11:765151. doi: 10.3389/fonc.2021.765151

INTRODUCTION

The main cause of cancer-related fatalities in patients is metastasis, a multistep process enabling tumor cells to spread through blood circulation and to form metastasis in distant organs. Stromal cells such as fibroblasts, endothelial and immune cells are integral parts of both primary tumor and metastatic lesions (1, 2). Tumor cells together with stromal cells produce cytokines that orchestrate

the formation of a tumor microenvironment, which promotes cancer progression. The TGFβ family of cytokines are directly linked to tumorigenesis, where they actively promote tumorigenesis through a modulation of the tumor microenvironment during metastasis (3–5).

TGFβ cytokines are involved in a wide range of biological processes, such as cell proliferation, differentiation, wound healing, and immune cell regulation (3). TGFβ-signaling is initiated by binding to TGFβ receptor I (TGFβRI), which recruits and phosphorylates TGFβ receptor II (TGFβRII), and results in activation of: the canonical pathway, involving SMAD proteins regulating a wide range of genes; and the non-canonical pathway that includes MAPK and PI3K signaling (4). In the context of cancer, TGFβ1 can act both as a tumor suppressor, in the early stages of cancer, and as a tumor promoter, in the later stages of tumor progression. In advanced cancers, however; TGFβ expression and activation strongly correlate with poor prognosis due to metastasis (4, 6).

TGFβ is an immunosuppressive cytokine produced by tumor cells and immune cells that polarizes both the innate and the adaptive immune system (7) and represents a primary mechanism of immune evasion (8). TGFβ inhibits NK cell function by decreasing cytokine production and in dendritic cells downregulates the expression of MHCII and co-stimulatory molecules. Within the tumor microenvironment, TGFβ signaling promotes immune suppression of macrophages and neutrophils, which results in alternatively polarized phenotypes of M2 and N2, respectively. In the lymphoid compartment, TGFβ dampens the activity of $CD4^+$ T helper and of $CD8^+$ cytotoxic T cells and promotes the activity of regulatory T (Treg) cells (7).

Myeloid cells promote immune suppression and formation of a metastatic niche and are abundantly present in cancer patients both as circulating cells in the blood and in tumor tissues (9–12). Systemic expansion of immature myeloid cells during cancer progression can be divided into two subpopulations of granulocytic ($CD11b^+/Ly6G^+$) and monocytic ($CD11b^+/Ly6C^{hi}$) myeloid-derived suppressor cells (9). In the tumor microenvironment TGFβ is an important factor promoting immune-suppressive polarization of myeloid-derived cells. Breast cancer metastasis to the lungs was dependent on myeloid cell recruitment and formation of pro-tumorigenic microenvironment (13). Inhibition of Tgfβ in tumor bearing-mice resulted in increased infiltration of cytotoxic $CD11b^+/Ly6G^+$-derived neutrophils and reduced tumor growth (14). Initial studies in mice with *Tgfbr2*-deficiency in myeloid cells showed reduced tumor growth, which was associated with an increased anti-tumor polarization of macrophages (15). Further studies in *Tgfbr2*-myeloid cell deficient mice showed reduced lung metastasis in 4T1 mammary tumor model (16, 17), which was ascribed to enhanced presence of cytotoxic $CD8^+$ T cells (16). Tumor-associated myeloid cells express CCL9 chemokine, which is upregulated in a TGFβ-dependent manner (17). The overexpression of CCL9 in *Tgfbr2*-deficient myeloid cells enabled metastasis. In a recent study, the CXCL1-CXCR2 axis was identified to mediate myeloid cell recruitment to the pre-metastatic liver (10). However, the contributing effects of TGFβ signaling during liver metastasis remain unclear.

The current study investigates and compares the tissue-specific role of TGFβ signaling in myeloid cells and its influence on the metastatic microenvironment in lung and liver metastasis using a LysMCre/$Tgfbr2^{fl/fl}$ mouse model.

MATERIALS AND METHODS

Cell Culture

MC-38GFP murine colon carcinoma cell line (18), LLC1.1 Lewis lung carcinoma, 3LL lung carcinoma, and B16-BL6 were grown in DMEM high glucose medium (Life Technologies) containing 10% fetal bovine serum (FBS) as described previously (19).

Mice

LysMCre/$Tgfbr2^{fl/fl}$ mouse in a C57BL/6J background was obtained from M. Heikewälder (University of Zurich). The mouse strain *ROSA-STOP*$^{fl/fl}$*-dTomato* was obtained from The Jackson Laboratory. All mice were in the C57BL76J background. Both males and female animals in the age of 7-10 weeks of age were used in all experiments. All animal experiments were performed according to the guidelines of the Swiss Animal Protection Law, and approved by the Veterinary Office of Kanton Zurich.

Metastasis Models

Spontaneous lung metastasis. Lewis lung carcinoma cells LLC1.1 (300,000 cells) were subcutaneously (s.c.) injected into a right flank of a mouse. The primary tumor was removed after 18 days and the extent of lung metastasis was evaluated two weeks after tumor removal. *Experimental liver metastasis.* MC-38GFP colon cancer cells (300,000 cells) were injected into the spleen of an anesthetized mouse. Splenectomy was performed three minutes after the tumor cell injection. Mice were terminated on day 28 and liver metastasis was evaluated. *Experimental lung metastasis.* MC-38GFP (300,000 cells) were intravenously injected and mice were terminated 28 days after the injection. 3LL and B16-BL6 cells (150,000 cells) were intravenously injected and lungs analyzed on day 14 (19). Surface metastasis were counted in perfused lung and liver tissues.

Immunohistochemistry

Tissues paraffin sections (3 μm) were stained with hematoxylin/eosin or the anti-GFP antibody (Fitzgerald Industries Int.) Ki67 (NeoMarkers) and cleaved caspase-3 (BD). Quantification of tumor cells in seven sections of lungs separated by 20 μm was performed. Staining was performed on a NEXES immunohistochemistry robot using an IVIEW DAB Detection Kit (Ventana Instruments, Switzerland). Images were digitalized on Zeiss MiraxMidi Slide Scanner and analyzed with Panoramic Viewer (3DHISTECH). For cryosections, tissues were fixed in 3% paraformaldehyde for 1 hour at 4°C, incubated in 20% sucrose overnight at 4°C, embedded in an OCT compound and snap-frozen in a bath containing methylbutane and dry ice.

Cryosections (10 μm) were blocked with phosphate buffer saline (PBS) containing 5% FCS and 5% rat serum, and incubated with AlexaFluor 647-coupled rat-anti-F4/80 antibody (Clone BM8, Biolegend). Slides were counterstained with DAPI and embedded in Prolong and evaluated on Leica Thunder Microscope.

Flow Cytometry Analysis

Mice were perfused with PBS and dissected tissues were minced and digested with Collagenase A and D (1 mg/mL, both from Roche), in 2 mL of RPMI medium containing 3% BSA for 1 hour at 37°C. The cell suspension was prepared by passing the homogenate five times through 18G needle followed by a 100μm cell strainer. In case of liver, the cell suspension was centrifuged at 500 rpm for one minute to separate the parenchyma. After centrifugation of the single cell suspension, erythrocytes lysed with ACK buffer and cells were passed through a 70μm cell strainer. The pellet was resuspended in a FACS buffer (PBS/2% FBS/5mM EDTA) and stained with Zombie Fixable Viability Kit (Biolegend), followed by incubation with anti-mouse CD16/32 mAb for 10 min on ice. Single cell suspensions were stained with the following antibodies: anti-CD45 (clone 30-F11), anti-CD11b (clone M1/70), anti-F4/80 (clone BM8), anti-Ly6G (clone 1A8), anti-Ly6C (clone HK1.4), anti-MHCII (clone M5/114.15.2), anti-CD31 (clone 390), CD4 (clone GK1.5), anti-CD8 (clone 53-6.7) and anti-PD1 (clone 29F.1A12) (all from Biolegend) for 30 min on ice. Data was acquired on a FACSCanto II (BD Biosciences), during cell quantification together with CountBright absolute counting beads (Life Technologies) and analyzed using Flow Jo software v. 7.6.5 (Tree Star). Samples for CD8 cell activation assessment were fixed and permeabilized using FoxP3/Transcription Factor Staining Buffer Set (eBioscience). Subsequently samples were stained for intra-cellular markers with the following antibodies: anti-Granzyme B (clone GB11) and anti-Perforin (clone S16009A) from Biolegend. CD8 cell activation was analyzed using the Cytek Aurora 5L – Spectral Analyzer from the Cytometry Facility at the University of Zurich.

Cell Sorting and Quantitative PCR

Tissues were processed the same way as described for flow cytometry analysis. Individual cell populations were sorted using a BD Aria III in FACS buffer at 4°C using a 100 μm nozzle. From at least 100'000 sorted cells RNA was isolated using the RNA Easy Plus Mini kit (Qiagen) and cDNA was prepared using 250 ng of RNA using Omniscript RT kit (Qiagen) according to the manufacturer's instructions. Real-time PCR was performed with KAPA Sybr FAST Universal (Sigma) using intron-spanning primers (**Supplementary Table S1**) and analyzed in a CFX96 Touch Real-Time PCR Detection System (Biorad). GAPDH was used as an internal control.

Fluorescent Beads Uptake Assay

Red fluorescence beads (Sigma) were diluted 1:20 in PBS and 100 μl was intravenously injected through a tail-vein per mouse. Mice were terminated after 9 hours, blood and organs were collected and processed as described in flow cytometry analysis.

Reactive Oxygen Species (ROS) Determination

Tumor bearing mice (subcutaneous LLC1.1 tumor) were anesthetized, the lungs perfused with PBS and through heart perfused with pre-warmed 5 μM CellROX® Oxidative Stress Green Reagent (Invitrogen) and the vessels clipped. After 30 min of incubation, the lungs were again perfused with PBS, digested with collagenase and single cell suspension stained with anti-Ly6G antibody and the ROS signal was quantified by flow cytometry.

Tumor Cell *In Vivo* Seeding Assay

MC-38-luciferase expressing cells (300,000) were injected through spleen in mice and at indicated time points, mice were anesthetized, subcutaneously injected with D-luciferin firefly (150 μg/g mouse) and after 8 min terminated. Mice were perfused with PBS and the luciferase activity in the liver was determined using IVIS imaging. After the intravenous injection of 300,000 MC-38GFP cells mice were terminated at indicated time points; mice perfused with PBS and lungs processed for histological analysis.

Antibody Depletion Experiments

Depletion of $CD8^+$ T cells in a lung metastasis model using LLC1.1 cells was performed with 10 μg anti-CD8 antibody (clone 2.43; BioXCell) i.v. injected one day prior to primary tumor removal. Mice received another 15 μg of the antibody by i.v. injection two days after the tumor removal. Control mice received the isotype control antibody (clone 2A3, BioXCell) in parallel. In the liver metastasis model, mice received 10 μg Ab injection 1 day before tumor cell injection and the second treatment with 15 μg Ab two days after tumor cell injection.

Neutrophil depletion was achieved by intraperitoneal injection (i.p.) of anti-Ly6G antibody (clone 1A8; BioXCell). Initial injection of 500 μg/mouse was performed 24 hours prior to intrasplenic injection of MC-38GFP cells. Mice were treated three times weekly with 100 μg i.p. until the termination at day 27. Control animals were injected with isotype-control Ab (clone 2A3, BioXCell) in parallel.

Cytokine Analysis

Snap-frozen tissues were homogenized using Polytron® in lysis buffer (FACS buffer containing 1x complete EDTA free proteinase inhibitor cocktail from Roche). After 15 min centrifugation at 14'000 rpm at 4°C, was determined the protein concentration in the supernatant was determined with BCA Protein Assay (Thermo Fischer). Cytokine concentrations were measured in a total of 200-500 μg of tissue lysate using the ProcartaPlex 23 Plex and the LegendPlex Mouse Proinflammatory Chemokine panel (Thermo Fischer) following the manufacturer's instructions. TGFβ1 was determined using the TGFβ Platinum Elisa (Thermo Fisher), where samples were activated with 1N HCl for 10 min at RT in a ratio of sample to HCl 5:1. The reaction was neutralized using 1 part of 1N NaOH/0.5M HEPES. Sorted tdT^+ $Ly6C^{hi}$ monocytes (20'000 cells/well) from livers of mice at day 14-post-intrasplenic injection of MC-38GFP cells were stimulated overnight (14 hrs) with PMA

(20 ng/ml), ionomycin (1μg/ml) and LPS (1 μg/ml). Cytokine production was detected in the supernatant after 14 h stimulation as described above.

RESULTS

Myeloid-Specific Deletion of Tgfbr2 Attenuates Lung and Liver Metastasis

Myeloid cells are the dominant population of immune cells associated with metastatic progression (20–22); and TGFβ is an immunosuppressive cytokine family that promotes metastases through modulations of the tumor microenvironment (7). To assess the role of Tgfβ-signaling in myeloid cells during lung and liver metastasis, we generated a mouse with myeloid cell-specific deletion of TGFβ receptor II (LysMCre^{+}/*Tgfbr2*$^{fl/fl}$ mouse, hereafter TR2^{my}KO) by crossing the *Tgfbr2*$^{fl/fl}$ mouse with a mouse expressing Cre under the control of the Lysozyme promoter (LysMCre). LysMCre^{neg}/*Tgfbr2*$^{fl/fl}$ (hereafter Ctrl) served as a control.

First, we tested the role of myeloid cell-derived Tgfβ-signaling during liver metastasis. We used an experimental liver metastasis model, where MC-38 murine colon carcinoma cells stably expressing GFP (MC-38GFP) were injected into the spleen. Significant reduction of metastatic foci and liver-body mass ratio was observed in TR2^{my}KO mice when compared to Ctrl mice (**Figure 1A**). The size of liver metastatic lesions was also significantly reduced in TR2^{my}KO mice (**Figure 1B**). To test whether myeloid cells affect tumor cell seeding to the liver in a Tgfβ-dependent manner, we intrasplenically injected MC-38-luciferase expressing cells and analyzed livers 9 and 24 hours post-tumor cell-injection using bioluminescence imaging (**Figure 1C**). No difference in tumor cell detection in the liver was observed between TR2^{my}KO and Ctrl mice, indicating that Tgfβ-signaling pathway in myeloid cells is not affecting initial tissue colonization.

Second, we tested whether Tgfβ-signaling deficiency in myeloid cells affects lung metastasis. Myeloid cells were previously shown to promote metastatic seeding to the lungs (22–24). Using three different cell lines, MC-38, Lewis lung carcinoma 3LL and B16-Bl6 melanoma in experimental lung metastasis models, we observed reduced metastasis in TR2^{my}KO mice (**Figure 1D** and **Supplementary Figures 1A, B**). To assess the effect of myeloid Tgfβ-deficiency on lung metastasis, we analyzed tissues sections two, four and seven days post-tumor cell injection. While the number of single tumor cells was similar in TR2^{myelo}KO and Ctrl mice at every time point, we observed a significant reduction of small clusters (2-10 tumor cells) and large cluster (more than 10 tumor cells) at day 4 and day 7 post-tumor cell challenge in TR2^{my}KO mice (**Figure 1E**). These findings indicate that the metastatic outgrowth in TR2^{my}KO mice has been greatly hampered (2-10 cells foci) or impaired (>10 cells foci). Next, we used the spontaneous lung metastasis model, where mice were subcutaneously (s.c.) injected with Lewis lung carcinoma (LLC1.1) cells. At day 18 the primary tumor was surgically removed and after another 14 days lung metastasis was analyzed. While no difference in the primary tumor growth between TR2^{my}KO and Ctrl mice was observed (**Supplementary Figure 1C**), a significant reduction of lung metastasis was detected in TR2^{my}KO mice (**Figure 1F**).

Increased Presence of Tgfβ-Responsive Myeloid Cells During Liver Metastasis

To understand the role of myeloid cell Tgfβ-signaling during liver metastasis, we analyzed these cells in metastatic livers at two different time points after tumor cell injection: 14 days – microscopic metastasis, 28 days – macroscopic metastasis, and compared the changes to naïve mice. We observed increased numbers of inflammatory monocytes (Ly6C^{hi}) and neutrophils (Ly6G^{+}) in Ctrl mice, which were significantly reduced in TR2^{my}KO at day 28 (**Figure 2A**). There were no changes in lymphoid CD4^{+} or CD8^{+} cells at any time point. Next, we analyzed cytokine levels in metastatic livers (**Figure 2B**). Increased levels of Ccl2, Ccl7, Cxcl1, and Cxcl10 chemokines both at day 14 and at day 28 in Ctrl mice correlated well with respective increased cytokine levels (**Figure 2C**). Both lower levels of cytokines and reduced myeloid cell number were detected in TR2^{my}KO mice. Increased amounts of Tgfβ1 cytokine were detected in metastatic livers at day 14, irrespective of mouse genotype, which decreased to levels observed in naïve mice at day 28 (**Figure 2D**).

Next, we aimed to detect myeloid cells in liver metastatic lesions. We prepared a mouse by breeding of LysMCre^{+}/*Tgfbr2*$^{fl/fl}$ strain into a transgenic mouse, Ai14, carrying loxP-flanked STOP cassette followed by tdTomato inserted into the ROSA26 locus. We analyzed myeloid cells from naïve LysMCre^{+}/*Tgfbr2*$^{fl/fl}$/tdT^{+} mice (TR2^{my}KO/tdT) and LysMCre/*Tgfbr2*^{wt}/tdT^{+}, wild-type allele (Ctrl/tdT) mice, and detected over 90% tdT^{+} Ly6G^{+} and over 30% tdT^{+} of Ly6C^{hi} cells in liver, lungs and spleen (**Supplementary Figure 2**). When MC-38GFP tumor cells were injected intrasplenically into TR2^{my}KO/tdT and Ctrl/tdT mice, we observed increased numbers of both Ly6C^{hi} and Ly6G^{+} cells in Ctrl/tdT mice by flow cytometry, while in TR2^{my}KO/tdT mice these myeloid cells were hardly present in the metastatic lesions (**Figure 3A**). These results confirm our previous data (**Figure 2A**). The histological analysis of liver sections at day 14 and 28 days post-tumor cell injection substantiated the finding of a pronounced reduction of tdT-positive cells within metastatic foci in TR2^{my}KO/tdT when compared to Ctrl/tdT mice (**Figure 3B**). Furthermore, large proportion of tdT-positive cells were positive for an F4/80 antigen (**Figure 3C**), indicating differentiation of myeloid-derived cells into macrophages. Histological analysis of metastatic livers for proliferating cells (Ki67^{+} cells) and for apoptotic cells (cleave-caspase3^{+} cells) revealed no obvious differences between Ctrl and TR2^{my}KO mice (**Supplementary Figure 3**). These data show a reduced presence of Tgfβ-responsive myeloid cells inside the growing metastatic foci, which correlated with decreased amounts of chemokines in the metastatic livers in TR2^{my}KO mice.

Tgfβ-Mediated Polarization of Monocytic Myeloid Cells Promotes Liver Metastasis

To assess how Tgfβ-responsive myeloid cells promote liver metastasis, we first analyzed myeloid cells from metastatic

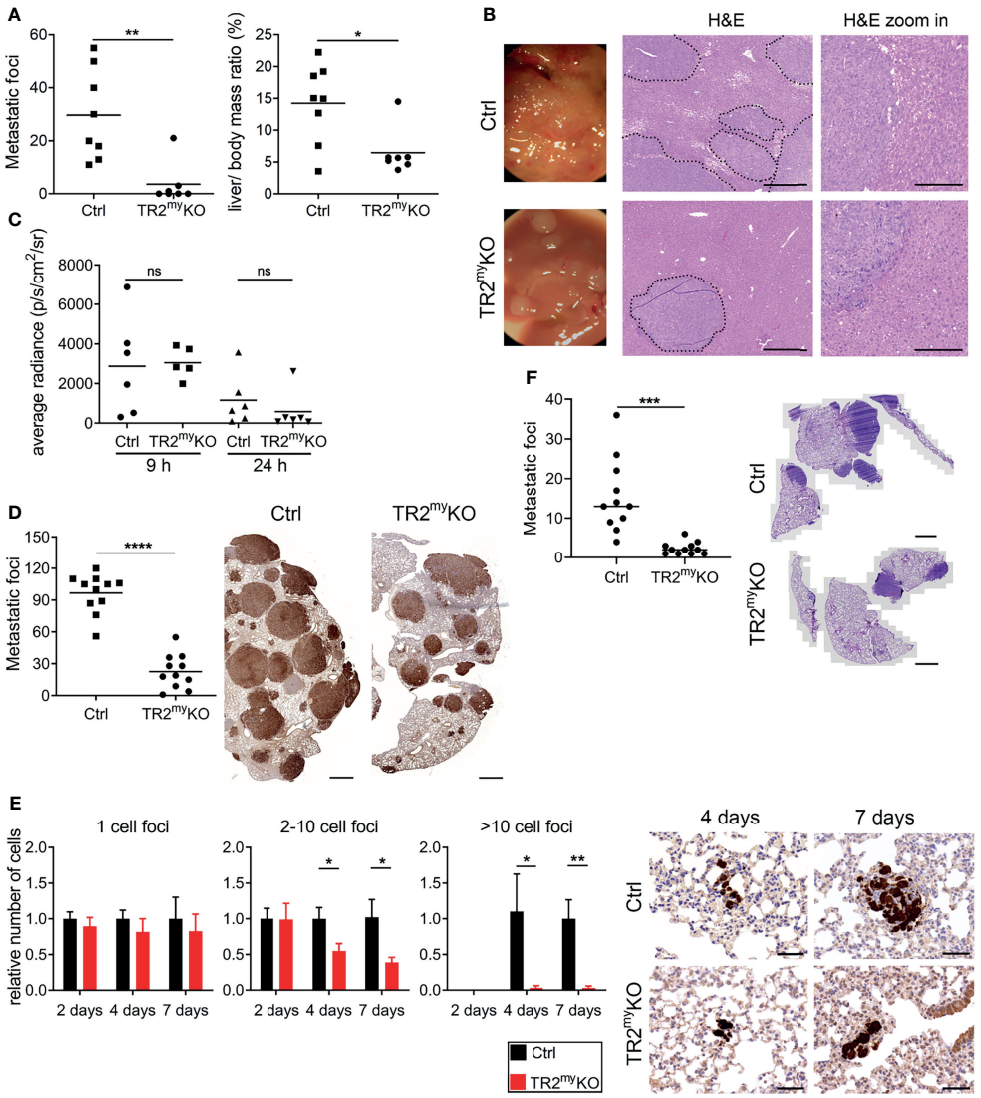

FIGURE 1 | Attenuation of liver and lung metastases in mice with myeloid cell-deletion of Tgfbr2. **(A)** Macroscopic quantification of liver metastatic foci and the ratio of liver weight to the total body mass (%) in TR2^{my}KO and control (Ctrl) mice 28 days after the intraspenic injection of MC-38GFP cells. **(B)** Representative macroscopic liver images and hematoxylin/eosin (H&E) stained liver sections indicating liver metastasis. Dotted line represents the edge of metastatic foci (middle panel). Bar = 500 µm; bar zoom-in = 200 µm. **(C)** Liver seeding of MC-38 luciferase-expressing cells determined at 9 and 24 hours post-intrasplenic injection of MC-38 luciferase cells using quantification of luciferase signal in the perfused liver. **(D)** Macroscopic quantification of lung metastasis in TR2^{my}KO compared to control (ctrl) mice 30 days after intravenous injection of MC-38GFP cells. Representative images (right panel) of pulmonary metastasis stained with anti-GFP antibodies (brown). Bar = 1 mm. **(E)** Quantification of GFP$^+$ cells in lung sections at 2, 4 and 7 days post-tumor cell injection as tumor cell clusters divided into: 1 cell, 2-10 cell foci and >10 cell foci. Representative images of lung sections from day 4 and 7 stained for GFP (brown). n = 4-6 mice per time point and genotype. Bar = 50 µm. **(F)** Spontaneous lung metastasis of LLC1.1 cells subcutaneously injected in TR2^{myelo}KO and Ctrl mice terminated at days 32. Representative H&E stained lung sections of respective genotype. Bar = 1 mm. For panels **(A–D, F)** each dot represents a mouse. Statistical significance was assessed using Mann-Whitney t-test: ns, not significant; *p < 0.05; **p < 0.01; ***p < 0.001.

livers of TR2^{my}KO and Ctrl mice. First, the phagocytic activity of myeloid-derived (CD11b$^+$) cells was tested. We analyzed Ly6C$^+$ monocytes and Ly6G^{lo}/Ly6C$^-$ macrophages isolated from livers of mice intrasplenically injected with MC-38 cells at day 14, during early metastasis. No differences in phagocytic capacity of monocytic cells were observed between the respective mouse genotypes (**Figure 4A**). A recent study using a murine breast cancer model with 4T1 tumor cells in LysMCre$^+$/Tgfbr2$^{fl/fl}$ mice showed that CD8$^+$ T cells control lung metastasis (16). Thus, we depleted CD8$^+$ T cells to test whether myeloid cells modulate CD8$^+$ T cells and thereby promote liver metastasis. While efficient depletion of CD8$^+$ T cells in the blood liver and lungs has been achieved (**Supplementary Figure 4A**), no effect on liver metastasis has been observed (**Figure 4B**). This finding points to a different mechanism of Tgfβ-stimulated pro-metastatic myeloid cell involvement during liver metastases. To determine

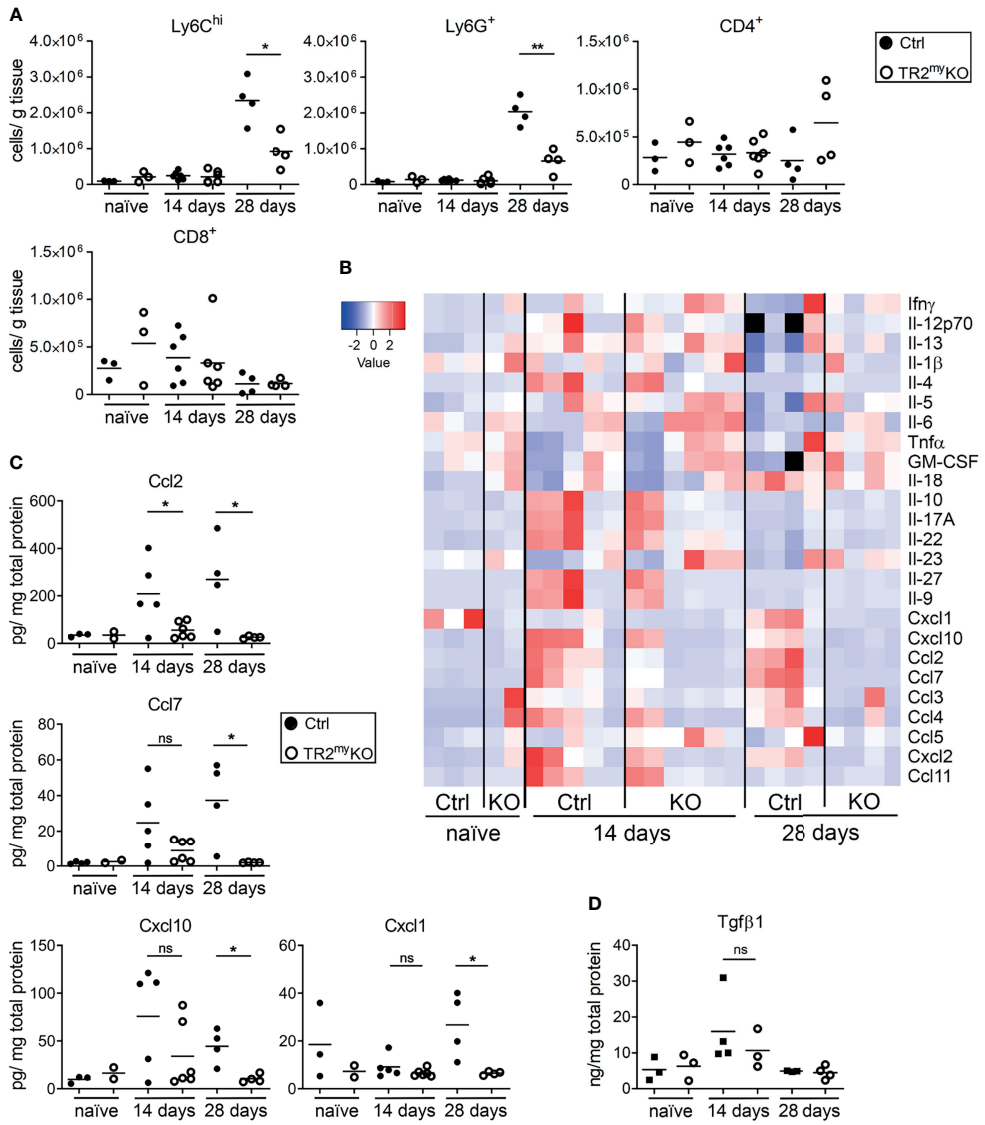

FIGURE 2 | Analysis of liver metastasis in Tgfbr2-myeloid cell-deficient mice. **(A)** Flow cytometry analysis of Ly6C^{hi}, Ly6G^{+} myeloid-derived cells and CD4^{+} and CD8^{+} lymphocytes in livers of TR2^{my}KO and Ctrl mice upon intrasplenic injection of MC-38GFP cells that were terminated at day 14 or 28, respectively; and compared to naïve mice. **(B)** Determination of cytokine amounts in the perfused liver homogenates of TR2^{my}KO and Ctrl mice at day 14 and 28 post-intrasplenic injection with MC-38GFP cells. **(C)** Quantification of selected cytokines amounts with significant changes among TR2^{my}KO and Ctrl mice samples. **(D)** Tgfβ1 levels in the liver of mice after intrasplenic injection of MC-38GFP cells 14 and 28 days post-injection when compared to naïve mice without any tumor cell injection. Statistical significance was assessed using Mann-Whitney test: ns, not significant; *p < 0.05; **p < 0.01.

the subpopulation of myeloid cells involved in liver metastasis, we depleted Ly6G^{+} cells during experimental liver metastasis. Depletion of neutrophils showed no difference in liver metastasis neither in Ctrl nor in TR2^{my}KO mice (**Figure 4C**), suggesting the involvement of myeloid-derived monocytic cells.

The altered polarization of monocytes/macrophages and neutrophils towards M2 and N2 phenotype, respectively, was previously associated with cancer progression (25, 26). Therefore, we sorted Ly6C^{hi} monocytes and Ly6G^{+} neutrophils from metastatic livers of TR2^{my}KO and Ctrl mice and analyzed the gene expression associated with M1 and M2 polarization (27) and N1 and N2 polarization (28), respectively. We observed an increased expression in seven out of eight genes in monocytic cells from TR2^{my}KO mice, which were mostly M1 genes (**Figure 4D**). Specifically, increased expression of ICAM1, TNFα and SOCS3, and decreased expression of M2 genes, CCL2 and Arg1 was detected in Ly6C^{hi} cells from TR2^{my}KO mice (**Figure 4D**). However, we observed no significant changes in polarization of Ly6G^{+} cells, while only the ICAM1 was increased in cells from TR2^{my}KO mice. To confirm the altered polarization of monocytes, we sorted Ly6C^{hi} cells from metastatic livers and measured cytokine production *in vitro*

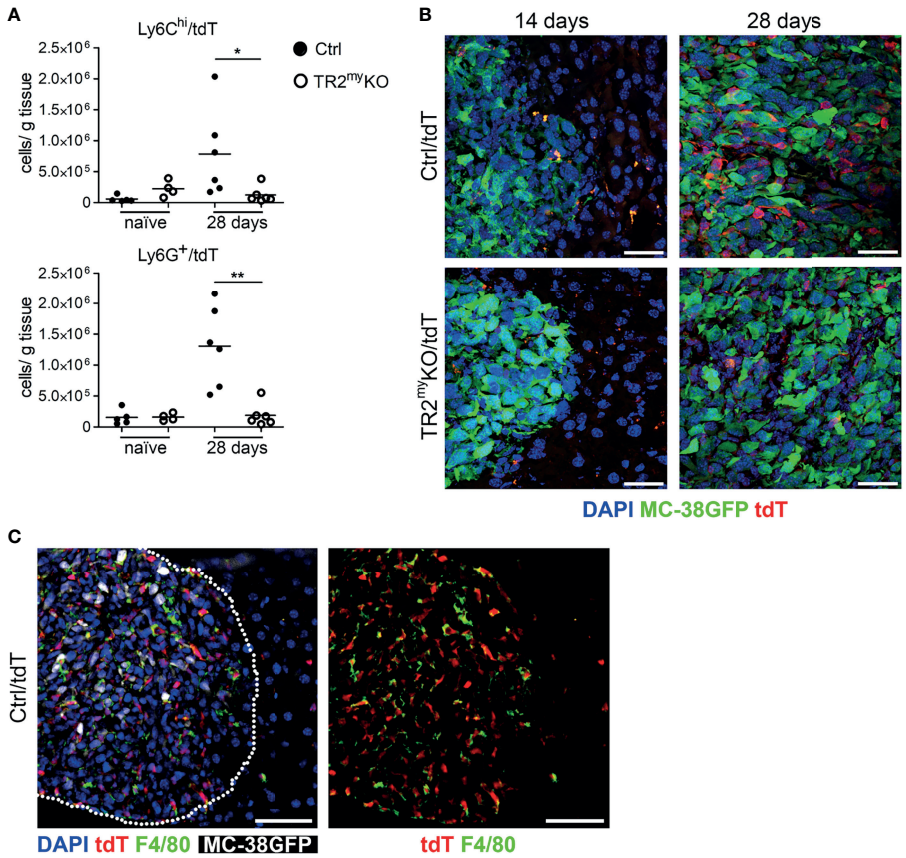

FIGURE 3 | Reduced myeloid cell recruitment to liver metastatic foci in *Tgfbr2*-myeloid cell-deficient mice. Analysis of tdTomato reporter expression in TR2^{my}KO (LysMCre^{+}/*Tgfbr2*$^{fl/fl}$/tdT^{+}) and Ctrl mice (LysMCre^{+}/*Tgfbr2*^{wt}/tdT^{+}). **(A)** Flow cytometry analysis of tdT-positive Ly6C^{hi} and Ly6G^{+} myeloid cells in perfused livers from TR2^{my}KO and Ctrl mice at day 28 post-intrasplenic tumor cell injection compared to non-injected mice (naïve). **(B)** Representative images of metastatic liver foci at day 14 and 28 post-tumor cell injection in TR2^{my}KO and Ctrl mice showing tumor cells (green), and myeloid cells (red) and counterstained with DAPI (blue). Bar = 30 μm. **(C)** Immunofluorescence analysis of F4/80-stained macrophages in livers 28 days after MC-38GFP splenic injection in Ctrl mice. Dotted line represents the edge of a metastatic focus (left panel); tdTomato channel and F4/80 staining (right panel) Bar = 50 μm. Statistical significance was assessed using Mann-Whitney test: *$p < 0.05$; **$p < 0.01$.

(**Figure 4E**). Ly6C^{hi} cells from TR2^{my}KO mice showed increased production of Il-1β, and partially increased Tnfα levels when compared to monocytes from Ctrl mice. Reduced levels of several cytokines, such as Il-6, Ccl2, Ccl3, Ccl5, Cxcl1 and Cxcl10, but also Il-10 were detected in Ly6C^{hi} cells from TR2^{my}KO mice (**Figure 4E** and **Supplementary Figure 4B**). Changes in cytokine production in Ly6C^{hi} cells supports the active role of Tgfβ-signaling in modulation of myeloid-derived cells that facilitates liver metastasis.

Unchanged Levels of Myeloid Cells During Lung Metastasis

We studied how the absence of Tgfb-signaling in myeloid cells reduces lung metastasis. The cellular composition of metastatic lungs in the LLC1.1 spontaneous metastatic model was analyzed. We selected day 21, which is 5 days after the primary tumor removal, as an early metastatic time point; and day 32, as a late metastatic phase. No differences in the presence of Ly6C^{hi} monocytes, Ly6G^{+} granulocytes and CD4^{+} T cells were detected between TR2^{my}KO and Ctrl mice at any time point (**Figure 5A**). However, we observed increased numbers of CD8^{+} T cells in the lungs of TR2^{my}KO mice at day 32 (**Figure 5A**). Of note, reduced numbers of F4/80^{+} macrophages was observed in the lungs of TR2^{my}KO mice at day 21, but not at day 32, when compared to control mice (**Supplementary Figure 5A**). Next, we analyzed cytokine levels in metastatic lungs at day 21 (**Figure 5B**). There was an overall decrease in cytokines in TR2^{my}KO mice when compared to Ctrl mice, specifically a significant reduction of Ifnγ, Il-4, Il-5,Ccl2 and Ccl11 was observed. Since tumor-associated myeloid cells can inhibit immune cell functions (20), the observed decrease in Il-4 and Il-5 together with a tendency of Il-10 in TR2^{my}KO mice suggests a possible reduced polarization of T cells. The reduced Ccl2 levels detected in TR2^{my}KO mice corresponds well with reduced macrophages in the lungs. Finally, we measured the amounts of Tgfβ1 cytokine in the lungs of tumor-bearing mice and compared them with non-injected (naïve) mice (**Figure 5C**).

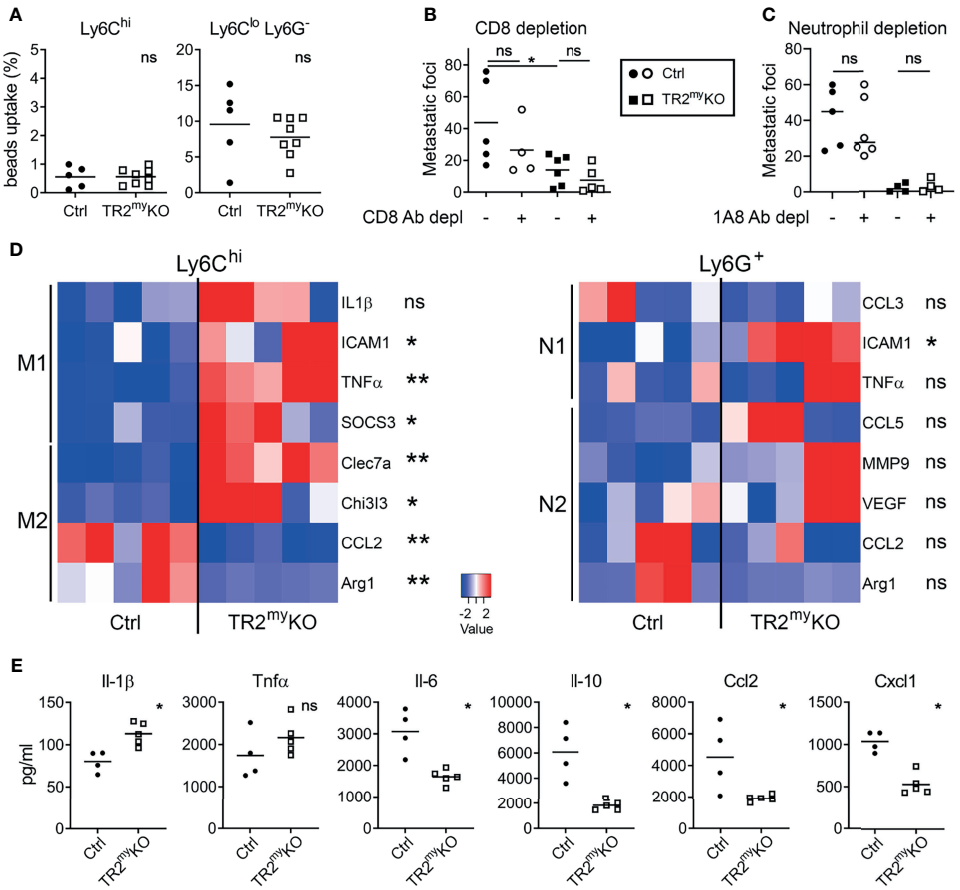

FIGURE 4 | Altered polarization of *Tgfbr2*-deficient monocytic cells resulted in reduced liver metastasis. Characterization of myeloid cells from TR2^{my}KO and Ctrl mice at day 14 post-intrasplenic injection of MC-38GFP cells. **(A)** The phagocytic capacity of Ly6C^{hi} monocytes and Ly6C^{lo}/Ly6G^{-} macrophages isolated from metastatic livers 9 hours after the intravenous injection of fluorescent beads. **(B)** Liver metastasis of MC-38GFP cells upon anti-CD8 antibody or isotype control depletion in TR2^{my}KO and Ctrl mice. Mice were terminated at day 28 and liver metastasis quantified. **(C)** Liver metastasis of MC-38GFP cells upon anti-Ly6G (1A8) antibody or isotype control depletion in TR2^{my}KO and Ctrl mice. Mice were terminated at day 28, and liver metastasis quantified. **(D)** Gene expression analysis of Ly6C^{hi}/tdT^{+} monocytes and Ly6G^{+}/tdT^{+} neutrophils sorted from livers of tdT-reporter TR2^{my}KO and Ctrl mice at day 14 post-tumor cell injection performed by qPCR. A panel of genes associated with M1 and M2 macrophage polarization and N1 and N2 neutrophil polarization was analyzed. **(E)** Analysis of cytokine production by tdT^{+} sorted Ly6C^{hi} monocytes from livers of TR2^{my}KO and Ctrl mice 14 days post-intrasplenic injection of MC-38GFP cells. Cells were stimulated overnight and secreted cytokines were measured in supernatants. Statistical significance was assessed using Mann-Whitney test: ns, not significant; *$p < 0.05$; **$p < 0.01$.

We observed an increase in Tgfβ1 levels in the lungs of tumor-bearing mice at day 14, while at day 28 there was no difference when compared to the lungs of naïve mice. When we analyzed metastatic lungs from TR2^{my}KO/tdT and Ctrl/tdT mice at day 32 days after LLC1.1 s.c. injection, we observed no changes in the presence of tdT-positive Ly6C^{hi} and Ly6G^{+} cells between mouse phenotypes as determined by flow cytometry (**Supplementary Figure 5B**).

Lung Metastasis Are Controlled Through Tgfβ-Myeloid Cell Suppression of CD8^{+} T Cells

Next, we tested whether attenuated lung metastasis is associated with altered polarization of Tgfβ-signaling deficient myeloid cells, when no major changes in myeloid cell presence in lungs of TR2^{my}KO/tdT and Ctrl/tdT mice were detected (**Figure 5A**). First, the phagocytic activity of myeloid-derived (CD11b^{+}) cells was tested. We analyzed Ly6C^{+} monocytes and Ly6G^{lo}/Ly6C^{-} macrophages isolated from lungs of mice injected with LLC1.1 cells at day 21, during early metastasis. No changes in uptake of beads neither in monocytic cells nor myeloid-derived macrophages isolated from TR2^{my}KO and Ctrl mice could be detected (**Figure 6A**). Second, we tested the production of reactive oxygen species (ROS) by myeloid-derived Ly6G^{+} cells, which was similar in both mouse genotypes (**Figure 6B**). These data indicate no functional changes in *Tgfbr2*-deficient myeloid cells in metastatic sites. TGFβ signaling is a critical mediator of immune cell polarization (7). Therefore, we sorted Ly6C^{hi} monocytes and Ly6G^{+} neutrophils from the lungs at day 21, early metastasis, and analyzed their polarization status on a transcriptional level. However, we detected no significant

changes in expression of genes linked to respective polarization patterns of myeloid cells (**Figure 6C**). Since we observed enhanced infiltration of lungs metastasis with $CD8^+$ T cells in $TR2^{my}KO$ mice (**Figure 5A**), we tested their role in control of lung metastasis. Depletion of $CD8^+$ T cells in a LLC1.1 model 24 h before the primary tumor removal and during the metastatic phase resulted in increased lung metastasis in $TR2^{my}KO$ mice to similar levels as observed in Ctrl mice (**Figure 6D**), indicating that Tgfβ-signaling-deficient myeloid cells control lung metastasis through modulation of $CD8^+$ T cells. The analysis of $CD8^+$ T cells from metastatic lungs (**Supplementary Figure 6**) showed a significantly increased levels of $perforin^+$ $CD8^+$ T cells in $TR2^{my}KO$ mice when compared to Ctrl mice (**Figure 6E**). However, no major differences in granzyme B expression, nor alteration in PD1 expression has been observed. These data provide evidence that the absence of Tgfβ-signaling in myeloid cells results in increased levels of functional $CD8^+$ T cells, which control metastatic outgrowth in the lungs.

DISCUSSION

Cytokines have a key role in orchestrating the tumor microenvironment both during tumorigenesis and metastasis (29). TGFβ signaling affects primarily the immune compartment of a tumor and stimulates immune suppressive polarization of myeloid-derived cells (3). The abrogation of TGFβ signaling in mammary carcinoma resulted in an increased chemokine production;

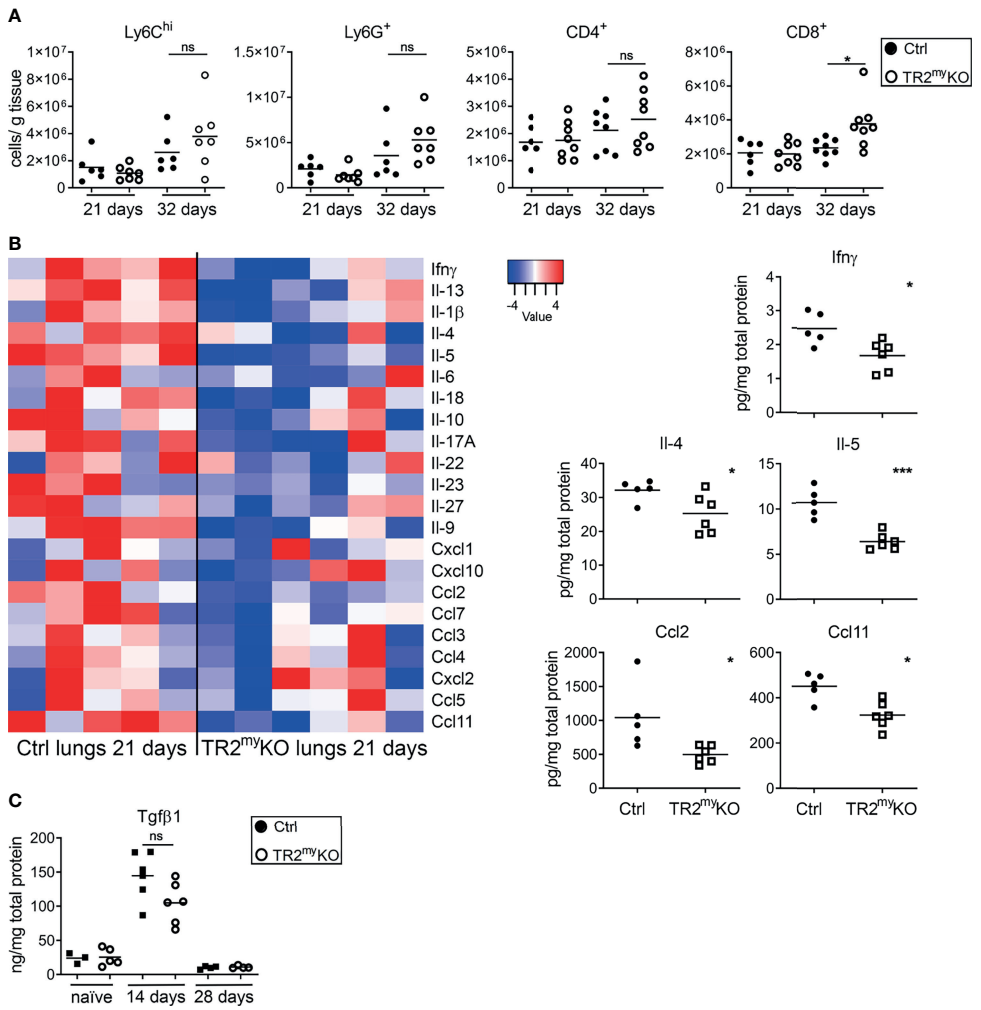

FIGURE 5 | Analysis of spontaneous lung metastasis in *Tgfbr2*-myeloid cell-deficient mice. **(A)** Flow cytometry analysis of the myeloid cells, $Ly6C^{hi}$, $Ly6G^+$; and lymphocytes, $CD4^+$ and $CD8^+$ cells in lungs at day 21 and 32 after the subcutaneous injection of LLC1.1 cells in $TR2^{myelo}KO$ mice and Ctrl mice, respectively. **(B)** Determination of cytokine amounts in the perfused lung homogenates of $TR2^{my}KO$ and Ctrl mice at day 21. Quantification of selected cytokines amounts (panels) with significant changes among $TR2^{my}KO$ and Ctrl mice samples. **(C)** Tgfβ1 levels in the lungs of tumor-bearing mice at day 14 and 28 after subcutaneous injection of LLC1.1 cells, when compared to naïve mice. Statistical significance was assessed using Mann-Whitney test: ns, not significant; *$p < 0.05$; ***$p < 0.001$.

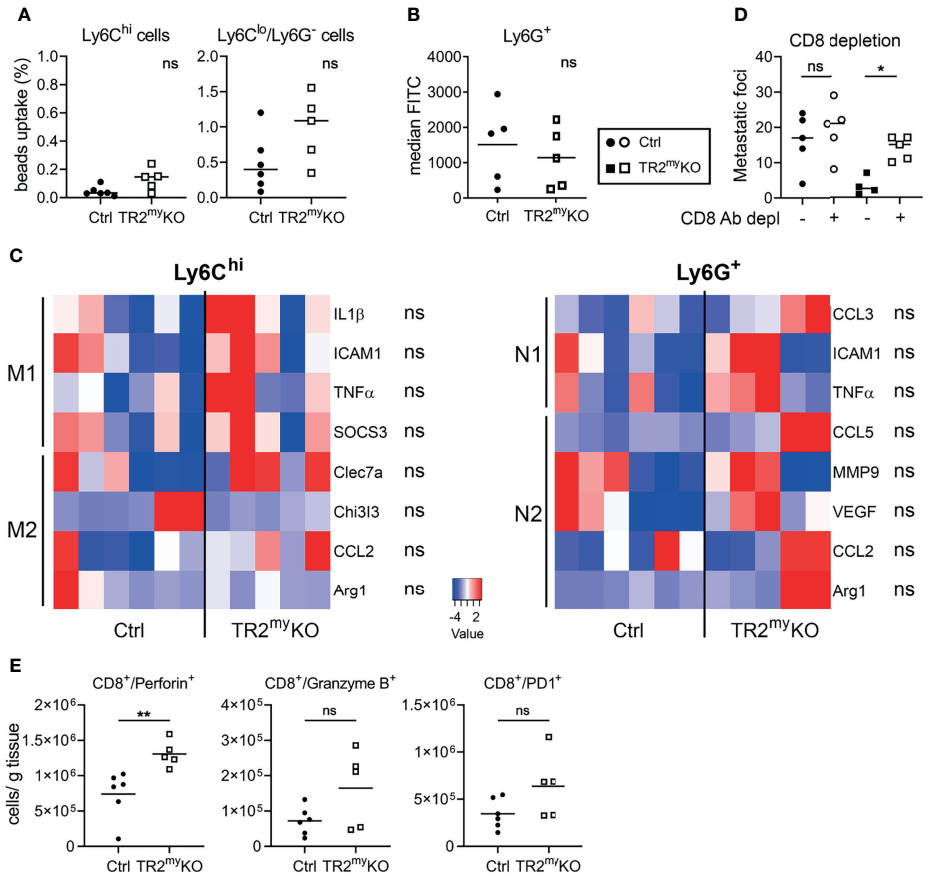

FIGURE 6 | Lung metastasis in *Tgfbr2*-myeloid cell-deficient mice are controlled by CD8 cells. Characterization of myeloid cells from TR2^{my}KO and Ctrl mice at day 21 (early metastatic lungs) post-subcutaneous injection of LLC1.1 cells. **(A)** The phagocytic capacity of Ly6C^{hi} monocytes and Ly6C^{lo}/Ly6G^{-} macrophages isolated from metastatic lungs 9 hours after the intravenous injection of fluorescent beads. **(B)** Reactive oxygen species (ROS) levels in neutrophils isolated from the lungs of mice perfused with the CellROX® dye *in vivo*. Data are presented in median fluorescent intensity (MFI). **(C)** Gene expression analysis of Ly6C^{hi}/tdT^{+} monocytes and Ly6G^{+}/tdT^{+} neutrophils sorted from metastasis lungs of tdT-reporter TR2^{my}KO and Ctrl mice at day 21 post-tumor cell injection and 5 days after the tumor removal performed by qPCR. A panel of genes associated with M1 and M2 macrophage polarization and N1 and N2 neutrophil polarization was analyzed. **(D)** Spontaneous lung metastasis of LLC1.1 cells upon anti-CD8 antibody or isotype control depletion in TR2^{my}KO and Ctrl mice. Mice were terminated at day 32, and lung metastasis quantified. **(E)** Analysis of effector CD8^{+} cells from metastatic lungs at day 32 in a spontaneous lung metastasis model LLC1.1 using flow cytometry analysis for detection of perforin, granzyme B and PD-1. Statistical significance was assessed using Mann-Whitney test: ns, not significant; *p < 0.05; **p < 0.01.

recruitment of myeloid cells and promotion of lung metastasis (22). On contrary, the absence of Tgfβ signaling in myeloid cells attenuated lung metastasis in a murine mammary tumor model (16, 22). Here we confirmed that functional TGFβ signaling in the myeloid compartment is essential for lung metastasis and provided the first evidence for its involvement also in liver metastasis.

The tumor microenvironment varies between primary tumors and metastatic sites and the composition dynamically changes throughout cancer progression (1, 30, 31). Therefore, we analyzed composition of metastatic lungs and livers for the presence of myeloid cells both in early metastatic phase and in fully developed metastasis. A strong infiltration of tdTomato-positive myeloid cells was observed in metastatic liver foci of Ctrl mice. However, in the very few metastatic foci detected in TR2^{my}KO mice, we observed virtually no tdT^{+} cells, indicating that myeloid cells with non-functional TGFβ signaling are unable either to get recruited or to survive in the liver metastatic niche. Closer analysis of liver metastasis, revealed that the majority of tdT^{+} monocytic cells differentiate into macrophages (F4/80^{+} cells).

In a colon cancer mouse model, myeloid cells were shown to promote liver metastasis (10). Tumor cell-triggered increased production of CXCL1 by tumor-associated macrophages resulted in increased myeloid cell recruitment to the premetastatic liver tissue. In agreement with these data, we observed reduced levels of CXCL1, CXCL10 but also CCL2, CCL3 and CCL5 in monocytes (Ly6C^{+} cells) from metastatic livers of TR2^{my}KO, with reduced liver metastasis, when compared with Ctrl mice. Importantly, an overall reduction of chemokines responsible for recruitment of myeloid cells was observed in TR2^{my}KO mice that correlated with a minimal number of myeloid cells, both monocytic and granulocytic, in liver metastatic foci. Since

depletion of neutrophils did not alter liver metastasis, the presence of monocytic myeloid cells is expected to modulate this process. Tgfβ-signaling deficiency in myeloid cells resulted in increased anti-tumorigenic polarization, associated with increased TNFα and decreased IL-6 production in subcutaneous mammary and lung tumors (15). In a mammary tumor model, increased production of Il-6 was shown to be responsible for myeloid cell recruitment to tumor microenvironment (11). Likewise, we observed reduced production of Il-6 and increased expression levels of TNFα in monocytic cells from livers of $TR2^{my}KO$ mice. High levels of pro-inflammatory chemokines, e.g. CCL2 and CCL5, in circulation are associated with poor prognosis for cancer patients (32, 33). Particularly, CCL2 is an apparent key immunosuppressive cytokine in tumors (34). We observed a strong shift in polarization of monocytic myeloid cells in $TR2^{my}KO$ mice, associated with reduced expression of CCL2, CCL3, and CCL5 that was confirmed on both transcription and protein levels.

Attenuation of lung metastasis observed in a mammary mouse model of *Tgfbr2*-deficient myeloid cells was associated with decreased production of type II cytokines, Tgfβ1 and Ccl2 (16, 22). We observed similar reduction in Ccl2 amounts in metastatic lungs. Interestingly, reduced amounts of Ccl11, Il-4 and Il-5 were also detected, which is in agreement with reduced alternative polarization of immune cells. Myeloid cell recruitment to the lungs during mammary carcinoma metastasis resulted in a decreased IFN-γ production and increase proinflammatory cytokines (13). The gene expression analysis of sorted monocytes ($Ly6C^+$) and neutrophils ($Ly6G^+$) showed small differences in inflammatory genes between $TR2^{my}KO$ and Ctrl mice. Finally, we provide evidence that spontaneous lung metastasis of LLC1.1 cells is controlled by $CD8^+$ T cells in $TR2^{my}KO$ mice.

The functional Tgfβ signaling in myeloid cells promotes lung metastasis of mammary tumors through immunosuppression (16, 22). We detected no significant difference in Tgfβ levels in metastatic lungs nor livers between $TR2^{my}KO$ and Ctrl mice. However, the increased Tgfβ amounts during early metastasis suggests that Tgfβ affects this phase of the metastatic process. Both tumor cell lines, LLC1.1 and MC-38, produce significant amounts of Tgfβ1 (**Supplementary Figure 7**). Interestingly, MC-38 tumor cells deficient in Tgfβ1 production produced no experimental metastasis irrespective of target tissue (data not shown). Thus, tumor-derived Tgfβ appears to be essential during the early stages of metastasis. How other cells in the metastatic microenvironment, such as fibroblasts, contribute to Tgfβ levels and thereby metastasis requires further investigation.

Taken together, these data indicate that TGFβ modulates monocytic myeloid cells, and thereby promotes metastasis both in the lungs and the liver. While the function of myeloid cells during lung metastasis results in suppression of $CD8^+$ T cells, myeloid cells seems to contribute directly to liver metastasis. One caveat of this study is the use of the experimental liver metastasis model. Nevertheless, we observed pronounced differences in myeloid cell infiltration in liver metastatic foci, which was dependent on a functional Tgfβ-signaling in myeloid cells. Recently, the inefficacy of immunotherapy on liver metastasis was linked to the macrophage-assisted elimination of T cells (35), which indicates an involvement of macrophages in liver metastasis. Our findings demonstrate that monocytic myeloid cell infiltration of the liver directly contributes to tumor growth during liver metastasis. Further studies will show whether targeting of TGFβ-signaling during metastasis may lead to therapeutic application in cancer patients.

DATA AVAILABILITY STATEMENT

The original contributions presented in the study are included in the article/**Supplementary Material**. Further inquiries can be directed to the corresponding author.

ETHICS STATEMENT

The animal study was reviewed and approved by Veterinary Office of Kanton Zurich.

AUTHOR CONTRIBUTIONS

Conception and Design, LB and MH. Methodology, CS, MR, and MV. Data acquisition, CS, MV, and MR. Analysis and interpretation of data, CS, MV, MR, and LB. Writing/editing of manuscript, CS, MV, MR, MH, and LB. All authors contributed to the article and approved the submitted version.

FUNDING

This study was supported by the SNF grant #310030-173076 (LB) and by a research credit of the University of Zurich #K-41406-01 (MR). MH was supported by the SFB TR209 and an ERC Consolidator grant (HepatometaboPath).

ACKNOWLEDGMENTS

The authors acknowledge the assistance of the Laboratory Animal Services Center (LASC) – UZH, Center for Microscopy and Image Analysis, and the Flow Cytometry Center of the University of Zurich.

SUPPLEMENTARY MATERIAL

The Supplementary Material for this article can be found online at: https://www.frontiersin.org/articles/10.3389/fonc.2021.765151/full#supplementary-material

REFERENCES

1. Salmon H, Remark R, Gnjatic S, Merad M. Host Tissue Determinants of Tumour Immunity. *Nat Rev Cancer* (2019) 19(4):215–27. doi: 10.1038/s41568-019-0125-9
2. Quail DF, Joyce JA. Microenvironmental Regulation of Tumor Progression and Metastasis. *Nat Med* (2013) 19(11):1423–37. doi: 10.1038/nm.3394
3. Pickup M, Novitskiy S, Moses HL. The Roles of TGFbeta in the Tumour Microenvironment. *Nat Rev Cancer* (2013) 13(11):788–99. doi: 10.1038/nrc3603
4. Kubiczkova L, Sedlarikova L, Hajek R, Sevcikova S. TGF-Beta - An Excellent Servant But a Bad Master. *J Transl Med* (2012) 10:183. doi: 10.1186/1479-5876-10-183
5. Batlle E, Massague J. Transforming Growth Factor-Beta Signaling in Immunity and Cancer. *Immunity* (2019) 50(4):924–40. doi: 10.1016/j.immuni.2019.03.024
6. de Kruijf EM, Dekker TJ, Hawinkels LJ, Putter H, Smit VT, Kroep JR, et al. The Prognostic Role of TGF-Beta Signaling Pathway in Breast Cancer Patients. *Ann Oncol* (2013) 24(2):384–90. doi: 10.1093/annonc/mds333
7. Flavell RA, Sanjabi S, Wrzesinski SH, Licona-Limon P. The Polarization of Immune Cells in the Tumour Environment by TGFbeta. *Nat Rev Immunol* (2010) 10(8):554–67. doi: 10.1038/nri2808
8. Tauriello DVF, Palomo-Ponce S, Stork D, Berenguer-Llergo A, Badia-Ramentol J, Iglesias M, et al. TGFbeta Drives Immune Evasion in Genetically Reconstituted Colon Cancer Metastasis. *Nature* (2018) 554 (7693):538–43. doi: 10.1038/nature25492
9. Gabrilovich DI, Nagaraj S. Myeloid-Derived Suppressor Cells as Regulators of the Immune System. *Nat Rev Immunol* (2009) 9(3):162–74. doi: 10.1038/nri2506
10. Wang D, Sun H, Wei J, Cen B, DuBois RN. CXCL1 Is Critical for Premetastatic Niche Formation and Metastasis in Colorectal Cancer. *Cancer Res* (2017) 77(13):3655–65. doi: 10.1158/0008-5472.CAN-16-3199
11. Oh K, Lee OY, Shon SY, Nam O, Ryu PM, Seo MW, et al. A Mutual Activation Loop Between Breast Cancer Cells and Myeloid-Derived Suppressor Cells Facilitates Spontaneous Metastasis Through IL-6 Trans-Signaling in a Murine Model. *Breast Cancer Res* (2013) 15(5):R79. doi: 10.1186/bcr3473
12. Lesokhin AM, Hohl TM, Kitano S, Cortez C, Hirschhorn-Cymerman D, Avogadri F, et al. Monocytic CCR2(+) Myeloid-Derived Suppressor Cells Promote Immune Escape by Limiting Activated CD8 T-Cell Infiltration Into the Tumor Microenvironment. *Cancer Res* (2012) 72(4):876–86. doi: 10.1158/0008-5472.CAN-11-1792
13. Yan HH, Pickup M, Pang Y, Gorska AE, Li Z, Chytil A, et al. Gr-1+CD11b+ Myeloid Cells Tip the Balance of Immune Protection to Tumor Promotion in the Premetastatic Lung. *Cancer Res* (2010) 70(15):6139–49. doi: 10.1158/0008-5472.CAN-10-0706
14. Fridlender ZG, Sun J, Kim S, Kapoor V, Cheng G, Ling L, et al. Polarization of Tumor-Associated Neutrophil Phenotype by TGF-Beta: "N1" Versus "N2" TAN. *Cancer Cell* (2009) 16(3):183–94. doi: 10.1016/j.ccr.2009.06.017
15. Novitskiy SV, Pickup MW, Chytil A, Polosukhina D, Owens P, Moses HL. Deletion of TGF-Beta Signaling in Myeloid Cells Enhances Their Anti-Tumorigenic Properties. *J Leukoc Biol* (2012) 92(3):641–51. doi: 10.1189/jlb.1211639
16. Pang Y, Gara SK, Achyut BR, Li Z, Yan HH, Day CP, et al. TGF-Beta Signaling in Myeloid Cells Is Required for Tumor Metastasis. *Cancer Discov* (2013) 3 (8):936–51. doi: 10.1158/2159-8290.CD-12-0527
17. Yan HH, Jiang J, Pang Y, Achyut BR, Lizardo M, Liang X, et al. CCL9 Induced by TGFbeta Signaling in Myeloid Cells Enhances Tumor Cell Survival in the Premetastatic Organ. *Cancer Res* (2015) 75(24):5283–98. doi: 10.1158/0008-5472.CAN-15-2282-T
18. Borsig L, Wong R, Hynes RO, Varki NM, Varki A. Synergistic Effects of L- and P-Selectin in Facilitating Tumor Metastasis can Involve Non-Mucin Ligands and Implicate Leukocytes as Enhancers of Metastasis. *Proc Natl Acad Sci USA* (2002) 99(4):2193–8. doi: 10.1073/pnas.261704098
19. Hauselmann I, Roblek M, Protsyuk D, Huck V, Knopfova L, Grassle S, et al. Monocyte Induction of E-Selectin-Mediated Endothelial Activation Releases VE-Cadherin Junctions to Promote Tumor Cell Extravasation in the Metastasis Cascade. *Cancer Res* (2016) 76(18):5302–12. doi: 10.1158/0008-5472.CAN-16-0784
20. Gabrilovich DI, Ostrand-Rosenberg S, Bronte V. Coordinated Regulation of Myeloid Cells by Tumours. *Nat Rev Immunol* (2012) 12(4):253–68. doi: 10.1038/nri3175
21. Ferjancic S, Gil-Bernabe AM, Hill SA, Allen PD, Richardson P, Sparey T, et al. VCAM-1 and VAP-1 Recruit Myeloid Cells That Promote Pulmonary Metastasis in Mice. *Blood* (2013) 121(16):3289–97. doi: 10.1182/blood-2012-08-449819
22. Yang L, Huang J, Ren X, Gorska AE, Chytil A, Aakre M, et al. Abrogation of TGF Beta Signaling in Mammary Carcinomas Recruits Gr-1+CD11b+ Myeloid Cells That Promote Metastasis. *Cancer Cell* (2008) 13(1):23–35. doi: 10.1016/j.ccr.2007.12.004
23. Wolf MJ, Hoos A, Bauer J, Boettcher S, Knust M, Weber A, et al. Endothelial CCR2 Signaling Induced by Colon Carcinoma Cells Enables Extravasation *via* the JAK2-Stat5 and P38mapk Pathway. *Cancer Cell* (2012) 22(1):91–105. doi: 10.1016/j.ccr.2012.05.023
24. Läubli H, Stevenson JL, Varki A, Varki NM, Borsig L. L-Selectin Facilitation of Metastasis Involves Temporal Induction of Fut7-Dependent Ligands at Sites of Tumor Cell Arrest. *Cancer Res* (2006) 66(3):1536–42. doi: 10.1158/0008-5472.CAN-05-3121
25. Coffelt SB, Wellenstein MD, de Visser KE. Neutrophils in Cancer: Neutral No More. *Nat Rev Cancer* (2016) 16(7):431–46. doi: 10.1038/nrc.2016.52
26. Lewis CE, Pollard JW. Distinct Role of Macrophages in Different Tumor Microenvironments. *Cancer Res* (2006) 66(2):605–12. doi: 10.1158/0008-5472.CAN-05-4005
27. Kratochvill F, Neale G, Haverkamp JM, Van de Velde LA, Smith AM, Kawauchi D, et al. TNF Counterbalances the Emergence of M2 Tumor Macrophages. *Cell Rep* (2015) 12(11):1902–14. doi: 10.1016/j.celrep.2015.08.033
28. Shaul ME, Levy L, Sun J, Mishalian I, Singhal S, Kapoor V, et al. Tumor-Associated Neutrophils Display a Distinct N1 Profile Following TGFbeta Modulation: A Transcriptomics Analysis of Pro- vs. Antitumor TANs. *Oncoimmunology* (2016) 5(11):e1232221. doi: 10.1080/2162402X.2016.1232221
29. Dranoff G. Cytokines in Cancer Pathogenesis and Cancer Therapy. *Nat Rev Cancer* (2004) 4(1):11–22. doi: 10.1038/nrc1252
30. Kitamura T, Qian BZ, Pollard JW. Immune Cell Promotion of Metastasis. *Nat Rev Immunol* (2015) 15(2):73–86. doi: 10.1038/nri3789
31. Kalluri R. The Biology and Function of Fibroblasts in Cancer. *Nat Rev Cancer* (2016) 16(9):582–98. doi: 10.1038/nrc.2016.73
32. Nagarsheth N, Wicha MS, Zou W. Chemokines in the Cancer Microenvironment and Their Relevance in Cancer Immunotherapy. *Nat Rev Immunol* (2017) 17(9):559–72. doi: 10.1038/nri.2017.49
33. Qian BZ, Li J, Zhang H, Kitamura T, Zhang J, Campion LR, et al. CCL2 Recruits Inflammatory Monocytes to Facilitate Breast-Tumour Metastasis. *Nature* (2011) 475(7355):222–5. doi: 10.1038/nature10138
34. Fridlender ZG, Buchlis G, Kapoor V, Cheng G, Sun J, Singhal S, et al. CCL2 Blockade Augments Cancer Immunotherapy. *Cancer Res* (2010) 70(1):109–18. doi: 10.1158/0008-5472.CAN-09-2326
35. Yu J, Green MD, Li S, Sun Y, Journey SN, Choi JE, et al. Liver Metastasis Restrains Immunotherapy Efficacy *via* Macrophage-Mediated T Cell Elimination. *Nat Med* (2021) 27(1):152–64. doi: 10.1038/s41591-020-1131-x

Conflict of Interest: The authors declare that the research was conducted in the absence of any commercial or financial relationships that could be construed as a potential conflict of interest.

frontiers in Oncology

ORIGINAL RESEARCH
published: 03 December 2021
doi: 10.3389/fonc.2021.732501

Transcriptomic Profiling Revealed Plexin A2 Downregulation With Migration and Invasion Alteration in Dacarbazine-Treated Primary Melanoma Cells

Anna Tyumentseva[1,2†], Anton Averchuk[1†], Nadezhda Palkina[1†], Ivan Zinchenko[1†], Anton Moshev[3†], Andrey Savchenko[3†] and Tatiana Ruksha[1†]*

[1] Department of Pathophysiology, Krasnoyarsk State Medical University, Krasnoyarsk, Russia, [2] Federal Research Center Krasnoyarsk Science Center of the Siberian Branch of the Russian Academy of Sciences, Krasnoyarsk, Russia, [3] Laboratory of Cell Molecular Physiology and Pathology, Federal Research Center, Krasnoyarsk Science Center of The Siberian Branch of The Russian Academy of Sciences, Krasnoyarsk, Russia

Melanoma is highly heterogeneous type of malignant neoplasm that is responsible for the majority of deaths among other types of skin cancer. In the present study, we screened a list of differentially expressed genes in two primary, drug-naïve melanoma cell lines derived from patients with melanoma following treatment of the cells with the chemotherapeutic agent dacarbazine. The aim was to determine the transcriptomic profiles and associated alterations in the cell phenotype. We found the vascular endothelial growth factor A/vascular endothelial growth factor receptor 2, phosphoinositide 3-kinase/protein kinase B and focal adhesion signaling pathways to be top altered after dacarbazine treatment. In addition, we observed the expression levels of genes associated with tumor dissemination, integrin β8 and matrix metalloproteinase-1, to be diminished in both cell lines studied, the results of which were confirmed by reverse transcription-quantitative polymerase chain reaction. By contrast, plexin A2 expression was found to be upregulated in K2303 cells, where reduced migration and invasion were also observed, following dacarbazine treatment. Plexin A2 downregulation was associated with the promotion of migrative and invasive capacities in B0404 melanoma cells. Since plexin A2 is semaphorin co-receptor that is involved in focal adhesion and cell migration regulation, the present study suggested that plexin A2 may be implicated in the dacarbazine-mediated phenotypic shift of melanoma cells. We propose that the signature of cancer cell invasiveness can be revealed by using a combination of transcriptomic and functional approaches, which should be applied in the development of personalized therapeutic strategies for each patient with melanoma.

Keywords: migration, transcriptome, dacarbazine, PLNXA2, melanoma

OPEN ACCESS

Edited by:
Emilio Hirsch,
University of Turin, Italy

Reviewed by:
Jorg Kobarg,
State University of Campinas, Brazil
Ramray Bhat,
Indian Institute of Science (IISc), India

****Correspondence:***
Tatiana Ruksha
tatyana_ruksha@mail.ru

†ORCID:
Anna Tyumentseva
orcid.org/0000-0002-2269-0298
Anton Averchuk
orcid.org/0000-0002-1284-6711
Nadezhda Palkina
orcid.org/0000-0002-6801-3452
Ivan Zinchenko
orcid.org/0000-0001-7085-6304
Anton Moshev
orcid.org/0000-0003-3122-0420
Andrey Savchenko
orcid.org/0000-0001-5829-672X
Tatiana Ruksha
orcid.org/0000-0001-8142-4283

Specialty section:
This article was submitted to Molecular and Cellular Oncology, a section of the journal Frontiers in Oncology

Received: *29 June 2021*
Accepted: *16 November 2021*
Published: *03 December 2021*

Citation:
Tyumentseva A, Averchuk A, Palkina N, Zinchenko I, Moshev A, Savchenko A and Ruksha T (2021) Transcriptomic Profiling Revealed Plexin A2 Downregulation With Migration and Invasion Alteration in Dacarbazine-Treated Primary Melanoma Cells. Front. Oncol. 11:732501. doi: 10.3389/fonc.2021.732501

INTRODUCTION

Melanoma is a highly heterogeneous type of tumor in which surgical excision in the early stages of the disease confers high survival rates (1, 2). However, various treatment options, including targeted therapy, immunotherapy and chemotherapy, are not completely effective against advanced melanoma (3). Dacarbazine (DTIC) is a chemotherapeutic agent that is used as a form of monotherapy or combined chemotherapy for melanoma (4, 5). However, the overall response rate to DTIC rarely exceeds 17.6% (4, 5). Mechanistically, DTIC is an alkylating agent that promotes G_1-phase cell cycle arrest (6). Alkylating agents favor the formation of O6-alkylguanine derivatives, which bind to thymine instead of cytosine during DNA replication, thereby blocking cell division and causing cell death at the G_1 and S phases (7).

Drug resistance to alkylating agents develops in cancer cells through a number of mechanisms. Induction of tumor heterogeneity can be considered one such mechanism of this process, which results in genetic differences among different cell types within the tumor, in addition to the acquisition of epigenetic alterations by cancer cells during tumorigenesis (8). Indeed, a previous transcriptomic study revealed >70 differentially expressed genes between temozolomide-sensitive and temozolomide-resistant glioma cells (9). In addition, metabolic heterogeneity can give rise to differences in responses by cancer cells to oxidative stress, lactate uptake and pyruvate metabolism (10). It has been previously reported that cancer cells with metastatic phenotypes tend to exhibit enhanced rates of lactate transport, whilst oxidative stress suppresses metastasis (11). Various types of tumors have demonstrated the ability to create pro-tumorigenic hypoxic environments, such that they can create physical barriers by altering blood flow to reduce drug exposure (12). Pancreatic cancer cells provide hypoxia-inducible factor 1α-mediated sonic hedgehog ligand secretion to form fibrous tissue deposition causing a poor drug delivery (13). Non-small-cell lung cancer cells release increased amounts of lactate to potentiate hypoxic-acidic microenvironment and to suppress cytotoxic T-cell activation (14). Drug resistance of melanoma cells to DTIC was reported to be mediated by hypoxia through activation of the nodal signaling pathway (15). The protein kinase B (AKT)/mechanistic target of rapamycin (mTOR) signaling pathway was shown to be up-regulated in DTIC-treated T24.6.9 melanoma cells (16). Furthermore, insulin can weaken the sensitivity of melanoma cells to DTIC by triggering the phosphoinositide 3-kinase (PI3K)/mTOR signaling pathway (17). Therefore, manipulations to various molecular signaling pathways may be underlying the diminished efficacy of chemotherapeutic agents that operate by alkylation.

In this study, we analyzed the effect of DTIC on the melanoma transcriptomic profile. Specific focus was placed on the signal pathways that can regulate cell migration, invasion and adhesion, all of which are associated with shifts in their metastatic phenotypes.

MATERIALS AND METHODS

Tissue Samples and Cell Culture

The present study was approved by the Ethics Committee of the Krasnoyarsk State Medical University (protocol no. 73/2016; approval date, 16 December, 2016) and the Krasnoyarsk Regional Clinical Oncology Center named after A.I. Kryzhanovskiy (protocol no. 8, 14, June, 2017). All procedures were performed according to the Institutional Safety Instructions, which included biosecurity. All researchers are trained in Institutional Safety/Biosafety and follow-up instructions are provided periodically every 3 months, followed by signature confirmation. The present study was also approved by the Institutional Bioethical Commission (protocol no. 3; approval date, 27 October 2017).

The operative samples were obtained from the Department of General Oncosurgery of Krasnoyarsk Regional Clinical Oncology Center named after A.I. Kryzhanovskiy and primary cell lines were prepared as described previously (18). In the present study, two primary melanoma cell populations were obtained from two drug-naïve melanoma patients. Written informed consent was obtained from each patient before the study. Inclusion criteria were as follows: pathologically confirmed primary malignant melanoma and no know second primary malignancies; age more than 18 years old; no systemic treatment in the four weeks prior to surgical treatment. Tumor tissues predominantly consisted of tumor cells that did not contain an abundance of stromal or vascular cell types. They were processed immediately after surgical excision and melanoma cell suspensions were prepared within 3 h. Single cell suspensions were obtained by mechanical dissociation of tumor tissues. These two melanoma cell populations were named K2303 and B0404 thereafter.

K2303 cells were obtained from a 30-year-old female patient with the melanoma localized on the right leg. It exhibited a superficial type of spreading with a Breslow's depth of 2.2 mm. B0404 cells were obtained from a 55-year-old male patient, the melanoma was localized on the right shin with a superficial spreading type and Breslow's depth of 2.0 mm.

Cells were cultured in RPMI-1640 medium with L-glutamine (Gibco, Thermo Fisher Scientific, Inc.) and 10% fetal bovine serum (FBS; Gibco, Thermo Fisher Scientific, Inc.) in the presence of antibiotics and antimycotics (10,000 U/ml penicillin G, 10,000 μg/ml streptomycin and 25 μg/ml amphotericin B; HyClone; Cytiva) at 37°C and 5% CO_2 using a CO_2 incubator (Sanyo Electric Co., Ltd.).

DTIC Treatment and Cell Viability Evaluation

To estimate the 50% inhibitory concentration (IC_{50}) of DTIC, cells were treated with a series of DTIC (Sigma-Aldrich Co., USA) dilutions. For this purpose, melanoma cells were placed in a 96-well plate at a density of $1x10^4$ cells per ml and cultured for 48 h at 37°C. In total, four different concentrations of DTIC in

DMSO (Panreac Quimica S.A.) were added to the culture medium to achieve the final concentrations of 250, 500, 750 and 1,000 mg/l. Since each dose also contains 1% DMSO, 1% DMSO was used as the negative control. The cells were incubated with DTIC for 72 h at 37°C and 5% CO_2.

To evaluate cell viability, 3-(4,5-dimethylthiazol-2-yl)-2,5-diphenyltetrazolium bromide (MTT; Invitrogen; Thermo Fisher Scientific, Inc.) assay was used. The culture medium was first replaced with that without the drug before 0.5 mg/ml MTT was added. After 4 h at 37°C the cells were lysed with DMSO and the amount of formazan formed was evaluated using an EFOS-9305 spectrophotometer (Shvabe Photosystems, Jsc) at a wavelength of 560 nm to measure light absorbance. The experiment was performed in triplicate. Using the dose-dependency curve of DTIC-mediated inhibition, IC_{50} was calculated using the GraphPad Software Prism 7.05/e (San Diego, CA, USA).

Evaluation of Apoptosis in Melanoma Cells After DTIC Treatment

Melanoma cell lines were seeded into 24-well plates at a density of $1x10^5$ cells per ml. After 24 h the cells were treated with 5.5 mM DTIC or 1% DMSO. In parallel, 1% DMSO was used as the negative control. After 72 h at 37°C and 5% CO_2 incubation the cells were stained using an annexin V-fluorescein isothiocyanate (FITC)/7-aminoactinomycin D (7-AAD) kit (Immunotech; Beckman Coulter, Inc.) according to the manufacturer's protocol. For this, 10 µl of Annexin V-FITC and 20 µl of 7-AAD were added to each sample containing 100 µl of melanoma cell suspension in binding buffer at a concentration of $5x10^6$, incubated for 15 min in the dark on ice, then 400 µl of binding buffer was added followed by analysis using a Cytomics FC-500 flow cytometer (Beckman Coulter Inc.) with NAVIOS software v.1.3. (Beckman Coulter, Brea, USA).

After detection, with the distribution of cells displayed in their respective regions of two-parameter diagrams, living cells were defined as unstained. By contrast, cells were defined to be in early apoptosis if they stained positive for phosphatidylserine by annexin V-FITC but negative for 7-AAD due to preserved membrane integrity. Cells were defined to be at late-stage apoptosis and necrotic if there is evidence of violation in the integrity of the membranes and were stained simultaneously with both fluorescent dyes. Cells that stained positive for annexin V alone were defined as necrotic cells. The experiment was performed in triplicate.

Migration and Invasion Assay of Melanoma Cells Under DTIC Treatment

Melanoma cells were plated into six-well plates at a density of $1x10^5$ cells per ml. After 24 h at 37°C and 5% CO_2, the cells were treated with 5.5 mM DTIC or 1% DMSO. After 72 h, the cells were transferred to serum-free RPMI-1640 medium with 5.5 mM DTIC and diluted to a final density of $1x10^4$ cells per ml. Cell migration and invasion assays were performed using CytoSelect™ 24-Well Cell Migration and Invasion assays (8 µm, colorimetric format; Cell Biolabs, Inc.) according to the manufacturer's protocols. Briefly, a 300 µl suspension of melanoma cells in RPMI-1640 medium without serum was placed into the upper part of special chambers for migration and invasion. The bottom layer of the chambers for migration assays was made of a polycarbonate membrane with pores, whilst for measuring invasion it was lined additionally with a layer of Matrigel. The chambers containing the cell suspension were incubated in a CO_2 incubator at 37°C and 5% CO_2 for 24 h in the wells of a 24-well plate filled with RPMI-1640 medium containing 10% FBS, which constitutes the lower part of the chamber. After incubation, the chambers were removed and the Matrigel was mechanically removed. Cells that did not migrate or invade located on the membrane inside the chamber and the invasive and migratory cells located on the outer side of the membrane were fixed and, stained by Cell Stain Solution, washed in dH20, dried at room temperature for 10 min and then lysed by Extraction Solution. The color intensity levels of lysates were measured on an EFOS-9305 spectrophotometer at a wavelength 560 nm, which were used to calculate the levels of cell migration and invasion. The experiment was performed in triplicate.

Whole Transcriptome Assay

Total RNA was extracted using RecoverAll™ Total Nucleic Acid Isolation kit (Invitrogen™; Thermo Fisher Scientific, Inc.) according to the manufacturer's protocol, using on-column DNase digestion. Extracted RNA was examined using a Qubit® 2.0 fluorimeter (Invitrogen; Thermo Fisher Scientific, Inc.) with the use of a Qubit® RNA HS Assay kit (Invitrogen by Thermo Fisher Scientific, Inc.). In total, 10 ng total RNA was amplified, purified, reverse transcribed and labeled with biotin using the GeneChip™ WT Plus kit (cat # 902280, Affymetrix; Thermo Fisher Scientific, Inc.) following the manufacturer's protocols. The samples were then hybridized to GeneChip™ HuGene 2.1 ST Array Strips (cat # 902114, Applied Biosystems; Thermo Fisher Scientific, Inc.). Post-hybridization staining and washing were processed according to manufacturer's protocol using GeneAtlas™ Hybridization, Wash, and Stain kit for WT array strips (cat # 900720-C, Affymetrix; Thermo Fisher Scientific, Inc.). The strips were scanned in a GeneAtlas™ Imaging Station (Affymetrix; Thermo Fisher Scientific, Inc.). Data were collected using the Transcriptome Analysis Console software version 4.0.0 and subsequent releases (Thermo Fisher Scientific, Inc.).

A total of three replicates of each cell line before and after DTIC treatment at 5.5 mM for 72 h were prepared. Quality Control of the experiment was automatically estimated at the imaging stage and all arrays passed the quality controls. The data generated in the present study were deposited at the Array Express repository (accession no. E-MTAB-10359; https://www.ebi.ac.uk/arrayexpress/experiments/E-MTAB-10359/).

The expression data were used to perform principal components analysis using all probe sets by Transcriptome Analysis Console Software v.4.0.1. (Thermo Fisher Scientific, Inc.). The expression data were also used to cluster the samples using a hierarchical clustering method (19). All P-values were false discovery rate-corrected for multiple hypothesis testing. Differentially expressed probe sets were defined using the threshold of absolute fold change ≥2 and the Q-value ≤0.05. PANTHER™ v.10.0 classification system (URL: PanterDB.org) was used to interpret the biological function of the differentially expressed genes.

RNA Isolation and Reverse Transcription-Quantitative Polymerase Chain Reaction (RT-qPCR) for Gene Expression Studies

The cells were seeded at a density of $2x10^5$ cells per ml and cultured for 24 h at 37°C and 5% CO_2. The culture medium was then replaced and the cells were treated with DTIC at a final concentration of 5.5 mM, with 1% DMSO used as the negative control. The cells were then incubated for 72 h, detached with 0.25% trypsin-ethylenediaminetetraacetic acid and washed twice with cold 0.01 M phosphate buffered saline (Amresco LLC). Isolation of total RNA was performed using the RecoverAll™ Total Nucleic Acid Isolation kit (Ambion; Thermo Fisher Scientific, Inc.) according to the manufacturer's protocol. Total RNA was then subjected to reverse transcription with random primers using the MMLV RT kit (cat # SK021, Evrogen, Russia). The reaction was performed with incubation at 40°C for 50 min, and the enzyme was subsequently inactivated by incubation at 70°C for 10 min.

Amplification of the obtained cDNA in an amount of 2 µl was performed in a StepOne ™ Real-Time PCR System (Applied Biosystems; Thermo Fisher Scientific, Inc.) in 20 µl reaction mixture containing 1 µl probe and primers for the detection of integrin β8 (ITGB8), plexin-A2 (PLXNA2) and matrix metalloproteinase-1 (MMP-1) from the TaqMan™ Gene Expression Assay (Assay names, CYP1A1 Hs01054796_g1, CYP1A2 Hs00167927_ml, CYP2E1 Hs00559367_ml, ITGB8 Hs00174456_ml, PLXNA2 Hs00300697_ml and MMP1 Hs00899658_ml; cat. no. 4331182; Applied Biosystems, Thermo Fisher Scientific Inc.) and 8 µl 2.5X reaction mixture for RT-PCR (Syntol, Russia) in the presence of the reference ROX dye (Syntol, Russia), using the following thermocycling protocol: 50°C for 2 min and 95°C for 10 min, followed by 40 cycles of denaturation at 95°C for 15 sec and annealing and elongation at 60°C for 1 min. Endogenous normalizing controls were β-actin and hypoxanthine phosphoribosyltransferase-1 (Assay names, ACTB Hs01060665_g1 and HPRT1 Hs01003267_m1; TaqMan™ Gene Expression Assay; cat. no. 4331182; Applied Biosystems; Thermo Fisher Scientific, Inc.). Relative expression levels were calculated using the $2^{-\Delta\Delta Cq}$ method as previously described (20).

Statistical Analysis

Statistical analysis was performed using the non-parametric Mann-Whitney U-test for comparisons between two independent groups (DTIC-treated group vs. control untreated group) using the Statistica 6.1 software (StatSoft, Inc.). $P<0.05$ was considered to indicate a statistically significant difference.

RESULTS

Sensitivity of Melanoma Cells Derived From Different Patients to DTIC and CYP1A1 Expression

According to MTT analysis, the IC_{50} value of DTIC for the K2303 melanoma cells was calculated to 4.2 mM, whilst the IC50 of DTIC for B0404 melanoma cells equated to 10.3 mM (**Figure 1A**). The final concentration of DTIC was chosen to be 5.5 mM. Overall, K2303 melanoma cells were found to be more sensitive to DTIC treatment compared with B0404 cells. As DTIC metabolized extrahepatically by cytochrome P450 1A1 (CYP1A1), it's mRNA levels were estimated in K2303 and B0404 cells by qRT-PCR as well as CYP1A2 and CYP2E1 levels which can metabolize DTIC also (21). We determined CYP1A1 expression in both cell lines studied, CYP1A2 expression in B0404 and CYP2E1 expression in K2303 cells (**Figure 1B**). Relative expression level was.

DTIC Induces Apoptosis in Primary Melanoma Cells

To evaluate the sensitivity of the primary melanoma cells originated from the two patients to DTIC *in vitro*, the proportions of live and apoptotic cells were measured using flow cytometry before and after DTIC treatment. Both cell lines

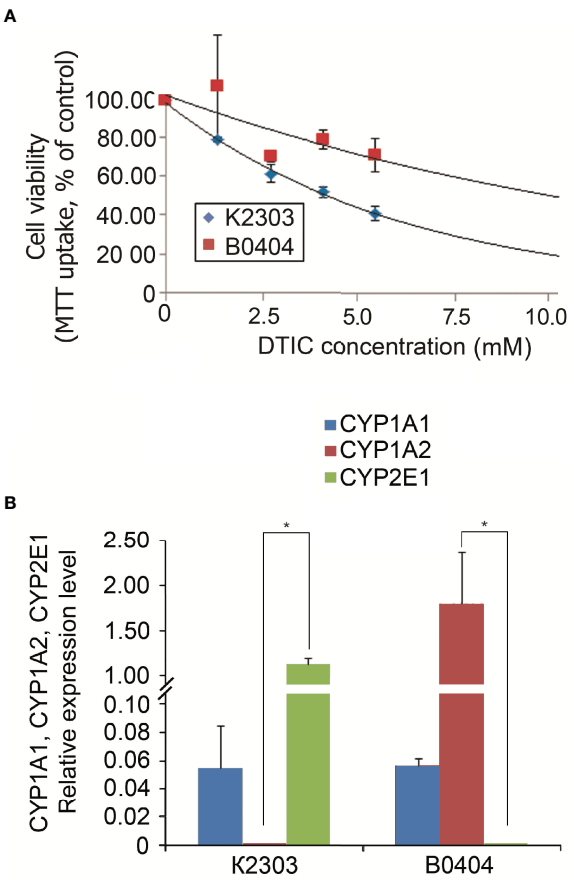

FIGURE 1 | **(A)** Sensitivity of melanoma cell lines K2303 and B0404 to dacarbazine. 3-(4,5-dimethylthiazol-2-yl)-2,5-diphenyltetrazolium bromide-assay-based dose-response curves were used to estimate the 50% inhibitory concentration. IC_{50} was calculated using the GraphPad Software Prism 7.05/e Data are presented as the mean ± SEM. **(B)** Relative *CYP1A1*, *CYP1A2* and *CYP2E1* gene expression levels according to reverse transcription-quantitative polymerase chain reaction in K2303 and B0404 melanoma cells. Data are presented as the mean ± SEM. *P<0.05 by Mann-Whitney U test for unpaired samples.

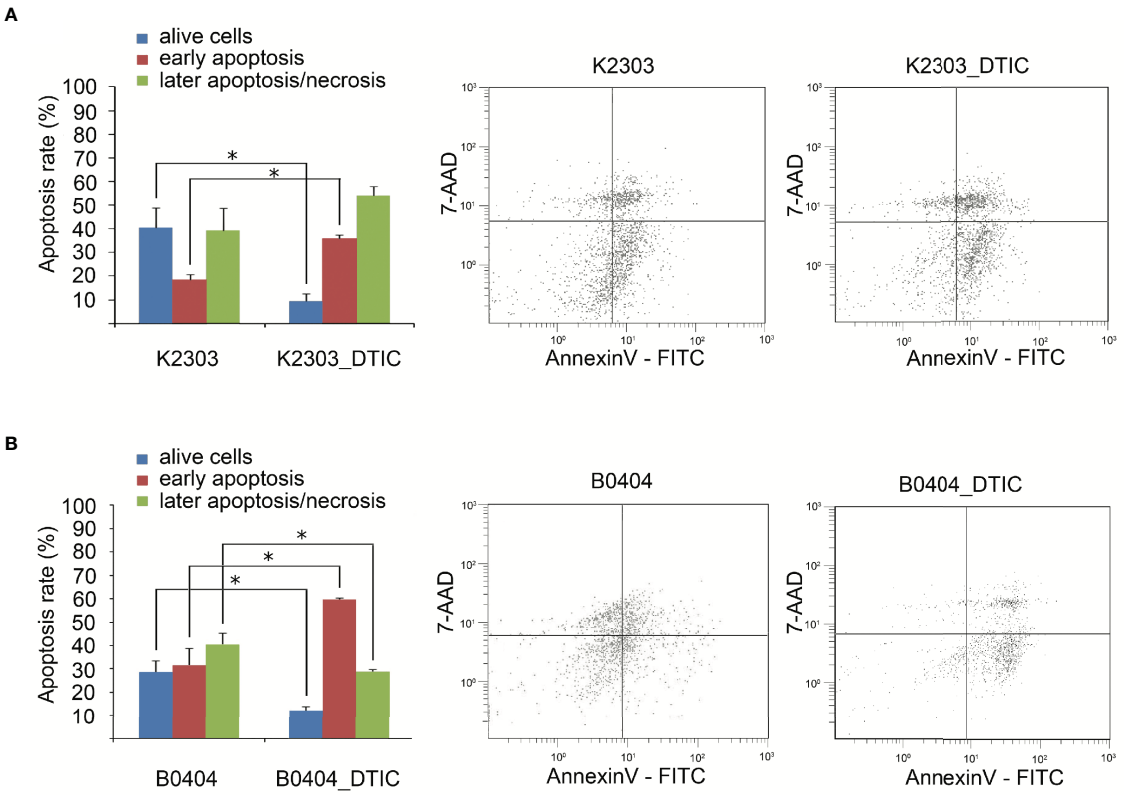

FIGURE 2 | Effect of dacarbazine at 5.5 mM on the apoptosis of melanoma cells according to the results of the annexin V/7-aminoactomycin flow cytometry assay. **(A)** The percentages of live, early-apoptotic, late-apoptotic and necrotic cells are shown in the two-parameter scatterplots for K2303 melanoma cells. **(B)** The percentages of live, early-apoptotic, late-apoptotic and necrotic cells are shown in the two-parameter scatterplots for B0404 melanoma cells. Data are presented as the mean ± SEM. *P<0.05 by Mann-Whitney U test for unpaired samples.

demonstrated notable responses to treatment, since DTIC increased the percentage of cells in early apoptosis by two-fold (**Figure 2**). The proportion of late apoptotic and necrotic cells was not altered in K2303 and reduced in B0404.

DTIC Treatment Results in Differential Migrative and Invasive Capacities in Melanoma Cells

The rates of migration and invasion were altered following DTIC treatment. We observed evident reductions in the migratory and invasive capacities of K2303 cells, whilst B0404 cells exhibited increased cell migration and invasion (**Figure 3**). Therefore, melanoma cells appeared to respond differentially in terms of the ability to disseminate in response to DTIC treatment in the present study.

Transcriptomic Profile of Primary Melanoma Cells Following DTIC Treatment Is Characterized by Signaling Pathway Induction Associated With Cell Motility

To reveal the phenotype of primary melanoma cells obtained from the two different patients, we performed a transcriptomic study (**Figures 4A–C**). We identified a total of 5,042 genes with altered expression in K2303 cells and 8906 in B0404 cells after DTIC treatment. Upregulated genes in K2303 were generally associated with apoptosis (*TNFRS 10D*), DNA repair (*TDP2*), extracellular matrix remodeling (*TFPI2* and *RPTN*) and cell proliferation (*EPGN*, *GPRC5A*, *VASN*, *FOSB*, *SCUBE3* and *SULF1*). Among the list of downregulated genes, we observed them to be associated with cell proliferation (*FRAS1* and *ACAN)* and extracellular matrix remodeling *(ACAN)*. In B0404 cells, it was found that the genes that were upregulated following DTIC treatment were typically associated with T-cell mediated immune response (*GAGE1*), apoptosis and DNA repair (*RHOB*). By contrast, genes that were associated with cell proliferation (*AREG* and *DKK1*) and extracellular matrix remodeling (*MXRA5*, *MMP-1*, *EDIL3*, *CCDC80*, *TNC*, *ITGA8*, *FN1* and *CCBE1*) were downregulated.

We next focused our attention on signaling pathways where the differentially expressed genes were also components. We observed the top downregulated genes in B0404 to be components of the vascular endothelial growth factor A (VEGFA)/vascular endothelial growth factor receptor R2 (VEGFR2), PI3K/AKT, focal adhesion, interleukin-18, mitogen-activated protein kinase (MAPK), RAS and

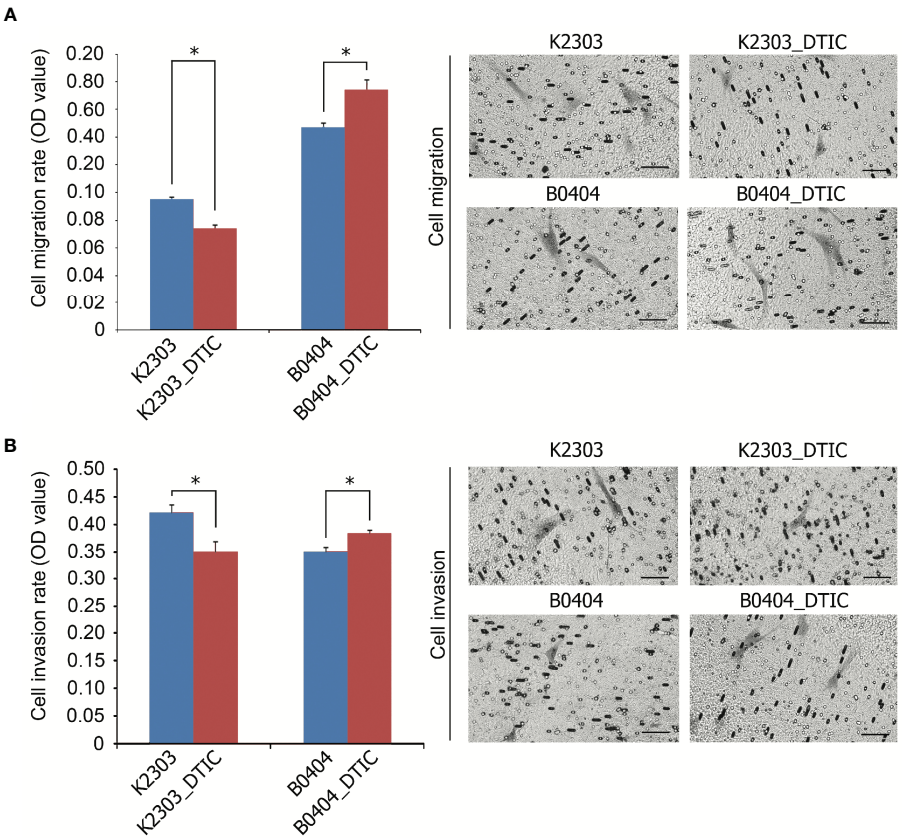

FIGURE 3 | Invasive and migratory potential of K2303 and B0404 melanoma cells after DTIC treatment. **(A)** Migration assay results of cells that were treated with 5.5 mM DTIC. Microscopic images of the polycarbonate membrane with migrated cells are shown. Migratory capacities of K2303 cells were reduced whilst B0404 cells exhibited increased cell migration. Data are presented as the mean ± SEM. *P<0.05 by Mann-Whitney U test for unpaired samples. DTIC, dacarbazine **(B)** Invasion assay results of cells that were treated with 5.5 mM DTIC. Microscopic images of the polycarbonate membrane with invasive cells are shown. Invasion rate of K2303 cells was reduced whilst the level of invasion of B0404 was increased. Data are presented as the mean ± SEM. *P<0.05 by Mann-Whitney U test for unpaired samples. DTIC, dacarbazine.

transforming growth factor (TGF)-β signaling pathways. Genes as components of PI3K/AKT, VEGFA/VEGFR2, focal adhesion, endothelin pathway, transforming growth factor (TGF)-β and hippo-Merlin signaling were downregulated in K2303 cells.

Since we found a clear dysregulation in the expression of genes associated with cell adhesion and migration, the expression levels of a number for these genes, components of up-regulated pathways were subsequently validated by RT-qPCR. Pathway Enrichment analysis was performed using the PANTHER database (http://pantherdb.org/). Gene Ontology (GO) terms associated with cancer cell biology ('biological adhesion', 'biological regulation', 'cellular process', 'developmental process', 'localization', 'locomotion', 'multicellular organismal process', 'response to stimulus' and 'signaling') were used to identify six genes matched to selected criteria, namely *ITGBL1*, *NOV*, *PLXNC1*, *ITGB3*, *ITGB8* and *PLXNA2*. Subsequently, *ITGB8* and *PLXNA2* were chosen as those most likely to be involved in the regulation of melanoma cell migration and invasion, as indicated in (22–24). *MMP1* was also selected as a key dysregulated gene in both cells following DTIC treatment, using the GO term 'cellular process'. Thus, the mRNA levels of ITGB8, plexin-A2 (PLNXA2) and MMP1 were measured in both cell lines before and after DTIC treatment. ITGB8 and MMP1 downregulation were found in both cell lines. However, PLNXA2 mRNA expression was increased in K2303 cells, whereas PLNXA2 expression was reduced in B0404 cells after DTIC treatment (**Figure 4D**). The expression levels of all three of these genes corresponded accurately with the microarray data in the present study, although the MMP1 levels showed a tendency to decrease according to the microarray result but a significant decrease was observed in the RT-qPCR data. Thus, PLNXA2 down-regulation was associated with migrative and invasive phenotype of primary melanoma cells.

DISCUSSION

Recently, a number of approaches have been implemented for melanoma treatment to provide beneficial effects, including anti-

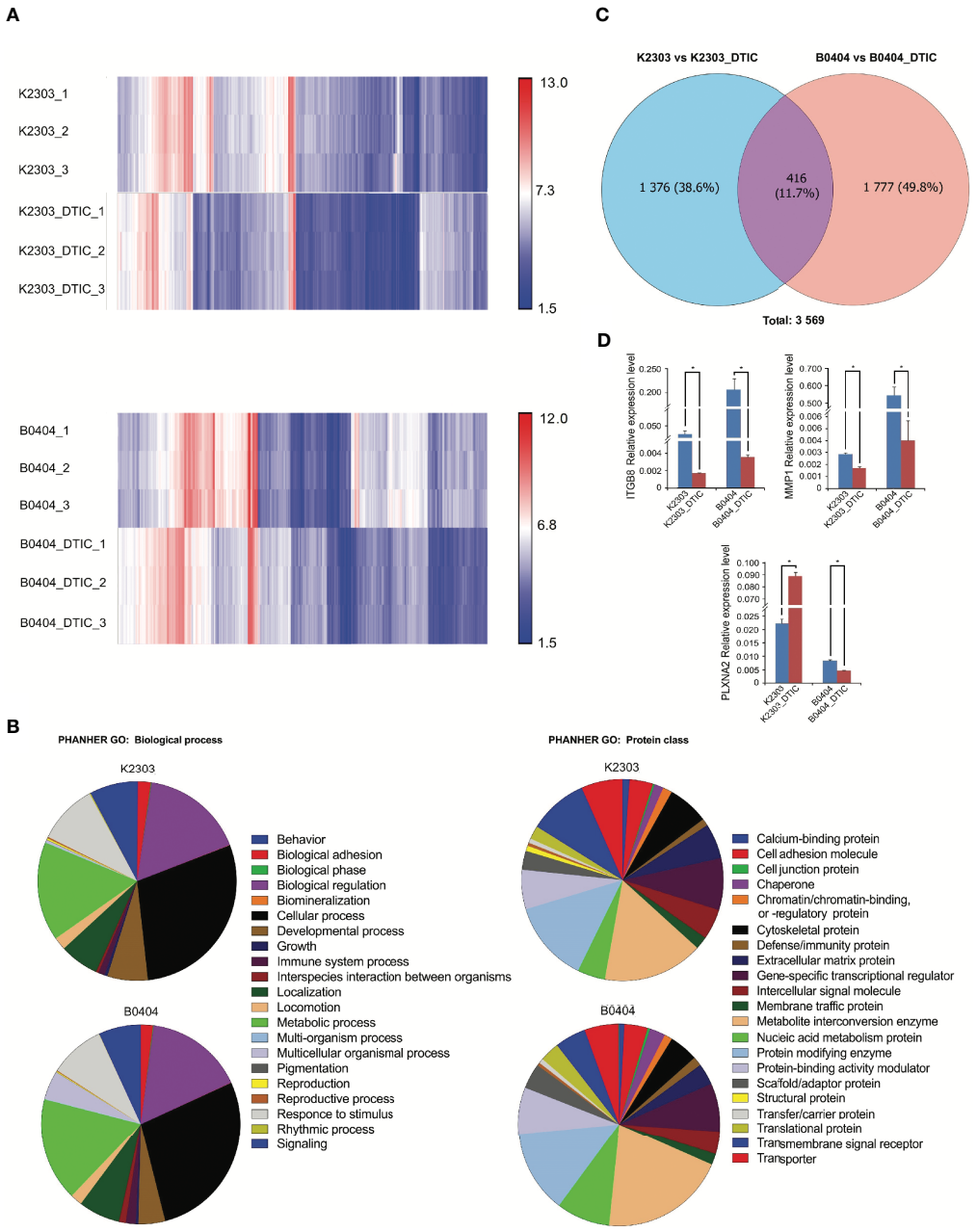

FIGURE 4 | Results of whole transcriptome analysis of K2303 and B0404 melanoma cells. **(A)** Heatmaps showing differentially altered transcripts in K2303 and B0404 melanoma cells after DTIC treatment. **(B)** Gene Ontology annotations for the two sub-trees, representing the biological process and protein class, for genes with dysregulated expression after exposure to DTIC in K2303 and B0404 melanoma cells. Plots were made using the PANTHER^{TM} v.16.0 classification system (http://www.pantherdb.org). **(C)** The Venn diagram shows the total number of altered transcripts in K2303 and B0404 melanoma cells after treatment with DTIC. **(D)** Changes in relative gene expression levels according to reverse transcription-quantitative polymerase chain reaction in K2303 and B0404 melanoma cells after 5.5 mM DTIC treatment. Data are presented as the mean ± SEM. *P<0.05 by Mann-Whitney U test for unpaired samples. DTIC, dacarbazine.

programed death-1 antibodies, BRAF and MEK inhibitors (25). However, chemotherapeutic agents remain to be in use in clinical oncology. Cancer cells utilize a diverse of set of mechanisms to mediate resistance to chemotherapeutic agents based on alkylation, which explains why sensitivity can vary greatly (26). In the present study, we administered DTIC to primary melanoma cell lines obtained from two different patients. Before it, we analyzed cytochrome P1A1, cytochrome P1A2, and cytochrome P2E1 expression revealed by microarray and RT-qPCR in terms of ability to activate DTIC. We revealed cytochrome P1A1 expression in both cell lines, whereas cytochrome P1A2 expressed in B0404 cells, cytochrome P2E1

in K2303 cells. The cells exhibited response to DTIC in terms of the levels of apoptosis. Indeed, K2303 and B0404 melanoma cells responded by increasing the number of early apoptotic cells. In addition, B0404 cells demonstrated enhanced migratory and invasive capacities following DTIC treatment, which was opposite to that observed in K2303 cells, where reduced rates in both of these characteristics were observed. To unravel the possible underlying mechanism of this finding we performed a transcriptomic analysis in both of these cell lines before and after treatment with DTIC.

Transcriptomic analysis revealed that 416 genes were dysregulated significantly in both cell lines, which constituted only 12% of all differentially expressed genes with a fold change ≥2. Such modest uniformity is in the line with the phenotypic diversity observed in response to DTIC. DTIC was also found to trigger the expression of genes associated with DNA repair and apoptosis. Among those that were upregulated after being treated with DTIC were *RHOB*, *GCLM* and *TGM2*. In addition, a number of downregulated signaling pathways such as growth factor A (VEGFA)/vascular endothelial growth factor receptor R2 (VEGFR2), PI3K/AKT, focal adhesion were found to be associated with metastasis in both cell lines after treatment with DTIC, including motility, migration, invasion and adhesion, according to the transcriptomic profile analysis. This caught our attention as these aforementioned characteristics may affect the overall patient response and survival rates (27, 28). Therefore, the expression levels of a number of these chosen genes that were found to be associated with the aforementioned processes related to metastasis were measured by RT-qPCR. ITGB8 and MMP1 expression levels were reduced after DTIC incubation, which concurred with results from transcriptomic analysis. All three molecules have been previously shown to be implicated in tumor progression and metastasis of various cancer types including melanoma (22–24, 29, 30). ITGB8 is involved in TGF-β activation (31, 32), which was found to be downregulated after DTIC treatment in the present study. MMP1 is an important enzyme that is activated by TGF-β and mediates extracellular matrix degradation, especially those of collagen type I, II and III (33, 34). Therefore, ITGB8 and MMP1 may act unidirectionally following altered TGF-β signaling.

By contrast, we observed a reduction in PLXNA2 expression in B0404 cells but elevated PLXNA2 expression in K2303 cells, which is opposite to the trend observed in the migration and invasion assays following DTIC treatment. PLXNA2 belongs to the semaphorin family of proteins that is more synonymous with nervous system development (35, 36). However, PLXNA2 has been later reported to be implicated in the proliferation and invasion of breast cancer cells (37). Melanoma is originated from melanocytes, which are cells of neuronal origin. Therefore, genes in the semaphorin/plexin signaling pathway may serve a role in the biology of neoplastic melanocytes (18). Class A plexins function as receptors for classes 3, 5 and 6 of semaphorins (38). The signaling consequences of PLXNA2-semaphorins have been extensively studied in cancers of the nervous system (29, 39). Semaphorin 3C downregulation was reported to be associated with a more metastatic phenotype in neuroblastoma cells (40), consistent with our present findings of increased B0404 melanoma cell invasion and migration. In addition, recent study also showed that gene upregulation specific for embryonic melanoblasts is necessary to facilitate melanoma dissemination (41). The results of a previous study demonstrated that PLXNA2 played a key role in the regulation of perineural invasion of prostate cancer (42). Moreover, Tivan TV et al. demonstrated that migration and invasion were increased in prostate cancer cells treated with PLXNA2 small interfering RNA (30). The use of PLXNA2-knockout mice also revealed that PLXNA2 controls retinal cell migration during retinal neurogenesis (43). However, the underlying mechanisms by which this membrane-bound molecule is involved in the regulation of cell migration remain to be fully elucidated.

Transcriptomic profiling of tumors is under extensive assessment as a potential prognostic tool and as a method for predicting anti-cancer agent efficacy (44). However, the accuracy for the application of tumor-based gene expression analysis remains unverified and additional evidence is required prior to its use in routine clinical practice (45). Tumor heterogeneity may yet prove to be an obstacle to its clinical applicability, since the genomic landscape within any single melanoma tumor is characterized by significant differences. Melanoma remains a type of skin cancer with a high rate of cancer-associated deaths (46).

Nevertheless, this study has some limitations: the number of cell lines was limited due to obtaining of operative material from melanoma patients, efficacy of primary melanoma cells isolation for experiments *in vitro* and costs of transcriptomic study. Second, the microarray analysis was performed in three replicates that was also limited because of aforementioned reasons. The present study lacks PLXNA2-based mechanistic experiments due to difficulties in the cultivation and transfection of primary melanoma cells. However, all results discussed in this paper were reaching statistical significance level. The role of PLXNA2 in the regulation of melanoma cell invasion and migration may be a novel marker for the characterization of melanoma cells based on invasive or proliferative phenotypes. Such phenotypes may be used in predicting patient prognosis. Further studies should provide a more complete understanding of melanoma resistance to chemotherapeutic agents and cancer cell chemoresistance.

CONCLUSIONS

Our findings suggest that other therapeutic options would need to be explored for melanoma. This is due to the high heterogeneity in the genetic landscape of the tumor and in the results from the functional study of cancer cells derived from individual patients. Data from the present study could be applied for further studies into phenotypic alterations in the tumor following the administration of anticancer agents.

DATA AVAILABILITY STATEMENT

The datasets presented in this study can be found in online repositories. The names of the repository/repositories and accession number(s) can be found in the article/supplementary material.

ETHICS STATEMENT

The study was approved by the ethics committee of the Krasnoyarsk State Medical University (protocol no. 73/2016; approval date, 16 December, 2016) and the Krasnoyarsk Regional Clinical Oncology Center named after A.I. Kryzhanovskiy (protocol no. 8, 14, June, 2017). The patients/participants provided their written informed consent to participate in this study.

AUTHOR CONTRIBUTIONS

All authors contributed to the concept and design of the study. All authors contributed to the article and approved the submitted version.

FUNDING

The study was supported by a grant from the Russian Science Foundation (project №19-15-00110).

REFERENCES

1. Rebecca VW, Somasundaram R, Herlyn M. Pre-Clinical Modeling of Cutaneous Melanoma. *Nat Commun* (2000) 11:2858. doi: 10.1038/s41467-020-15546-9
2. Wright FC, Souter LH, Kellett S, Easson A, Murray C, Toye J, et al. Primary Excision Margins, Sentinel Lymph Node Biopsy, and Completion Lymph Node Dissection in Cutaneous Melanoma: A Clinical Practice Guideline. *Curr Oncol* (2019) 26:e541–50. doi: 10.3747/co.26.4885
3. Biteghe FAN, Padayachee E, Davids LM, Chalomie NET, Ndong JC, Barth S. Desensitization of Metastatic Melanoma Cells to Therapeutic Treatment Through Repeated Exposure to Dacarbazine. *J Photochem Photobiol B* (2020) 211:111982. doi: 10.1016/j.jphotobiol.2020.111982
4. Narahira A, Yanagi T, Kitamura S, Maeda T, Hata H, Asano T, et al. Advanced Malignant Melanoma Successfully Treated With Dacarbazine Following Anti-PD-1/CTLA-4 Treatment. *Int J Dermatol* (2020) 59:e414–6. doi: 10.1111/ijd.14997
5. Pflugfelder A, Kochs C, Blum A, Capellaro M, Czeschik C, Dettenborn T, et al. Malignant Melanoma S3-Guideline "Diagnosis, Therapy and Follow-Up of Melanoma". *J Dtsch Dermatol Ges* (2012) 11(Suppl 6):1–116. doi: 10.1111/ddg.12113_suppl
6. Piotrowska A, Wierzbicka J, Rybarczyk A, Tuckey RC, Slominski AT, Żmijewski MA. Vitamin D and Its Low Calcemic Analogs Modulate the Anticancer Properties of Cisplatin and Dacarbazine in the Human Melanoma A375 Cell Line. *Int J Oncol* (2019) 54:1481–95. doi: 10.3892/ijo.2019.4725
7. Zhang J, Stevens MF, Bradshaw TD. Temozolomide: Mechanisms of Action, Repair and Resistance. *Curr Mol Pharmacol* (2012) 5:102–14. doi: 10.2174/1874467211205010102
8. Seoane J. Cancer: Division Hierarchy Leads to Cell Heterogeneity. *Nature* (2017) 549:164–6. doi: 10.1038/nature23546
9. Auger N, Thillet J, Wanherdrick K, Idbaih A, Legrier ME, Dutrillaux B, et al. Genetic Alterations Associated With Acquired Temozolomide Resistance in SNB-19, a Human Glioma Cell Line. *Mol Cancer Ther* (2006) 5:2182–92. doi: 10.1158/1535-7163.MCT-05-0428
10. Carmona-Fontaine C, Deforet M, Akkari L, Thompson CB, Joyce LA, Xavier JB. Metabolic Origins of Spatial Organization in the Tumor Microenvironment. *Proc Natl Acad Sci USA* (2017) 114:2934–9. doi: 10.1073/pnas.1700600114
11. Tasdogan A, Faubert B, Ramesh V, Ubellacker JM, Shen B, Solmonson A, et al. Metabolic Heterogeneity Confers Differences in Melanoma Metastatic Potential. *Nature* (2020) 577:115–20. doi: 10.1038/s41586-019-1847-2
12. Vasan N, Baselga J, Hyman DM. A View on Drug Resistance in Cancer. *Nature* (2019) 575:299–309. doi: 10.1038/s41586-019-1730-1
13. Spivak-Kroizman TR, Hostetter G, Posner R, Aziz M, Hu C, Demeure MJ, et al. Hypoxia Triggers Hedgehog-Mediated Tumor-Stromal Interactions in Pancreatic Cancer. *Cancer Res* (2013) 73:3235–47. doi: 10.1158/0008-5472.CAN-11-1433
14. Giatromanolaki A, Kouroupi M, Pouliliou S, Mitrakas A, Hasan F, Pappa A, et al. Ectonucleotidase CD73 and CD39 Expression in non-Small Cell Lung Cancer Relates to Hypoxia and Immunosuppressive Pathways. *Life Sci* (2020) 259:118389. doi: 10.1016/j.lfs.2020.118389
15. Li H, Chen J, Wang X, He M, Zhang Z, Cen Y. Nodal Induced by Hypoxia Exposure Contributes to Dacarbazine Resistance and the Maintenance of Stemness in Melanoma Cancer Stem–Like Cells. *Oncol Rep* (2018) 39:2855–64. doi: 10.3892/or.2018.6387
16. Erdmann S, Seidel D, Jahnke HG, Eichler M, Simon J-C, Robitzki AA. Induced Cross-Resistance of BRAFV600E Melanoma Cells to Standard Chemotherapeutic Dacarbazine After Chronic PLX4032 Treatment. *Sci Rep* (2019) 9. doi: 10.1038/s41598-018-37188-0
17. Chi M, Ye Y, Zhang XD, Chen J. Insulin Induces Drug Resistance in Melanoma Through Activation of the PI3K/Akt Pathway. *Drug Des Devel Ther* (2014) 8:255–62. doi: 10.2147/DDDT.S53568
18. Komina AV, Palkina NV, Aksenenko MB, Lavrentev SN, Moshev AV, Savchenko AA, et al. Semaphorin-5A Downregulation is Associated With Enhanced Migration and Invasion of BRAF-Positive Melanoma Cells Under Vemurafenib Treatment in Melanomas With Heterogeneous BRAF Status. *Melanoma Res* (2019) 29:544–8. doi: 10.1097/CMR.0000000000000621
19. Panach L, Pertusa C, Martínez-Rojas B, Acebrón A, Mifsut D, Tarín JJ, et al. Comparative Transcriptome Analysis Identifies CARM1 and DNMT3A as Genes Associated With Osteoporosis. *Sci Rep* (2020) 10:16298. doi: 10.1038/s41598-020-72870-2
20. Schmittgen TD, Livak KJ. Analyzing Real-Time PCR Data by the Comparative C(T) Method. *Nat Protoc* (2008) 3:1101–8. doi: 10.1038/nprot.2008.73
21. Reid JM, Kuffel MJ, Miller JK, Rios R, Ames MM. Metabolic Activation of Dacarbazine by Human Cytochromes P450: The Role of CYP1A1, CYP1A2, and CYP2E1. *Clin Cancer Res* (1999) 5:2192–7.
22. Ambrosi L, Khan S, Carvajal RD, Yang J. Novel Targets for the Treatment of Melanoma. *Curr Oncol Rep* (2019) 21:97. doi: 10.1007/s11912-019-0849-4
23. Strobel H, Baisch T, Fitzel R, Schilberg K, Siegelin MD, Karpel-Massler G, et al. Temozolomide and Other Alkylating Agents in Glioblastoma Therapy. *Biomedicines* (2019) 7:69. doi: 10.3390/biomedicines7030069
24. Tagliabue E, Ghirelli C, Squicciarini P, Aiello P, Colnaghi MI, Ménard S. Prognostic Value of Alpha 6 Beta 4 Integrin Expression in Breast Carcinomas Is Affected by Laminin Production From Tumor Cells. *Clin Cancer Res* (1998) 4:407–10.
25. Wong BS, Shah SR, Yankaskas CL, Bajpai VK, Wu PH, Chin D, et al. A Microfluidic Cell-Migration Assay for the Prediction of Progression-Free Survival and Recurrence Time of Patients With Glioblastoma. *Nat Biomed Eng* (2021) 5:26–40. doi: 10.1038/s41551-020-00621-9
26. Blackburn JS, Liu I, Coon CI, Brinckerhoff CE. A Matrix Metalloproteinase-1/Protease Activated Receptor-1 Signaling Axis Promotes Melanoma Invasion and Metastasis. *Oncogene* (2009) 28:4237–48. doi: 10.1038/onc.2009.272
27. Kidacki M, Lehman HL, Green MV, Warrick JI, Stairs DB. P120-Catenin Downregulation and PIK3CA Mutations Cooperate to Induce Invasion

Through MMP1 in HNSCC. *Mol Cancer Res* (2017) 15:1398–409. doi: 10.1158/1541-7786.MCR-17-0108
28. Mertens-Walker I, Fernandini BC, Maharaj MS, Rockstroh A, Nelson CC, Herington AC, et al. The Tumour-Promoting Receptor Tyrosine Kinase, EphB4, Regulates Expression of Integrin-β8 in Prostate Cancer Cells. *BMC Cancer* (2015) 15:164. doi: 10.1186/s12885-015-1164-6
29. Presta I, Donato A, Malara N, Russo E, Hribal ML, Donato G. Classical Differentiation Protocols Upregulate the Expression of the Axon Guidance Genes PLXNA2 and SEMA3C in SH-SY5Y Neuroblastoma Cells. *Hum Cell* (2019) 32:397–400. doi: 10.1007/s13577-019-00246-4
30. Tian TV, Tomavo N, Huot L, Flourens A, Bonnelye E, Flajollet S, et al. Identification of Novel TMPRSS2:ERG Mechanisms in Prostate Cancer Metastasis: Involvement of MMP9 and PLXNA2. *Oncogene* (2014) 33:2204–14. doi: 10.1038/onc.2013.176
31. Mu D, Cambier S, Fjellbirkeland L, Baron JL, Munger JS, Kawakatsu H, et al. The Integrin Alpha(V)Beta8 Mediates Epithelial Homeostasis Through MT1-MMP-Dependent Activation of TGF-Beta1. *J Cell Biol* (2002) 157:493–507. doi: 10.1083/jcb.200109100
32. Yang Y, Zenke Y, Hirai T, Kaplan DH. Keratinocyte-Derived Tgfβ is Not Required to Maintain Skin Immune Homeostasis. *J Dermatol Sci* (2019) 95:134. doi: 10.1016/j.jdermsci.2019.04.008
33. Hall MC, Young DA, Waters JG, Rowan AD, Chantry A, Edwards DR, et al. The Comparative Role of Activator Protein 1 and Smad Factors in the Regulation of Timp-1 and MMP-1 Gene Expression by Transforming Growth Factor-Beta 1. *J Biol Chem* (2003) 278:10304–13. doi: 10.1074/jbc.M212334200
34. Mekkat A, Poppleton E, An B, Visse R, Nagase H, Kaplan DL, et al. Effects of Flexibility of the α2 Chain of Type I Collagen on Collagenase Cleavage. *J Struct Biol* (2018) 203:247–54. doi: 10.1016/j.jsb.2018.05.002
35. Ebert AM, Childs SJ, Hehr CL, Cechmanek PB, McFarlane S. Sema6a and Plxna2 Mediate Spatially Regulated Repulsion Within the Developing Eye to Promote Eye Vesicle Cohesion. *Development* (2014) 141:2473–82. doi: 10.1242/dev.103499
36. Murakami Y, Suto F, Shimizu M, Shinoda T, Kameyama T, Fujisawa H. Differential Expression of Plexin-A Subfamily Members in the Mouse Nervous System. *Dev Dyn* (2001) 220:246–58. doi: 10.1002/1097-0177(20010301)220:3<246::AID-DVDY1112>3.0.CO;2-2
37. Gabrovska PN, Smith RA, Tiang T, Weinstein SR, Haupt LM, Griffiths LR. Semaphorin-Plexin Signalling Genes Associated With Human Breast Tumourigenesis. *Gene* (2011) 489:63–9. doi: 10.1016/j.gene.2011.08.024
38. Kong Y, Janssen BJ, Malinauskas T, Vangoor VR, Coles CH, Kaufmann R, et al. Structural Basis for Plexin Activation and Regulation. *Neuron* (2016) 91:548–60. doi: 10.1016/j.neuron.2016.06.018
39. Valiulyte I, Steponaitis G, Kardonaite D, Tamasauskas A, Kazlauskas A. A SEMA3 Signaling Pathway-Based Multi-Biomarker for Prediction of Glioma Patient Survival. *Int J Mol Sci* (2020) 21:7396. doi: 10.3390/ijms21197396
40. Delloye-Bourgeois C, Bertin L, Thoinet K, Jarrosson L, Kindbeiter K, Buffet T, et al. Microenvironment-Driven Shift of Cohesion/Detachment Balance Within Tumors Induces a Switch Toward Metastasis in Neuroblastoma. *Cancer Cell* (2017) 32:427–43. doi: 10.1016/j.ccell.2017.09.006
41. Marie KL, Sassano A, Yang HH, Michalowski AM, Michael HT, Guo T, et al. Melanoblast Transcriptome Analysis Reveals Pathways Promoting Melanoma Metastasis. *Nat Commun* (2020) 11:333. doi: 10.1038/s41467-019-14085-2
42. Yin L, Li J, Wang J, Pu T, Wei J, Li Q, et al. MAOA Promotes Prostate Cancer Cell Perineural Invasion Through SEMA3C/PlexinA2/NRP1-cMET Signaling. *Oncogene* (2021) 40:1362–74. doi: 10.1038/s41388-020-01615-2
43. Belle M, Parray A, Belle M, Chédotal A, Nguyen-Ba-Charvet KT. PlexinA2 and Sema6A Are Required for Retinal Progenitor Cell Migration. *Dev Growth Differ* (2016) 58:492–502. doi: 10.1111/dgd.12298
44. Rabbie R, Ferguson P, Molina-Aguilar C, Adams DJ, Robles-Espinoza CD. Melanoma Subtypes: Genomic Profiles, Prognostic Molecular Markers and Therapeutic Possibilities. *J Pathol* (2019) 247:539–51. doi: 10.1002/path.5213
45. Grossman D, Okwundu N, Bartlett EK, Marchetti MA, Othus M, Coit DG, et al. Prognostic Gene Expression Profiling in Cutaneous Melanoma: Identifying the Knowledge Gaps and Assessing the Clinical Benefit. *JAMA Dermatol* (2020) 156:1004–11. doi: 10.1001/jamadermatol.2020.1729
46. Gyrylova SN, Aksenenko MB, Gavrilyuk DV, Palkina NV, Dyhno YA, Ruksha TG, et al. Melanoma Incidence, Mortality Rates and Clinic-Pathological Types in the Siberian Area of the Russian Federation. *Asian Pacific J Cancer Prev* (2014) 15:2201–4. doi: 10.7314/APJCP.2014.15.5.2201

Conflict of Interest: The authors declare that the research was conducted in the absence of any commercial or financial relationships that could be construed as a potential conflict of interest.

Publisher's Note: All claims expressed in this article are solely those of the authors and do not necessarily represent those of their affiliated organizations, or those of the publisher, the editors and the reviewers. Any product that may be evaluated in this article, or claim that may be made by its manufacturer, is not guaranteed or endorsed by the publisher.

frontiers in Cell and Developmental Biology

ORIGINAL RESEARCH
published: 26 January 2022
doi: 10.3389/fcell.2022.805507

Association of Angiogenesis Gene Expression With Cancer Prognosis and Immunotherapy Efficacy

*Xin-yu Li[1,2†], Wei-Ning Ma[3†], Li-xin Su[1†], Yuchen Shen[1†], Liming Zhang[1], Yuhao Shao[1], Deming Wang[1], Zhenfeng Wang[1], Ming-Zhe Wen[1] and Xi-tao Yang[1]**

[1]Department of Interventional Therapy, Shanghai Ninth People's Hospital, Shanghai Jiao Tong University School of Medicine, Shanghai, China, [2]Department of Neurosurgery, Shanghai Ninth People's Hospital, Shanghai Jiao Tong University School of Medicine, Shanghai, China, [3]Department of Pediatrics, Shanghai General Hospital, Shanghai Jiao Tong University School of Medicine, Shanghai, China

OPEN ACCESS

Edited by:
Qiangzhe Zhang, Nankai University, China

Reviewed by:
Domenico Ribatti, University of Bari Aldo Moro, Italy
Antonio Giovanni Solimando, University of Bari Aldo Moro, Italy
Hussien Ahmed Khamees, Community College, Yemen

***Correspondence:**
Xi-tao Yang
xitao123456@126.com

†These authors have contributed equally to this work

Specialty section:
This article was submitted to Molecular and Cellular Oncology, a section of the journal Frontiers in Cell and Developmental Biology

Received: *30 October 2021*
Accepted: *03 January 2022*
Published: *26 January 2022*

Citation:
Li X-y, Ma W-N, Su L-x, Shen Y, Zhang L, Shao Y, Wang D, Wang Z, Wen M-Z and Yang X-t (2022) Association of Angiogenesis Gene Expression With Cancer Prognosis and Immunotherapy Efficacy. Front. Cell Dev. Biol. 10:805507. doi: 10.3389/fcell.2022.805507

Background: Several new blood vessels are formed during the process of tumor development. These new blood vessels provide nutrients and water for tumour growth, while spreading tumour cells to distant areas and forming new metastases in different parts of the body. The available evidence suggests that tumour angiogenesis is closely associated with the tumour microenvironment and is regulated by a variety of pro-angiogenic factors and/or angiogenic inhibitors.

Methods: In the present study, a comprehensive characterization of angiogenesis genes expression was performed in a pan-cancer analysis across the 33 human cancer types. Further, genetic data from several public databases were also used in the current study. An angiogenesis score was assigned to The Cancer Genome Atlas (TCGA) pan-cancer data, with one angiogenesis score as per sample for each tumour.

Results: It was found that angiogenesis genes vary across cancer types, and are associated with a number of genomic and immunological features. Further, it was noted that macrophages and iTreg infiltration were generally higher in tumours with high angiogenesis scores, whereas lymphocytes and B cells showed the opposite trend. Notably, NK cells showed significantly different correlations among cancer types. Furthermore, results of the present study showed that a high angiogenesis score was associated with poor survival and aggressive types of cancer in most of the cancer types.

Conclusion: In conclusion, the current study evidently showed that the expression of angiogenesis genes is a key feature of tumour biology that has a major impact on prognosis of patient with cancers.

Keywords: angiogenesis, pan-cancer, prognosis, methylation, gene expression

Abbreviations: TCGA, The Cancer Genome Atlas; DEGs, Differentially expressed genes; OS, Overall survival; FDR, False discovery rate; GO, Gene Ontology; KEGG, Kyoto Encyclopedia of Genes and Genomes; HR, Hazard ratio; CI: Confidence interval; See.

INTRODUCTION

Given that malignant tumours need supplies of oxygen and nutrients to survive and thrive, they require adequate vascularization to access the blood circulation system (Lugano et al., 2020). Previous studies have shown that rapid growth of tumours requires a large supply of nutrients from the blood as compared with dormant tumours. Therefore, it should be noted that initiation of tumour angiogenesis is a major factor for tumor development (Azoitei et al., 2010). Results of a previous clinical trial showed that anti-angiogenic therapy can be successfully used to treat cancer (Hurwitz et al., 2004). Recently, anti-tumour angiogenesis research has evolved from the early non-specific embolisation and severance of tumour vessels to a new level of specific and targeted blockade of tumour vessels (Hida et al., 2008; Mitsuhashi et al., 2015). However, it was found that the anti-angiogenesis therapy only provided a short-term relief and inhibition of tumour growth before resistance is developed (Lugano et al., 2020). Further, emerging evidence shows that angiogenesis and immunosuppression frequently occur simultaneously in response to this crosstalk. Accordingly, strategies combining both anti-angiogenic therapy and immunotherapy have potential to tip the balance of the tumor microenvironment and improve treatment response (Solimando et al., 2020).

The present study provides a comprehensive assessment of the genomic and clinical characteristics of angiogenesis genes in 33 solid tumours. In addition, the angiogenesis score of each patients with cancers was also assessed in the current study. Results of this study found that angiogenesis is correlated with distinct genomic and immunologic tumour characteristics. Moreover, it was found that expression of angiogenesis genes has prognostic and predictive value in outcomes of both patients and their response to immunotherapy. Therefore, the analyses reported in the current study provide the first comprehensive survey of angiogenesis genes expression across 33 cancer types.

MATERIALS AND METHODS

Datasets

The data of 33 tumors in The Cancer Genome Atlas (TCGA) including the mRNA data, mutation data, and clinical data were collected from UCSC Xena. The data on expression of gene for different tissues were retrieved from GTEx, whereas the angiogenesis relevant data was downloaded from the hallmark gene sets of the msigdb database. The flow of this articles is as presented in **Figure 1**.

Identification of Differential Genes

The present study analyzed differential expression of angiogenesis genes in tumour samples (from TCGA database) as compared with that of the normal samples (from TCGA and GTEx database). The "limma" R package was used to identify differentially expressed genes (DEGs), with FDR <0.05, and $|\log2FC| \geq 1$ as the cut-offs. Next, "ggplot" and "reshape" R packages were used to generate a heatmap to visualize the results obtained.

Survival Analysis of Angiogenesis Genes

The 'Survival' R package was used to conduct univariate Cox regression analysis for angiogenesis genes. Further, the *p*-value and HR-values were then extracted for heatmap presentation. The number of genes was then counted for which Cox analysis was significant in all tumours. Notably, a risk factor was considered if the score was increased by 1, whereas a protective factor was considered if the score was decreased by 1 and the final score was used as the risk score.

Genetic Correlation and Genetic Variation

In the present study, Pearson's r was used to explore correlations between different angiogenesis genes and the obtained results were presented using a heatmap. Genetic variation data was downloaded from the cbioportal database including mutations, fusions, amplifications, deletions, and multiple variants. Angiogenesis genes variants were then calculated for each

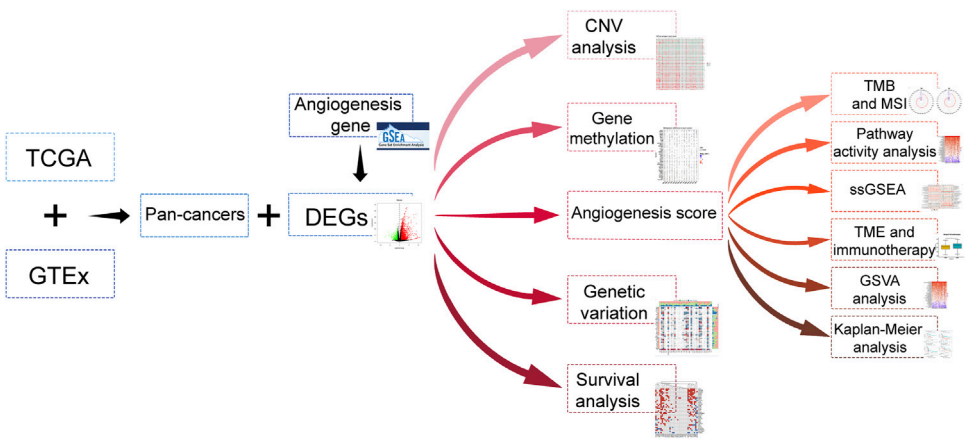

FIGURE 1 | Article flow diagram.

tumour. Finally, mutation of angiogenesis genes in different cancers was explored using Gene Set Cancer Analysis (GSCA) (http://bioinfo.life.hust.edu.cn/GSCA).

Gene Methylation Analysis and Copy Number Variation Analysis

Previous studies have suggested that DNA hypomethylation promote increased expression of many oncogenes, whereas DNA hypermethylation has also been shown to silence tumour suppressor genes (Wang et al., 2020). In the present study, the mRNA expression and methylation data for the angiogenesis genes were merged using the GSCA, followed by the analysis of the differential methylation. Further, a Student's *t* test was performed to determine the methylation difference between tumor and normal samples, and the *p*-value was adjusted using the FDR. Notably, FDR ≤0.05 was considered statistically significant. Pearson's or Spearman's correlation was then performed to explore the association between methylation and expression levels. Finally, HR for prognostic value of gene methylation status was calculated using Cox regression analysis. The information of copy number variations (CNVs) of the 33 types of tumors from the TCGA database and determined using GISTIC 2.0 software were also totally collected. In addition, the percentage of CNVs and CNVs correlation with mRNA were calculated by Spearman correlation analyses by corrplot package. The CNVs were classified into 2 categories (homozygous and heterozygous), including amplification and deletion, which represents the presence of CNVs on only one chromosome or two chromosomes. It is worth noting that only genes with CNV >5% in cancer were discussed in the present study. The associations between paired mRNA expression and paired CNV percentage samples were explored based on the Person's product moment correlation coefficient and t-distribution (Schlattl et al., 2011). The statistical significant threshold was set as FDR *p*-value ≤0.05.

Angiogenesis Score

The angiogenesis score for each sample in the present study was calculated using the "GSVA" R package (Kim et al., 2020). The size of the angiogenesis score in each tumour and explored the differences in angiogenesis score across clinical stages. Data visualization was done using "ggplot" R package (Shatalova et al., 2020). Next, the relationship between the angiogenesis score and prognoses in patients with cancer was explored. Survival estimates were calculated using Kaplan-Meier (KM) and Cox regression models. The "GSVA" R package was used to perform GSVA analysis, with t value >2 and FDR <0.05 as the cut-offs. Notably, the gene set used in this study was MsigDB dataset, HALLMARK pathway of the database. Single-sample gene set enrichment analysis (ssGSEA) was also employed to evaluate the enrichment scores for each sample. Therefore, the present study also evaluated the correlation between angiogenesis score and pathways. Finally, the correlation was visualized using "ggplot" R package (Shatalova et al., 2020).

Tumor Microenvironments and Immunotherapy

Immune and stromal scores were calculated using the ESTIMATE algorithm with the help of "limma" and "estimate" R packages. The relationship between the angiogenesis score and tumor microenvironment in accordance with a previous study was also assessed to validate the results obtained in the current study (Zeng et al., 2019). Finally, the data was plotted using the "pheatmap" R package. Considering the association of immune infiltration level with survival and prognosis in cancers, the correlation between angiogenesis score and immune infiltration level was hence explored. On the other hand, the CIBERSORT algorithm was used to estimate data on tumor-infiltrating immune cells (Thorsson et al., 2018; Huang et al., 2021). Immune Cell Abundance Identifier and TIMER2 were used to evaluate the correlation of angiogenesis score with immune infiltration across all tumors in the TCGA database. Plots were then performed using "ggplot" R package (Shatalova et al., 2020). The use of immunotherapy in cancer treatment has evolved rapidly and several therapeutic antibodies have reached the clinical practices in recent years (Hultqvist et al., 2017; Wu and Shih, 2018). Therefore, the present study used immunotherapy data to explore the impact of high or low angiogenesis score on the prognosis of immunotherapy patients. Specifically, immunotherapy data was used from IMvigor210 dataset, GSE78220, GSE135222, and GSCA.

Correlations Between Angiogenesis Score and Immunological Genes

The correlation between immune genes and angiogenesis score was also analyzed in the present study. The analyzed target genes included MHC genes, chemokines, chemokine receptors, and immunosuppressive genes. Recently, tumor mutation burden (TMB) has emerged as a predictive indicator for tumor immunotherapy, which aids in prognostic prediction of immunotherapy in some tumors such as lung cancer, malignant melanoma, and colon cancer (Kelley et al., 2020; Saeed and Salem, 2020). Microsatellite instability (MSI) is a genetic change that has been shown to be closely associated with tumor prognosis (De Palma et al., 2019; Li et al., 2020a). In the present study, the TMB score was calculated using R software and corrected by dividing the total length of the exon. In addition, the MSI scores for all samples were obtained from the somatic mutation data which was downloaded from TCGA database. Finally, Spearman correlation analysis was performed to assess the correlation of angiogenesis score with TMB and MSI scores.

RESULTS

Dysregulated Angiogenesis Genes in Various Cancer Types Are Associated With Prognosis

Using TCGA and GTEx datasets, we evaluated the differential expressions of angiogenesis-related genes between cancers

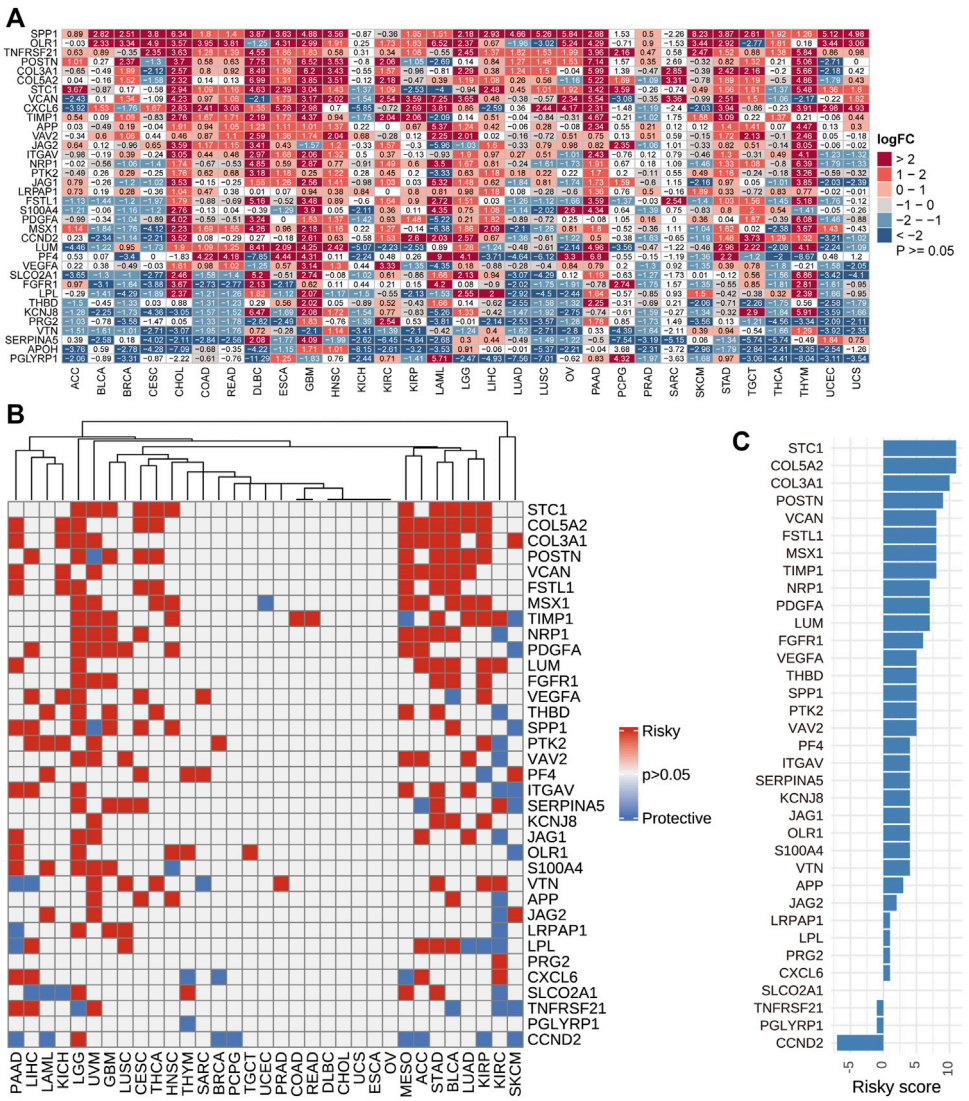

FIGURE 2 | (A): Differential expressions of angiogenesis-related genes. We found the angiogenesis genes were aberrantly expressed in 31 tumor types. **(B)**. Univariate Cox regression analysis of angiogenesis-associated genes in pan-cancer. Grey denotes $p > 0.05$, red represents $p < 0.05$ HR > 1while blue denotes HR < 1 **(C)**. The number of genes with significant cox analysis in all tumors was counted. As a risk factor +1, as a protective factor -1, the final score as risky score.

and normal tissues. The angiogenesis genes were aberrantly expressed in 31 tumor types ($p < 0.05$, **Figure 2A**). We found that angiogenesis genes tended to be significantly downregulated in BRCA (Breast invasive carcinoma) and UCES(Uterine Corpus Endometrial Carcinoma), but upregulated in PAAD (Pancreatic adenocarcinoma), GBM (Glioblastoma multiforme). These findings are consistent with several previous studies (Ardito et al., 2008; Liu et al., 2019). For example, SPP1 was upregulated in most tumor types. SPP1 enhances tumor development and its overexpression is associated with poor prognostic outcomes for melanoma, while its silencing suppresses melanoma cell proliferation, migration, as well as invasion (Komatsu et al., 2012; Deng et al., 2020). These findings imply that dysregulated expressions of angiogenesis-associated genes are involved in cancer initiation and development. Since angiogenesis-related genes play critical roles in cancer metastasis (Firestone and Sundar, 2009), we evaluated the associations between their expression levels and survival outcomes. In at least one cancer type, all angiogenesis-related genes were associated with overall survival outcomes (**Figure 2B**). In many cancer types, patients with elevated angiogenesis-associated gene levels have significantly poor survival outcomes, compared to those with suppressed levels. Risk scores revealed that most genes were unfavourable for patient prognosis. These findings imply that angiogenesis-related gene levels are associated with prognostic outcomes in many human cancer types, with suppressed levels exhibiting protective effects (**Figure 2C**).

Analysis of Angiogenesis Gene Variants and Methylation

The relationship between angiogenesis genes was established to be positively significant (**Supplementary Figure S1A**), suggesting that these genes could function individually or cooperatively. Notably, BRCA samples exhibited the highest number of variant genes. Genetic variabilities of *STC1* and *LPL* genes were highest, and they were dominated by deletions while gene fusions were dominant among the other gene variants (**Supplementary Figure S1B**). The development of many tumors has been associated with point mutations and deletions (Agirre et al., 2006). The single nucleotide variation (SNV) was dominated by C > T (50%) (**Supplementary Figures S2A-S2B**). **Supplementary Figure S2C** show the frequencies of deleterious mutations in pan-caner. For instance, elevated *VCAN* levels in gastric cancer independently predict poor prognostic outcomes, and patients with *VCAN* mutations have a lower tumor grade, compared to those without (Li et al., 2020b; Li et al., 2020c). Moreover, **Supplementary Figure S2D** shows survival differences between mutant (deleterious) and wild type in the selected cancers. Aberrant methylation status are correlated with the development of various diseases, including cancer (Shao et al., 2017). Evaluation of the methylation status of angiogenesis-associated genes in this study was aimed at identifying epigenetic regulation. **Supplementary Figure S2E** shows the differences between tumor and normal samples with regards to gene methylation. In different tumors, the methylations of angiogenesis-associated genes were highly heterogeneous. Relative to hypomethylated genes, there were more hypermethylated genes in BRCA, prostate adenocarcinoma (PRAD), uterine corpus endometrial carcinoma (UCEC), and colon adenocarcinoma (COAD). In addition, in most cancers, *PGLYRP1, KCNJ8,* and *LPL* were hypermethylated while *OLR1*, *VEGFA,* and *SPP1* were hypomethylated (**Supplementary Figure S2E**). Correlation analysis revealed that mRNA levels of angiogenesis-associated genes were negatively correlated with their methylation levels. However, in PRAD, skin cutaneous melanoma (SKCM), BRCA, liver hepatocellular carcinoma (LIHC), and uveal melanoma (UVM), *PTK1* exhibited positive correlations between methylation and mRNA expression levels (**Supplementary Figure S2F**). Survival analysis showed that in most cancers, hypermethylations of *PGLYRP1, PTK2, THBD,* and *CCND2* as well as hypomethylations of *VAV2, OLR1,* and *ITGAV* were associated with poor survival outcomes (**Supplementary Figure S3**). Hypermethylation of CCND2 was associated with female lung cancer and lung adenocarcinoma (Hung et al., 2018). Hypermethylation of CCND2 in lung and breast cancer is a potential biomarker and drug target (Hung et al., 2018).

CNV of Angiogenesis Genes Are Associated With Prognosis

CNV has been confirmed to have diagnostic, prognostic or therapeutic significances in various types of cancer (Su et al., 2018). In the present study, heterozygous amplifications and deletions were the main CNV types (**Supplementary Figure S4A**). For instance, CNV percentage analysis revealed that homozygous amplifications of *PTK2* in OV, ESCA, BRCA LIHC, and UVM as well as *CCND2, KCNJ8,* and *OLR1* in TGCT were all greater than 35% (**Supplementary Figure S4B**). Homozygous deletions of *LPL* and *STC1* in PRAD were all greater than 35% (**Supplementary Figure S4B**). Heterozygous analysis showed that the amplified gene (*PTGFA*) in TGCT, READ, GBM, and KIRP was greater than 35% in all cases, while *STC1* deletion in OV, LUSC, and LUAD was greater than 35% in all cases (**Supplementary Figure S4C**). **Supplementary Figure S5** shows the differences in survival outcomes between CNV and wild types for selected cancers. These results imply that the CNV of angiogenesis-associated genes mediate their abnormal expressions, suggesting that it plays a significant role in cancer development.

Associations Among Angiogenesis Scores, Clinical Stage and Patient Outcomes

For the 33 tumors, the highest angiogenesis scores were in PAAD while the lowest were in LAML (**Supplementary Figure S6A**). The scores in ACC, BLCA, BRCA, COAD, ESCA, LUSC, SKCM, STAD, and UVM varied across clinical stages. As clinical staging increased, so did the angiogenesis scores (**Supplementary Figures S6B-J**). **Supplementary Figures S7A-D** shows the associations between angiogenesis scores and pan-cancer overall survival (OS), disease free interval (DFI), progression-free interval (PFI), as well as disease-specific survival (DSS). Notably, HR was evaluated in the Cox proportional hazard models. In most cancers, high angiogenesis scores were associated with poor survival outcomes (**Supplementary Figure S8**). These results suggest a close association between angiogenesis scores and patient outcomes.

Pathway Activity Analysis and Enrichment Analysis

The related pathways network indicated that angiogenesis scores were significantly involved in cancer-related signaling pathways, including Kras signaling, TGF-beta signaling, apoptosis, IL-2 STAT5 signaling, TNF-a signaling via NFK-b, inflammatory responses, IL-6 JAK STAT3 signaling, notch signaling, and the P53 pathway (**Figure 3A**). However, these associations differed among tumors. For instance, in all cancer types, the IL-2 STAT5 signaling pathway was positively correlated with angiogenesis scores, while the DNA repair pathway exhibited the opposite trend. Besides, some pathways, such as those in pancreatic beta cells, exhibited different associations in different tumors. Using breast cancer as an example, enrichment analysis revealed a predominant enrichment in the PI3K-Akt signaling pathway, proteoglycans in cancer, human papillomavirus infections, and the relaxin signaling pathway (**Figure 3B**).

High Angiogenesis Scores Are Associated With Hot Tumor Microenvironments

The tumor microenvironment (TME) modulates tumor progression and treatment efficacy (Blanco-Fernandez et al., 2021). Therefore, we evaluated the relationship between the angiogenesis score and the TME. Angiogenesis was significantly correlated with the TME

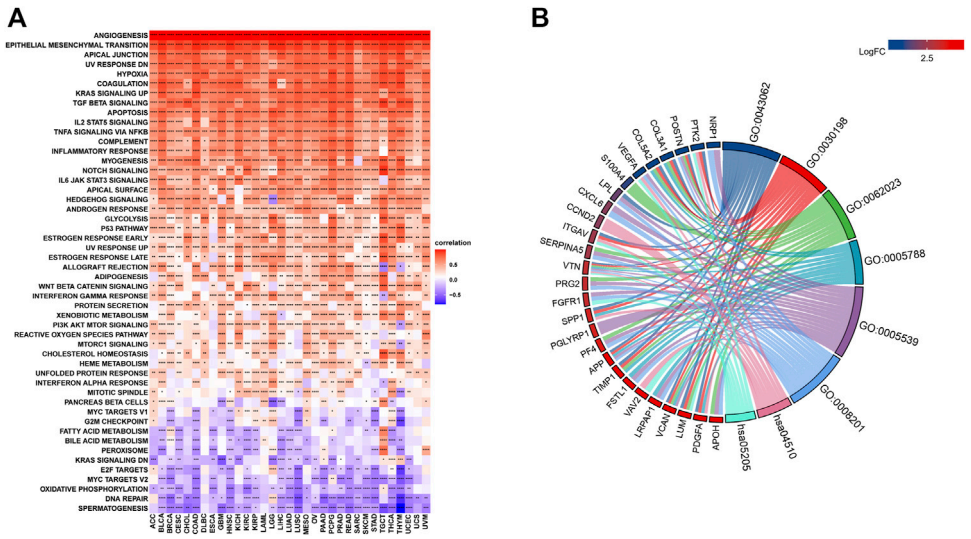

FIGURE 3 | (A). Gene Set Variant Analysis (Red represents positive correlations while blue represents negative correlations. Angiogenesis scores were significantly involved in cancer-related signaling pathways, including Kras signaling, TGF-beta signaling, apoptosis, IL-2 STAT5 signaling, TNF-a signaling via NFK-b, inflammatory responses, IL-6 JAK STAT3 signaling, notch signaling, and the P53 pathway. *** denotes $p < 0.001$, ** denotes $p < 0.01$, while * denotes $p < 0.05$). **(B)**. Enrichment analysis A predominant enrichment in the PI3K-Akt signaling pathway, proteoglycans in cancer, human papillomavirus infections, and the relaxin signaling pathway in BRCA.

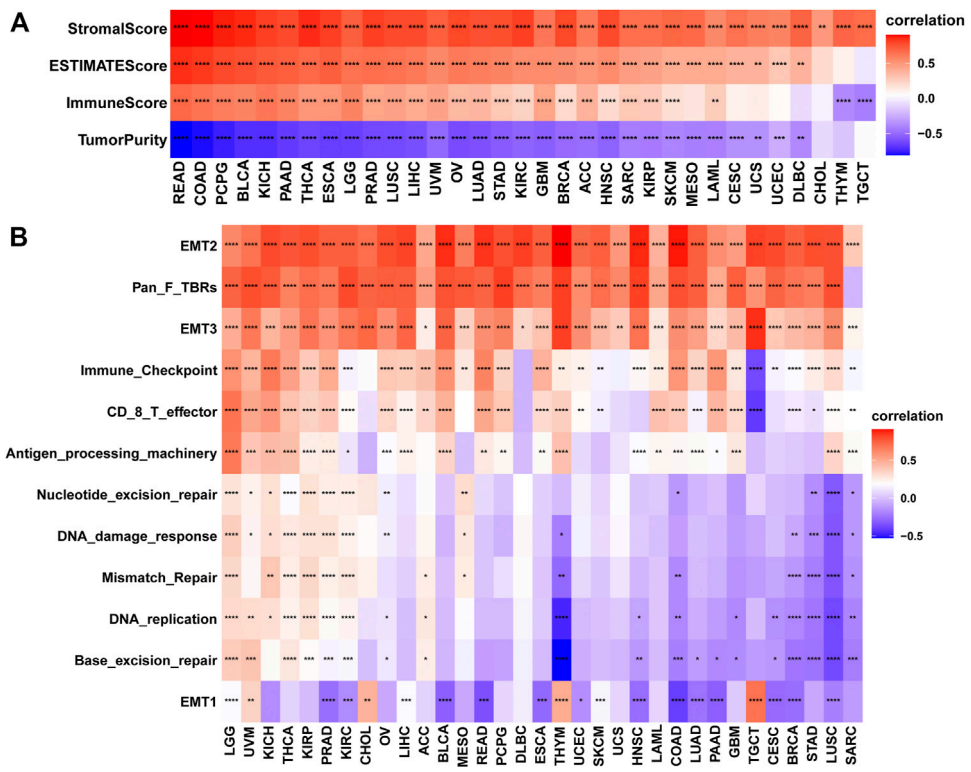

FIGURE 4 | Analysis of the tumor microenvironment. (*** denotes $p < 0.001$, ** denotes $p < 0.01$, while * denotes $p < 0.05$) **(A)**. Correlations between angiogenesis scores and ImmuneScores, Stromalcores, ESTIMATEScores and TumorPurity. **(B)**. Relationship between angiogenesis scores and pathways (Immune-related pathways, Stromal/transfer-related pathways and DNA damage repair-related pathways).

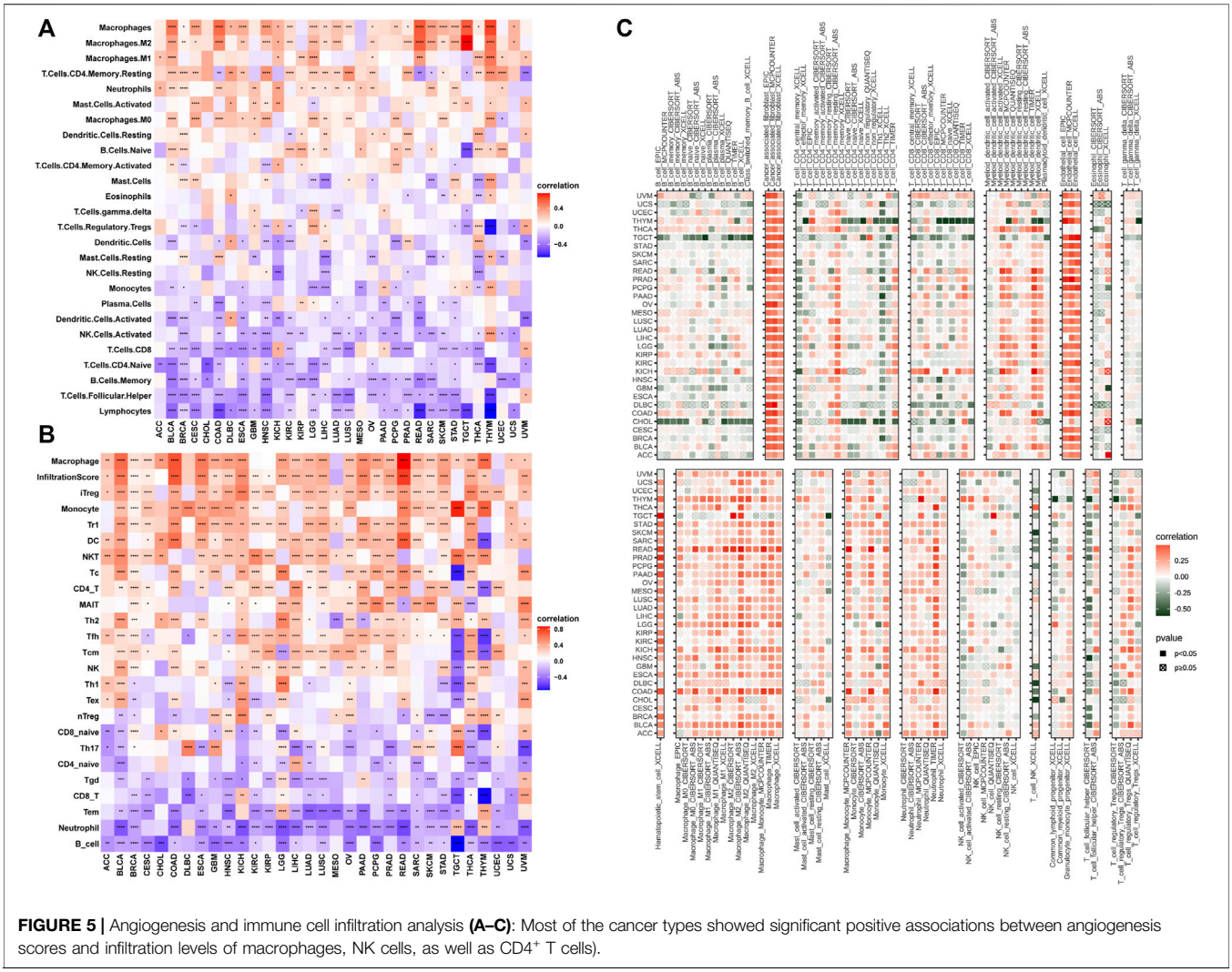

FIGURE 5 | Angiogenesis and immune cell infiltration analysis **(A–C)**: Most of the cancer types showed significant positive associations between angiogenesis scores and infiltration levels of macrophages, NK cells, as well as CD4$^+$ T cells).

(immune and stromal) (**Figure 4A**) while angiogenesis scores were strongly correlated with immune and stromal/metastasis-related pathways (**Figure 4B**). Next, the association between angiogenesis scores and infiltration levels of different immune cell types in 33 cancer types were evaluated. Most of the cancer types showed significant positive associations between angiogenesis scores and infiltration levels of macrophages, NK cells, as well as CD4$^+$ T cells (**Figures 5A,B**), implying that angiogenesis scores are associated with a hot TME. For instance, THYM revealed a highly significant positive correlation between angiogenesis scores and infiltration levels of NK cells. In contrast, NK cells exhibited significant negative correlations with angiogenesis scores in TGCT, and weak or no correlations in ACC (**Figures 5A–C**).

Angiogenesis Scores Were Associated With Immune-Related Genes in Many Cancer Types

The core function of the immune system is to recognize self and eliminate non-self antigens to maintain normal physiological activities and fight disease (Bai et al., 2020; Forster and Radpour, 2020). This function is largely mediated by the major histocompatibility complex (MHC). The significance of MHC in tumor diagnosis and treatment is being evaluated in immunotherapy (Baba et al., 2007; Marcu et al., 2021). Chemokines are also involved in responses to cancer therapies, therefore, they are potential targets for immunotherapy and chemokine-targeted therapy (Samaniego et al., 2018). We found strong associations between angiogenesis scores and the above related genes (**Supplementary Figures S9A-C**). Then, we investigated the correlation between angiogenesis scores and expressions of immune checkpoints. In 33 cancer types, the angiogenesis score was positively correlated with expression levels of most of the immune checkpoints (**Supplementary Figure S9D**). A previous study revealed that TMB is associated with immunotherapeutic responses (Abou Khouzam et al., 2020). We found that angiogenesis scores were significantly correlated with TMB in STAD, HNSC, LUAD, KIRP, LIHC, CHOL, THYM, LAM, and LGG (**Supplementary Figure S9E**). MSI are repeated DNA sequences (Page and Graham, 2008).

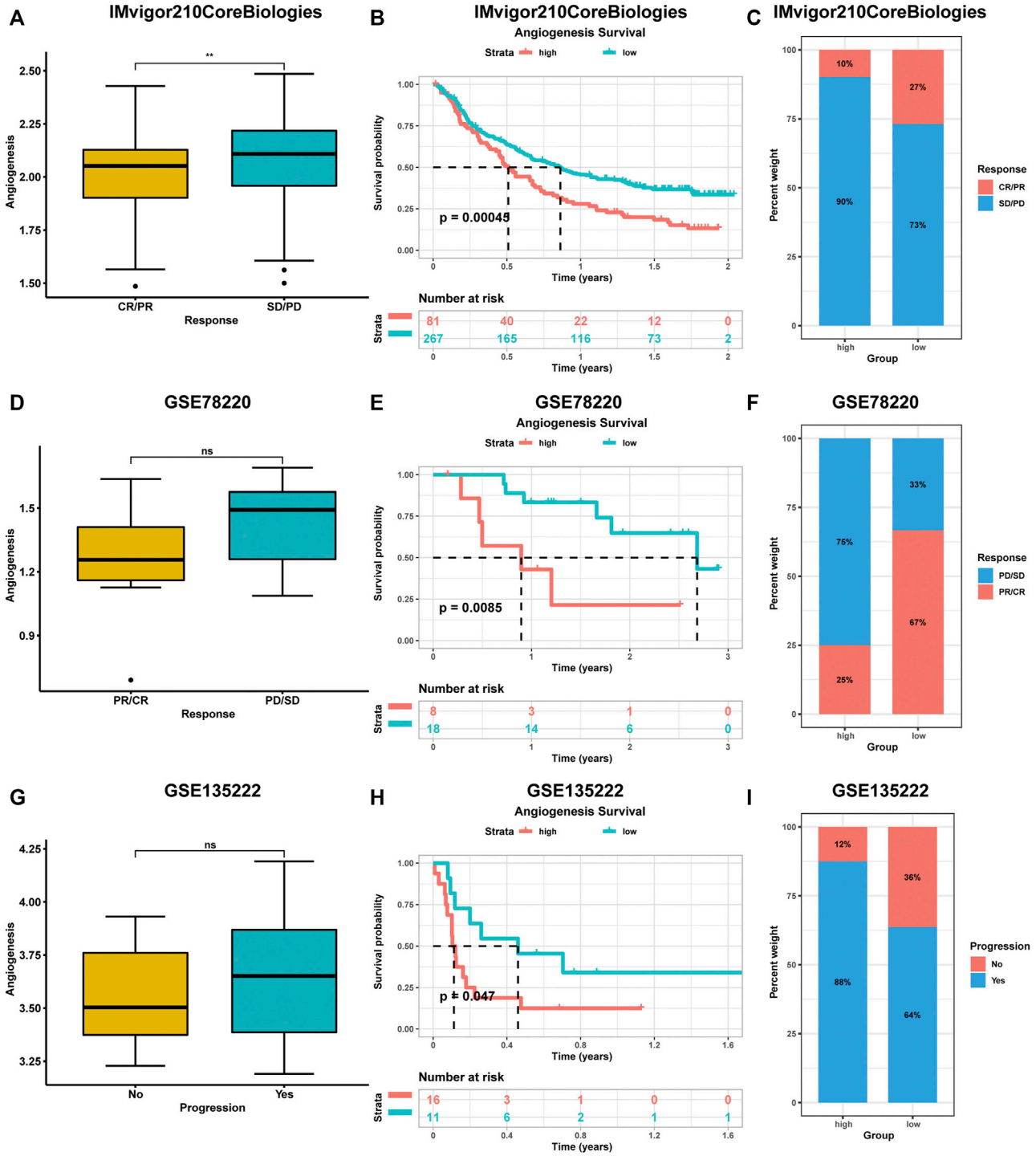

FIGURE 6 | The impact of angiogenesis scores on the prognostic outcome of immunotherapy patients was analysed using multiple datasets **(A-I)**. Patients with high angiogenesis scores exhibited poorer prognostic outcomes after immunotherapy. complete responses (CR), partial responses (PR), progressive disease (PD), stable disease (SD).

Impaired mismatch repair-associated MSI may be a mechanism in gastric cancer development, therefore, its significance is being evaluated by various studies. Our results showed a strong correlation between angiogenesis scores and MSI in BRCA, LUAD, LUSC, STAD, HNSC, and TGCT (**Supplementary Figure S9F**).

Angiogenesis Scores Were Correlated With Immunotherapeutic Responses

During the evaluation of angiogenesis-associated TME characteristics, we observed strong positive correlations between immune checkpoint levels and angiogenesis genes. Due to advances in cancer immunotherapy, we evaluated the expressions of angiogenesis-associated genes in immunotherapy-treated patients. We collected three datasets containing pre-treatment samples and immunotherapeutic data. These datasets had various patient information, including clinical manifestations (complete responses (CR) or partial responses (PR)) or no clinical benefits (progressive disease (PD) or stable disease (SD)). Compared to patients with low angiogenesis scores, patients with high angiogenesis scores exhibited poorer prognostic outcomes after immunotherapy. Higher scores were observed in progressive phase patients (**Figure 6**).

Drug Sensitivity Analysis

Currently, surgery and chemotherapy are the main therapeutic strategies for cancer, however, resistance to chemotherapeutic drugs and molecularly targeted therapies is a major barrier to cancer treatment (Wu et al., 2020). Spearman's correlation analysis showed that drug sensitivity towards YM155, ZG-10, GW843682X, and S–Trityl–L–cysteine correlated with *APP* levels (positive correlation with IC50). However, resistance towards EHT 1864 and lisitinib correlated with expressions of *APOH* (negative correlation with IC50) (**Supplementary Figure S10**). In conclusion, dysregulated expressions of angiogenesis-associated genes may be involved in resistance to cancer therapies.

miRNA and lncRNAs Regulation Analysis

Non-coding RNAs (ncRNAs) are involved gene expression regulation. To ascertain whether angiogenesis genes are modulated by some ncRNAs, first, we predicted upstream miRNAs that have the potential to bind angiogenesis-associated genes. Network visualization was achieved using the Cytoscape software (**Supplementary Figure S12**). Hsa-miR-106a-5p was regulated and was central to most angiogenesis-associated genes. Therefore, in pan-cancer, hsa-miR-106a-5p might be a potential regulatory miRNA of angiogenesis-associated genes. Next, upstream lncRNAs of hsa-miR-106a-5p were predicted using the starbase database. Sixty eight potential lncRNAs were identified. Relationships visualization was performed using the Cytoscape software (**Supplementary Figure S12**). These results indicate that ncRNAs regulation of angiogenesis-associated genes might be involved in cancer progression.

DISCUSSION

Angiogenesis, the formation of new blood vessels, is important for tumor progression (Lin et al., 2010). In 1971, Folkman proposed that tumor growth is dependent on angiogenesis and that inhibition of angiogenesis is a potential therapeutic paradigm for solid tumors (Folkman, 1971). To trigger angiogenesis, tumors overexpress various angiogenic factors and cytokines, as well as endogenous angiogenesis enhancers (Folkman, 1996). Various angiogenic factors have been identified, their corresponding inhibitors developed, and their efficacies in cancer treatment demonstrated (Cao, 2010; Cao and Langer, 2010; Cao et al., 2011; Cao, 2014). Therefore, to understand tumorigenesis, and to investigate potential targets for clinical treatment, elucidation of angiogenesis in cancer is necessary.

In this study, we reveal multiple potential mechanisms of angiogenesis in cancer, including common angiogenesis-associated cancer pathways. According to the results of this study, we found a high frequency of CNVs of angiogenesis-associated genes. Moreover, the CNVs were positively correlated with angiogenesis-associated gene expressions, indicating that copy number variations may affect angiogenesis-associated gene expressions, contributing to tumorigenesis. For example, *S100A4* was frequently amplified in PAAD and was associated with poor patient survival outcomes, consistent with findings from previous studies (Matsubara et al., 2005; Li and Bresnick, 2006). Hypermethylated CCND2 was associated with poor survival rates of KICH, implying that hypermethylated CCND2 may be a driver gene for KICH progression. This is in tandem with findings from previous studies that concluded that hypermethylation of *CCND2* is associated with the progression of various cancers (Hung et al., 2018; Ding et al., 2019). However, in this study, there were inconsistencies between methylation levels and prognostic outcomes, therefore, we postulated that in certain contexts, genetic and epigenetic alterations of angiogenesis-associated genes might result in angiogenesis dysfunctions and promote tumorigenesis. Therefore, studies should be conducted to assess this postulate.

The TME is hypoxic and acidic in nature, and in this environment, tumor cells recruit a number of innate immune cells, the most representative of which are tumor-associated macrophages (TAMs), neutrophils, myeloid-derived suppressor cells (MDSC) and natural killer cells (NK) (Hamaguchi et al., 2020). TAMs are involved in every step of tumor angiogenesis (Komohara and Takeya, 2017). In early stages of tumor development, neutrophils play a key role in promoting angiogenesis. Neutrophils can release MMP-9 to activate endothelial cell growth signals and to promote angiogenesis (Eyileten et al., 2016). They also secrete myeloperoxidase (MPO), which is important for macrophage recruitment and platelet activation (Heslop et al., 2010). In addition, reduction in neutrophil counts significantly inhibits the link between VEGF and its receptors (Li et al., 2012).

Despite its significance in tumor therapy, immunotherapeutic responses are suboptimal, which may be attributed to immunosuppressive tumor microenvironments (Chan et al., 2020). The tumor vasculature carries essential nutrients and oxygen to the tumor tissue and plays an important role in the growth as well as progression of malignant tumors. Abnormal blood vessels can form a physical barrier that limits immunotherapeutic efficacies (Jain, 2005). Abnormal tumor vasculature may inhibit immunotherapeutic effectiveness

through hypoxia and development of an acidic microenvironment, which enhances immunosuppression (Jain, 2005). In addition, it can induce a decrease in micro-environmental pH, affecting immune cell functions, therefore, anti-tumor immune cells, such as T lymphocytes and NK cells can become unresponsive in acidic environments and subsequently, undergo apoptosis (Huber et al., 2017). In contrast, immunosuppressive components (such as myeloid and Treg cells) enhance tumor growth in acidic environments (Huber et al., 2017). The combination of anti-angiogenic therapy and immunotherapy has improved prognostic outcomes for patients with different cancer types, including liver, kidney and breast cancers (Rini et al., 2019; Finn et al., 2020; Liu et al., 2020), resulting in improved PFS and OS. This combination provides additional clinical options for patients with liver metastases and positive driver genes (Finn et al., 2020). In addition, this combination has not increased toxicity but has an increased efficacy, while the overall safety profile is manageable.

Drug sensitivity analyses were performed to identify potential drugs that can modulate angiogenesis-associated genes. For instance, a positive correlation was found between *APP* and YM155, ZG-10, GW843682X, and S−Trityl−L−cysteine, suggesting that patients with elevated *APP* gene expressions may be resistant to these drugs. Thus, we postulate that targeting angiogenesis-associated genes may be an effective anticancer treatment approach. Our findings, which revealed variations in angiogenesis at all regulation levels, elucidate on regulation of angiogenesis-associated genes in tumors. These variations may in turn lead to differences in drug efficacies, treatment responses and patient survival outcomes. However, more studies should comprehensively investigate cancer heterogeneity and individual-based treatment approaches.

CONCLUSION

This study provides the first comprehensive description of angiogenesis-associated gene expressions in various tumor types. Moreover, we systematically investigated the impact of changes in expressions of all angiogenesis-associated genes on clinical outcomes of various cancer types. Angiogenesis-associated gene expressions were correlated with different genomic and immunological tumor characteristics, implying that they have prognostic values in both immunotherapeutic and standard settings.

DATA AVAILABILITY STATEMENT

The datasets presented in this study can be found in online repositories. The names of the repository/repositories and accession number(s) can be found in the article/**Supplementary Material**.

ETHICS STATEMENT

Written informed consent was obtained from the individual(s) for the publication of any potentially identifiable images or data included in this article.

AUTHOR CONTRIBUTIONS

X-tY designed the experiments; W-NM, X-yL, YS, LZ, ZW, DW, L-xS, M-ZW, and YS performed the experiments and wrote the manuscript while X-tY reviewed the manuscript. The corresponding author of this article is X-tY. X-yL, W-NM, L-xS, and YS contributed equally to this work.

FUNDING

This study received Fundamental research program funding of Ninth People's Hospital affiliated to Shanghai Jiao Tong University School of Medicine (No. JYZZ076), Clinical Research Program of Ninth People's Hospital, Shanghai Jiao Tong University School of Medicine (No. JYLJ201801, JYLJ201911), the China Postdoctoral Science Foundation (No. 2017M611585) and the National Natural Science Foundation of China (No. 81871458).

ACKNOWLEDGMENTS

Home for Researchers editorial team (www.home-for-researchers.com).

SUPPLEMENTARY MATERIAL

The Supplementary Material for this article can be found online at: https://www.frontiersin.org/articles/10.3389/fcell.2022.805507/full#supplementary-material

REFERENCES

Abou Khouzam, R., Goutham, H. V., Zaarour, R. F., Chamseddine, A. N., Francis, A., Buart, S., et al. (2020). Integrating Tumor Hypoxic Stress in Novel and More Adaptable Strategies for Cancer Immunotherapy. *Semin. Cancer Biol.* 65, 140–154. doi:10.1016/j.semcancer.2020.01.003

Agirre, X., Román-Gómez, J., Vázquez, I., Jiménez-Velasco, A., Garate, L., Montiel-Duarte, C., et al. (2006). Abnormal Methylation of the commonPARK2andPACRGpromoter Is Associated with Downregulation of Gene Expression in Acute Lymphoblastic Leukemia and Chronic Myeloid Leukemia. *Int. J. Cancer* 118 (8), 1945–1953. doi:10.1002/ijc.21584

Ardito, C. M., Briggs, C. D., and Crawford, H. C. (2008). Targeting of Extracellular Proteases Required for the Progression of Pancreatic Cancer. *Expert Opin. Ther. Targets* 12 (5), 605–619. doi:10.1517/14728222.12.5.605

Azoitei, N., Pusapati, G. V., Kleger, A., Moller, P., Kufer, R., Genze, F., et al. (2010). Protein Kinase D2 Is a Crucial Regulator of Tumour Cell-Endothelial Cell Communication in Gastrointestinal Tumours. *Gut* 59 (10), 1316–1330. doi:10.1136/gut.2009.206813

Baba, T., Hanagiri, T., Ichiki, Y., Kuroda, K., Shigematsu, Y., Mizukami, M., et al. (2007). Lack and Restoration of Sensitivity of Lung Cancer Cells to Cellular Attack with Special Reference to Expression of Human Leukocyte Antigen Class I And/or Major Histocompatibility Complex Class I Chain Related

Molecules A/B. *Cancer Sci.* 98 (11), 1795–1802. doi:10.1111/j.1349-7006.2007.00586.x

Bai, B., Yang, Y., Wang, Q., Li, M., Tian, C., Liu, Y., et al. (2020). NLRP3 Inflammasome in Endothelial Dysfunction. *Cell Death Dis* 11 (9), 776. doi:10.1038/s41419-020-02985-x

Blanco-Fernandez, B., Gaspar, V. M., Engel, E., and Mano, J. F. (2021). Proteinaceous Hydrogels for Bioengineering Advanced 3D Tumor Models. *Adv. Sci.* 8 (4), 2003129. doi:10.1002/advs.202003129

Cao, Y., Arbiser, J., D'Amato, R. J., D'Amore, P. A., Ingber, D. E., Kerbel, R., et al. (2011). Forty-Year Journey of Angiogenesis Translational Research. *Sci. Transl. Med.* 3 (114), 113r–114r. doi:10.1126/scitranslmed.3003149

Cao, Y., and Langer, R. (2010). Optimizing the Delivery of Cancer Drugs that Block Angiogenesis. *Sci. Transl. Med.* 2 (15), 13p–15p. doi:10.1126/scitranslmed.3000399

Cao, Y. (2010). Off-tumor Target-Beneficial Site for Antiangiogenic Cancer Therapy? *Nat. Rev. Clin. Oncol.* 7 (10), 604–608. doi:10.1038/nrclinonc.2010.118

Cao, Y. (2014). VEGF-targeted Cancer Therapeutics-Paradoxical Effects in Endocrine Organs. *Nat. Rev. Endocrinol.* 10 (9), 530–539. doi:10.1038/nrendo.2014.114

Chan, J. Y., Lim, J. Q., Yeong, J., Ravi, V., Guan, P., Boot, A., et al. (2020). Multiomic Analysis and Immunoprofiling Reveal Distinct Subtypes of Human Angiosarcoma. *[J]. J. Clin. Invest.* 130 (11), 5833–5846. doi:10.1172/JCI139080

De Palma, F., D'Argenio, V., Pol, J., Kroemer, G., Maiuri, M., and Salvatore, F. (2019). The Molecular Hallmarks of the Serrated Pathway in Colorectal Cancer. *Cancers* 11 (7), 1017. doi:10.3390/cancers11071017

Deng, G., Zeng, F., Su, J., Zhao, S., Hu, R., Zhu, W., et al. (2020). BET Inhibitor Suppresses Melanoma Progression via the Noncanonical NF-Kb/spp1 Pathway. *Theranostics* 10 (25), 11428–11443. doi:10.7150/thno.47432

Ding, Z. y., Li, R., Zhang, Q. j., Wang, Y., Jiang, Y., Meng, Q. y., et al. (2019). Prognostic Role of Cyclin D2/D3 in Multiple Human Malignant Neoplasms: A Systematic Review and Meta-analysis. *Cancer Med.* 8 (6), 2717–2729. doi:10.1002/cam4.2152

Eyileten, C., Majchrzak, K., Pilch, Z., Tonecka, K., Mucha, J., Taciak, B., et al. (2016). Immune Cells in Cancer Therapy and Drug Delivery. *Mediators Inflamm.* 2016, 1–13. doi:10.1155/2016/5230219

Finn, R. S., Qin, S., Ikeda, M., Galle, P. R., Ducreux, M., Kim, T.-Y., et al. (2020). Atezolizumab Plus Bevacizumab in Unresectable Hepatocellular Carcinoma. *N. Engl. J. Med.* 382 (20), 1894–1905. doi:10.1056/NEJMoa1915745

Firestone, G. L., and Sundar, S. N. (2009). Anticancer Activities of Artemisinin and its Bioactive Derivatives. *Expert Rev. Mol. Med.* 11, e32. doi:10.1017/S1462399409001239

Folkman, J. (1971). Tumor Angiogenesis: Therapeutic Implications. *N. Engl. J. Med.* 285 (21), 1182–1186. doi:10.1056/NEJM197111182852108

Folkman, J. (1996). Tumor Angiogenesis and Tissue Factor. *Nat. Med.* 2 (2), 167–168. doi:10.1038/nm0296-167

Forster, S., and Radpour, R. (2020). Molecular Immunotherapy: Promising Approach to Treat Metastatic Colorectal Cancer by Targeting Resistant Cancer Cells or Cancer Stem Cells. *Front. Oncol.* 10, 569017. doi:10.3389/fonc.2020.569017

Hamaguchi, R., Narui, R., and Wada, H. (2020). Effects of Alkalization Therapy on Chemotherapy Outcomes in Metastatic or Recurrent Pancreatic Cancer. *Anticancer Res.* 40 (2), 873–880. doi:10.21873/anticanres.14020

Heslop, C. L., Frohlich, J. J., and Hill, J. S. (2010). Myeloperoxidase and C-Reactive Protein Have Combined Utility for Long-Term Prediction of Cardiovascular Mortality after Coronary Angiography. *J. Am. Coll. Cardiol.* 55 (11), 1102–1109. doi:10.1016/j.jacc.2009.11.050

Hida, K., Hida, Y., and Shindoh, M. (2008). Understanding Tumor Endothelial Cell Abnormalities to Develop Ideal Anti-angiogenic Therapies. *Cancer Sci.* 99 (3), 459–466. doi:10.1111/j.1349-7006.2007.00704.x

Huang, C., Huang, R., Chen, H., Ni, Z., Huang, Q., Huang, Z., et al. (2021). Chromatin Accessibility Regulates Gene Expression and Correlates with Tumor-Infiltrating Immune Cells in Gastric Adenocarcinoma. *Front. Oncol.* 10, 609940. doi:10.3389/fonc.2020.609940

Huber, V., Camisaschi, C., Berzi, A., Ferro, S., Lugini, L., Triulzi, T., et al. (2017). Cancer Acidity: An Ultimate Frontier of Tumor Immune Escape and a Novel Target of Immunomodulation. *Semin. Cancer Biol.* 43, 74–89. doi:10.1016/j.semcancer.2017.03.001

Hultqvist, G., Syvänen, S., Fang, X. T., Lannfelt, L., and Sehlin, D. (2017). Bivalent Brain Shuttle Increases Antibody Uptake by Monovalent Binding to the Transferrin Receptor. *Theranostics* 7 (2), 308–318. doi:10.7150/thno.17155

Hung, C.-S., Wang, S.-C., Yen, Y.-T., Lee, T.-H., Wen, W.-C., and Lin, R.-K. (2018). Hypermethylation of CCND2 in Lung and Breast Cancer Is a Potential Biomarker and Drug Target. *Ijms* 19 (10), 3096. doi:10.3390/ijms19103096

Hurwitz, H., Fehrenbacher, L., Novotny, W., Cartwright, T., Hainsworth, J., Heim, W., et al. (2004). Bevacizumab Plus Irinotecan, Fluorouracil, and Leucovorin for Metastatic Colorectal Cancer. *N. Engl. J. Med.* 350 (23), 2335–2342. doi:10.1056/nejmoa032691

Jain, R. K. (2005). Normalization of Tumor Vasculature: an Emerging Concept in Antiangiogenic Therapy. *Science* 307 (5706), 58–62. doi:10.1126/science.1104819

Kelley, R. K., Bridgewater, J., Gores, G. J., and Zhu, A. X. (2020). Systemic Therapies for Intrahepatic Cholangiocarcinoma. *J. Hepatol.* 72 (2), 353–363. doi:10.1016/j.jhep.2019.10.009

Kim, Y. J., Lee, S. C., Kim, S. E., Kim, S. H., Kim, S. K., and Lee, C. S. (2020). YAP Activity Is Not Associated with Survival of Uveal Melanoma Patients and Cell Lines. *Sci. Rep.* 10 (1), 6209. doi:10.1038/s41598-020-63391-z

Komatsu, Y., Waku, T., Iwasaki, N., Ono, W., Yamaguchi, C., and Yanagisawa, J. (2012). Global Analysis of DNA Methylation in Early-Stage Liver Fibrosis. *BMC Med. Genomics* 5, 5. doi:10.1186/1755-8794-5-5

Komohara, Y., and Takeya, M. (2017). CAFs and TAMs: Maestros of the Tumour Microenvironment. *J. Pathol.* 241 (3), 313–315. doi:10.1002/path.4824

Li, K., Luo, H., Huang, L., Luo, H., and Zhu, X. (2020). Microsatellite Instability: a Review of what the Oncologist Should Know. *Cancer Cell Int* 20, 16. doi:10.1186/s12935-019-1091-8

Li, W., Han, F., Fu, M., and Wang, Z. (2020). High Expression of VCAN Is an Independent Predictor of Poor Prognosis in Gastric Cancer. *J. Int. Med. Res.* 48 (1), 030006051989127. doi:10.1177/0300060519891271

Li, Y., Wang, J.-S., Zhang, T., Wang, H.-C., and Li, L.-P. (2020). Identification of New Therapeutic Targets for Gastric Cancer with Bioinformatics. *Front. Genet.* 11, 865. doi:10.3389/fgene.2020.00865

Li, Z.-H., and Bresnick, A. R. (2006). The S100A4 Metastasis Factor Regulates Cellular Motility via a Direct Interaction with Myosin-IIA. *Cancer Res.* 66 (10), 5173–5180. doi:10.1158/0008-5472.can-05-3087

Li, Z.-J., Zhu, H., Ma, B.-Y., Zhao, F., Mao, S.-H., Liu, T.-G., et al. (2012). Inhibitory Effect of Bifidobacterium Infantis-Mediated sKDR Prokaryotic Expression System on Angiogenesis and Growth of Lewis Lung Cancer in Mice. *BMC cancer* 12, 155. doi:10.1186/1471-2407-12-155

Lin, Y., Bai, L., Chen, W., and Xu, S. (2010). The NF-Kb Activation Pathways, Emerging Molecular Targets for Cancer Prevention and Therapy. *Expert Opin. Ther. Targets* 14 (1), 45–55. doi:10.1517/14728220903431069

Liu, J. J., Liu, Q., Li, Y., Li, Q., Su, F., Yao, H., et al. (2020). Efficacy and Safety of Camrelizumab Combined with Apatinib in Advanced Triple-Negative Breast Cancer: an Open-Label Phase II Trial]. *J. Immunother. Cancer* 8 (1), e000696. doi:10.1136/jitc-2020-000696

Liu, W., Zha, Z., and Wang, H. (2019). Upregulation of microRNA-27a Inhibits Synovial Angiogenesis and Chondrocyte Apoptosis in Knee Osteoarthritis Rats through the Inhibition of PLK2. *J. Cell Physiol* 234 (12), 22972–22984. doi:10.1002/jcp.28858

Lugano, R., Ramachandran, M., and Dimberg, A. (2020). Tumor Angiogenesis: Causes, Consequences, Challenges and Opportunities. *Cell. Mol. Life Sci.* 77 (9), 1745–1770. doi:10.1007/s00018-019-03351-7

Marcu, A., Bichmann, L., Kuchenbecker, L., Kowalewski, D. J., Freudenmann, L. K., Backert, L., et al. (2021). HLA Ligand Atlas: a Benign Reference of HLA-Presented Peptides to Improve T-Cell-Based Cancer Immunotherapy. *J. Immunother. Cancer* 9 (4), e002071. doi:10.1136/jitc-2020-002071

Matsubara, D., Niki, T., Ishikawa, S., Goto, A., Ohara, E., Yokomizo, T., et al. (2005). Differential Expression of S100A2 and S100A4 in Lung Adenocarcinomas: Clinicopathological Significance, Relationship to P53 and Identification of Their Target Genes. *Cancer Sci.* 96 (12), 844–857. doi:10.1111/j.1349-7006.2005.00121.x

Mitsuhashi, A., Goto, H., Saijo, A., Trung, V. T., Aono, Y., Ogino, H., et al. (2015). Fibrocyte-like Cells Mediate Acquired Resistance to Anti-angiogenic Therapy with Bevacizumab. *Nat. Commun.* 6, 8792. doi:10.1038/ncomms9792

Page, K., and Graham, E. A. M. (2008). Cancer and Forensic Microsatellites. *Forensic Sci. Med. Pathol.* 4 (1), 60–66. doi:10.1007/s12024-008-9027-y

Rini, B. I., Powles, T., Atkins, M. B., Escudier, B., McDermott, D. F., Suarez, C., et al. (2019). Atezolizumab Plus Bevacizumab versus Sunitinib in Patients with Previously Untreated Metastatic Renal Cell Carcinoma (IMmotion151): a Multicentre, Open-Label, Phase 3, Randomised Controlled Trial. *The Lancet* 393 (10189), 2404–2415. doi:10.1016/S0140-6736(19)30723-8

Saeed, A., and Salem, M. E. (2020). Prognostic Value of Tumor Mutation burden (TMB) and INDEL burden (IDB) in Cancer: Current View and Clinical Applications. *Ann. Transl Med.* 8 (9), 575. doi:10.21037/atm-2020-75

Samaniego, R., Gutiérrez-González, A., Gutiérrez-Seijo, A., Sánchez-Gregorio, S., García-Giménez, J., Mercader, E., et al. (2018). CCL20 Expression by Tumor-Associated Macrophages Predicts Progression of Human Primary Cutaneous Melanoma. *Cancer Immunol. Res.* 6 (3), 267–275. doi:10.1158/2326-6066.CIR-17-0198

Schlattl, A., Anders, S., Waszak, S. M., Huber, W., and Korbel, J. O. (2011). Relating CNVs to Transcriptome Data at fine Resolution: Assessment of the Effect of Variant Size, Type, and Overlap with Functional Regions. *Genome Res.* 21 (12), 2004–2013. doi:10.1101/gr.122614.111

Shao, Z., Xu, P., Xu, W., Li, L., Liu, S., Zhang, R., et al. (2017). Discovery of Novel DNA Methyltransferase 3A Inhibitors via Structure-Based Virtual Screening and Biological Assays. *Bioorg. Med. Chem. Lett.* 27 (2), 342–346. doi:10.1016/j.bmcl.2016.11.023

Shatalova, A., Shatalov, I., and Lebedin, Y. (2020). X6: A Novel Antibody for Potential Use in Gluten Quantification. *Molecules* 25 (14), 3107. doi:10.3390/molecules25143107

Solimando, A. G., Summa, S. D., Vacca, A., and Ribatti, D. (2020). Cancer-Associated Angiogenesis: The Endothelial Cell as a Checkpoint for Immunological Patrolling. *Cancers* 12 (11), 3380. doi:10.3390/cancers12113380

Su, C., Li, D., Li, N., Du, Y., Yang, C., Bai, Y., et al. (2018). Studying the Mechanism of PLAGL2 Overexpression and its Carcinogenic Characteristics Based on 3'-untranslated Region in Colorectal Cancer. *Int. J. Oncol.* 52 (5), 1479–1490. doi:10.3892/ijo.2018.4305

Thorsson, V., Gibbs, D. L., Brown, S. D., Wolf, D., Bortone, D. S., Ou Yang, T. H., et al. (2018). The Immune Landscape of Cancer. *Immunity* 48 (4), 812–e14. doi:10.1016/j.immuni.2018.03.023

Wang, R., Zhao, A., Cao, N., Li, Z., Zhang, G., and Liu, F. (2020). The Value of Circulation Tumor DNA in Predicting Postoperative Recurrence of Colorectal Cancer: a Meta-Analysis. *Int. J. Colorectal Dis.* 35 (8), 1463–1475. doi:10.1007/s00384-020-03667-y

Wu, S.-G., and Shih, J.-Y. (2018). Management of Acquired Resistance to EGFR TKI-Targeted Therapy in Advanced Non-small Cell Lung Cancer. *Mol. Cancer* 17 (1), 38. doi:10.1186/s12943-018-0777-1

Wu, Z. X., Yang, Y., Wang, G., Wang, J. Q., Teng, Q. X., Sun, L., et al. (2020). Dual TTK/CLK2 Inhibitor, CC-671, Selectively Antagonizes ABCG2-mediated Multidrug Resistance in Lung Cancer Cells. *Cancer Sci.* 111 (8), 2872–2882. doi:10.1111/cas.14505

Zeng, D., Li, M., Zhou, R., Zhang, J., Sun, H., Shi, M., et al. (2019). Tumor Microenvironment Characterization in Gastric Cancer Identifies Prognostic and Immunotherapeutically Relevant Gene Signatures. *Cancer Immunol. Res.* 7 (5), 737–750. doi:10.1158/2326-6066.CIR-18-0436

Conflict of Interest: The authors declare that the research was conducted in the absence of any commercial or financial relationships that could be construed as a potential conflict of interest.

Publisher's Note: All claims expressed in this article are solely those of the authors and do not necessarily represent those of their affiliated organizations, or those of the publisher, the editors and the reviewers. Any product that may be evaluated in this article, or claim that may be made by its manufacturer, is not guaranteed or endorsed by the publisher.

frontiers in Oncology

ORIGINAL RESEARCH
published: 31 January 2022
doi: 10.3389/fonc.2022.818182

Pigment Epithelium Derived Factor Is Involved in the Late Phase of Osteosarcoma Metastasis by Increasing Extravasation and Cell-Cell Adhesion

Sei Kuriyama[1*†], *Gentaro Tanaka*[1,2], *Kurara Takagane*[1], *Go Itoh*[1] *and Masamitsu Tanaka*[1†]

[1] Department of Molecular Medicine and Biochemistry, Graduate School and Faculty of Medicine, Akita University, Akita City, Japan, [2] Department of Lifescience, Faculty and Graduate School of Engineering and Resource Science, Akita University, Akita City, Japan

OPEN ACCESS

Edited by:
Qiangzhe Zhang,
Nankai University, China

Reviewed by:
Jormay Lim,
National Taiwan University, Taiwan
Alessandro De Vita,
Scientific Institute of Romagna for the Study and Treatment of Tumors (IRCCS), Italy

***Correspondence:**
Sei Kuriyama
seikury@med.akita-u.ac.jp

[†]*These authors share the senior authorship*

Specialty section:
This article was submitted to Molecular and Cellular Oncology, a section of the journal Frontiers in Oncology

Received: *19 November 2021*
Accepted: *07 January 2022*
Published: *31 January 2022*

Citation:
Kuriyama S, Tanaka G, Takagane K, Itoh G and Tanaka M (2022) Pigment Epithelium Derived Factor Is Involved in the Late Phase of Osteosarcoma Metastasis by Increasing Extravasation and Cell-Cell Adhesion. Front. Oncol. 12:818182. doi: 10.3389/fonc.2022.818182

Organ tropism of metastatic cells is not well understood. To determine the key factors involved in the selection of a specific organ upon metastasis, we established metastatic cell lines and analyzed their homing to specific tissues. Toward this, 143B osteosarcoma cells were injected intracardially until the kidney-metastasizing sub-cell line Bkid was established, which significantly differed from the parental 143B cells. The candidate genes responsible for kidney metastasis were validated, and SerpinF1/Pigment epithelium derived factor (PEDF) was identified as the primary target. Bkid cells with PEDF knockdown injected intracardially did not metastasize to the kidneys. In contrast, PEDF overexpressing 143B cells injected into femur metastasized to the lungs and kidneys. PEDF triggered mesenchymal-to-epithelial transition (MET) *in vitro* as well as *in vivo*. Based on these results, we hypothesized that the MET might be a potential barrier to extravasation. PEDF overexpression in various osteosarcoma cell lines increased their extravasation to the kidneys and lungs. Moreover, when cultured close to the renal endothelial cell line TKD2, Bkid cells disturbed the TKD2 layer and hindered wound healing *via* the PEDF-laminin receptor (lamR) axis. Furthermore, novel interactions were observed among PEDF, lamR, lysyl oxidase-like 1 (Loxl1), and SNAI3 (Snail-like transcription factor) during endothelial-to-mesenchymal transition (EndoMT). Collectively, our results show that PEDF induces cancer cell extravasation by increasing the permeability of kidney and lung vasculature acting *via* lamR and its downstream genes. We also speculate that PEDF promotes extravasation *via* inhibiting EndoMT, and this warrants investigation in future studies.

Keywords: osteosarcoma, pigment epithelium derived factor (PEDF), metastasis, mesenchymal to epithelial transition (MET), extravasation

INTRODUCTION

Despite being a rare type of cancer, osteosarcoma (OS) is the most common bone cancer, and occurs mainly in children and young adults. Most of the currently used surgical treatments that are combined with multiple-agent chemotherapy had been established during the 70s–80s. The survival rate of OS patients had improved at that time; however, further significant treatments have not been developed (1, 2). OS has heterogenous characteristics, and lacks any consistent unifying event that could lead to its pathogenesis (1). High-grade osteosarcomas have a high propensity for pulmonary metastasis; over 75% of metastatic OS cases involve the lung. Other organ metastases are extremely rare; however, the renal metastasis of OS is often found with pulmonary metastasis after death (3), and the hepatic metastasis of OS is found microscopically after chemotherapy (4). Usually the OS metastasize hematogeneously to lung and bones but rarely to lymph nodes (5). It is crucial to determine the mechanism by which osteosarcomas prefer to metastasize to specific organs, as may be applicable to other cancers. However, most established OS cell lines were found to be non-metastatic.

A v-Ki-ras-transformed cell line derived from the human osteosarcoma (HOS) cell line 143B showed better growth and survival in mice than HOS. It has been reported that 143B cells form pulmonary metastases from orthotopic transplantations into the tibia (6–8), even from a cutaneous tumor (9). Therefore, we designed an experiment in which the orthotopic implantation of 143B caused distant metastatic lesions in the various organs. However, our 143B cells did not show such strong phenotypes from the knee joint injection or subcutaneous injection (data not shown). We then tried to examine the intracardiac injection to mimic circulating OS. In the orthotopic experimental model, OS partially digests the bone, which may provide TGF-ß, subsequently experiences neovascularization, intravasation, migration toward the distant organ, anoikis resistance, and extravasation. Finally, OS proliferates in the secondary site (10). However, OS can start as the circulating population in the intracardiac injection model. Therefore, the key function would be to elucidate the mechanism of OS survival, arrest on a particular organ, extravasation, and proliferation under suitable conditions. Anoikis resistance and anchoring on the particular sites of the endothelial cells could be mediated by various molecules, but it is ultimately consolidated into the Akt pathway (10). Additionally, SDF1-CXCR4 could be involved in the lung preference of OS metastasis (11, 12). However, the cell surface anchor between OS and endothelial cells remains unclear.

We successfully created metastatic sub-cell lines, and identified the genes potentially responsible for the specificity of metastasized organ. The details are presented in the following result section. Furthermore, we identified SERPINF1/pigment epithelium-derived factor (PEDF) as the gene responsible for the renal metastasis from the established renal metastatic cell line, Bkid.

PEDF is a Serine protease inhibitor family protein displaying no inhibitory activity against serine protease (13). PEDF has strong anti-angiogenesis activity, and its signaling is mediated by laminin receptor (lamR), which is also known as RPSA (40S ribosomal protein SA) (14, 15). PEDF is multifunctional, and has another PEDF receptor, which is also known as PNPLA2, and is a membrane-bound lipase molecule (16, 17). PEDF has been reported to have anti-angiogenesis, anti-tumor, and anti-metastasis properties in cancer (18–20). Particularly in OS, PEDF was tested using SaOS-2, and it was found that PEDF overexpression reduced the volume of the tumor and microvessels in a mouse model (20). Furthermore, the administration of recombinant PEDF protein in the orthotopic spontaneous metastasis model using SaOS-2 showed therapeutic effects in the primary and secondary OS lesions (21, 22). However, a recent study reported that the role of endogenous PEDF in cancer metastasis remains controversial and dependent on the context of cancer cell types (23). Furthermore, endogenous PEDF expression was observed in almost all osteosarcomas (**Supplemental Figure 1A**). Therefore, we hypothesized that endogenous PEDF may play an unknown role in cancer metastasis.

In the present study, loss of PEDF function in Bkid tumors blocked renal metastasis, and gain-of-function exhibited pulmonary and renal metastasis. We also found that PEDF expression increased the potency of mesenchymal-to-epithelial transition (MET); however, we expected that MET might block extravasation before forming nodules in the organs. Contrary to this expectation, PEDF overexpression increased extravasation in various osteosarcomas. Therefore, we examined the mechanism underlying the extravasation. As it was expressed in the kidneys and lungs, we further investigated the downstream signaling of lamR, which is one of the receptor of PEDF (14) in the renal endothelial cell line TKD2. As a result, lysyl oxidase-like 1 (Loxl1) (24) and SNAI3 (25) worked through the PEDF-lamR axis in TKD2, and we elucidated that their direct molecular interactions, while Snail2 and the other EMT/MET factors were regulated in cancer. Collectively, these results suggest that PEDF might increase extravasation, which is controlled by endogenous receptor expression. Therefore, it exhibited organ specificity, and extravasated cancer cells may undergo MET to form secondary lesions. This study demonstrated a new role for endogenous PEDF, particularly in the late phase of metastasis.

MATERIALS AND METHODS

Cell Lines and Culture Methods

We obtained 143B cells from the RIKEN BRC Cell Bank (Cat# RCB0701, RRID: CVCL_9W36). Other osteosarcoma cell lines were obtained from our collaborator (26). The osteosarcoma cells were maintained in Eagle's modified essential medium (EMEM) (Millipore Sigma, Burlington, MA, USA) with 10% fetal bovine serum (FBS) and sodium pyruvate at 37°C and 5% CO_2. The modified or subcloned cell lines of 143B and the other osteosarcoma cell lines with lentivirus/retrovirus constructs (see **Supplemental Text**) were also cultured in EMEM+10% FBS along with the selection antibiotic G418 sulfate (800 μg/mL, Inalco Pharmaceuticals, CA, USA), puromycin (2 μg/mL), or

hygromycin B (400 μg/mL, Wako-Fujifilm, Osaka, Japan). Mouse kidney endothelial TKD2 cells (RCB Cat# RCB0752, RRID: CVCL_5598) were maintained in Dulbecco's modified essential medium (DMEM) containing 4500 mg/mL L-glucose, 2% FBS, sodium pyruvate, ITS-X supplement (x1 from x100 stock solution, Wako-Fujifilm), and 2.5 μg/mL EGF at 33°C, and 5% CO_2.

Lentivirus and Retrovirus Preparation

A modified CSII-CMV-vector with a puromycin-resistant gene was used to establish the 143B cell line, as described previously (27). The selection of the cells with antibiotics and the information on the vector are described in the **Supplemental Text**.

Animal Experiments and *In Vivo* Imaging

All animal experiments were approved by the Akita University Ethical Committee for Experimental Animals. The 143B cells were cultured until subconfluent, rinsed with PBS, resuspended in Hank's buffered saline (HBSS), and injected into the left cardiac ventricle of nude mice (Balb/c Slc, SLC JAPAN, five-weeks-old) using 31G needle syringes containing 4×10^5 cells/100 μL. The tumors were monitored once per week by administering *aLuciferin* (250 μL/25 g nude mouse, 15 mg/mL in PBS) (Avidin Ltd, Szeged, Hungary) and were observed using the IVIS imaging suite (IVIS Lumina, Perkin-Elmer, Waltham, MA, USA). In a separate experiment, mice were anesthetized using isoflurane vapor, and 5×10^4 cells, 2×10^6 cells in 10 μL were injected into their knee joints using a Hamilton syringe.

Microarray Analyses

RNA was obtained from established cell lines, and gene expression was analyzed using a Gene Chip (Human v.2.0, GE Healthcare, Chicago, IL, USA). Gene expression analyses and drawing of the graphs or charts were performed using Transcriptome Analysis Console 4.0 software (Affymetrix Transcriptome Analysis Console Software, RRID : SCR_018718).

RNA Extraction, cDNA Synthesis, and Quantitative Polymerase Chain Reaction

The cells were cultured under the appropriate conditions for each experiment. RNA was extracted using PureLink RNA Mini Kit (Thermo Fisher Scientific, Waltham, MA, USA). cDNA was synthesized using the PrimeScript 1st strand cDNA Synthesis Kit (Takara Bio Inc., Shiga, JAPAN). Quantitative PCR was performed on a LightCycler Nano system (Roche Molecular systems Inc, Pleasanton, CA, USA) using Brilliant III Ultra-Fast SYBR Green master mix (Agilent Technologies, Santa Clara, CA, USA). The sequential steps of reverse transcript and quantitative PCR will be referred as qRT-PCR.

Oligonucleotides

All qRT-PCR primers and oligonucleotides used for gene editing are listed in the **Supplemental Text**.

The guide RNAs were transcribed using an all-in-one CRISPR/Cas9 system (Thermo Fisher Scientific). Human and mouse laminin receptor genome sequences were edited using the PITCh method (Precise Integration into Target Chromosome) (28, 29). The target sequences were also listed in **Supplemental Data**.

Western Blots and Antibodies

The cells were lysed using PLC buffer (100 mM Tris-HCl, 1% TritonX-100, 10% glycerol, 50 mM sodium vanadate, 1 mM PMSF, and 1 × protease inhibitor cocktail). Before obtaining their organs, the mice were perfused with PBS to remove blood from the organs. Each mouse organ was dissected briefly using scissors and homogenized in PLC buffer. Large fragments were removed by centrifugation, and the cleared samples were treated as described above. The antibodies used in this study were follows: Anti-PEDF/SerpinF1 (R&D Systems Cat# AF1177, RRID : AB_2187173), Anti-Cadherin-11 (R&D Systems Cat# MAB1790, RRID : AB_2076970), Anti-N-cadherin (BD Biosciences Cat# 610920, RRID : AB_2077527), Anti-K-cadherin (Millipore Cat# MAB2013, RRID : AB_11210468), Anti-CD31 (Abcam Cat# ab28364, RRID : AB_72636), Anti-SPARC (Sigma-Aldrich Cat# HPA003020, RRID : AB_1079531), Anti-laminin receptor (RPSA/67LR) (GeneTex Cat# GTX23099, RRID : AB_367077), Anti-PNPLA2 (R&D Systems Cat# AF5365, RRID : AB_2165678), Anti-phosphor-Akt (Ser473 (D9E)XP, Cell Signaling Technology Cat# 5012, RRID : AB_2224726), Anti-Akt (CST, Cat# 9272, RRID : AB_329827), Anti-phospho p38 (CST, Cat# 9210, RRID : AB_330710), Anti-p38 MAPK (CST, Cat# 9212, RRID : AB_330713), Anti-phospho p42/44 MAPK (CST, Cat# 4094, RRID : AB_10694057), Anti-p42/44 MAPK (CST, Cat# 9102, RRID : AB_330744), Anti-Slug (Snail2) (CST, Cat# 9585, RRID : AB_2239535), Anti-MMP9 (Millipore Cat# AB19016, RRID : AB_91090), Anti-MMP14 (Abcam Cat# ab51074, RRID : AB_881234), Anti-MMP15 (Abcam Cat# ab15475, RRID : AB_301885), Anti-Lipoma preferred partner (LPP) (Abcam Cat# ab63621, RRID : AB_956113) Anti-ß-catenin (Abcam Cat# ab79089, RRID : AB_1603423), Anti-alpha-tubulin (Sigma-Aldrich Cat# T5168, RRID : AB_477579).

Immunohistochemistry (IHC) and Immunofluorescence (IF)

The procedures of immunostaining have been described previously (30). The preparation of the paraffin-embedded samples and sectioning of the paraffin blocks were provided by Akita University Bioscience Education-Research Support Center.

Miles Assay

We followed the procedure described in the text and video of a previous study (31). The stock solution (5%) of Evans blue (EB) (Wako-Fujifilm) was prepared in PBS, and the diluted (0.5%) solution was sterilized using a 0.45 μm syringe filter (SARSTEDT AG&Co.KG, Nümbrecht, Germany). EB was introduced through the tail vein of mice injected with MG63 cells two weeks ago. After each organ was dissected, the weights of each organ were

measured, and the EB in each organ was extracted using formamide solution for 24 h. The absorbance of EB was measured at 610 nm using a Multiskan FC system (Thermo Fisher Scientific).

Double-Sided Culture of Cancer Cluster and the Endothelial Layer

GFP-expressing TKD2 (TKD2-GFP) cell line was established. The TKD2-GFP cells were cultured on the bottom side of the culture insert by flipping the atelocollagen membrane insert (AteloCell CM-24, Koken, Japan). Next, 143B and 143B+PEDF cells were separately cultured on low-adherent culture dishes for 2 days, and 143B/143B+PEDF spheroids were prepared. After obtaining the confluent layer of TKD2-GFP cells, the culture insert was flipped again, and a few spheroids of 143B/143B+PEDF were placed on the opposite side of the membrane over the TKD2-GFP cell layer (see schematic diagram in **Figure 6E**). After 2 days, the culture inserts were briefly fixed with 4% PFA, washed and permealized by PBS +0.01% TritonX-100, and immuno-stained with anti-ß-catenin antibody. Next, the membranes were cut out from the culture insert, and the samples were mounted on a slide with Mowiol (Sigma). The images were obtained under the confocal microscope LSM780 (Carl Zeiss Microscopy GmbH, Jena, Germany), and the Z-stack images were reconstructed by IMARIS software (Imaris, RRID : SCR_007370).

Cell Proliferation and Wound Healing Assay

To obtain data on cell proliferation and wound healing assays, we performed experiments on the Holomonitor M4 (HoloMonitor system, RRID : SCR_019231). For cell proliferation counting, six-well plates were used (SARSTEDT), the multiple positions were imaged, and the cell numbers were analyzed using Hstudio software (version 2.7.3, PHI AB). For wound healing assay of TKD2, we used the culture-insert two-well plate to separate the monolayer of the culture cells (ibidi #80206, Martinsrid, Germany). The cell-free area of the wound was imaged, and the reduction in the area was also analyzed using Hstudio software.

Immunoprecipitation and HaloTag Pulldown

For FLAG-tag immunoprecipitation (IP), cells were lysed using RIPA buffer (50mM TrisHCl, 150mM NaCl, 0.5% Sodium Deoxycholate, 0.1% Sodium dodecyl sulfate, 1% NP-40). The input was taken before IP. FLAG-M2 affinity agarose gels (Sigma, A2220) were washed by RIPA buffer several times until washing solution became clear, blocked using 0.1% BSA in RIPA buffer for 30 minutes, washed once, and mixed with 0.5 mg/mL protein lysates for 3 hours at 4°C. The agarose bed was washed using RIPA buffer three times for 5 minute at 4°C. The washed agarose bed was incubated with 100μg/mL of 3xFLAG peptides (Sigma) in TBST buffer for 1 hour. The eluates were separated from the bed by centrifuge. For HaloTag purification, cells were lysed using HaloTag purification buffer (50mM HEPES, 1mM Dithiothreitol, 1mM EDTA, 1mM EGTA, 0.05% NP-40). HaloTag acryl beads were rinsed twice with HaloTag purification buffer, and mixed with 0.5 mg/mL protein lysate for 30 minutes at room temperature. The beads were washed with HaloTag purification buffer three times for 5 minutes at room temperature. The beads was boiled for 3 minutes to extract the proteins.

RESULTS

Establishment of the Sub-Cell Lines From the Intracardiac Injections of 143B

According to the previous paper, 143B, an osteosarcoma cell line, could metastasize into lung even from the cutaneous tumor (9). We were especially interested in the highly metastatic potential of 143B; therefore, we prepared our own 143B +mCherry-IRES-luciferase2 sub-cell line (referred to as 143B). However, 143B did not show pulmonary metastasis for four–six weeks, both from orthotopic or subcutaneous injection (data not shown). Therefore, we performed intracardiac injection of 143B; the cells were monitored by luciferase imaging and were soon observed in the adrenal glands (**Figures 1A–D**). We further followed the secondary metastatic lesions (data not shown) and enhanced the organ-tropism of metastasis by repeated injections to establish different sub-cell lines (**Figure 1E**). Once 143B cells consistently metastasized into the liver (called Bliv), they were used for several repeated injections, following which the cells were suddenly biased to renal metastasis (**Figure 1F**) or lymph node metastasis (**Figure 1G**). The initial metastasis in the specific organ was observed very weakly after four to five weeks from the cardiac injection, however, the repeated injections increased the aggressiveness of these sub-cell lines, and the luciferase signals could be observed within three weeks after the third time injection since the sub-population was detected in the specific organs (data not shown). Finally, we established two biased metastatic sub-cell lines from 143B: the renal-specific Bkid and lymph node-specific Blym.

PEDF Is Upregulated in Sub-Cell Lines That Frequently Infiltrate into the Kidney

After establishing the sub-cell lines of 143B, we performed gene chip (Human Gene 2.0 ST array, Affymetrix) analyses of 143B +mCherryIRES-luc2 (143B), Bkid (renal metastasis), and Blym (lymph node metastasis). A total of 48226 transcript clusters (tc) were analyzed; 523 tc (> 2.0-fold increase) was found in the comparison between Bkid and 143B, whereas 273 tc (> 2.0-fold increase) was found in the comparison between Blym and 143B. Therefore, Bkid was considered the most significantly different subclone of 143B. We then selected genes that were increased in Bkid compared to 143B. The results are summarized in **Table 1**. A hierarchy plot between 143B and Bkid revealed the most effectively upregulated genes in Bkid (**Figure 2A**). We further validated these results using quantitative real time polymerase chain reaction (qRT-PCR) (**Figures 2B–G**). The levels of SLC14A1 (32), LAMC2 (33), LURAP1 (34), and DDIT4 (35) were slightly different from the results of the microarray analyses (**Figures 2A–D**). Serin proteinase inhibitor

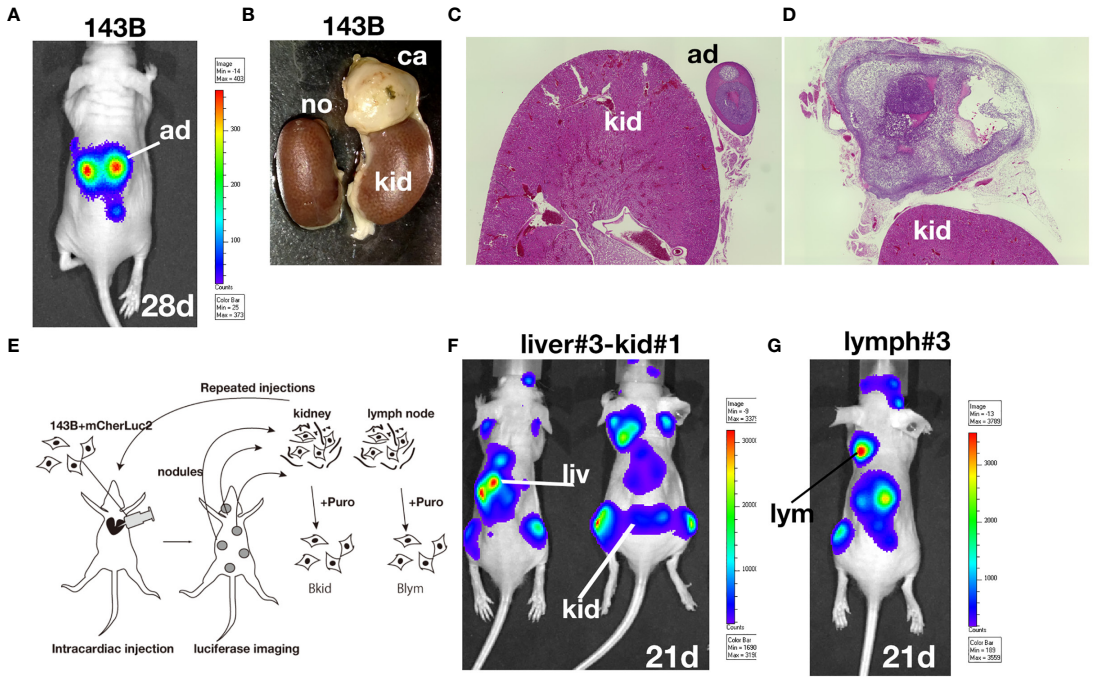

FIGURE 1 | Establishment of osteosarcoma sub-cell lines. **(A)** *In vivo* luciferase imaging of 143B expressing mCherry-IRES-luciferase 2 (143B) after four weeks. Signals in the adrenal glands were detected after two–three weeks. **(B)** Kidneys dissected with the adrenal gland of 143B-injected mice. **(C)** There was no renal metastatic lesion on the left side of **(B)**. **(D)** Cancer cells infiltrated the adrenal gland, while no renal metastasis was observed. **(E)** Schematic diagram of repeated intracardiac injections of osteosarcoma cells. **(F, G)** Results of intracardiac injections of the aggressive cell line. **(F)** The lesions quickly spread throughout the nude mice within three weeks. The cells metastasized to the liver three times and started to infiltrate the kidney. Note that the renal signals of luciferase appeared before the adrenal gland signal became dense. **(G)** Metastatic lesions in the shoulder lymph node after two-repeated injections gathered from lymph node metastasis. The luciferase signal in the lymph node was higher than that in the adrenal glands.

family F1/Pigment epithelium derived factor (SERPINF1/PEDF) (36), slit-related kinase 6 (Slitrk6) (37), and Amelotin (38) (data not shown) remained as candidates (**Figures 2F, G**). Further validation of the gene expression profiles of these upregulated genes showed that PEDF was expressed in various osteosarcoma cell lines (**Supplementary Figure 1A**), whereas Slitrk6 protein was truncated in the SaOS-2 cell line (**Supplementary Figure 1B**). Bkid cells were derived from the hepatic metastasized sub-cell line (Bliv), as described above. Thus, we examined whether PEDF was acquired by 143B cells (**Figure 2H**). Immunoblot analysis revealed that PEDF did not increase in Bliv and accumulated after Bkid differentiation (**Figure 2H**). Thus, PEDF was considered the best candidate gene for kidney-specific metastasis in 143B cells.

Regarding cell morphology, Bkid formed a cohesive sheet compared to 143B (**Figure 2I**). Thus, we searched for cell-cell adhesion molecules in the microarray and found that R-, K-, and N-cadherin were upregulated in Bkid cells (**Figure 2J**). N-cadherin upregulation was unique to Bkid cells (**Figure 2K**). To choose the target of interest among the candidates, we examined them by overexpressed them in 143B cells (data not shown), and found that N-, OB-, and K-cadherin were increased when PEDF was overexpressed in 143B cells (**Figure 2L**). Therefore, we investigated the role of PEDF in Bkid cells.

PEDF Knockdown in Bkid Cells Blocks Renal Metastasis

To determine whether PEDF is responsible for the renal metastasis of Bkid cells, we performed loss-of-function analyses. PEDF protein was mostly reduced by transfection with the microRNA (miR) expression vector (**Figure 3A**). Next, we examined the renal metastasis of Bkid cells with PEDFmiR, and confirmed that Bkid cells had metastasized into the kidney 20 days after their cardiac injection (**Figure 3B**, left), whereas PEDF-knockdown Bkid cells (Bkid+PEDFmiR cells) did not metastasize to the kidney (**Figure 3B**, right column). However, PEDF knockdown did not block the hepatic metastasis (**Figure 3C**). A tumor was found inside the kidney of Bkid-injected mice (**Figure 3D**, left, met), but not in Bkid+PEDFmiR-injected mice (**Figure 3D**, right). In the liver, both cells formed nodules (**Figure 3E**), with no difference in the number or size between the hepatic lesions of Bkid and Bkid +PEDFmiR cells. First, the overall levels of PEDF were tested in the Bkid tumor compared to Bkid+PEDFmiR (**Figure 3F**). The specificity of PEDF-IHC was tested by staining the gel-embedded cells (**Figure 3G**). To determine whether the cells still have osteosarcoma properties, we examined SPARC/osteonectin expression (39) in the kidney (**Figures 3H, I**). SPARC expression was observed in both the kidney and adrenal glands

TABLE 1 | Gene expression comparison between 143B and Bkid cells.

ID	Bkid Avg	143B Avg	Fold Change	Gene Symbol	Description
16852179	8.68	3.75	30.51	SLC14A1	solute carrier family 14 (urea transporter),
16674845	8.94	4.36	23.76	LAMC2	laminin, gamma 2
16829570	9.13	5.03	17.16	SERPINF1	pigment epithelium derived factor), member 1
16967513	7.04	3.45	12.07	AMTN	amelotin
16670185	9.03	5.55	11.15	LOC284561	uncharacterized LOC284561
16996415	6.51	3.14	10.38	ACTBL2	actin, beta-like 2
17083614	8.52	5.3	9.37	LURAP1L	leucine rich adaptor protein 1-like
16705961	8.34	5.38	7.79	DDIT4	DNA damage inducible transcript 4
16803754	7.08	4.29	6.93	CEMIP	cell migration inducing protein
16686271	8.68	5.89	6.92	RNU5F-1	RNA, U5F small nuclear 1
16766578	6.52	3.9	6.15	DDIT3	DNA-damage-inducible transcript 3
16942367	4.43	1.85	5.98		Unknown
16780133	6.18	3.64	5.84	SLITRK6	SLIT and NTRK-like family, member 6
17088446	6.71	4.18	5.8	LOC105376235	uncharacterized LOC105376235
17117867	7.71	5.34	5.18		Unknown
16734877	4.85	7.3	-5.46	HBE1	hemoglobin, epsilon 1
17001985	2.12	4.62	-5.68	LINC01470	long intergenic non-protein coding RNA 1470
17088527	3.76	6.35	-6.03	TLR4	toll-like receptor 4
16708796	3.3	6.03	-6.66	INA	internexin neuronal intermediate filament protein, alpha
17070482	3.77	6.67	-7.44		Unknown
16940203	3.69	6.62	-7.61	RTP3	receptor (chemosensory) transporter protein 3
16734902	3.81	6.78	-7.85	OR51I1;	olfactory receptor, family 51, subfamily I,
16865782	4.71	7.72	-8.05	RFPL4AL1	ret finger protein-like 4A-like 1
16921456	5.47	8.56	-8.52		Unknown
16853375	4.34	7.65	-9.91		Unknown
17024315	3.18	7.11	-15.35		Unknown
16734898	2.23	6.22	-15.88	OR51B2	olfactory receptor, family 51, subfamily B, member 2 (gene/pseudogene)
16734886	3.37	7.57	-18.31	HBG2; HBE1	hemoglobin, gamma G; hemoglobin, epsilon 1
17020497	3.01	7.37	-20.54		Unknown
16734883	3.13	7.9	-27.2	OR51B4	olfactory receptor, family 51, subfamily B, member 4

Gene chips (Human Gene 2.0 ST array, Affymetrix) were hybridized with 143B, Bkid, and Blym RNA each other. Total 48226 transcript clusters (tc) were analyzed, and the results were initially cut by the threshold 2.0 of fold increase. Bkid vs 143B showed unique 523 tc, and Blym vs 143B showed unique 273 tc. Thus, Bkid cells were most differentiated cell line. We further increased the threshold to 5, and cut off the genes in the comparison between Bkid vs 143B. The results were listed in the table.

of Bkid (**Figure 3H**, left, arrows), whereas only in adrenal gland of Bkid+PEDFmiR (**Figure 3H**, right).

PEDF Ligands Are Found on the Cellular Surface of Kidney or Kidney Vein Cells

Next, we investigated the expression of PEDF-related genes (**Figures 3J, K**). PEDF expression was diffusible, which was mostly observed in the cavity of the adrenal gland lesions rather than in the cancer cells (**Figure 3F**). Close observation revealed that PEDF expression was localized on the surface of podocytes around the glomerulus and inside the glomerulus (**Figure 3J**). We presumed that the PEDF ligand might be anchored to the cell surface receptor. In a similar section, we found that one of the PEDF receptor molecules, laminin receptor/67lr (lamR) (14), accumulated on podocytes and glomeruli (**Figure 3K**); however, PEDF and lamR were faint or negative in the kidneys of Bkid+PEDFmiR-injected mice (**Figures 3J, K**, right columns). Therefore, PEDF proteins may be secreted from infiltrated cancer cells and attached to kidney podocytes or kidney vascular cells (**Figure 3L**).

PEDF Reduced Blood Vessels in Liver Tumors

Both Bkid and Bkid+PEDFmiR cells were able to infiltrate the liver (**Figures 3C, E**), possibly because the acquisition of PEDF in Bkid occurred after differentiation from Bliv cells (**Figure 2H**). PEDF is known to inhibit angiogenesis or tumor neovascularization (13, 20). We were not able to compare this function in the kidney because only Bkid had renal metastasis; thus, we performed IHC of CD31 in liver tissues (**Figures 3M, N**) (40). In Bkid-injected mice, CD31-positive cells did not shape the closed blood vessels (**Figure 3M**, above), while the closed vessels were observed in Bkid+PEDFmiR tumors (**Figure 3N**, above), and the tumor-liver tissue border showed it more clearly (**Figures 3M, N**, below). The number of closed vessels was significantly lower in the Bkid tumors (**Figure 3O**).

Therefore, these data suggest that either Bkid or Bkid lacking PEDF could form hepatic metastatic lesions in the 143B nature; however, the function of PEDF as a neovascularization inhibitor was intact in the liver tumor. Moreover, hepatic phenotypes were not involved in the PEDF acquisition in Bkid.

143B+PEDF Quickly Causes Pulmonary Metastasis

The most common destination for osteosarcoma metastasis is the lung; thus, to test the lung infiltration ability of 143B or 143B +PEDF, we performed knee-joint injections of these cell lines and monitored them using *in vivo* imaging (**Figure 4A**). The 143B +PEDF cell line metastasized to the lung within 28 days

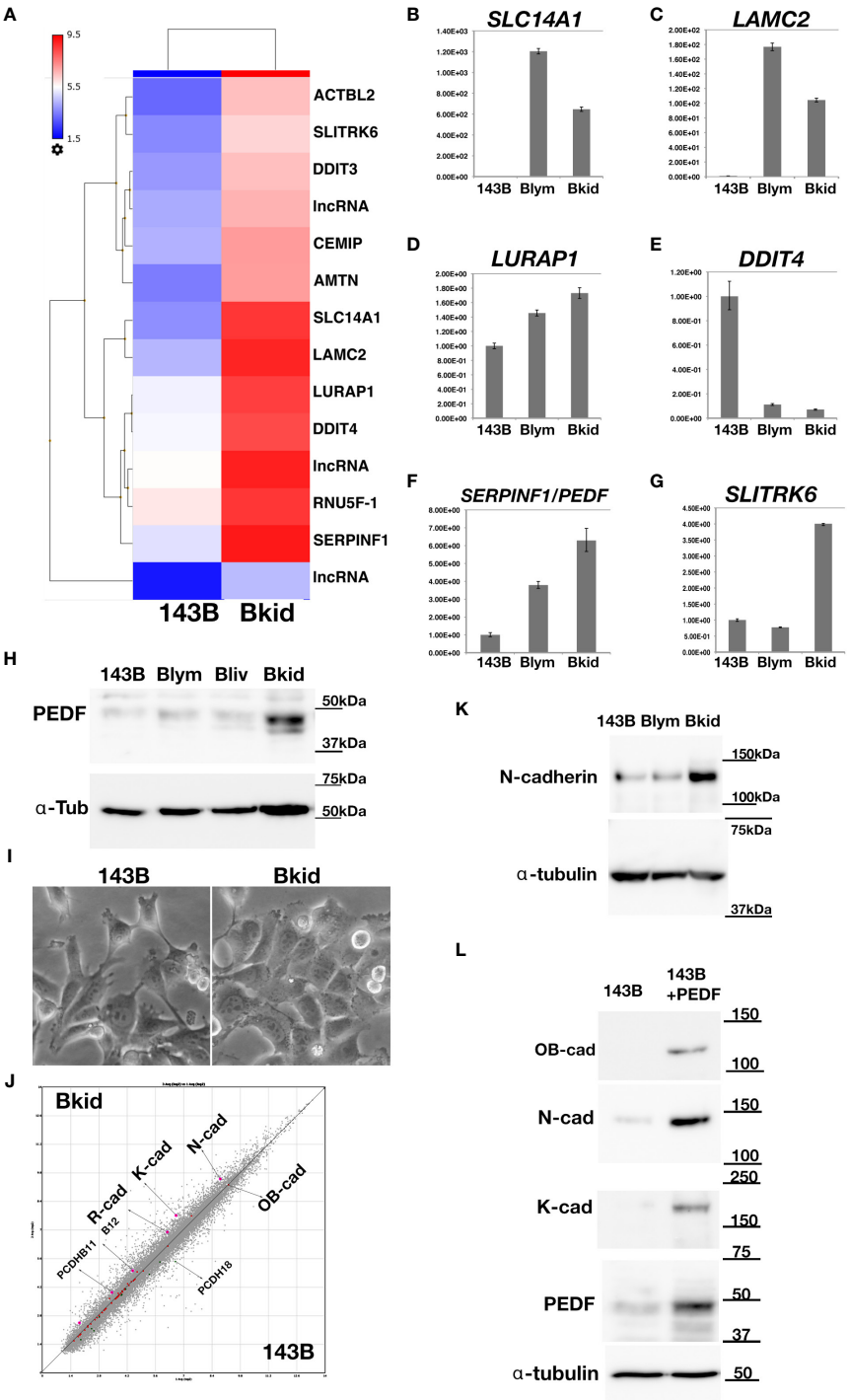

FIGURE 2 | Gene expression profile between 143B parental (143B) and 143B renal metastatic cells (Bkid). **(A)** The hierarchy plot of the gene expression profiles of the comparison between 143B and Bkid. **(B–G)** The validations of gene-tip analyses by quantitative RT-PCR (qRT-PCR). The results of qPCR with the primer sets: **(B)** *SLC14A1*, urea transporter gene **(C)** laminin C2 chain gene (*LAMC2*). **(D)** *LURAP1* **(E)** *DDIT4* **(F)** *Serin protease inhibitor F1/pigment epithelium derived factor* (*PEDF*) **(G)** *Slit related kinase 6* (*Slitrk6*) **(H)** Immunoblot by anti-PEDF antibody or anti-alpha tubulin among sub-cell lines. Blym is a cell line from lesion of lymph node. Bliv is a cell line from hepatic metastasis, later developed as Bkid. **(I)** The morphological changes between 143B and Bkid cells. **(J)** The scatter plot of the gene expression profiles of cadherin family genes between 143B and Bkid. Cdh6 (K-cadherin), Cdh2 (N-cadherin) and Cdh4 (R-cadherin) expression levels were upregulated. **(K)** The endogenous N-cadherin increased in Bkid cells. **(L)** PEDF overexpression in 143B reproduced Bkid phenotypes. OB-cad, N-cad, and K-cad were increased co-incidentally with PEDF overexpression.

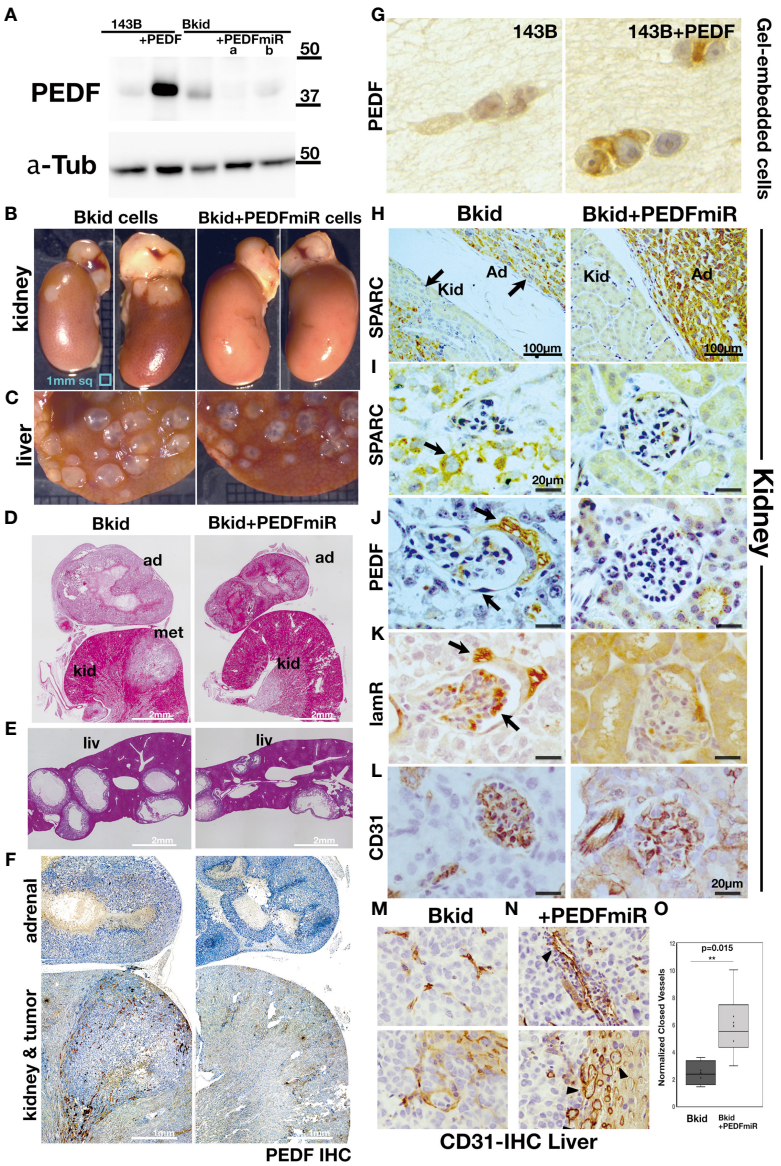

FIGURE 3 | Loss-of-function analyses of PEDF in Bkid cells. **(A)** PEDF micro RNA (miR) expressing vector was transfected into Bkid cells. Immunoblot by anti-PEDF antibody showed the reduction of PEDF proteins by miRs. **(B)** The renal and the hepatic lesions of the results of the intracardiac injections of Bkid cells or Bkid +PEDFmiR cells. The adrenal metastasis was observed. Also, by Bkid cell injections, the renal metastasis was observed frequently (left, 12-positive/12), while no renal nodule was observed in Bkid+PEDFmiR injected mouse (right, 17-negative/18). The ruler is 1mm square. **(C)** The hepatic metastases of both cells were not inhibited with or without PEDF. **(D)** The section Hematoxylin/Eosin (H&E) staining of the similar samples to **(B)**. The adrenal hypertrophy was observed both in Bkid- and Bkid+PEDFmiR-injected mouse organs. The renal metastatic lesion (met) was seen as the lighter color. The scale is 2 mm. **(E)** The hepatic metastasis. Both tumors had the cavity. **(F)** PEDF-immunohistochemistry (IHC) of the section **(D)**. PEDF staining was observed inside of the adrenal gland cystic vesicle of Bkid tumors. The overall staining level of PEDF in Bkid tumor was higher than Bkid+PEDFmiR cells. The scale is 1 mm. **(G)** IHC for PEDF on paraffin sections of collagen gel-embedded 143B and 143B+PEDF cells. (H-L) The renal section IHC by various antibodies. **(H)** Anti-SPARC (osteonectin)-IHC indicates that the lesions are derived from the injected osteosarcoma. In the section of kidney from Bkid-injected mouse, there is SPARC-positive tumor both in kidney and adrenal gland sides. On the right, the kidney from Bkid+PEDFmiR-injected mouse had SPARC-positive cells only in adrenal gland. The scale indicates 100 μm. **(I–L)** The scale indicates 20 μm. **(I)** The higher magnified picture of the tissue surrounded glomerulus. There is SPARC-positive cells were seen around the glomerulus of Bkid-injected mouse (arrow), while no signal was seen in Bkid+PEDFmiR-injected mouse, **(J)** PEDF-IHC. PEDF was accumulated in the podocytes around the glomerulus. **(K)** 67kDa laminin receptor (lamR)-IHC. lamR is a potential PEDF receptor. Arrows indicated lamR signals in the podocytes around and the vein in the glomerulus. **(L)** CD31-IHC in glomerulus. **(M, N)** The liver section IHCs with CD31 antibody. The vascular formation was observed. **(M)** No closed blood vessel was seen in Bkid tumor (above). Near the tumor-liver boundary in Bkid sample (below). **(N)** The blood vessels could be seen as the closed oval form in Bkid+PEDFmiR tumor (above). Tumor-liver boundary of Bkid+PEDFmiR (below). There were a lot of the closed blood vessels (arrowheads). **(O)** The closed shapes of CD31-staining were counted only in the tumor regions, and the results were normalized by CD31-positive area. PEDF expression severely disturbed the formation of blood vessels (p=0.015). ad, adrenal gland; kid, kidney; met, metastatic lesion; liv, liver.

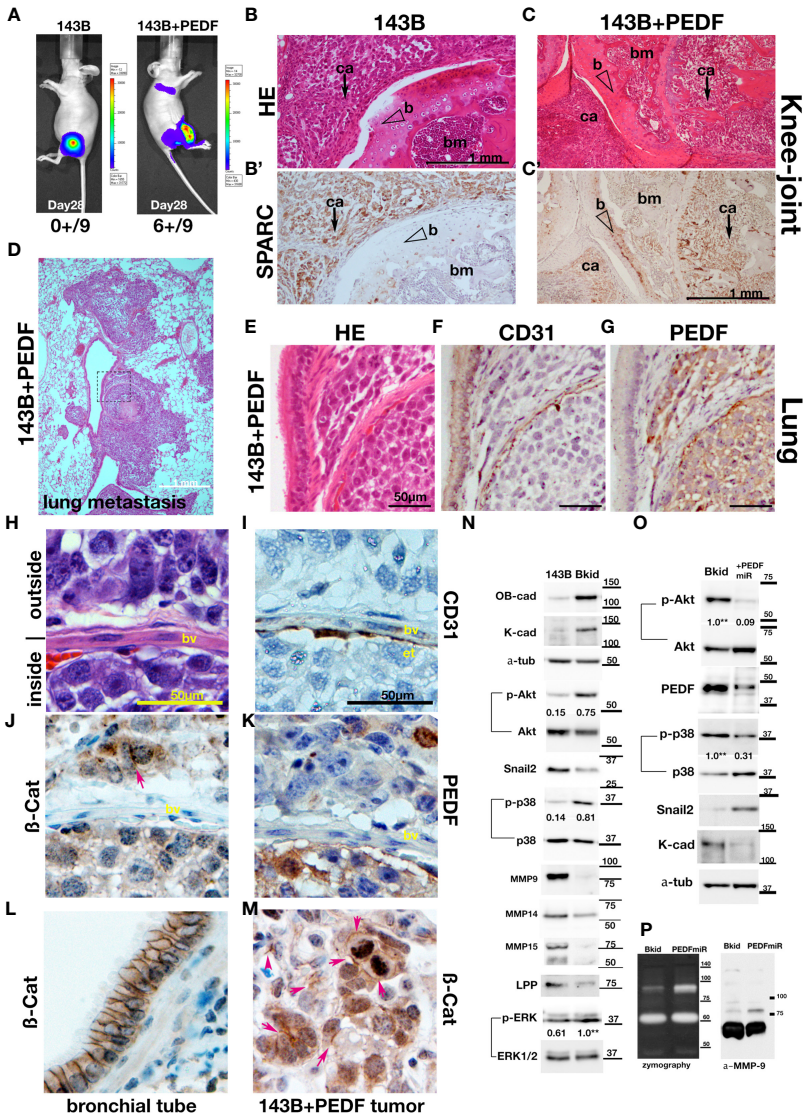

FIGURE 4 | PEDF overexpression promoted the MET-like behavior in pulmonary metastasis. **(A–K, M)** The results of higher doses (2 x 10^6 cells) injections into the knee joints. **(A)** *In vivo* luciferase-imaging of 143B/143B+PEDF cells after 28 days from the injection. The signals were observed in the lung of 143B+PEDF cell-injected mice (right, six positive/10: one dead), while no signal was seen in thorasic region of 143B-injected mice (left, zero positive/nine). **(B, C)** The H&E stain of knee joint and femur section. The scale bar indicates 1mm. **(B', C')** SPARC-IHC of the adjacent section of **(B, C)**. The scale bar indicates 1 mm. **(B)** The 143B cells (ca; arrow) were mainly observed outside of the knee bone. **(B')** SPARC-IHC. The cells outside of the joint were osteosarcomas. **(C)** 143B+PEDF cells were observed inside of the bone (ca; arrow). **(C')** SPARC-IHC of **(C)**. The SPARC-positive cancer cells were seen both in the bone marrow (bm) and the joint. The opened arrowheads mean the position of the bone. **(D)** The H&E stain of the pulmonary metastatic lesion of the 143B+PEDF-injected mouse. The square of the broken line is the region of interest in **(E–G)**. **(E–G)** The lung vascular border in 143B+PEDF cell-injected mouse at higher magnification. The cancer cells inside and outside the vasculature are connected with each other. The scale bar indicates 50 μm. **(E)** shows H&E staining of these sections. **(F)** shows IHC for CD31 on a similar section. The endothelial cell layer is very thin. **(G)** shows IHC for PEDF. PEDF-positive cells are present both inside and outside the vein. (H–K, M) The 143B +PEDF tumor in the lung at higher magnification. The scale bar indicates 50 μm. **(H)** shows H&E staining of the inside and outside of vasculature. **(I)** shows IHC for CD31 indicating the endothelial layer. **(J)** shows IHC for ß-catenin on both sides of the boundary. **(K)** shows IHC for PEDF also on both the sides. **(L)** IHC for ß-catenin-in the normal bronchial tube near the tumor lesion. **(M)** IHC for ß-catenin in the tumor far away from the vascular boundary. Arrowheads indicate strong staining on cell–cell junctions. **(N)** Immunoblot of 143B and Bkid cell lysates. OB-cadherin and K-cadherin was upregulated, whereas Snail2 was downregulated. The ratios of phosphorylated to whole Akt for each sample are shown between the blots. The ratio of phosphorylated to whole p38MAPK, and the ratio of phosphorylated to whole ERK1/2 are also shown between each blot. Expression of MMP9 was diminished in Bkid cells, whereas that of MMP14, MMP15, and LPP was decreased. **(O)** Comparisons between Bkid and Bkid+PEDFmiR cell lysates. The amount of PEDF were reduced. The ratios of phosphorylated to whole Akt and phospho-p38MAPK to whole p38 are also shown between the blots. The phosphorylation level decreased upon PEDF knockdown. Snail2 was upregulated in Bkid +PEDFmiR, whereas K-cadherin was downregulated. **(P)** Zymography indicating that metalloprotease activity was increased upon PEDF knockdown. The upregulated MMP was mainly MMP9.

(**Figure 4A**, right; six positive out of nine mice, one died earlier), whereas 143B parental cell lines did not show any metastasis during the same period (**Figure 4A**, left; zero positive in thorasic level out of nine mice). The 143B cells were observed around the knee joint (**Figure 4B**), whereas 143B +PEDF cells efficiently invaded the bone marrow of the femur (**Figure 4C**), which was confirmed by SPARC staining (**Figures 4B, C**). We also analyzed the pulmonary metastatic lesions (**Figures 4D–G**) and found that 143B cells were not seen in the lungs (data not shown), whereas the 143B +PEDF cells infiltrated the lung tissues or blood vessels (**Figure 4D**). The vascular wall (endothelial cells) had already been thin in the metastatic lesion (**Figures 4E, F**); further, PEDF staining was observed in these tumors (**Figure 4G**). We closely observed the cell-cell adhesions inside and outside the blood vessels (**Figures 4H–K, M**). The endothelial layer was shown by CD31 staining (**Figure 4I**), and both β-catenin and PEDF signals were observed on both sides of the vascular boundary (**Figures 4J, K**), and ß-catenin IHC was accumulated in the cell-cell junctions (**Figure 4J**, arrow). When we looked at the position far away from the blood vessels, many 143B +PEDF cells formed cell-cell adhesions in the lung (**Figure 4M**), while the bronchial tube showed similar staining (**Figure 4L**). Therefore, these data suggest that PEDF may promote mesenchymal-to-epithelial transition (MET) after extravasation.

PEDF Promotes Mesenchymal-to-Epithelial Transition (MET)

To understand why PEDF increased metastatic lesions, we analyzed the protein expression of 143B/Bkid. As mentioned above, K- and OB-cadherins were upregulated by PEDF (**Figure 4N**). Phosphorylation of Akt and p38MAPK signaling was also upregulated in Bkid cells (**Figure 4N**). We found that epithelial-to-mesenchymal transition (EMT)-related markers, such as Snail2, MMP9, and MMP14, were downregulated in Bkid cells (**Figure 4N**). Moreover, we previously reported that MMP15, under the control of the transcriptional co-factor LPP, digests N-cadherin in lung cancer cells, and that loss of LPP function caused abnormal stabilization of N-cadherin (27). Similarly, in Bkid cells, MMP15 and LPP were downregulated (**Figure 4N**). Thus, these results indicate that Bkid partially promotes MET. To determine if this MET phenotype is due to PEDF expression, we compared Bkid cells and PEDF-knockdown cells (**Figure 4O**). PEDF-knockdown in Bkid cells resulted in a reduction in the phosphorylation of Akt and p38MAPK, and upregulation of Snail2 (**Figure 4O**). Moreover, K-cadherin expression was reduced (**Figure 4O**). Further, zymography of Bkid and PEDFmiR cell supernatants showed that the activity of MMP-9 was also upregulated in PEDF-knockdown cells (**Figure 4P**). Therefore, PEDF expression in Bkid cells promoted MET phenotypes, at least partially.

PEDF Delays Cell Delamination Without Affecting Cell Proliferation

The experiments above showed that PEDF caused an MET-promoting phenotype; thus, we examined the MET marker expression to determine the general role in the osteosarcomas; however, the basal expressions of osteosarcomas were very different from each other (data not shown). Therefore, we examined whether PEDF overexpression had similar effects on other osteosarcomas. First, the effect of PEDF on cell proliferation was tested in 143B, MG63, and U2OS cells (**Figures 5A–C**). The proliferation of PEDF-overexpressing cells was slightly higher than that of the control cells (**Figure 5A-C**). Furthermore, we examined the autocrine effects of PEDF in Bkid cells (**Figure 5D**). Neither PEDF knockdown nor laminin receptor knockout affected cell proliferation (**Figure 5D**). We also examined the wound healing abilities of each cell line because PEDF might block cell delamination by increasing the epithelial-like character (**Figures 5E–H**). PEDF significantly delayed wound healing in MG63 and U2OS cells, similar to that in 143B cells (**Figures 5E–G**). Loss-of-PEDF or lamR showed faster healing (**Figure 5H**), while only the targeted protein was reduced (**Figure 5I**). Therefore, PEDF expression caused MET-promoting phenotypes in other osteosarcoma cells without changing cell proliferation.

Low Numbers of 143B+PEDF Cells Infiltrate Into the Liver and Kidney

As mentioned above, the orthotopic injection of PEDF-overexpressing 143B caused pulmonary metastasis (**Figure 4**), and the mice died of respiratory failure before showing renal metastasis. Thus, we injected smaller amounts of cancer cells and observed them for a much longer period (**Supplementary Figure 2**). The leg tumors of 143B +PEDF were larger than those of 143B (**Supplementary Figures 2A, B**). While the hepatic metastasis was not obvious because the superficial nodules did not appear (**Supplementary Figure 2C**), and the renal phenotype was clearly observed (**Supplementary Figure 2D**). In the liver sections, the inflammatory cells accumulated around the central vein; however, no apparent metastatic tumor was observed (**Supplementary Figures 2E–H**). On the other hand, a renal metastatic tumor was observed (**Supplementary Figures 2I, J**), and the cancer cells surrounded the glomerulus in 143B +PEDF cell-injected mice (**Supplementary Figures 2K–N**). Therefore, PEDF overexpression in 143B could also bias metastasis toward the kidney.

PEDF-R and Laminin Receptor Expression in the Kidney, Liver, and Lung

To understand why Bkid cells prefer to infiltrate the kidney or lung, an understanding of endogenous receptor expression in mouse organs is necessary. The phospholipase molecule PNPLA2 is a putative PEDF receptor (41). The other receptor molecule laminin receptor/67lr (lamR) (14), has already been described above. Thus, we performed western blot analyses of the endogenous protein levels of these genes in mouse organs (**Figure 6A**). PNPLA2 was strongly expressed in the liver and weakly expressed in the lungs and kidneys (**Figure 6A**, arrow). LamR was clearly expressed in the kidneys and lungs (**Figure 6A**, arrow), whereas it was truncated in the liver (**Figure 6A**,

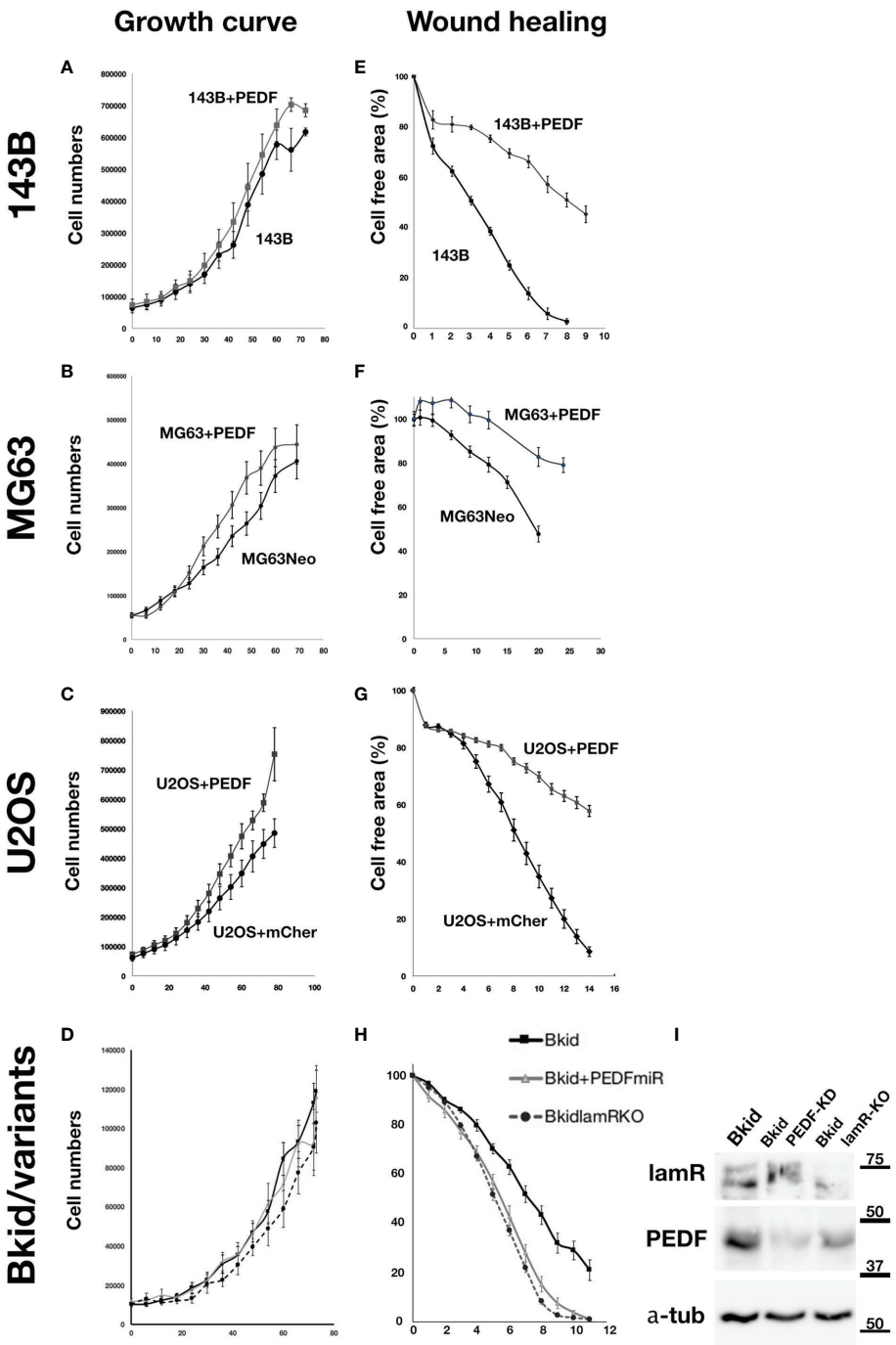

FIGURE 5 | PEDF did not inhibit the proliferation but inhibited the migration. **(A–D)** Cell numbers over time. **(E–H)** The decrease ratio of the cell free area by wound healing. **(A)** The growth curves of 143B and 143B+PEDF cells. PEDF overexpression slightly increased the cell proliferation, but the differences were not significant. **(B)** The cell numbers of MG63+MOC vector (MG63Neo) and MG63+PEDF in cell culture. MG63+PEDF grow slightly faster than MG63Neo. **(C)** The cell numbers of U2OS+mCherry vector and U2OS+PEDF in cell culture. Likely U2OS+PEDF grow faster than that of U2OS+mCherry. **(D)** The comparisons among Bkid, Bkid +PEDFmiR, and Bkid lamR knockout cells. The proliferations were not significantly changed by loss-of-function. **(E)** Wound healing abilities of 143B and 143B+PEDF cells. PEDF overexpression decreased cell motility of 143B. **(F)** Wound healing of MG63Neo and MG63+PEDF. MG63+PEDF delayed the healing. **(G)** Wound healing of U2OS+mCherry and U2OS+PEDF. Same as other cells, U2OS+PEDF significantly delayed the healing. **(H)** The wound healing phenotype of Bkid was cancelled by the knockdown of PEDF-lamR pathway. **(I)** Western blot of the effect of gene knockdown and gene knockout cell lysates. LamR knockout and PEDF knock down did not affect on the other's expression each other.

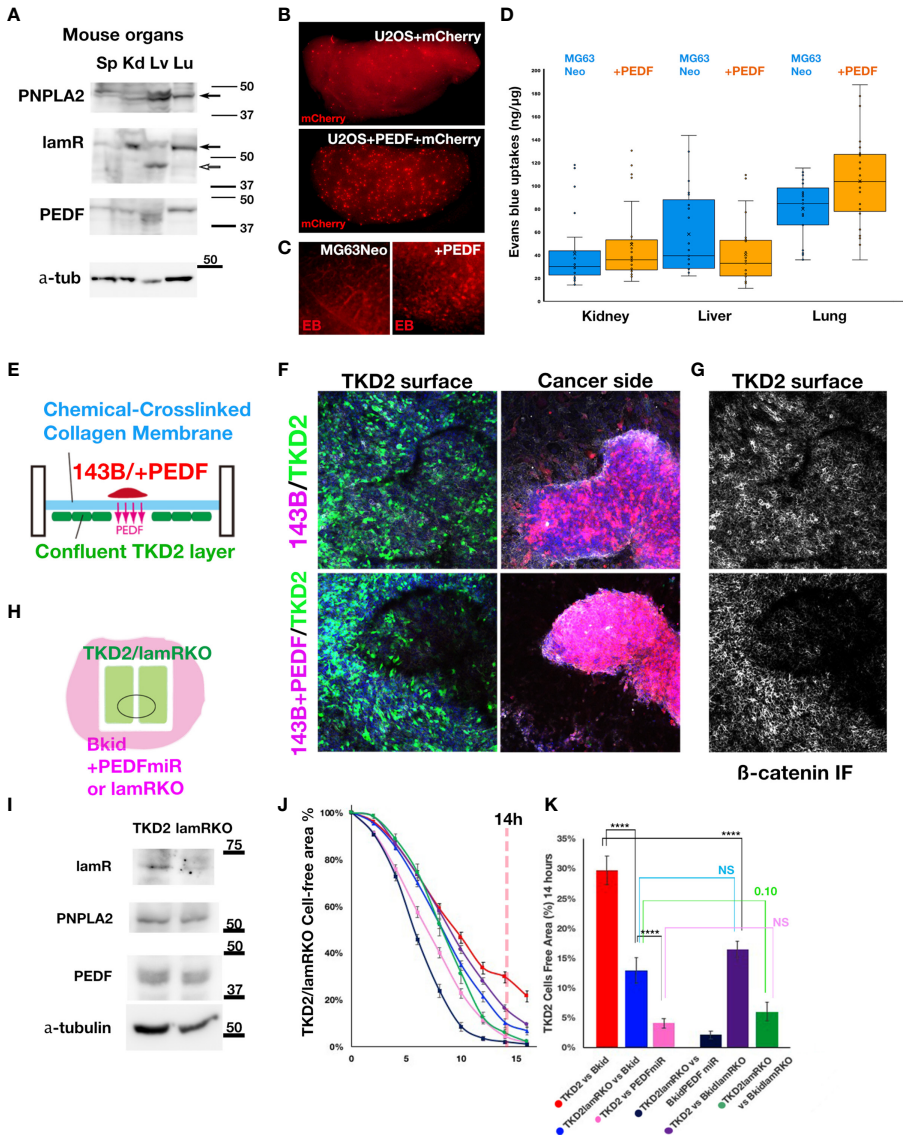

FIGURE 6 | The effects of PEDF on extravasation and inhibition of EndoMT. **(A)** Immunoblot of mouse spleen (Sp), kidney (Kd), liver (Lv), and lung (Lu) lysates by anti-PEDF receptor molecules. PNPLA2/PEDF-R was expressed in liver and lung. Laminin receptor/67lr (lamR) was expressed in the kidney and the lung (arrow). The lamR in liver sample was truncated (open arrow). The endogenous PEDF was not significantly different among these organs. **(B)** The cells extravasated in the lung of tail intravenous injected U2OS+mCherry (above). The cells extravasated in the lung of U2OS+PEDF (+mCherry) injected mouse. The mCherry-positive cells were observed everywhere in the lung (below). **(C)** After two weeks of the intracardiac injection of MG63Neo or MG63+PEDF, Evans Blue (EB) dye was injected from the tail vein two hours before the sacrifice. EB dye was visualized as the red fluorescence, and when the vascular permeability was increased, the EB dye remained in the organs (See *Materials & Methods*). In MG63+PEDF-injected mouse lung, the large puncta of EB remained (right) while the small vein was stained in control (left). **(D)** The quantitative analyses of Milles assay shown in **(C)**. The remained EB dyes were extracted from each dissected organ by the heated formamide and quantified by OD_{600}. **(E)** The schematic illustration of the double-sided cell culture on the atelocollagen membrane. The mouse kidney endothelial cell line, TKD2 cells expressing GFP (TKD2-GFP) were cultured on the one side of the chemically cross-linked atelocollagen membrane, and the appropriate size of 143B cell cluster was transferred on the other side of the membrane. We could see the localized effects of PEDF because only secretory molecules could go across this cross-linked membrane (See *Material and Methods*). **(F, G)** The Z-stack images were taken under the confocal microscopy. The nucleus of the cells (blue), TKD2-GFP (green), osteosarcomas (red), and ß-catenin immunofluorescence (IF) (white) images were merged. **(F)** TKD2 layer was disturbed by 143B+PEDF. The optical section of TKD2 side (above). The projection image of cancer side (below). **(G)** ß-catenin IF of TKD2 layer. ß-catenin staining was disappeared from the region where the opposite side were occupied by the cancer cells. **(H)** The schematic diagram of the wound healing assay of TKD2-derived cell layers. TKD2 cell layers were formed inside of the silicon molds. The cancer cells were cultured around the mold, and time-lapse images were captured after removing the mold. **(I)** Western blot analyses of TKD2-laminin receptor knockout cells (lamRKO). The PEDF or its receptor expressions were not changed. **(J, K)** [TKD2 migrations with Bkid (red)], [TKD2 with Bkid+PEDFmiR (pink)], [TKD2-lamRKO cell migrations with Bkid (blue)] and [TKD2-lamRKO with Bkid+PEDFmiR (dark blue)], [TKD2 with Bkid-lamRKO(purple)] and [lamRKO-TKD2 with Bkid-lamRKO (green)]. **(K)** The graph indicated the cell free area at 14 hours after the start. PEDF knockdown in Bkid cells or lamR knockout in TKD2 accelerated the endothelial cell migration. NS, Not significant. The symbol **** means 4 digit below the decimal point, enough significant difference according to the result of t-test.

open arrow). Thus, the phenotype of Bkid in the kidney may be mediated by the laminin receptor.

PEDF Overexpression Induces Extravasation of Osteosarcoma Cell Lines

We hypothesized that MET phenotypes caused by PEDF overexpression might obstruct extravasation. Then, we performed tail vein injection of U2OS+mCherry cells with or without PEDF, and fixed the lung two hour after injection (**Figure 6B**). Contrary to our initial expectation, PEDF increased the extravasation of cells in the lung (**Figure 6B**). To confirm these results, we injected MG63+Neo (MOC vector) cells or MG63+PEDF cells in the heart, and after two weeks, we injected Evans Blue (EB) dye from the tail vein, and then dissected the lung (**Figure 6C**). Because the molecular weight of EB dye is almost the same as the membrane pore size, the Milles assay can be used to indicate increased vascular permeability (31). MG63 could not survive for more than two weeks (data not shown), suggesting that PEDF overexpression increased vascular permeability (**Figure 6C**, right). We further quantified the remaining EB in each organ (**Figure 6D**). The estimated amounts of EB seemed to be increased in the kidneys and lungs by PEDF overexpression (**Figure 6D**), while the liver did not show such an increase. These data suggest that PEDF overexpression in osteosarcoma may increase vascular permeability in the kidneys and lungs.

PEDF Inhibits Endothelial Cell Layer Formation *via* Laminin Receptor

To determine how PEDF affects extravasation, we focused on the layer-forming ability of TKD2, a kidney endothelial cell line. TKD2 could be a model for the glomerular endothelial cells (42), which may be suitable for testing the extravasation. Thus, we designed the assay to observe the interaction between the endothelial layer and the cancer cells (**Figure 6E**). A confluent TKD2 cell layer was prepared on the bottom side of the culture insert, and a cancer cluster was prepared separately, which was then placed on the atelocollagen membrane. The membrane is chemically cross-linked; thus, the cells never across the membrane. However, the effect of the secretory molecules can be distinctly observed (**Figure 6E**). The cluster of 143B+PEDF reduced the number of TKD2 cells on the opposite side of the cancer cluster (**Figure 6F**, below), whereas the cluster of 143B did not disturb theTKD2 layer (**Figure 6F**, above). The ß-catenin immuno fluorescence staining showed the cell-cell adhesions of TKD2 were highly disturbed by PEDF overexpression (**Figure 6G**, below). We conducted similar assay with Bkid and Bkid+PEDFmiR cells (**Supplementary Figure 3A, B**), and observed that Bkid+PEDFmiR cells did not disturb the TKD2 layer (**Supplementary Figure 3B**). Therefore, we inferred that the close contact between PEDF-overexpressing and endothelial cells might have increased cell permeability. Next, to analyze the cell-cell interactions more quantitatively, TKD2 and 143B cells (or derivative cells) were separated using a silicon mold, and the cell-free area between TKD2 layers was then observed (**Figure 6H**). TKD2 migrated rapidly when co-cultured with 143B cells, whereas PEDF overexpression delayed their migration over time (**Supplementary Figure 3C**). We established a TKD2-lamR knockout cell line without changing the expression of PNPLA2 or PEDF (**Figure 6I**). Next, we tested various combinations of TKD2 with or without lamR, and Bkid with or without PEDF (**Figure 6J**). When lamR expression in TKD2 cells and PEDF expression in Bkid cells was inhibited, the endothelial cells migrated at the highest speed (**Figure 6J**, dark blue). The results at 14 h were compared (**Figure 6K**, pANOVA=3.37E-15), and the t-test of each pair was also performed (**Figure 6K**, ****p<0.001). These data suggest that PEDF expression in Bkid cells effectively inhibited the layer formation process in renal endothelial cells, and the signals for this inhibitory process might be mediated by lamR in TKD2 cells.

PEDF-lamR Downstream in TKD2-Endothelial Cells

The PEDF-lamR axis is known to be mediated by Akt phosphorylation (43). First, we analyzed the expression of Snail2 or the other MET-related markers by western blotting, as shown in **Figure 4**; however, mouse Snail2 was not detected by this method (data not shown). Therefore, we investigated the genes targeted by lamR using the Akt inhibitor wortmannin (WMN) (**Figure 7A**). The condensed Bkid supernatant (Bkid sup) increased Akt phosphorylation, and the basal level of phosphorylation was high because TKD2 culture medium supplemented with epidermal growth factor. WMN treatment reduced Akt phosphorylation (**Figure 7A**), and the expression of various genes involved in this process was analyzed (**Figure 7B**). *Lysyl oxidase-like 1* (*Loxl1*) expression was upregulated by Bkid stimulation and inhibited by the addition of WMN. We analyzed the expressions of Snail1 and 2, however, no significant change in their expression was observed (**Figure 7B**, data not shown). We found that *SNAI3* expression was inhibited by the Bkid supernatant and upregulated by the addition of WMN. Thus, we identified Loxl1 and SNAI3 as candidate LamR downstream genes. SNAI3 overexpression in TKD2 cells increased the expression of marker associated with endothelial-to-mesenchymal transition (EndoMT), and co-expression SNAI3 with PEDF cancelled the EndoMT-upregulation by SNAI3 (**Figure 7C**). *Tcf12* is an osteopontin upstream gene that is involved in EndoMT (44). *S100A4* and *ACTA2* are both fibroblastic markers (45, 46), and their upregulation may indicate transient EndoMT. *SM-22a*, also known as *transgelin*, is a smooth muscle cell protein, which serves as an EndoMT marker (47). *SM-22a* upregulation by SNAI3 overexpression was not inhibited by co-expression of PEDF; thus, we inferred that strict regulation of SNAI3 expression was required for the maintenance of the endothelial cell layer. We also found that the known EMT marker, metadherin (48), was expressed with the occurrence of EndoMT. Endogenous *SNAI3* levels in SNAI3 overexpressing TKD2 cells was monitored; however, no significant difference was observed in *SNAI3* levels (**Figure 7C**). We established Loxl1-overexpressing TKD2 and conducted the same assay, as shown in **Figure 6E**. TKD2-Loxl1 blocked the effects of PEDF-knockdown Bkid cells (**Figure 7D**).

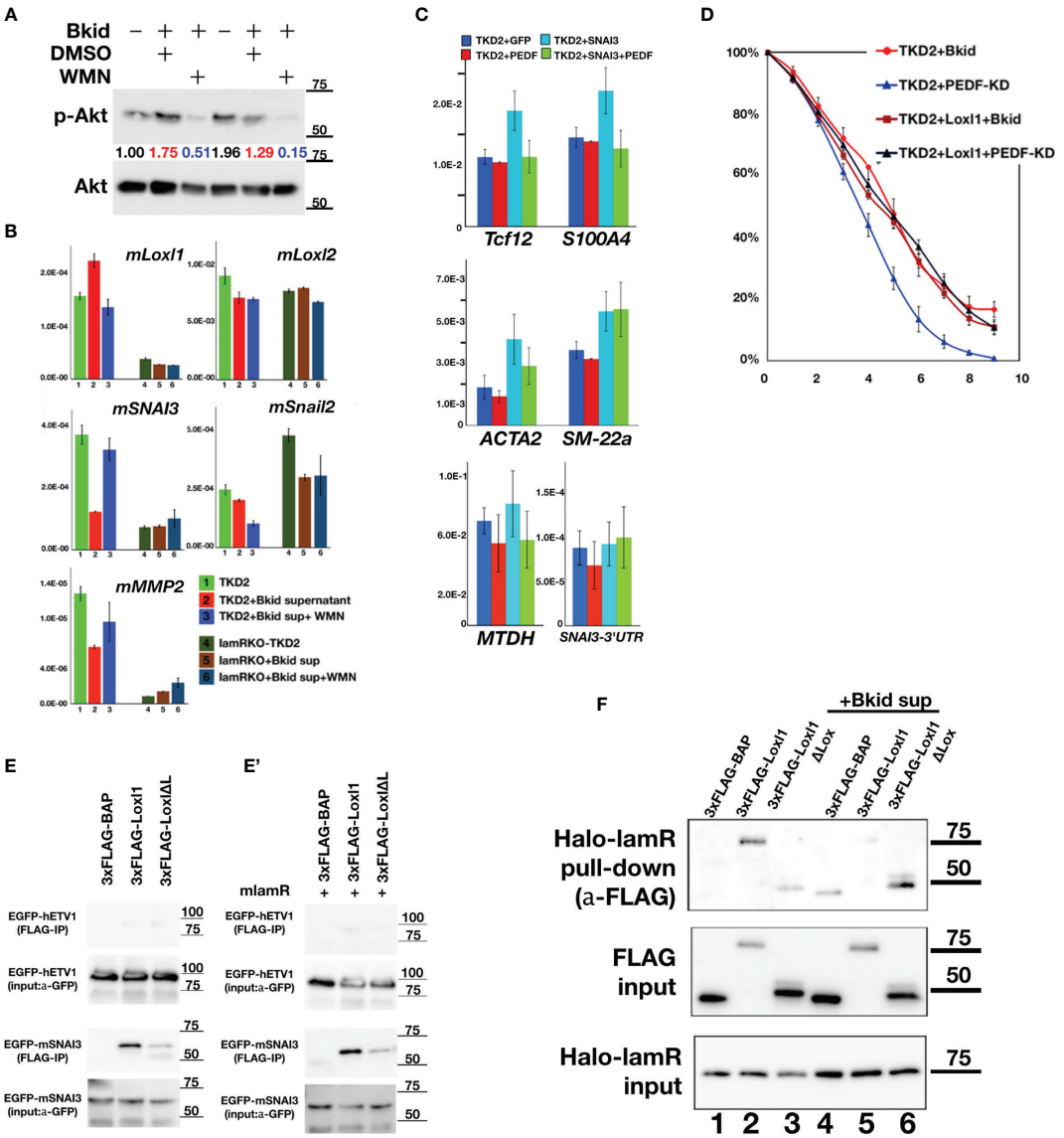

FIGURE 7 | PEDF-lamR downstream in TKD2 endothelial cells. **(A)** The phosphorylation of Akt in TKD2 cells were stimulated by Bkid supernatant and inhibited by wortmanin (WMN) treatment. The numbers showed the ratio of phosphorylated Akt to Akt. **(B)** The qPCR of the same sample as **(A)**. *Lysyl-oxidase like 1*(*Loxl1*) was increased by Bkid stimulation and blocked by WMN. Conversely, *SNAI3* (*Snail3*) expression was downregulated by Bkid and increased by Bkid+WMN, while *Loxl2* and *Snail2* were not affected by such stimulations. *MMP2* were regulated similarly to *SNAI3*. **(C)** The gene expressions of PEDF-overexpressing, SNAI3-overexpressing and SNAI3+PEDF-coexpressing TKD2. Endothelial-to-mesenchymal Transition (EndoMT) markers were tested. *Tcf12*, *S100A4* (fibroblastic), *ACTA2* (fibroblastic) markers indicated that SNAI3 overexpression promoted the EndoMT, and SNAI3 function was blocked by PEDF-coexpression. *SM-22a* (smooth muscle protein) was not inhibited by PEDF. The known EMT marker, *Metadherin* (*MTDH*) was also upregulated by SNAI3 overexpression. The endogenous *SNAI3* was not significantly changed by the overexpression. **(D)** TKD2+Loxl1 cell line was established. The layer formation of TKD2 with Bkid+PEDF-KD was promoted, however, TKD2+Loxl1 with Bkid+PEDF-KD was inhibited as same as that of TKD2+Bkid. **(E, E')** The co-immunoprecipitation between 3xFLAG-Loxl1 and EGFP-ETV1 (negative control of EGFP-tag) and EGFP-SNAI3. FLAG-tagged bovine alkaline phosphatase (3xFLAG-BAP) was negative control of FLAG-tag. Loxl1 pulled down SNAI3 while Loxl1 lacking Lox domain (Loxl1ΔL) could not bind to SNAI3 same way as full-length Loxl1, thus, the center of binding between SNAI3 and Loxl1 is the Lox domain of Loxl1. **(E')** The co-expression of lamR protein did not affect on the binding between Loxl1 and SNAI3. **(F)** The binding between HaloTag-fusion protein of laminin receptor (Halo-lamR) and 3xFLAG-Loxl1 was tested with or without Bkid stimulations. Loxl1 could bind to lamR (lane 2), while Bkid stimulation released Loxl1 from Halo-lamR (lane 5). Non-specific binding was slightly increased after adding Bkid proteins (lane 4).

We infer that SNAI3 promotes EndoMT, and its expression is enhanced by Akt inhibition. In contrast, Loxl1 inhibits EndoMT, and its expression is promoted by Bkid cell stimulation. Next, we tested whether SNAI3 and Loxl1 directly interacted with each other; For this purpose, we first examined the binding affinity between Loxl1 and SNAI3 (**Figure 7E**). SNAI3 mainly bound to the Lox domain of Loxl1 (**Figure 7E**), and lamR expression did not disrupt the binding affinity between SNAI3 and Loxl1

(**Figure 7E'**). Next, we then tested the binding affinity between lamR and Loxl1 (**Figure 7F**). In absence of Bkid sup stimulation, Loxl1 bound to lamR (**Figure 7F**, lane 2). However, the binding affinity was disrupted under the Bkid sup stimulation (**Figure 7F**, lane 5). In summary, Loxl1 may associate with lamR until Bkid cell stimulation, and the released Loxl1 may bind to SNAI3 and inhibit EndoMT upon endothelial layer formation.

Collectively, our results suggest that PEDF expression increases the permeability of kidney and lung vasculature owing to its association with endogenous lamR expression. Thus, the PEDF-lamR axis may promote the extravasation of cancer cells and may be involved in target organ specificity.

DISCUSSION

We sought to identify the mechanisms underlying the organ tropism of metastasis in osteosarcoma; however, the candidate for the renal metastasis-specific gene was unexpectedly an anti-cancer molecule, PEDF. Until now, PEDF function has been examined in a wide range of cancers, including osteosarcoma, prostate cancer, breast cancer, and hepatocellular carcinoma (19, 20, 43, 49–51). PEDF shows anti-angiogenic, anti-tumor, and anti-metastatic effects (18, 19, 22, 23, 52). However, the role of endogenous PEDFs in cancer cells has not been thoroughly investigated. Here, we discuss the differences between previous studies and the present study. Interestingly, we found that PEDF only affected renal and pulmonary metastases; therefore, we could conclude that the PEDF-lamR axis also controlled organ tropism.

PEDF is a promising candidate for anticancer drugs. However, we observed contrasting effects of PEDF in osteosarcoma cell lines, possibly because of the following reasons. First, the anti-angiogenic activity of PEDF was shown to inhibit tumor vascular formation (49, 53). Similar to previous observations, the inhibitory effect of PEDF on tumor vasculature was observed (**Figure 3O**); however, it did not interfere with hepatic metastasis (**Figure 3C**). This study suggests that organ vascular inhibition by PEDF may promote extravasation into the target organ (**Figures 6B–D**). At least some part, the phenotype of the extravasation was reproduced by the co-culture assay shown in **Figures 6E–G**.

The anti-tumorigenic activity of PEDF in OS has been previously reported in SaOS-2 (18). The synthetic peptide of PEDF has been demonstrated to exert anti-tumorigenic activity (52, 54). In addition, the administration of recombinant PEDF protein showed the therapeutic effects on the primary OS and the secondary pulmonary tumor in an orthotopic animal model using SaOS-2 (22). However, the researchers also reported that there were no significant differences in the mean number of pulmonary micrometastasis between treatment and non-treatment groups (22), and the similar observation from the synthetic peptides test was also reported (52). It was speculated that the proliferation in the secondary lesions may be involved in these phenotypes (22). In our study, PEDF overexpression in 143B increased the pulmonary metastatic lesions (**Figure 4D**) and MET (**Figure 4M**), which may be favorable for the local growth of metastasized cells in the lung. Moreover, PEDF also exerted anti-oxidative stress activity (16, 55). In fact, the cell survival signal was increased in Bkid cells but reduced following PEDF knockdown, as evidenced by the increase in the phosphorylation of Akt and p38MAPK (**Figures 4N, O**). Cell proliferation was slightly increased in three different cell lines (**Figure 5**), whereas PEDF inhibited proliferation and induced apoptosis in SaOS-2 (19). Additionally, PEDF causes necrosis in prostate cancer (49). Although Fas or death receptors are frequently negative in the pulmonary metastatic lesions of OS (1), cell death is still involved in the development of the secondary lesions. Therefore, the effects of endogenous PEDF on micrometastasis, cell survival, cell death, and the cell type-dependent differences should be carefully analyzed in future studies.

Third, PEDF has shown anti-metastatic effects in epithelial cancer cells (14, 19, 20). Notably, we showed that Bkid cells showed a decrease in EMT factors, which were reversed by PEDF knockdown (**Figures 4N, O**). It was reported that PEDF downregulated MMP9 and inhibit invasion in malignant U251 glioma (53), MMP downregulation is same as our result, but the output is opposite. Our study was performed in osteosarcoma, which is mesenchymal, and we skipped the early phase of metastasis, such as EMT and intravasation, by intracardiac injection (**Figures 1**, **3**). If PEDF blocked EMT in epithelial cancer cells in the early phase of metastasis, we also concluded that PEDF had anti-metastatic function; however, the same function could be used for MET after extravasation (**Figure 4**).

We also found novel molecular interactions among PEDF-lamR-Loxl1-SNAI3 (**Figure 7**). In Bkid cells, gain-of-function and loss-of-function analyses of PEDF showed the regulation of Snail2 (**Figures 4N, O**). We examined gene expression in TKD2, a renal endothelial cell line, but Snail2 expression was not detected in TKD2 using the same antibody used in **Figure 4N** (data not shown). We found the RNA expression of mouse Snail2 later in the qRT-PCR (**Figure 7B**); however, it still did not respond to PEDF stimulation (**Figure 7B**, data not shown). Thus, we once examined Snail1; however, it did not work as well (data not shown). Finally, we found that SNAI3 responded to Bkid stimulation and WMN treatment (**Figures 7A, B**). It has been reported that lysyl oxidase-like 2 (Loxl2) interacts with Snail (56). Again, Loxl2 did not respond to PEDF stimulation (**Figure 7B**). We examined Loxl1-4 expression (data not shown), and found that Loxl1 responds to stimulation (**Figure 7B**). The laminin receptor can bind to laminin and PEDF in the extracellular space, and it is also known as ribosomal protein SA (Rpsa) (15), which works at the inner cellular. Loxl proteins are extracellular enzymes involved in matrix modification (24), which work upon EMT (57–59); however, their cellular function has also been reported. Therefore, both Loxls and lamR have multi-distribution properties. We found that lamR could bind to Loxl1, and Bkid stimulation released Loxl1 freely. Because lamR did not interfere with the binding between Loxl1 and SNAI3 (**Figure 7E**), free Loxl1 may bind to SNAI3. We also found that Loxl1

overexpression was like PEDF overexpression in terms of inhibition of TKD2 migration (**Figures 6J**, **7D**), and that Loxl1 is promoted by Bkid stimulation under the control of lamR/Akt signaling (**Figures 7A, B**). Conversely, SNAI3 gene regulation was opposite to that in Loxl1, while SNAI3 enhanced EndoMT gene expression (**Figure 7C**). Therefore, it is reasonable to conclude that Loxl1 binds to SNAI3 to block transcription, and subsequently blocks EndoMT. Recently, the extracellular roles of lysyl oxidase (LOX) and these Loxl proteins have been reported (24, 58–61). LOX antibody-conjugated liposome was used for cancer-targeting drug deliverly because cancer cells secrete LOX during EMT (60). Further study on the inner cellular and extracellular roles and the potential feedback regulation of Loxl1 *via* PEDF is encouraged. Interestingly, pseudoexfoliation syndrome was associated with Loxl1 gene function (62), and it has been recently shown that PEDF expression level was also correlated with pseudoexfoliation (63). So far, there is no direct relationship between these studies, however, our finding may give them some connection.

Further study on patient specimens is a viable direction for future research. Our data suggested that the signal flow from PEDF to SNAI3 and its downstream molecules may control the extravasation and reorganization of tumor in specific target organs. In addition, the various combinations of these proteins may be key to predicting organ tropism of metastasis.

DATA AVAILABILITY STATEMENT

The datasets presented in this study can be found in online repositories. The names of the repository/repositories and accession number(s) can be found below: https://www.ncbi.nlm.nih.gov/geo/query/acc.cgi?acc=GSE188984.

ETHICS STATEMENT

The animal study was reviewed and approved by Akita University Ethical Committee for Experimental Animals.

AUTHOR CONTRIBUTIONS

SK contributed to conception, design of this study, wrote the first draft of this manuscript, and edited the latest version of manuscript. GT, KT, and GI did data curation. MT read and edited the draft. All authors approved the submitted edition.

FUNDING

SK was supported by JSPS KAKENHI (15K06822, 17KT0104, 18K07192, 21K07090) and the Takeda Science Foundation. MT was supported by JSPS KAKENHI (19H03495) and research grant from Princess Takamatsu Cancer Research Fund (19–25123).

ACKNOWLEDGMENTS

We would like to thank Editage (www.editage.com) for English language editing.

SUPPLEMENTARY MATERIAL

The Supplementary Material for this article can be found online at: https://www.frontiersin.org/articles/10.3389/fonc.2022.818182/full#supplementary-material

REFERENCES

1. Durfee RA, Mohammed M, Luu HH. Review of Osteosarcoma and Current Management. *Rheumatol Ther* (2016) 3(2):221–43. doi: 10.1007/s40744-016-0046-y
2. Carrle D, Bielack SS. Current Strategies of Chemotherapy in Osteosarcoma. *Int Orthop* (2006) 30(6):445–51. doi: 10.1007/s00264-006-0192-x
3. Akasbi Y, Arifi S, Lahlaidi K, Namad T, Mellas N, El Fassi MJ, et al. Renal Metastases of a Femur Osteosarcoma: A Case Report and a Review of the Literature. *Case Rep Urol* (2012) 2012:259193. doi: 10.1155/2012/259193
4. Daw NC, Kaste SC, Hill DA, Kun LE, Pratt CB. Metastatic Osteosarcoma to the Liver After Treatment for Synovial Sarcoma: A Case Report. *Pediatr Hematol Oncol* (2001) 18(2):123–8. doi: 10.1080/088800101300002955
5. Dirik Y, Çınar A, Yumrukçal F, Eralp L. Popliteal Lymph Node Metastasis of Tibial Osteoblastic Osteosarcoma. *Int J Surg Case Rep* (2014) 5(11):840–4. doi: 10.1016/j.ijscr.2014.09.029
6. McGary EC, Weber K, Mills L, Doucet M, Lewis V, Lev DC, et al. Inhibition of Platelet-Derived Growth Factor-Mediated Proliferation of Osteosarcoma Cells by the Novel Tyrosine Kinase Inhibitor STI571. *Clin Cancer Res* (2002) 8(11):3584–91.
7. Berlin O, Samid D, Donthineni-Rao R, Akeson W, Amiel D, Woods VL Jr. Development of a Novel Spontaneous Metastasis Model of Human Osteosarcoma Transplanted Orthotopically Into Bone of Athymic Mice. *Cancer Res* (1993) 53(20):4890–5.
8. Luu HH, Kang Q, Park JK, Si W, Luo Q, Jiang W, et al. An Orthotopic Model of Human Osteosarcoma Growth and Spontaneous Pulmonary Metastasis [Internet]. *Clin Exp Metastasis* (2005) 22:319–29. doi: 10.1007/s10585-005-0365-9
9. Mohseny AB, Machado I, Cai Y, Schaefer K-L, Serra M, Hogendoorn PCW, et al. Functional Characterization of Osteosarcoma Cell Lines Provides Representative Models to Study the Human Disease. *Lab Invest* (2011) 91 (8):1195–205. doi: 10.1038/labinvest.2011.72
10. Ando K, Mori K, Verrecchia F, Marc B, Rédini F, Heymann D. Molecular Alterations Associated With Osteosarcoma Development. *Sarcoma* (2012) 2012:12. doi: 10.1155/2012/523432
11. Huang C-Y, Lee C-Y, Chen M-Y, Yang W-H, Chen Y-H, Chang C-H, et al. Stromal Cell-Derived Factor-1/CXCR4 Enhanced Motility of Human Osteosarcoma Cells Involves MEK1/2, ERK and NF-kappaB-Dependent Pathways. *J Cell Physiol* (2009) 221(1):204–12. doi: 10.1002/jcp.21846
12. Lin F, Zheng S-E, Shen Z, Tang L-N, Chen P, Sun Y-J, et al. Relationships Between Levels of CXCR4 and VEGF and Blood-Borne Metastasis and Survival in Patients With Osteosarcoma. *Med Oncol* (2011) 28(2):649–53. doi: 10.1007/s12032-010-9493-4
13. Dawson DW, Volpert OV, Gillis P, Crawford SE, Xu H, Benedict W, et al. Pigment Epithelium-Derived Factor: A Potent Inhibitor of Angiogenesis. *Science* (1999) 285(5425):245–8. doi: 10.1126/science.285.5425.245
14. Bernard A, Gao-Li J, Franco CA, Bouceba T. Laminin Receptor Involvement in the Anti-Angiogenic Activity of Pigment Epithelium-Derived Factor. *J Biol* (2009) 284:10480–90. doi: 10.1074/jbc.M809259200
15. Qiao J, Su X, Wang Y, Yang J, Kouadir M, Zhou X, et al. Cloning and Characterization of Full-Length Coding Sequence (CDS) of the Ovine 37/67-

kDa Laminin Receptor (RPSA). *Mol Biol Rep* (2009) 36(8):2131–7. doi: 10.1007/s11033-008-9426-x
16. Zhuang W, Zhang H, Pan J, Li Z, Wei T, Cui H, et al. PEDF and PEDF-Derived Peptide 44mer Inhibit Oxygen–Glucose Deprivation-Induced Oxidative Stress Through Upregulating Pparγ *via* PEDF-R in H9c2 Cells. *Biochem Biophys Res Commun* (2016) 472:482–8. doi: 10.1016/j.bbrc.2016.02.110
17. Subramanian P, Locatelli-Hoops S, Kenealey J, DesJardin J, Notari L, Patricia Becerra S. Pigment Epithelium-Derived Factor (PEDF) Prevents Retinal Cell Death *via* PEDF Receptor (PEDF-R). *J Biol Chem* (2013) 288:23928–42. doi: 10.1074/jbc.m113.487884
18. Ek ETH, Dass CR, Choong PFM. Pigment Epithelium-Derived Factor: A Multimodal Tumor Inhibitor. *Mol Cancer Ther* (2006) 5(7):1641–6. doi: 10.1158/1535-7163.MCT-06-0107
19. Ek ETH, Dass CR, Contreras KG, Choong PFM. Inhibition of Orthotopic Osteosarcoma Growth and Metastasis by Multitargeted Antitumor Activities of Pigment Epithelium-Derived Factor. *Clin Exp Metastasis* (2007) 24(2):93–106. doi: 10.1007/s10585-007-9062-1
20. Ek ETH, Dass CR, Contreras KG, Choong PFM. Pigment Epithelium-Derived Factor Overexpression Inhibits Orthotopic Osteosarcoma Growth, Angiogenesis and Metastasis. *Cancer Gene Ther* (2007) 14(7):616–26. doi: 10.1038/sj.cgt.7701044
21. Dass CR, Ek ET, Contreras KG, Choong PF. A Novel Orthotopic Murine Model Provides Insights Into Cellular and Molecular Characteristics Contributing to Human Osteosarcoma. *Clin Exp Metastasis* (2006) 23(7–8):367–80. doi: 10.1007/s10585-006-9046-6
22. Broadhead ML, Dass CR, Choong PFM. Systemically Administered PEDF Against Primary and Secondary Tumours in a Clinically Relevant Osteosarcoma Model. *Br J Cancer* (2011) 105(10):1503–11. doi: 10.1038/bjc.2011.410
23. Abooshahab R, Al-Salami H, Dass CR. The Increasing Role of Pigment Epithelium-Derived Factor in Metastasis: From Biological Importance to a Promising Target. *Biochem Pharmacol* (2021) 193:114787. doi: 10.1016/j.bcp.2021.114787
24. Liu X, Zhao Y, Gao J, Pawlyk B, Starcher B, Spencer JA, et al. Elastic Fiber Homeostasis Requires Lysyl Oxidase–Like 1 Protein. *Nat Genet* (2004) 36(2):178–82. doi: 10.1038/ng1297
25. Katoh M, Katoh M. Comparative Genomics on SNAI1, SNAI2, and SNAI3 Orthologs. *Oncol Rep* (2005) 14(4):1083–6. doi: 10.3892/or.14.4.1083
26. Park Y-B, Park MJ, Kimura K, Shimizu K, Lee SH, Yokota J. Alterations in the INK4a/ARF Locus and Their Effects on the Growth of Human Osteosarcoma Cell Lines. *Cancer Genet Cytogenet* (2002) 133(2):105–11. doi: 10.1016/S0165-4608(01)00575-1
27. Kuriyama S, Yoshida M, Yano S, Aiba N, Kohno T, Minamiya Y, et al. LPP Inhibits Collective Cell Migration During Lung Cancer Dissemination. *Oncogene* (2016) 35(8):952–64. doi: 10.1038/onc.2015.155
28. Sakuma T, Nakade S, Sakane Y, Suzuki K-IT, Yamamoto T. MMEJ-Assisted Gene Knock-in Using TALENs and CRISPR-Cas9 With the PITCh Systems. *Nat Protoc* (2016) 11(1):118–33. doi: 10.1038/nprot.2015.140
29. Nakamae K, Nishimura Y, Takenaga M, Nakade S, Sakamoto N, Ide H, et al. Establishment of Expanded and Streamlined Pipeline of PITCh Knock-in – a Web-Based Design Tool for MMEJ-Mediated Gene Knock-in, PITCh Designer, and the Variations of PITCh, PITCh-TG and PITCh-KIKO. *Bioengineered* (2017) 8(3):302–8. doi: 10.1080/21655979.2017.1313645
30. Kuriyama S, Tsuji T, Sakuma T, Yamamoto T, Tanaka M. PLEKHN1 Promotes Apoptosis by Enhancing Bax-Bak Hetro-Oligomerization Through Interaction With Bid in Human Colon Cancer. *Cell Death Discov* (2018) 4:11. doi: 10.1038/s41420-017-0006-5
31. Radu M, Chernoff J. An *In Vivo* Assay to Test Blood Vessel Permeability. *J Vis Exp* (2013) 73):e50062. doi: 10.3791/50062
32. Klein JD, Blount MA, Sands JM. Urea Transport in the Kidney. *Compr Physiol* (2011) 1(2):699–729. doi: 10.1002/cphy.c100030
33. Moon YW, Rao G, Kim JJ, Shim H-S, Park K-S, An SS, et al. LAMC2 Enhances the Metastatic Potential of Lung Adenocarcinoma. *Cell Death Differ* (2015) 22(8):1341–52. doi: 10.1038/cdd.2014.228
34. Cheng X-N, Shao M, Li J-T, Wang Y-F, Qi J, Xu Z-G, et al. Leucine Repeat Adaptor Protein 1 Interacts With Dishevelled to Regulate Gastrulation Cell Movements in Zebrafish. *Nat Commun* (2017) 8(1):1353. doi: 10.1038/s41467-017-01552-x
35. Ellisen LW, Ramsayer KD, Johannessen CM, Yang A, Beppu H, Minda K, et al. REDD1, a Developmentally Regulated Transcriptional Target of P63 and P53, Links P63 to Regulation of Reactive Oxygen Species. *Mol Cell* (2002) 10(5):995–1005. doi: 10.1016/S1097-2765(02)00706-2
36. Steele FR, Chader GJ, Johnson LV, Tombran-Tink J. Pigment Epithelium-Derived Factor: Neurotrophic Activity and Identification as a Member of the Serine Protease Inhibitor Gene Family. *Proc Natl Acad Sci USA* (1993) 90(4):1526–30. doi: 10.1073/pnas.90.4.1526
37. Aruga J, Mikoshiba K. Identification and Characterization of Slitrk, a Novel Neuronal Transmembrane Protein Family Controlling Neurite Outgrowth. *Mol Cell Neurosci* (2003) 24(1):117–29. doi: 10.1016/S1044-7431(03)00129-5
38. Iwasaki K, Bajenova E, Somogyi-Ganss E, Miller M, Nguyen V, Nourkeyhani H, et al. Amelotin—a Novel Secreted, Ameloblast-Specific Protein. *J Dent Res* (2005) 84(12):1127–32. doi: 10.1177/154405910508401207
39. Dalla-Torre CA, Yoshimoto M, Lee C-H, Joshua AM, de Toledo SRC, Petrilli AS, et al. Effects of THBS3, SPARC and SPP1 Expression on Biological Behavior and Survival in Patients With Osteosarcoma. *BMC Cancer* (2006) 6:237. doi: 10.1186/1471-2407-6-237
40. Miettinen M, Lindenmayer AE, Chaubal A. Endothelial Cell Markers CD31, CD34, and BNH9 Antibody to H- and Y-Antigens–Evaluation of Their Specificity and Sensitivity in the Diagnosis of Vascular Tumors and Comparison With Von Willebrand Factor. *Mod Pathol* (1994) 7(1):82–90.
41. Notari L, Baladron V, Aroca-Aguilar JD, Balko N, Heredia R, Meyer C, et al. Identification of a Lipase-Linked Cell Membrane Receptor for Pigment Epithelium-Derived Factor. *J Biol Chem* (2006) 281(49):38022–37. doi: 10.1074/jbc.M600353200
42. Ueda S, Tominaga T, Ochi A, Sakurai A, Nishimura K, Shibata E, et al. TGF-β1 is Involved in Senescence-Related Pathways in Glomerular Endothelial Cells *via* P16 Translocation and P21 Induction. *Sci Rep* (2021) 11(1):21643. doi: 10.1038/s41598-021-01150-4
43. Hong H, Zhou T, Fang S, Jia M, Xu Z, Dai Z, et al. Pigment Epithelium-Derived Factor (PEDF) Inhibits Breast Cancer Metastasis by Down-Regulating Fibronectin. *Breast Cancer Res Treat* (2014) 148(1):61–72. doi: 10.1007/s10549-014-3154-9
44. Fan C-S, Chen W-S, Chen L-L, Chen C-C, Hsu Y-T, Chua KV, et al. Osteopontin-Integrin Engagement Induces HIF-1α-TCF12-Mediated Endothelial-Mesenchymal Transition to Exacerbate Colorectal Cancer. *Oncotarget* (2018) 9(4):4998–5015. doi: 10.18632/oncotarget.23578
45. Kato T, Sekiguchi A, Sagara K, Tanabe H, Takamura M, Kaneko S, et al. Endothelial-Mesenchymal Transition in Human Atrial Fibrillation. *J Cardiol* (2017) 69(5):706–11. doi: 10.1016/j.jjcc.2016.10.014
46. Ghosh AK, Nagpal V, Covington JW, Michaels MA, Vaughan DE. Molecular Basis of Cardiac Endothelial-to-Mesenchymal Transition (EndMT): Differential Expression of microRNAs During EndMT. *Cell Signal* (2012) 24(5):1031–6. doi: 10.1016/j.cellsig.2011.12.024
47. Moonen J-RAJ, Lee ES, Schmidt M, Maleszewska M, Koerts JA, Brouwer LA, et al. Endothelial-To-Mesenchymal Transition Contributes to Fibro-Proliferative Vascular Disease and Is Modulated by Fluid Shear Stress. *Cardiovasc Res* (2015) 108(3):377–86. doi: 10.1093/cvr/cvv175
48. Li X, Kong X, Huo Q, Guo H, Yan S, Yuan C, et al. Metadherin Enhances the Invasiveness of Breast Cancer Cells by Inducing Epithelial to Mesenchymal Transition. *Cancer Sci* (2011) 102(6):1151–7. doi: 10.1111/j.1349-7006.2011.01919.x
49. Doll JA, Stellmach VM, Bouck NP, Bergh ARJ, Lee C, Abramson LP, et al. Pigment Epithelium–Derived Factor Regulates the Vasculature and Mass of the Prostate and Pancreas. *Nat Med* (2003) 9(6):774–80. doi: 10.1038/nm870
50. Guan M, Jiang H, Xu C, Xu R, Chen Z, Lu Y. Adenovirus-Mediated PEDF Expression Inhibits Prostate Cancer Cell Growth and Results in Augmented Expression of PAI-2. *Cancer Biol Ther* (2007) 6(3):419–25. doi: 10.4161/cbt.6.3.3757
51. Hou J, Ge C, Cui M, Liu T, Liu X, Tian H, et al. Pigment Epithelium-Derived Factor Promotes Tumor Metastasis Through an Interaction With Laminin Receptor in Hepatocellular Carcinomas. *Cell Death Dis* (2017) 8(8):e2969. doi: 10.1038/cddis.2017.359
52. Broadhead ML, Choong PFM, Dass CR. Efficacy of Continuously Administered PEDF-Derived Synthetic Peptides Against Osteosarcoma Growth and Metastasis. *J BioMed Biotechnol* (2012) 2012:230298. doi: 10.1155/2012/230298

53. Guan M, Pang C-P, Yam H-F, Cheung K-F, Liu W-W, Lu Y. Inhibition of Glioma Invasion by Overexpression of Pigment Epithelium-Derived Factor. *Cancer Gene Ther* (2004) 11(5):325–32. doi: 10.1038/sj.cgt.7700675
54. Mirochnik Y, Aurora A, Schulze-Hoepfner FT, Deabes A, Shifrin V, Beckmann R, et al. Short Pigment Epithelial-Derived Factor-Derived Peptide Inhibits Angiogenesis and Tumor Growth. *Clin Cancer Res* (2009) 15(5):1655–63. doi: 10.1158/1078-0432.CCR-08-2113
55. Gao X, Zhang H, Zhuang W, Yuan G, Sun T, Jiang X, et al. PEDF and PEDF-Derived Peptide 44mer Protect Cardiomyocytes Against Hypoxia-Induced Apoptosis and Necroptosis *via* Anti-Oxidative Effect. *Sci Rep* (2014) 4:5637. doi: 10.1038/srep05637
56. Peinado H, Del Carmen Iglesias-de la Cruz M, Olmeda D, Csiszar K, Fong KSK, Vega S, et al. A Molecular Role for Lysyl Oxidase-Like 2 Enzyme in Snail Regulation and Tumor Progression. *EMBO J* (2005) 24(19):3446–58. doi: 10.1038/sj.emboj.7600781
57. Hu Q, Masuda T, Kuramitsu S, Tobo T, Sato K, Kidogami S, et al. Potential Association of LOXL1 With Peritoneal Dissemination in Gastric Cancer Possibly *via* Promotion of EMT. *PloS One* (2020) 15(10):e0241140. doi: 10.1371/journal.pone.0241140
58. Xiao Q, Ge G. Lysyl Oxidase, Extracellular Matrix Remodeling and Cancer Metastasis. *Cancer Microenviron* (2012) 5(3):261–73. doi: 10.1007/s12307-012-0105-z
59. Moon H-J, Finney J, Xu L, Moore D, Welch DR, Mure M. MCF-7 Cells Expressing Nuclear Associated Lysyl Oxidase-Like 2 (LOXL2) Exhibit an Epithelial-to-Mesenchymal Transition (EMT) Phenotype and are Highly Invasive In Vitro. *J Biol Chem* (2013) 288(42):30000–8. doi: 10.1074/jbc.C113.502310
60. De Vita A, Liverani C, Molinaro R, Martinez JO, Hartman KA, Spadazzi C, et al. Lysyl Oxidase Engineered Lipid Nanovesicles for the Treatment of Triple Negative Breast Cancer. *Sci Rep* (2021) 11(1):5107. doi: 10.1038/s41598-021-84492-3
61. Johnston KA, Lopez KM. Lysyl Oxidase in Cancer Inhibition and Metastasis. *Cancer Lett* (2018) 417:174–81. doi: 10.1016/j.canlet.2018.01.006
62. Schlötzer-Schrehardt U. Molecular Pathology of Pseudoexfoliation Syndrome/Glaucoma–New Insights From LOXL1 Gene Associations. *Exp Eye Res* (2009) 88(4):776–85. doi: 10.1016/j.exer.2008.08.012
63. Utlu B, Akyol Salman İ, Öztürk N. Pigment Epithelial-Derived Factor in the Lens Anterior Capsule of Patients With Senile Cataract With Pseudoexfoliation. *Clin Exp Optom* (2020) 103(2):207–11. doi: 10.1111/cxo.12922

Conflict of Interest: The authors declare that the research was conducted in the absence of any commercial or financial relationships that could be construed as a potential conflict of interest.

Publisher's Note: All claims expressed in this article are solely those of the authors and do not necessarily represent those of their affiliated organizations, or those of the publisher, the editors and the reviewers. Any product that may be evaluated in this article, or claim that may be made by its manufacturer, is not guaranteed or endorsed by the publisher.

frontiers in Oncology

ORIGINAL RESEARCH
published: 23 February 2022
doi: 10.3389/fonc.2022.774988

Tspan9 Induces EMT and Promotes Osteosarcoma Metastasis *via* Activating FAK-Ras-ERK1/2 Pathway

Shijie Shao[1†], Lianhua Piao[2†], Jiangsong Wang[1], Liwei Guo[1], Jiawen Wang[1], Luhui Wang[1], Lei Tong[1], Xiaofeng Yuan[1], Xu Han[1], Sheng Fang[1], Junke Zhu[1] and Yimin Wang[1*]*

[1] Department of Orthopedics, The Third Affiliated Hospital of Soochow University, Changzhou, China, [2] Institute of Bioinformatics and Medical Engineering, Jiangsu University of Technology, Changzhou, China

OPEN ACCESS

Edited by:
Guisheng Song,
University of Minnesota, United States

Reviewed by:
Eswari Dodagatta-Marri,
University of California, San Francisco, United States
Luigi Ippolito,
University of Florence, Italy

***Correspondence:**
Yimin Wang
doctorwym51346@163.com
Lianhua Piao
piaolianhua@jsut.edu.cn

[†]These authors have contributed equally to this work

Specialty section:
This article was submitted to Molecular and Cellular Oncology, a section of the journal Frontiers in Oncology

Received: 13 September 2021
Accepted: 21 January 2022
Published: 23 February 2022

Citation:
Shao S, Piao L, Wang J, Guo L, Wang J, Wang L, Tong L, Yuan X, Han X, Fang S, Zhu J and Wang Y (2022) Tspan9 Induces EMT and Promotes Osteosarcoma Metastasis via Activating FAK-Ras-ERK1/2 Pathway. Front. Oncol. 12:774988. doi: 10.3389/fonc.2022.774988

Object: At present, there are few effective treatment options available to patients suffering from osteosarcoma (OS). Clarifying the signaling pathways that govern OS oncogenesis may highlight novel approaches to treating this deadly form of cancer. Recent experimental evidence suggests that the transmembrane protein tetraspanin-9 (Tspan9) plays a role in tumor development. This study was thus formulated to assess the molecular role of Tspan9 as a regulator of OS cell metastasis.

Methods: Gene expression in OS cell lines was evaluated *via* qRT-PCR, while CCK-8, colony formation, Transwell, and wound healing assays were used to explore the *in vitro* proliferative, invasive, and migratory activities of OS cells. The relationship between Tspan9 and *in vivo* OS cell metastasis was assessed by injecting these cells into the tail vein of nude mice. Interactions between the Tspan9 and integrin β1 proteins were explored through mass spectrometric and co-immunoprecipitation, and Western blotting to assess the functional mechanisms whereby Tspan9 shapes OS pathogenesis.

Results: Both primary OS tumors and OS cell lines commonly exhibited Tspan9 upregulation, and the knockdown of this tetraspanin suppressed the migration, invasion, and epithelial-mesenchymal transition (EMT) activity in OS cells, whereas Tspan9 overexpression resulted in opposite phenotypes. Tumor lung metastasis were significantly impaired in mice implanted with HOS cells in which Tspan9 was downregulated as compared to mice implanted with control HOS cells. Tspan9 was also found to interact with β1 integrin and to contribute to OS metastasis *via* the amplification of integrin-mediated downstream FAK/Ras/ERK1/2 signaling pathway.

Conclusion: These data suggest that Tspan9 can serve as a promising therapeutic target in OS.

Keywords: osteosarcoma, Tspan9, EMT, integrin β1, metastasis, FAK-Ras-ERK1/2 pathway

INTRODUCTION

Osteosarcoma (OS) is the most prevalent form of primary bone malignancy affecting children and adolescences, most commonly manifesting in the epiphyseal region of the proximal tibia and distal femur (1). The treatment of OS is currently primarily focused on a combination of surgical resection, adjuvant chemotherapy, and postoperative chemotherapy (2). However, as OS tumors are highly malignant and aggressive, patients generally exhibit poor 5-year survival rates, particularly in individuals with early lung metastases in whom these rates are < 30% (3). Efficacious OS treatment is hindered by the emergence of chemoresistant OS tumors (4) and by chemotherapy -induced organ damage (5). At present, no biomarkers or therapeutic targets specific for OS have been identified or leveraged in a clinical context, and there is thus a clear need to further explore the molecular mechanisms governing OS pathogenesis and metastasis in order to design more effective treatments capable of prolonging the survival of affected patients.

The tetraspanin family of conserved 4-transmembrane proteins (TM4SF) proteins each harbor a small extracellular loop (EC1), a large extracellular loop (EC2), N- and C-terminal cytoplasmic tails, and four hydrophobic transmembrane domains (TM1-4) (6). To date, 33 human tetraspanins have been identified and found to be expressed in most tissues, including Tspan8, CD63, CD82, and CD151 (7). These tetraspanins can bind with surface proteins and other molecules at the plasma membrane in tetraspanin-enriched membrane microdomains (TEMs). By interacting with integrins, receptor molecules, and other signaling intermediaries, tetraspanins can activate downstream signaling to control key physiological processes including apoptosis, adhesion, differentiation, oncogenesis, and metastatic tumor progression (8–10).

Tspan9 (NET-5, PP1057) is a tetraspanin that has been shown to promote platelet aggregation (11) and alphavirus transport (12). Prior evidence also suggests that Tspan9 can suppress the development of gastric cancer. Indeed, Li et al. (13) determined that Tspan9 was able to inhibit SGC7901 cell proliferation *via* suppressing the G1/S phase transition while simultaneously promoting MMP-9 downregulation *via* the ERK1/2 pathway to compromise cellular migratory and invasive activity. The overexpression of Tspan9 can also impair FAK-Ras-ERK signaling and EMT induction to hamper metastatic gastric cancer progression (14). Tspan9 can further enhance tumor cell 5-fluorouracil resistance *via* the inhibition of the PI3K/Akt/mTOR pathway and the induction of autophagic activity (15). Given that different TM4SF proteins play distinct roles as suppressors or promoters of oncogenesis in a context-dependent manner, however, it is impossible to reliably predict the functional role of Tspan9 as a regulator of OS tumor cell survival, migration, or metastasis. For example, both CD9 and CD82 are tetraspanins that function to primarily suppress tumor growth, whereas Tspan8 and CD151 are primarily oncogenic. However, in ovarian cancer and invasive lobular breast cancer, CD151 can bind to integrin α3β1 to regulate signaling pathways downstream of this complex, ultimately impairing tumor progression (16, 17). Tspan7 can similarly inhibit bladder cancer, liver cancer, and multiple myeloma, yet it promotes non-small cell lung cancer. No studies to date have clarified the functional importance of Tspan9 in OS, and the mechanistic role of this tetraspanin in this cancer remains to be elucidated, particularly in the context of EMT induction and tumor metastasis.

Distant tumor cell metastasis remains a major barrier to effective OS patient treatment. Epithelial-mesenchymal transition (EMT) is a process integral to metastatic progression wherein tumor cells shed their epithelial-like properties and instead acquire more motile mesenchymal characteristics. EMT induction is critical to malignant cell dissemination in the context of OS progression (18, 19), and EMT-regulating transcription factors including the zinc-finger- binding transcription factors Snai1 and Slug, zinc finger E–box –binding homeobox 1 (ZEB1), and the Twist1 and Twist2 basic helix-loop-helix (bHLH) factors have been shown to control this process in OS cells and to regulate associated metastasis (20–22). Integrins, which are heterodimeric receptors with α and β subunits that bind to the extracellular matrix, also regulate tumor malignancy. For example, the αvβ3 and β1 integrins have been linked to worse clinical outcomes and to enhanced metastasis in OS (23–25). By binding to specific ECM ligands and cell surface molecules, integrins can trigger context-appropriate intracellular signaling that can shape a variety of physiological or pathological processes (26). The focal adhesion kinase (FAK) and extracellular regulated protein kinases (ERK) enzymes are essential mediators of proliferative and migratory activity in cancer cells, and they are also directly involved in signaling downstream of integrin activation (27–29). As molecular scaffolds, tetraspanins such as CD9, CD63, CD81, CD82, CD151, and Tspan8 commonly bind to specific integrins within TEM domains. However, whether Tspan9 can interact with integrins and whether these interactions are related to OS cell aggression remain to be established.

Herein, we assessed Tspan9 expression in OS and found it to be upregulated in both OS patient tumor tissues and in OS cell lines. Through *in vitro* and *in vivo* analyses of the mechanistic importance of Tspan9 in OS, we found that it was able to not only promote EMT induction as a means of driving tumor cell metastasis, but also to interact with integrin β1 and to thereby enhance FAK-Ras-ERK1/2 signaling activity within tumor cells. Overall, our study offers new insight into the role of Tspan9 in OS and highlights its promise as a potential diagnostic biomarker and therapeutic target in this oncogenic context.

MATERIALS AND METHODS

Microarray Data Collection

Microarray datasets related to gene expression profiles in OS samples were downloaded from the Gene Expression Omnibus (GEO) database (http://www.ncbi.nlm.nih.gov/geo). These include the GSE12865 dataset [2 normal osteoblast (OB) samples and 12 OS tissue samples], the GSE33383 dataset [11 normal mesenchymal stem cells (MSC) samples, 3 OB samples,

and 84 primary OS tissue samples], and the GSE42352 dataset (11 MSC samples, 3 OB samples, and 19 primary OS cell lines), all of which were used for differential gene expression analyses.

Cell Culture

HEK293T cells and the human hFOB1.19, HOS, U2OS, and Mg63 OS cell lines were obtained from the Chinese Academy of Cell Resource Center and were cultured in DMEM/MEM (Gibco, CA, USA) containing 10% fetal bovine serum (ScienCell, USA) and penicillin/streptomycin in a 5% CO_2 incubator at 37°C.

RNA Extraction and Quantitative Real-Time Polymerase Chain Reaction (qRT-PCR)

A qRT-PCR approach was used to assess change in gene expression. Briefly, a total of $1x10^6$ cells in 6-well plates were lysed to prepare RNA with a MiniBEST Universal RNA Extraction kit (Takara, Dalian, China), after which a First Strand cDNA Synthesis kit (Takara) was used to prepared cDNA based on provided directions. SYBR Premix Ex Taq (Takara) and a Step-One Plus RT-PCR System (Applied Biosystems, Shanghai, China) were used to perform qRT-PCR reactions with the following settings: 30 s at 95°C; 40 cycles of 5 s at 95°C and 34 s at 60°C. The $2^{-\Delta\Delta Ct}$ method was used to assess relative gene expression, with GAPDH being used for normalization. Primers used in this study are listed in **Table 1**.

Transfection

To knockdown Tspan9, OS cells were transfected with Tspan9-specific siRNA oligonucleotide duplexes (siTspan9#1, siTspan9#2, siTspan9#3) or a control siNC construct purchased from Biolino Nucleic Acid Technology Co., Ltd. Briefly, cells were grown to 30-50% confluency, at which time they were transfected with siNC or siTspan9 (100 nM) in serum-free Opti-MEM using Lipofectamine 3000 (Thermo Fisher Scientific, Inc.) based on provided directions. At 6 h post-transfection, Opti-MEM was exchanged for complete media, and knockdown efficiency was subsequently confirmed *via* qRT-PCR.

TABLE 1 | The siRNA and shRNA sequences used in this study.

Name		Sequences
Tspan9	Forward	AACGAGAACGCCAAGAAGGA
	Reverse	CGTTGTTCTCGGTGTGGTACA
GAPDH	Forward	ATGGAAATCCCATCACCATCTT
	Reverse	CGCCCCACTTGATTTTGG
Tspan9 siRNAs		
siTspan9#1	Sense	UGGACAAGGUGAACGAGAATT
	Antisense	UUCUCGUUCACCUUGUCCATT
siTspan9#2	Sense	CUGAAGAACGCCUGGAACATT
	Antisense	UGUUCCAGGCGUUCUUCAGTT
siTspan9#3	Sense	CCAAGAAGGACCUGAAGGATT
	Antisense	UCCUUCAGGUCCUUCUUGGTT
Negative Control (siNC)	Sense	UUCUCCGAACGUGUCACGUTT
	Antisense	ACGUGACACGUUCGGAGAATT
Tspan9 shRNAs		
shTspan9#1	5'-3'	TGGACAAGGTGAACGAGAA
shTspan9#2	5'-3'	CTGAAGAACGCCTGGAACA
Negative Control (shNC)	5'-3'	TTCTCCGAACGTGTCACGT

Stable Cell Line Establishment

To stably knock down Tspan9, two shRNAs specific for this gene and one control shRNA were purchased from Shanghai GenePharma Co.,Ltd. HOS cells were then transduced with lentiviruses encoding shTspan9#1, shTspan9#2, or shNC sequences in media supplemented with 10% FBS and 8 μg/mL polybrene. At 48 h post-transduction, puromycin (2 mg/mL) was added to cells, which were then cultured for 1 week to yield stably transduced cell lined as confirmed based upon fluorescence microscopy analyses of green fluorescent protein (GFP) positivity.

A FLAG-tagged PGMLV-6946 Tspan9 expression vector was purchased from GenePharma Technology Co., Ltd (Shanghai, China). U2OS cells were transduced with prepared lentiviral particles encoding this construct, and stably transduced cells were then selected with blasticidin (2 mg/mL). In addition, stable Tspan9 overexpression and knockdown were confirmed through qRT-PCR and Western blotting. All shRNA sequences used herein are listed in **Table 1**.

RNA-Sequencing (RNA-Seq)

Total RNA was extracted from HOS cells stably transduced with shTspan9 or shNC, and an Agilent Bioanalyzer 2100 (Agilent Technologies, Inc., USA) was used to confirm RNA integrity. An Illumina HiSeq 2000 instrument (Illumina, Inc., USA) was then used to perform deep RNA-sequencing of these samples. Differentially expressed genes (DEGs) were then identified ($P < 0.05$, and fold-change ≥ 2) and subjected to Gene Ontology (GO; http://www.geneontology.org) and KEGG (https://www.genome.jp/kegg) enrichment analyses aimed at identifying the signaling pathways whereby Tspan9 influences the development of OS.

Viability and Proliferation Assays

A CCK-8 assay was used to evaluate cell viability. Briefly, siRNA-treated cells were seeded in 96-well plates (2000/well) in triplicate, and after 72 h, 10 uL of CCK8 solution (Dojindo Molecular Technologies, Inc., China) was added per well. After a 1 h incubation in the dark, absorbance at 450 nm was measured *via* microplate reader (Thermo Fisher Scientific, Inc.). Colony formation assays were also used to evaluate OS cell proliferation. Briefly, cells were added to 6-well plates (5000/well) and subjected to siRNA transfection. After incubation for 10-14 days, colonies were fixed for 15 min with methanol, stained for 30 min with 0.1% crystal violet, rinsed using distilled water, and colony numbers were then quantified.

Migration and Invasion Assays

Wound healing and Transwell assays were conducted to evaluate OS cell migration. In wound healing assays, OS cells stably expressing shTspan9 or shNC were grown to 95% confluency in 6-well plates. Following starvation for 24 h in serum-free media, three horizontal and three vertical scratch wounds were generated in the cell monolayer using a sterile 1 mL pipette tip. Wounds were imaged at 0, 24, and 48 h in at least 16 fields of view per well *via* microscopy, and ImageJ was used to quantify

migration as follows: migration rate (%) = [1 - (wound area at 24 h or 48 h/wound area at 0 h)] × 100%. The mean value was calculated based on 10 random fields of view. In Transwell migration assays, 2 x 10^4 cells in 150 uL of serum-free media were added to the upper chamber of a 24-well Tranwell insert (#3464, Corning, USA), while the lower chamber was filled with 600 μL of media supplemented with 10% FBS. Following an 18 h incubation, PBS was used to wash cells two times, and they were then fixed with methanol, stained with crystal violet, and non-migratory cells were removed with a cotton swab. Transwell invasion assays were conducted *via* a similar approach using Matrigel-coated Transwell inserts (#354480, BD, USA). IN those assays, 500 μL of serum-free medium containing 1x10^5 cells was added to the upper chamber of this insert in a 24-well plate, while the lower chamber was filled with 700 μL of media containing 10% FBS. Following a 20 h incubation, non-invasive cells were removed, while invasive cells were fixed and stained. For both Transwell assays, cells in 6 random fields of view were imaged *via* microscopy and counted.

Western Blotting

Cells were grown to ~95% confluence in cell culture plates, at which time chilled RIPA buffer (Roche Applied Science, Penzberg, Germany) was used to extract proteins from cells for 10 min, after which samples were sonicated to facilitate lysis (Ningbo Scientz Biotechnology, Zhejiang, China). After centrifugation for 1 min at 12,000 rpm, supernatant protein levels were measured *via* BCA assay (Biyuntian Biotechnology, Shanghai, China). Next, 6-12% SDS-PAGE was used to separate protein samples prior to their transfer onto 0.45 μm PVDF membranes (Millipore, USA). Blots were then blocked for 1 h at room temperature with 5% non-fat milk in TBST, followed by overnight incubation with appropriate primary antibodies at 4°C and a subsequent 45 min incubation with secondary antibodies. Tanon Image Software v1.0 (Tanon Science and Technology Co., Ltd.) was then used to detect protein bands, with β-actin serving as a loading control. Primary antibodies specific for Tspan9 (1:300, #ab106412, Abcam), β-Catenin (1:1000, #8480, CST), N-Cadherin (1:1000, #13116, CST), FN1 (1:1000, #A12932, ABclonal), Vimentin (1:1000, #5741, CST), Snai1 (1:1000, #3879, CST), total-FAK (1:1000, #ab40794, Abcam), phospho-FAK (1:500, #AP0302, ABclonal), Ras (1:1000, #ab52939, Abcam), total-ERK1/2 (1:1000, #4695, CST), phospho-ERK1/2 (1:1000, #4370, CST), Flag (1:1000, #F7425, Sigma), and integrin β1/ITGB1 (1:500, #A2217, ABclonal) were utilized, while anti-rabbit and anti-mouse IgG (1:5000, CST) were employed as secondary antibodies.

Immunoprecipitation (IP) Assay

U2OS cells expressing FLAG-tagged Tspan9 or control constructs were cultured in 10 cm dishes and then lysed using chilled RIPA buffer supplemented with protease inhibitors. The resultant lysates were subjected to sonication, centrifuged for 1 min at 12,000 rpm, and supernatants were transferred to a fresh tube. For IP assays, 250 μL of anti-Flag M2 agarose beads (#A2220, Sigma) were rinsed three times using PBS (2 min/wash), collected *via* centrifugation at 8,000 rpm, and combined with lysates. These samples were then incubated at 4°C for 2 h under constant agitation. Precipitates were then collected, washed three times using PBS, combined with sample loading buffer, boiled, and used for Western blotting analyses as above.

Mass Spectrometric Analysis

HEK 293T cells were transfected with FLAG-Tspan9 or FLAG empty vector. At 48 h post-transfection, cells were immunoprecipitated with anti-FLAG M2 agarose beads. The Tspan9-interacting proteins were identified by mass spectrometry.

Ras Inhibition

U2OS cells stably expressing the MOCK or OE-Tspan9 constructs were treated for 48 h with the Ras inhibitor Salirasib (50 μM; #HY-14754), after which they were used in assays of migratory and invasion activity. Changes in intracellular signaling proteins were assessed *via* Western blotting.

In Vivo Metastasis Assay

The Animal Ethics Committee of the Third Affiliated Hospital of Soochow University approved this study. Female BALB/c nude mice (5-6 weeks old, Qinglong Mountain Animal Breeding Center, Nanjing, China) were housed in a climate-controlled animal facility (26 °C, 12h light/dark cycle) with sterile bedding, food, and water that were replaced every other day. To establish a model of murine lung metastasis, these mice received an intravenous injection of HOS cells (shNC or shTspan9#1) *via* the lateral tail vein (2.0 × 10^6 cells/animal). After 4 weeks, all animals were euthanized and lungs were collected, immersed for 24 h in phosphate-buffered formalin, and metastases visible on the lung surface and bottom were counted by eye. Whole lungs were then embedded, cut into sections, and subjected to hematoxylin-eosin (H&E) staining. Prepared sections were imaged at 5 x and 10 x magnification.

Statistical Analysis

SPSS v 21.0 (IBM Corp., NY, USA) was used for all statistical testing. qRT-PCR data are given as means ± standard error values, while other data are given as means ± standard deviation. $P < 0.05$ was the threshold of significance, and all studies were repeated in duplicate or triplicate.

RESULTS

Human OS Tissue Samples and Cell Lines Exhibit Tspan9 Upregulation

We began by evaluating extant microarray datasets from the GEO database (GSE12865, GSE33383, and GSE42352) to analyze the expression of Tspan9 in human OS samples. In the GSE12865 dataset, we observed significant Tspan9 upregulation in OS tissues relative to normal osteoblast cells (OBs) (fold-change = 2.131, $P = 0.0037$) (**Figure 1A**). It was also upregulated in OS tissues compared to healthy mesenchymal stem cells (MSCs) (fold-change = 1.9651, $P = 0.0004$) and OBs (fold-change = 3.5611, $P = 0.0005$) according to the GSE33383

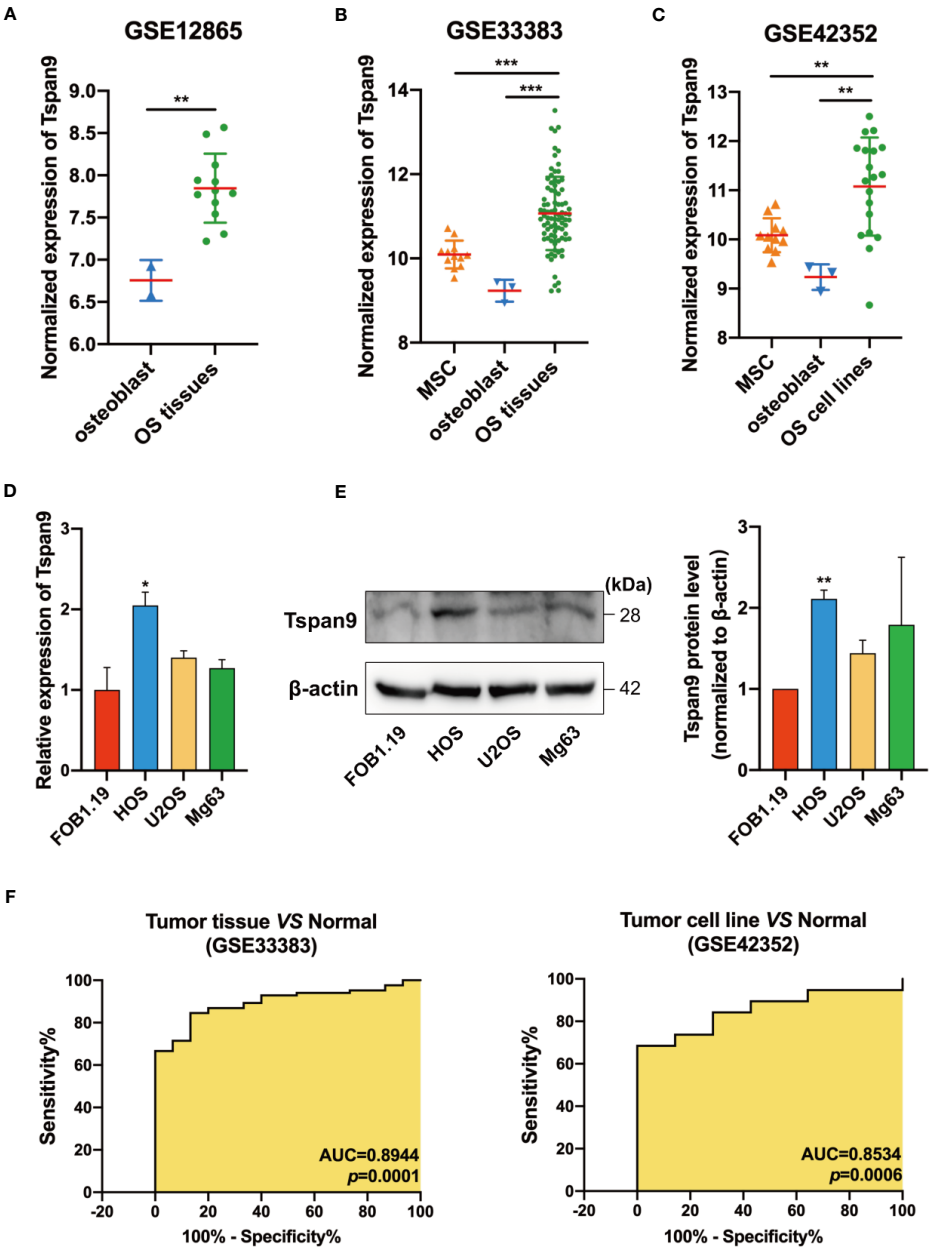

FIGURE 1 | Human OS cells and tumor tissue samples exhibit Tspan9 upregulation. **(A–C)** Tspan9 mRNA levels were significantly elevated in OS tumor tissues and cell lines in the GSE12865, GSE33383, and GSE42352 datasets relative to levels in normal MSCs and OBs. **(D)** Relative Tspan9 mRNA levels were markedly increased in HOS cells relative to control hFOB1.19 cells, whereas no changes were evident in U2OS or Mg63 cells as assessed *via* qRT-PCR. GAPDH served as a normalization control. **(E)** Western blotting results revealed that Tspan9 protein expression in HOS but not U2OS and Mg63 was significantly higher compared to hFOB1.19 cells. β-actin was used as a loading control and for normalization. Data are means ± SD from two independent experiments. **(F)** ROC curves and AUC values were determined using the GSE33383 and GSE42352 datasets. *$P < 0.05$; **$P < 0.01$; ***$P < 0.001$; Student's t-test. Tspan9, Tetraspanin-9; MSC, mesenchymal stem cell; OB: osteoblast; OS: osteosarcoma; GEO: Gene Expression Omnibus; qRT-PCR, quantitative reverse -transcription polymerase chain reaction; GAPDH, glyceraldehyde-3-phosphate dehydrogenase; SD, standard deviation; ROC, receiver operating characteristic; AUC, area under the curve.

(**Figure 1B**). Similarly, in the GSE42352 dataset, Tspan9 was significantly upregulated in OS cell lines as compared to corresponding MSC (fold-change = 1.9787, $P = 0.0037$) and OB (fold-change = 3.5857, $P = 0.0054$) control samples (**Figure 1C**). We further evaluated Tspan9 expression levels in a series of human OS cell lines and found that HOS cells exhibited significantly higher Tspan9 mRNA and protein levels relative to the normal osteoblast hFOB1.19 cell line when

analyzed *via* qRT-PCR (**Figure 1D**) and Western blotting assays (**Figure 1E**). Receiver operating characteristic (ROC) curves were then generated using the GSE33383 and GSE42352 datasets, and analyses of these curves indicated that Tspan9 can serve as a valuable biomarker capable of differentiating between OS tumors or cells and corresponding normal control samples (**Figure 1F**). Prior research has indicated that Tspan9 can play an anti-oncogenic function in gastric cancer. In contrast, our present results suggest that Tspan9 is upregulated in OS, suggesting that it may serve as a positive regulator of OS progression.

Tspan9 Knockdown Suppresses the Proliferation of OS Cells

To clarify the functional role of Tspan9 as a regulator of OS cell proliferation, we utilized three siRNA constructs specific for this tetraspanin (siTspan9#1, siTspan9#2, siTspan9#3) to knock down its expression in HOS cells, with qRT-PCR being used to confirm Tspan9 silencing at 72 h post-transfection relative to the siNC control group (**Figure 2A**). We then conducted a CCK-8 assay to evaluate the viability of these HOS cells, and found that Tspan9 knockdown was associated with a significant decrease in HOS cell survival over a 72 h period relative to control treatment (**Figure 2B**). Colony formation assays were further conducted to explore the relationship between Tspan9 expression and the proliferation of HOS cells. On day 12 post-transfection, significantly fewer colonies were observed in the siTspan9 group relative to the siNC group (**Figure 2C**). These results thus suggest that Tspan9 may play an oncogenic role in OS cells.

RNA-Seq-Based Identification of Downstream Tspan9 Target Genes

To determine the targets downstream of Tspan9 in OS cells, we next conducted an RNA-seq analysis of cells in which this tetraspanin had been stably knocked down (shTspan9#1 and shTspan9#2) and compared these cells to control (shNC) cells. This approach revealed 211 genes that were differentially expressed, including 96 and 115 that were upregulated and downregulated, respectively, following Tspan9 knockdown ($P <$

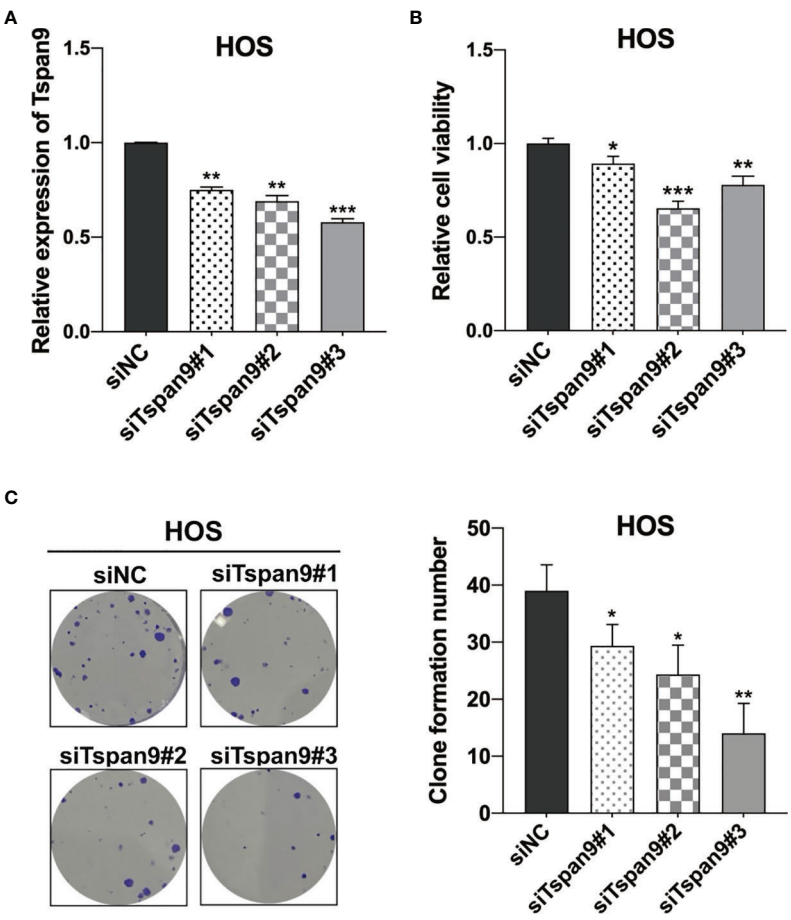

FIGURE 2 | Tspan9 knockdown suppresses OS cell proliferation. **(A)** Tspan9 mRNA levels in siTspan9 cells (siTspan9#1, #2, and #3) were significantly lower than those in siNC cells, as measured *via* qRT-PCR. **(B)** The viability of HOS cells in the siNC and siTspan9 HOS cells was assessed *via* CCK-8 assay. **(C)** The impact of Tspan9 knockdown on HOS cell proliferation was measured *via* colony formation assay. Statistical results of colony formation numbers normalized to shNC were presented. *$P < 0.05$; **$P < 0.01$; ***$P < 0.001$; Student's t-test. NC, negative control; si, small interfering RNA.

0.05, fold-change ≥ 2) (**Figures 3A, B**). Notably, fibronectin 1 (FN1), which is an interstitial biomarker related to EMT induction, was found to be significantly downregulated in OS cells in which Tspan9 had been knocked down as compared to shNC cells, indicating that this tetraspanin may regulate this EMT-related gene (**Table 2**). To further elucidate the functional role of Tspan9 in this oncogenic setting, we performed a GO enrichment analysis (including cellular component, biological process, and molecular function) of these identified DEGs and found the downregulated DEGs to be enriched in the regulation of ERK1/2 cascade (GO:0070372), leukocyte migration (GO:0050900), extracellular structure organization (GO:0043062), extracellular matrix organization (GO:0030198), positive regulation of cell growth (GO:0030307) and cell adhesion (GO:0045785), and integrin activation (GO:0033622) (**Figure 3C**). Upregulated DEGs were mostly associated with the response to lipopolysaccharide (GO:0032496) and response to molecule of bacterial origin (GO:0002237) (**Figure 3D**). Besides, to explore the potential pathways enriched in DEGs, a KEGG pathway enrichment analysis of these DEGs was additionally performed (**Figure 3E**; cutoff: $P < 0.05$). we revealed these downregulated DEGs to be enriched in the HIF-1 (hsa04066), Rap1 (hsa04015), and PPAR (hsa03320) signaling pathways, and upregulated DEGs were significantly related to IL-17 signaling pathway (hsa04657), TGF-beta signaling pathway (hsa04350), and Kaposi sarcoma-associated herpesvirus infection (hsa05167) (**Figure 3F**).

Tspan9 Enhances the *In Vitro* Migratory and Invasive Activity of OS Cells

The above RNA-seq results highlighted a potential role for Tspan9 as a regulator of OS cell migration and invasion. To analyze the metastatic role of this gene, highly metastatic HOS and U2OS cells were thus utilized for subsequent assays. We began by knocking down Tspan9 in HOS cells, which expressed high basal levels of this gene, and confirmed stable knockdown therein by fluorescent microscopy, qRT-PCR, and Western blotting (**Figure 4A**). In subsequent woundhealing and Transwell assays, we found that this reduction in Tspan9 expression was associated with significantly impaired migratory activity (**Figures 4B, C**). Similarly, Tspan9 knockdown decreased HOS cell invasivity in a Matrigel-based invasion assay relative to control cells (**Figure 4C**). We additionally overexpressed Tspan9 in U2OS cells which expressed low endogenous Tspan9 levels (**Figure 4D**), and found that the upregulation of this tetraspanin increased tumor cell migratory (**Figures 4E, F**) and invasive (**Figure 4G**) activity. Together, these data suggest that Tspan9 serves as a positive regulator of *in vitro* OS cell metastasis.

Tspan9 Knockdown Impairs EMT Induction and *In Vivo* OS Cell Metastasis

The EMT process is an early and essential step in the metastatic process that enables tumor cells to migrate away from the primary tumor site. Several prior reports have demonstrated that tetraspanins are closely linked to EMT initiation (30, 31). Our RNA-seq analysis, notably, identified FN1, which is a mesenchymal EMT marker, as an important regulatory target of Tspan9. FN1 is also involved in certain cancer metastasis-related GO processes such as regulation cell adhesion and extracellular structure organization. Through Western blotting, we found that Tspan9 overexpression was associated with marked FN1 upregulation in these OS tumor cells (**Figures 5A, B**). To test the ability of Tspan9 to control EMT induction in this oncogenic context, we thus analyzed the expression of EMT-related proteins. Western blotting analysis revealed that Tspan9 knockdown was associated with a decrease in the expression of both mesenchymal markers (N-cadherin and Vimentin) and EMT-regulating transcription factor (Snai1) (**Figures 5A, B**), while related to an increasing in epithelial cell marker (β-catenin). In contrast, the expression of mesenchymal markers and Snai1 were elevated while the epithelial marker β-catenin was downregulated after overexpressing Tspan9 in U2OS cells (**Figures 5A, B**). Furthermore, the changes in ZEB and Twist families as EMT transcriptional factors are shown in **Figure S1**. RT-PCR analysis revealed that the mRNA levels of ZEB1, ZEB2 and Twist1 were not affected by Tspan9 knockdown and overexpression.

HOS cells in which Tspan9 had been stably knocked down exhibited impaired migratory and proliferative activity, together with impaired EMT initiation, whereas these changes were reversed when this Tspan9 protein was overexpressed in U2OS cells. To further confirm the ability of Tspan9 to similarly regulate metastatic progression *in vivo*, we injected shNC and shTspan9 HOS cells into the lateral tail vein of female BALB/c nude mice and then assessed pulmonary metastases. Following a 4-week period, 4 mice in the control group developed metastatic lung nodules, whereas they were evident in just 2 mice in the shTspan9 group. Representative lung images are shown in **Figure 5C**, while corresponding H&E-stained tissue sections are shown in **Figure 5D**. Statistical analyses revealed that there were significantly fewer pulmonary metastases in mice that were injected with HOS cells expressing shTspan9 as compared to mice injected with control tumor cells (**Figure 5E**). Lung weight values were also significantly lower in the shTspan9 group relative to the control group (**Figure 5F**), although body weight was comparable between these groups (**Figure 5G**). Together, these results provided robust evidence for the role of Tspan9 as a driver of OS cell metastasis *in vitro* and *in vivo* in part owing to its ability to initiate the EMT process.

Tspan9 Regulates OS Cell Metastasis Through Interactions With Integrin β1 and the Activation of Downstream FAK-Ras-ERK1/2 Signaling

Distant metastases of OS, especially lung metastases, are difficult to control and usually have a poor prognosis. As such, we sought to further understand the mechanisms whereby Tspan9 influences OS cell metastasis at the molecular level. Tetraspanins are known to form TEM complexes with a variety of different proteins at the plasma membrane, including integrins. These tetraspanins further serve as essential regulators

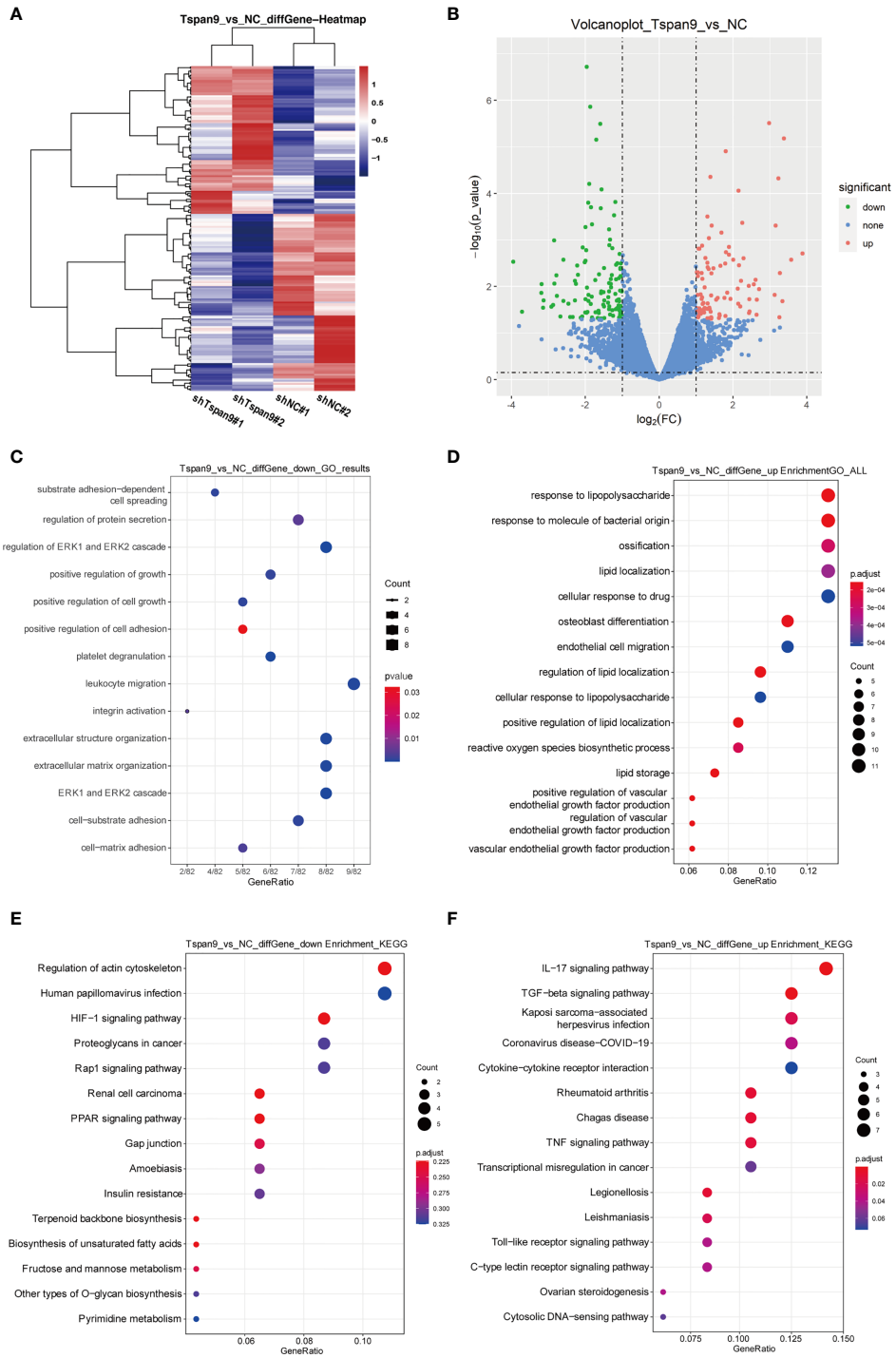

FIGURE 3 | RNA-seq-mediated identification of the biological roles of Tspan9 in OS cells. **(A)** Heatmaps demonstrating DEGs identified *via* RNA-seq in HOS cells in which shTspan9 or shNC were stably expressed. **(B)** DEGs (n=211) are represented in a volcano plot, including 96 upregulated DEGs (red) and 115 downregulated DEGs (green), with DEGs having been identified using the following criteria: adjusted log fold-change ≥ 1 and $P \leq 0.05$. **(C, D)** GO analyses of DEGs identified following Tspan9 knockdown were conducted, with top enriched biological processes, molecular functions, and cellular components being shown in a bubble chart in which darker coloration is indicative of more significant enrichment. **(E, F)** KEGG pathway enrichment analyses of identified DEGs were conducted, with the results being shown in a bubble chart in which bubble size is proportional to the number of DEGs in a given pathway, and the bubble color is indicative of P-value significance (red = significant, blue = non-significant). DEGs, differentially expressed genes; GO, Gene Ontology; KEGG, Kyoto Encyclopedia of Genes and Genomes.

TABLE 2 | Eleven of 82 differential genes enriched in certain cancer metastasis-related GO processes (regulation of cell adhesion and extracellular matrix organization) based on RNA-Seq.

Gene names	Expression value -shTspan9#1	Expression value -shTspan9#2	Expression value -shNC#1	Expression value -shNC#2	Log^2 fold change	*p*-value
PDGFB	2.026756025	1.684725714	2.268746532	3.530040241	-4.528380789	*p<0.05*
TGFB2	0.722634952	0.559786978	1.872658528	0.826405003	-3.186123662	*p*<0.05
ITGA8	1.023664948	1.196609075	1.978711921	1.449654294	-2.254178833	*p<0.05*
TEK	0.722634952	0.559786978	1.361928673	1.35788392	-2.34444508	*p*<0.05
FN1	**3.546946779**	**3.470766925**	**3.595974438**	**4.341457148**	**-1.998509785**	***p*<0.05**
COL7A1	3.551294849	3.251163207	3.958601588	4.015726844	-1.864478412	*p*<0.05
LCP1	1.826926919	1.735878237	1.908130846	2.513041272	-1.733824821	*p<0.05*
COL5A1	3.712021197	3.592540008	4.045844797	4.211975531	-1.595678527	*p<0.05*
CITED2	3.19830614	3.026160239	3.047824772	3.759892291	-1.37840773	*p*<0.05
DYSF	1.938234753	1.480605732	2.095430327	2.24800893	-1.349043777	*p*<0.05
GAS6	2.722014088	2.60641219	2.904711187	3.053262573	-1.051382751	*p<0.05*

The significance of row given in bold in the table is to highlight the direction of research.

of integrin compartmentalization and signal transduction. Through a mass spectrometry approach (**Table S1**) and co-IP analyses (**Figure 6A**), we found that Tspan9 can interact with integrin β1. Integrin β1 binding to collagen triggers intracellular signaling *via* FAK, which becomes autophosphorylated at the Tyr397 or Tyr925 residues to generate SH2-bearing sites capable of further triggering Ras-dependent MAPK signaling (32). To explore the relationship between integrin β1 signaling and Tspan9, we evaluated FAK and ERK1/2 expression and phosphorylation levels, as well as Ras in OS cell lines in which Tspan9 had been knocked down or overexpressed. Western blotting results showed that Tspan9 knockdown in HOS cells was associated with reduced pFAK (Try397), Ras, and pERK1/2 levels as compared to control cells, whereas Tspan9 overexpression in U2OS cells yielded the opposite effect (**Figures 6B, C**). To further determine whether these migratory and invasive changes were linked to Tspan9-β1 complex mediated cell signaling, we treated these cells with a Ras inhibitor (Salirasib) and then analyzed the relative signaling proteins involved in FAK-Ras-ERK1/2 and the metastatic activity of OS cells. This treatment approach resulted in the marked suppression of ERK1/2 phosphorylation downstream of Ras (**Figure 6D**). Ras inhibitor treatment also decreased OS cell migration and invasion relative to that observed for control cells (**Figure 6E**). In addition, we established stable β1 integrin-knockdown cells by shRNA in Tspan9-overexpression U2OS cells. Compared with shControl, shIntegrin β1 resulted in a reduce in the expression of Ras (**Figure S2A**). Also, highly invasive OE-Tspan9 U2OS cells stably down-regulating integrin β1 exhibited impaired capacity of migration and invasion as compared with their counterparts (**Figure S2B**). Together, these data indicate that Tspan9 at least partially promotes OS cell invasive and migratory activity *via* binding to integrin β1 integrin and thereby inducing integrin β1 mediated downstream FAK-Ras-ERK1/2 signaling (**Figure 6F**).

DISCUSSION

Tetraspanin-9 is a 27 kD protein encoded on chromosome 12p13.33-p13.32 in humans, and is expressed at high levels in renal, cardiac, and placental tissues. Recent studies of Tspan9 have highlighted its function as a suppressor of migratory, invasive, and autophagic activity in gastric cancer cells. The mechanisms whereby Tspan9 achieves these regulatory activities, however, have yet to be defined, particularly in other tumor types. This study is the first to have clarified the functional role of Tspan9 in the context of OS development.

Herein, we evaluated the expression of Tspan9 in OS cell lines and tissues and found it to be significantly upregulated in both analyses of extant GEO datasets. When Tspan9 expression was knocked down in OS cells, this suppressed their viability and proliferation, suggesting that Tspan9 plays an oncogenic role distinct from its function as a tumor suppressor in gastric cancer. We subsequently generated HOS and U2OS cell lines in which Tspan9 was stably knocked down or overexpressed, respectively, and further confirmed that the stable knockdown of this tetraspanin inhibited OS cell migration and invasion *in vitro* and *in vivo*. Conversely, the overexpression of Tspan9 enhanced the metastasis of these cells, confirming its carcinogenic role in this cancer type.

To better explore the role of Tspan9 as a regulator of OS onset and progression, we conducted an RNA-seq analysis in which we identified 96 and 115 genes that were respectively up- and downregulated in cells in which Tspan9 was stably knocked down. FN1 was notably detected among these downregulated DEGs, and is associated with GO terms including regulating cell adhesin, extracellular structure organization, and cell-matrix adhesion, suggesting that Tspan9 may play an important role as a regulator of OS cell migratory and invasive activity. In addition, FN1 serves as an important biomarker associated with EMT induction that is known to influence adhesion, invasion, and migration (33, 34). Metastatic progression is a primary cause of death among OS patients, and EMT induction is central to the initiation of invasive pro-metastatic activity. During the EMT process, epithelial-like cells acquire mesenchymal characteristics including increased motility and reductions in cell-cell adhesion (35). A growing body of evidence suggests that many tetraspanins can shape oncogenic processes through the suppression or induction of the EMT process. For example, Qi et al. (14) reported that the knockdown of Tspan9 in gastric cancer cells led to increases in the levels of N-cadherin,

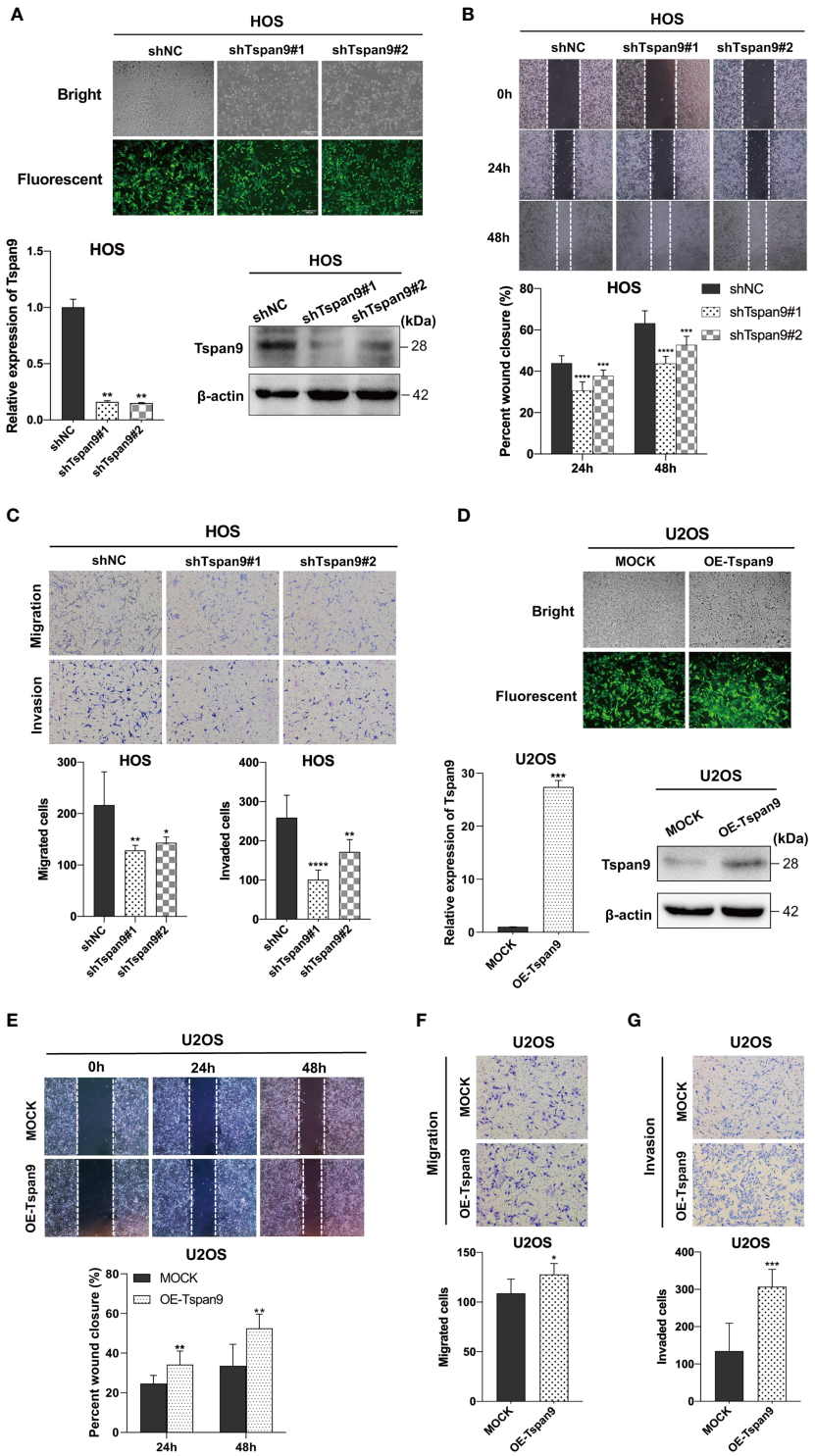

FIGURE 4 | Tspan9 promotes *in vitro* OS cell migration and invasion. **(A)** GFP expression was indicative of stable lentiviral transduction of HOS cells with shTspan9 (shTspan9#1 or shTspan9#2) or shNC constructs at near 100% efficiency (fluorescent microscopy). Tspan9 knockdown efficiency was also confirmed *via* qRT-PCR (lower left panel) and Western blotting (lower right panel). **(B)** OS cell migration was assessed in a wound-healing assay using cells stably expressing shTspan9 or shNC. **(C)** The impact of Tspan9 knockdown on OS cell migration and invasion was assessed *via* a Transwell approach. **(D)** GFP expression was indicative of successful Tspan9 overexpression, as confirmed *via* qRT-PCR and Western blotting relative to Mock control. Wound-healing **(E)** and Transwell assays **(F, G)** were conducted to assess the impact of Tspan9 on the migratory and invasive activity of OS cells. $^{*}P < 0.05$; $^{**}P < 0.01$; $^{***}P < 0.001$; $^{****}P < 0.0001$; Student's t-test. GFP, green fluorescent protein; sh, short hairpin RNA.

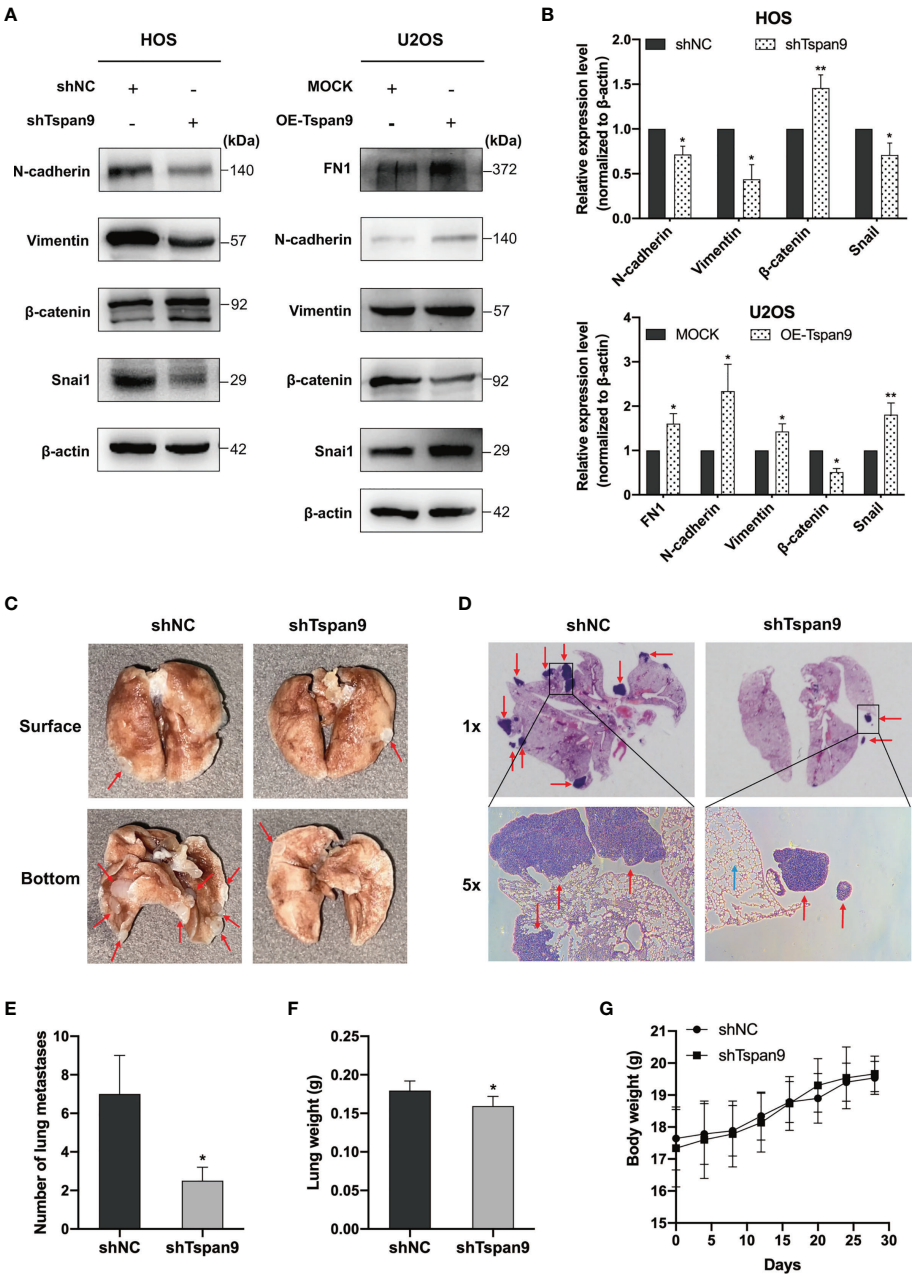

FIGURE 5 | Tspan9 regulates EMT, and knocking down of it impairs *in vivo* OS cell metastasis. **(A)** EMT marker protein levels and associated transcription factor expression were assessed in HOS and U2OS cells stably expressing shTspan9/OE-Tspan9 or control constructs. **(B)** Quantification of the Western blotting results presented in **(A)**. **(C, D)** HOS cells stably expressing shTspan9 or control constructs were injected *via* the lateral tail vein into nude mice to establish a model of pulmonary metastasis (n=5/group). Left: representative lung images; Right: representative H&E staining results (1x and 5x). Pulmonary nodules are indicated by red arrows, while normal alveolar tissue is indicated by blue arrows. **(E)** Numbers of metastatic pulmonary nodules in the indicated groups. **(F)** Lung weights on day 28 post-HOS tumor cell injection. **(G)** Murine body weight was assessed every 4 days. $^{*}P < 0.05$; $^{**}P < 0.01$.

Vimentin, Twist, and ZEB1 in these cells, together with decreased E-cadherin expression, thus suggesting that Tspan9 regulated gastric cancer cell metastasis in part *via* modulating EMT induction. CD82 is a tetraspanin that, when expressed at low levels and in the context of elevated Vimentin expression, was associated with a worse lung cancer patient prognosis (36). Lee et al. (37) also found that CD82 was able to suppress prostate cancer cell EMT induction and metastasis *via* disrupting TGF-β1/Smad and Wnt/β-catenin signaling activity. Other tetraspanin proteins including CD63, CD73, CD151, and Tspan8 have also been shown to modulate the EMT process and tumor progression in colorectal cancer, gastric cancer,

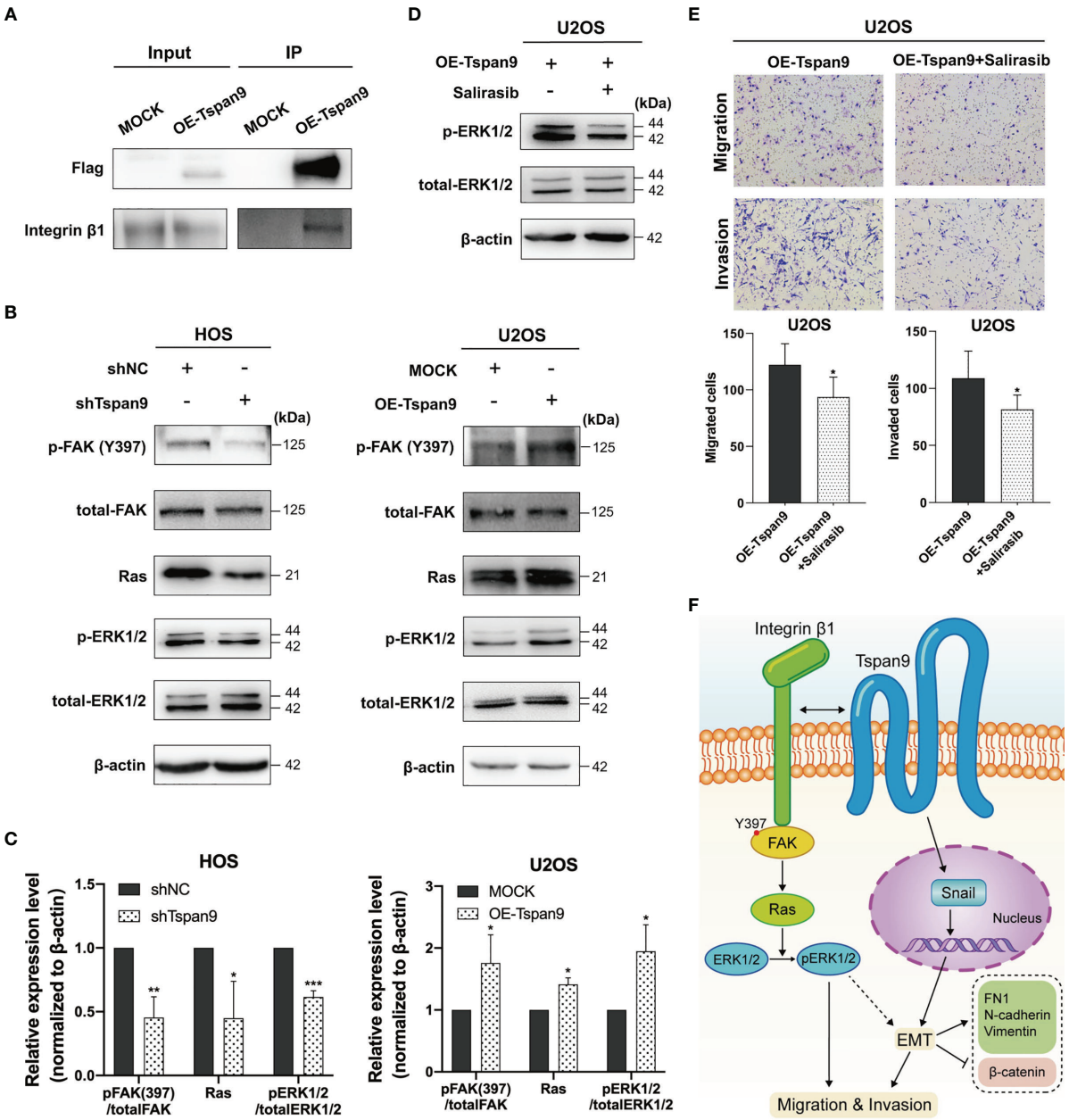

FIGURE 6 | Tspan9-β1 interactions promote FAK-Src-Ras-ERK1/2 pathway signaling and OS metastasis. **(A)** Interactions between Tspan9 and integrin β1 were detected in a co-IP assay. **(B)** FAK-Ras-ERK1/2 pathway proteins (FAK^{Y397}, total-FAK, Ras, pERK1/2, and total-ERK1/2) were analyzed *via* western blotting, with β-actin as a loading control. **(C)** Quantification of the Western blotting results presented in **(B)**. **(D)** Western blotting was used to assess Ras downstream signaling in OE-Tspan9 U2OS cells following Salirasib treatment (50μM). **(E)** Following treatment with Salirasib (50μM), OE-Tspan9 cells were analyzed in migration and invasion assays, with representative cells being shown. **(F)** Schematic presentation of mechanism underlying Tspan9-mediated OS metastasisis. All analyzes were repeated two or three times. Data are means ± SD. $^{*}P < 0.05$; $^{**}P < 0.01$; $^{***}P < 0.001$.

melanoma, and renal cell carcinoma (38–41). In light of the above findings, we further analyzed FN1 expression in our experimental model system and found FN1 to be upregulated following Tspan9 overexpression in U2OS cells, with these changes also correlated with the increased expression of EMT markers and transcription factors including N-cadherin, Vimentin, and Snai1. In contrast, the opposite findings were observed upon Tspan9 knockdown. Together, our findings thus suggest that Tspan9 can promote the migratory and invasive activity of OS cells at least in part by promoting EMT induction.

Tetraspanins exhibit a unique ability to form TEM membrane structures wherein they interact with specific enzymes and/or

receptors to influence intracellular signaling activity *via* the control of the functionality or trafficking of these molecules and the facilitation of interactions between specific molecules (42). Herein, we explored the relationship between key integrins known to promote OS cell metastasis and Tspan9. Li et al. (25) previously demonstrated the ability of integrin β1 to inhibit OS cell apoptosis and to thus enhance the migratory activity of these cells, while Jiang et al. (24) further observed increased EMT induction and invasive activity in OS cells upon integrin β1 upregulation. Ren et al. (43) found that the αvβ3 integrin was able to induce ERK1/2 signaling in OS cells to promote their invasion and migration, and specific interactions between tetraspanin proteins and this integrin have been shown to govern tumor metastasis (44). These prior findings suggest that integrins can serve to stimulate OS cell metastasis *via* ERK signaling and/or EMT induction. Interactions between particular tetraspanin proteins and integrin β1 have also been explored, as in the case of CD82, which can suppress tumor metastasis by interacting with integrin β1 in TEM domains and thereby disrupting the ability of this integrin to interact with the fibronectin matrix, impairing associated intracellular signaling (45, 46). In contrast, the migration and invasion of glioma cells are enhanced by the CD151-α3β1 complex, which promotes FAK^{Y397} activation and associated GTPase signaling (47). Herein, we confirmed that Tspan9 was able to directly interact with integrin β1 through mass spectrometry and co-IP analyses, while we further identified a role for Tspan9 as a regulator of ERK1/2 pathway activation through RNA-seq assays. The recruitment of integrin β1 to the ECM promotes FAK^{Y397} autophosphorylation, in turn leading to the recruitment of Src family kinases and the consequent phosphorylation of other FAK residues including Try925, thereby triggering downstream Ras-ERK signaling (32, 48, 49). Lee et al. determined that CD82 can interact with the α3β1/α5β1 integrins in prostate cancer cells, ultimately impairing EMT induction by inhibiting FAK/Src signaling (46). Wang et al. further demonstrated that in cholangiocarcinoma cells, Tspan1 can drive the EMT process through interactions with integrin α6β1 and the consequent amplification of downstream signaling (31). The Ras-ERK pathway and associated downstream factors are closely tied to the EMT (50, 51). Interactions between Tspan9 and integrin β1 may thus strongly impact the ability of OS cells to proliferate and metastasize by shaping intracellular signaling activity. Herein we evaluated FAK and ERK1/2 phosphorylation, and found that these, together with Ras expression, were positively correlated with Tspan9 expression. The Ras inhibitor Salirasib was also able to inhibit Tspan9 overexpression-induced ERK1/2 phosphorylation, migration, and invasion in OS cells. Furthermore, compared with highly invasive Tspan9-overexpression group, stable integrin β1-knockdown in OE-Tspan9 U2OS cells showed inhibited Ras expression, reduced migration and invasion ability. As such, Tspan9 may promote OS cell metastatic progression by binding to integrin β1 and thereby promoting FAK-Ras-ERK1/2 signaling activity, thus leading to EMT induction. However, further research will be necessary to explore the mechanisms whereby Tspan9 modulates this EMT process in OS cells.

CONCLUSION

We herein found for the first time that Tspan9 can function to promote human OS progression. Both OS tumor tissue samples and cell lines exhibited marked Tspan9 upregulation, and the overexpression of this gene was associated with enhanced proliferation, EMT induction, and metastasis in OS cells through a mechanism whereby Tspan9 interacts with integrin β1 to augment downstream integrin-mediated FAK-Ras-ERK1/2 signaling. Together, our results provide a firm foundation for future analyses of the specific mechanisms governing OS progression and may highlight novel approaches to improving OS patient therapeutic outcomes.

DATA AVAILABILITY STATEMENT

The original contributions presented in the study are included in the article/**Supplementary Material**. Further inquiries can be directed to the corresponding authors.

ETHICS STATEMENT

The animal study was reviewed and approved by Ethics Committee of the Third Affiliated Hospital of Soochow University (approval number: 2021-007).

AUTHOR CONTRIBUTIONS

YW and LP conceptualized the study. JSW contributed to the data curation. LG conducted the formal analysis. SS, JWW, and LW investigated the study. LT contributed to the methodology. XY and XH conducted the project administration. SF and JZ conducted the visualization. SS wrote the original draft. SS and LP wrote, reviewed, and edited the manuscript. All authors contributed to the article and approved the submitted version.

FUNDING

The present study was supported by the National Natural Science Foundation of China (grant No. 81903661), and the Project of State Key Laboratory of Radiation Medicine and Protection of Soochow University (grant No. GZK1202129).

SUPPLEMENTARY MATERIAL

The Supplementary Material for this article can be found online at: https://www.frontiersin.org/articles/10.3389/fonc.2022.774988/full#supplementary-material

REFERENCES

1. Rainusso N, Wang LL, Yustein JT. The Adolescent and Young Adult With Cancer: State of the Art – Bone Tumors. *Curr Oncol Rep* (2013) 15:296–307. doi: 10.1007/s11912-013-0321-9
2. Biazzo A, De Paolis M. Multidisciplinary Approach to Osteosarcoma. *Acta Orthop Belg* (2016) 82:690–8.
3. Bacci G, Rocca M, Salone M, Balladelli A, Ferrari S, Palmerini E, et al. High Grade Osteosarcoma of the Extremities With Lung Metastases at Presentation: Treatment With Neoadjuvant Chemotherapy and Simultaneous Resection of Primary and Metastatic Lesions. *J Surg Oncol* (2008) 98:415–20. doi: 10.1002/jso.21140
4. Lilienthal I, Herold N. Targeting Molecular Mechanisms Underlying Treatment Efficacy and Resistance in Osteosarcoma: A Review of Current and Future Strategies. *Int J Mol Sci* (2020) 21(18):6885. doi: 10.3390/ijms21186885
5. Janeway KA, Grier HE. Sequelae of Osteosarcoma Medical Therapy: A Review of Rare Acute Toxicities and Late Effects. *Lancet Oncol* (2010) 11:670–8. doi: 10.1016/S1470-2045(10)70062-0
6. Maecker HT, Todd SC, Levy S. The Tetraspanin Superfamily: Molecular Facilitators. *FASEB J* (1997) 11:428–42. doi: 10.1096/fasebj.11.6.9194523
7. Boucheix C, Rubinstein E. Tetraspanins. *Cell Mol Life Sci* (2001) 58:1189–205. doi: 10.1007/PL00000933
8. Levy S, Shoham T. The Tetraspanin Web Modulates Immune-Signalling Complexes. *Nat Rev Immunol* (2005) 5:136–48. doi: 10.1038/nri1548
9. Sala-Valdes M, Ailane N, Greco C, Rubinstein E, Boucheix C. Targeting Tetraspanins in Cancer. *Expert Opin Ther Targets* (2012) 16:985–97. doi: 10.1517/14728222.2012.712688
10. Erfani S, Hua H, Pan Y, Zhou BP, Yang XH. The Context-Dependent Impact of Integrin-Associated CD151 and Other Tetraspanins on Cancer Development and Progression: A Class of Versatile Mediators of Cellular Function and Signaling, Tumorigenesis and Metastasis. *Cancers (Basel)* (2021) 13(9):2005. doi: 10.3390/cancers13092005
11. Haining EJ, Matthews AL, Noy PJ, Romanska HM, Harris HJ, Pike J, et al. Tetraspanin Tspan9 Regulates Platelet Collagen Receptor GPVI Lateral Diffusion and Activation. *Platelets* (2017) 28:629–42. doi: 10.1080/09537104.2016.1254175
12. Stiles KM, Kielian M. Role of TSPAN9 in Alphavirus Entry and Early Endosomes. *J Virol* (2016) 90:4289–97. doi: 10.1128/JVI.00018-16
13. Li PY, Lv J, Qi WW, Zhao SF, Sun LB, Liu N, et al. Tspan9 Inhibits the Proliferation, Migration and Invasion of Human Gastric Cancer SGC7901 Cells *via* the ERK1/2 Pathway. *Oncol Rep* (2016) 36:448–54. doi: 10.3892/or.2016.4805
14. Qi Y, Lv J, Liu S, Sun L, Wang Y, Li H, et al. TSPAN9 and EMILIN1 Synergistically Inhibit the Migration and Invasion of Gastric Cancer Cells by Increasing TSPAN9 Expression. *BMC Cancer* (2019) 19:630. doi: 10.1186/s12885-019-5810-2
15. Qi Y, Qi W, Liu S, Sun L, Ding A, Yu G, et al. TSPAN9 Suppresses the Chemosensitivity of Gastric Cancer to 5-Fluorouracil by Promoting Autophagy. *Cancer Cell Int* (2020) 20:4. doi: 10.1186/s12935-019-1089-2
16. Romanska HM, Potemski P, Krakowska M, Mieszkowska M, Chaudhri S, Kordek R, et al. Lack of CD151/integrin Alpha3beta1 Complex is Predictive of Poor Outcome in Node-Negative Lobular Breast Carcinoma: Opposing Roles of CD151 in Invasive Lobular and Ductal Breast Cancers. *Br J Cancer* (2015) 113:1350–7. doi: 10.1038/bjc.2015.344
17. Baldwin LA, Hoff JT, Lefringhouse J, Zhang M, Jia C, Liu Z, et al. CD151-Alpha3beta1 Integrin Complexes Suppress Ovarian Tumor Growth by Repressing Slug-Mediated EMT and Canonical Wnt Signaling. *Oncotarget* (2014) 5:12203–17. doi: 10.18632/oncotarget.2622
18. Wang Y, Hao W, Wang H. miR-557 Suppressed the Malignant Behaviours of Osteosarcoma Cells by Reducing HOXB9 and Deactivating the EMT Process. *Artif Cells Nanomed Biotechnol* (2021) 49:230–9. doi: 10.1080/21691401.2021.1890100
19. Shen S, Huang K, Wu Y, Ma Y, Wang J, Qin F, et al. A miR-135b-TAZ Positive Feedback Loop Promotes Epithelial-Mesenchymal Transition (EMT) and Tumorigenesis in Osteosarcoma. *Cancer Lett* (2017) 407:32–44. doi: 10.1016/j.canlet.2017.08.005
20. Yang G, Yuan J, Li K. EMT Transcription Factors: Implication in Osteosarcoma. *Med Oncol* (2013) 30:697. doi: 10.1007/s12032-013-0697-2
21. Qiu M, Chen D, Shen C, Shen J, Zhao H. And He Y: Sex-Determining Region Y-Box Protein 3 Induces Epithelial-Mesenchymal Transition in Osteosarcoma Cells via Transcriptional Activation of Snail1. *J Exp Clin Cancer Res* (2017) 36:46. doi: 10.1186/s13046-017-0515-3
22. Feng T, Zhu Z, Jin Y, Wang H, Mao X, Liu D, et al. The Microrna7085p/ZEB1/EMT Axis Mediates the Metastatic Potential of Osteosarcoma. *Oncol Rep* (2020) 43:491–502. doi: 10.3892/or.2019.7452
23. Shi K, Wang SL, Shen B, Yu FQ, Weng DF, Lin JH. Clinicopathological and Prognostic Values of Fibronectin and Integrin Alphavbeta3 Expression in Primary Osteosarcoma. *World J Surg Oncol* (2019) 17:23. doi: 10.1186/s12957-019-1566-z
24. Jiang Y, Luo Y. LINC01354 Promotes Osteosarcoma Cell Invasion by Up-Regulating Integrin Beta1. *Arch Med Res* (2020) 51:115–23. doi: 10.1016/j.arcmed.2019.12.016
25. Li R, Shi Y, Zhao S, Shi T, Zhang G. NF-kappaB Signaling and Integrin-Beta1 Inhibition Attenuates Osteosarcoma Metastasis via Increased Cell Apoptosis. *Int J Biol Macromol* (2019) 123:1035–43. doi: 10.1016/j.ijbiomac.2018.11.003
26. Luo BH, Carman CV, Springer TA. Structural Basis of Integrin Regulation and Signaling. *Annu Rev Immunol* (2007) 25:619–47. doi: 10.1146/annurev.immunol.25.022106.141618
27. Lakshmanan I, Rachagani S, Hauke R, Krishn SR, Paknikar S, Seshacharyulu P, et al. MUC5AC Interactions With Integrin Beta4 Enhances the Migration of Lung Cancer Cells Through FAK Signaling. *Oncogene* (2016) 35:4112–21. doi: 10.1038/onc.2015.478
28. Shen M, Jiang YZ, Wei Y, Ell B, Sheng X, Esposito M, et al. Tinagl1 Suppresses Triple-Negative Breast Cancer Progression and Metastasis by Simultaneously Inhibiting Integrin/FAK and EGFR Signaling. *Cancer Cell* (2019) 35:64–80 e67. doi: 10.1016/j.ccell.2018.11.016
29. Sheng W, Chen C, Dong M, Wang G, Zhou J, Song H, et al. Calreticulin Promotes EGF-Induced EMT in Pancreatic Cancer Cells *via* Integrin/EGFR-ERK/MAPK Signaling Pathway. *Cell Death Dis* (2017) 8:e3147. doi: 10.1038/cddis.2017.547
30. Wang X, Lin M, Zhao J, Zhu S, Xu M, Zhou X. TSPAN7 Promotes the Migration and Proliferation of Lung Cancer Cells *via* Epithelial-to-Mesenchymal Transition. *Onco Targets Ther* (2018) 11:8815–22. doi: 10.2147/OTT.S167902
31. Wang Y, Liang Y, Yang G, Lan Y, Han J, Wang J, et al. Tetraspanin 1 Promotes Epithelial-to-Mesenchymal Transition and Metastasis of Cholangiocarcinoma *via* PI3K/AKT Signaling. *J Exp Clin Cancer Res* (2018) 37:300. doi: 10.1186/s13046-018-0969-y
32. Schlaepfer DD, Hanks SK, Hunter T, van der Geer P. Integrin-Mediated Signal Transduction Linked to Ras Pathway by GRB2 Binding to Focal Adhesion Kinase. *Nature* (1994) 372:786–91. doi: 10.1038/372786a0
33. Cai X, Liu C, Zhang TN, Zhu YW, Dong X, Xue P. Down-Regulation of FN1 Inhibits Colorectal Carcinogenesis by Suppressing Proliferation, Migration, and Invasion. *J Cell Biochem* (2018) 119:4717–28. doi: 10.1002/jcb.26651
34. Son H, Moon A. Epithelial-Mesenchymal Transition and Cell Invasion. *Toxicol Res* (2010) 26:245–52. doi: 10.5487/TR.2010.26.4.245
35. Acloque H, Adams MS, Fishwick K, Bronner-Fraser M, Nieto MA. Epithelial-Mesenchymal Transitions: The Importance of Changing Cell State in Development and Disease. *J Clin Invest* (2009) 119:1438–49. doi: 10.1172/JCI38019
36. Zhou L, Yu L, Wu S, Feng Z, Song W, Gong X. Clinicopathological Significance of KAI1 Expression and Epithelial-Mesenchymal Transition in non-Small Cell Lung Cancer. *World J Surg Oncol* (2015) 13:234. doi: 10.1186/s12957-015-0657-8
37. Lee MS, Lee J, Kim YM, Lee H. The Metastasis Suppressor CD82/KAI1 Represses the TGF-Beta 1 and Wnt Signalings Inducing Epithelial-to-Mesenchymal Transition Linked to Invasiveness of Prostate Cancer Cells. *Prostate* (2019) 79:1400–11. doi: 10.1002/pros.23837
38. Yu Y, Liang C, Wang S, Zhu J, Miao C, Hua Y, et al. CD151 Promotes Cell Metastasis *via* Activating TGF-Beta1/Smad Signaling in Renal Cell Carcinoma. *Oncotarget* (2018) 9:13313–23. doi: 10.18632/oncotarget.24028
39. Lupia A, Peppicelli S, Witort E, Bianchini F, Carloni V, Pimpinelli N, et al. CD63 Tetraspanin is a Negative Driver of Epithelial-to-Mesenchymal

Transition in Human Melanoma Cells. *J Invest Dermatol* (2014) 134:2947–56. doi: 10.1038/jid.2014.258
40. Xu Z, Gu C, Yao X, Guo W, Wang H, Lin T, et al. CD73 Promotes Tumor Metastasis by Modulating RICS/RhoA Signaling and EMT in Gastric Cancer. *Cell Death Dis* (2020) 11:202. doi: 10.1038/s41419-020-2403-6
41. Zhang HS, Liu HY, Zhou Z, Sun HL, Liu MY. TSPAN8 Promotes Colorectal Cancer Cell Growth and Migration in LSD1-Dependent Manner. *Life Sci* (2020) 241:117114. doi: 10.1016/j.lfs.2019.117114
42. Yunta M, Lazo PA. Tetraspanin Proteins as Organisers of Membrane Microdomains and Signalling Complexes. *Cell Signal* (2003) 15:559–64. doi: 10.1016/S0898-6568(02)00147-X
43. Ren P, Sun D, Xin D, Ma W, Chen P, Gao H, et al. Serum Amyloid A Promotes Osteosarcoma Invasion *via* Upregulating Alphavbeta3 Integrin. *Mol Med Rep* (2014) 10:3106–12. doi: 10.3892/mmr.2014.2635
44. Detchokul S, Williams ED, Parker MW, Frauman AG. Tetraspanins as Regulators of the Tumour Microenvironment: Implications for Metastasis and Therapeutic Strategies. *Br J Pharmacol* (2014) 171:5462–90. doi: 10.1111/bph.12260
45. Lee HA, Park I, Byun HJ, Jeoung D, Kim YM, Lee H. Metastasis Suppressor KAI1/CD82 Attenuates the Matrix Adhesion of Human Prostate Cancer Cells by Suppressing Fibronectin Expression and Beta1 Integrin Activation. *Cell Physiol Biochem* (2011) 27:575–86. doi: 10.1159/000329979
46. Lee J, Byun HJ, Lee MS, Jin YJ, Jeoung D, Kim YM, et al. The Metastasis Suppressor CD82/KAI1 Inhibits Fibronectin Adhesion-Induced Epithelial-to-Mesenchymal Transition in Prostate Cancer Cells by Repressing the Associated Integrin Signaling. *Oncotarget* (2017) 8:1641–54. doi: 10.18632/oncotarget.13767
47. Zhou P, Erfani S, Liu Z, Jia C, Chen Y, Xu B, et al. CD151-Alpha3beta1 Integrin Complexes are Prognostic Markers of Glioblastoma and Cooperate With EGFR to Drive Tumor Cell Motility and Invasion. *Oncotarget* (2015) 6:29675–93. doi: 10.18632/oncotarget.4896
48. Mitra SK, Schlaepfer DD. Integrin-Regulated FAK-Src Signaling in Normal and Cancer Cells. *Curr Opin Cell Biol* (2006) 18:516–23. doi: 10.1016/j.ceb.2006.08.011
49. Zhao J, Singleton PA, Brown ME, Dudek SM, Garcia JG. Phosphotyrosine Protein Dynamics in Cell Membrane Rafts of Sphingosine-1-Phosphate-Stimulated Human Endothelium: Role in Barrier Enhancement. *Cell Signal* (2009) 21:1945–60. doi: 10.1016/j.cellsig.2009.09.002
50. Fan D, Yu S, Yang Y, Qu S. Low Expression of Rasal2 Promotes Non-Small Cell Lung Cancer Metastasis Through Ras/ERK Pathway. *Biol Pharm Bull* (2021) 44:992–8. doi: 10.1248/bpb.b21-00231
51. Ge P, Wei L, Zhang M, Hu B, Wang K, Li Y, et al. TRPC1/3/6 Inhibition Attenuates the TGF-Beta1-Induced Epithelial-Mesenchymal Transition in Gastric Cancer *via* the Ras/Raf1/ERK Signaling Pathway. *Cell Biol Int* (2018) 42:975–84. doi: 10.1002/cbin.10963

Conflict of Interest: The authors declare that the research was conducted in the absence of any commercial or financial relationships that could be construed as a potential conflict of interest.

Publisher's Note: All claims expressed in this article are solely those of the authors and do not necessarily represent those of their affiliated organizations, or those of the publisher, the editors and the reviewers. Any product that may be evaluated in this article, or claim that may be made by its manufacturer, is not guaranteed or endorsed by the publisher.

frontiers in Oncology

ORIGINAL RESEARCH
published: 25 February 2022
doi: 10.3389/fonc.2022.801230

Ionizing Radiation-Induced GDF15 Promotes Angiogenesis in Human Glioblastoma Models by Promoting VEGFA Expression Through p-MAPK1/SP1 Signaling

Hyejin Park[1,2], *Ki-Seok Nam*[1], *Hae-June Lee*[1,2*] *and Kwang Seok Kim*[1,2*]

[1] Division of Radiation Biomedical Research, Korea Institute of Radiological and Medical Sciences, Seoul, South Korea,
[2] School of Radiological and Medico-Oncological Sciences, University of Science and Technology, Daejeon, South Korea

OPEN ACCESS

Edited by:
Qiangzhe Zhang,
Nankai University, China

Reviewed by:
Fanghsin Chen,
Chang Gung University, Taiwan
Eva Andreuzzi,
Aviano Oncology Reference Center (IRCCS), Italy

***Correspondence:**
Kwang Seok Kim
kskim@kirams.re.kr
Hae-June Lee
hjlee@kirams.re.kr

Specialty section:
This article was submitted to Molecular and Cellular Oncology, a section of the journal Frontiers in Oncology

Received: 25 October 2021
Accepted: 02 February 2022
Published: 25 February 2022

Citation:
Park H, Nam K-S, Lee H-J and Kim KS (2022) Ionizing Radiation-Induced GDF15 Promotes Angiogenesis in Human Glioblastoma Models by Promoting VEGFA Expression Through p-MAPK1/SP1 Signaling. Front. Oncol. 12:801230. doi: 10.3389/fonc.2022.801230

Glioblastoma multiforme (GBM), the most aggressive cancer type that has a poor prognosis, is characterized by enhanced and aberrant angiogenesis. In addition to surgical resection and chemotherapy, radiotherapy is commonly used to treat GBM. However, radiation-induced angiogenesis in GBM remains unexplored. This study examined the role of radiation-induced growth/differentiation factor-15 (GDF15) in regulating tumor angiogenesis by promoting intercellular cross-talk between brain endothelial cells (ECs) and glioblastoma cells. Radiation promoted GDF15 secretion from human brain microvascular endothelial cells (HBMVECs). Subsequently, GDF15 activated the transcriptional promoter *VEGFA* in the human glioblastoma cell line U373 through p-MAPK1/SP1 signaling. Upregulation of vascular endothelial growth factor (VEGF) expression in U373 cells resulted in the activation of angiogenic activity in HBMVECs *via* KDR phosphorylation. Wound healing, tube formation, and invasion assay results revealed that the conditioned medium of recombinant human GDF15 (rhGDF15)-stimulated U373 cell cultures promoted the angiogenic activity of HBMVECs. In the HBMVEC-U373 cell co-culture, *GDF15* knockdown mitigated radiation-induced VEGFA upregulation in U373 cells and enhanced angiogenic activity of HBMVECs. Moreover, injecting rhGDF15-stimulated U373 cells into orthotopic brain tumors in mice promoted angiogenesis in the tumors. Thus, radiation-induced GDF15 is essential for the cross-talk between ECs and GBM cells and promotes angiogenesis. These findings indicate that GDF15 is a putative therapeutic target for patients with GBM undergoing radio-chemotherapy.

Keywords: GDF15, glioblastoma, endothelial cells, radiotherapy, angiogenesis

Abbreviations: CM, Conditioned medium; ECs, Endothelial cells; GBM, Glioblastoma; HBMVECs, Human brain microvascular endothelial cells; H-E, Hematoxylin and Eosin; IR, Ionizing radiation; KDR, Vascular endothelial growth factor receptor 2; rhGDF15, Recombinant human GDF15; RT, Room temperature; VEGF, Vascular endothelial growth factor.

INTRODUCTION

Glioblastoma multiforme (GBM), which is the most common malignant brain tumor in adults, is characterized by enhanced vascularization and a complex vascular phenotype (1, 2). Angiogenesis plays an important role in the progression of glioma (3, 4). To maintain proliferation, cancer cells secrete multiple factors that promote the formation of new blood vessels, which supply oxygen and nutrition to them (5, 6). Therefore, anti-angiogenesis drugs are commonly used to treat GBM (2, 4, 7). Additionally, GBM is treated using radiotherapy to inhibit angiogenesis. However, angiogenesis is reactivated within a short duration of treatment cessation (8, 9).

Vascular endothelial growth factor (VEGF) is an essential paracrine factor involved in maintaining vascular homeostasis and mediating pathological angiogenesis. Generally, endothelial cells (ECs) produce VEGF only in response to radiation doses of > 10 Gy (10). However, radiation activates hypoxia-inducible factor-1 (HIF1) in tumors and promotes the survival and proliferation of ECs through the induction of VEGF expression (11).

Growth/differentiation factor-15 (GDF15), a 34 kDa secretory protein belonging to the transforming growth factor-beta (TGFβ) superfamily, is involved in the development and regulation of cardiac vascular diseases, as well as in hormone responses that maintain systemic homeostasis (12, 13). Previous studies have reported that upregulated GDF15 expression protects against ischemia/reperfusion injury (also called acute EC apoptosis) during heart transplantation (14). In ECs, irradiation upregulates GDF15 levels, which leads to enhanced oxidative stress and cellular senescence (15). Although GDF15 has been well characterized, its role in cancer progression remains unclear. Inhibition of the p38/MEK signaling pathway mitigates the GDF15 overexpression-induced invasion and proliferation of ovarian cancer cells (16). Osteocyte-derived GDF15 enhances prostate cancer cell proliferation and invasion by promoting the interaction between osteocytes and prostate cancer cells (17). In non-small cell lung cancer cells, GDF15 arrests the cell cycle at the G0/G1 phase, leading to cellular apoptosis (18). However, the role of GDF15 in cancer progression has not been elucidated as its expression levels vary among patients and cancer types (19, 20).

In this study, we hypothesized that irradiation-induced GDF15 promotes angiogenesis in glioblastoma by functioning as a cytokine in the tumor microenvironment. This study aimed to examine the role of GDF15 in the cross-talk between a human GBM cell line (U373) and human brain microvascular endothelial cells (HBMVECs; representative ECs). In addition, the mechanisms underlying GDF15-mediated regulation of angiogenesis in GBM were examined.

MATERIALS AND METHODS

Materials

Recombinant human GDF15 (rhGDF15) was purchased from PeproTech (#120-28C, Cranbury, NJ, USA). U0126, a MEK/MAPK1 specific inhibitor, was obtained from Promega Co. (#V112A, Madison, WI, USA). Anti-VEGF antibody (#MAB293) was obtained from R&D Systems (Abingdon, UK).

Cell Culture

HBMVECs purchased from iXCells Biotechnologies (CA, USA) were cultured in EGM™-2 Endothelial Cell Growth Medium-2 BulletKit™ (#CC-3162, Lonza, MD, USA) at 37°C and 5% CO_2 in a humidified incubator. Cells passaged for 5–7 times were used for the experiments. For conducting ionizing radiation (IR) experiments, the cells were irradiated with γ-rays at a dose of 3.5 Gy/min using a ^{137}Cs γ-ray source (Atomic Energy of Canada, Ltd., ON, Canada). U373 cells were cultured in Dulbecco's modified Eagle's medium supplemented with 10% fetal bovine serum (FBS; #35-015-CV, Corning, NY, USA) and 1% penicillin-streptomycin (#15240-062, Thermo Fisher Scientific, UK). To analyze cell growth, U373 cells were cultured in 12-well plates (5×10^4 cells/well) for 3 days. Cells cultured under different serum concentrations (2% and 10%) were counted daily.

Wound Healing Assay

U373 cells (3×10^5 cells/well) and HBMVECs (1.5×10^5 cells/well) were seeded in 12-well cell culture plates and incubated overnight. A scratch was introduced in the monolayer using a pipette tip. The culture medium was replaced to remove cell debris. After washing, three or more images were taken, and then the cells were cultivated for 24 h with rhGDF15 (#120-28C, PeproTech, NJ, USA). The next day, images of the same location as that of the previous day were taken. Using ImageJ line tool, a line was drawn along the area newly filled by proliferated cells. The areas calculated by ImageJ were averaged (three or more images per group) and normalized to the control group.

Tube Formation Assay

Individual wells of a 24-well cell culture plate were coated with 250 μL of Matrigel (#354234, Matrigel® Basement Membrane Matrix, LDEV-free, Corning, NY, USA) for 1 h before cell seeding. HBMVECs (1×10^5 cells/well) were seeded in the coated wells and cultured for 12 h. The tube shapes were analyzed using ImageJ software (ver.1.52a with angiogenesis analyzer plugin).

Co-Culture of HBMVECs and U373 Cells

HBMVECs and U373 cells were cultured in a co-culture system. A 12-mm Transwell with a polycarbonate membrane insert (pore size: 0.4 μm; #CLS3413, Corning, NY, USA) was used. In the upper well, U373 cells (5×10^4 cells) were seeded in culture medium supplemented with 2% FBS. HBMVECs (1.5×10^5 cells) were seeded in the bottom well containing EC culture medium supplemented with 2% FBS. The monolayer of HBMVECs was scratched with a tip to introduce a wound. The culture medium was replaced with a fresh culture medium. Next, the cells were irradiated with 8 Gy IR.

Quantitative Reverse Transcription Polymerase Chain Reaction (qRT-PCR)

Total RNA was extracted using QIAzol Lysis Reagent (#79306, Qiagen, Hilden, Germany), following the manufacturer's instructions. The isolated RNA was reverse-transcribed into

cDNA using amfiRivert cDNA Synthesis Platinum Master Mix (#R5600, GenDEPOT, Barker, TX, USA). qRT-PCR analysis was performed using the SYBR Green 2× Master Mix kit (#18303, Mbiotech, Inc., Gyeonggi, Korea) and a CFX96 Touch™ Real-Time PCR detection system (Bio-Rad, Hercules, CA, USA). The PCR conditions were as follows: initial denaturation at 95°C for 2 min, followed by 45 cycles at 95°C for 10 s, 60°C for 5 s, and 72°C for 12 s. The results were analyzed using CFX Manager™ software, version 2.1. The expression of target genes was normalized to that of 18S RNA. The following primers were used: *GDF15*, 5′-GACATCACTAGGCCCCTGA-3′ (forward) and 5′-CCCGTAAGCGCAGTTCC-3′ (reverse); *VEGFA*, 5′-TCAGTTCGAGGAAAGGGAAA-3′ (forward) and 5′-GAGGCTCCAGGGCATTAGAC-3′ (reverse); *kinase insert domain receptor* (*KDR*), 5′-CGGTCAACAAAGTCGGGAGA-3′ (forward) and 5′-CAGTGCACCACAAAGACACG-3′ (reverse); and 18S RNA, 5′-GGCCCTGTAATTGGAATGAGTC-3′ (forward) and 5′-CCACGATCCAACTACGAGCTT-3′ (reverse).

Western Blotting

Cells were lysed in ice-cold protein extraction solution (#EBA-1049, ELPIS-BIOTECH, Daejeon, Korea). Equal amounts of protein (40 μg) were subjected to sodium dodecyl sulfate (SDS)-polyacrylamide gel electrophoresis. The resolved proteins were transferred to a nitrocellulose membrane. The membrane was probed with the following primary antibodies: anti-GDF15 (1:1000, #SC66904, Santa Cruz Biotechnology, Inc., TX, USA), anti-MAPK1 (1:1000, #9102, Cell Signaling Technology, Inc., MA, USA), anti-p-MAPK1 (1:1000, #9101, Cell Signaling Technology, Inc.), anti-SP1 (1:1000, #SC14027, Santa Cruz, CA, USA), anti-VEGF (1:1000, #SC1836, Santa Cruz Biotechnology, Inc.), anti-KDR (1:1000, #9698 Cell Signaling Technology, Inc.), anti-p-KDR (1:500, #3817, Cell Signaling Technology, Inc.), and anti-ACTB (1:3000 #SC47778, Santa Cruz Biotechnology, Inc.) antibodies. ACTB was used as the loading control. Immunoreactive signals were developed using enhanced chemiluminescence.

Promoter Assay

Variant VEGF constructs were used as luciferase-based reporters for the *VEGFA* promoter region (pGL4.10-VEGFprom −1000 to −1, −950 to −700, −1000 to −500, and −500 to −1 bp). The following VEGFA constructs were purchased from Addgene (MA, USA): pGL4.10-VEGFprom −1000 to −1 (plasmid #66128); pGL4.10-VEGFprom −950 to −700 (plasmid #66133); pGL4.10-VEGFprom −1000 to −500 (plasmid #66129); and pGL4.10-VEGFprom −500 to −1 (plasmid #66130). The constructs were transfected into 293T cells, and the cells were treated with 50 ng/mL of rhGDF15. The cells were lysed using the Nano-Glo® Dual-Luciferase® Reporter Assay System (Promega, WI, USA). The luminescence intensity in the lysate was measured using a GloMax® Discover System.

Chromatin Immunoprecipitation (ChIP)

U373 cells were treated with 10 μM U0126 for 1 h, followed by treatment with 100 ng/mL rhGDF15. The cells were harvested, lysed in SDS with 50 mM Tris-HCl (pH 8.1) and 1 mM ethylenediaminetetraacetic acid (EDTA), and sonicated for 1 h at 4°C. The supernatant was evenly split and incubated with 2 μg of anti-SP1 antibody overnight at 4°C with rotation. The reaction mixture was incubated with protein A beads (60 μL/reaction) for 1 h at 4°C. The beads were then washed thrice. The eluted supernatants and input DNA samples were incubated at 65°C for 4 h to allow de-crosslinking. The DNA was then precipitated with ethanol and treated with proteinase K for 30 min at 37°C. The samples were extracted with phenol/chloroform, precipitated with ethanol, and resuspended in 20 μL of distilled water. The promoter-binding activity was measured using qRT-PCR analysis with specific promoter primers (forward, 5′-GGGTAGCTCGGAGGTCGT-3′; reverse, 5′-GGGAATGGCAAGCAAAAA-3′).

Immunocytochemistry

HBMVECs were seeded in 12-well dishes on coverslips. The cells were fixed in 3.7% formaldehyde/phosphate-buffered saline (PBS) for 10 min at room temperature (RT) and permeabilized with ice-cold 0.5% Triton X-100/PBS for 10 min. The permeabilized cells were blocked with 0.5% bovine serum albumin (BSA)/PBS for 1 h at RT and incubated with anti-GDF15 antibodies overnight at 4°C. Next, the cells were treated with goat anti-rabbit IgG (H+L) Alexa Fluor® 488 (#A27034, Invitrogen Inc., Carlsbad, CA, USA) for 1 h. The coverslips were mounted on glass slides with Fluoromount-G™ Mounting Medium (#0100-01, Southern Biotech, AL, USA).

Enzyme-Linked Immunosorbent Assay (ELISA)

To analyze the concentration of soluble proteins (GDF15 and VEGFA), the cultured media were passed through 0.45-μm filter membranes and concentrated using Vivaspin® 20 centrifugal concentrators (Sartorius, Göttingen, Germany). ELISA was performed using commercial kits (GDF15, #DGD150; VEGF, #DVE00; R&D Systems, Inc., MN, USA), following the manufacturer's instructions. Briefly, the standard was prepared by serially diluting recombinant proteins. The samples were then loaded into the plates with anti-GDF15 or anti-VEGFA antibodies for 2 h at RT. Next, the plate wells were incubated with the substrate solution for 30 min, followed by incubation with a stop solution. The absorbance of the reaction mixture was measured at 450 nm.

Small Interfering RNA (siRNA) Transfection

To knockdown *GDF15*, HBMVECs were transfected with *GDF15* siRNAs (siGDF15; 50 nM, ON-TARGETplus siRNAs, Dharmacon Inc., CO, USA) or control siRNA (siCon) using Lipofectamine 2000 (Invitrogen Inc., CA, USA), following the manufacturers' instructions. Briefly, 1×10^6 cells were seeded in a 60 mm culture dish and cultured overnight. Lipofectamine was incubated with 50 ng/mL siRNA for 20 min. The cells were washed twice with PBS, and the culture medium was replaced with EBM™-2 Endothelial Cell Growth Basal Medium (#CC-3156, Lonza). Next, the cells were incubated with the siRNA/Lipofectamine mixture for 6 h. The medium was then replaced with EGM™-2 Endothelial Cell

Growth Medium-2 BulletKit™ (#CC-3162, Lonza). The cells were harvested 48 h after transfection.

Orthotopic Brain Tumor Model

All animal experiments were approved by the Institutional Animal Care and Use Committee of the Korea Institute of Radiological and Medical Sciences (Approval no. KIRAMS2018-0079). Athymic BALB/c nu/nu mice were purchased from Orient Bio Inc. (Seoul, Korea). The mice were provided standard food and tap water under specific pathogen-free conditions. Prior to injecting the U373 cells into the mouse brain, the cells were treated with GDF15 by adding rhGDF15 to the culture medium for 14 days. The culture medium was changed every three days with fresh rhGDF15-containing medium. For injecting U373 cells (1×10^5/3 μL), the head of each mouse was fixed on a stereotactic device. The cells were injected into the left frontal cortex using a microinjector. On day 10 post-injection, mouse brain samples were harvested, fixed in 4% paraformaldehyde solution, embedded in paraffin, and cut into 5 μm-thick sections using a microtome (Leica, Nussloch, Germany).

Tumor Size Evaluation

The brain tissue was coronally sectioned to a thickness of 5 μm using a microtome (Leica, Nussloch, Germany). The sections were hydrated and stained with hematoxylin and eosin (H-E). The area of the tumor with the greatest longitudinal diameter and transverse diameter was measured. The U373 cell-derived tumor was manually traced along the tumor margin, and the area was measured using ImageJ.

Immunofluorescence Analysis of Brain Tumor

The embedded brain tissues were sectioned to a thickness of 5 μm using a microtome (Leica, Nussloch, Germany). The sections were mounted on coated slides (#631-1349, Adhesion slides, Menzel Gläser, Polysine®, Thermo Fisher Scientific, UK), hydrated, and boiled in citrate buffer (pH 6.0) for antigen retrieval. After washing twice with 0.1% Triton X-100/PBS for 5 min, the sections were blocked with 1.5% normal horse serum for 1 h at RT to inhibit non-specific signals. The sections were subsequently incubated overnight at 4°C with anti-VEGFA (1:200, #SC1836, Santa Cruz Biotechnology), anti-CD31 (1:200, # AF3628, R&D Systems, MN, USA), anti-p-MAPK1 (#9102, Cell Signaling Technology, Inc), and anti-SP-1 antibodies, followed by incubation with the appropriate secondary antibodies for 1 h at RT. The slides were observed using an Olympus BX53 fluorescence microscope with DP73 digital camera (Olympus, Tokyo, Japan). Three fields were arbitrarily photographed for each tumor, and the average value of the three fields was used as a representative value for one tumor. The fluorescence intensity was analyzed by Image J using the following formula: Corrected Total Cell Fluorescence (CTCF) = Integrated Density − (Area of selected cell × Mean fluorescence of background readings).

Statistical Analysis

All data are presented as mean ± standard deviation. The means between two groups were compared using Student's *t*-tests, whereas those among more than two groups were compared using one-way or two-way analysis of variance. Differences were considered significant at $p < 0.05$. All statistical analyses were performed using GraphPad Prism Software version 8.3 (GraphPad Software, La Jolla, CA, USA).

RESULTS

IR Upregulates GDF15 and Promotes Its Secretion From HBMVECs

The effect of different doses of IR (2, 4, and 8 Gy) on *GDF15* mRNA expression in HBMVECs was examined 24 h post-irradiation. *GDF15* mRNA levels in cells irradiated with IR at doses of ≥ 4 Gy were significantly upregulated compared to those in the nonirradiated cells (**Figure 1A**). Consistent with its effect on *GDF15* mRNA levels, IR increased intracellular GDF15 immunofluorescence signals (**Figure 1B**). qRT-PCR analysis revealed that the upregulation of *GDF15* mRNA levels was significant 4 h post-irradiation onward (**Figure 1C**). Immunoblotting analysis revealed that GDF15 protein levels were upregulated in cell lysates and cell culture media (secreted GDF15) 24 h post-irradiation (**Figure 1D**). Consistently, ELISA results revealed that IR promoted GDF15 secretion into the culture medium of HBMVECs (**Figure 1E**). These results indicate that IR upregulated endogenous/cytosolic GDF15 expression and secretion in HBMVECs. The cytosol and extracellular milieu are important components of the tumor microenvironment.

GDF15 Promotes VEGFA Expression in U373 Cells But Not U373 Cell Invasion or Proliferation

To investigate the role of GDF15 in glioblastoma, the effect of GDF15 on the *in vitro* proliferation and invasion of U373 cells was examined. GDF15 is reported to promote cancer cell growth (16, 17). Hence, the effect of rhGDF15 on the proliferation and migration of U373 cells was examined in this study. U373 cells were cultured for up to 3 days in the presence of rhGDF15 (in the medium supplemented with 10% serum or a serum substitute); rhGDF15 did not affect the proliferation rate of U373 cells (**Figure 2A**). The results of the wound healing assay revealed that rhGDF15 increased the migration of U373 cells, although the change was not statistically significant ($p = 0.4248$; **Figure 2B**).

GDF15, which has a structure similar to that of TGFβ, is a member of the TGFβ superfamily. The TGFβ superfamily members can stimulate cytokine-inducible factors, including HIF1a, C-X-C motif chemokine ligands (CXCLs), and VEGF, in cancer cells (4). Thus, the effect of GDF15 on VEGFA expression in U373 cells was examined. The mRNA and secretory levels of VEGFA in rhGDF15-treated U373 cells were examined. Interestingly, *VEGFA* mRNA levels in the rhGDF15-stimulated U373 cells were upregulated by 1.78-fold compared to those in the control U373 cells ($p = 0.0032$; **Figure 2C**). Meanwhile, soluble VEGFA levels in the culture medium of rhGDF15-treated cells were significantly higher than those in the culture medium of control cells ($p = 0.0131$ and $p = 0.0008$ at days 2 and 3 post-rhGDF15 treatment, respectively; **Figure 2D**).

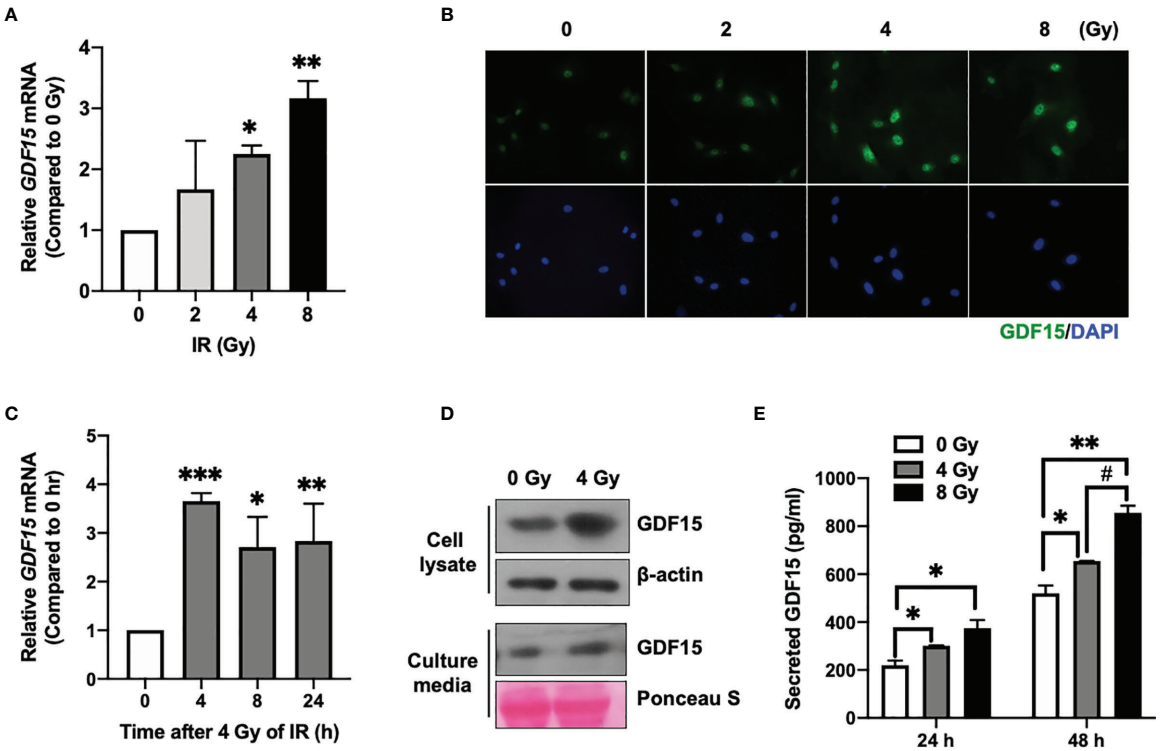

FIGURE 1 | Effect of ionizing radiation (IR) on GDF15 expression in human brain microvascular endothelial cells (HBMVECs). **(A)** Effect of different doses of IR on *GDF15* mRNA expression in HBMVECs. Cultured cells were harvested 24 h post-IR exposure, and *GDF15* mRNA levels were analyzed using quantitative reverse transcription polymerase chain reaction (qRT-PCR). **(B)** Effect of different doses of IR (0 – 8 Gy) on GDF15 protein levels in HBMVECs. GDF15 protein expression was detected by immunofluorescence analysis using anti-GDF15 antibody (green). Nuclei were stained with 4′,6-diamidino-2-phenylindole (DAPI) (blue) (Magnification: 400×); **(C)** Time course of *GDF15* mRNA expression after irradiation with 4 Gy of IR. *GDF15* mRNA levels measured using qRT-PCR at the indicated time points. **(D)** Immunoblotting analysis of GDF15 in the cell lysate and culture medium reveals that IR upregulated GDF15 protein levels. Cells and culture media were harvested at 24 h post-IR exposure. **(E)** IR promotes the secretion of GDF15. The secretion of GDF15 into the culture medium was measured using a human GDF15 enzyme-linked immunosorbent assay kit at 24 and 48 h post-irradiation with 4 or 8 Gy of IR. Data are presented as the mean ± standard deviation of three experiments. $^{*}p < 0.05$, $^{**}p < 0.01$, and $^{***}p < 0.001$ compared with the control. $^{\#\#}p < 0.05$ compared with 4 Gy.

We also examined the effect of GDF15 on HBMVECs. We observed that GDF15 increased the viability, wound recovery ability, and tube formation ability of these cells; however, these observations were not statistically significant. Additionally, we observed no significant effect on pMAPK by western blotting (**Supplementary Figure S1**).

GDF15 Stimulates *VEGFA* Promoter Activity in U373 Cells *via* the p-MAPK1/SP-1 Pathway

To investigate the mechanism underlying GDF15-mediated regulation of VEGFA expression, the effects of rhGDF15 on the luciferase activity of various *VEGFA* promoter-reporter constructs were examined. GDF15 activated the GC-rich *VEGFA* promoter containing an SP1-binding site (from −500 to −1) (**Figure 3A**). Transcription factors, such as NF-κB and STAT3 can bind to the GC-rich *VEGFA* promoter (21). However, GDF15 did not activate NF-κB and STAT3 expression in U373 cells (**Supplementary Figure S2**). This indicated that VEGFA is induced by the MAPK1 signaling pathway through the transcription factor SP1 (22, 23). In order to inactivate MAPK1, U373 cells were treated with U0126 1 h before the addition of recombinant hGDF15. The cells were incubated for 6 h and then harvested for western blotting. rhGDF15 treatment increased MAPK1 phosphorylation and SP1 levels in U373 cells (**Figure 3B**). U0126 suppressed SP1 expression and MAPK1 phosphorylation in rhGDF15-stimulated and control U373 cells (**Figure 3B**). To confirm the role of GDF15-induced VEGFA expression, *VEFGA* expression was examined by qRT-PCR analysis 12 h after incubation with rhGDF15 and/or U0126. qRT-PCR analysis revealed that U0126 mitigated the GDF15-induced upregulation of *VEGFA* mRNA levels (**Figure 3C**). Next, the effect of GDF15 on the direct binding of SP1 to the *VEGFA* promoter was examined using a ChIP assay to confirm the GDF15-mediated regulation of VEGFA expression through MAPK1/SP1 signaling. The results of a series of ChIP assays using anti-SP1 antibodies revealed that GDF15 promoted the binding of SP1 to the *VEGFA* promoter and that U0126 mitigated the GDF15-induced SP1 promotor binding (**Figure 3D**). These data suggest that GDF15 activates

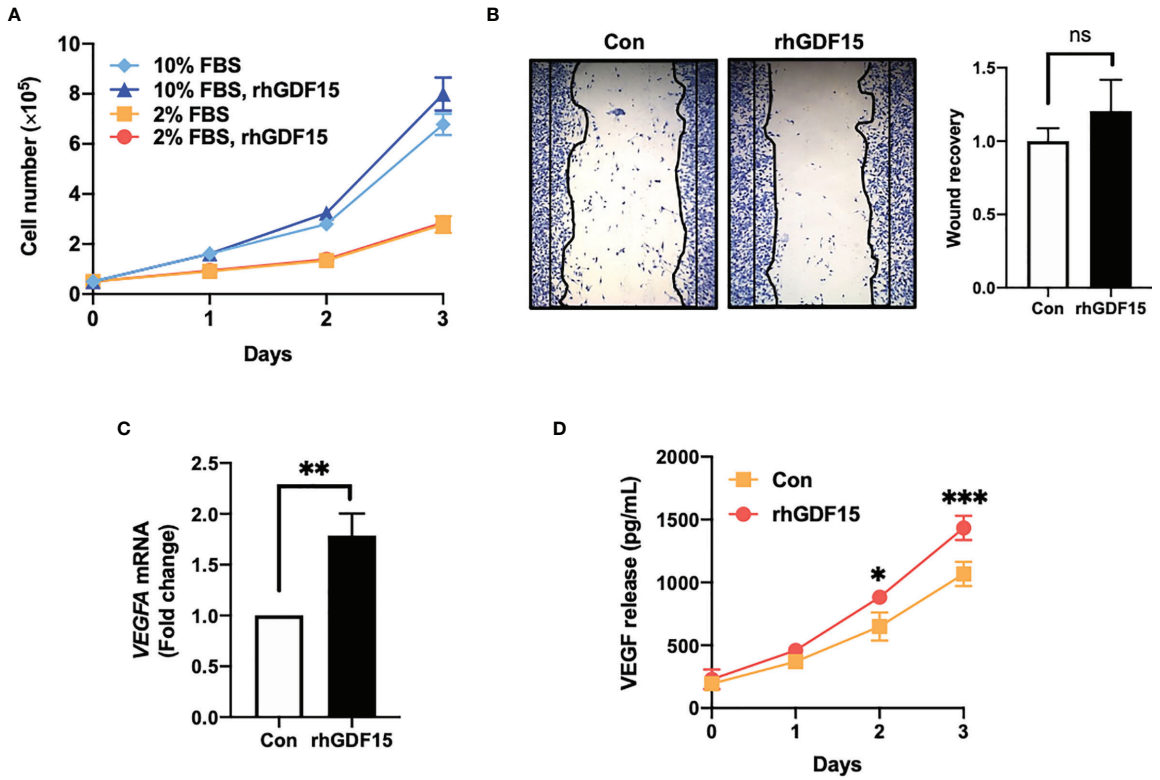

FIGURE 2 | GDF15 promotes VEGFA expression in U373 glioblastoma cells but not proliferation and migration of U373 cells. **(A)** U373 cells were treated with 100 ng/mL rhGDF15 protein for 3 days in a medium with different serum concentrations (2% or 10% fetal bovine serum) and the cells were counted daily. **(B)** The cells were seeded on 12-well plates (3×10^5 cells/well) and cultured for 1 day. The monolayer was scratched and incubated for 24 h in a medium containing 2% serum. Subsequently, the cells were stained with a fixation solution containing trypan blue. **(C)** The *VEGFA* mRNA levels in rhGDF15-stimulated U373 cells were measured using quantitative reverse transcription polymerase chain reaction. **(D)** Soluble VEGF was quantified in the enriched culture medium containing 2% serum using enzyme-linked immunosorbent assay from days 1–3. Data are presented as the mean ± standard deviation of three experiments. $^*p < 0.05$, $^{**}p < 0.01$, and $^{***}p < 0.001$ compared with control group. ns, no significance.

transcription of the *VEGFA* promoter through p-MAPK1/SP1 signaling.

GDF15 Modulates the Interaction Between ECs and Glioblastoma Cells

To investigate the role of GDF15 in the interaction between ECs and glioblastoma cells, GDF15-induced VEGFA expression in glioblastoma cells and its effects on ECs were examined. The effect of conditioned medium (CM) derived from rhGDF15-stimulated U373 cell cultures (GDF15-CM) on HBMVEC cultures was examined (**Figure 4A**). As GDF15-CM contains secreted VEGFA, KDR levels were examined in HBMVECs. GDF15-CM upregulated *KDR* mRNA levels and increased KDR phosphorylation in HBMVECs (**Figure 4B, C**). Next, HBMVECs cultured in GDF15-CM were subjected to wound healing and tube formation assays. The migration (2.3-fold; $p < 0.05$) and tube formation (1.2-fold; $p < 0.001$) abilities of HBMVECs cultured in GDF15-CM were significantly higher than those of HBMVECs cultured in Con-CM (control CM, culture media derived from U373 cells not treated with rhGDF15) (**Figure 4D, E**). Further, to validate GDF15-induced VEGF secretion, we performed would healing assay and tube formation assays using a neutralizing VEGF antibody (α-VEGF). We added neutralizing VEGF antibody (1 ng/mL) to Con-CM and GDF15-CM, which were incubated with HBMVECs for 24 h. By neutralizing VEGF, the migration (27%, $p < 0.05$) and tube formation (53%, $p < 0.01$) abilities of both cultures were notably blocked compared to those in the absence of α-VEGF (**Figure 5**).

SiRNA-Mediated Knockdown of *GDF15* Suppresses Radiation-Induced HBMVEC Migration

In addition to ablating cancer cells, IR promotes angiogenesis. IR stimulates the angiogenic activity of ECs in the tumor (24, 25). To examine the involvement of GDF15 in IR-induced tumor angiogenesis through VEGFA regulation, the effect of *GDF15* knockdown on HBMVEC angiogenic activity was examined using the HBMVEC–U373 co-culture system (**Figure 6A**). We confirmed that siGDF15 treatment inhibited the protein levels of GDF15 in HBMVECs (**Figure 6B**). IR-induced GDF15 expression in siCon-transfected HBMVECs was upregulated 2.49-fold ($p = 0.0027$) compared with that in siGDF15-

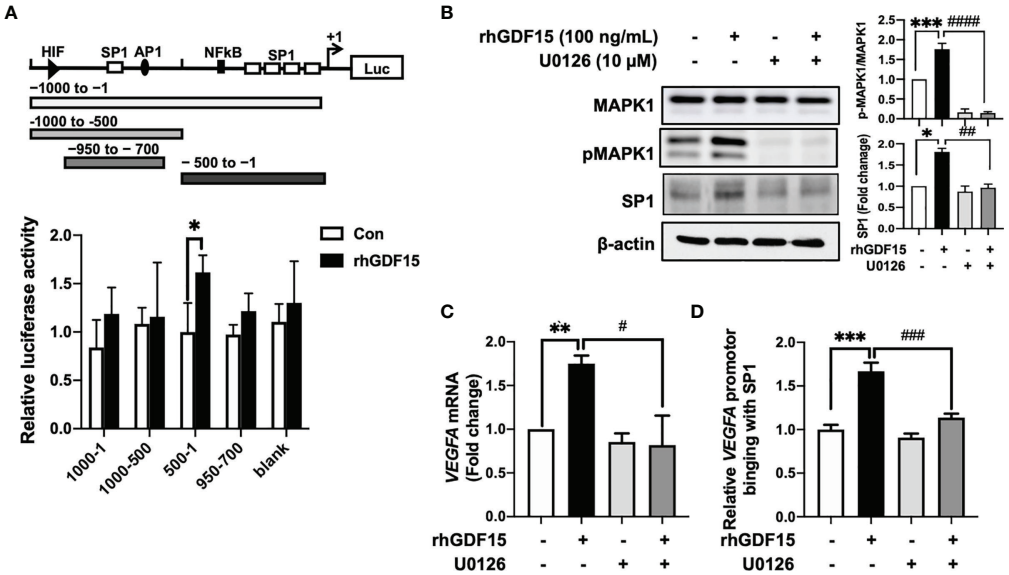

FIGURE 3 | GDF15 upregulates *VEGFA* transcription by promoting the binding of SP1 to its promoter. **(A)** 293T cells were transfected with a luciferase construct containing different *VEGFA* promotor regions or control vectors and treated with recombinant human GDF15 (rhGDF15). Data are presented as the mean ± standard deviation of three experiments (*$p < 0.05$). **(B)** For immunoblotting analysis of MAPK1, p-MAPK1, and SP1 in U373 cells, the cells were incubated for 1 h in the presence or absence of a MAPK1 inhibitor (U0126) and treated with rhGDF15 for 6 h. **(C)** Quantitative reverse transcription polymerase chain reaction (qRT-PCR) analysis of *VEGFA* mRNA expression in U373 cells treated with rhGDF15 and/or U0126. qRT-PCR analysis was performed using samples extracted 12 h post-rhGDF15 treatment. For inhibition studies, U373 cells were incubated with 10 μM U0126 for 1 h before treatment with 100 ng/mL rhGDF15. **(D)** Cells were incubated with or without rhGDF15 and U0126 and subjected to chromatin immunoprecipitation (ChIP) assay using anti-SP1 or IgG isotype control antibodies. Bar graphs represent the qRT-PCR results for immunoprecipitated *VEGFA* promoter. Data are presented as the mean ± standard error (**$p < 0.01$ and ***$p < 0.001$ compared with control group; $^{\#}p < 0.05$, $^{\#\#}p < 0.01$, $^{\#\#\#}p < 0.001$ and $^{\#\#\#\#}p < 0.0001$ compared with rhGDF15-treated group.

transfected HBMVECs. In contrast, IR did not affect GDF15 expression in siGDF15-transfected HBMVECs (**Figure 6C**). IR-induced VEGFA expression in U373 cells co-cultured with siCon-transfected HBMVECs ($p = 0.0198$) was 1.87-fold higher than that in U373 cells co-cultured with siGDF15-transfected HBMVECs. Irradiation with IR did not affect VEGF expression in U373 cells co-cultured with siGDF15-transfected HBMVECs (**Figure 6D**). To investigate the effects of *GDF15* knockdown on angiogenic activity mediated by the interaction between glioblastoma cells and ECs, the effect of IR on wound healing in siCon-transfected or siGDF15-transfected HBMVECs co-cultured with U373 cells was examined. Transfected HBMVECs in the lower well were scratched, irradiated with IR, and incubated with U373 cells for 24 h. Irradiation with IR did not affect the wound recovery rates in siGDF15-transfected HBMVECs (**Figure 6E**). In contrast, the wound recovery rates in siCon-transfected HBMVECs increased 1.33-fold compared to those in siGDF15-transfected HBMVECs ($p = 0.0268$).

GDF15 Accelerates *In Vivo* Glioma Angiogenesis by Stimulating VEGFA Secretion

To investigate the effect of GDF15 on brain tumors *in vivo*, orthotropic brain tumors were injected with rhGDF15-stimulated U373 cells (1×10^5 cells; cultured in the presence of 50 ng/mL rhGDF15 for 2 weeks). Mice with orthotropic brain tumors injected with control U373 cells (not treated with rhGDF15) served as a control group. The *VEGFA* mRNA expression levels in rhGDF15-stimulated U373 cells were confirmed using qRT-PCR before stereotactically injecting the cells into the brain tumors (**Supplementary Figure S3**). The mice were euthanized, and the tumor size was measured in the H-E-stained brain sections on day 10 post-injection. The tumor size was significantly higher in the rhGDF15-stimulated U373 cell-injected group than in the control U373 cell-injected group (**Figure 7A**). Immunofluorescence analysis of the tumor sections revealed that the EC density (represented by CD31-positive vessels) in the rhGDF15-stimulated U373 cell-injected tumors was significantly higher than that in the control U373 cell-injected tumors. VEGFA-positive signals in both cancer cells and ECs of the rhGDF15-stimulated U373 cell-injected tumors were significantly higher than those in both cancer cells and ECs of the control U373 cell-injected tumors (**Figure 7B**). We also performed immunofluorescence analysis of p-MAPK1 and SP1 levels in the control- and GDF15-treated tumors. Consistent with the *in vitro* results, the rhGDF15-treated U373 cell-injected tumors exhibited higher levels of both p-MAPK1 and SP1 than control tumors (**Figure 7C**). We also analyzed the expression *GDF15* and *VEGFA* mRNA in the tumors from the control and rhGDF15-treated groups using qRT-PCR. The mRNA expression of both *GDF15* and *VEGFA* was higher in the rhGDF15-treated group than in the control group (**Supplementary Figure S4**).

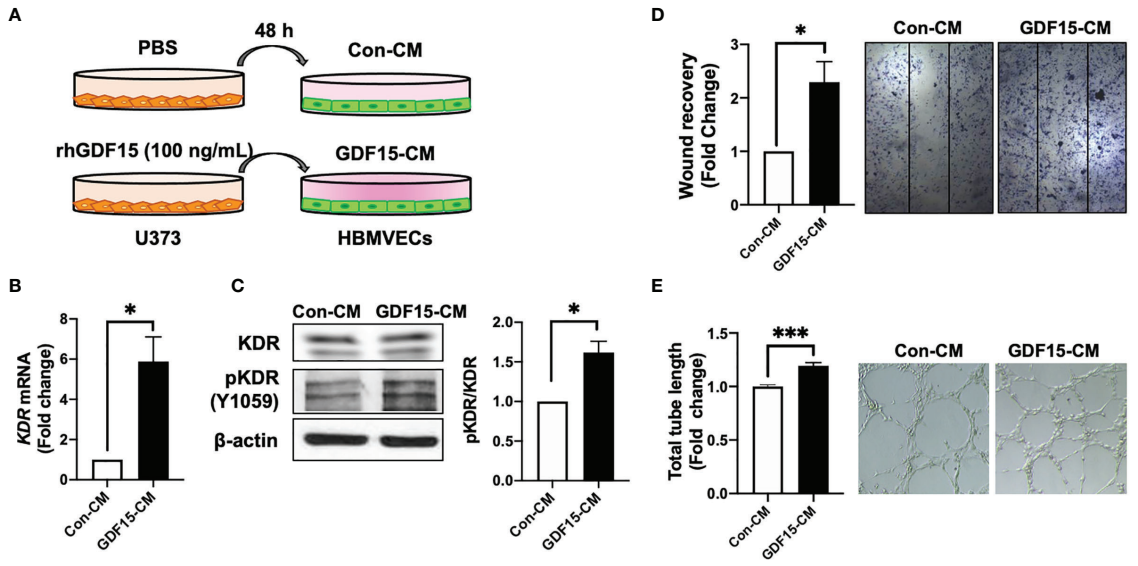

FIGURE 4 | GDF15-induced VEGFA activates angiogenesis. **(A)** Schematic representing human brain microvascular endothelial cells (HBMVECs) cultured in control conditioned medium (Con-CM; conditioned medium from U373 cells) or GDF15-CM (conditioned medium from rhGDF15-stimulated U373 cells); **(B)** *KDR* mRNA expression in HBMVECs was measured using quantitative reverse transcription polymerase chain reaction (qRT-PCR). **(C)** Phosphorylation of KDR was examined using western blotting (β-actin as used as loading control); **(D)** Wound healing assay results. The day before the experiment, HBMVECs were seeded in 12-well plates (1.5×10^5/well). The monolayer was scratched to introduce a wound and treated with Con-CM or GDF15-CM. The migration of cells into the wound area was analyzed after 24 h (significance compared with the cells cultured in Con-CM). **(E)** Tube formation assay results. HBMVECs (1.5×10^5 cells) were incubated on Matrigel matrix for 3 days with Con-CM or GDF15-CM. The tube length was measured using ImageJ angiogenesis analyzer (significance was compared with the cells cultured in Con-CM). ($^*p < 0.05$ and $^{***}p < 0.001$ compared with the cells cultured in Con-CM).

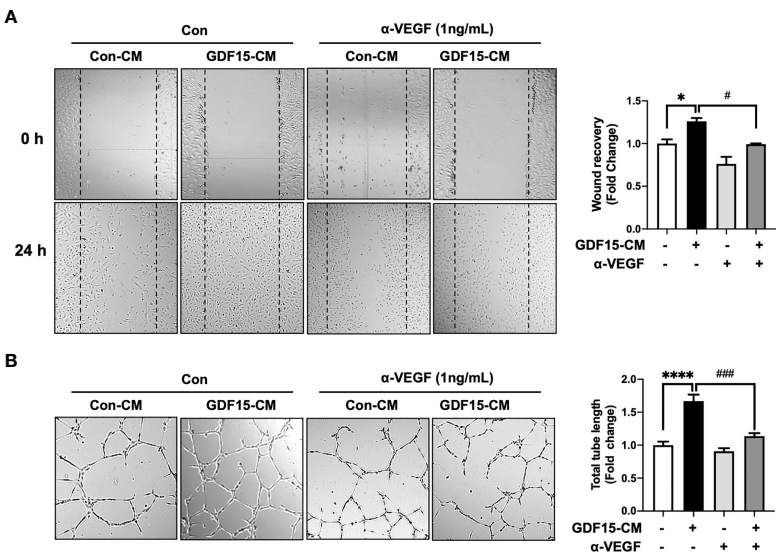

FIGURE 5 | Anti-VEGF antibody blocks GDF15 mediated angiogenesis. **(A)** Wound healing assay was performed using human brain microvascular endothelial cells (HBMVECs) in the absence/presence of anti-VEGF antibody. The day before the experiment, HBMVECs were seeded in 12-well plates (1.5×10^5/well). The monolayer was scratched to introduce a wound and cells were cultured with control conditioned medium (Con-CM; conditioned medium from HBMVECs) or GDF15-CM HBMVECs (conditioned medium from rhGDF15-stimulated HBMVECs) with added control antibody or α-VEGF (1 ng/mL each). The wounded areas were photographed at 0 h and 24 h and the cell migration as percent mean distance migration was assessed. **(B)** Representative photographs of tube formation assay. HBMVECs (1.5×10^5 cells) were incubated on Matrigel matrix for 12 h with Con-CM or GDF15-CM in the presence or absence of α-VEGF (1 ng/mL). The tube length was measured using ImageJ angiogenesis analyzer (significance was compared with the group Con-CM in the absence of α-VEGF). Data are presented as the mean ± standard error ($^*p < 0.01$ and $^{****}p < 0.001$ compared with the non-treated CM control; $^{\#}p < 0.05$ and $^{\#\#\#}p < 0.001$ compared with rhGDF15- CM group).

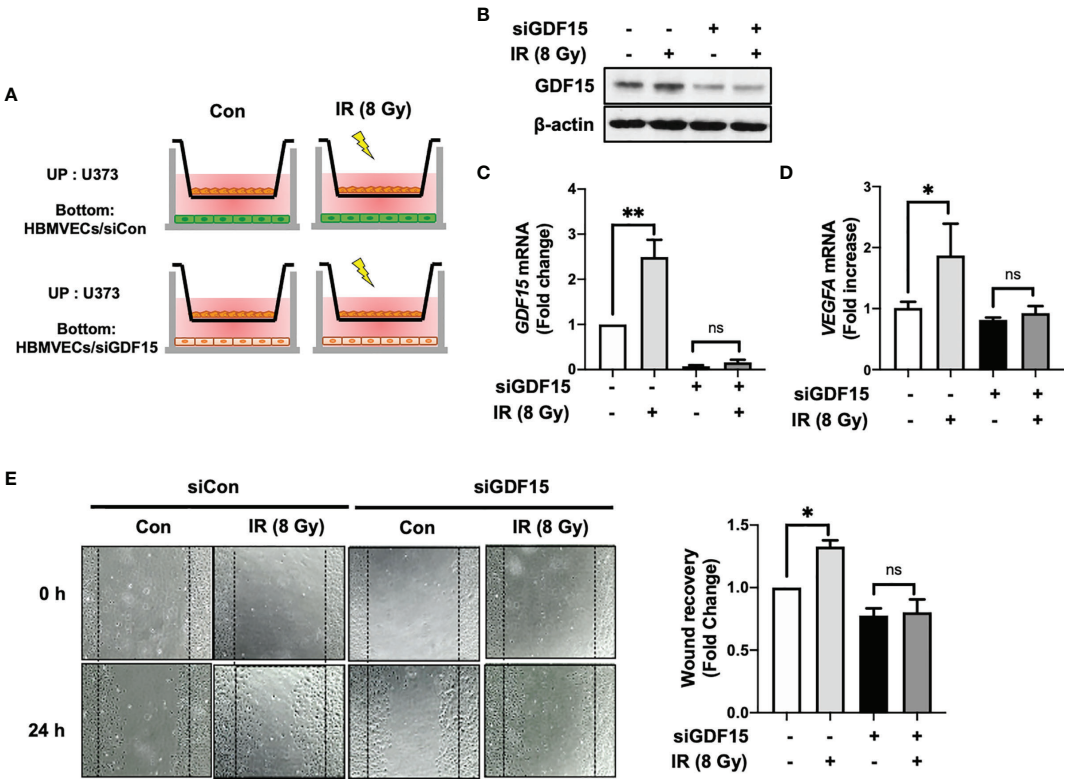

FIGURE 6 | *GDF15* knockdown suppresses ionizing radiation (IR)-induced wound recovery. **(A)** Graphic experimental scheme; for the co-culture of U373 cells and human brain microvascular endothelial cells (HBMVECs), U373 cells were seeded on the upper well and the siGDF15-transfected or siCon-transfected HBMVECs were seeded on the bottom well. After irradiation with 8 Gy IR, U373 cells and HBMVECs were co-cultured for 24 h. **(B)** In HBMVECs, the protein levels of GDF15 were examined by immunoblotting analysis 24 h post-IR exposure. **(C)** In HBMVECs, the levels of *GDF15* mRNA were determined using quantitative reverse transcription polymerase chain reaction 24 h post-IR exposure. **(D)** In U373 cells, the levels of *VEGFA* mRNA were determined using qRT-PCR 24 h post-IR exposure. **(E)** For the wound healing assay, the HBMVECs on the plate were scratched and incubated for 24 h after irradiation with 8 Gy IR. The wound recovery rates were assessed using ImageJ. Data are presented as the mean ± standard deviation of three experiments. $^{*}p < 0.05$ and $^{**}p < 0.01$ compared with siCon-transfected and nonirradiated HBMVECs. ns, no significance.

DISCUSSION

As angiogenesis is a key event for the progression of GBM, various studies have proposed chemotherapy, radiation, or combined treatment modalities to inhibit this process in GBM (3, 4). However, radiation can stimulate angiogenesis by promoting the release of various cytokines from different cell types, including cancer cells, immune cells, and ECs, into the glioma microenvironment (26, 27). To inhibit radiation-induced angiogenesis, the interactions between various components of the tumor microenvironment must be elucidated. Therefore, this study examined the role of GDF15, which is one of the cytokines released from the tumor microenvironment, in the cross-talk between ECs and glioma cells irradiated with IR. The findings of this study indicated that radiation-induced HBMVEC-derived GDF15 promoted VEGFA production in U373 glioma cells and consequently enhanced angiogenesis in glioma.

In this study, IR directly upregulated GDF15 expression and secretion in HBMVECs (**Figure 1**). The upregulated GDF15 levels in the blood or cerebrospinal fluid are reported to be correlated with poor survival in patients with GBM (28). Hence, the effect of rhGDF15 on the proliferation and migration abilities of glioma cells was examined in this study. Ideally, the CM should be collected from the ECs following IR. However, radiation stimulates the release of diverse angiocrine factors from ECs post IR (29). Since the irradiated CM would contain other cytokines in addition to GDF15, we cannot be certain whether the induction of VEGF expression is caused by GDF15 alone or by other factors. Therefore, we determined whether GDF15 directly modulated proliferation/migration of glioma cells or induced VEGF expression in U373 cells (**Figure 2**). GDF15 is reported to promote the growth of ovarian and prostate cancers (16, 17). However, rhGDF15 treatment did not affect the proliferation and migration of U373 cells in this study but markedly promoted VEGFA production in U373 cells through the p-MAPK1/SP1 pathway. This finding is consistent with that of Griner et al. (16) who reported that exogenous GDF15 treatment and endogenous GDF15 overexpression stimulated the phosphorylation of p38, Erk1/2, and Akt. Consistent with the findings of this study, Mielcarska et al.

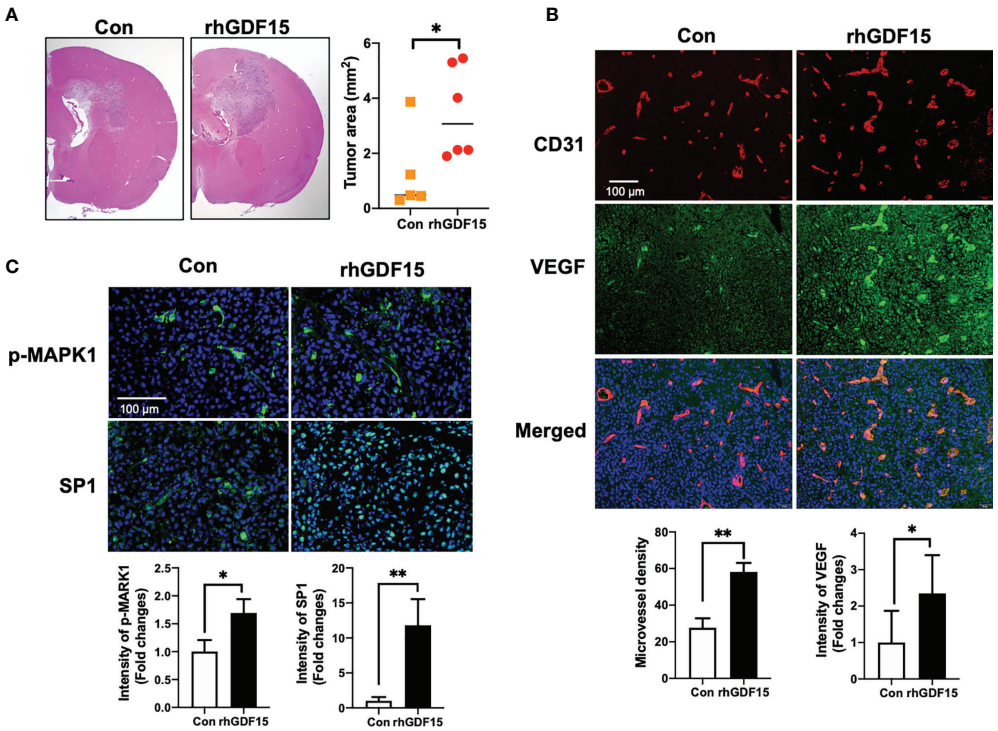

FIGURE 7 | GDF15 promotes angiogenesis by stimulating VEGFA secretion in the brain tumor. **(A)** Representative section of the brain tumors from mice injected with control U373 cells and rhGDF15-stimulated U373 cells. The brain sections were stained with hematoxylin and eosin. The brain tumor area was measured using ImageJ. **(B)** VEGFA (green) and CD31-positive endothelial cells (red) in mouse brain tumor tissues were analyzed using immunofluorescence staining. Microvessel density was counted as the number of CD31-positive vessels. Scale bar = 100 μm. **(C)** Representative image of immunofluorescence analysis of the phosphorylation of MAPK1 (p-MAPK1; upper panel; green) and expression of SP1 (upper panel; green) counterstained with 4′,6-diamidino-2-phenylindole (DAPI) (blue). Scale bar = 100 μm. Fluorescence intensity was calculated using ImageJ as follows: Corrected total cell fluorescence = integrated density – (area of selected cell × mean fluorescence of background readings). Data are presented as the mean ± standard (control group, n = 5; rhGDF15-treated group; n = 6), * $p < 0.05$ and ** $p < 0.01$ compared with control group.

reported that increased GDF15 levels were correlated with VEGFA production in colorectal cancer. These findings demonstrate the mechanism of GDF15 in radiation-induced angiogenesis in glioma. As shown in **Figure 8**, GDF15 promotes tumor angiogenesis through a positive feedback loop comprising EC-secreted GDF15, glioma-derived VEGFA, and KDR on ECs. IR promotes GDF15 secretion from the ECs, which leads to the secretion of VEGF from the glioma cells. VEGF activates ECs by binding to KDR and consequently promotes angiogenesis. To the best of our knowledge, this is the first study to propose a mechanism for GDF15-mediated angiogenesis involving the cross-talk between ECs and glioma cells.

Furthermore, this study demonstrated the *in vivo* effect of GDF15 on brain tumor angiogenesis. Consistent with the *in vitro* results, we observed that orthotopic brain tumors injected with rhGDF15-exposed glioma cells showed increased VEGF expression and enhanced angiogenesis than control tumors. However, this study has some limitations. First, to validate whether the observed angiogenesis in the tumors is mediated by an increase in VEGF expression levels in U373 cells, further *in vivo* studies using VEGF inhibiting agents or VEGF-knockdown U373 cells are needed. Second, this study only examined the interaction between ECs and glioma cells using rhGDF15. Generally, IR dose fractionation is administered to brain tumor patients over several weeks. In fact, brain tumor cells are continuously and repeatedly exposed to the GDF15-secreting ECs. We treated U373 cells with rhGDF15 for 2 weeks prior to injecting them into the mouse brains to mimic the secretion of GDF15 from ECs to the tumor microenvironment. Therefore, our method does not sufficiently mimic the actual tumor microenvironment *in vivo*. Nevertheless, we can reveal the association of tumor growth and angiogenesis with GDF15 alone. Finally, complex intercellular communication is involved in tumor progression and angiogenesis. Therefore, further studies are required to examine the interaction of GDF15 with other components of the tumor microenvironment, including macrophages and fibroblasts.

In summary, this study demonstrated that IR directly promotes the secretion of GDF15 from brain ECs and that GDF15 activates the *VEGFA* promoter in glioma cells through

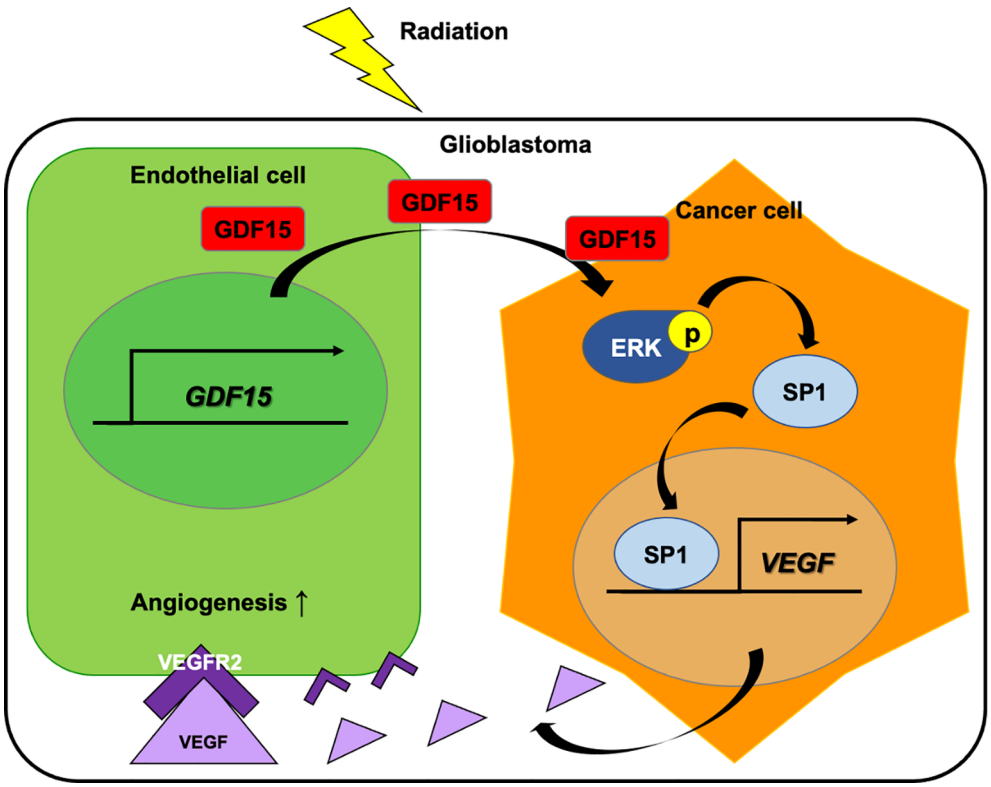

FIGURE 8 | Role of GDF15 in ionizing radiation (IR)-induced angiogenesis in glioblastoma. Radiation upregulates GDF15 expression in the endothelial cells (ECs). EC-derived GDF15 activates the p-MAPK1/SP1 pathway in glioblastoma cells. SP1 stimulates the promoter activity of VEGF. The upregulated VEGF levels induce angiogenesis in glioblastoma through p-KDR on ECs.

the p-MAPK1/SP1 pathway and consequently enhances angiogenesis in orthotopic brain tumors. These results suggest that radiotherapy-induced GDF15 secretion may contribute to tumor recurrence or therapy resistance by mediating the cross-talk between brain cancer cells and ECs. Therefore, GDF15 is a potential therapeutic target for glioblastoma.

DATA AVAILABILITY STATEMENT

The datasets presented in this study can be found in online repositories. The names of the repository/repositories and accession number(s) can be found in the article/**Supplementary Material**.

ETHICS STATEMENT

The animal study was reviewed and approved by Institutional Animal Care and Use Committee of the Korea Institute of Radiological and Medical Sciences (Approval no. KIRAMS2018-0079). Written informed consent was obtained from the owners for the participation of their animals in this study.

AUTHOR CONTRIBUTIONS

HP and K-SN performed molecular and cellular experiments. HP generated and analyzed the data. HP and H-JL designed and performed animal experiments. H-JL and KK reviewed the data, prepared the manuscript, and supervised the work. All authors contributed to the article and approved the submitted version.

FUNDING

This work was supported by grants from the National Research Foundation (NRF-2020M2C8A2069337) and a grant from the Korea Institute of Radiological and Medical Sciences (50531–2021), which is funded by the Ministry of Science and Information and Communications Technology of the Korean government.

SUPPLEMENTARY MATERIAL

The Supplementary Material for this article can be found online at: https://www.frontiersin.org/articles/10.3389/fonc.2022.801230/full#supplementary-material

REFERENCES

1. Bulnes S, Bengoetxea H, Ortuzar N, Argandona EG, Garcia-Blanco A, Rico-Barrio I, et al. Angiogenic Signalling Pathways Altered in Gliomas: Selection Mechanisms for More Aggressive Neoplastic Subpopulations With Invasive Phenotype. *J Signal Transduct* (2012) 2012:597915. doi: 10.1155/2012/597915
2. Plate KH, Scholz A, Dumont DJ. Tumor Angiogenesis and Anti-Angiogenic Therapy in Malignant Gliomas Revisited. *Acta Neuropathol* (2012) 124 (6):763–75. doi: 10.1007/s00401-012-1066-5
3. Ahir BK, Engelhard HH, Lakka SS. Tumor Development and Angiogenesis in Adult Brain Tumor: Glioblastoma. *Mol Neurobiol* (2020) 57(5):2461–78. doi: 10.1007/s12035-020-01892-8
4. Wong ML, Prawira A, Kaye AH, Hovens CM. Tumour Angiogenesis: Its Mechanism and Therapeutic Implications in Malignant Gliomas. *J Clin Neurosci* (2009) 16(9):1119–30. doi: 10.1016/j.jocn.2009.02.009
5. Hida K, Maishi N, Annan DA, Hida Y. Contribution of Tumor Endothelial Cells in Cancer Progression. *Int J Mol Sci* (2018) 19(5):1272. doi: 10.3390/ijms19051272
6. Zuazo-Gaztelu I, Casanovas O. Unraveling the Role of Angiogenesis in Cancer Ecosystems. *Front Oncol* (2018) 8:248. doi: 10.3389/fonc.2018.00248
7. Tamura R, Tanaka T, Miyake K, Yoshida K, Sasaki H. Bevacizumab for Malignant Gliomas: Current Indications, Mechanisms of Action and Resistance, and Markers of Response. *Brain Tumor Pathol* (2017) 34(2):62–77. doi: 10.1007/s10014-017-0284-x
8. Yock TI, Tarbell NJ. Technology Insight: Proton Beam Radiotherapy for Treatment in Pediatric Brain Tumors. *Nat Clin Pract Oncol* (2004) 1(2):97–103. doi: 10.1038/ncponc0090
9. Seo YS, Ko IO, Park H, Jeong YJ, Park JA, Kim KS, et al. Radiation-Induced Changes in Tumor Vessels and Microenvironment Contribute to Therapeutic Resistance in Glioblastoma. *Front Oncol* (2019) 9:1259. doi: 10.3389/fonc.2019.01259
10. Kim EJ, Lee H, Lee YJ, Sonn JK, Lim YB. Ionizing Radiation Regulates Vascular Endothelial Growth Factor-A Transcription in Cultured Human Vascular Endothelial Cells *Via* the PERK/eIF2alpha/ATF4 Pathway. *Int J Radiat Oncol Biol Phys* (2020) 107(3):563–70. doi: 10.1016/j.ijrobp.2020.03.003
11. Moeller BJ, Cao Y, Li CY, Dewhirst MW. Radiation Activates HIF-1 to Regulate Vascular Radiosensitivity in Tumors: Role of Reoxygenation, Free Radicals, and Stress Granules. *Cancer Cell* (2004) 5(5):429–41. doi: 10.1016/s1535-6108(04)00115-1
12. Coll AP, Chen M, Taskar P, Rimmington D, Patel S, Tadross JA, et al. GDF15 Mediates the Effects of Metformin on Body Weight and Energy Balance. *Nature* (2020) 578(7795):444–8. doi: 10.1038/s41586-019-1911-y
13. Ost M, Igual Gil C, Coleman V, Keipert S, Efstathiou S, Vidic V, et al. Muscle-Derived GDF15 Drives Diurnal Anorexia and Systemic Metabolic Remodeling During Mitochondrial Stress. *EMBO Rep* (2020) 21(3):e48804. doi: 10.15252/embr.201948804
14. Kempf T, Eden M, Strelau J, Naguib M, Willenbockel C, Tongers J, et al. The Transforming Growth Factor-Beta Superfamily Member Growth-Differentiation Factor-15 Protects the Heart From Ischemia/Reperfusion Injury. *Circ Res* (2006) 98(3):351–60. doi: 10.1161/01.RES.0000202805.73038.48
15. Park H, Kim CH, Jeong JH, Park M, Kim KS. GDF15 Contributes to Radiation-Induced Senescence Through the ROS-Mediated P16 Pathway in Human Endothelial Cells. *Oncotarget* (2016) 7(9):9634–44. doi: 10.18632/oncotarget.7457
16. Griner SE, Joshi JP, Nahta R. Growth Differentiation Factor 15 Stimulates Rapamycin-Sensitive Ovarian Cancer Cell Growth and Invasion. *Biochem Pharmacol* (2013) 85(1):46–58. doi: 10.1016/j.bcp.2012.10.007
17. Wang W, Yang X, Dai J, Lu Y, Zhang J, Keller ET. Prostate Cancer Promotes a Vicious Cycle of Bone Metastasis Progression Through Inducing Osteocytes to Secrete GDF15 That Stimulates Prostate Cancer Growth and Invasion. *Oncogene* (2019) 38(23):4540–59. doi: 10.1038/s41388-019-0736-3
18. Lu X, He X, Su J, Wang J, Liu X, Xu K, et al. EZH2-Mediated Epigenetic Suppression of GDF15 Predicts a Poor Prognosis and Regulates Cell Proliferation in Non-Small-Cell Lung Cancer. *Mol Ther Nucleic Acids* (2018) 12:309–18. doi: 10.1016/j.omtn.2018.05.016
19. Vanhara P, Hampl A, Kozubik A, Soucek K. Growth/differentiation Factor-15: Prostate Cancer Suppressor or Promoter? *Prostate Cancer Prostatic Dis* (2012) 15(4):320–8. doi: 10.1038/pcan.2012.6
20. Wang X, Baek SJ, Eling TE. The Diverse Roles of Nonsteroidal Anti-Inflammatory Drug Activated Gene (NAG-1/GDF15) in Cancer. *Biochem Pharmacol* (2013) 85(5):597–606. doi: 10.1016/j.bcp.2012.11.025
21. Ramanathan M, Giladi A, Leibovich SJ. Regulation of Vascular Endothelial Growth Factor Gene Expression in Murine Macrophages by Nitric Oxide and Hypoxia. *Exp Biol Med (Maywood)* (2003) 228(6):697–705. doi: 10.1177/153537020322800608
22. Curry JM, Eubank TD, Roberts RD, Wang Y, Pore N, Maity A, et al. M-CSF Signals Through the MAPK/ERK Pathway *via* Sp1 to Induce VEGF Production and Induces Angiogenesis *In Vivo*. *PloS One* (2008) 3(10): e3405. doi: 10.1371/journal.pone.0003405
23. Feng J, Zhang Y, Xing D. Low-Power Laser Irradiation (LPLI) Promotes VEGF Expression and Vascular Endothelial Cell Proliferation Through the Activation of ERK/Sp1 Pathway. *Cell Signal* (2012) 24(6):1116–25. doi: 10.1016/j.cellsig.2012.01.013
24. Yana I, Sagara H, Takaki S, Takatsu K, Nakamura K, Nakao K, et al. Crosstalk Between Neovessels and Mural Cells Directs the Site-Specific Expression of MT1-MMP to Endothelial Tip Cells. *J Cell Sci* (2007) 120(Pt 9):1607–14. doi: 10.1242/jcs.000679
25. Bouquet F, Pal A, Pilones KA, Demaria S, Hann B, Akhurst RJ, et al. TGFbeta1 Inhibition Increases the Radiosensitivity of Breast Cancer Cells *In Vitro* and Promotes Tumor Control by Radiation *In Vivo*. *Clin Cancer Res* (2011) 17 (21):6754–65. doi: 10.1158/1078-0432.CCR-11-0544
26. Tabatabai G, Frank B, Mohle R, Weller M, Wick W. Irradiation and Hypoxia Promote Homing of Haematopoietic Progenitor Cells Towards Gliomas by TGF-Beta-Dependent HIF-1alpha-Mediated Induction of CXCL12. *Brain* (2006) 129(Pt 9):2426–35. doi: 10.1093/brain/awl173
27. Zhou W, Jiang Z, Li X, Xu Y, Shao Z. Cytokines: Shifting the Balance Between Glioma Cells and Tumor Microenvironment After Irradiation. *J Cancer Res Clin Oncol* (2015) 141(4):575–89. doi: 10.1007/s00432-014-1772-6
28. Codo P, Weller M, Kaulich K, Schraivogel D, Silginer M, Reifenberger G, et al. Control of Glioma Cell Migration and Invasiveness by GDF-15. *Oncotarget* (2016) 7(7):7732–46. doi: 10.18632/oncotarget.6816
29. Nolan DJ, Ginsberg M, Israely E, Palikuqi B, Poulos MG, James D, et al. Molecular Signatures of Tissue-Specific Microvascular Endothelial Cell Heterogeneity in Organ Maintenance and Regeneration. *Dev Cell* (2013) 26 (2):204–19. doi: 10.1016/j.devcel.2013.06.017

Conflict of Interest: The authors declare that the research was conducted in the absence of any commercial or financial relationships that could be construed as a potential conflict of interest.

frontiers in Cell and Developmental Biology

REVIEW
published: 02 March 2022
doi: 10.3389/fcell.2022.752818

Tumor-Derived Exosomes Modulate Primary Site Tumor Metastasis

*Suwen Bai[1,2†], Zunyun Wang[2†], Minghua Wang[1], Junai Li[1], Yuan Wei[1], Ruihuan Xu[1] and Juan Du[1]**

[1]*Longgang District People's Hospital of Shenzhen, The Second Affiliated Hospital of The Chinese University of Hong Kong, Shenzhen, China,* [2]*School of Basic Medical Sciences, Anhui Medical University, Hefei, China*

Tumor-derived exosomes (TDEs) are actively produced and released by tumor cells and carry messages from tumor cells to healthy cells or abnormal cells, and they participate in tumor metastasis. In this review, we explore the underlying mechanism of action of TDEs in tumor metastasis. TDEs transport tumor-derived proteins and non-coding RNA to tumor cells and promote migration. Transport to normal cells, such as vascular endothelial cells and immune cells, promotes angiogenesis, inhibits immune cell activation, and improves chances of tumor implantation. Thus, TDEs contribute to tumor metastasis. We summarize the function of TDEs and their components in tumor metastasis and illuminate shortcomings for advancing research on TDEs in tumor metastasis.

Keywords: tumor-derived exosomes, metastasis, pre-metastatic niche, angiogenesis, immunosuppression

OPEN ACCESS

Edited by:
Peti Thuwajit,
Mahidol University, Thailand

Reviewed by:
Nabanita Chatterjee,
The Ohio State University, United States
Paola Massimi,
International Centre for Genetic Engineering and Biotechnology, Italy

****Correspondence:***
Juan Du
dujuan@cuhk.edu.cn

[†]These authors have contributed equally to this work and share first authorship

Specialty section:
This article was submitted to Molecular and Cellular Oncology, a section of the journal Frontiers in Cell and Developmental Biology

Received: *03 August 2021*
Accepted: *10 February 2022*
Published: *02 March 2022*

Citation:
Bai S, Wang Z, Wang M, Li J, Wei Y, Xu R and Du J (2022) Tumor-Derived Exosomes Modulate Primary Site Tumor Metastasis. Front. Cell Dev. Biol. 10:752818. doi: 10.3389/fcell.2022.752818

BACKGROUND

Exosomes are extracellular vesicles, approximately 30–150 nm in diameter, that contain functional biomolecules, such as proteins, RNA, DNA, and lipids, and can interact with recipient cells (Balaj et al., 2011; Choi et al., 2013; Peinado et al., 2011; Raposo and Stoorvogel, 2013; Skog et al., 2008; Thakur et al., 2014; Thery et al., 2009; Valadi et al., 2007). Exosomes are present in various body fluids and are regarded as a key component of intercellular communication. Tumor cell-, stromal cell-, or even normal cell–derived exosomes play an important role in tumor progression and can induce angiogenesis and accelerate metastasis (Hood et al., 2011; Luga et al., 2012; Peinado et al., 2012). The components and functions of the exosomes depend on the cell types; some studies have shown many differences in the contents and release rate in different types of cells. But, the complete mechanism and process have not yet been elucidated and need to be further explored. Metastasis is the leading cause of tumor-induced death and is a complex process involving local invasion, survival, and evasion from immunosurveillance, invasion into circulation, and extravasation at secondary organs (Fidler and Kripke, 2015; Wan et al., 2013). Tumor-derived exosomes (TDEs) are a significant component of the tumor microenvironment and are involved in promoting tumor metastasis through several mechanisms, including acquiring primary tumor migration capacity, tumor angiogenesis, escaping immune system organotropic metastasis, forming the pre-metastatic niche, and metastatic tumor growth in the secondary site.

In this review, we summarize the function of exosomes in every aspect of cancer metastasis (**Figure 1**) to provide a better systematic comprehension of the role of exosomes in tumor metastasis and propose practical implications of early diagnosis, treatment, and prognostic methods for cancer.

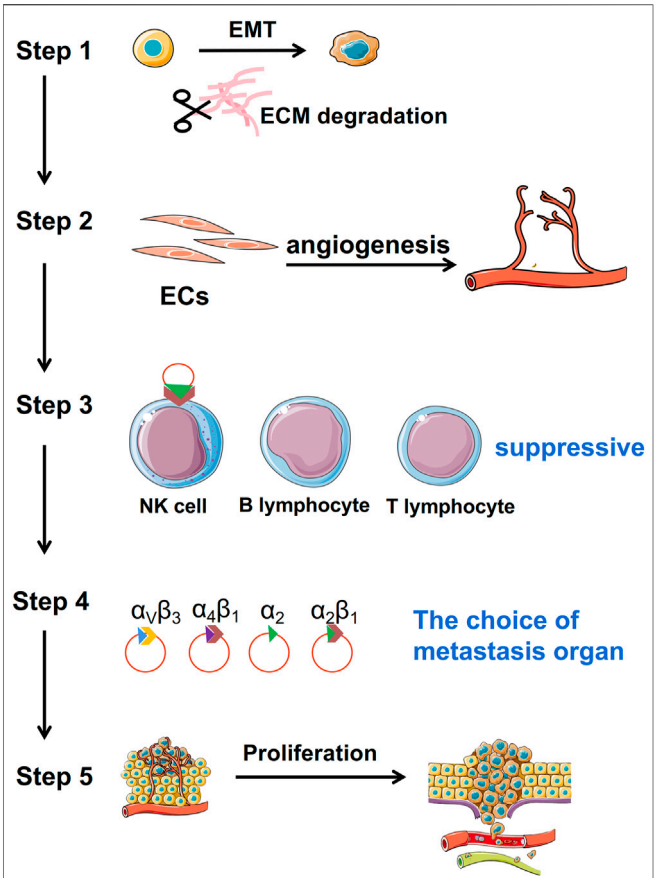

FIGURE 1 | Function of TDEs in tumor metastasis. TDEs are mainly involved in tumor metastasis through five aspects. Step 1: acquisition of tumor migration ability; Step 2: angiogenesis; Step 3: immunosuppression; Step 4: localization of metastatic sites; and Step 5: enhancement of proliferation ability of tumor cells after migration.

TUMOR-DERIVED EXOSOMES ENHANCE THE MIGRATION ABILITY OF TUMOR CELLS

Tumor-Derived Exosomes Promote Epithelial–Mesenchymal Transition to Initiate Metastasis

Epithelial–mesenchymal transition (EMT) frequently initiates the metastatic process (Li et al., 2021). Epithelial tumor cells acquire mesenchymal characteristics under the influence of cancer-associated fibroblasts (CAFs) in the tumor stroma (Diepenbruck and Christofori, 2016). Epithelial markers, including E-cadherin, zona occludens 1 (ZO-1), cytokeratins, desmoplakin, and laminin, are downregulated, and mesenchymal markers, including N-cadherin, β-catenin, and vimentin, are upregulated (Sommers et al., 1994; Li Y. et al., 2019). During EMT, tumor cells lose their apical–basal polarity, basement anchoring, and cell–cell junctions and switch to a low proliferation state with enhanced migratory and invasion capabilities (Basil et al., 2020). Once the tumor cells reach a distant pre-metastatic niche, the reversed process takes place (Maren, 2016). This so-called mesenchymal–epithelial transition (MET) returns tumor cells to a high proliferative state and enables the formation of micrometastases (Bakir et al., 2019). TDEs play an important regulatory role in mediating the EMT and MET transformation (Bigagli et al., 2019). There has been increasing research showing the signaling pathway involved in inducing cancer-related EMT. We propose that the critical components in TDEs can serve to promote EMT.

The latest hypothesis is TDEs may be conduits for initiating signals for EMT. For example, TDEs carry EMT derivers, such as transforming growth factor-beta (TGF-β), tumor necrosis factor-alpha (TNF-α), hypoxia-inducible factor 1 alpha (HIF-1α), protein kinase B (AKT), caveolin-1, platelet-derived growth factors (PDGFs), and β-catenin Wnt pathway modulators, that directly enhance the process of EMT (Aga et al., 2014; Kucharzewska et al., 2013; Luga et al., 2012; Ramteke et al., 2015). TDEs transmit non-coding RNA, such as, miR-128-3p, miR-27, LINC00960, linc02470, circ-PVT1, and circ-CPA4, that upregulate EMT (Huang C.-S. et al., 2020; Liu et al., 2019; Wang J. et al., 2018). Therefore, many studies have shown that tumor

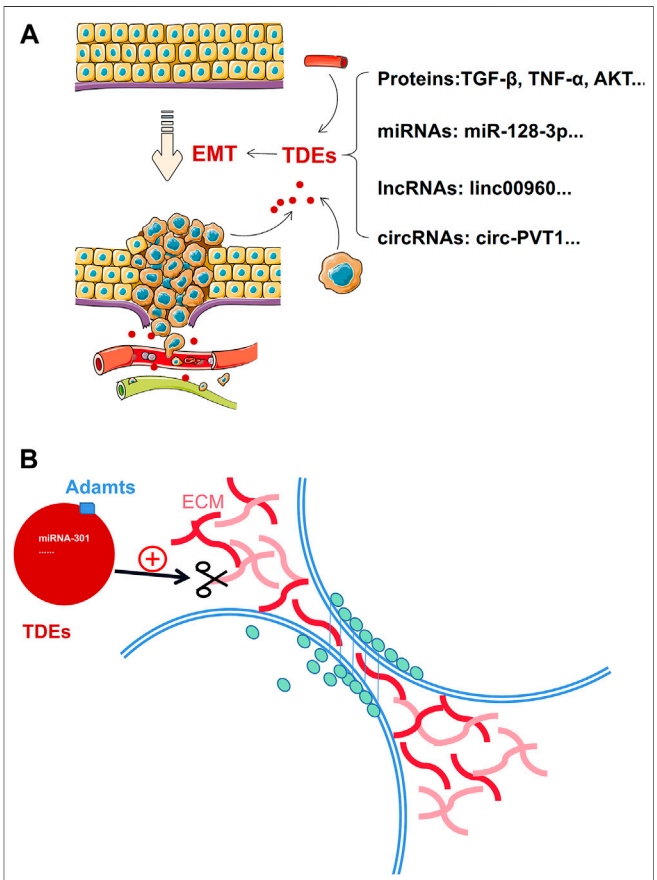

FIGURE 2 | TDEs enhance the migration ability of tumor cells by promoting EMT and degrading the ECM. **(A):** Exosomes carry proteins, miRNA, lncRNA, and circRNA to promote the occurrence and development of EMT. **(B)**: TDEs carry proteins or non-coding RNA to initiate degradation of the ECM.

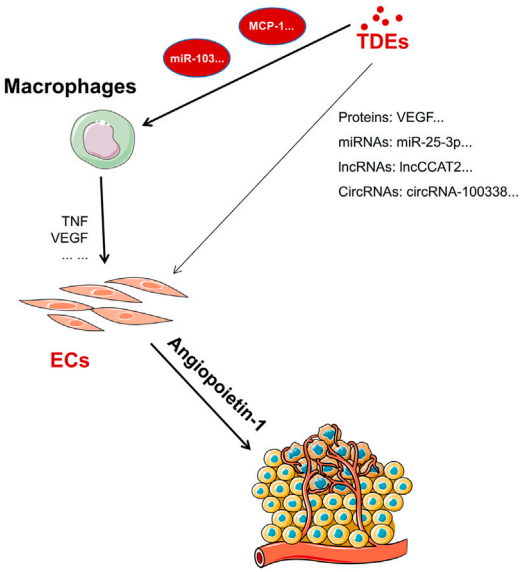

FIGURE 3 | Exosomes directly or indirectly promote angiogenesis. TDEs promote macrophages to release TNF and VEGF to promote angiogenesis factors by carrying miRNAs or proteins. In addition, TDEs carry proteins, miRNAs, lncRNA, or circRNA to promote angiogenesis directly by targeting endothelial cells.

cells can secrete exosomes into the extracellular space and promote the EMT through their effectors: proteins, miRNAs, circRNAs, and lncRNAs (**Figure 2A**).

Tumor-Derived Exosomes Promote Extracellular Matrix Degradation

The extracellular matrix (ECM) is a scaffold for tissues and organs (Eble and Niland, 2019). The ECM is a complex network combined with proteins, proteoglycans, and glycoproteins that can regulate cell growth, survival, motility, and differentiation through specific receptors, such as integrin, syndecan, and discoidin receptors (Leitinger, 2011; Xian et al., 2010). Cancer-associated ECM is not only an integral feature of a tumor but also actively contributes to its histopathology and malignant behavior (Levental et al., 2009; Provenzano et al., 2008). From tumor initiation to metastasis, ECM molecules bind with cell surface receptors and activate intracellular signaling pathways. ECM adhesion–induced signals promote self-sufficient growth through mitogen-activated protein kinase (MAPK) and phosphatidylinositol 3-kinase (PI3K) (Pylayeva et al., 2009). Focal adhesion kinase (FAK) signaling inhibits p15 and p21, which are growth suppressors, and p53 to limit the induction of apoptosis (Kim et al., 2008). TGF-β and RhoA/Rac signaling promote EMT induction and enhance promigratory pathways (Leight et al., 2012). The ECM can also enhance angiogenesis and strengthen vascular endothelial growth factor (VEGF) signaling in endothelial cells (Liu and Agarwal, 2010).

TDEs mediate tumor–tumor and tumor–host cell crosstalk (Kalluri, 2016). TDEs interact with and regulate the synthesis of ECM components and are involved in ECM remodeling (Rackov et al., 2018). The proteins on the surface of TDEs promote the activation of membrane-associated proteinases, such as Adamts1, Adamts4, and Adamts5, thus improving proteolytic activity (Ginestra et al., 1997; Lo Cicero et al., 2012). In addition, matrix metalloproteinases (MMPs) derived from TDEs participate in localized degradation and ECM proteolysis during cellular migration and metastasis (Ginestra et al., 1997; Atay et al., 2014). However, besides exosomal surface proteins, non-coding RNA also mediates ECM degradation. For example, breast cancer–derived exosomes carry miR-301 to regulate matrix modulation (Morad et al., 2020). Gastric cancer cell–derived exosomal miR-27a reshapes the ECM at adjacent sites and promotes tumor progression by downregulating CSRP2 expression and upregulating α-SMA expression (Wang et al., 2018). Currently, there are no direct reports on other non-coding RNAs, such as lncRNA and cicrRNA, but TDE-derived lncRNA and circRNA can influence fibroblast, chondrocyte, and epithelial cell function, secreting ECM components into the extracellular space (Tan et al., 2020).

Some data suggested that the ECM is a prerequisite for tumor cell invasion and metastasis (Tan et al., 2020). When the tumor cells metastasize, they detach from the ECM. Furthermore, the exosomes participate in this process (**Figure 2B**).

TUMOR-DERIVED EXOSOMES PROMOTE ANGIOGENESIS DIRECTLY OR INDIRECTLY

Regardless of tumor size, metastasis may occur; however, in most cases, metastasis is associated with large primary neoplasms (Fidler and Kripke, 2015). If a tumor mass exceeds 1 mm in diameter, angiogenesis is bound to occur (Folkman, 1971; Nagy and Dvorak, 2012). Therefore, exploring tumor angiogenesis is an important way to understand tumor metastasis.

Tumor-Derived Exosomes Promote Angiogenesis by Activating Macrophages

Cancer-derived exosomes stimulate macrophage infiltration and polarization for establishing a pre-metastatic niche. For example, exosomes derived from CT-26, a colon cancer cell, can provoke macrophages to secrete significantly high levels of monocyte chemoattractant protein-1 (MCP-1) and TNF, thus promoting the growth and migration of colorectal cancer cells. Lung cancer cell–derived exosomes containing miRNA-103 upregulate angiogenic VEGF-A and angiopoietin-1 expression from M2 macrophages (Hsu et al., 2018; Wu et al., 2019). Therefore, TDEs can motivate the angiogenic property of macrophages such as secretion of VEGF (Wu et al., 2019). It can induce angiogenesis by tumor cells. In addition, other immune cells also contribute to tumor angiogenesis, such as neutrophils, myeloid precursor cells (MPCs), and dendritic cells (DCs) (Albini et al., 2018). But, there are no reports about TDE-educated neutrophils, MPCs, or DCs to promote angiogenesis in metastasis.

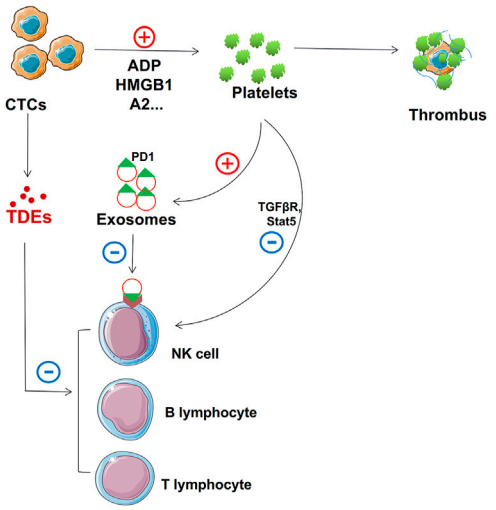

FIGURE 4 | Role of TDEs in protecting CTCs. TDEs from CTCs and activated platelets suppress NK cell, T cell, and B cell function. In addition, activated platelets can form thrombi that adhere to the surface to protect CTCs.

Tumor-Derived Exosomes Carry Non-coding RNA and Proteins to Promote Angiogenesis Directly

TDEs carry non-coding RNAs, including microRNA, lncRNA, and circRNA, that play an indispensable role in angiogenesis. TDEs carry miR-25-3p that regulates VEGFR2, ZO-1, occludin, and claudin5 expression in ECs by targeting KLF2 and KLF4 and eventually promotes vascular permeability and angiogenesis (Felcht et al., 2012; Wu et al., 2019). TDEs deliver miR-130a to vascular cells to promote angiogenesis by targeting c-MYB (Yang et al., 2018). Exosomal miR-155-5p can induce angiogenesis through the SOCS1/JAK2/STAT3 signaling pathway (Zhou X. et al., 2018). Exosomal miR-135b promotes angiogenesis by inhibiting FOXO1 expression. Exosomal miR-23a induces angiogenesis by targeting TSGA10, prolyl hydroxylase, tight junction protein ZO-1, and SIRT1 (Sruthi et al., 2018; Bai et al., 2019). Exosomal miR-1229 promotes angiogenesis by targeting HIPK2. Exosomal miR-21 promotes angiogenesis by targeting STAT3 (Liu and Cao et al., 2016). In addition, lncRNA containing lncCCAT2, lncMALAT1, lncRNA-p21, and lncPOU3F3 or circRNA, such as TDE-derived circRNA-100338, also promote angiogenesis (Castellano et al., 2020; Huang X.-Y. et al., 2020; Lang, Hu, & Chen et al., 2017; Lang, Hu, &; Zhang Z. et al., 2017; Qiu J.-J. et al., 2018). LncRNA and circRNA are often used as "sponges" to regulate miRNA expression in cells. Moreover, TDEs carry a variety of angiogenic proteins, such as VEGF, IGFBP3, MMP2, ICAM-1, and IL-8, thus enhancing angiogenesis through *in vitro* and *in vivo* ligand/receptor signaling (Ludwig and Whiteside, 2018). Therefore, a combination of multiple non-coding RNAs and exosomal proteins promotes tumor angiogenesis.

The importance of angiogenesis in tumor metastasis cannot be understated, TDEs can carry proteins and non-coding RNAs that directly promote angiogenesis or they can mediate angiogenesis indirectly by "educating" macrophages to release proangiogenic factors (**Figure 3**).

TUMOR-DERIVED EXOSOMES CAN PROTECT TUMOR CELLS DURING METASTASIS

Tumor cells shed from primary or secondary tumors are called circulating tumor cells (CTCs) (Paoletti and Hayes, 2016). CTCs invade the bloodstream and attach to the endothelium in the target organ. They then invade the surrounding parenchyma to form new tumors (Garcia et al., 2018). Blood is an unfavorable environment for CTCs, and they struggle with circulating immune cells (Agarwal et al., 2018). TDEs help CTCs metastasize smoothly by inhibiting immune cell activity and conferring a protective layer on them, thus maintaining cellular integrity (**Figure 4**).

Tumor-Derived Exosomes can Suppress Immune Cells to Protect CTCs

The immune system inhibits the progression of cancer cells. Many immune cells are found circulating in human blood, including T lymphocytes, natural killer (NK) cells, and B lymphocytes (de la Cruz-Merino et al., 2008; Grivennikov et al., 2010; McCarthy, 2001). These immune cells play crucial roles in immune surveillance, immunosuppression, and killing effects and mainly act on CTCs (Deepak and Acharya, 2010; Pahl and Cerwenka, 2017; Wernersson and Pejler, 2014; Ye et al., 2017). Immune cells can recognize and attack CTCs under normal circumstances; therefore, immunosuppression is necessary for the metastasis of CTCs (Guo et al., 2019). Many researchers have found that TDEs can suppress immune cells. Exosomes carry bioactive molecules that can impair immune cell function (Becker et al., 2016; Kalluri, 2016; Robbins and Morelli, 2014). Programmed cell death receptor ligand 1 (PD-L1) can bind to programmed cell death protein 1 (PD-1) to inactivate T cells through its extracellular domain (L. Chen and Han, 2015; Chen et al., 2015; Garcia-Diaz et al., 2019). TDEs carry PD-L1 on their surface and suppress $CD8^+$ T cell function in metastatic melanoma (Chen et al., 2018). In addition to PD-1, TDEs can also carry others to inhibit T cell function, and prolyl hydroxylase can inhibit $CD4^+$ and $CD8^+$ T cell functions by oxygen sensing (Clever et al., 2016). TDEs block T cell activation and enhance T cell apoptosis (Czernek and Dutchler, 2017; Ludwig et al., 2017). TDEs can also cause NK cell dysfunction. NK cells do not express PD-1; however, TDEs interfere with the TGFβ/TGFβRI/II pathway and other common molecular pathways, such as the adenosine pathway, eventually driving NK cell responses (Hong et al., 2017). In addition, TDEs can inhibit NK cell cytotoxicity by suppressing STAT5 activation (Zhang et al., 2007). B cells play a critical role in immunoglobulin, antigen, and proinflammatory cytokine secretion (Mauri and Bosma, 2012). TDE HMGB1 regulates the proliferation of T cell Ig and mucin domain-1^+ ($TIM\text{-}1^+$) B cells and fosters cancer cell immune evasion (Ye et al.,

TABLE 1 | Chart for organotropic metastasis with respect to cancer types.

Cancer type	Organotropic metastasis	References
Acute myeloid leukemia	Liver metastasis	Wang H. et al. (2020); Wang N. et al. (2020)
Breast cancer	Bone metastasis	Salvador et al. (2019); Tahara et al. (2019); Ma et al. (2020a)
	Lung metastasis	Kim et al. (2018); Yousefi et al. (2018); Tyagi et al. (2021)
	Brain metastasis	Pedrosa et al. (2018); Chang et al. (2020); Hosonaga et al. (2020)
	Lymph node metastasis	Zhang H. et al. (2017); Qiu et al. (2020); Zhang Q. et al. (2017); Xu et al. (2021)
	Liver metastasis	Ma et al. (2015); Yousefi et al. (2018); Bale et al. (2019); Ji et al. (2020)
Bladder cancer	Bone metastasis	Fan et al. (2020)
	Lymph node metastasis	Doshi et al. (2013); Tuncer et al. (2014)
	Lung metastasis	
	Liver metastasis	
	Mediastinum	
	Adrenal gland	
Colon cancer	Liver metastasis	Yao et al. (2017); Tokoro et al. (2018); Kim et al. (2019a); Li K. et al., (2019); Zhu et al. (2020)
	Lung metastasis	Yao et al. (2017); Tokoro et al. (2018)
	Lymph node metastasis	(El-Halabi et al. (2014)
	Brain metastasis	Yoshida et al. (2012); Tokoro et al. (2018)
Cervical cancer	Lung metastasis	Ali et al. (2017); Chen et al. (2020); Hsieh et al. (2021)
	Brain metastasis	Hwang et al. (2013); Sato et al. (2015); Fetcko et al. (2017); Kim et al. (2019b); Sun et al. (2020)
	Lymph node metastasis	Wu et al. (2020); Zhang C. et al. (2020); Zhang Q. et al. (2020); Zhong et al. (2020)
	Bone metastasis	Yoon et al. (2013); Nartthanarung et al. (2014); Kanayama et al., (2015); Makino et al. (2016)
	Liver metastasis	Nance et al. (2020); Liu et al. (2021)
Gastrointestinal stromal tumor	Liver metastasis	Yamanaka et al. (2013); Yamashita et al. (2016); Cumsille et al. (2019)
	Bone metastasis	Aktan et al. (2015); Suzuki et al. (2015)
	Lymph node metastasis	Canda et al. (2008); Gong et al. (2011); Kubo and Takeuchi, (2017)
	Brain metastasis	Naoe et al. (2011)
	Lung metastasis	Xu et al. (2020a); Carvalho et al. (2020)
Gastric cancer	Lung metastasis	Qiu et al. (2018a); Wang et al. (2019d); Abe et al. (2020)
	Brain metastasis	York et al. (1999); Peng et al. (2014); Yang et al. (2016); Qiu et al., (2018b); Cavanna et al. (2018)
	Lymph node metastasis	Chen et al. (2019); Wang J. et al. (2020); Wang Y. et al. (2020); Kim et al. (2021)
	Bone metastasis	Ubukata et al. (2011); Mikami et al. (2017); Qiu et al. (2018a); Fujita et al. (2020); Imura et al. (2020)
	Liver metastasis	Zhang G. et al. (2017); Qiu et al. (2018b); Luo et al. (2019); Ohara et al. (2020)
Glioblastoma	Lung metastasis	Hoffman et al. (2017)
	Lymph node metastasis	Dolman, (1974); Jamjoom et al. (1997); Datta et al. (1998); Alhoulaiby et al. (2020)
	Bone metastasis	Ricard et al. (2019); Nagata et al. (2020)
	Liver metastasis	Yung et al. (1983); Shuto et al. (1995)
Hepatocellular carcinoma	Bone metastasis	Zhang et al. (2019b); Park et al. (2019); Ma et al. (2020b); Hu et al. (2020)
	Lymph node metastasis	Xu et al. (2016); Ikegami et al. (2017); Liu et al. (2018a)
	Stomach and colon	Kim et al. (2020)
	Brain metastasis	Yamakawa et al. (2015); Lin et al. (2017); Nam et al. (2019)
	Lung metastasis	Zhang et al. (2019a); Kapoor et al. (2020)
Head and neck cancer	Lung metastasis	Nishino et al. (1996); AlShammari et al. (2020)
	Brain metastasis	Nishino et al. (1996); Kofler et al. (2017)
	Lymph node metastasis	Zhou X. et al. (2018); Nienstedt et al. (2018); Zhou Z. et al. (2018); Mermod et al. (2019); Fang et al. (2020); Nishio et al. (2021)
	Bone metastasis	Bhandari and Jain, (2013); Chi et al. (2021)
	Liver metastasis	Chen et al. (2014)
Lung cancer	Liver metastasis	Sridhar et al. (2019); Wang B. et al. (2020); Lu et al. (2020)
	Bone metastasis	Liu et al. (2017); Okabe et al. (2018); da Silva et al. (2019); Wang et al. (2019b); Ai et al. (2020)
	Lymph node metastasis	Xia et al. (2015); Kong et al. (2017); Wang C.-F. et al. (2020); Wang L. et al. (2020)
	Brain metastasis	Aljohani et al. (2018); Waqar et al. (2018); Wang et al. (2019a); Luo et al. (2020b); Fujimoto et al. (2020)
Melanoma	Liver metastasis	Nakamura et al. (2017a); Ryu et al. (2017); Grossniklaus, (2019); Bustamante et al. (2021)
	Bone metastasis	Uluckan, (2019); Caldaria et al. (2020); Mannavola et al. (2020)
	Lymph node metastasis	Merkow et al. (2016); Moy et al. (2017); Muhsin-Sharafaldine et al. (2017); Faries et al. (2018); Soler-Cardona et al. (2018)
	Brain metastasis	Kircher et al. (2016); Katona et al. (2017); Redmer, (2018); Schwarz et al. (2019)
	Lung metastasis	Zhu et al. (2016); Hyun et al. (2020); Park et al. (2020); Stansel et al. (2020)
Multiple myeloma (BM-MSC)	Liver metastasis	Estelles Piera et al. (1993)
Mesothelioma	Liver metastasis	Etoh et al. (1997); Marzullo et al. (2020)
	Bone metastasis	Laurini, (1974); Swayne et al. (1992); Roegel et al. (1993); Huang et al. (2019)
	Lymph node metastasis	Sussman and Rosai, (1990); Yan et al. (2006); Abdel Rahman et al. (2008); Takehara et al. (2014)
	Brain metastasis	Asoh et al. (1990); Kawai et al. (1997); Hirooka et al. (2016)
Ovarian cancer	Lung metastasis	Ueda et al. (1973)
	Brain metastasis	Pakneshan et al. (2014); Stasenko et al. (2019)

(Continued on following page)

TABLE 1 | (*Continued*) Chart for organotropic metastasis with respect to cancer types.

Cancer type	Organotropic metastasis	References
	Lymph node metastasis	Kleppe et al. (2011); Zhou et al. (2016); Hong et al. (2018); Longo et al. (2020)
	Bone metastasis	Kumar et al. (1992); Tiwari et al. (2007); Zhang and Sun, (2013)
	Liver metastasis	Xu et al. (2017); Wang et al. (2019c); Zhuo et al. (2020)
Pancreatic cancer	Lung metastasis	Park et al. (2017); Sakimura et al. (2019); Uesato et al. (2020)
	Brain metastasis	Matsumura et al. (2009); Lemke et al. (2013); Matsumoto and Yoshida, (2015); Sasaki et al. (2019)
	Lymph node metastasis	Kanda et al. (2011); Liu et al., 2018b; Ma et al., 2018; Seifert et al. (2020)
	Bone metastasis	Saif et al. (2010); Guan et al. (2017); Outani et al. (2018)
	Liver metastasis	Ho et al. (2020); Wang et al. (2021a)
Prostate cancer	Lung metastasis	Polistina et al. (2020)
	Brain metastasis	Hernandez-Esquivel et al. (2018); Marchand Crety et al. (2020); Shida et al. (2020)
	Lymph node metastasis	Li F. et al. (2019); Xu et al. (2020b); Zhao et al. (2020); Klingenberg et al. (2021)
	Bone metastasis	Berish et al. (2018); Zhang, (2019); Wen et al. (2020)
	Liver metastasis	Simons et al. (2020); Ma B. et al. (2021)

2018). We can design therapeutic modalities to enhance immune cell surveillance and killing of these tumors by understanding these signaling pathways.

CTCs Activate Platelets Directly or by Releasing Exosomes

Platelets play major roles in hemostasis and coagulation and regulate the efficiency of canceration, tumor angiogenesis, tumor metastasis, and chemotherapy (Sharma et al., 2014). Platelets and cancer cells interact, thus affecting tumor growth and metastasis (Sharma P. et al., 2018). During blood circulation, other nontumor help is essential, for example, platelets can protect CTCs from blood flow shear forces by providing a protective layer. CTCs release soluble mediators, such as adenosine diphosphate (ADP), thromboxane (TX) A2, or high-mobility group box 1 (HMGB1), that can ligate toll-like receptor 4 (TLR4) to instigate localized platelet activation and form thrombus encasing tumor cells, thus protecting them from cytolysis by NK cells (Aitokallio-Tallberg et al., 1985; Nieswandt et al., 1999; Yu et al., 2014; Zucchella et al., 1989).

The interaction between platelets and CTCs can lead to platelet activation, and platelets release cytokines conducive to the survival and proliferation of tumor cells. When platelets combine with circulating tumor cells, platelet-derived soluble factors (TGF β and PDGF) mediate and prevent NK cells from detecting and dissolving tumor cells (Lambert et al., 2017; Lee J.-K. et al., 2013).

Finally, platelets prevent tumor cells from being eliminated by the immune system. Platelet-derived TGF-β can downregulate NKG2D expression and inactivate NK cells (Y. Chen et al., 2015; Kopp et al., 2009). The platelet expression profile in tumor and nontumor patients varies substantially (Santarpia et al., 2018). The interaction between CTCs and platelets can protect CTCs from immune surveillance during circulation and help tumor cells adhere to the endothelial cells at the metastasis site (Santarpia et al., 2018). Kuznetsov et al. showed that luminal breast cancer cells carried platelets that loaded factors with the effect of pro-inflammatory and pro-angiogenic activities and confirmed that these factors were released at distant tumors sites (Kuznetsov et al., 2012). Platelets are essential for releasing proangiogenic cytokines and recruiting angiogenic vascular endothelial growth factor receptor 2^+ ($VEGFR2^+$) cells that promote malignant progression (Schlesinger, 2018). Moreover, studies have shown that platelets may not just have a secondary role but may also drive malignant progression (or metastasis) (Kuo et al., 2011).

In human blood, platelets are considered to be the major contributors of exosomes (Caby et al., 2005). Goetzl et al. showed that endothelial cells absorb platelet-derived exosomes and enhance their adhesion by increasing endothelial cell adhesion protein expression and anti-adhesion factor production, thereby promoting CTC adhesion in vascular endothelial cells (Goetzl et al., 2016). Platelet-derived exosomes also increase platelet adhesion to monocytes and consequently monocyte activation, thus promoting the formation of inflammatory phenotypes (Goetzl et al., 2016).

Therefore, many researchers believe that blood platelets may be a potential source of biomarkers to aid cancer diagnosis. Nonetheless, the mechanism using which CTC-educated platelets mediate CTCs to avoid damage in the circulatory system still needs further research. We firmly believe that these CTC-educated platelet-derived exosomes play an important role in preventing damage to CTCs.

INTEGRINS OF TUMOR-DERIVED EXOSOMES DETERMINE ORGANOTROPIC METASTASIS

That different types of cancer cells preferentially colonize and metastasize to different organs is the salient feature of metastasis (Nguyen et al., 2009). Current research shows that tumors mainly metastasize to lung, brain, lymph node, bone, and liver tissues. We have summarized organotropic metastasis with respect to cancer types (**Table 1**). Many studies focus on tumor cell

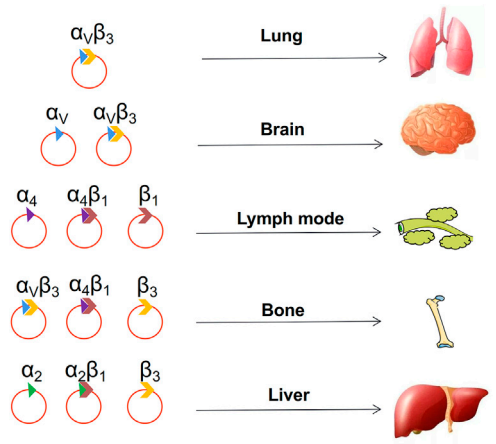

FIGURE 5 | Choice of metastatic organs. The integrin on the surface of the exosome determines where the tumor metastasizes.

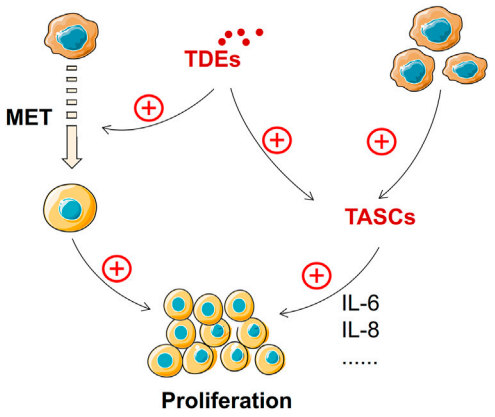

FIGURE 6 | TDEs promote tumor growth at the metastasis site. MET and TASCs promote tumor growth at metastatic sites, and TDEs can derive MET and TASC formation.

adhesion function, and extracellular matrix molecules, such as integrins, have been determined to be related to the choice of organotropic metastasis (Valastyan and Weinberg, 2011).

Integrins, a large family of adhesion molecules, can mediate cell–cell and cell–extracellular matrix interactions (Desgrosellier and Cheresh, 2010). Many integrins are associated with tumor angiogenesis, such as αvβ3, αvβ5, and α5β1 (Cascone et al., 2005; Lee et al., 2013a; Huang and Rofstad, 2018). β1 integrins bind to vascular cell adhesion molecule 1 (VCAM-1) on ECs and play an important role in trans-endothelial migration (Klemke et al., 2007). Integrins participate in tumor angiogenesis by interacting with the VEGF–VEGFR and ANG–TIE pathways (Klemke et al., 2007). αvβ3 integrin binds to the adhesion molecule L1 on ECs driving trans-endothelial migration (Voura et al., 2001). αvβ3 integrin is the most abundant and influential receptor among integrins on ECs and can regulate angiogenesis (De et al., 2005; Mahabeleshwar et al., 2008; Shattil and Ginsberg, 1997). It can be activated and colocalized with VEGFR-2 on ECs of proliferating blood vessels (Mahabeleshwar et al., 2008). VEGF-stimulated c-Src can be the phosphorylate β3 subunit on ECs, promoting VEGFR-2 phosphorylation and activation (De et al., 2005; Mahabeleshwar et al., 2008; Mahabeleshwar et al., 2007). In addition, αvβ3 is necessary for the survival and maturation of new blood vessels, and proliferative angiogenic EC apoptosis occurs after treatment with αvβ3 antagonists (Brooks et al., 1994). Briefly, integrin subunits α1, α2, α3, α4, α5, α6, α9, αv, β1, β3, and β5 are involved in physiological or pathological angiogenesis. Exosomes affect several steps of angiogenesis including motility, cytokine production, cell adhesion, and cell signaling (Taverna et al., 2012). These can improve the tumor survival environment before metastasis.

Although integrins are secreted by tumor cells, it is transported by exosomes to a distant organ (Peinado et al., 2017). Lyden et al. showed that tumor exosome integrins can determine organotropic metastasis. They suggested that tumor exosome integrins can fuse with organ-specific resident cells and activate Src phosphorylation and proinflammatory S100 expression to establish a pre-metastatic niche (Hoshino et al., 2015). In addition, more bodies of evidence identified that different integrins on the surface of exosomes play varied roles in metastasis to specific organs (Alderton, 2015; Hoshino et al., 2015; Paolillo and Schinelli, 2017). For instance, exosomal integrins α6β4 and α6β1 preferentially direct tumor cells to the lungs, and αvβ5 induces liver metastasis (Hoshino et al., 2015). Tumor exosomes can prepare pre-metastatic niches to facilitate organ-specific metastasis, even for cancer cells equipped to metastasize (**Figure 5**).

TUMOR CELL GROWTH AT THE METASTASIS SITE

Once tumor cells migrate to tissues and organs, TDEs provide them with a good growth environment and the ability to promote their growth.

Tumor-Derived Exosomes Promote Pre-metastatic Niche Formation

A pre-metastasis niche is a primary tumor in secondary organs and tissues that creates a favorable microenvironment for subsequent metastasis. Tumor-derived molecules secreted by primary tumors play a key role in preparing distant sites for the formation of new pre-metastasis niches, promoting metastasis and even determining the orientation of metastatic organs. These major tumor-derived molecules are usually tumor-derived secretory factors, extracellular vesicles (EVs), and other molecular components (Minciacchi et al., 2015). Exosomes containing protein, mRNA, or DNA fragments promote the pre-metastasis niche formation by mediating the communication between tumor cells and surrounding components or transferring their contents to recipient cells (Chin and Wang, 2016; Zhou et al., 2014).

Tumor cells are “seeds”. With tumor-secreting factors, tumor cell–secreting vesicles, and exosomes acting as catalysts, tumor

TABLE 2 | Role and target of the components of TDEs in tumor metastasis.

Cancer type	Exosome component	Target cells	Potential regulation	Roles in metastasis steps	References
AML	TGF-β	NK cells	NKG2D	Step 3: immunosuppressive	Szczepanski et al. (2011)
	DPP4	Bone	-	Step 5	Namburi et al. (2021)
	TGFβ/TGFβRI/II	NK-92	-	Step 3: immunosuppressive	Hong et al. (2017)
Breast cancer	miR-10b	Mammary epithelial cells	HOXD10 and KLF4	Step 1: enhance invasion ability	Singh et al. (2014)
	miR-122	Lung fibroblast neurons	PKM	Step 2: non-coding RNA influence angiogenesis	Fong et al. (2015)
	RN7SL1	Breast cancer cells	PRR RIG-I	Step 5	Nabet et al. (2017)
	miR-200c, miR-141	Breast cancer cells	FOXP3-KAT2B	Enhance metastases	Zhang G. et al. (2017)
	miRNA-503	Microglia	-	Step 3: immunosuppressive	Xing et al. (2018)
	Caveolin-1	Breast cancer cells	-	Enhance metastases	Campos et al. (2018)
	miR-193b	Breast cancer cells	RAB22A	Step 1: enhance invasion ability	Sun et al. (2018)
	CEMIP	Brain endothelial and microglial cells	-	Step 2: angiogenesis	Rodrigues et al. (2019)
	hsa-miR-940	Osteoblastic	ARHGAP1 and FAM134A	Step 5	Hashimoto et al. (2018)
	miR-126a	Lung	S100A8/A9	Step 2	Deng et al. (2017)
	miR-222	Breast cancer cells	NF-κB	Step 1	Ding et al. (2018)
	miR-130a-3p	Breast cancer cells	RAB5B	Step 1	Kong et al. (2018)
	miR-939	Breast cancer cells	VE-cadherin	Step 2: non-coding RNA influence angiogenesis	Di Modica et al. (2017)
	miR-770	TNBCs	STMN1	Decrease metastases	Li Y. et al. (2018)
	miR-4443	Breast cancer cells	TIMP2	Step 4	Wang H. et al. (2020)
	miR-210	Endothelial cells	-	Step 2: non-coding RNA influence angiogenesis	Kosaka et al. (2013)
	miR-1910-3p	Breast cancer cells	MTMR3	Step 1: enhance invasion ability	Wang B. et al. (2020)
	miR-146a	CAFs	TXNIP	Step 5	Yang et al. (2020b)
	miR-4443	Liver	-	Step 1: enhances invasion ability	Wang J. et al. (2020)
Bladder Cancer	LINC02470, LINC00960	Bladder cancer cells	-	Step 1: EMT	Huang et al. (2020b)
CML	miR-92a	EC	Integrin α5	Step 2: non-coding RNA influence angiogenesis	Umezu et al. (2014)
Colon cancer	hsp 70	MDSC	STAT3	Step 3: immunosuppressive	Chalmin et al. (2010)
	KRAS mutation	Colon CA cells	-	Step 5: tumor growth	Demory Beckler et al. (2013)
	TF	EC	-	Step 3: platelet activation	Garnier et al. (2012)
	miR-193a	Colon cancer cells	Caprin1	Step 5: decrease the growth of cells	Teng et al. (2017)
	miR-92a-3p	Colon cancer cells	-	Step 1: EMT	Hu J. L. et al. (2019)
	lncRNA H19	Colon cancer cells	miR-141	Step 5: MET	Ren et al. (2018)
	miR-21-5p; miR-155-5p	Colon cancer cells	BRG1	Step 5	Lan et al. (2019)
	miR-182-3p	Colon cancer cells	FOXO4	Step 1: EMT	Liu et al. (2019)
	GDF15	HUVECs	Smad	Step 2	Zheng et al. (2020)
	MCP-1; TNF	Macrophages	-	Step 2: activating macrophages	Chen et al. (2016)
	miR-25-3p	ECs	VEGFR, ZO-1, occludin, and claudin5	Step 2: angiogenesis	Zeng et al. (2018)
	miR-1229	ECs	HIPK2	Step 2: angiogenesis	Hu H.-Y. et al. (2019)
Cervical cancer	Survivin	Cervical cancer cells	-	Step 5: tumor growth	(Khan et al., 2009; Khan et al., 2011)
	Cicr-PVT1	Cervical cancer cells	MiR-1286	Step 1: EMT	Wang H. et al. (2020)
	miR-221-3p	HLEC	VASH1	Step 2: Lymphatic vessel formation	Zhou et al. (2019)
	miR-663b	Cervical cancer cells	MGAT3	Step 1: EMT	You et al. (2021b)
GIST	KIT	Progenitor muscle cells	MMP1	Step 1: Influence the relationship between tumor cells and cell matrix	You et al. (2021b)
Gastric cancer	miR-27a	CAFs	-	Step 1: EMT	Wang J. et al. (2018)
	miR-130a	ECs	C-MYB	Step 2: angiogenesis	Yang et al. (2018)
	miR-135b	ECs	FOX1	Step 2: angiogenesis	Bai et al. (2019)
Glioblastoma	EGFR vIII	Glioblastoma cells	VEGF, Bcl-x (L), p27	Step 5: tumor growth	Al-Nedawi et al. (2008)
	matrix metalloproteinases, IL-8, PDGFs, and caveolin 1	Glioblastoma cells	PI3K/AKT	Step 1: EMT	Kucharzewska et al. (2013)
	L1CAM	Glioblastoma cells	FAK; FGFR	Enhance metastases	Pace et al. (2019)
	miR-148a	Glioblastoma cells	CADM1	Step 1	Cai et al. (2018)
	MDA-9/Syntenin	Glioblastoma cells	CD63-AP-2	Step 1	Das et al. (2018)

(Continued on following page)

TABLE 2 | (*Continued*) Role and target of the components of TDEs in tumor metastasis.

Cancer type	Exosome component	Target cells	Potential regulation	Roles in metastasis steps	References
	LncRNA CCAT2	ECs	-	Step 2: angiogenesis	Lang et al. (2017a)
	LncRNA POU3F3	ECs	-	Step 2: angiogenesis	Lang et al. (2017b)
HCC	miR-584, 517c, 378	HCC cells	TAK1	Step 5: tumor growth	Kogure et al. (2011)
	miR-1247-3p	Fibroblasts	B4GALT3	Step 5: TASCs	Fang T. et al. (2018)
	miR-122	HCC cells		Step 5: tumor growth	Qian and Pollard, (2010)
	miR-27b-3p/miR-92a-3p	HCC cells	IGF1R	Step 5: tumor growth	Basu and Bhattacharyya et al. (2014)
	miR-103	ECs	VE-cadherin	Step 2: non-coding RNA influence angiogenesis	Basu and Bhattacharyya et al. (2014), Fang J. H. et al. (2018)
	miR-21, miR-10b	HCC cells	-	Step 1	Tian et al. (2019)
	SMAD3	HCC cells	ROS	Step 4: attach Step 5: tumor growth	Fu et al. (2018)
	LOXL4	HUVECs	FAK/Src	Step 2: angiogenesis	Li R. et al. (2019)
	Vps4A	HCC cells	β-catenin	Step 1: EMT	Han et al. (2019)
	miR-320a	HCC cells	CDK2, MMP2	Step 1: EMT Step 5: TASCs	Zhang Z. et al. (2017)
	lncRNA FAL1	HCC cells	miR-1236	Enhance metastases	Li B. et al. (2018)
	p120-catenin	HCC cells	STAT3	Enhance metastases	Cheng et al. (2019)
	miR-372-3p	HCC cells	Rab11a	Enhance metastases	Cao et al. (2019)
	Alpha-enolase	HCC cells	Integrin α6β4	Enhance metastases	Jiang et al. (2020)
	circ_MMP2	HCC cells	MMP2	Enhance metastases	Liu et al. (2020)
	miR-92a-3p	HCC cells	PTEN/Akt	Step 1: EMT	Liu et al. (2020)
	Linc00161	HUVECs	miR-590-3p/ROCK	Step 2: angiogenesis	You et al. (2021a)
	miR-30a; miR-222	HCC cells	MIA3	Enhance metastases	Du et al. (2021)
	S100A4	HCC cells	STAT3	Enhance metastases	Sun et al. (2021)
	miR-1290	ECs	SMEK1	Step 2: angiogenesis	Wang et al. (2021b)
	circRNA-100338	HUVECs	-	Step 2: angiogenesis	Huang et al. (2020b)
	TIM11	B cells	TLR/MAPK	Step 3: immunosuppressive	Ye et al. (2018)
HNC	FasL	T cells	Jurkat	Step 3: immunosuppressive	Kim et al. (2005)
	miR-23a	HUVECs	TSGA10	Step 2: angiogenesis	Bao et al. (2018)
	-	NK cells	NKG2D	Step 3: immunosuppressive	Ludwig et al. (2017)
Lung Cancer	miR-103	M2 macrophages	VEGF-A	Step 2: angiogenesis	(Hsu et al., 2018; Wu et al., 2019)
	miR-23a	ECs	ZO-1	Step 2: angiogenesis	Hsu et al. (2017)
	miR-21	HUVECs	-	Step 2: angiogenesis	Liu et al. (2016a)
	LncRNA-p21	HUVECs	-	Step 2: angiogenesis	Castellano et al. (2020)
Melanoma	MET	BM progenitor cells	-	Step 5: tumor growth	Peinado et al. (2012)
	PD-L1	T cells	PD-1	Step 3: immunosuppressive	Chen et al. (2018)
	snRNA	Lung epithelial cells	TLR3	Step 5: TASCs	Liu et al. (2016b)
	CD151	Lung, lymph node and stromal cells	-	Step 4: location	Malla et al. (2018)
	Fas	T cells	MMP9	Step 3: immunosuppressive	Cai et al. (2012)
	miR-191; let-7a	Melanoma cells	-	Step 1: EMT	Xiao et al. (2016)
	Immunomodulatory, proangiogenic factors	Melanoma cells	-	Step 2: angiogenesis Step 3: immunosuppressive	Ekstrom et al. (2014)
	HSP70	NK cells	-	Step 3: immunosuppressive	Elsner et al. (2007)
	uPAR	HMVECs; ECFCs	ERK1,2	Step 2: angiogenesis	Biagioni et al. (2021)
	miR-106b-5p	Melanoma cells	EphA4	Step 5: MET	Luan et al. (2021)
	miR-155-5p	CAFs	SOCS1/JAK2/STAT3	Step 2: angiogenesis	Zhou X. et al. (2018)
Multiple myeloma (BM-MSC)	miR-15a	MM cells	FAK	Step 1: enhance invasion ability	Roccaro et al. (2013)
	miR-let-7c	ECs	-	Step 2: TDEs promote angiogenesis by activating macrophages	Tian et al. (2021)
	miR-135b	EC	HIF-FIH	Step 2	Umezu et al. (2014)
Mesothelioma	TGF-β	Fibroblasts	SMAD	Step 1: influence the relationship between tumor cells and cell matrix	Webber et al. (2010)
NPC	HIF1α	NPC cells	LMP1	Step 1	Aga et al. (2014)
	miR-23a	EC	TSGA10	Step 2: angiogenesis	Bao et al. (2018)
	MMP13	NPC cells	-	Step 1 Step 2: angiogenesis	You et al. (2015)
	circMYC	NPC cells	-	Enhance metastases	Luo et al. (2020a)

(Continued on following page)

TABLE 2 | (*Continued*) Role and target of the components of TDEs in tumor metastasis.

Cancer type	Exosome component	Target cells	Potential regulation	Roles in metastasis steps	References
	LMP1	NPC cells	-	Step 1: EMT	Aga et al. (2014)
Ovarian cancer	FasL	T cells	CD3-zeta	Step 3: immunosuppressive	Taylor et al. (2003)
	ATF2; MTA1; ROCK1/2	HUVECs	-	Step 2: angiogenesis	Yi et al. (2015)
	GNA12; EPHA2; COIA1	MSCs; ECs	-	Step 5	Sharma et al. (2018b)
	CD44	HPMCs	-	Step 1	Nakamura et al. (2017a)
	circWHSC1	HPMCs	miR-145; miR-1182	Step 2	Nakamura et al. (2017b); Zong et al. (2019)
	miR-375	Ovarian cancer cells	CA-125	Enhance metastases	Su et al. (2019)
	miR-7	EOC	EGFR, AKT, ERK1/2	Decrease metastases	Hu et al. (2017)
	LncRNA FAL1	Ovarian cancer cells	PTEN/AKT	Enhance metastases	Hu et al. (2017)
	miR-6780b-5p	Ovarian cancer cells	-	Step 1: EMT	Cai et al. (2021)
	circRNA051239	Ovarian cancer cells	-	Step 5	Ma R. et al. (2021)
	LncRNA MALAT1	HUVECs	-	Step 2: angiogenesis	Qiu et al. (2018a)
Pancreatic	MIF	Liver Kupfer cells	-	Step 5: tumor growth	Costa-Silva et al. (2015)
cancer	miR-301a-3p	Macrophages	PTEN/PI3Kγ	Step 2: active macrophages	Wang X. et al. (2018)
	circ-IARS	HUVECs	-	Enhance metastases	Li J. et al. (2018)
	Lin28B	CAFs	let-7, HMGA2, PDGFB	Step 5	Zhang et al. (2019c)
	miR-501-3p	Pancreatic ductal adenocarcinoma	TGFBR3, TGF-β	Enhance metastases	Yin et al. (2019)
	lncRNA Sox2ot	Pancreatic ductal adenocarcinoma	-	Step 1: EMT	Li Z. et al. (2018)
	CD151, Tspan8	ASML	-	Step 1: matrix degradation	Yue et al. (2015)
	miR92a-3p	Pancreatic ductal adenocarcinoma	PTEN/Akt	Step 1: EMT	Yang et al. (2020a)
	CD44v6/C1QBP	Pancreatic ductal adenocarcinoma	-	Step 5	Xie et al. (2021)
Prostate cancer	αvβ6 Integrin	Prostate cancer cells	-	Step 4	Lazaro-Ibanez et al. (2014)
	miR-1246	Prostate cancer cells	N-cadherin; vimentin	Step 1: EMT	Bhagirath et al. (2018)
	miR-940	Osteoblastic	ARHGAP1, FAM134A	Enhance metastases	Bhagirath et al. (2018)
	miR-26a	Prostate cancer cells	-	Step 1: EMT	Wang et al. (2019f)
	PKM2	BMSCs	CXCL12	Step 5	Dai et al. (2019)
	PSGR	Prostate cancer cells	-	Step 1: EMT	Li et al. (2021)
	TGF-β2, TNF1α, IL6, TSG101, Akt, ILK, β-catenin	Prostate cancer cells	-	Step 1: matrix degradation	Ramteke et al. (2015)

The role of exosomes in various cancer metastases. AML: acute myeloid leukemia. CML: chronic myeloid leukemia. GIST: gastrointestinal stromal tumor. HCC: hepatocellular carcinoma. HNC: head and neck cancer. NPC: nasopharyngeal carcinoma.

cells can promote the formation of the "soil" (host microenvironment) in a distant metastasis site and promote the growth of cancer cells. Cancer metastasis is preceded by the interaction between the seed and soil (Y. Chen et al., 2015; Lambert et al., 2017; Liu and Cao, 2016; Minciacchi et al., 2015). Primary tumor cells influence and change the microenvironment at secondary organs by promoting pre-metastasis niche factor before tumor cells arrive (Chin and Wang, 2016; He et al., 2017).

The characteristics of a pre-metastasis niche include the following six aspects. First, pre-metastasis niche formation is accompanied by the recruitment of bone marrow–derived cells (BMDC) (Y. Chen et al., 2015; Minciacchi et al., 2015). Literature suggests that extracellular matrix metalloproteinase inducer (EMMPRIN) in cancer cells can induce the secretion and expression of many factors, such as SDF and VEGF, which mediate the recruitment of BMDC to the liver and lungs (Y. Chen et al., 2015; Minciacchi et al., 2015). Second, the immune cells involved in the pre-transfer niche formation are heterogenous. Pre-metastasis niche formation involves not only the recruitment of foreign cells but also the reprogramming of resident stromal cells, promoting metastasis. Pre-metastasis niche formation also involves the change of the ECM. Niche formation before transfer is accompanied by a change in the vascular system. Metastatic breast cancer cells reduce tight junctions between endothelial cells by secreting exosomes containing mir-105, thus inducing systemic vascular leakage and promoting metastasis (Kong et al., 2019). Breast cancer cells secrete exosomes containing miR-122, which are absorbed by niche cells, and reduce glucose consumption by targeting pyruvate kinase, thus increasing the proliferation rate and survival rate of cancer cells and promoting metastasis (Fong et al., 2015). Pancreatic cancer–derived exosomes, rich in macrophage migration inhibitory factors, recruit macrophages and induce pre-metastasis niche formation in the liver (Costa-Silva et al., 2015). Modulation of the pre-metastatic niche formation by controlling TDEs is a new area for future chemotherapy research.

Tumor-Derived Exosomes Promote the Growth of Metastasis Tumor

The growth of metastatic tumors requires suitable "soil". MET returns the cancer cells to a highly proliferative state but with the

loss of their migration characteristics, enabling tumor growth at the metastasis site (Li K. et al., 2019). The characteristics of MET are increased expression of mesenchymal markers, such as vimentin, and decreased expression of epithelial markers, such as E-cadherin, compared with that of EMT (Wells et al., 2008). MET supports the reacquisition of epithelial features to promote metastasis (Brabletz et al., 2001). Several signaling pathways are involved in regulating MET, including transforming growth factor (TGF), fibroblast growth factors (FGFs), bone morphogenic protein (BMP), epidermal growth factor receptor (EGFR), hepatocyte growth factor (HGF), Wnt/β-catenin, and Notch pathways (Said and Williams, 2011). TDEs can support tumor progression and remodel surrounding parenchymal tissues at the metastatic site (Greening et al., 2015). TDEs play an important regulatory role mediating EMT and transforming MET (Bigagli et al., 2019). Gastric cancer cell–derived exosomes can mediate the stimulation of proinflammatory cytokine IL-1β secretion and activate the Akt and MAPK pathways to promote tumor growth at the metastatic site (Che et al., 2018; Wang et al., 2019e). In addition, TDEs can transform stromal cells into tumor-associated stromal cells (TASCs) that can secrete many pro-tumorigenic factors, including IL-6 and IL-8. These factors can enhance the proliferation ability of tumor cells (Bussard et al., 2016). Hence, TDEs can enable tumor cells to acquire proliferation capacity directly through the MET process or promote tumor proliferation by inducing TASC formation and releasing related factors (**Figure 6**). Nevertheless, there is still a dearth of research on exosomes and their contribution to MET.

CONCLUSION

Exosomes play an important role in every step leading to tumor metastasis. Although there are many reports on the role of exosomes in metastasis, much is left to be explored of the potential mechanisms underlying metastasis. Although a few studies still have unclear results, we have summarized the published literature on the substances that exosomes carry, their main functions in different tumors, the target cells affected, and steps involved in metastasis. (**Table 2**). Exploring these underlying mechanisms will enlighten us about cancer biology and contribute to the prevention of and therapeutic strategies for malignancies. We can manipulate TDEs to impede not just metastasis formation but even established metastases.

AUTHOR CONTRIBUTIONS

SB and ZW developed the first draft of the manuscript. All authors contributed to the planning, organization, data collection, and writing of the manuscript. JD completed all figures and provided critical edits. The final version of the manuscript was approved by all authors.

FUNDING

The study was supported by grants from the National Natural Science Foundation of China (Grant Nos. 81972539 and U1732157).

REFERENCES

Abdel Rahman, A. R. M., Gaafar, R. M., Baki, H. A., El Hosieny, H. M., Aboulkasem, F., Farahat, E. G., et al. (2008). Prevalence and Pattern of Lymph Node Metastasis in Malignant Pleural Mesothelioma. *Ann. Thorac. Surg.* 86 (2), 391–395. doi:10.1016/j.athoracsur.2008.04.012

Abe, Y., Suzuki, M., Tsuji, K., Sato, M., Kimura, H., Kimura, H., et al. (2020). Lung Metastasis from Gastric Cancer Presenting as Diffuse Ground-Glass Opacities. *Respir. Med. Case Rep.* 30, 101104. doi:10.1016/j.rmcr.2020.101104

Aga, M., Bentz, G. L., Raffa, S., Torrisi, M. R., Kondo, S., Wakisaka, N., et al. (2014). Exosomal HIF1α Supports Invasive Potential of Nasopharyngeal Carcinoma-Associated LMP1-Positive Exosomes. *Oncogene* 33 (37), 4613–4622. doi:10.1038/onc.2014.66

Agarwal, A., Balic, M., El-Ashry, D., and Cote, R. J. (2018). Circulating Tumor Cells. *Cancer J.* 24 (2), 70–77. doi:10.1097/PPO.0000000000000310

Ai, C., Ma, G., Deng, Y., Zheng, Q., Gen, Y., Li, W., et al. (2020). Nm23-H1 Inhibits Lung Cancer Bone-specific Metastasis by Upregulating miR-660-5p Targeted SMARCA5. *Thorac. Cancer* 11 (3), 640–650. doi:10.1111/1759-7714.13308

Aitokallio-Tallberg, A., Kärkkäinen, J., Pantzar, P., Wahlström, T., and Ylikorkala, O. (1985). Prostacyclin and Thromboxane in Breast Cancer: Relationship between Steroid Receptor Status and Medroxyprogesterone Acetate. *Br. J. Cancer* 51 (5), 671–674. doi:10.1038/bjc.1985.101

Aktan, M., Koc, M., Yavuz, B. B., and Kanyilmaz, G. (2015). Two Cases of Gastrointestinal Stromal Tumor of the Small Intestine with Liver and Bone Metastasis. *Ann. Transl Med.* 3 (17), 259. doi:10.3978/j.issn.2305-5839.2015.09.46

Al-Nedawi, K., Meehan, B., Micallef, J., Lhotak, V., May, L., Guha, A., et al. (2008). Intercellular Transfer of the Oncogenic Receptor EGFRvIII by Microvesicles Derived from Tumour Cells. *Nat. Cel Biol* 10 (5), 619–624. doi:10.1038/ncb1725

Albini, A., Bruno, A., Noonan, D. M., and Mortara, L. (2018). Contribution to Tumor Angiogenesis from Innate Immune Cells within the Tumor Microenvironment: Implications for Immunotherapy. *Front. Immunol.* 9, 527. doi:10.3389/fimmu.2018.00527

Alderton, G. K. (2015). Directions to Metastatic Sites. *Nat. Rev. Cancer* 15 (12), 696–697. doi:10.1038/nrc4046

Alhoulaiby, S., Abdulrahman, A., Alouni, G., Mahfoud, M., and Shihabi, Z. (2020). Extra-CNS Metastasis of Glioblastoma Multiforme to Cervical Lymph Nodes and Parotid Gland: A Case Report. *Clin. Case Rep.* 8 (9), 1672–1677. doi:10.1002/ccr3.2985

Ali, A., Kim, S. H., Kim, M. J., Choi, M. Y., Kang, S. S., Cho, G. J., et al. (2017). O-GlcNAcylation of NF-kappaB Promotes Lung Metastasis of Cervical Cancer Cells via Upregulation of CXCR4 Expression. *Mol. Cell* 40 (7), 476–484. doi:10.14348/molcells.2017.2309

Aljohani, H. M., Aittaleb, M., Furgason, J. M., Amaya, P., Deeb, A., Chalmers, J. J., et al. (2018). Genetic Mutations Associated with Lung Cancer Metastasis to the Brain. *Mutagenesis* 33 (2), 137–145. doi:10.1093/mutage/gey003

AlShammari, A., Almasri, T., Sarraj, J., AlAshgar, O., Ahmed, M. H., AlKattan, K., et al. (2020). Pulmonary Metastasis of Head and Neck Cancer: Surgical Removal Outcomes from a Tertiary Care center. *Indian J. Thorac. Cardiovasc. Surg.* 36 (3), 199–206. doi:10.1007/s12055-019-00866-3

Asoh, Y., Nakamura, M., Maeda, T., Shiogai, T., Ogashiwa, M., Takeuchi, K., et al. (1990). Brain Metastasis from Primary Pericardial Mesothelioma. *Neurol. Med. Chir.(Tokyo)* 30 (11 Spec No), 884–887. doi:10.2176/nmc.30.884

Atay, S., Banskota, S., Crow, J., Sethi, G., Rink, L., and Godwin, A. K. (2014). Oncogenic KIT-Containing Exosomes Increase Gastrointestinal Stromal Tumor Cell Invasion. *Proc. Natl. Acad. Sci.* 111 (2), 711–716. doi:10.1073/pnas.1310501111

Bai, M., Li, J., Yang, H., Zhang, H., Zhou, Z., Deng, T., et al. (2019). miR-135b Delivered by Gastric Tumor Exosomes Inhibits FOXO1 Expression in Endothelial Cells and Promotes Angiogenesis. *Mol. Ther.* 27 (10), 1772–1783. doi:10.1016/j.ymthe.2019.06.018

Bakir, B., Chiarella, A. M., Pitarresi, J. R., and Rustgi, A. K. (2020). EMT, MET, Plasticity, and Tumor Metastasis. *Trends Cel Biol.* 30 (10), 764–776. doi:10.1016/j.tcb.2020.07.003

Balaj, L., Lessard, R., Dai, L., Cho, Y.-J., Pomeroy, S. L., Breakefield, X. O., et al. (2011). Tumour Microvesicles Contain Retrotransposon Elements and Amplified Oncogene Sequences. *Nat. Commun.* 2, 180. doi:10.1038/ncomms1180

Bale, R., Putzer, D., and Schullian, P. (2019). Local Treatment of Breast Cancer Liver Metastasis. *Cancers* 11 (9), 1341. doi:10.3390/cancers11091341

Bao, L., You, B., Shi, S., Shan, Y., Zhang, Q., Yue, H., et al. (2018). Metastasis-associated miR-23a from Nasopharyngeal Carcinoma-Derived Exosomes Mediates Angiogenesis by Repressing a Novel Target Gene TSGA10. *Oncogene* 37 (21), 2873–2889. doi:10.1038/s41388-018-0183-6

Basu, S., and Bhattacharyya, S. N. (2014). Insulin-like Growth Factor-1 Prevents miR-122 Production in Neighbouring Cells to Curtail its Intercellular Transfer to Ensure Proliferation of Human Hepatoma Cells. *Nucleic Acids Res.* 42 (11), 7170–7185. doi:10.1093/nar/gku346

Becker, A., Thakur, B. K., Weiss, J. M., Kim, H. S., Peinado, H., and Lyden, D. (2016). Extracellular Vesicles in Cancer: Cell-To-Cell Mediators of Metastasis. *Cancer Cell* 30 (6), 836–848. doi:10.1016/j.ccell.2016.10.009

Berish, R. B., Ali, A. N., Telmer, P. G., Ronald, J. A., and Leong, H. S. (2018). Translational Models of Prostate Cancer Bone Metastasis. *Nat. Rev. Urol.* 15 (7), 403–421. doi:10.1038/s41585-018-0020-2

Bhagirath, D., Yang, T. L., Bucay, N., Sekhon, K., Majid, S., Shahryari, V., et al. (2018). microRNA-1246 Is an Exosomal Biomarker for Aggressive Prostate Cancer. *Cancer Res.* 78 (7), 1833–1844. doi:10.1158/0008-5472.CAN-17-2069

Bhandari, V., and Jain, R. (2013). A Retrospective Study of Incidence of Bone Metastasis in Head and Neck Cancer. *J. Can. Res. Ther.* 9 (1), 90–93. doi:10.4103/0973-1482.110385

Biagioni, A., Laurenzana, A., Menicacci, B., Peppicelli, S., Andreucci, E., Bianchini, F., et al. (2021). uPAR-Expressing Melanoma Exosomes Promote Angiogenesis by VE-Cadherin, EGFR and uPAR Overexpression and Rise of ERK1,2 Signaling in Endothelial Cells. *Cell. Mol. Life Sci.* 78 (6), 3057–3072. doi:10.1007/s00018-020-03707-4

Bigagli, E., Cinci, L., D'Ambrosio, M., and Luceri, C. (2019). Transcriptomic Characterization, Chemosensitivity and Regulatory Effects of Exosomes in Spontaneous EMT/MET Transitions of Breast Cancer Cells. *Cancer Genomics Proteomics* 16 (3), 163–173. doi:10.21873/cgp.20122

Brabletz, T., Jung, A., Reu, S., Porzner, M., Hlubek, F., Kunz-Schughart, L. A., et al. (2001). Variable -catenin Expression in Colorectal Cancers Indicates Tumor Progression Driven by the Tumor Environment. *Proc. Natl. Acad. Sci.* 98 (18), 10356–10361. doi:10.1073/pnas.171610498

Brooks, P. C., Montgomery, A. M. P., Rosenfeld, M., Reisfeld, R. A., Hu, T., Klier, G., et al. (1994). Integrin αvβ3 Antagonists Promote Tumor Regression by Inducing Apoptosis of Angiogenic Blood Vessels. *Cell* 79 (7), 1157–1164. doi:10.1016/0092-8674(94)90007-8

Bussard, K. M., Mutkus, L., Stumpf, K., Gomez-Manzano, C., and Marini, F. C. (2016). Tumor-associated Stromal Cells as Key Contributors to the Tumor Microenvironment. *Breast Cancer Res.* 18 (1), 84. doi:10.1186/s13058-016-0740-2

Bustamante, P., Piquet, L., Landreville, S., and Burnier, J. V. (2021). Uveal Melanoma Pathobiology: Metastasis to the Liver. *Semin. Cancer Biol.* 71, 65–85. doi:10.1016/j.semcancer.2020.05.003

Caby, M.-P., Lankar, D., Vincendeau-Scherrer, C., Raposo, G., and Bonnerot, C. (2005). Exosomal-like Vesicles Are Present in Human Blood Plasma. *Int. Immunol.* 17 (7), 879–887. doi:10.1093/intimm/dxh267

Cai, J., Gong, L., Li, G., Guo, J., Yi, X., and Wang, Z. (2021). Exosomes in Ovarian Cancer Ascites Promote Epithelial-Mesenchymal Transition of Ovarian Cancer Cells by Delivery of miR-6780b-5p. *Cell Death Dis* 12 (2), 210. doi:10.1038/s41419-021-03490-5

Cai, Q., Zhu, A., and Gong, L. (2018). Exosomes of Glioma Cells Deliver miR-148a to Promote Proliferation and Metastasis of Glioblastoma via Targeting CADM1. *Bull. du Cancer* 105 (7-8), 643–651. doi:10.1016/j.bulcan.2018.05.003

Cai, Z., Yang, F., Yu, L., Yu, Z., Jiang, L., Wang, Q., et al. (2012). Activated T Cell Exosomes Promote Tumor Invasion via Fas Signaling Pathway. *J.I.* 188 (12), 5954–5961. doi:10.4049/jimmunol.1103466

Caldaria, A., Giuffrida, R., di Meo, N., Massari, L., Dianzani, C., Cannavò, S. P., et al. (2020). Diagnosis and Treatment of Melanoma Bone Metastasis: A Multidisciplinary Approach. *Dermatol. Ther.* 33 (6), e14193. doi:10.1111/dth.14193

Campos, A., Salomon, C., Bustos, R., Díaz, J., Martínez, S., Silva, V., et al. (2018). Caveolin-1-containing Extracellular Vesicles Transport Adhesion Proteins and Promote Malignancy in Breast Cancer Cell Lines. *Nanomedicine* 13 (20), 2597–2609. doi:10.2217/nnm-2018-0094

Canda, A. E., Ozsoy, Y., Nalbant, O. A., and Sagol, O. (2008). Gastrointestinal Stromal Tumor of the Stomach with Lymph Node Metastasis. *World J. Surg. Onc* 6, 97. doi:10.1186/1477-7819-6-97

Cao, S.-Q., Zheng, H., Sun, B.-C., Wang, Z.-L., Liu, T., Guo, D.-H., et al. (2019). Long Non-coding RNA Highly Up-Regulated in Liver Cancer Promotes Exosome Secretion. *Wjg* 25 (35), 5283–5299. doi:10.3748/wjg.v25.i35.5283

Carvalho, J., Teixeira, M., Silva, F. T., Esteves, A., Ribeiro, C., and Guerra, D. (2020). Esophageal Gastrointestinal Stromal Tumor with Rare Intracranial Metastasis. *Case Rep. Gastrointest. Med.* 2020, 1–4. doi:10.1155/2020/8842006

Cascone, I., Napione, L., Maniero, F., Serini, G., and Bussolino, F. (2005). Stable Interaction between α5β1 Integrin and Tie2 Tyrosine Kinase Receptor Regulates Endothelial Cell Response to Ang-1. *J. Cel Biol* 170 (6), 993–1004. doi:10.1083/jcb.200507082

Castellano, J. J., Marrades, R. M., Molins, L., Viñolas, N., Moises, J., Canals, J., et al. (2020). Extracellular Vesicle lincRNA-P21 Expression in Tumor-Draining Pulmonary Vein Defines Prognosis in NSCLC and Modulates Endothelial Cell Behavior. *Cancers* 12 (3), 734. doi:10.3390/cancers12030734

Cavanna, L., Seghini, P., Di Nunzio, C., Orlandi, E., Michieletti, E., Stroppa, E., et al. (2018). Gastric Cancer with Brain Metastasis and the Role of Human Epidermal Growth Factor 2 Status. *Oncol. Lett.* 15 (4), 5787–5791. doi:10.3892/ol.2018.8054

Chalmin, F., Ladoire, S., Mignot, G., Vincent, J., Bruchard, M., Remy-Martin, J.-P., et al. (2010). Membrane-associated Hsp72 from Tumor-Derived Exosomes Mediates STAT3-dependent Immunosuppressive Function of Mouse and Human Myeloid-Derived Suppressor Cells. *J. Clin. Invest.* 120 (2), 457–471. doi:10.1172/JCI40483

Chang, G., Shi, L., Ye, Y., Shi, H., Zeng, L., Tiwary, S., et al. (2020). YTHDF3 Induces the Translation of m6A-Enriched Gene Transcripts to Promote Breast Cancer Brain Metastasis. *Cancer Cell* 38 (6), 857–871. doi:10.1016/j.ccell.2020.10.004

Che, Y., Geng, B., Xu, Y., Miao, X., Chen, L., Mu, X., et al. (2018). *Helicobacter pylori* -induced Exosomal MET Educates Tumour-Associated Macrophages to Promote Gastric Cancer Progression. *J. Cel Mol Med* 22 (11), 5708–5719. doi:10.1111/jcmm.13847

Chen, D., Chen, G., Jiang, W., Fu, M., Liu, W., Sui, J., et al. (2019). Association of the Collagen Signature in the Tumor Microenvironment with Lymph Node Metastasis in Early Gastric Cancer. *JAMA Surg.* 154 (3), e185249. doi:10.1001/jamasurg.2018.5249

Chen, G., Huang, A. C., Zhang, W., Zhang, G., Wu, M., Xu, W., et al. (2018). Exosomal PD-L1 Contributes to Immunosuppression and Is Associated with Anti-PD-1 Response. *Nature* 560 (7718), 382–386. doi:10.1038/s41586-018-0392-8

Chen, L., and Han, X. (2015). Anti-PD-1/PD-L1 Therapy of Human Cancer: Past, Present, and Future. *J. Clin. Invest.* 125 (9), 3384–3391. doi:10.1172/JCI80011

Chen, P. G., Schoeff, S. S., Watts, C. A., Reibel, J. F., Levine, P. A., Shonka, D. C., Jr., et al. (2014). Utility of Abdominal Imaging to Assess for Liver Metastasis in Patients with Head and Neck Cancer and Abnormal Liver Function Tests. *Am. J. Otolaryngol.* 35 (2), 137–140. doi:10.1016/j.amjoto.2013.10.004

Chen, X., Chen, L., Zhu, H., and Tao, J. (2020). Risk Factors and Prognostic Predictors for Cervical Cancer Patients with Lung Metastasis. *J. Cancer* 11 (20), 5880–5889. doi:10.7150/jca.46258

Chen, Y., Gou, X., Kong, D. K., Wang, X., Wang, J., Chen, Z., et al. (2015). EMMPRIN Regulates Tumor Growth and Metastasis by Recruiting Bone Marrow-Derived Cells through Paracrine Signaling of SDF-1 and VEGF. *Oncotarget* 6 (32), 32575–32585. doi:10.18632/oncotarget.5331

Chen, Z., Yang, L., Cui, Y., Zhou, Y., Yin, X., Guo, J., et al. (2016). Cytoskeleton-centric Protein Transportation by Exosomes Transforms Tumor-Favorable Macrophages. *Oncotarget* 7 (41), 67387–67402. doi:10.18632/oncotarget.11794

Cheng, Z., Lei, Z., Yang, P., Si, A., Xiang, D., Tang, X., et al. (2019). Exosome-transmitted P120-catenin Suppresses Hepatocellular Carcinoma Progression via STAT3 Pathways. *Mol. Carcinog* 58 (8), 1389–1399. doi:10.1002/mc.23022

Chi, C., Fan, Z., Yang, B., Sun, H., and Zheng, Z. (2021). The Clinical Characteristics and Prognostic Nomogram for Head and Neck Cancer Patients with Bone Metastasis. *J. Oncol.* 2021, 1–12. doi:10.1155/2021/5859757

Chin, A. R., and Wang, S. E. (2016). Cancer Tills the Premetastatic Field: Mechanistic Basis and Clinical Implications. *Clin. Cancer Res.* 22 (15), 3725–3733. doi:10.1158/1078-0432.CCR-16-0028

Choi, D.-S., Kim, D.-K., Kim, Y.-K., and Gho, Y. S. (2013). Proteomics, Transcriptomics and Lipidomics of Exosomes and Ectosomes. *Proteomics* 13 (10-11), 1554–1571. doi:10.1002/pmic.201200329

Clever, D., Roychoudhuri, R., Constantinides, M. G., Askenase, M. H., Sukumar, M., Klebanoff, C. A., et al. (2016). Oxygen Sensing by T Cells Establishes an Immunologically Tolerant Metastatic Niche. *Cell* 166 (5), 1117–1131 e1114. doi:10.1016/j.cell.2016.07.032

Costa-Silva, B., Aiello, N. M., Ocean, A. J., Singh, S., Zhang, H., Thakur, B. K., et al. (2015). Pancreatic Cancer Exosomes Initiate Pre-metastatic Niche Formation in the Liver. *Nat. Cel Biol* 17 (6), 816–826. doi:10.1038/ncb3169

Cumsille, P., Godoy, M., Gerdtzen, Z. P., and Conca, C. (2019). Parameter Estimation and Mathematical Modeling for the Quantitative Description of Therapy Failure Due to Drug Resistance in Gastrointestinal Stromal Tumor Metastasis to the Liver. *PLoS One* 14 (5), e0217332. doi:10.1371/journal.pone.0217332

Czernek, L., and Düchler, M. (2017). Functions of Cancer-Derived Extracellular Vesicles in Immunosuppression. *Arch. Immunol. Ther. Exp.* 65 (4), 311–323. doi:10.1007/s00005-016-0453-3

da Silva, G. T., Bergmann, A., and Thuler, L. C. S. (2019). Incidence and Risk Factors for Bone Metastasis in Non-small Cell Lung Cancer. *Asian Pac. J. Cancer Prev.* 20 (1), 45–51. doi:10.31557/APJCP.2019.20.1.45

Dai, J., Escara-Wilke, J., Keller, J. M., Jung, Y., Taichman, R. S., Pienta, K. J., et al. (2019). Primary Prostate Cancer Educates Bone Stroma through Exosomal Pyruvate Kinase M2 to Promote Bone Metastasis. *J. Exp. Med.* 216 (12), 2883–2899. doi:10.1084/jem.20190158

Das, S. K., Pradhan, A. K., Bhoopathi, P., Talukdar, S., Shen, X.-N., Sarkar, D., et al. (2018). The MDA-9/Syntenin/IGF1R/STAT3 Axis Directs Prostate Cancer Invasion. *Cancer Res.* 78 (11), 2852–2863. doi:10.1158/0008-5472.CAN-17-2992

Datta, C. K., Weinstein, J. D., Bland, J. E., Brager, P. M., and Stewart, M. A. (1998). A Case of Cervical Lymph Node Metastasis Resulting from Glioblastoma Multiforme. *W V Med. J.* 94 (5), 276–278.

de la Cruz-Merino, L., Grande-Pulido, E., Albero-Tamarit, A., and Codes-Manuel de Villena, M. E. (2008). Cancer and Immune Response: Old and New Evidence for Future Challenges. *Oncologist* 13 (12), 1246–1254. doi:10.1634/theoncologist.2008-0166

De, S., Razorenova, O., McCabe, N. P., O'Toole, T., Qin, J., and Byzova, T. V. (2005). VEGF-integrin Interplay Controls Tumor Growth and Vascularization. *Proc. Natl. Acad. Sci.* 102 (21), 7589–7594. doi:10.1073/pnas.0502935102

Deepak, P., and Acharya, A. (2010). Anti-tumor Immunity and Mechanism of Immunosuppression Mediated by Tumor Cells: Role of Tumor-Derived Soluble Factors and Cytokines. *Int. Rev. Immunol.* 29 (4), 421–458. doi:10.3109/08830185.2010.483027

Demory Beckler, M., Higginbotham, J. N., Franklin, J. L., Ham, A.-J., Halvey, P. J., Imasuen, I. E., et al. (2013). Proteomic Analysis of Exosomes from Mutant KRAS colon Cancer Cells Identifies Intercellular Transfer of Mutant KRAS. *Mol. Cell Proteomics* 12 (2), 343–355. doi:10.1074/mcp.M112.022806

Deng, Z., Rong, Y., Teng, Y., Zhuang, X., Samykutty, A., Mu, J., et al. (2017). Exosomes miR-126a Released from MDSC Induced by DOX Treatment Promotes Lung Metastasis. *Oncogene* 36 (5), 639–651. doi:10.1038/onc.2016.229

Desgrosellier, J. S., and Cheresh, D. A. (2010). Integrins in Cancer: Biological Implications and Therapeutic Opportunities. *Nat. Rev. Cancer* 10 (1), 9–22. doi:10.1038/nrc2748

Dey, M., Fetcko, K., Gondim, D., and Bonnin, J. (2017). Cervical Cancer Metastasis to the Brain: A Case Report and Review of Literature. *Surg. Neurol. Int.* 8, 181. doi:10.4103/sni.sni_111_17

Di Modica, M., Regondi, V., Sandri, M., Iorio, M. V., Zanetti, A., Tagliabue, E., et al. (2017). Breast Cancer-Secreted miR-939 Downregulates VE-Cadherin and Destroys the Barrier Function of Endothelial Monolayers. *Cancer Lett.* 384, 94–100. doi:10.1016/j.canlet.2016.09.013

Diepenbruck, M., and Christofori, G. (2016). Epithelial-mesenchymal Transition (EMT) and Metastasis: Yes, No, Maybe? *Curr. Opin. Cel Biol.* 43, 7–13. doi:10.1016/j.ceb.2016.06.002

Ding, J., Xu, Z., Zhang, Y., Tan, C., Hu, W., Wang, M., et al. (2018). Exosome-mediated miR-222 Transferring: An Insight into NF-Kb-Mediated Breast Cancer Metastasis. *Exp. Cel Res.* 369 (1), 129–138. doi:10.1016/j.yexcr.2018.05.014

Dolman, C. L. (1974). Lymph Node Metastasis as First Manifestation of Glioblastoma. *J. Neurosurg.* 41 (5), 607–609. doi:10.3171/jns.1974.41.5.0607

Doshi, T. V., Doshi, J. V., Makaryus, J. N., and Makaryus, A. N. (2013). A Rare Case of Successfully Treated Cardiac Metastasis from Transitional Cell Bladder Cancer. *Am. J. Ther.* 20 (3), 307–310. doi:10.1097/MJT.0b013e3181f6c131

Du, Q., Ye, X., Lu, S.-R., Li, H., Liu, H.-Y., Zhai, Q., et al. (2021). Exosomal miR-30a and miR-222 Derived from colon Cancer Mesenchymal Stem Cells Promote the Tumorigenicity of colon Cancer through Targeting MIA3. *J. Gastrointest. Oncol.* 12 (1), 52–68. doi:10.21037/jgo-20-513

Eble, J. A., and Niland, S. (2019). The Extracellular Matrix in Tumor Progression and Metastasis. *Clin. Exp. Metastasis* 36 (3), 171–198. doi:10.1007/s10585-019-09966-1

Ekström, E. J., Bergenfelz, C., von Bülow, V., Serifler, F., Carlemalm, E., Jönsson, G., et al. (2014). WNT5A Induces Release of Exosomes Containing Pro-angiogenic and Immunosuppressive Factors from Malignant Melanoma Cells. *Mol. Cancer* 13, 88. doi:10.1186/1476-4598-13-88

El-Halabi, M. M., Chaaban, S. A., Meouchy, J., Page, S., and Salyers, W. J., Jr. (2014). Colon Cancer Metastasis to Mediastinal Lymph Nodes without Liver or Lung Involvement: A Case Report. *Oncol. Lett.* 8 (5), 2221–2224. doi:10.3892/ol.2014.2426

Elsner, L., Muppala, V., Gehrmann, M., Lozano, J., Malzahn, D., Bickeböller, H., et al. (2007). The Heat Shock Protein HSP70 Promotes Mouse NK Cell Activity against Tumors that Express Inducible NKG2D Ligands. *J. Immunol.* 179 (8), 5523–5533. doi:10.4049/jimmunol.179.8.5523

Estelles Piera, F., Peris Godoy, M., Saro Pérez, E., and Calabuig Alborch, J. R. (1993). Multiple Myeloma and Adenocarcinoma Liver Metastasis. *Med. Interna* 10 (7), 363.

Etoh, T., Baba, H., Adachi, E., Kohnoe, S., Seo, Y., Saito, T., et al. (1997). A Case of Liver Metastasis of Malignant Peritoneal Mesothelioma Successfully Treated by Surgery. *Oncol. Rep.* 4 (4), 803–805. doi:10.3892/or.4.4.803

Fan, Z., Huang, Z., Hu, C., Tong, Y., and Zhao, C. (2020). Risk Factors and Nomogram for Newly Diagnosis of Bone Metastasis in Bladder Cancer. *Medicine (Baltimore)* 99 (42), e22675. doi:10.1097/MD.0000000000022675

Fang, J. H., Zhang, Z. J., Shang, L. R., Luo, Y. W., Lin, Y. F., Yuan, Y., et al. (2018). Hepatoma Cell-secreted Exosomal microRNA-103 Increases Vascular Permeability and Promotes Metastasis by Targeting junction Proteins. *Hepatology* 68 (4), 1459–1475. doi:10.1002/hep.29920

Fang, T., Lv, H., Lv, G., Li, T., Wang, C., Han, Q., et al. (2018). Tumor-derived Exosomal miR-1247-3p Induces Cancer-Associated Fibroblast Activation to foster Lung Metastasis of Liver Cancer. *Nat. Commun.* 9 (1), 191. doi:10.1038/s41467-017-02583-0

Fang, W.-Y., Kuo, Y.-Z., Chang, J.-Y., Hsiao, J.-R., Kao, H.-Y., Tsai, S.-T., et al. (2020). The Tumor Suppressor TGFBR3 Blocks Lymph Node Metastasis in Head and Neck Cancer. *Cancers* 12 (6), 1375. doi:10.3390/cancers12061375

Faries, M. B., Han, D., Reintgen, M., Kerivan, L., Reintgen, D., and Caracò, C. (2018). Lymph Node Metastasis in Melanoma: a Debate on the Significance of Nodal Metastases, Conditional Survival Analysis and Clinical Trials. *Clin. Exp. Metastasis* 35 (5-6), 431–442. doi:10.1007/s10585-018-9898-6

Felcht, M., Luck, R., Schering, A., Seidel, P., Srivastava, K., Hu, J., et al. (2012). Angiopoietin-2 Differentially Regulates Angiogenesis through TIE2 and Integrin Signaling. *J. Clin. Invest.* 122 (6), 1991–2005. doi:10.1172/JCI58832

Fidler, I. J., and Kripke, M. L. (2015). The challenge of Targeting Metastasis. *Cancer Metastasis Rev.* 34 (4), 635–641. doi:10.1007/s10555-015-9586-9

Fong, M. Y., Zhou, W., Liu, L., Alontaga, A. Y., Chandra, M., Ashby, J., et al. (2015). Breast-cancer-secreted miR-122 Reprograms Glucose Metabolism in Premetastatic Niche to Promote Metastasis. *Nat. Cel Biol* 17 (2), 183–194. doi:10.1038/ncb3094

Fu, Q., Zhang, Q., Lou, Y., Yang, J., Nie, G., Chen, Q., et al. (2018). Primary Tumor-Derived Exosomes Facilitate Metastasis by Regulating Adhesion of Circulating Tumor Cells via SMAD3 in Liver Cancer. *Oncogene* 37 (47), 6105–6118. doi:10.1038/s41388-018-0391-0

Fujimoto, T., Nakagawa, S., Morofuji, Y., Watanabe, D., Ujifuku, K., Horie, N., et al. (2020). Pericytes Suppress Brain Metastasis from Lung Cancer *In Vitro*. *Cell Mol Neurobiol* 40 (1), 113–121. doi:10.1007/s10571-019-00725-0

Fujita, I., Toyokawa, T., Makino, T., Matsueda, K., Omote, S., and Horii, J. (2020). Small Early Gastric Cancer with Synchronous Bone Metastasis: A Case Report. *Mol. Clin. Onc* 12 (3), 202–207. doi:10.3892/mco.2020.1985

García, S. A., Weitz, J., and Schölch, S. (2018). Circulating Tumor Cells. *Methods Mol. Biol.* 1692, 213–219. doi:10.1007/978-1-4939-7401-6_18

Garcia-Diaz, A., Shin, D. S., Moreno, B. H., Saco, J., Escuin-Ordinas, H., Rodriguez, G. A., et al. (2019). Interferon Receptor Signaling Pathways Regulating PD-L1 and PD-L2 Expression. *Cel Rep.* 29 (11), 3766. doi:10.1016/j.celrep.2019.11.113

Garnier, D., Magnus, N., Lee, T. H., Bentley, V., Meehan, B., Milsom, C., et al. (2012). Cancer Cells Induced to Express Mesenchymal Phenotype Release Exosome-like Extracellular Vesicles Carrying Tissue Factor. *J. Biol. Chem.* 287 (52), 43565–43572. doi:10.1074/jbc.M112.401760

Ginestra, A., Monea, S., Seghezzi, G., Dolo, V., Nagase, H., Mignatti, P., et al. (1997). Urokinase Plasminogen Activator and Gelatinases Are Associated with Membrane Vesicles Shed by Human HT1080 Fibrosarcoma Cells. *J. Biol. Chem.* 272 (27), 17216–17222. doi:10.1074/jbc.272.27.17216

Goetzl, E. J., Goetzl, L., Karliner, J. S., Tang, N., and Pulliam, L. (2016). Human Plasma Platelet-derived Exosomes: Effects of Aspirin. *FASEB j.* 30 (5), 2058–2063. doi:10.1096/fj.201500150R

Greening, D. W., Gopal, S. K., Xu, R., Simpson, R. J., and Chen, W. (2015). Exosomes and Their Roles in Immune Regulation and Cancer. *Semin. Cel Dev. Biol.* 40, 72–81. doi:10.1016/j.semcdb.2015.02.009

Grivennikov, S. I., Greten, F. R., and Karin, M. (2010). Immunity, Inflammation, and Cancer. *Cell* 140 (6), 883–899. doi:10.1016/j.cell.2010.01.025

Grossniklaus, H. E. (2019). Understanding Uveal Melanoma Metastasis to the Liver: The Zimmerman Effect and the Zimmerman Hypothesis. *Ophthalmology* 126 (4), 483–487. doi:10.1016/j.ophtha.2018.09.031

Guan, Z., Lan, H., Chen, X., Jiang, X., Wang, X., and Jin, K. (2017). Individualized Drug Screening Based on Next Generation Sequencing and Patient Derived Xenograft Model for Pancreatic Cancer with Bone Metastasis. *Mol. Med. Rep.* 16 (4), 4784–4790. doi:10.3892/mmr.2017.7213

Guo, Y., Ji, X., Liu, J., Fan, D., Zhou, Q., Chen, C., et al. (2019). Effects of Exosomes on Pre-metastatic Niche Formation in Tumors. *Mol. Cancer* 18 (1), 39. doi:10.1186/s12943-019-0995-1

Han, Q., Lv, L., Wei, J., Lei, X., Lin, H., Li, G., et al. (2019). Vps4A Mediates the Localization and Exosome Release of β-catenin to Inhibit Epithelial-Mesenchymal Transition in Hepatocellular Carcinoma. *Cancer Lett.* 457, 47–59. doi:10.1016/j.canlet.2019.04.035

Hashimoto, K., Ochi, H., Sunamura, S., Kosaka, N., Mabuchi, Y., Fukuda, T., et al. (2018). Cancer-secreted Hsa-miR-940 Induces an Osteoblastic Phenotype in the Bone Metastatic Microenvironment via Targeting ARHGAP1 and FAM134A. *Proc. Natl. Acad. Sci. USA* 115 (9), 2204–2209. doi:10.1073/pnas.1717363115

He, J., Shi, J., Zhang, K., Xue, J., Li, J., Yang, J., et al. (2017). Sox2 Inhibits Wnt-β-Catenin Signaling and Metastatic Potency of Cisplatin-Resistant Lung Adenocarcinoma Cells. *Mol. Med. Rep.* 15 (4), 1693–1701. doi:10.3892/mmr.2017.6170

Hernández-Esquivel, M. A., Pérez-Torres, A., Romero-Romero, L., Reyes-Matute, A., Loaiza, B., Mellado-Sánchez, G., et al. (2018). The Dialyzable Leukocyte Extract TransferonTM Inhibits Tumor Growth and Brain Metastasis in a Murine Model of Prostate Cancer. *Biomed. Pharmacother.* 101, 938–944. doi:10.1016/j.biopha.2018.03.012

Hirooka, A., Tamiya, A., Kanazu, M., Nonaka, J., Yonezawa, T., Asami, K., et al. (2016). Brain Metastasis of Pleural Mesothelioma after a Subarachnoid Hemorrhage. *Intern. Med.* 55 (7), 779–781. doi:10.2169/internalmedicine.55.3765

Ho, T. T. B., Nasti, A., Seki, A., Komura, T., Inui, H., Kozaka, T., et al. (2020). Combination of Gemcitabine and Anti-PD-1 Antibody Enhances the Anticancer Effect of M1 Macrophages and the Th1 Response in a Murine Model of Pancreatic Cancer Liver Metastasis. *J. Immunother. Cancer* 8 (2), e001367. doi:10.1136/jitc-2020-001367

Hoffman, H. A., Li, C. H., Everson, R. G., Strunck, J. L., Yong, W. H., and Lu, D. C. (2017). Primary Lung Metastasis of Glioblastoma Multiforme with Epidural Spinal Metastasis: Case Report. *J. Clin. Neurosci.* 41, 97–99. doi:10.1016/j.jocn.2017.03.033

Hong, C.-S., Sharma, P., Yerneni, S. S., Simms, P., Jackson, E. K., Whiteside, T. L., et al. (2017). Circulating Exosomes Carrying an Immunosuppressive Cargo Interfere with Cellular Immunotherapy in Acute Myeloid Leukemia. *Sci. Rep.* 7 (1), 14684. doi:10.1038/s41598-017-14661-w

Hong, L., Qiu, H., Mei, Z., Zhang, H., Liu, S., and Cao, H. (2018). Ovarian Cancer Initially Presenting with Supra-clavicular L-ymph N-ode M-etastasis: A C-ase R-eport. *Oncol. Lett.* 16 (1), 505–510. doi:10.3892/ol.2018.8664

Hood, J. L., San, R. S., and Wickline, S. A. (2011). Exosomes Released by Melanoma Cells Prepare sentinel Lymph Nodes for Tumor Metastasis. *Cancer Res.* 71 (11), 3792–3801. doi:10.1158/0008-5472.CAN-10-4455

Hoshino, A., Costa-Silva, B., Shen, T.-L., Rodrigues, G., Hashimoto, A., Tesic Mark, M., et al. (2015). Tumour Exosome Integrins Determine Organotropic Metastasis. *Nature* 527 (7578), 329–335. doi:10.1038/nature15756

Hosonaga, M., Saya, H., and Arima, Y. (2020). Molecular and Cellular Mechanisms Underlying Brain Metastasis of Breast Cancer. *Cancer Metastasis Rev.* 39 (3), 711–720. doi:10.1007/s10555-020-09881-y

Hsieh, Y.-S., Chu, S.-C., Huang, S.-C., Kao, S.-H., Lin, M.-S., and Chen, P.-N. (2021). Gossypol Reduces Metastasis and Epithelial-Mesenchymal Transition by Targeting Protease in Human Cervical Cancer. *Am. J. Chin. Med.* 49 (1), 181–198. doi:10.1142/S0192415X21500105

Hsu, Y.-L., Hung, J.-Y., Chang, W.-A., Jian, S.-F., Lin, Y.-S., Pan, Y.-C., et al. (2018). Hypoxic Lung-Cancer-Derived Extracellular Vesicle MicroRNA-103a Increases the Oncogenic Effects of Macrophages by Targeting PTEN. *Mol. Ther.* 26 (2), 568–581. doi:10.1016/j.ymthe.2017.11.016

Hsu, Y.-L., Hung, J.-Y., Chang, W.-A., Lin, Y.-S., Pan, Y.-C., Tsai, P.-H., et al. (2017). Hypoxic Lung Cancer-Secreted Exosomal miR-23a Increased Angiogenesis and Vascular Permeability by Targeting Prolyl Hydroxylase and Tight junction Protein ZO-1. *Oncogene* 36 (34), 4929–4942. doi:10.1038/onc.2017.105

Hu, C., Yang, J., Huang, Z., Liu, C., Lin, Y., Tong, Y., et al. (2020). Diagnostic and Prognostic Nomograms for Bone Metastasis in Hepatocellular Carcinoma. *BMC Cancer* 20 (1), 494. doi:10.1186/s12885-020-06995-y

Hu, H.-Y., Yu, C.-H., Zhang, H.-H., Zhang, S.-Z., Yu, W.-Y., Yang, Y., et al. (2019). Exosomal miR-1229 Derived from Colorectal Cancer Cells Promotes Angiogenesis by Targeting HIPK2. *Int. J. Biol. Macromolecules* 132, 470–477. doi:10.1016/j.ijbiomac.2019.03.221

Hu, J. L., Wang, W., Lan, X. L., Zeng, Z. C., Liang, Y. S., Yan, Y. R., et al. (2019). CAFs Secreted Exosomes Promote Metastasis and Chemotherapy Resistance by Enhancing Cell Stemness and Epithelial-Mesenchymal Transition in Colorectal Cancer. *Mol. Cancer* 18 (1), 91. doi:10.1186/s12943-019-1019-x

Hu, Y., Li, D., Wu, A., Qiu, X., Di, W., Huang, L., et al. (2017). TWEAK-stimulated Macrophages Inhibit Metastasis of Epithelial Ovarian Cancer via Exosomal Shuttling of microRNA. *Cancer Lett.* 393, 60–67. doi:10.1016/j.canlet.2017.02.009

Huang, C.-S., Ho, J.-Y., Chiang, J.-H., Yu, C.-P., and Yu, D.-S. (2020a). Exosome-Derived LINC00960 and LINC02470 Promote the Epithelial-Mesenchymal Transition and Aggressiveness of Bladder Cancer Cells. *Cells* 9 (6), 1419. doi:10.3390/cells9061419

Huang, R., and Rofstad, E. K. (2018). Integrins as Therapeutic Targets in the Organ-specific Metastasis of Human Malignant Melanoma. *J. Exp. Clin. Cancer Res.* 37 (1), 92. doi:10.1186/s13046-018-0763-x

Huang, R., Wu, J., Zheng, Z., Wang, G., Song, D., Yan, P., et al. (2019). The Construction and Analysis of ceRNA Network and Patterns of Immune Infiltration in Mesothelioma with Bone Metastasis. *Front. Bioeng. Biotechnol.* 7, 257. doi:10.3389/fbioe.2019.00257

Huang, X.-Y., Huang, Z.-L., Huang, J., Xu, B., Huang, X.-Y., Xu, Y.-H., et al. (2020b). Exosomal circRNA-100338 Promotes Hepatocellular Carcinoma Metastasis via Enhancing Invasiveness and Angiogenesis. *J. Exp. Clin. Cancer Res.* 39 (1), 20. doi:10.1186/s13046-020-1529-9

Hwang, J. H., Yoo, H. J., Lim, M. C., Seo, S.-S., Kang, S., Kim, J.-Y., et al. (2013). Brain Metastasis in Patients with Uterine Cervical Cancer. *J. Obstet. Gynaecol. Res.* 39 (1), 287–291. doi:10.1111/j.1447-0756.2012.01927.x

Hyun, Y.-M., Seo, S.-U., Choi, W. S., Kwon, H.-J., Kim, D.-Y., Jeong, S., et al. (2020). Endogenous DEL-1 Restrains Melanoma Lung Metastasis by Limiting Myeloid Cell-Associated Lung Inflammation. *Sci. Adv.* 6 (45). doi:10.1126/sciadv.abc4882

Ikegami, T., Yoshizumi, T., Kawasaki, J., Nagatsu, A., Uchiyama, H., Harada, N., et al. (2017). Surgical Resection for Lymph Node Metastasis after Liver Transplantation for Hepatocellular Carcinoma. *Ar* 37 (2), 891–896. doi:10.21873/anticanres.11395

Imura, Y., Tateiwa, D., Sugimoto, N., Inoue, A., Wakamatsu, T., Outani, H., et al. (2020). Prognostic Factors and Skeletal-related E-vents in P-atients with B-one

M-etastasis from G-astric C-ancer. *Mol. Clin. Oncol.* 13 (4), 31. doi:10.3892/mco.2020.2101

Jamjoom, A. B., Jamjoom, Z. A. B., Rahman, N.-U., and Al-Rikabi, A. C. (1997). Cervical Lymph Node Metastasis from a Glioblastoma Multiforme in a Child: Report of a Case and a Review of the Literature. *Ann. Saudi Med.* 17 (3), 340–343. doi:10.5144/0256-4947.1997.340

Ji, L., Fan, L., Zhu, X., Gao, Y., and Wang, Z. (2020). A Prognostic Model for Breast Cancer with Liver Metastasis. *Front. Oncol.* 10, 1342. doi:10.3389/fonc.2020.01342

Jiang, K., Dong, C., Yin, Z., Li, R., Mao, J., Wang, C., et al. (2020). Exosome-derived ENO1 Regulates Integrin α6β4 Expression and Promotes Hepatocellular Carcinoma Growth and Metastasis. *Cel Death Dis* 11 (11), 972. doi:10.1038/s41419-020-03179-1

Jie, G. N., Sing, W. C., Ching, C. Y., and Tiffany, fnm. (2011). Is Lymph Node Metastasis a Common Feature of Gastrointestinal Stromal Tumor? *Clin. Nucl. Med.* 36 (8), 678–682. doi:10.1097/RLU.0b013e318219ad31

Kalluri, R. (2016). The Biology and Function of Exosomes in Cancer. *J. Clin. Invest.* 126 (4), 1208–1215. doi:10.1172/JCI81135

Kanayama, T., Mabuchi, S., Shimura, K., Hisamatsu, T., Isohashi, F., Hamasaki, T., et al. (2015). Prognostic Factors for Survival in Cervical Cancer Patients with Bone Metastasis. *Eur. J. Gynaecol. Oncol.* 36 (3), 290–293.

Kanda, M., Fujii, T., Nagai, S., Kodera, Y., Kanzaki, A., Sahin, T. T., et al. (2011). Pattern of Lymph Node Metastasis Spread in Pancreatic Cancer. *Pancreas* 40 (6), 951–955. doi:10.1097/MPA.0b013e3182148342

Kapoor, H., Sanampudi, S., Owen, J., and Raissi, D. (2020). Lung Metastasis Postradioembolization of Hepatocellular Carcinoma with Tumor in Vein. *ACG Case Rep. J.* 7 (2), e00322. doi:10.14309/crj.0000000000000322

Katona, F., Murnyák, B., Marko-Varga, G., and Hortobágyi, T. (2017). A Melanoma És Az Agyi Áttétképződés Molekuláris Háttere. *Orvosi Hetilap* 158 (28), 1083–1091. doi:10.1556/650.2017.30793

Kawai, A., Nagasaka, Y., Muraki, M., Fukuoka, M., Satou, T., Kimura, M., et al. (1997). Brain Metastasis in Malignant Pleural Mesothelioma. *Intern. Med.* 36 (8), 591–594. doi:10.2169/internalmedicine.36.591

Khan, S., Aspe, J. R., Asumen, M. G., Almaguel, F., Odumosu, O., Acevedo-Martinez, S., et al. (2009). Extracellular, Cell-Permeable Survivin Inhibits Apoptosis while Promoting Proliferative and Metastatic Potential. *Br. J. Cancer* 100 (7), 1073–1086. doi:10.1038/sj.bjc.6604978

Khan, S., Jutzy, J. M. S., Aspe, J. R., McGregor, D. W., Neidigh, J. W., and Wall, N. R. (2011). Survivin Is Released from Cancer Cells via Exosomes. *Apoptosis* 16 (1), 1–12. doi:10.1007/s10495-010-0534-4

Kim, E.-K., Song, M.-J., Jung, Y., Lee, W.-S., and Jang, H. H. (2019a). Proteomic Analysis of Primary Colon Cancer and Synchronous Solitary Liver Metastasis. *Cancer Genomics Proteomics* 16 (6), 583–592. doi:10.21873/cgp.20161

Kim, H., Lee, K. K., Heo, M. H., and Kim, J. Y. (2019b). The Prognostic Factors Influencing Overall Survival in Uterine Cervical Cancer with Brain Metastasis. *Korean J. Intern. Med.* 34 (6), 1324–1332. doi:10.3904/kjim.2018.051

Kim, J., Piao, H.-L., Kim, B.-J., Yao, F., Han, Z., Wang, Y., et al. (2018). Long Noncoding RNA MALAT1 Suppresses Breast Cancer Metastasis. *Nat. Genet.* 50 (12), 1705–1715. doi:10.1038/s41588-018-0252-3

Kim, J. W., Wieckowski, E., Taylor, D. D., Reichert, T. E., Watkins, S., and Whiteside, T. L. (2005). Fas Ligand-Positive Membranous Vesicles Isolated from Sera of Patients with Oral Cancer Induce Apoptosis of Activated T Lymphocytes. *Clin. Cancer Res.* 11 (3), 1010–1020. doi:10.1158/1078-0432.ccr-05-1346

Kim, R., Song, J., and Kim, S. B. (2020). Concurrent Hepatocellular Carcinoma Metastasis to Stomach, colon, and Brain: A Case Report. *Wjcc* 8 (16), 3534–3541. doi:10.12998/wjcc.v8.i16.3534

Kim, S., Bae, W. J., Ahn, J. M., Heo, J.-H., Kim, K.-M., Choi, K. W., et al. (2021). MicroRNA Signatures Associated with Lymph Node Metastasis in Intramucosal Gastric Cancer. *Mod. Pathol.* 34 (3), 672–683. doi:10.1038/s41379-020-00681-x

Kim, W., Seok Kang, Y., Soo Kim, J., Shin, N.-Y., Hanks, S. K., and Song, W. K. (2008). The Integrin-Coupled Signaling Adaptor p130Cas Suppresses Smad3 Function in Transforming Growth Factor-β Signaling. *MBoC* 19 (5), 2135–2146. doi:10.1091/mbc.E07-10-0991

Kircher, D., Silvis, M., Cho, J., and Holmen, S. (2016). Melanoma Brain Metastasis: Mechanisms, Models, and Medicine. *Ijms* 17 (9), 1468. doi:10.3390/ijms17091468

Klemke, M., Weschenfelder, T., Konstandin, M. H., and Samstag, Y. (2007). High Affinity Interaction of Integrin α4β1 (VLA-4) and Vascular Cell Adhesion Molecule 1 (VCAM-1) Enhances Migration of Human Melanoma Cells across Activated Endothelial Cell Layers. *J. Cel. Physiol.* 212 (2), 368–374. doi:10.1002/jcp.21029

Kleppe, M., Wang, T., Van Gorp, T., Slangen, B. F. M., Kruse, A. J., and Kruitwagen, R. F. P. M. (2011). Lymph Node Metastasis in Stages I and II Ovarian Cancer: a Review. *Gynecol. Oncol.* 123 (3), 610–614. doi:10.1016/j.ygyno.2011.09.013

Klingenberg, S., Jochumsen, M. R., Ulhøi, B. P., Fredsøe, J., Sørensen, K. D., Borre, M., et al. (2021). 68Ga-PSMA PET/CT for Primary Lymph Node and Distant Metastasis NM Staging of High-Risk Prostate Cancer. *J. Nucl. Med.* 62 (2), 214–220. doi:10.2967/jnumed.120.245605

Kofler, B., Kerschbaumer, J., Schartinger, V. H., Posch, A., Gizewski, E. R., and Widmann, G. (2017). Hirnmetastase versus Strahlennekrose nach Kopf-Hals-Karzinom. *Radiologe* 57 (5), 392–396. doi:10.1007/s00117-017-0219-x

Kogure, T., Lin, W.-L., Yan, I. K., Braconi, C., and Patel, T. (2011). Intercellular Nanovesicle-Mediated microRNA Transfer: a Mechanism of Environmental Modulation of Hepatocellular Cancer Cell Growth. *Hepatology* 54 (4), 1237–1248. doi:10.1002/hep.24504

Kong, J., Tian, H., Zhang, F., Zhang, Z., Li, J., Liu, X., et al. (2019). Extracellular Vesicles of Carcinoma-Associated Fibroblasts Creates a Pre-metastatic Niche in the Lung through Activating Fibroblasts. *Mol. Cancer* 18 (1), 175. doi:10.1186/s12943-019-1101-4

Kong, M., Jin, J., Cai, X., Shen, J., Ma, D., Ye, M., et al. (2017). Characteristics of Lymph Node Metastasis in Resected Adenosquamous Lung Cancer. *Medicine (Baltimore)* 96 (48), e8870. doi:10.1097/MD.0000000000008870

Kong, X., Zhang, J., Li, J., Shao, J., and Fang, L. (2018). MiR-130a-3p Inhibits Migration and Invasion by Regulating RAB5B in Human Breast Cancer Stem Cell-like Cells. *Biochem. Biophysical Res. Commun.* 501 (2), 486–493. doi:10.1016/j.bbrc.2018.05.018

Kopp, H.-G., Placke, T., and Salih, H. R. (2009). Platelet-Derived Transforming Growth Factor-β Down-Regulates NKG2D Thereby Inhibiting Natural Killer Cell Antitumor Reactivity. *Cancer Res.* 69 (19), 7775–7783. doi:10.1158/0008-5472.CAN-09-2123

Kosaka, N., Iguchi, H., Hagiwara, K., Yoshioka, Y., Takeshita, F., and Ochiya, T. (2013). Neutral Sphingomyelinase 2 (nSMase2)-dependent Exosomal Transfer of Angiogenic microRNAs Regulate Cancer Cell Metastasis. *J. Biol. Chem.* 288 (15), 10849–10859. doi:10.1074/jbc.M112.446831

Kubo, N., and Takeuchi, N. (2017). Gastrointestinal Stromal Tumor of the Stomach with Axillary Lymph Node Metastasis: A Case Report. *Wjg* 23 (9), 1720–1724. doi:10.3748/wjg.v23.i9.1720

Kucharzewska, P., Christianson, H. C., Welch, J. E., Svensson, K. J., Fredlund, E., Ringner, M., et al. (2013). Exosomes Reflect the Hypoxic Status of Glioma Cells and Mediate Hypoxia-dependent Activation of Vascular Cells during Tumor Development. *Proc. Natl. Acad. Sci.* 110 (18), 7312–7317. doi:10.1073/pnas.1220998110

Kumar, L., Bhargava, V. L., Rao, R. C. K., Rath, G. K., and Kataria, S. P. (1992). Bone Metastasis in Ovarian Cancer. *Asia Oceania J. Obstet. Gynaecol.* 18 (4), 309–313. doi:10.1111/j.1447-0756.1992.tb00324.x

Kuo, S.-W., Ke, F.-C., Chang, G.-D., Lee, M.-T., and Hwang, J.-J. (2011). Potential Role of Follicle-Stimulating Hormone (FSH) and Transforming Growth Factor (TGFβ1) in the Regulation of Ovarian Angiogenesis. *J. Cel. Physiol.* 226 (6), 1608–1619. doi:10.1002/jcp.22491

Kuznetsov, H. S., Marsh, T., Markens, B. A., Castaño, Z., Greene-Colozzi, A., Hay, S. A., et al. (2012). Identification of Luminal Breast Cancers that Establish a Tumor-Supportive Macroenvironment Defined by Proangiogenic Platelets and Bone Marrow-Derived Cells. *Cancer Discov.* 2 (12), 1150–1165. doi:10.1158/2159-8290.CD-12-0216

Lal, P., Tiwari, A., Kumar, N., and Bajpai, R. (2007). Bone Metastasis from Ovarian Cancer. *J. Can. Res. Ther.* 3 (1), 34–36. doi:10.4103/0973-1482.31969

Lambert, A. W., Pattabiraman, D. R., and Weinberg, R. A. (2017). Emerging Biological Principles of Metastasis. *Cell* 168 (4), 670–691. doi:10.1016/j.cell.2016.11.037

Lan, J., Sun, L., Xu, F., Liu, L., Hu, F., Song, D., et al. (2019). M2 Macrophage-Derived Exosomes Promote Cell Migration and Invasion in Colon Cancer. *Cancer Res.* 79 (1), 146–158. doi:10.1158/0008-5472.CAN-18-0014

Lang, H.-L., Hu, G.-W., Zhang, B., Kuang, W., Chen, Y., Wu, L., et al. (2017b). Glioma Cells Enhance Angiogenesis and Inhibit Endothelial Cell Apoptosis

through the Release of Exosomes that Contain Long Non-coding RNA CCAT2. *Oncol. Rep.* 38 (2), 785–798. doi:10.3892/or.2017.5742

Lang, H. L., Hu, G. W., Chen, Y., Liu, Y., Tu, W., Lu, Y. M., et al. (2017a). Glioma Cells Promote Angiogenesis through the Release of Exosomes Containing Long Non-coding RNA POU3F3. *Eur. Rev. Med. Pharmacol. Sci.* 21 (5), 959–972.

Laurini, R. N. (1974). Diffuse Pleural Mesothelioma with Distant Bone Metastasis. *Acta Pathol. Microbiol. Scand. A.* 82A (2), 296–298. doi:10.1111/j.1699-0463.1974.tb03854.x

Lázaro-Ibáñez, E., Sanz-Garcia, A., Visakorpi, T., Escobedo-Lucea, C., Siljander, P., Ayuso-Sacido, Á., et al. (2014). Different gDNA Content in the Subpopulations of Prostate Cancer Extracellular Vesicles: Apoptotic Bodies, Microvesicles, and Exosomes. *Prostate* 74 (14), 1379–1390. doi:10.1002/pros.22853

Lee, J.-K., Park, S.-R., Jung, B.-K., Jeon, Y.-K., Lee, Y.-S., Kim, M.-K., et al. (2013b). Exosomes Derived from Mesenchymal Stem Cells Suppress Angiogenesis by Down-Regulating VEGF Expression in Breast Cancer Cells. *PLoS One* 8 (12), e84256. doi:10.1371/journal.pone.0084256

Lee, J., Kim, K. E., Choi, D.-K., Jang, J. Y., Jung, J.-J., Kiyonari, H., et al. (2013a). Angiopoietin-1 Guides Directional Angiogenesis through Integrin α V β 5 Signaling for Recovery of Ischemic Retinopathy. *Sci. Transl. Med.* 5 (203), 203ra127. doi:10.1126/scitranslmed.3006666

Leight, J. L., Wozniak, M. A., Chen, S., Lynch, M. L., and Chen, C. S. (2012). Matrix Rigidity Regulates a Switch between TGF-B1-Induced Apoptosis and Epithelial-Mesenchymal Transition. *MBoC* 23 (5), 781–791. doi:10.1091/mbc.E11-06-0537

Leitinger, B. (2011). Transmembrane Collagen Receptors. *Annu. Rev. Cel Dev. Biol.* 27, 265–290. doi:10.1146/annurev-cellbio-092910-154013

Lemke, J., Scheele, J., Kapapa, T., Wirtz, C., Henne-Bruns, D., and Kornmann, M. (2013). Brain Metastasis in Pancreatic Cancer. *Ijms* 14 (2), 4163–4173. doi:10.3390/ijms14024163

Levental, K. R., Yu, H., Kass, L., Lakins, J. N., Egeblad, M., Erler, J. T., et al. (2009). Matrix Crosslinking Forces Tumor Progression by Enhancing Integrin Signaling. *Cell* 139 (5), 891–906. doi:10.1016/j.cell.2009.10.027

Li, B., Mao, R., Liu, C., Zhang, W., Tang, Y., and Guo, Z. (2018). LncRNA FAL1 Promotes Cell Proliferation and Migration by Acting as a CeRNA of miR-1236 in Hepatocellular Carcinoma Cells. *Life Sci.* 197, 122–129. doi:10.1016/j.lfs.2018.02.006

Li, F., Dai, Y., Xu, H., Huang, K., Zhou, Y., Luo, D., et al. (2019). XPNPEP2 Is Associated with Lymph Node Metastasis in Prostate Cancer Patients. *Sci. Rep.* 9 (1), 10078. doi:10.1038/s41598-019-45245-5

Li, J., Li, Z., Jiang, P., Peng, M., Zhang, X., Chen, K., et al. (2018). Circular RNA IARS (Circ-IARS) Secreted by Pancreatic Cancer Cells and Located within Exosomes Regulates Endothelial Monolayer Permeability to Promote Tumor Metastasis. *J. Exp. Clin. Cancer Res.* 37 (1), 177. doi:10.1186/s13046-018-0822-3

Li, K., Chen, Y., Li, A., Tan, C., and Liu, X. (2019). Exosomes Play Roles in Sequential Processes of Tumor Metastasis. *Int. J. Cancer* 144 (7), 1486–1495. doi:10.1002/ijc.31774

Li, R., Wang, Y., Zhang, X., Feng, M., Ma, J., Li, J., et al. (2019). Exosome-mediated Secretion of LOXL4 Promotes Hepatocellular Carcinoma Cell Invasion and Metastasis. *Mol. Cancer* 18 (1), 18. doi:10.1186/s12943-019-0948-8

Li, Y., Li, Q., Li, D., Gu, J., Qian, D., Qin, X., et al. (2021). Exosome Carrying PSGR Promotes Stemness and Epithelial-Mesenchymal Transition of Low Aggressive Prostate Cancer Cells. *Life Sci.* 264, 118638. doi:10.1016/j.lfs.2020.118638

Li, Y., Liang, Y., Sang, Y., Song, X., Zhang, H., Liu, Y., et al. (2018). MiR-770 Suppresses the Chemo-Resistance and Metastasis of Triple Negative Breast Cancer via Direct Targeting of STMN1. *Cel Death Dis* 9 (1), 14. doi:10.1038/s41419-017-0030-7

Li, Y., Xi, Y., Zhu, G., Jia, J., Huang, H., Liu, Y., et al. (2019). Downregulated IGFBP7 Facilitates Liver Metastasis by Modulating Epithelial-mesenchymal T-ransition in colon C-ancer. *Oncol. Rep.* 42 (5), 1935–1945. doi:10.3892/or.2019.7303

Li, Z., Jiang, P., Li, J., Peng, M., Zhao, X., Zhang, X., et al. (2018). Tumor-derived Exosomal Lnc-Sox2ot Promotes EMT and Stemness by Acting as a ceRNA in Pancreatic Ductal Adenocarcinoma. *Oncogene* 37 (28), 3822–3838. doi:10.1038/s41388-018-0237-9

Lin, W.-H., Chang, Y.-W., Hong, M.-X., Hsu, T.-C., Lee, K.-C., Lin, C., et al. (2021). STAT3 Phosphorylation at Ser727 and Tyr705 Differentially Regulates the EMT-MET Switch and Cancer Metastasis. *Oncogene* 40 (4), 791–805. doi:10.1038/s41388-020-01566-8

Lin, Y., Huang, S.-T., Jiang, Y.-M., and Pan, X.-B. (2017). Hemorrhage of Brain Metastasis Is a Poor Prognostic Factor in Hepatocellular Carcinoma Patients. *Oncotarget* 8 (54), 93245–93250. doi:10.18632/oncotarget.21449

Liu, D., Kang, H., Gao, M., Jin, L., Zhang, F., Chen, D., et al. (2020). Exosome-transmitted circ_MMP2 Promotes Hepatocellular Carcinoma Metastasis by Upregulating MMP2. *Mol. Oncol.* 14 (6), 1365–1380. doi:10.1002/1878-0261.12637

Liu, H., Ye, X., Li, D., Yao, Q., and Li, Y. (2021). Incidence, Clinical Risk and Prognostic Factors for Liver Metastasis in Patients with Cervical Cancer: a Population-Based Retrospective Study. *BMC Cancer* 21 (1), 421. doi:10.1186/s12885-021-08127-6

Liu, J., and Agarwal, S. (2010). Mechanical Signals Activate Vascular Endothelial Growth Factor Receptor-2 to Upregulate Endothelial Cell Proliferation during Inflammation. *J.I.* 185 (2), 1215–1221. doi:10.4049/jimmunol.0903660

Liu, T., Zhang, X., Du, L., Wang, Y., Liu, X., Tian, H., et al. (2019). Exosome-transmitted miR-128-3p Increase Chemosensitivity of Oxaliplatin-Resistant Colorectal Cancer. *Mol. Cancer* 18 (1), 43. doi:10.1186/s12943-019-0981-7

Liu, Y., and Cao, X. (2016). Characteristics and Significance of the Pre-metastatic Niche. *Cancer Cell* 30 (5), 668–681. doi:10.1016/j.ccell.2016.09.011

Liu, Y., Gu, Y., Han, Y., Zhang, Q., Jiang, Z., Zhang, X., et al. (2016a). Tumor Exosomal RNAs Promote Lung Pre-metastatic Niche Formation by Activating Alveolar Epithelial TLR3 to Recruit Neutrophils. *Cancer Cell* 30 (2), 243–256. doi:10.1016/j.ccell.2016.06.021

Liu, Y., Luo, F., Wang, B., Li, H., Xu, Y., Liu, X., et al. (2016b). STAT3-regulated Exosomal miR-21 Promotes Angiogenesis and Is Involved in Neoplastic Processes of Transformed Human Bronchial Epithelial Cells. *Cancer Lett.* 370 (1), 125–135. doi:10.1016/j.canlet.2015.10.011

Liu, Y., Ren, W., Bai, Y., Wan, L., Sun, X., Liu, Y., et al. (2018a). Oxyresveratrol Prevents Murine H22 Hepatocellular Carcinoma Growth and Lymph Node Metastasis via Inhibiting Tumor Angiogenesis and Lymphangiogenesis. *J. Nat. Med.* 72 (2), 481–492. doi:10.1007/s11418-018-1173-2

Liu, Y., Wu, T., Lu, D., Zhen, J., and Zhang, L. (2018b). CD44 Overexpression Related to Lymph Node Metastasis and Poor Prognosis of Pancreatic Cancer. *Int. J. Biol. Markers* 33 (3), 308–313. doi:10.1177/1724600817746951

Liu, Z.-L., Wang, C., Chen, H.-J., Li, X., Dai, L.-J., and Ding, Z.-Y. (2017). Bone Metastasis from Lung Cancer Identified by Genetic Profiling. *Oncol. Lett.* 13 (2), 847–850. doi:10.3892/ol.2016.5458

Lo Cicero, A., Majkowska, I., Nagase, H., Di Liegro, I., and Troeberg, L. (2012). Microvesicles Shed by Oligodendroglioma Cells and Rheumatoid Synovial Fibroblasts Contain Aggrecanase Activity. *Matrix Biol.* 31 (4), 229–233. doi:10.1016/j.matbio.2012.02.005

Longo, R., Bastien, C., Campitiello, M., Plastino, F., and Rozzi, A. (2020). Breast and Axillary Lymph Node Metastasis from Ovarian Cancer: A Case Report. *Am. J. Case Rep.* 21, e925089. doi:10.12659/AJCR.925089

Lu, Y.-J., Yang, Y., Yuan, Y.-H., Wang, W.-J., Cui, M.-T., Tang, H.-Y., et al. (2020). A Novel Nomogram Based on SEER Database for the Prediction of Liver Metastasis in Patients with Small-Cell Lung Cancer. *Ann. Palliat. Med.* 9 (5), 3123–3137. doi:10.21037/apm-20-886

Luan, W., Ding, Y., Xi, H., Ruan, H., Lu, F., Ma, S., et al. (2021). Exosomal miR-106b-5p Derived from Melanoma Cell Promotes Primary Melanocytes Epithelial-Mesenchymal Transition through Targeting EphA4. *J. Exp. Clin. Cancer Res.* 40 (1), 107. doi:10.1186/s13046-021-01906-w

Ludwig, N., and Whiteside, T. L. (2018). Potential Roles of Tumor-Derived Exosomes in Angiogenesis. *Expert Opin. Ther. Targets* 22 (5), 409–417. doi:10.1080/14728222.2018.1464141

Ludwig, S., Floros, T., Theodoraki, M.-N., Hong, C.-S., Jackson, E. K., Lang, S., et al. (2017). Suppression of Lymphocyte Functions by Plasma Exosomes Correlates with Disease Activity in Patients with Head and Neck Cancer. *Clin. Cancer Res.* 23 (16), 4843–4854. doi:10.1158/1078-0432.CCR-16-2819

Luga, V., Zhang, L., Viloria-Petit, A. M., Ogunjimi, A. A., Inanlou, M. R., Chiu, E., et al. (2012). Exosomes Mediate Stromal Mobilization of Autocrine Wnt-PCP Signaling in Breast Cancer Cell Migration. *Cell* 151 (7), 1542–1556. doi:10.1016/j.cell.2012.11.024

Luo, K.-J., Chen, C.-X., Yang, J.-P., Huang, Y.-C., Cardenas, E. R., and Jiang, J. X. (2020a). Connexins in Lung Cancer and Brain Metastasis. *Front. Oncol.* 10, 599383. doi:10.3389/fonc.2020.599383

Luo, Y., Ma, J., Liu, F., Guo, J., and Gui, R. (2020b). Diagnostic Value of Exosomal circMYC in Radioresistant Nasopharyngeal Carcinoma. *Head & Neck* 42 (12), 3702–3711. doi:10.1002/hed.26441

Luo, Z., Rong, Z., and Huang, C. (2019). Surgery Strategies for Gastric Cancer with Liver Metastasis. *Front. Oncol.* 9, 1353. doi:10.3389/fonc.2019.01353

Ma, B., Wells, A., Wei, L., and Zheng, J. (2021). Prostate Cancer Liver Metastasis: Dormancy and Resistance to Therapy. *Semin. Cancer Biol.* 71, 2–9. doi:10.1016/j.semcancer.2020.07.004

Ma, J., Zhang, J., Weng, Y. C., and Wang, J. C. (2018). EZH2-Mediated microRNA-139-5p Regulates Epithelial-Mesenchymal Transition and Lymph Node Metastasis of Pancreatic Cancer. *Mol. Cell* 41 (9), 868–880. doi:10.14348/molcells.2018.0109

Ma, R., Ye, X., Cheng, H., Cui, H., and Chang, X. (2021). Tumor-derived Exosomal circRNA051239 Promotes Proliferation and Migration of Epithelial Ovarian Cancer. *Am. J. Transl Res.* 13 (3), 1125–1139.

Ma, R.-Y., Zhang, H., Li, X.-F., Zhang, C.-B., Selli, C., Tagliavini, G., et al. (2020a). Monocyte-derived Macrophages Promote Breast Cancer Bone Metastasis Outgrowth. *J. Exp. Med.* 217 (11). doi:10.1084/jem.20191820

Ma, R., Feng, Y., Lin, S., Chen, J., Lin, H., Liang, X., et al. (2015). Mechanisms Involved in Breast Cancer Liver Metastasis. *J. Transl Med.* 13, 64. doi:10.1186/s12967-015-0425-0

Ma, Z.-j., Wang, Y., Li, H.-f., Liu, M.-H., Bi, F.-r., Ma, L., et al. (2020b). LncZEB1-AS1 Regulates Hepatocellular Carcinoma Bone Metastasis via Regulation of the miR-302b-EGFR-Pi3k-AKT axis. *J. Cancer* 11 (17), 5118–5128. doi:10.7150/jca.45995

Mahabeleshwar, G. H., Chen, J., Feng, W., Somanath, P. R., Razorenova, O. V., and Byzova, T. V. (2008). Integrin Affinity Modulation in Angiogenesis. *Cell Cycle* 7 (3), 335–347. doi:10.4161/cc.7.3.5234

Mahabeleshwar, G. H., Feng, W., Reddy, K., Plow, E. F., and Byzova, T. V. (2007). Mechanisms of Integrin-Vascular Endothelial Growth Factor Receptor Cross-Activation in Angiogenesis. *Circ. Res.* 101 (6), 570–580. doi:10.1161/CIRCRESAHA.107.155655

Makino, H., Nishio, S., Tsubamoto, H., Shimada, M., Nishikawa, R., Kai, K., et al. (2016). Treatment and Prognosis of Bone Metastasis from Cervical Cancer (KCOG-G1202s). *J. Obstet. Gynaecol. Res.* 42 (6), 701–706. doi:10.1111/jog.12956

Malla, R. R., Pandrangi, S., Kumari, S., Gavara, M. M., and Badana, A. K. (2018). Exosomal Tetraspanins as Regulators of Cancer Progression and Metastasis and Novel Diagnostic Markers. *Asia-pac J. Clin. Oncol.* 14 (6), 383–391. doi:10.1111/ajco.12869

Mannavola, F., Mandala, M., Todisco, A., Sileni, V. C., Palla, M., Minisini, A. M., et al. (2020). An Italian Retrospective Survey on Bone Metastasis in Melanoma: Impact of Immunotherapy and Radiotherapy on Survival. *Front. Oncol.* 10, 1652. doi:10.3389/fonc.2020.01652

Marchand Crety, C., Ettalhaoui, L., and Servagi Vernat, S. (2020). Cystic Brain Metastasis from Prostate Cancer: A Case Report and Literature Review. *Urol. Case Rep.* 32, 101219. doi:10.1016/j.eucr.2020.101219

Marzullo, A., Serio, G., Pezzuto, F., Fortarezza, F., Cazzato, G., Caporusso, C., et al. (2020). A Single Liver Metastasis from Pleural Biphasic Mesothelioma. *Diagnostics* 10 (8), 555. doi:10.3390/diagnostics10080555

Matsumoto, H., and Yoshida, Y. (2015). Brain Metastasis from Pancreatic Cancer: A Case Report and Literature Review. *Asian J. Neurosurg.* 10 (1), 35–39. doi:10.4103/1793-5482.151507

Matsumura, T., Ohzato, H., Yamamoto, T., Ota, K., Mabuchi, E., Miwa, H., et al. (2009). A Case of Postoperative Brain Metastasis Originated from Pancreatic Cancer Which Was Successfully Treated by Resection and Postoperative Irradiation. *Gan To Kagaku Ryoho* 36 (12), 2433–2435.

Mauri, C., and Bosma, A. (2012). Immune Regulatory Function of B Cells. *Annu. Rev. Immunol.* 30, 221–241. doi:10.1146/annurev-immunol-020711-074934

McCarthy, D. H. (2001). Letters to the Editor. *Prog. Transpl.* 11 (3), 162. doi:10.7182/prtr.11.3.hh6665126211678310.1177/152692480101100302

Merkow, J., Paniccia, A., Jones, E., Jones, T., Hodges, M., Stovall, R., et al. (2016). Association of sentinel Lymph Node Diameter with Melanoma Metastasis. *Am. J. Surg.* 212 (2), 315–320. doi:10.1016/j.amjsurg.2015.09.022

Mermod, M., Bongiovanni, M., Petrova, T., Goun, E., Simon, C., Tolstonog, G., et al. (2019). Prediction of Occult Lymph Node Metastasis in Head and Neck Cancer with CD31 Vessel Quantification. *Otolaryngol. Head Neck Surg.* 160 (2), 277–283. doi:10.1177/0194599818791779

Mikami, J., Kimura, Y., Makari, Y., Fujita, J., Kishimoto, T., Sawada, G., et al. (2017). Clinical Outcomes and Prognostic Factors for Gastric Cancer Patients with Bone Metastasis. *World J. Surg. Onc* 15 (1), 8. doi:10.1186/s12957-016-1091-2

Minciacchi, V. R., Freeman, M. R., and Di Vizio, D. (2015). Extracellular Vesicles in Cancer: Exosomes, Microvesicles and the Emerging Role of Large Oncosomes. *Semin. Cel Dev. Biol.* 40, 41–51. doi:10.1016/j.semcdb.2015.02.010

Moy, A. P., Mochel, M. C., Muzikansky, A., Duncan, L. M., and Kraft, S. (2017). Lymphatic Invasion Predicts sentinel Lymph Node Metastasis and Adverse Outcome in Primary Cutaneous Melanoma. *J. Cutan. Pathol.* 44 (9), 734–739. doi:10.1111/cup.12969

Muhsin-Sharafaldine, M.-R., Saunderson, S. C., Dunn, A. C., and McLellan, A. D. (2017). Melanoma Growth and Lymph Node Metastasis Is Independent of Host CD169 Expression. *Biochem. Biophysical Res. Commun.* 486 (4), 965–970. doi:10.1016/j.bbrc.2017.03.138

Nabet, B. Y., Qiu, Y., Shabason, J. E., Wu, T. J., Yoon, T., Kim, B. C., et al. (2017). Exosome RNA Unshielding Couples Stromal Activation to Pattern Recognition Receptor Signaling in Cancer. *Cell* 170 (2), 352 e313–366. doi:10.1016/j.cell.2017.06.031

Nagata, A., Kanemasa, Y., Kikuchi, M., Otani, R., Yamada, R., Motoi, T., et al. (2020). Bone Marrow Metastasis of Glioblastoma Multiforme Mimicking Acute Myeloid Leukemia. *Oxf Med. Case Rep.* 2020 (6), omaa040. doi:10.1093/omcr/omaa040

Nagy, J. A., and Dvorak, H. F. (2012). Heterogeneity of the Tumor Vasculature: the Need for New Tumor Blood Vessel Type-specific Targets. *Clin. Exp. Metastasis* 29 (7), 657–662. doi:10.1007/s10585-012-9500-6

Nakamara, N., Matsui, T., Ishibashi, Y., Sotokawauchi, A., Fukami, K., Higashimoto, Y., et al. (2017b). RAGE-aptamer Attenuates the Growth and Liver Metastasis of Malignant Melanoma in Nude Mice. *Mol. Med.* 23, 295–306. doi:10.2119/molmed.2017.00099

Nakamura, K., Sawada, K., Kinose, Y., Yoshimura, A., Toda, A., Nakatsuka, E., et al. (2017a). Exosomes Promote Ovarian Cancer Cell Invasion through Transfer of CD44 to Peritoneal Mesothelial Cells. *Mol. Cancer Res.* 15 (1), 78–92. doi:10.1158/1541-7786.MCR-16-0191

Nam, H. C., Sung, P. S., Song, D. S., Kwon, J. H., Nam, S. W., Yoon, D. J., et al. (2019). Control of Intracranial Disease Is Associated with Improved Survival in Patients with Brain Metastasis from Hepatocellular Carcinoma. *Int. J. Clin. Oncol.* 24 (6), 666–676. doi:10.1007/s10147-019-01407-z

Namburi, S., Broxmeyer, H. E., Hong, C.-S., Whiteside, T. L., and Boyiadzis, M. (2021). DPP4+ Exosomes in AML Patients' Plasma Suppress Proliferation of Hematopoietic Progenitor Cells. *Leukemia* 35 (7), 1925–1932. doi:10.1038/s41375-020-01047-7

Nance, M. E., Biedermann, G. B., Bhat, A. P., and Davis, R. M. (2020). Chemorefractory Liver Metastasis from Cervical Cancer Successfully Treated with a Combination of Yttrium-90 and Immunotherapy. *Radiol. Case Rep.* 15 (8), 1359–1365. doi:10.1016/j.radcr.2020.06.010

Naoe, H., Kaku, E., Ido, Y., Gushima, R., Maki, Y., Saito, H., et al. (2011). Brain Metastasis from Gastrointestinal Stromal Tumor: a Case Report and Review of the Literature. *Case Rep. Gastroenterol.* 5 (3), 583–589. doi:10.1159/000333403

Nartthanarung, A., Thanapprapasr, K., Udomsubpayakul, U., and Thanapprapasr, D. (2014). Age and Survival of Cervical Cancer Patients with Bone Metastasis. *Asian Pac. J. Cancer Prev.* 15 (19), 8401–8404. doi:10.7314/apjcp.2014.15.19.8401

Nguyen, D. X., Bos, P. D., and Massagué, J. (2009). Metastasis: from Dissemination to Organ-specific Colonization. *Nat. Rev. Cancer* 9 (4), 274–284. doi:10.1038/nrc2622

Nienstedt, J. C., Schroeder, C., Clauditz, T., Simon, R., Sauter, G., Muenscher, A., et al. (2018). EZH2 Overexpression in Head and Neck Cancer Is Related to Lymph Node Metastasis. *J. Oral Pathol. Med.* 47 (3), 240–245. doi:10.1111/jop.12673

Nieswandt, B., Hafner, M., Echtenacher, B., and Männel, D. N. (1999). Lysis of Tumor Cells by Natural Killer Cells in Mice Is Impeded by Platelets. *Cancer Res.* 59 (6), 1295–1300.

Nishino, H., Abe, K., Igarashi, M., Miyata, M., and Kitamura, K. (1996). Chemotherapy with Low-Dose Consecutive Cisplatin (Cddp) for Patients with Recurrent and Distant Metastasis of Head and Neck Cancer. *Nippon Jibiinkoka Gakkai Kaiho* 99 (9), 1218–1222. doi:10.3950/jibiinkoka.99.1218

Nishio, N., van den Berg, N. S., Martin, B. A., van Keulen, S., Fakurnejad, S., Rosenthal, E. L., et al. (2021). Photoacoustic Molecular Imaging for the Identification of Lymph Node Metastasis in Head and Neck Cancer Using

an Anti-EGFR Antibody-Dye Conjugate. *J. Nucl. Med.* 62 (5), 648–655. doi:10.2967/jnumed.120.245241

Ohara, H., Ishibashi, Y., Yoshimura, S., Yamazaki, R., Hatao, F., Koshiishi, T., et al. (2020). Intratumoral Pseudoaneurysm within a Liver Metastasis of Gastric Cancer: a Case Report. *Surg. Case Rep.* 6 (1), 39. doi:10.1186/s40792-020-00806-z

Okabe, H., Aoki, K., Yogosawa, S., Saito, M., Marumo, K., and Yoshida, K. (2018). Downregulation of CD24 Suppresses Bone Metastasis of Lung Cancer. *Cancer Sci.* 109 (1), 112–120. doi:10.1111/cas.13435

Outani, H., Akita, H., Nakai, T., Takada, R., Imura, Y., Tanaka, T., et al. (2018). Clinical Features and Prognosis of Patients with the Bone Metastasis of Pancreatic Cancer. *Pancreas* 47 (7), e43–e46. doi:10.1097/MPA.0000000000001098

Pace, K. R., Dutt, R., and Galileo, D. S. (2019). Exosomal L1CAM Stimulates Glioblastoma Cell Motility, Proliferation, and Invasiveness. *Ijms* 20 (16), 3982. doi:10.3390/ijms20163982

Pahl, J., and Cerwenka, A. (2017). Tricking the Balance: NK Cells in Anti-cancer Immunity. *Immunobiology* 222 (1), 11–20. doi:10.1016/j.imbio.2015.07.012

Pakneshan, S., Safarpour, D., Tavassoli, F., and Jabbari, B. (2014). Brain Metastasis from Ovarian Cancer: a Systematic Review. *J. Neurooncol.* 119 (1), 1–6. doi:10.1007/s11060-014-1447-9

Paoletti, C., and Hayes, D. F. (2016). Circulating Tumor Cells. *Adv. Exp. Med. Biol.* 882, 235–258. doi:10.1007/978-3-319-22909-6_10

Paolillo, M., and Schinelli, S. (2017). Integrins and Exosomes, a Dangerous Liaison in Cancer Progression. *Cancers* 9 (8), 95. doi:10.3390/cancers9080095

Park, J.-M., Han, Y.-M., Jeong, M., Chung, M. H., Kwon, C. I., Ko, K. H., et al. (2017). Synthetic 8-hydroxydeoxyguanosine Inhibited Metastasis of Pancreatic Cancer through Concerted Inhibitions of ERM and Rho-GTPase. *Free Radic. Biol. Med.* 110, 151–161. doi:10.1016/j.freeradbiomed.2017.06.003

Park, S., Byun, H. K., and Seong, J. (2019). Irradiation-Related Lymphopenia for Bone Metastasis from Hepatocellular Carcinoma. *Liver Cancer* 8 (6), 468–479. doi:10.1159/000500461

Park, S. M., Do-Thi, V. A., Lee, J. O., Lee, H., and Kim, Y. S. (2020). Interleukin-9 Inhibits Lung Metastasis of Melanoma through Stimulating Anti-tumor M1 Macrophages. *Mol. Cell* 43 (5), 479–490. doi:10.14348/molcells.2020.0047

Pedrosa, R. M. S. M., Mustafa, D. A., Soffietti, R., and Kros, J. M. (2018). Breast Cancer Brain Metastasis: Molecular Mechanisms and Directions for Treatment. *Neuro Oncol.* 20 (11), 1439–1449. doi:10.1093/neuonc/noy044

Peinado, H., Alečković, M., Lavotshkin, S., Matei, I., Costa-Silva, B., Moreno-Bueno, G., et al. (2012). Melanoma Exosomes Educate Bone Marrow Progenitor Cells toward a Pro-metastatic Phenotype through MET. *Nat. Med.* 18 (6), 883–891. doi:10.1038/nm.2753

Peinado, H., Lavotshkin, S., and Lyden, D. (2011). The Secreted Factors Responsible for Pre-metastatic Niche Formation: Old Sayings and New Thoughts. *Semin. Cancer Biol.* 21 (2), 139–146. doi:10.1016/j.semcancer.2011.01.002

Peinado, H., Zhang, H., Matei, I. R., Costa-Silva, B., Hoshino, A., Rodrigues, G., et al. (2017). Pre-metastatic Niches: Organ-specific Homes for Metastases. *Nat. Rev. Cancer* 17 (5), 302–317. doi:10.1038/nrc.2017.6

Peng, Z., Xu, S., Li, H., Sun, C., Fu, M., and Gao, M. (2014). Advanced Gastric Cancer with Brain Metastasis Effectively Treated by Arterial Infusion Chemotherapy: A Case Report. *Oncol. Lett.* 7 (2), 449–451. doi:10.3892/ol.2013.1699

Polistina, G. E., Matarese, A., Cariello, P., Caroppo, D., and Zamparelli, A. S. (2020). Cavitary Lung Metastasis as Relapse of Prostate Cancer. *Respir. Med. Case Rep.* 29, 100973. doi:10.1016/j.rmcr.2019.100973

Provenzano, P. P., Inman, D. R., Eliceiri, K. W., Knittel, J. G., Yan, L., Rueden, C. T., et al. (2008). Collagen Density Promotes Mammary Tumor Initiation and Progression. *BMC Med.* 6, 11. doi:10.1186/1741-7015-6-11

Pylayeva, Y., Gillen, K. M., Gerald, W., Beggs, H. E., Reichardt, L. F., and Giancotti, F. G. (2009). Ras- and PI3K-dependent Breast Tumorigenesis in Mice and Humans Requires Focal Adhesion Kinase Signaling. *J. Clin. Invest.* 119 (2), 252–266. doi:10.1172/JCI37160

Qian, B.-Z., and Pollard, J. W. (2010). Macrophage Diversity Enhances Tumor Progression and Metastasis. *Cell* 141 (1), 39–51. doi:10.1016/j.cell.2010.03.014

Qiu, J.-J., Lin, X.-J., Tang, X.-Y., Zheng, T.-T., Lin, Y.-Y., and Hua, K.-Q. (2018a). Exosomal Metastasis-Associated Lung Adenocarcinoma Transcript 1 Promotes Angiogenesis and Predicts Poor Prognosis in Epithelial Ovarian Cancer. *Int. J. Biol. Sci.* 14 (14), 1960–1973. doi:10.7150/ijbs.28048

Qiu, M.-Z., Shi, S.-M., Chen, Z.-H., Yu, H.-E., Sheng, H., Jin, Y., et al. (2018b). Frequency and Clinicopathological Features of Metastasis to Liver, Lung, Bone, and Brain from Gastric Cancer: A SEER-Based Study. *Cancer Med.* 7 (8), 3662–3672. doi:10.1002/cam4.1661

Qiu, X., Jiang, Y., Zhao, Q., Yan, C., Huang, M., and Jiang, T. a. (2020). Could Ultrasound-Based Radiomics Noninvasively Predict Axillary Lymph Node Metastasis in Breast Cancer? *J. Ultrasound Med.* 39 (10), 1897–1905. doi:10.1002/jum.15294

Rackov, G., Garcia-Romero, N., Esteban-Rubio, S., Carrión-Navarro, J., Belda-Iniesta, C., and Ayuso-Sacido, A. (2018). Vesicle-Mediated Control of Cell Function: The Role of Extracellular Matrix and Microenvironment. *Front. Physiol.* 9, 651. doi:10.3389/fphys.2018.00651

Ramteke, A., Ting, H., Agarwal, C., Mateen, S., Somasagara, R., Hussain, A., et al. (2015). Exosomes Secreted under Hypoxia Enhance Invasiveness and Stemness of Prostate Cancer Cells by Targeting Adherens junction Molecules. *Mol. Carcinog.* 54 (7), 554–565. doi:10.1002/mc.22124

Raposo, G., and Stoorvogel, W. (2013). Extracellular Vesicles: Exosomes, Microvesicles, and Friends. *J. Cel Biol* 200 (4), 373–383. doi:10.1083/jcb.201211138

Redmer, T. (2018). Deciphering Mechanisms of Brain Metastasis in Melanoma - the Gist of the Matter. *Mol. Cancer* 17 (1), 106. doi:10.1186/s12943-018-0854-5

Ren, J., Ding, L., Zhang, D., Shi, G., Xu, Q., Shen, S., et al. (2018). Carcinoma-associated Fibroblasts Promote the Stemness and Chemoresistance of Colorectal Cancer by Transferring Exosomal lncRNA H19. *Theranostics* 8 (14), 3932–3948. doi:10.7150/thno.25541

Ricard, J. A., Cramer, S. W., Charles, R., Gil Tommee, C., Le, A., Bell, W. R., et al. (2019). Infratentorial Glioblastoma Metastasis to Bone. *World Neurosurg.* 131, 90–94. doi:10.1016/j.wneu.2019.07.142

Robbins, P. D., and Morelli, A. E. (2014). Regulation of Immune Responses by Extracellular Vesicles. *Nat. Rev. Immunol.* 14 (3), 195–208. doi:10.1038/nri3622

Roccaro, A. M., Sacco, A., Maiso, P., Azab, A. K., Tai, Y.-T., Reagan, M., et al. (2013). BM Mesenchymal Stromal Cell-Derived Exosomes Facilitate Multiple Myeloma Progression. *J. Clin. Invest.* 123 (4), 1542–1555. doi:10.1172/JCI66517

Rodrigues, G., Hoshino, A., Kenific, C. M., Matei, I. R., Steiner, L., Freitas, D., et al. (2019). Tumour Exosomal CEMIP Protein Promotes Cancer Cell Colonization in Brain Metastasis. *Nat. Cel Biol* 21 (11), 1403–1412. doi:10.1038/s41556-019-0404-4

Roegel, J. C., Bressollette, L., Fouilhoux, A. C., Martin, F., Morand, C., and Mottier, D. (1993). Peritoneal Mesothelioma with Bone Metastasis: a Radionuclide Follow-Up. *Ann. Med. Interne (Paris)* 144 (6), 425.

Ryu, S.-H., Heo, S.-H., Park, E. Y., Choi, K.-C., Ryu, J.-W., Lee, S. H., et al. (2017). Selumetinib Inhibits Melanoma Metastasis to Mouse Liver via Suppression of EMT-Targeted Genes. *Ar* 37 (2), 607–614. doi:10.21873/anticanres.11354

Said, N. A. B. M., and Williams, E. D. (2011). Growth Factors in Induction of Epithelial-Mesenchymal Transition and Metastasis. *Cells Tissues Organs* 193 (1-2), 85–97. doi:10.1159/000320360

Saif, M. W., Galanina, N., Ravage-Mass, L., Kaley, K., Cornfeld, D., Lamb, L., et al. (20102010). Bone Metastasis as the Only Metastatic Site in a Patient with Pancreatic Cancer Following Distal Pancreatectomy. *Case Rep. Med.* 2010, 1–3. doi:10.1155/2010/634975

Sakimura, C., Hori, T., Deguchi, S., Masuda, G., Tendo, M., Nakata, B., et al. (2019). A Case Report of Lung Resection for Lung Metastasis from Pancreatic Cancer. *Gan To Kagaku Ryoho* 46 (13), 1934–1936.

Salvador, F., Llorente, A., and Gomis, R. R. (2019). From Latency to Overt Bone Metastasis in Breast Cancer: Potential for Treatment and Prevention. *J. Pathol.* 249 (1), 6–18. doi:10.1002/path.5292

Santarpia, M., Liguori, A., D'Aveni, A., Karachaliou, N., Gonzalez-Cao, M., Daffinà, M. G., et al. (2018). Liquid Biopsy for Lung Cancer Early Detection. *J. Thorac. Dis.* 10 (Suppl. 7), S882–S897. doi:10.21037/jtd.2018.03.81

Sasaki, T., Sato, T., Nakai, Y., Sasahira, N., Isayama, H., and Koike, K. (2019). Brain Metastasis in Pancreatic Cancer. *Medicine (Baltimore)* 98 (4), e14227. doi:10.1097/MD.0000000000014227

Sato, Y., Tanaka, K., Kobayashi, Y., Shibuya, H., Nishigaya, Y., Momomura, M., et al. (2015). Uterine Cervical Cancer with Brain Metastasis as the Initial Site of Presentation. *J. Obstet. Gynaecol. Res.* 41 (7), 1145–1148. doi:10.1111/jog.12668

Schwarz, D., Niederle, T., Münch, P., Hielscher, T., Hassel, J. C., Schlemmer, H. P., et al. (2019). Susceptibility-weighted Imaging in Malignant Melanoma Brain Metastasis. *J. Magn. Reson. Imaging* 50 (4), 1251–1259. doi:10.1002/jmri.26692

Seifert, A. M., Eymer, A., Heiduk, M., Wehner, R., Tunger, A., von Renesse, J., et al. (2020). PD-1 Expression by Lymph Node and Intratumoral Regulatory T Cells Is Associated with Lymph Node Metastasis in Pancreatic Cancer. *Cancers* 12 (10), 2756. doi:10.3390/cancers12102756

Sharma, D., Brummel-Ziedins, K. E., Bouchard, B. A., and Holmes, C. E. (2014). Platelets in Tumor Progression: a Host Factor that Offers Multiple Potential Targets in the Treatment of Cancer. *J. Cel. Physiol* 229 (8), 1005–1015. doi:10.1002/jcp.24539

Sharma, P., Ludwig, S., Muller, L., Hong, C. S., Kirkwood, J. M., Ferrone, S., et al. (2018a). Immunoaffinity-based Isolation of Melanoma Cell-Derived Exosomes from Plasma of Patients with Melanoma. *J. Extracellular Vesicles* 7 (1), 1435138. doi:10.1080/20013078.2018.1435138

Sharma, S., Alharbi, M., Kobayashi, M., Lai, A., Guanzon, D., Zuñiga, F., et al. (2018b). Proteomic Analysis of Exosomes Reveals an Association between Cell Invasiveness and Exosomal Bioactivity on Endothelial and Mesenchymal Cell Migration *In Vitro*. *Clin. Sci. (Lond)* 132 (18), 2029–2044. doi:10.1042/CS20180425

Shattil, S. J., and Ginsberg, M. H. (1997). Integrin Signaling in Vascular Biology. *J. Clin. Invest.* 100 (11 Suppl. l), S91–S95. doi:10.1172/jci119500

Sherwood, L. M., Parris, E. E., and Folkman, J. (1971). Tumor Angiogenesis: Therapeutic Implications. *N. Engl. J. Med.* 285 (21), 1182–1186. doi:10.1056/NEJM197111182852108

Shida, Y., Hakariya, T., Miyata, Y., and Sakai, H. (2020). Three Cases of Brain Metastasis from Castration-resistant Prostate Cancer. *Clin. Case Rep.* 8 (1), 96–99. doi:10.1002/ccr3.2587

Shuto, T., Fujino, H., Inomori, S., Nakayama, S., Satoh, H., Ideguchi, H., et al. (1995). Glioblastoma Multiforme with Liver Metastasis-Ccase Report. *No To Shinkei* 47 (8), 772–777.

Simons, B. W., Dalrymple, S., Rosen, M., Zheng, L., and Brennen, W. N. (2020). A Hemi-spleen Injection Model of Liver Metastasis for Prostate Cancer. *Prostate* 80 (14), 1263–1269. doi:10.1002/pros.24055

Singh, R., Pochampally, R., Watabe, K., Lu, Z., and Mo, Y.-Y. (2014). Exosome-mediated Transfer of miR-10b Promotes Cell Invasion in Breast Cancer. *Mol. Cancer* 13, 256. doi:10.1186/1476-4598-13-256

Skog, J., Würdinger, T., van Rijn, S., Meijer, D. H., Gainche, L., Curry, W. T., et al. (2008). Glioblastoma Microvesicles Transport RNA and Proteins that Promote Tumour Growth and Provide Diagnostic Biomarkers. *Nat. Cel Biol* 10 (12), 1470–1476. doi:10.1038/ncb1800

Soler-Cardona, A., Forsthuber, A., Lipp, K., Ebersberger, S., Heinz, M., Schossleitner, K., et al. (2018). CXCL5 Facilitates Melanoma Cell-Neutrophil Interaction and Lymph Node Metastasis. *J. Invest. Dermatol.* 138 (7), 1627–1635. doi:10.1016/j.jid.2018.01.035

Sommers, C. L., Byers, S. W., Thompson, E. W., Torri, J. A., and Gelmann, E. P. (1994). Differentiation State and Invasiveness of Human Breast Cancer Cell Lines. *Breast Cancer Res. Tr* 31 (2-3), 325–335. doi:10.1007/BF00666165

Sridhar, S., Paz-Ares, L., Liu, H., Shen, K., Morehouse, C., Rizvi, N., et al. (2019). Prognostic Significance of Liver Metastasis in Durvalumab-Treated Lung Cancer Patients. *Clin. Lung Cancer* 20 (6), e601–e608. doi:10.1016/j.cllc.2019.06.020

Sruthi, T. V., Edatt, L., Raji, G. R., Kunhiraman, H., Shankar, S. S., Shankar, V., et al. (2018). Horizontal Transfer of miR-23a from Hypoxic Tumor Cell Colonies Can Induce Angiogenesis. *J. Cel Physiol* 233 (4), 3498–3514. doi:10.1002/jcp.26202

Stansel, T., A. Wickline, S., and Pan, H. (2020). NF-κB Inhibition Suppresses Experimental Melanoma Lung Metastasis. *J. Cancer Sci. Clin. Ther.* 04 (3), 256–265. doi:10.26502/jcsct.5079070

Stasenko, M., Cybulska, P., Feit, N., Makker, V., Konner, J., O'Cearbhaill, R. E., et al. (2019). Brain Metastasis in Epithelial Ovarian Cancer by BRCA1/2 Mutation Status. *Gynecol. Oncol.* 154 (1), 144–149. doi:10.1016/j.ygyno.2019.05.004

Su, Y. Y., Sun, L., Guo, Z. R., Li, J. C., Bai, T. T., Cai, X. X., et al. (2019). Upregulated Expression of Serum Exosomal miR-375 and miR-1307 Enhance the Diagnostic Power of CA125 for Ovarian Cancer. *J. Ovarian Res.* 12 (1), 6. doi:10.1186/s13048-018-0477-x

Sun, H., Wang, C., Hu, B., Gao, X., Zou, T., Luo, Q., et al. (2021). Exosomal S100A4 Derived from Highly Metastatic Hepatocellular Carcinoma Cells Promotes Metastasis by Activating STAT3. *Sig Transduct Target. Ther.* 6 (1), 187. doi:10.1038/s41392-021-00579-3

Sun, L., He, M., Xu, N., Xu, D.-H., Ben-David, Y., Yang, Z.-Y., et al. (2018). Regulation of RAB22A by Mir-193b Inhibits Breast Cancer Growth and Metastasis Mediated by Exosomes. *Int. J. Oncol.* 53 (6), 2705–2714. doi:10.3892/ijo.2018.4571

Sun, S., Lian, X., Liu, X., Ma, J., Hou, X., Zhang, F., et al. (2020). Multimodal Therapy Is a Better Choice for Patients with Brain Metastasis from Cervical Cancer. *Cmar* Vol 12, 12395–12402. doi:10.2147/CMAR.S283673

Sussman, J., and Rosai, J. (1990). Lymph Node Metastasis. *Am. J. Surg. Pathol.* 14 (9), 819–828. doi:10.1097/00000478-199009000-00003

Suzuki, K., Yasuda, T., Nagao, K., Hori, T., Watanabe, K., Kanamori, M., et al. (2015). Bone Metastasis of a Gastrointestinal Stromal Tumor: A Report of Two Cases. *Oncol. Lett.* 9 (4), 1814–1818. doi:10.3892/ol.2015.2976

Swayne, L. C., Hediger, R. G., and Wolff, M. (1992). Bone Scan Detection of Pelvic Metastasis from Pleural Mesothelioma. *Clin. Nucl. Med.* 17 (12), 965–966. doi:10.1097/00003072-199212000-00013

Szczepanski, M. J., Szajnik, M., Welsh, A., Whiteside, T. L., and Boyiadzis, M. (2011). Blast-derived Microvesicles in Sera from Patients with Acute Myeloid Leukemia Suppress Natural Killer Cell Function via Membrane-Associated Transforming Growth Factor- 1. *Haematologica* 96 (9), 1302–1309. doi:10.3324/haematol.2010.039743

Tahara, R. K., Brewer, T. M., Theriault, R. L., and Ueno, N. T. (2019). Bone Metastasis of Breast Cancer. *Adv. Exp. Med. Biol.* 1152, 105–129. doi:10.1007/978-3-030-20301-6_7

Takehara, Y., Endo, S., Mori, Y., Nakahara, K., Takayanagi, D., Shimada, S., et al. (2014). Malignant Peritoneal Mesothelioma with Lymph Node Metastasis that Originated in the Transverse colon. *World J. Surg. Onc* 12, 112. doi:10.1186/1477-7819-12-112

Tan, S., Xia, L., Yi, P., Han, Y., Tang, L., Pan, Q., et al. (2020). Exosomal miRNAs in Tumor Microenvironment. *J. Exp. Clin. Cancer Res.* 39 (1), 67. doi:10.1186/s13046-020-01570-6

Taverna, S., Flugy, A., Saieva, L., Kohn, E. C., Santoro, A., Meraviglia, S., et al. (2012). Role of Exosomes Released by Chronic Myelogenous Leukemia Cells in Angiogenesis. *Int. J. Cancer* 130 (9), 2033–2043. doi:10.1002/ijc.26217

Taylor, D. D., Gerçel-Taylor, C., Lyons, K. S., Stanson, J., and Whiteside, T. L. (2003). T-cell Apoptosis and Suppression of T-Cell receptor/CD3-Zeta by Fas Ligand-Containing Membrane Vesicles Shed from Ovarian Tumors. *Clin. Cancer Res.* 9 (14), 5113–5119.

Teng, Y., Ren, Y., Hu, X., Mu, J., Samykutty, A., Zhuang, X., et al. (2017). MVP-mediated Exosomal Sorting of miR-193a Promotes colon Cancer Progression. *Nat. Commun.* 8, 14448. doi:10.1038/ncomms14448

Thakur, B. K., Zhang, H., Becker, A., Matei, I., Huang, Y., Costa-Silva, B., et al. (2014). Double-stranded DNA in Exosomes: a Novel Biomarker in Cancer Detection. *Cell Res* 24 (6), 766–769. doi:10.1038/cr.2014.44

Théry, C., Ostrowski, M., and Segura, E. (2009). Membrane Vesicles as Conveyors of Immune Responses. *Nat. Rev. Immunol.* 9 (8), 581–593. doi:10.1038/nri2567

Tian, X.-P., Wang, C.-Y., Jin, X.-H., Li, M., Wang, F.-W., Huang, W.-J., et al. (2019). Acidic Microenvironment Up-Regulates Exosomal miR-21 and miR-10b in Early-Stage Hepatocellular Carcinoma to Promote Cancer Cell Proliferation and Metastasis. *Theranostics* 9 (7), 1965–1979. doi:10.7150/thno.30958

Tian, X., Sun, M., Wu, H., Chen, C., Li, H., Qiu, S., et al. (2021). Exosome-derived miR-Let-7c Promotes Angiogenesis in Multiple Myeloma by Polarizing M2 Macrophages in the Bone Marrow Microenvironment. *Leuk. Res.* 105, 106566. doi:10.1016/j.leukres.2021.106566

Tokoro, T., Nakamura, K., Hirose, A., Nakanuma, S., Okamoto, K., Kinoshita, J., et al. (2018). A Case of Colon Cancer with Brain, Liver and Lung Metastasis Successfully Treated with Bevacizumab Plus Xelox Therapy. *Gan To Kagaku Ryoho* 45 (3), 521–523.

Tuncer, M., Faydaci, G., Altin, G., Erdogan, B. A., Kibar, S., Sanli, A., et al. (2014). Metastasis of Non-muscle-invasive Bladder Cancer into the Thyroid Gland: a Literature Review Accompanied by a Rare Case. *Korean J. Urol.* 55 (3), 222–225. doi:10.4111/kju.2014.55.3.222

Tyagi, A., Sharma, S., Wu, K., Wu, S.-Y., Xing, F., Liu, Y., et al. (2021). Nicotine Promotes Breast Cancer Metastasis by Stimulating N2 Neutrophils and Generating Pre-metastatic Niche in Lung. *Nat. Commun.* 12 (1), 474. doi:10.1038/s41467-020-20733-9

Ubukata, H., Motohashi, G., Tabuchi, T., Nagata, H., Konishi, S., and Tabuchi, T. (2011). Overt Bone Metastasis and Bone Marrow Micrometastasis of Early Gastric Cancer. *Surg. Today* 41 (2), 169–174. doi:10.1007/s00595-010-4389-7

Ueda, S., Ooka, H., Yamaguchi, M., Hayashi, H., and Okayasu, T. (1973). Case of Pulmonary Metastasis of Ovarian Cancer Erroneously Diagnosed and Treated as Pulmonary Tuberculosis for a Long Time. *Nihon Kyobu Shikkan Gakkai Zasshi* 11 (11), 684–687.

Uesato, Y., Tamashiro, K., and Takatsuki, M. (2020). Long-term Survival after Repeated Resection for Lung Metastasis Originating from Pancreatic Cancer: a Case Report. *Surg. Case Rep.* 6 (1), 66. doi:10.1186/s40792-020-00832-x

Uluçkan, Ö. (2019). Mouse Models of Melanoma Bone Metastasis. *Methods Mol. Biol.* 1914, 343–348. doi:10.1007/978-1-4939-8997-3_19

Umezu, T., Tadokoro, H., Azuma, K., Yoshizawa, S., Ohyashiki, K., and Ohyashiki, J. H. (2014). Exosomal miR-135b Shed from Hypoxic Multiple Myeloma Cells Enhances Angiogenesis by Targeting Factor-Inhibiting HIF-1. *Blood* 124 (25), 3748–3757. doi:10.1182/blood-2014-05-576116

Valadi, H., Ekström, K., Bossios, A., Sjöstrand, M., Lee, J. J., and Lötvall, J. O. (2007). Exosome-mediated Transfer of mRNAs and microRNAs Is a Novel Mechanism of Genetic Exchange between Cells. *Nat. Cel Biol* 9 (6), 654–659. doi:10.1038/ncb1596

Valastyan, S., and Weinberg, R. A. (2011). Tumor Metastasis: Molecular Insights and Evolving Paradigms. *Cell* 147 (2), 275–292. doi:10.1016/j.cell.2011.09.024

Voura, E. B., Ramjeesingh, R. A., Montgomery, A. M. P., and Siu, C.-H. (2001). Involvement of Integrin αvβ3and Cell Adhesion Molecule L1 in Transendothelial Migration of Melanoma Cells. *MBoC* 12 (9), 2699–2710. doi:10.1091/mbc.12.9.2699

Wan, L., Pantel, K., and Kang, Y. (2013). Tumor Metastasis: Moving New Biological Insights into the Clinic. *Nat. Med.* 19 (11), 1450–1464. doi:10.1038/nm.3391

Wang, B., Mao, J.-h., Wang, B.-y., Wang, L.-x., Wen, H.-y., Xu, L.-j., et al. (2020). Exosomal miR-1910-3p Promotes Proliferation, Metastasis, and Autophagy of Breast Cancer Cells by Targeting MTMR3 and Activating the NF-Kb Signaling Pathway. *Cancer Lett.* 489, 87–99. doi:10.1016/j.canlet.2020.05.038

Wang, C.-F., Peng, S.-J., Liu, R.-Q., Yu, Y.-J., Ge, Q.-M., Liang, R.-B., et al. (2020). The Combination of CA125 and NSE Is Useful for Predicting Liver Metastasis of Lung Cancer. *Dis. Markers* 2020, 1–10. doi:10.1155/2020/8850873

Wang, G., Xu, J., Qi, Y., Xiu, J., Li, R., and Han, M. (2019a). Distribution of Brain Metastasis from Lung Cancer. *Cmar* Vol 11, 9331–9338. doi:10.2147/CMAR.S222920

Wang, H., Deng, Q., Lv, Z., Ling, Y., Hou, X., Chen, Z., et al. (2019b). N6-methyladenosine Induced miR-143-3p Promotes the Brain Metastasis of Lung Cancer via Regulation of VASH1. *Mol. Cancer* 18 (1), 181. doi:10.1186/s12943-019-1108-x

Wang, H., Wei, M., Kang, Y., Xing, J., and Zhao, Y. (2020). Circular RNA circ_PVT1 Induces Epithelial-Mesenchymal Transition to Promote Metastasis of Cervical Cancer. *aging* 12 (20), 20139–20151. doi:10.18632/aging.103679

Wang, J., Guan, X., Zhang, Y., Ge, S., Zhang, L., Li, H., et al. (2018a). Exosomal miR-27a Derived from Gastric Cancer Cells Regulates the Transformation of Fibroblasts into Cancer-Associated Fibroblasts. *Cell Physiol Biochem* 49 (3), 869–883. doi:10.1159/000493218

Wang, J., Zhang, Q., Wang, D., Yang, S., Zhou, S., Xu, H., et al. (2020). Microenvironment-induced TIMP2 Loss by Cancer-secreted Exosomal miR-4443 Promotes Liver Metastasis of Breast Cancer. *J. Cel Physiol* 235 (7-8), 5722–5735. doi:10.1002/jcp.29507

Wang, L., Tantai, J., and Zhu, X. (2020). Katanin P60: a Potential Biomarker for Lymph Node Metastasis and Prognosis for Non-small Cell Lung Cancer. *World J. Surg. Onc* 18 (1), 157. doi:10.1186/s12957-020-01939-z

Wang, M., Chao, C.-C., Chen, P.-C., Liu, P.-I., Yang, Y.-C., Su, C.-M., et al. (2019c). Thrombospondin Enhances RANKL-dependent Osteoclastogenesis and Facilitates Lung Cancer Bone Metastasis. *Biochem. Pharmacol.* 166, 23–32. doi:10.1016/j.bcp.2019.05.005

Wang, M., Zhou, J., Zhang, L., Zhao, Y., Zhang, N., Wang, L., et al. (2019d). Surgical Treatment of Ovarian Cancer Liver Metastasis. *Hepatobiliary Surg. Nutr.* 8 (2), 129–137. doi:10.21037/hbsn.2018.12.06

Wang, N., Feng, Y., Xie, J., Han, H., Dong, Q., and Wang, W. (2020). Long Non-coding RNA ZNF667-AS1 Knockdown Curbs Liver Metastasis in Acute Myeloid Leukemia by Regulating the microRNA-206/AKAP13 Axis. *Cmar* Vol 12, 13285–13300. doi:10.2147/CMAR.S269258

Wang, Q., Wang, G., Niu, L., Zhao, S., Li, J., Zhang, Z., et al. (2021a). Exosomal MiR-1290 Promotes Angiogenesis of Hepatocellular Carcinoma via Targeting SMEK1. *J. Oncol.* 2021, 1–13. doi:10.1155/2021/6617700

Wang, X., Hu, L.-P., Qin, W.-T., Yang, Q., Chen, D.-Y., Li, Q., et al. (2021b). Identification of a Subset of Immunosuppressive P2RX1-Negative Neutrophils in Pancreatic Cancer Liver Metastasis. *Nat. Commun.* 12 (1), 174. doi:10.1038/s41467-020-20447-y

Wang, X., Luo, G., Zhang, K., Cao, J., Huang, C., Jiang, T., et al. (2018). Hypoxic Tumor-Derived Exosomal miR-301a Mediates M2 Macrophage Polarization via PTEN/PI3Kγ to Promote Pancreatic Cancer Metastasis. *Cancer Res.* 78 (16), 4586–4598. doi:10.1158/0008-5472.CAN-17-3841

Wang, X., Wang, B., Zhan, W., Kang, L., Zhang, S., Chen, C., et al. (2019e). Melatonin Inhibits Lung Metastasis of Gastric Cancer *In Vivo*. *Biomed. Pharmacother.* 117, 109018. doi:10.1016/j.biopha.2019.109018

Wang, X., Wang, X., Zhu, Z., Li, W., Yu, G., Jia, Z., et al. (2019f). Prostate Carcinoma Cell-Derived Exosomal MicroRNA-26a Modulates the Metastasis and Tumor Growth of Prostate Carcinoma. *Biomed. Pharmacother.* 117, 109109. doi:10.1016/j.biopha.2019.109109

Wang, Y., Liu, W., Yu, Y., Liu, J.-j., Xue, H.-d., Qi, Y.-f., et al. (2020). CT Radiomics Nomogram for the Preoperative Prediction of Lymph Node Metastasis in Gastric Cancer. *Eur. Radiol.* 30 (2), 976–986. doi:10.1007/s00330-019-06398-z

Waqar, S. N., Samson, P. P., Robinson, C. G., Bradley, J., Devarakonda, S., Du, L., et al. (2018). Non-small-cell Lung Cancer with Brain Metastasis at Presentation. *Clin. Lung Cancer* 19 (4), e373–e379. doi:10.1016/j.cllc.2018.01.007

Webber, J., Steadman, R., Mason, M. D., Tabi, Z., and Clayton, A. (2010). Cancer Exosomes Trigger Fibroblast to Myofibroblast Differentiation. *Cancer Res.* 70 (23), 9621–9630. doi:10.1158/0008-5472.CAN-10-1722

Wells, A., Yates, C., and Shepard, C. R. (2008). E-cadherin as an Indicator of Mesenchymal to Epithelial Reverting Transitions during the Metastatic Seeding of Disseminated Carcinomas. *Clin. Exp. Metastasis* 25 (6), 621–628. doi:10.1007/s10585-008-9167-1

Wen, S., Wei, Y., Zen, C., Xiong, W., Niu, Y., and Zhao, Y. (2020). Long Non-coding RNA NEAT1 Promotes Bone Metastasis of Prostate Cancer through N6-Methyladenosine. *Mol. Cancer* 19 (1), 171. doi:10.1186/s12943-020-01293-4

Wernersson, S., and Pejler, G. (2014). Mast Cell Secretory Granules: Armed for Battle. *Nat. Rev. Immunol.* 14 (7), 478–494. doi:10.1038/nri3690

Wu, H., Song, S., Yan, A., Guo, X., Chang, L., Xu, L., et al. (2020). RACK1 Promotes the Invasive Activities and Lymph Node Metastasis of Cervical Cancer via Galectin-1. *Cancer Lett.* 469, 287–300. doi:10.1016/j.canlet.2019.11.002

Wu, J., Li, H., Xie, H., Wu, X., and Lan, P. (2019). The Malignant Role of Exosomes in the Communication Among Colorectal Cancer Cell, Macrophage and Microbiome. *Carcinogenesis* 40 (5), 601–610. doi:10.1093/carcin/bgy138

Xia, Y., Zhang, B., Zhang, H., Li, W., Wang, K. P., and Shen, H. (2015). Evaluation of Lymph Node Metastasis in Lung Cancer: Who Is the Chief justice? *J. Thorac. Dis.* 7 (Suppl. 4), S231–S237. doi:10.3978/j.issn.2072-1439.2015.11.63

Xian, X., Gopal, S., and Couchman, J. R. (2010). Syndecans as Receptors and Organizers of the Extracellular Matrix. *Cell Tissue Res* 339 (1), 31–46. doi:10.1007/s00441-009-0829-3

Xiao, D., Barry, S., Kmetz, D., Egger, M., Pan, J., Rai, S. N., et al. (2016). Melanoma Cell-Derived Exosomes Promote Epithelial-Mesenchymal Transition in Primary Melanocytes through Paracrine/autocrine Signaling in the Tumor Microenvironment. *Cancer Lett.* 376 (2), 318–327. doi:10.1016/j.canlet.2016.03.050

Xie, Z., Gao, Y., Ho, C., Li, L., Jin, C., Wang, X., et al. (2021). Exosome-delivered CD44v6/C1QBP Complex Drives Pancreatic Cancer Liver Metastasis by Promoting Fibrotic Liver Microenvironment. *Gut* 71, 568–579. doi:10.1136/gutjnl-2020-323014

Xing, F., Liu, Y., Wu, S.-Y., Wu, K., Sharma, S., Mo, Y.-Y., et al. (2018). Loss of XIST in Breast Cancer Activates MSN-C-Met and Reprograms Microglia via Exosomal miRNA to Promote Brain Metastasis. *Cancer Res.* 78 (15), 4316–4330. doi:10.1158/0008-5472.CAN-18-1102

Xu, D., Lin, X., and Qiu, X. (2020a). The Epithelioid Gastrointestinal Stromal Tumor with Pulmonary Metastasis. *Medicine (Baltimore)* 99 (9), e19346. doi:10.1097/MD.0000000000019346

Xu, H., Xu, G. L., Li, X. D., Su, Q. H., and Dong, C. Z. (2021). Correlation between the Contrast-Enhanced Ultrasound Image Features and Axillary Lymph Node Metastasis of Primary Breast Cancer and its Diagnostic Value. *Clin. Transl Oncol.* 23 (1), 155–163. doi:10.1007/s12094-020-02407-6

Xu, L., Xue, F., Wang, B., Yan, D., Ding, W., Yin, J., et al. (2016). Hoarseness Due to Lymph Node Metastasis of Hepatocellular Carcinoma: A Case Report. *Oncol. Lett.* 12 (2), 918–920. doi:10.3892/ol.2016.4687

Xu, N., Chen, S. H., Lin, T. T., Cai, H., Ke, Z. B., Dong, R. N., et al. (2020b). Development and Validation of Hub Genes for Lymph Node Metastasis in Patients with Prostate Cancer. *J. Cel Mol Med* 24 (8), 4402–4414. doi:10.1111/jcmm.15098

Xu, Y. Y., Lu, X., Mao, Y. L., Xiong, J. P., Bian, J., Huang, H. C., et al. (2017). The Surgical Treatment of Ovarian Cancer Metastasis between Liver and Diaphragm: a Report of 83 Cases. *Zhonghua Wai Ke Za Zhi* 55 (11), 838–841. doi:10.3760/cma.j.issn.0529-5815.2017.11.004

Yamakawa, Y., Moriguchi, M., Aramaki, T., Mitsuya, K., Asakura, K., Sawada, A., et al. (2015). Brain Metastasis from Hepatocellular Carcinoma: The Impact of Radiotherapy on Control of Intracranial Hemorrhage. *Hepatol. Res.* 45 (11), 1071–1075. doi:10.1111/hepr.12457

Yamanaka, T., Takaki, H., Nakatsuka, A., Uraki, J., Fujimori, M., Hasegawa, T., et al. (2013). Radiofrequency Ablation for Liver Metastasis from Gastrointestinal Stromal Tumor. *J. Vasc. Interv. Radiol.* 24 (3), 341–346. doi:10.1016/j.jvir.2012.11.021

Yamashita, K., Baba, Y., Kurashige, J., Iwatsuki, M., Imai, K., Hashimoto, D., et al. (2016). Co-occurrence of Liver Metastasis of Gastrointestinal Stromal Tumor and Hepatocellular Carcinoma: a Case Report. *Surg. Case Rep.* 2 (1), 86. doi:10.1186/s40792-016-0212-z

Yan, T. D., Yoo, D., and Sugarbaker, P. H. (2006). Significance of Lymph Node Metastasis in Patients with Diffuse Malignant Peritoneal Mesothelioma. *Eur. J. Surg. Oncol. (Ejso)* 32 (9), 948–953. doi:10.1016/j.ejso.2006.05.009

Yang, B., Feng, X., Liu, H., Tong, R., Wu, J., Li, C., et al. (2020a). High-metastatic Cancer Cells Derived Exosomal miR92a-3p Promotes Epithelial-Mesenchymal Transition and Metastasis of Low-Metastatic Cancer Cells by Regulating PTEN/Akt Pathway in Hepatocellular Carcinoma. *Oncogene* 39 (42), 6529–6543. doi:10.1038/s41388-020-01450-5

Yang, G.-L., Luo, T.-H., Zhang, H.-Q., Ling, C.-Q., and Li, B. (2016). A Case Report of Gastric Cancer with Brain Metastasis: Rare Peripheral Nervous System Symptoms. *Oncol. Lett.* 11 (4), 2893–2895. doi:10.3892/ol.2016.4288

Yang, H., Zhang, H., Ge, S., Ning, T., Bai, M., Li, J., et al. (2018). Exosome-Derived miR-130a Activates Angiogenesis in Gastric Cancer by Targeting C-MYB in Vascular Endothelial Cells. *Mol. Ther.* 26 (10), 2466–2475. doi:10.1016/j.ymthe.2018.07.023

Yang, S.-S., Ma, S., Dou, H., Liu, F., Zhang, S.-Y., Jiang, C., et al. (2020b). Breast Cancer-Derived Exosomes Regulate Cell Invasion and Metastasis in Breast Cancer via miR-146a to Activate Cancer Associated Fibroblasts in Tumor Microenvironment. *Exp. Cel Res.* 391 (2), 111983. doi:10.1016/j.yexcr.2020.111983

Yao, K., Peng, C., Zhang, Y., Zykova, T. A., Lee, M.-H., Lee, S.-Y., et al. (2017). RSK2 Phosphorylates T-Bet to Attenuate colon Cancer Metastasis and Growth. *Proc. Natl. Acad. Sci. USA* 114 (48), 12791–12796. doi:10.1073/pnas.1710756114

Ye, L., Zhang, F., Li, H., Yang, L., Lv, T., Gu, W., et al. (2017). Circulating Tumor Cells Were Associated with the Number of T Lymphocyte Subsets and NK Cells in Peripheral Blood in Advanced Non-small-cell Lung Cancer. *Dis. Markers* 2017, 1–6. doi:10.1155/2017/5727815

Ye, L., Zhang, Q., Cheng, Y., Chen, X., Wang, G., Shi, M., et al. (2018). Tumor-derived Exosomal HMGB1 Fosters Hepatocellular Carcinoma Immune Evasion by Promoting TIM-1+ Regulatory B Cell Expansion. *J. Immunotherapy Cancer* 6 (1), 145. doi:10.1186/s40425-018-0451-6

Yi, H., Ye, J., Yang, X. M., Zhang, L. W., Zhang, Z. G., and Chen, Y. P. (2015). High-grade Ovarian Cancer Secreting Effective Exosomes in Tumor Angiogenesis. *Int. J. Clin. Exp. Pathol.* 8 (5), 5062–5070.

Yin, Z., Ma, T., Huang, B., Lin, L., Zhou, Y., Yan, J., et al. (2019). Macrophage-derived Exosomal microRNA-501-3p Promotes Progression of Pancreatic Ductal Adenocarcinoma through the TGFBR3-Mediated TGF-β Signaling Pathway. *J. Exp. Clin. Cancer Res.* 38 (1), 310. doi:10.1186/s13046-019-1313-x

Yoon, A., Choi, C. H., Kim, H.-J., Park, J.-Y., Lee, Y.-Y., Kim, T.-J., et al. (2013). Contributing Factors for Bone Metastasis in Uterine Cervical Cancer. *Int. J. Gynecol. Cancer* 23 (7), 1311–1317. doi:10.1097/IGC.0b013e31829da127

York, J. E., Stringer, J., Ajani, J. A., Wildrick, D. M., and Gokaslan, Z. L. (1999). Gastric Cancer and Metastasis to the Brain. *Ann. Surg. Oncol.* 6 (8), 771–776. doi:10.1007/s10434-999-0771-3

Yoshida, Y., Hoshino, S., Miyake, T., Fukuda, S., Yamada, K., Naoya, A., et al. (2012). Early Start of Chemotherapy after Resection of Brain Metastasis from colon Cancer with Synchronous Multiple Liver Metastases. *Case Rep. Oncol.* 5 (2), 290–295. doi:10.1159/000339614

You, L.-N., Tai, Q.-W., Xu, L., Hao, Y., Guo, W.-J., Zhang, Q., et al. (2021a). Exosomal LINC00161 Promotes Angiogenesis and Metastasis via Regulating miR-590-3p/ROCK axis in Hepatocellular Carcinoma. *Cancer Gene Ther.* 28 (6), 719–736. doi:10.1038/s41417-020-00269-2

You, X., Wang, Y., Meng, J., Han, S., Liu, L., Sun, Y., et al. (2021b). Exosomal miR-663b E-xposed to TGF-β1 P-romotes C-ervical C-ancer M-etastasis and E-pithelial-mesenchymal T-ransition by T-argeting MGAT3. *Oncol. Rep.* 45 (4). doi:10.3892/or.2021.7963

You, Y., Shan, Y., Chen, J., Yue, H., You, B., Shi, S., et al. (2015). Matrix Metalloproteinase 13-containing Exosomes Promote Nasopharyngeal Carcinoma Metastasis. *Cancer Sci.* 106 (12), 1669–1677. doi:10.1111/cas.12818

Yousefi, M., Nosrati, R., Salmaninejad, A., Dehghani, S., Shahryari, A., and Saberi, A. (2018). Organ-specific Metastasis of Breast Cancer: Molecular and Cellular Mechanisms Underlying Lung Metastasis. *Cell Oncol.* 41 (2), 123–140. doi:10.1007/s13402-018-0376-6

Yu, L.-X., Yan, L., Yang, W., Wu, F.-Q., Ling, Y., Chen, S.-Z., et al. (2014). Platelets Promote Tumour Metastasis via Interaction between TLR4 and Tumour Cell-Released High-Mobility Group Box1 Protein. *Nat. Commun.* 5, 5256. doi:10.1038/ncomms6256

Yue, S., Mu, W., Erb, U., and Zöller, M. (2015). The Tetraspanins CD151 and Tspan8 Are Essential Exosome Components for the Crosstalk between Cancer Initiating Cells and Their Surrounding. *Oncotarget* 6 (4), 2366–2384. doi:10.18632/oncotarget.2958

Yung, W. K. A., Tepper, S. J., and Young, D. F. (1983). Diffuse Bone Marrow Metastasis by Glioblastoma: Premortem Diagnosis by Peroxidase-Antiperoxidase Staining for Glial Fibrillary Acidic Protein. *Ann. Neurol.* 14 (5), 581–585. doi:10.1002/ana.410140514

Zeng, Z., Li, Y., Pan, Y., Lan, X., Song, F., Sun, J., et al. (2018). Cancer-derived Exosomal miR-25-3p Promotes Pre-metastatic Niche Formation by Inducing Vascular Permeability and Angiogenesis. *Nat. Commun.* 9 (1), 5395. doi:10.1038/s41467-018-07810-w

Zhang, C., Liao, Y., Liu, P., Du, Q., Liang, Y., Ooi, S., et al. (2020). FABP5 Promotes Lymph Node Metastasis in Cervical Cancer by Reprogramming Fatty Acid Metabolism. *Theranostics* 10 (15), 6561–6580. doi:10.7150/thno.44868

Zhang, G., Zhang, W., Li, B., Stringer-Reasor, E., Chu, C., Sun, L., et al. (2017). MicroRNA-200c and microRNA- 141 Are Regulated by a FOXP3-Kat2b axis and Associated with Tumor Metastasis in Breast Cancer. *Breast Cancer Res.* 19 (1), 73. doi:10.1186/s13058-017-0858-x

Zhang, H.-G., Kim, H., Liu, C., Yu, S., Wang, J., Grizzle, W. E., et al. (2007). Curcumin Reverses Breast Tumor Exosomes Mediated Immune Suppression of NK Cell Tumor Cytotoxicity. *Biochim. Biophys. Acta (Bba) - Mol. Cel Res.* 1773 (7), 1116–1123. doi:10.1016/j.bbamcr.2007.04.015

Zhang, H., Deng, T., Liu, R., Bai, M., Zhou, L., Wang, X., et al. (2017). Exosome-delivered EGFR Regulates Liver Microenvironment to Promote Gastric Cancer Liver Metastasis. *Nat. Commun.* 8, 15016. doi:10.1038/ncomms15016

Zhang, J., Gao, Y., Han, H., Zou, C., Feng, Y., and Zhang, H. (2019a). Matrine Suppresses Lung Metastasis of Human Hepatocellular Carcinoma by Directly Targeting Matrix Metalloproteinase-9. *Biochem. Biophysical Res. Commun.* 515 (1), 57–63. doi:10.1016/j.bbrc.2019.04.063

Zhang, L., Niu, H., Ma, J., Yuan, B.-Y., Chen, Y.-H., Zhuang, Y., et al. (2019b). The Molecular Mechanism of LncRNA34a-Mediated Regulation of Bone Metastasis in Hepatocellular Carcinoma. *Mol. Cancer* 18 (1), 120. doi:10.1186/s12943-019-1044-9

Zhang, M., and Sun, J. (2013). Bone Metastasis from Ovarian Cancer. Clinical Analysis of 26 Cases. *Saudi Med. J.* 34 (12), 1270–1273.

Zhang, Q., Len, T. Y., Zhang, S. X., Zhao, Q. H., and Yang, L. H. (2020). Exosomes Transferring Long Non-coding RNA FAL1 to Regulate Ovarian Cancer Metastasis through the PTEN/AKT Signaling Pathway. *Eur. Rev. Med. Pharmacol. Sci.* 24 (21), 10921. doi:10.26355/eurrev_202011_23560

Zhang, Q., Suo, J., Chang, W., Shi, J., and Chen, M. (2017). Dual-modal Computer-Assisted Evaluation of Axillary Lymph Node Metastasis in Breast Cancer Patients on Both Real-Time Elastography and B-Mode Ultrasound. *Eur. J. Radiol.* 95, 66–74. doi:10.1016/j.ejrad.2017.07.027

Zhang, X. (2019). Interactions between Cancer Cells and Bone Microenvironment Promote Bone Metastasis in Prostate Cancer. *Cancer Commun.* 39 (1), 76. doi:10.1186/s40880-019-0425-1

Zhang, Y.-F., Zhou, Y.-Z., Zhang, B., Huang, S.-F., Li, P.-P., He, X.-M., et al. (2019c). Pancreatic Cancer-Derived Exosomes Promoted Pancreatic Stellate Cells Recruitment by Pancreatic Cancer. *J. Cancer* 10 (18), 4397–4407. doi:10.7150/jca.27590

Zhang, Z., Li, X., Sun, W., Yue, S., Yang, J., Li, J., et al. (2017). Loss of Exosomal miR-320a from Cancer-Associated Fibroblasts Contributes to HCC Proliferation and Metastasis. *Cancer Lett.* 397, 33–42. doi:10.1016/j.canlet.2017.03.004

Zhao, Z., Liang, S., and Sun, F. (2020). LncRNA DLX6-AS1 Promotes Malignant Phenotype and Lymph Node Metastasis in Prostate Cancer by Inducing LARGE Methylation. *Front. Oncol.* 10, 1172. doi:10.3389/fonc.2020.01172

Zheng, X., Ma, N., Wang, X., Hu, J., Ma, X., Wang, J., et al. (2020). Exosomes Derived from 5-Fluorouracil-Resistant colon Cancer Cells Are Enriched in GDF15 and Can Promote Angiogenesis. *J. Cancer* 11 (24), 7116–7126. doi:10.7150/jca.49224

Zhong, Y., Lu, Q., Qiu, W., and Luo, Y. (2020). LINC00636 Promotes Lymph Node Metastasis and Cervical Cancer through Targeting NM23. *Biosci. Rep.* 40 (10). doi:10.1042/BSR20200367

Zhou, C.-F., Ma, J., Huang, L., Yi, H.-Y., Zhang, Y.-M., Wu, X.-G., et al. (2019). Cervical Squamous Cell Carcinoma-Secreted Exosomal miR-221-3p Promotes Lymphangiogenesis and Lymphatic Metastasis by Targeting VASH1. *Oncogene* 38 (8), 1256–1268. doi:10.1038/s41388-018-0511-x

Zhou, J., Sun, J.-Y., Wu, S.-G., Wang, X., He, Z.-Y., Chen, Q.-H., et al. (2016). Risk Factors for Lymph Node Metastasis in Ovarian Cancer: Implications for Systematic Lymphadenectomy. *Int. J. Surg.* 29, 123–127. doi:10.1016/j.ijsu.2016.03.039

Zhou, W., Fong, M. Y., Min, Y., Somlo, G., Liu, L., Palomares, M. R., et al. (2014). Cancer-secreted miR-105 Destroys Vascular Endothelial Barriers to Promote Metastasis. *Cancer Cell* 25 (4), 501–515. doi:10.1016/j.ccr.2014.03.007

Zhou, X., Yan, T., Huang, C., Xu, Z., Wang, L., Jiang, E., et al. (2018). Melanoma Cell-Secreted Exosomal miR-155-5p Induce Proangiogenic Switch of Cancer-Associated Fibroblasts via SOCS1/JAK2/STAT3 Signaling Pathway. *J. Exp. Clin. Cancer Res.* 37 (1), 242. doi:10.1186/s13046-018-0911-3

Zhou, Z., Chen, L., Sher, D., Zhang, Q., Shah, J., Pham, N.-L., et al. (2018). Predicting Lymph Node Metastasis in Head and Neck Cancer by Combining Many-objective Radiomics and 3-dimensioal Convolutional Neural Network through Evidential Reasoning*. *Annu. Int. Conf. IEEE Eng. Med. Biol. Soc.*, 1–4. doi:10.1109/EMBC.2018.8513070

Zhu, H., Jia, Z., Trush, M. A., and Li, Y. R. (2016). Nrf2 Deficiency Promotes Melanoma Growth and Lung Metastasis. *Ros* 2 (4), 308–314. doi:10.20455/ros.2016.853

Zhu, Y.-J., Chen, Y., Hu, H.-Y., Zhou, Y.-W., Zhu, Y.-T., and Liu, J.-Y. (2020). Predictive Risk Factors and Online Nomograms for Synchronous Colon Cancer with Liver Metastasis. *Front. Oncol.* 10, 1681. doi:10.3389/fonc.2020.01681

Zhuo, S., Zhou, J., Ruan, G., Zeng, S., Ma, H., Xie, C., et al. (2020). Percutaneous Microwave Ablation versus Surgical Resection for Ovarian Cancer Liver Metastasis. *Int. J. Hyperthermia* 37 (1), 28–36. doi:10.1080/02656736.2019.1706767

Zong, Z.-H., Du, Y.-P., Guan, X., Chen, S., and Zhao, Y. (2019). CircWHSC1 Promotes Ovarian Cancer Progression by Regulating MUC1 and hTERT through Sponging miR-145 and miR-1182. *J. Exp. Clin. Cancer Res.* 38 (1), 437. doi:10.1186/s13046-019-1437-z

Zucchella, M., Dezza, L., Pacchiarini, L., Meloni, F., Tacconi, F., Bonomi, E., et al. (1989). Human Tumor Cells Cultured "*In Vitro*" Activate Platelet Function by Producing ADP or Thrombin. *Haematologica* 74 (6), 541–545.

Conflict of Interest: The authors declare that the research was conducted in the absence of any commercial or financial relationships that could be construed as a potential conflict of interest.

Publisher's Note: All claims expressed in this article are solely those of the authors and do not necessarily represent those of their affiliated organizations, or those of the publisher, the editors, and the reviewers. Any product that may be evaluated in this article, or claim that may be made by its manufacturer, is not guaranteed or endorsed by the publisher.

frontiers in Cell and Developmental Biology

ORIGINAL RESEARCH
published: 18 March 2022
doi: 10.3389/fcell.2022.778286

Angiogenesis-Related Gene Signature-Derived Risk Score for Glioblastoma: Prospects for Predicting Prognosis and Immune Heterogeneity in Glioblastoma

Gang Wang[1], *Jin-Qu Hu*[1], *Ji-Yuan Liu*[1] *and Xiao-Mei Zhang*[2]*

[1]*Department of Neurosurgery, The First Affiliated Hospital of China Medical University, Shenyang, China,* [2]*Department of Rheumatology and Immunology, ShengJing Hospital of China Medical University, Shenyang, China*

OPEN ACCESS

Edited by:
Hamid Morjani, Université de Reims Champagne-Ardenne, France

Reviewed by:
Lucia Di Marcotullio, Sapienza University of Rome, Italy
Juliano Andreoli Miyake, Federal University of Santa Catarina, Brazil

***Correspondence:**
Xiao-Mei Zhang
20142260@cmu.edu.cn

Specialty section:
This article was submitted to Molecular and Cellular Oncology, a section of the journal Frontiers in Cell and Developmental Biology

Received: *16 September 2021*
Accepted: *15 February 2022*
Published: *18 March 2022*

Citation:
Wang G, Hu J-Q, Liu J-Y and Zhang X-M (2022) Angiogenesis-Related Gene Signature-Derived Risk Score for Glioblastoma: Prospects for Predicting Prognosis and Immune Heterogeneity in Glioblastoma. Front. Cell Dev. Biol. 10:778286. doi: 10.3389/fcell.2022.778286

Background: Glioblastoma multiforme (GBM) is the most common malignant tumor in the central nervous system with poor prognosis and unsatisfactory therapeutic efficacy. Considering the high correlation between tumors and angiogenesis, we attempted to construct a more effective model with angiogenesis-related genes (ARGs) to better predict therapeutic response and prognosis.

Methods: The ARG datasets were downloaded from the NCBI-Gene and Molecular Signatures Database. The gene expression data and clinical information were obtained from TCGA and CGGA databases. The differentially expressed angiogenesis-related genes (DE-ARGs) were screened with the R package "DESeq2". Univariate Cox proportional hazards regression analysis was used to screen for ARGs related to overall survival. The redundant ARGs were removed by least absolute shrinkage and selection operator (LASSO) regression analysis. Based on the gene signature of DE-ARGs, a risk score model was established, and its effectiveness was estimated through Kaplan–Meier analysis, ROC analysis, etc.

Results: A total of 626 DE-ARGs were explored between GBM and normal samples; 31 genes were identified as key DE-ARGs. Then, the risk score of ARG signature was established. Patients with high-risk score had poor survival outcomes. It was proved that the risk score could predict some medical treatments' response, such as temozolomide chemotherapy, radiotherapy, and immunotherapy. Besides, the risk score could serve as a

Abbreviations: ARG, angiogenesis-related gene; AUC, area under receiver operating characteristic curve; Ang, angiopoietin; bFGF, basic fibroblast growth factor; BP, biological processes; CC, cellular component; CGGA, Chinese glioma genome atlas; DE-ARG, differentially expressed angiogenesis-related gene; GBM, glioblastoma multiforme; G-CIMP, glioma CpG island methylator phenotype; GO gene ontology; HGF, hepatocyte growth factor; IDH, isocitrate dehydrogenases; IFN, interferon; KEGG, Kyoto Encyclopedia of Genes and Genomes; LASSO, least absolute shrinkage and selection operator; MF, molecular function; MMP, matrix metalloproteinase; OS, overall survival; pDC, plasmacytoid dendritic cell; PDGF, platelet-derived growth factor; PPI, protein–protein interaction; ROC, receiver operating characteristic curve; TCGA, The Cancer Genome Atlas; TGF-β, transforming growth factor-β; TIDE, tumor immune dysfunction and exclusion; uPA/uPAR, urokinase/urokinase-type plasminogen activator receptor; VEGF, vascular endothelial growth factor; WHO, World Health Organization.

promising prognostic predictor. Three key prognostic genes (PLAUR, ITGA5, and FMOD) were selected and further discussed.

Conclusion: The angiogenesis-related gene signature-derived risk score is a promising predictor of prognosis and treatment response in GBM and will help in making appropriate therapeutic strategies.

Keywords: glioblastoma, angiogenesis, gene signature, prognostic model, risk score

BACKGROUND

Glioblastoma, also known as glioblastoma multiforme (GBM), which is classified by the World Health Organization (WHO) as a grade IV glioma, is a highly heterogeneous and aggressive type of nervous system tumor, with a 5-year survival rate of less than 7% (Ostrom et al., 2019). There has been great progress in surgical resection, radiotherapy, and chemotherapy. Immunotherapy, as a new promising treatment, has particularly caught worldwide attention (Bush et al., 2017; Xu et al., 2020). Nevertheless, the prognosis for GBM patients remains dismal.

Angiogenesis, which refers to the process of neovascularization from existing vessels, has been substantiated to be highly related to tumorigenesis, metastasis, and migration in glioblastoma (Onishi et al., 2011). Some angiogenesis regulators, including vascular endothelial growth factor (VEGF), basic fibroblast growth factor (bFGF), hepatocyte growth factor (HGF), platelet-derived growth factor (PDGF), transforming growth factor-β (TGF-β), matrix metalloproteinases (MMPs), and angiopoietins (Angs), are demonstrated to modulate several important cancer-related pathways and are promising prognostic biomarkers of GBM patients (Ahir et al., 2020). Inhibition of growth factors/signaling pathways necessary for tumor angiogenesis is viewed as one of the most practical approaches to hinder tumor progression (Ahir et al., 2020; Bazan et al., 2021).

Recently, with the advancement of next-generation sequencing technology, numerous studies have focused on the molecular changes underlying GBM. In 2016, for the first time, the World Health Organization (WHO) incorporated molecular marker-based classification into diagnosis, indicating that the treatment and diagnosis of GBM have entered a molecular era (Komori, 2017). Although increasing molecular studies in GBM have been reported recently, the appropriate prognostic biomarkers and predictors of therapeutic responses are still not clear. Increasing studies have investigated the roles of angiogenesis-related genes (ARGs) in the development and progression of glioma. The expression of ARGs is dysregulated in GBM and correlated with prognosis (Fei et al., 2015; Rostami et al., 2019; Simon et al., 2020). Therefore, ARGs are promising therapeutic targets and prognostic predictors in GBM.

In the present study, based on the global gene expression profile, we aimed to develop an angiogenesis-related gene expression signature and a nomogram model to predict prognosis and therapeutic targets in GBM. The related immunological features are also evaluated.

MATERIALS AND METHODS

Gene Expression and Clinical Data Acquisition

The study was carried out according to the workflow shown in **Figure 1A**. The ARG sets were downloaded from the NCBI-Gene (https://www.ncbi.nlm.nih.gov/gene) and Molecular Signatures Database (MSigDB, http://www.broad.mit.edu/gsea/msigdb). A total of 1,603 ARGs were obtained from NCBI-Gene with the keyword "angiogenesis" in *Homo sapiens* and 48 ARGs were downloaded from MSigDB (**Supplementary Table S1**).

The level III gene expression profiles and corresponding clinical information of GBM patients were downloaded from The Cancer Genome Atlas (TCGA, https://portal.gdc.cancer.gov) and the Chinese Glioma Genome Atlas (CGGA, http://www.cgga.org.cn) databases, respectively. The TCGA-GBM cohort containing 167 tumor samples and 5 normal samples was used as the training set (**Figure 1B**), while the CGGA cohort containing 388 GBM samples was selected as the validation set. A total of 219 GBM samples in The Repository for Molecular Brain Neoplasia Data (REMBRANDT, http://cainteGrator-info.nci.nih.gov/REMBRANDT) and 159 GBM samples in GSE16011 database (https://www.ncbi.nlm.nih.gov/geo/) were also obtained and used as the validation set. The expression data regarding the efficacy of angiogenesis inhibitors in GBM was obtained from the GSE79671 database (https://www.ncbi.nlm.nih.gov/geo/). Protein–protein interaction (PPI) network data were obtained using the STRING database (http://string-db.org) (Szklarczyk et al., 2021). No ethical approval or informed consent was required in this study due to the public availability of the data.

Identification of Differentially Expressed Genes and Functional Enrichment Analysis

The differentially expressed angiogenesis-related genes (DE-ARGs) between GBM and normal samples in the TCGA cohort were screened with the R language package "DESeq2", using a cutoff of log2 fold change (log2FC) ≥1 and adjusted $p \leq 0.01$ (Love et al., 2014). GO and KEGG pathway enrichment analyses were performed using the R package "clusterProfiler" (Yu et al., 2012).

Development and Validation of Prognostic Signatures Based on ARGs

Univariate Cox proportional hazards regression analysis was used to screen for ARGs related to overall survival (OS). Then, the redundant ARGs were removed by least absolute shrinkage and

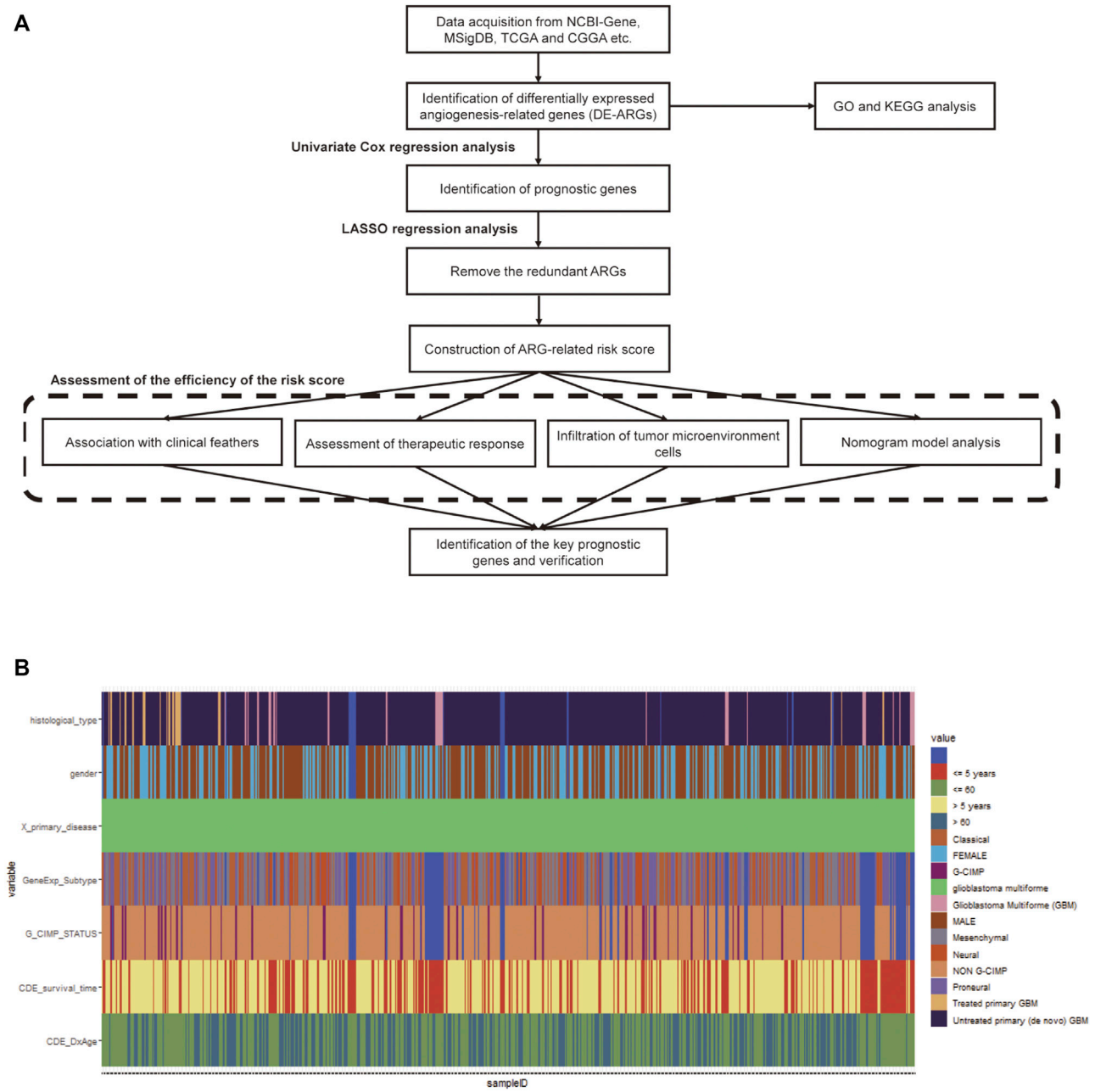

FIGURE 1 | Workflow chart and the clinicopathological features of the data. **(A)** The workflow chart of the whole analysis in this study. **(B)** Heatmap of clinicopathological features of the TCGA-GBM data.

selection operator (LASSO) regression analysis using the R package "glmnet"; thus, only 31 key ARGs remained (Friedman et al., 2009). The LASSO regression coefficients were weighted with mRNA expression levels to calculate the risk score.

By the risk score, patients were divided into high- or low-risk groups, respectively. With the R package "survival" and "survminer", Kaplan–Meier survival analysis was carried out to compare the prognostic difference between the two groups, and then the results were verified by ROC analysis.

Assessment of the Immune Landscape of GBM

In the present study, we analyzed the specific gene expression signature of immune and stromal cells in GBM tissues using the R package "estimate" (Yoshihara et al., 2013). By calculating the purity score, and immune and stromal scores with ESTIMATE algorithm, the infiltration of tumor microenvironment cells was predicted. Then, based on the normalized gene expression data, the proportions of 16 types of infiltrating immune cells

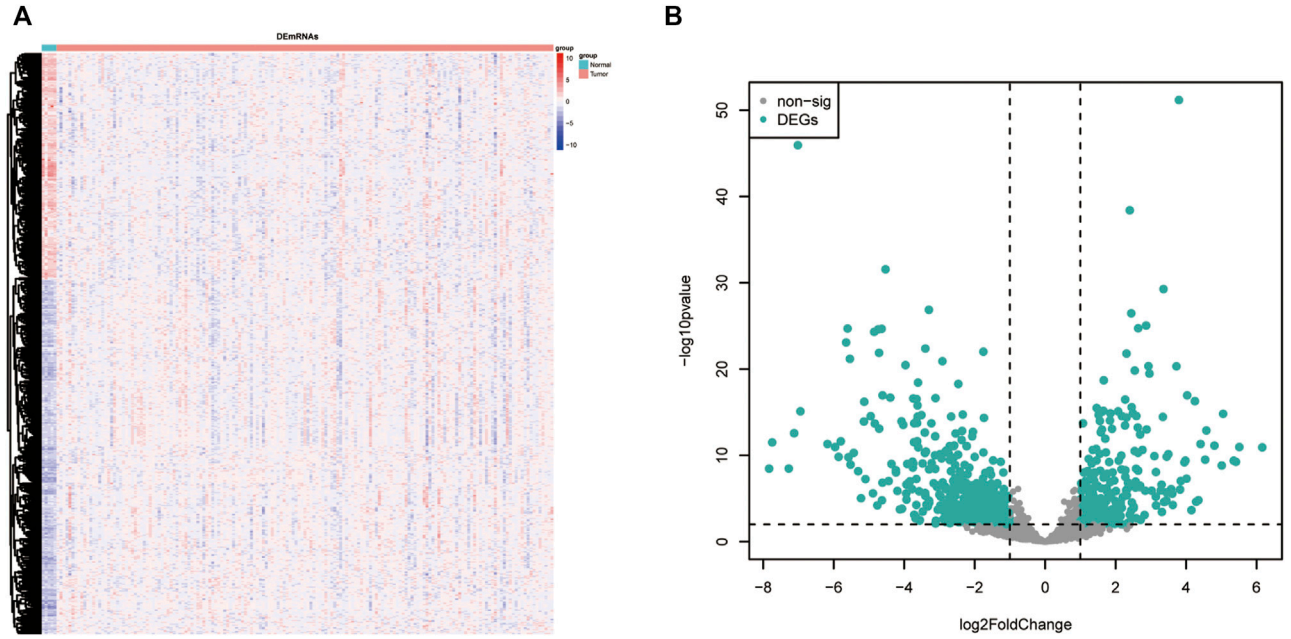

FIGURE 2 | DE-ARGs between GBM and normal brain tissues. **(A)** Heatmap of the DE-ARGs. **(B)** Volcano plots presenting the differences between GBM and normal brain tissues. The blue dots represent DE-ARGs (adj. p-value < 0.01 and |log2(FC)| > 1). DE-ARGs, differentially expressed angiogenesis-related genes.

were calculated by the CIBERSORT algorithm (Newman et al., 2015).

Evaluation of the Prediction Efficiency of the Risk Score on Chemotherapy and Immunotherapy

We evaluated the distribution of the non-responding group and the responding group in high- and low-risk groups separately by analyzing the data from GSE79671. Tumor immune dysfunction and exclusion (TIDE) algorithm was used to predict tumor immune evasion (Jiang et al., 2018). The prognostic value on immunotherapy was verified by ROC analysis.

Construction and Evaluation of the Nomogram

Furthermore, we plotted a nomogram based on the risk score groups and clinical traits by the multivariable Cox regression analysis. Then, validations were conducted utilizing the R package "rms" (version 6.2–0; http://cran.r-project.org/web/packages/rms). The calculation of concordance index (C-index) is to estimate the probability that the predicted result is consistent with the actual outcome.

Identification of Key Genes

The network of 74 DE-ARGs was constructed by *Cytoscape* software (version 3.8.2) and the top hub genes were selected through the MCODE plugin. The prognostic value was examined by Kaplan–Meier survival analysis through the GlioVis data portal (http://gliovis.bioinfo.cnio.es) (Bowman et al., 2017). A Venn diagram analysis was carried out between the 31 key ARGs, 10 hub genes, and 8 prognostic hub genes previously identified; ultimately, 3 key genes were identified using venn tools in Hiplot (https://hiplot.com.cn) (Hiplot: A Free and Comprehensive Cloud Platform for Scientific Computation and Visualization, 2021).

Statistical Analysis

Differences between the high- or low-risk groups were compared with the Wilcoxon test. Survival curves were generated by the Kaplan–Meier method and compared with the Log-rank test. Experiments were conducted three times independently and data were presented as mean ± SEM. p < 0.05 (*), p < 0.01 (**), and p < 0.001 (***) represent statistical significance. The time-dependent receiver operating characteristic (ROC) curves were built using the R package "pROC" to test the prognostic performance of the ARG-risk signature (Robin et al., 2011). All statistical analyses were conducted with SPSS 19.0 (IBM, Armonk, New York), GraphPad Prism 8.0 (GraphPad Software, La Jolla, California), or R software (www.r-project.org).

RESULTS

Identification of Differentially Expressed Genes and Functional Enrichment Analysis

The TCGA-GBM dataset was screened to identify the differentially expressed angiogenesis-related genes (DE-ARGs) between GBM and normal samples with the R language package "DESeq2", using a cutoff of |log2FC| ≥1 and adj.p < 0.01. As

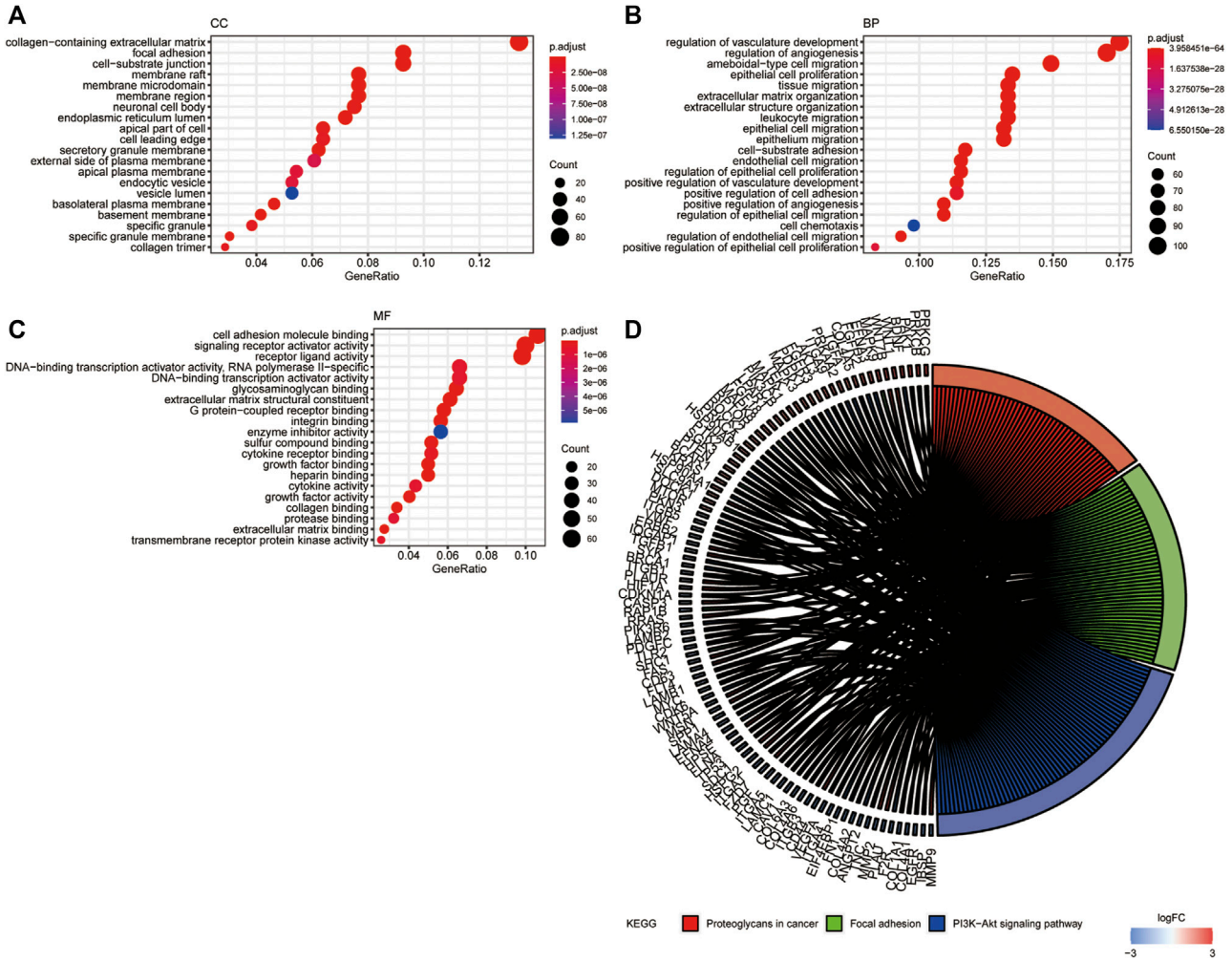

FIGURE 3 | GO and KEGG functional enrichment analysis of DE-ARGs. **(A–C)** The top 20 enriched terms in CC, BP, and MF are presented. **(D)** The top 100 genes and 3 pathways enriched in KEGG analysis. GO, Gene Ontology; CC, cellular component; MF, molecular function; BP, biological process; KEGG, Kyoto Encyclopedia of Genes and Genomes. DE-ARGs, differentially expressed angiogenesis-related genes.

shown in **Figure 2**, there were 626 DE-ARGs in total; 243 genes were upregulated and 383 genes were downregulated (**Figure 2**).

GO and KEGG pathway enrichment analyses were performed with a cutoff of $p < 0.05$. The top 20 most enriched terms are shown in **Figure 3**. GO analysis showed that the DE-ARGs were mainly enriched in cellular components like collagen-containing extracellular matrix, focal adhesion, and cell–substrate junction; biological processes like regulation of angiogenesis, regulation of vasculature development, and ameboidal-type cell migration; and molecular functions like cell adhesion molecule binding, signaling receptor activator activity, and receptor–ligand activity (**Figures 3A–C**). Meanwhile, KEGG analysis showed that the proteoglycans in cancer, focal adhesion, and PI3K-AKT signaling pathway were highly enriched. All the results suggested that the genes had a broad impact on tumor progression *via* angiogenesis regulation.

Identification of Prognostic ARGs and Establishment of the ARG-Related Prognostic Model

Univariate Cox regression analysis was conducted to detect prognostic DE-ARGs. Seventy-four DE-ARGs were shown to be highly related with prognosis. The expression levels and OS curves of the top 6 are shown in **Figure 4**. Subsequently, 31 genes were selected as key factors from the above 74 DE-ARGs by LASSO Cox regression analysis (**Figure 5**).

With the 31 key factors, we established an ARG-related risk score model to predict the prognosis. The formula of the risk score of ARG signature reads as follows:

$$\text{riskscore} = e^{\sum_{k=1}^{n} c_k \exp ression_k}$$

In the above equation, n is the number of selected key ARGs, e refers to the natural constant, k represents the kth prognostic gene with a non-zero dimension reduction coefficient of Lasso, c is its coefficient, and $expression_k$ is its expression value.

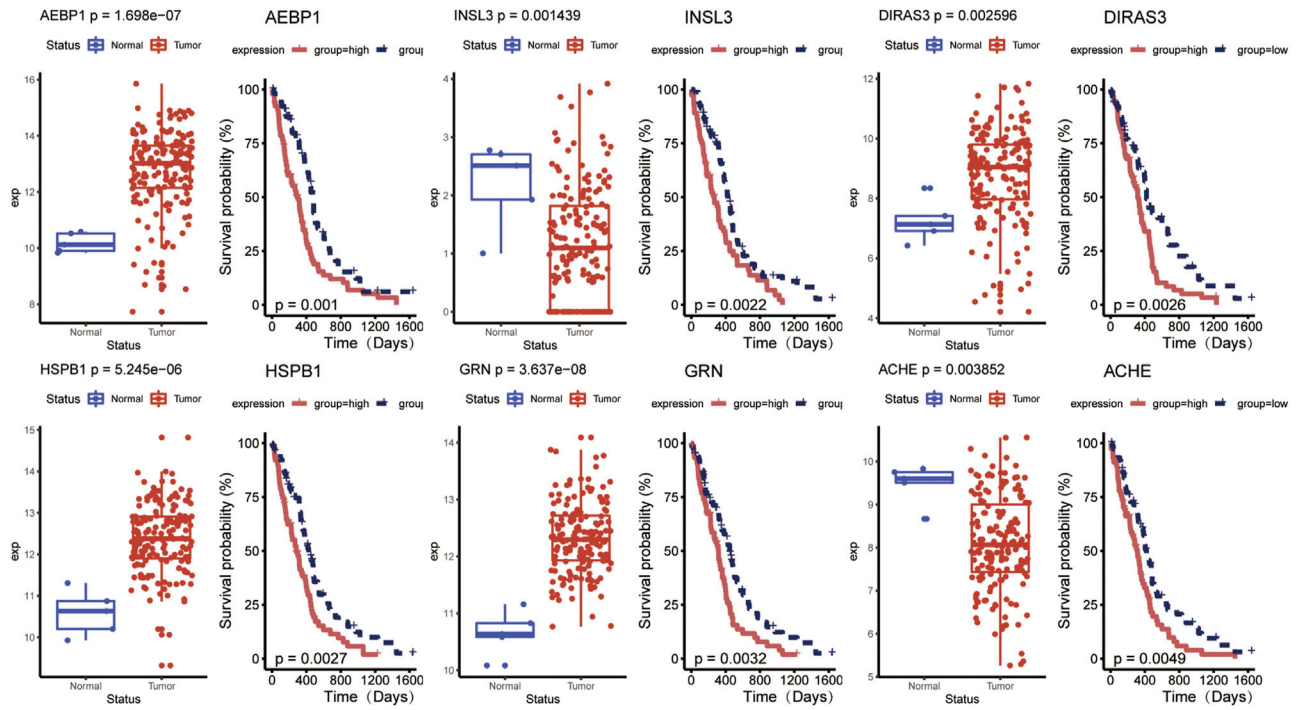

FIGURE 4 | Top 6 prognostic DE-ARGs' expression and their Kaplan–Meier survival curves. DE-ARGs, differentially expressed angiogenesis-related genes.

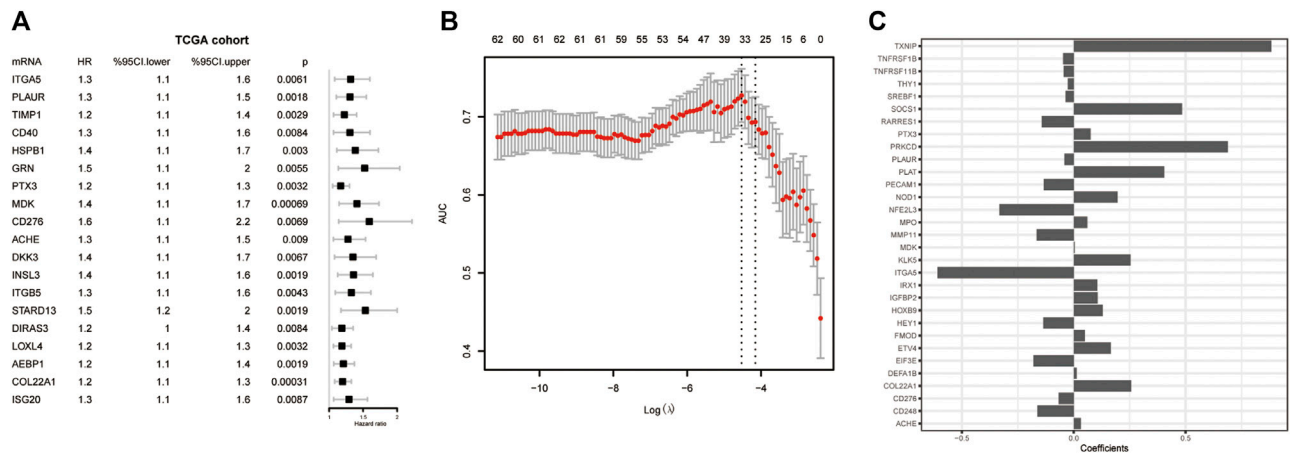

FIGURE 5 | Screening for the key genes from the DE-ARGs. **(A)** Cox regression analysis. **(B)** LASSO penalized Cox regression analysis of the DE-ARGs. **(C)** The weight coefficient of key DE-ARGs. DE-ARGs, differentially expressed angiogenesis-related genes. LASSO, the least absolute shrinkage and selection operator.

Hereafter, we sought to explore the relationship between the risk score and prognosis. We used the median value of the risk score as a cutoff to divide the patients into high- and low-risk groups (**Figures 6A,B**). Compared to the low-risk group, the high-risk group has a significant low OS, suggesting a worse prognosis (**Figure 6C**). Receiver operating characteristic (ROC) curve analysis showed that the ARG-related risk score had good predictive accuracy for prognosis in the TCGA cohort (**Figure 6D**). For independent validation, we further assessed the risk score model using the CGGA, Rembrandt, and Gravendeel database (**Figure 6**E). Consistent results were obtained.

Association Between the Risk Score and Clinical Features

In order to explore the correlation between ARG-related risk score and clinical features, we respectively compared the

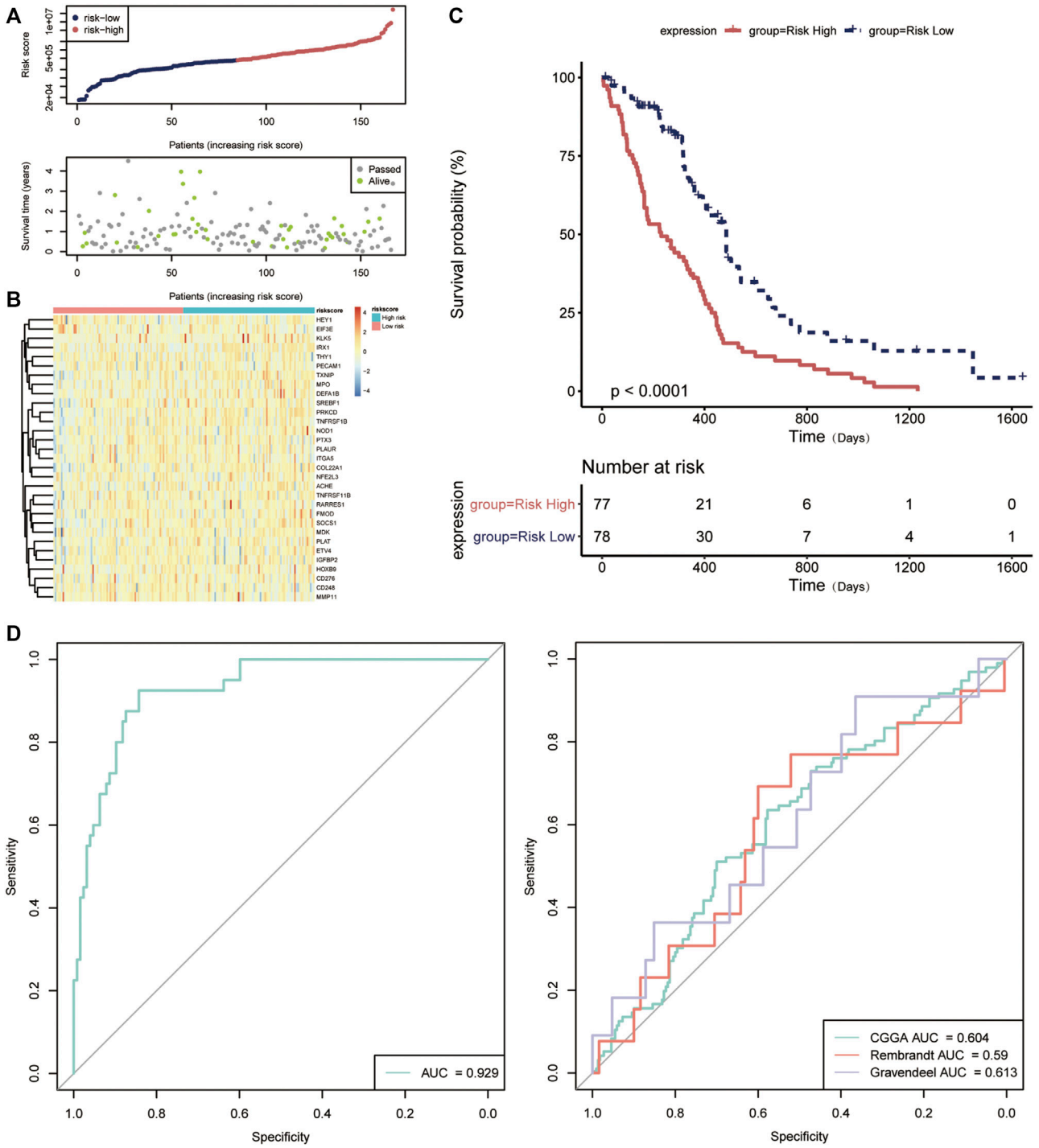

FIGURE 6 | Validation of the prognostic value of the angiogenesis-related risk score model. **(A)** The distribution of the risk score model and patient survival status. **(B)** Heatmap presenting the expression of 31 key DE-ARGs in the high- and low-risk group classified by the risk score model. **(C)** Kaplan–Meier curves for overall survival in the high- and low-risk group. **(D)** The receptor operating characteristic (ROC) curve of the risk score in TCGA database (left) and other databases (right). AUC, area under the curve.

differences between the high- and low-risk groups in survival time, Glioma CpG island methylator phenotype (G-CIMP) status, gene expression subtype, isocitrate dehydrogenase (IDH) mutant status, etc. It was shown that the risk score did reveal a relationship with some clinical traits, especially in G_CIMP status and IDH mutant status (**Figure 7**).

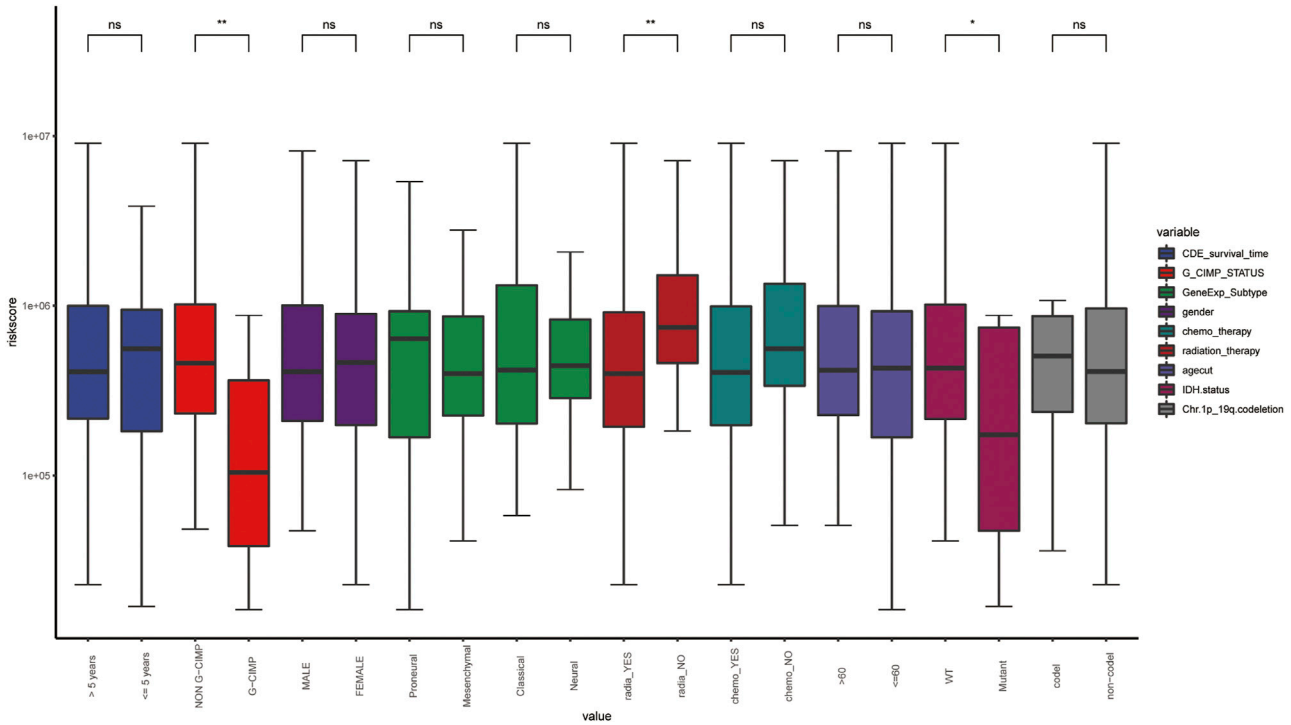

FIGURE 7 | The distribution of clinical features in the different risk groups. WT, wild type; *, *p*-value < 0.05; **, *p*-value < 0.01; ns, non-significant.

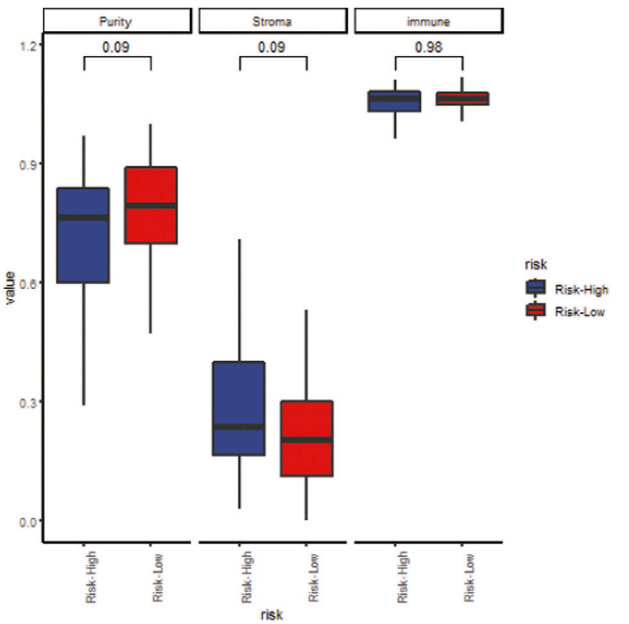

FIGURE 8 | The correlation between the risk score and tumor purity (left), stroma score (middle) and immune score (right).

The Risk Score Predicts the Infiltration of Tumor Microenvironment Cells

We analyzed the specific gene expression signature of purity, immune, and stroma scores in GBM tissues using the R package "estimate". As shown in **Figure 8**, there was no difference between the two groups in tumor purity. Even though the differences were not significant, the high-risk group did show a higher stroma score and immune score, indicating a poorer prognosis (**Figure 8**). To estimate the immunological functioning in the high- and low-risk groups, the proportions of 16 types of infiltrating immune cell and 13 types of immune-related functions were calculated by the CIBERSORT algorithm using the TCGA database. High-risk score was shown to be correlated with many immune-related functions, especially type I interferon (IFN) antiviral response and para-inflammation function. Furthermore, the distribution of immune cell also differed; the high-risk group had higher proportion of plasmacytoid dendritic cells (pDCs) and neutrophils (**Figure 9**).

The Risk Score Predicts the Medical Treatment Response

The targeted drug bevacizumab, which is well known as an anti-angiogenesis drug, has been proven effective on many malignant tumors. Nevertheless, not all the patients could benefit from it. In order to examine the prognostic ability on anti-angiogenesis

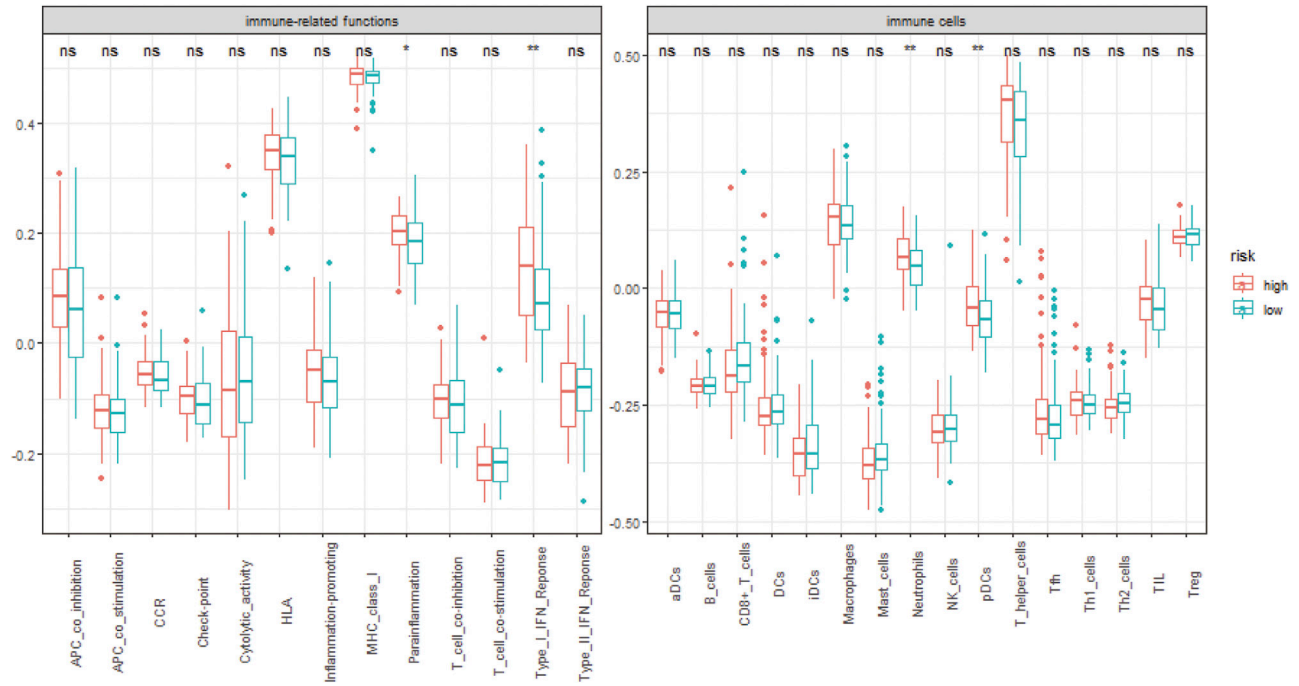

FIGURE 9 | The distribution of 13 different immune-related functions and 16 types of infiltrating immune cell in the different risk groups. *, p-value < 0.05; **, p-value < 0.01; ns, non-significant.

treatment, the efficacy of bevacizumab was compared between the two groups. As shown in **Figure 10**, there were more patients who responded to the drugs in the low-risk score group. Meanwhile, the non-responding group has higher risk scores relatively (**Figures 10A,B**).

Predictive potential of immunotherapy responsiveness among the two groups in TCGA-GBM was estimated by TIDE algorithm. The high-risk group revealed a higher TIDE score (**Figures 10C,D**).

The Risk Score Was an Independent Prognostic Predictor

To access whether the angiogenesis-related risk score is a promising prognostic predictor, univariate and multivariate Cox regression was conducted with the TCGA-GBM dataset. The results revealed that the risk score, G-CIMP status, IDH mutant status, 1p/19q co-deletion, chemotherapy, and radiation therapy were significantly correlated with clinical outcome and prognosis (**Figure 11**). Similar results were obtained with the CGGA dataset. Taken together, the angiogenesis-related risk score was validated to be an independent prognostic predictor.

Build Nomogram Combined the Risk Score With Clinical Features

In order to explore a new model for predicting, a nomogram was generated with the above independent prognostic clinical features to predict the probability of the 12- and 24-month OS in the TCGA cohort (**Figure 12A**). As is shown in **Figure 12**, the predicted OS was closely related to the actual OS (**Figure 12B**).

Identification of the Key Prognostic Genes

The prognostic 31 DE-ARGs' interaction network was constructed by *Cytoscape* software (**Figure 13A**), and the top 10 hub genes were identified through the MCODE plugin (**Figure 13B**). The Kaplan–Meier survival analysis was conducted and 8 genes were shown to be prognostic on OS (**Figures 13C–L**). Venn diagram analysis indicated that 3 key genes [PLAUR (plasminogen activator, urokinase receptor), ITGA5, and FMOD (fibromodulin)] were the intersection of the 31 DE-ARGs, 10 hub genes, and 8 prognostic hub genes (**Figure 14**).

DISCUSSION

GBM is a highly heterogeneous malignant tumor, and despite the great advances in multimodality therapy, the overall prognosis remains poor. Recently, numerous studies have focused on the molecular changes underlying GBM, supplying abundant high-throughput data. Based on the data, people tried to explore molecular characteristics to facilitate predicting the prognosis and improving individualized treatment (Cao et al., 2019; Wang et al., 2019; Niu et al., 2020). Nevertheless, the most appropriate models remain controversial to date. It is widely believed that angiogenesis is highly related to tumorigenesis, metastasis, and migration; anti-angiogenesis therapy has been viewed as a

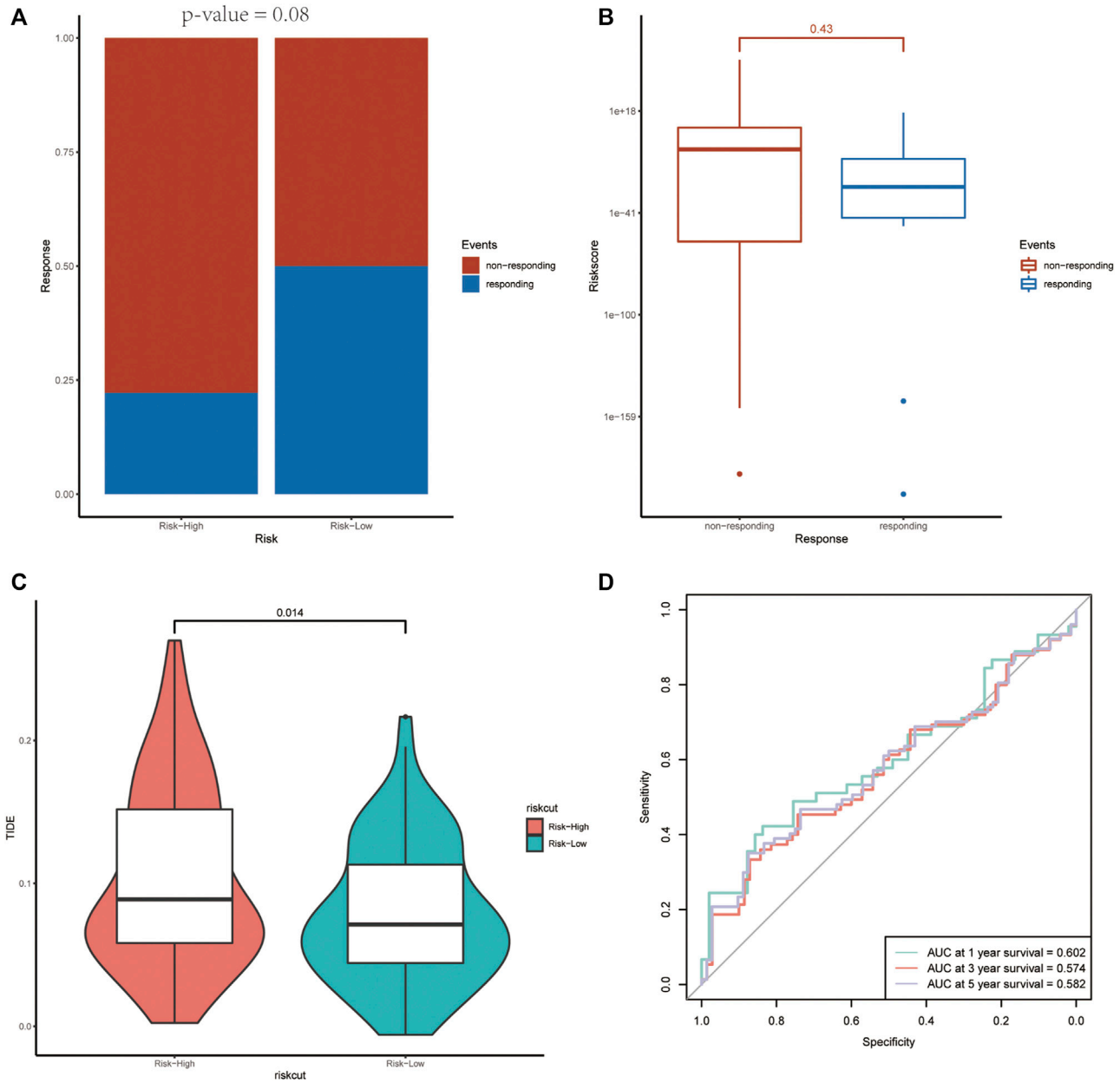

FIGURE 10 | The association between the risk score and the treatment efficiency of anti-angiogenesis therapy and immunotherapy. **(A)** The responding ratio differs in the high- and low-risk groups. **(B)** The average risk score of the non-responding group was higher than that of the responding group. **(C, D)** The high-risk group revealed a higher TIDE score and the ROC curve demonstrated the prognostic value of the risk score on immunotherapy.

promising treatment for GBM patients (Ahir et al., 2020), but a prediction model concerning angiogenesis has not been developed yet. In the current study, we established an angiogenesis-related gene signature-derived risk score for the first time.

The performance evaluation analysis revealed that the risk score worked well in predicting OS in both the training set and the validation set. The correlations between the risk score and clinical traits were also estimated. Many existing studies demonstrated that non-G-CIMP and IDH wild type were associated with worse prognosis (Tan et al., 2020). Our risk score showed high correlation with G-CIMP and IDH status, which further implied its potential in predicting prognosis.

Tumor microenvironment, as one of the hottest topics, has received extensive attention these past few years. In our study, the high-risk score group revealed a close correlation with type I IFN antiviral response and a higher infiltration proportion of plasmacytoid dendritic cells (pDCs) and neutrophils. It is well-known that both innate and adaptive immune response could promote angiogenesis through releasing pro-angiogenic

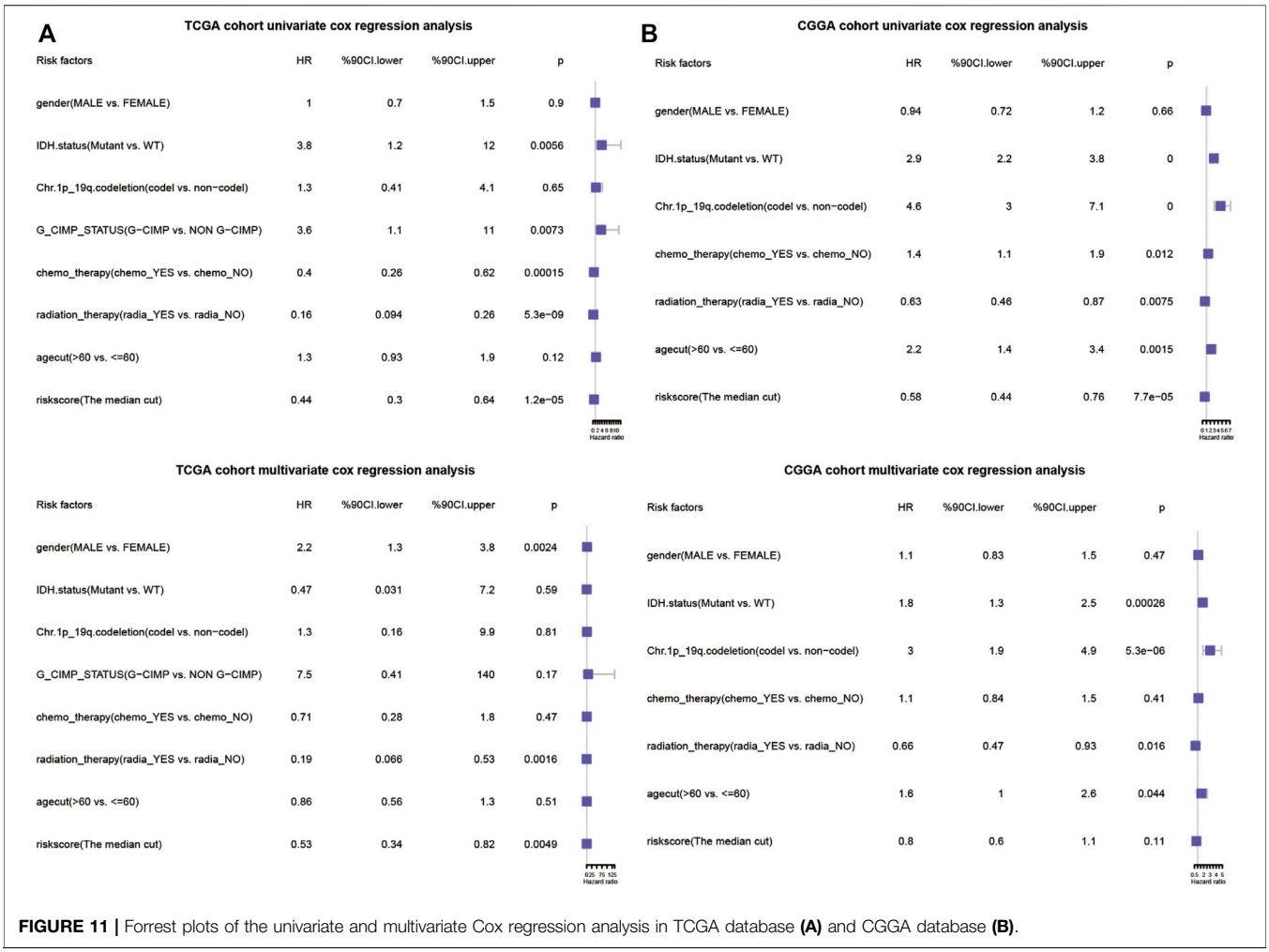

FIGURE 11 | Forrest plots of the univariate and multivariate Cox regression analysis in TCGA database **(A)** and CGGA database **(B)**.

mediators and then activating endothelial cell proliferation and migration (Ribatti and Crivellato, 2009). The type I IFN family was capable of exerting its anti-tumor activity *via* regulating a wide range of immune cells and inhibiting angiogenesis (Hong et al., 2000; Enomoto et al., 2017; Snell et al., 2017). pDCs, as an important class of antigen-presenting cells (APCs), play a critical role in regulating the immune response to antigens (Megjugorac et al., 2004). Depending on the different microenvironments or stimuli, they could induce either immunogenicity or immune tolerance (Villadangos and Young, 2008; Panda et al., 2017; Waisman et al., 2017). pDC dysfunction induced by impaired IFN-α secretion and upregulation of immune checkpoint mediators was often observed in tumors, including gliomas (Gousias et al., 2013; Aspord et al., 2014; Mitchell et al., 2018). As for neutrophils, they are the most abundant white blood cells in the human circulatory system, involved in the innate immunity (Amulic et al., 2012). Recent studies have demonstrated their complex role in promoting angiogenesis and tumorigenesis (Kim and Bae, 2016; Wu et al., 2020). Both pDCs and neutrophils play a critical role in pro-angiogenesis and immunosuppression (Stockmann et al., 2014; Albini et al., 2018). It is for this reason that our ARG-related risk score has a satisfactory prognostic efficiency.

Chemotherapy, such as anti-angiogenic therapy and immunotherapy, has been expected to be a promising adjunct to traditional surgery and radiotherapy for GBM treatment (Tan et al., 2020). Anti-angiogenic therapy using bevacizumab is a type of targeted anti-cancer therapy that aims to inhibit tumor growth *via* controlling tumor vessel growth. Some studies found that bevacizumab prolonged progression-free survival in both newly diagnosed and recurrent GBM. On the other hand, not all patients could benefit from it because of its increased toxicity (Chinot et al., 2014; Gilbert et al., 2014). Here, we found that the high-risk group had a higher rate of non-response, indicating that the risk score could serve as an attractive stratification tool to screen suitable patients. Likewise, the risk score was applied to predict the efficiency of immunotherapy. In recent years, there is a growing interest in immunotherapeutic treatments and their intrinsic mechanisms. Though immunotherapy has apparently improved the management of many other tumors, GBM

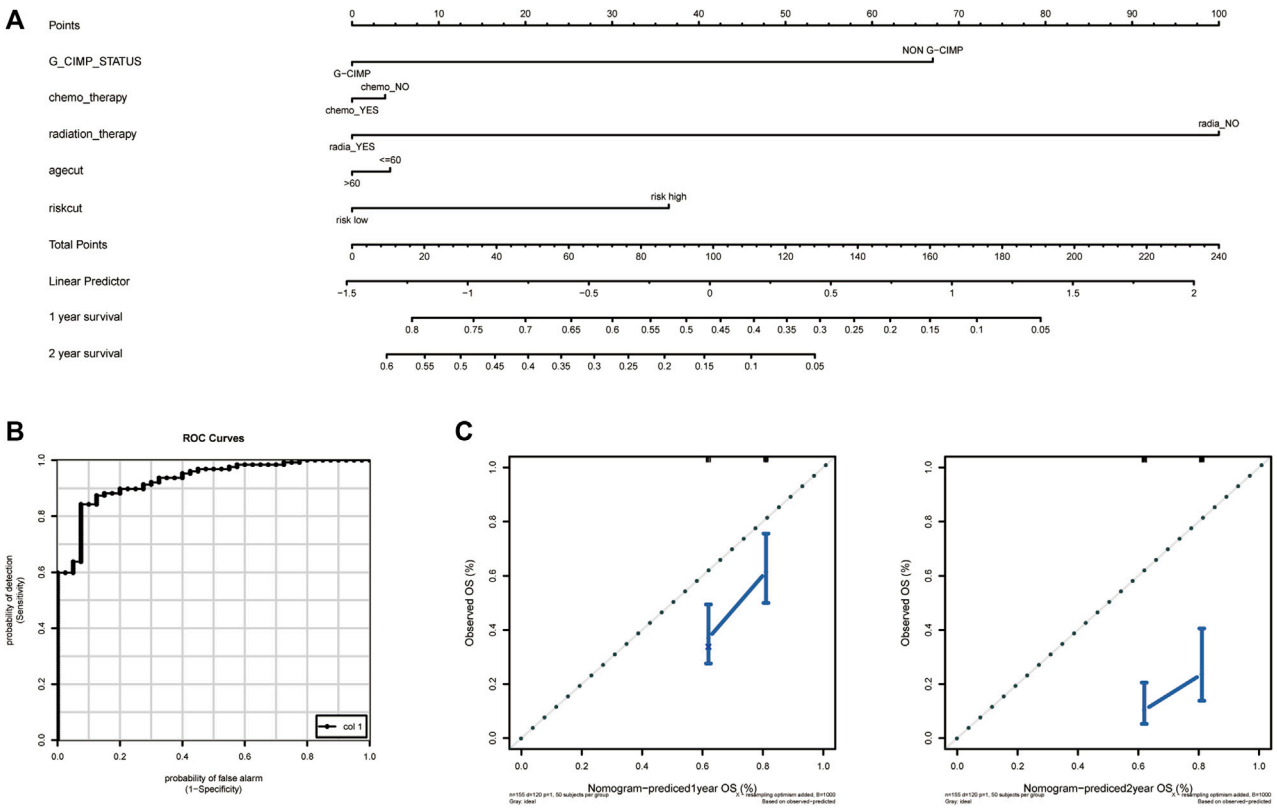

FIGURE 12 | Establishment and validation of the nomogram to predict the prognosis. **(A)** Calibration plot of nomogram. **(B)** The ROC curve of the risk score. **(C)** The efficiency of nomogram on predicting 1 year OS (left) and 2 year OS (right). OS, overall survival.

exhibits a high resistance to it (Lim et al., 2018). As discussed above, there is a cross-talk between immune responses and tumor angiogenesis (Albini et al., 2018). Potential response to immune checkpoint blockage therapy was estimated with TIDE algorithm. The results confirmed the potential prognostic efficiency of the risk score on immunotherapy. In general, the risk score we presented would help with providing individualized regimens on GBM.

Furthermore, a nomogram incorporating the angiogenesis-related gene signature, gender, G-CIMP status, IDH status, 1p19q co-deletion status, etc. was generated to predict the OS of GBM. The efficiency was validated by ROC curve. As expected, the performance of the nomogram was satisfactory, which implied a good prospect in clinical practice.

It should be noted that the model has been examined only in a few databases; further validation in multicenter, prospective clinical trials is still needed. Besides, it is derived from 31 genes; the quantity of genes is larger than those of other models, which may hinder its application. Henceforth, we would make further efforts in optimizing and simplifying this angiogenesis-related prognostic model and verifying it in prospective studies.

In the present study, three genes (PLAUR, ITGA5, and FMOD) were finally identified to be key hub genes through construction of a PPI network and screening hub genes with *Cytoscape* software. PLAUR, which is also known as CD87, UPAR, URKR, and U-PAR, is found to be overexpressed in multiple cancers including GBM, and contributes to tumor angiogenesis, cell migration, and invasion (Raghu et al., 2011; Raghu et al., 2012; Schuler et al., 2012; Hu et al., 2015; Loft et al., 2017). It encodes urokinase-type plasminogen activator receptor (uPAR), a GPI-anchored cell membrane receptor, which could bind with urokinase (uPA) and stimulate the intracellular signals associated with tumorigenesis. Raghu et al. validated its over-expression in glioma cell lines and found that specific knockdown of uPA/uPAR could attenuate tumor growing and invasion *via* Notch-1 signaling pathway (Raghu et al., 2011). Besides, some other pro-oncogenic factors like sphingosine-1-phosphate and nitric oxide synthase are also reported to exert their effects through the uPA/uPAR system in glioma (Young et al., 2009; Zhuang et al., 2013). ITGA5, which forms heterodimers together with integrin β1, is known as an important subtype of the integrin α chain family. It was validated to be overexpressed in glioma and play a role in predicting prognosis and therapeutic response (Cosset et al., 2012; Blandin et al., 2021; Chen et al., 2021). FMOD was an epigenetically regulated gene, encoding extracellular matrix

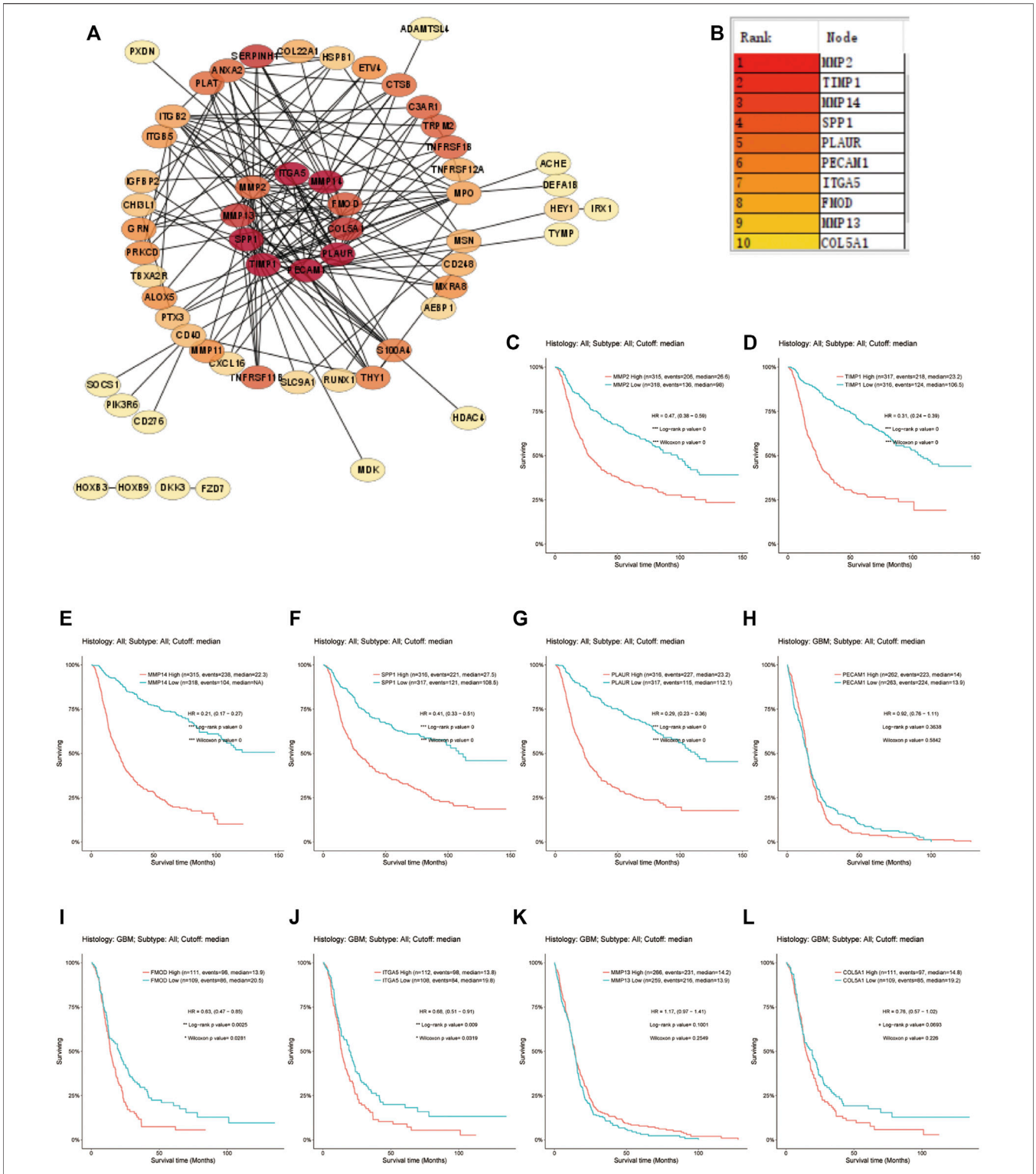

FIGURE 13 | Screening for the hub genes. **(A)** PPI network of the DE-ARGs. **(B)** The top 10 hub genes selected by MCODE algorithm. **(C–L)** The correlation between the expression of hub gene and OS. PPI, protein–protein interaction; DE-ARGs, differentially expressed angiogenesis-related genes; OS, overall survival.

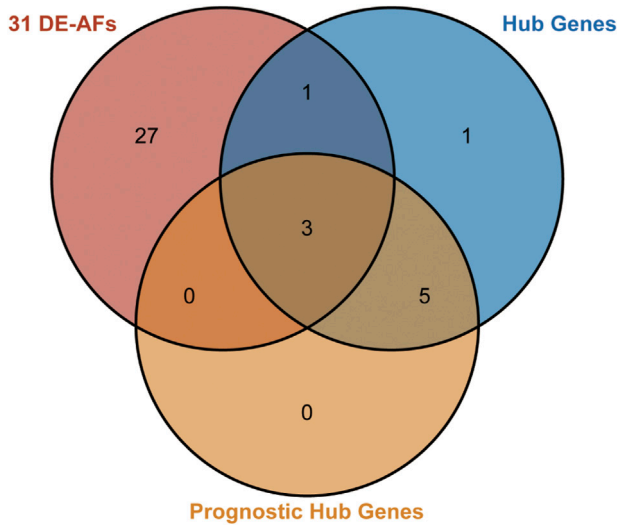

FIGURE 14 | Venn diagram for identifying the key factors. The pink circle represents the 31 DE-ARGs. The blue circle represents the 10 hub genes. The orange circle represents the 8 prognostic genes selected by Kaplan–Meier survival curves. The overlap area represents the 3 genes that were predicted to play central roles.

small leucine-rich proteoglycans. It has been demonstrated to promote cell migration in GBM *via* inducing filamentous actin stress fiber formation, depending on the TGF-β1 pathway (Mondal et al., 2017). It was also suggested to be a mediator in VEGF expression and associated with angiogenesis (Chen et al., 2018). Overall, the current findings indicate that the three genes have a complex relationship with GBM. The underlying mechanisms of the three hub genes demand further explorations.

CONCLUSION

In conclusion, we established a reliable angiogenesis-related risk score model that is verified to be effective in predicting the OS and therapeutic responses, suggesting a high likelihood of making individualized treatment strategies for GBM patients. Further studies are needed to optimize the model and explore the inner mechanisms of the key genes in tumorigenesis, metastasis, and migration.

DATA AVAILABILITY STATEMENT

Publicly available datasets were analyzed in this study. These data can be found here: TCGA-GBM, https://portal.gdc.cancer.gov; CGGA-GBM, http://www.cgga.org.cn; the Repository for Molecular Brain Neoplasia Data (REMBRANDT, http://cainteGrator-info.nci.nih.gov/REMBRANDT); and GSE16011 and GSE79671 databases (https://www.ncbi.nlm.nih.gov/geo/).

AUTHOR CONTRIBUTIONS

GW designed the study and performed the analysis. X-MZ and GW were the major contributors in writing the manuscript. J-YL and J-QH helped in drafting the manuscript and figures. All authors read and approved the final manuscript.

SUPPLEMENTARY MATERIAL

The Supplementary Material for this article can be found online at: https://www.frontiersin.org/articles/10.3389/fcell.2022.778286/full#supplementary-material

REFERENCES

Ahir, B. K., Engelhard, H. H., and Lakka, S. S. (2020). Tumor Development and Angiogenesis in Adult Brain Tumor: Glioblastoma. *Mol. Neurobiol.* 57 (5), 2461–2478. doi:10.1007/s12035-020-01892-8

Albini, A., Bruno, A., Noonan, D. M., and Mortara, L. (2018). Contribution to Tumor Angiogenesis from Innate Immune Cells within the Tumor Microenvironment: Implications for Immunotherapy. *Front. Immunol.* 9, 527. doi:10.3389/fimmu.2018.00527

Amulic, B., Cazalet, C., Hayes, G. L., Metzler, K. D., and Zychlinsky, A. (2012). Neutrophil Function: From Mechanisms to Disease. *Annu. Rev. Immunol.* 30, 459–489. doi:10.1146/annurev-immunol-020711-074942

Aspord, C., Leccia, M. T., Charles, J., and Plumas, J. (2014). Melanoma Hijacks Plasmacytoid Dendritic Cells to Promote its Own Progression. *Oncoimmunology* 3, e27402. doi:10.4161/onci.27402

Bazan, N. G., Reid, M. M., Flores, V. A. C., Gallo, J. E., Lewis, W., and Belayev, L. (2021). Multiprong Control of Glioblastoma Multiforme Invasiveness: Blockade of Pro-inflammatory Signaling, Anti-angiogenesis, and Homeostasis Restoration. *Cancer Metastasis Rev.* 40 (3), 643–647. doi:10.1007/s10555-021-09987-x

Blandin, A.-F., Cruz Da Silva, E., Mercier, M.-C., Glushonkov, O., Didier, P., Dedieu, S., et al. (2021). Gefitinib Induces EGFR and α5β1 Integrin Co-endocytosis in Glioblastoma Cells. *Cell. Mol. Life Sci.* 78 (6), 2949–2962. doi:10.1007/s00018-020-03686-6

Bowman, R. L., Wang, Q., Carro, A., Verhaak, R. G. W., and Squatrito, M. (2017). GlioVis Data portal for Visualization and Analysis of Brain Tumor Expression Datasets. *Neuonc* 19 (1), 139–141. doi:10.1093/neuonc/now247

Bush, N. A. O., Chang, S. M., and Berger, M. S. (2017). Current and Future Strategies for Treatment of Glioma. *Neurosurg. Rev.* 40 (1), 1–14. doi:10.1007/s10143-016-0709-8

Cao, M., Cai, J., Yuan, Y., Shi, Y., Wu, H., Liu, Q., et al. (2019). A Four-Gene Signature-Derived Risk Score for Glioblastoma: Prospects for Prognostic and Response Predictive Analyses. *Cancer Biol. Med.* 16 (3), 595–605. doi:10.20892/j.issn.2095-3941.2018.0277

Chen, M., Ba, H., Lu, C., Dai, J., and Sun, J. (2018). Glial Cell Line-Derived Neurotrophic Factor (GDNF) Promotes Angiogenesis through the Demethylation of the Fibromodulin (FMOD) Promoter in Glioblastoma. *Med. Sci. Monit.* 24, 6137–6143. doi:10.12659/msm.911669

Chen, J., Wang, H., Wang, J., Niu, W., Deng, C., and Zhou, M. (2021). LncRNA NEAT1 Enhances Glioma Progression via Regulating the miR-128-3p/ITGA5 Axis. *Mol. Neurobiol.* 58, 5163. doi:10.1007/s12035-021-02474-y

Chinot, O. L., Wick, W., Mason, W., Henriksson, R., Saran, F., Nishikawa, R., et al. (2014). Bevacizumab Plus Radiotherapy-Temozolomide for Newly Diagnosed Glioblastoma. *N. Engl. J. Med.* 370 (8), 709–722. doi:10.1056/nejmoa1308345

Cosset, E. C., Godet, J., Entz-Werlé, N., Guérin, E., Guenot, D., Froelich, S., et al. (2012). Involvement of the TGFβ Pathway in the Regulation of α5β1 Integrins by Caveolin-1 in Human Glioblastoma. *Int. J. Cancer* 131 (3), 601–611. doi:10.1002/ijc.26415

Enomoto, H., Tao, L., Eguchi, R., Sato, A., Honda, M., Kaneko, S., et al. (2017). The *In Vivo* Antitumor Effects of Type I-Interferon against Hepatocellular Carcinoma: the Suppression of Tumor Cell Growth and Angiogenesis. *Sci. Rep.* 7 (1), 12189. doi:10.1038/s41598-017-12414-3

Fei, F., Li, S., Fei, Z., and Chen, Z. (2015). The Roles of CD147 in the Progression of Gliomas. *Expert Rev. Anticancer Ther.* 15 (11), 1351–1359. doi:10.1586/14737140.2015.1092874

Friedman, J., Hastie, T., and Tibshirani, R. (2009). Glmnet: Lasso and Elastic-Net Regularized Generalized Linear Models.

Gilbert, M. R., Dignam, J. J., Armstrong, T. S., Wefel, J. S., Blumenthal, D. T., Vogelbaum, M. A., et al. (2014). A Randomized Trial of Bevacizumab for Newly Diagnosed Glioblastoma. *N. Engl. J. Med.* 370 (8), 699–708. doi:10.1056/nejmoa1308573

Gousias, K., von Ruecker, A., Voulgari, P., and Simon, M. (2013). Phenotypical Analysis, Relation to Malignancy and Prognostic Relevance of ICOS+T Regulatory and Dendritic Cells in Patients with Gliomas. *J. Neuroimmunol.* 264 (1-2), 84–90. doi:10.1016/j.jneuroim.2013.09.001

Hiplot: A Free and Comprehensive Cloud Platformfor Scientific Computation and Visualization (2021). Hiplot: A Free and Comprehensive Cloud Platform for Scientific Computation and visualization[J]. Openbiox Community. Unpublished. Available at: http://hiplot.com.cn/basic/venn.

Hong, Y. K., Chung, D. S., Joe, Y. A., Yang, Y. J., Kim, K. M., Park, Y. S., et al. (2000). Efficient Inhibition of *In Vivo* Human Malignant Glioma Growth and Angiogenesis by Interferon-Beta Treatment at Early Stage of Tumor Development. *Clin. Cancer Res.* 6 (8), 3354–3360.

Hu, J., Muller, K. A., Furnari, F. B., Cavenee, W. K., VandenBerg, S. R., and Gonias, S. L. (2015). Neutralizing the EGF Receptor in Glioblastoma Cells Stimulates Cell Migration by Activating uPAR-Initiated Cell Signaling. *Oncogene* 34 (31), 4078–4088. doi:10.1038/onc.2014.336

Jiang, P., Gu, S., Pan, D., Fu, J., Sahu, A., Hu, X., et al. (2018). Signatures of T Cell Dysfunction and Exclusion Predict Cancer Immunotherapy Response. *Nat. Med.* 24 (10), 1550–1558. doi:10.1038/s41591-018-0136-1

Kim, J., and Bae, J. S. (2016). Tumor-Associated Macrophages and Neutrophils in Tumor Microenvironment. *Mediators Inflamm.* 2016, 6058147. doi:10.1155/2016/6058147

Komori, T. (2017). The 2016 WHO Classification of Tumours of the Central Nervous System: The Major Points of Revision. *Neurol. Med. Chir.(Tokyo)* 57 (7), 301–311. doi:10.2176/nmc.ra.2017-0010

Lim, M., Xia, Y., Bettegowda, C., and Weller, M. (2018). Current State of Immunotherapy for Glioblastoma. *Nat. Rev. Clin. Oncol.* 15 (7), 422–442. doi:10.1038/s41571-018-0003-5

Loft, M. D., Sun, Y., Liu, C., Christensen, C., Huang, D., Kjaer, A., et al. (2017). Improved Positron Emission Tomography Imaging of Glioblastoma Cancer Using Novel 68Ga-labeled Peptides Targeting the Urokinase-type Plasminogen Activator Receptor (uPAR). *Amino Acids* 49 (6), 1089–1100. doi:10.1007/s00726-017-2407-4

Love, M. I., Huber, W., and Anders, S. (2014). Moderated Estimation of Fold Change and Dispersion for RNA-Seq Data with DESeq2. *Genome Biol.* 15 (12), 550. doi:10.1186/s13059-014-0550-8

Megjugorac, N. J., Young, H. A., Amrute, S. B., Olshalsky, S. L., and Fitzgerald-Bocarsly, P. (2004). Virally Stimulated Plasmacytoid Dendritic Cells Produce Chemokines and Induce Migration of T and NK Cells. *J. Leukoc. Biol.* 75 (3), 504–514. doi:10.1189/jlb.0603291

Mitchell, D., Chintala, S., and Dey, M. (2018). Plasmacytoid Dendritic Cell in Immunity and Cancer. *J. Neuroimmunol.* 322, 63–73. doi:10.1016/j.jneuroim.2018.06.012

Mondal, B., Patil, V., Shwetha, S. D., Sravani, K., Hegde, A. S., Arivazhagan, A., et al. (2017). Integrative Functional Genomic Analysis Identifies Epigenetically Regulated Fibromodulin as an Essential Gene for Glioma Cell Migration. *Oncogene* 36 (1), 71–83. doi:10.1038/onc.2016.176

Newman, A. M., Liu, C. L., Green, M. R., Gentles, A. J., Feng, W., Xu, Y., et al. (2015). Robust Enumeration of Cell Subsets from Tissue Expression Profiles. *Nat. Methods* 12 (5), 453–457. doi:10.1038/nmeth.3337

Niu, X., Sun, J., Meng, L., Fang, T., Zhang, T., Jiang, J., et al. (2020). A Five-lncRNAs Signature-Derived Risk Score Based on TCGA and CGGA for Glioblastoma: Potential Prospects for Treatment Evaluation and Prognostic Prediction. *Front. Oncol.* 10, 590352. doi:10.3389/fonc.2020.590352

Onishi, M., Ichikawa, T., Kurozumi, K., and Date, I. (2011). Angiogenesis and Invasion in Glioma. *Brain Tumor Pathol.* 28 (1), 13–24. doi:10.1007/s10014-010-0007-z

Ostrom, Q. T., Cioffi, G., Gittleman, H., Patil, N., Waite, K., Kruchko, C., et al. (2019). CBTRUS Statistical Report: Primary Brain and Other Central Nervous System Tumors Diagnosed in the United States in 2012-2016. *Neuro Oncol.* 21 (Suppl. 5), v1. doi:10.1093/neuonc/noz150

Panda, S. K., Kolbeck, R., and Sanjuan, M. A. (2017). Plasmacytoid Dendritic Cells in Autoimmunity. *Curr. Opin. Immunol.* 44, 20–25. doi:10.1016/j.coi.2016.10.006

Raghu, H., Gondi, C. S., Dinh, D. H., Gujrati, M., and Rao, J. S. (2011). Specific Knockdown of uPA/uPAR Attenuates Invasion in Glioblastoma Cells and Xenografts by Inhibition of Cleavage and Trafficking of Notch -1 Receptor. *Mol. Cancer* 10, 130. doi:10.1186/1476-4598-10-130

Raghu, H., Nalla, A. K., Gondi, C. S., Gujrati, M., Dinh, D. H., and Rao, J. S. (2012). uPA and uPAR shRNA Inhibit Angiogenesis via Enhanced Secretion of SVEGFR1 Independent of GM-CSF but Dependent on TIMP-1 in Endothelial and Glioblastoma Cells. *Mol. Oncol.* 6 (1), 33–47. doi:10.1016/j.molonc.2011.11.008

Ribatti, D., and Crivellato, E. (2009). Immune Cells and Angiogenesis. *J. Cel Mol. Med.* 13 (9a), 2822–2833. doi:10.1111/j.1582-4934.2009.00810.x

Robin, X., Turck, N., Hainard, A., Tiberti, N., Lisacek, F., Sanchez, J.-C., et al. (2011). pROC: an Open-Source Package for R and S+ to Analyze and Compare ROC Curves. *BMC Bioinformatics* 12 (1), 77. doi:10.1186/1471-2105-12-77

Rostami, N., Nikkhoo, A., Ajjoolabady, A., Azizi, G., Hojjat-Farsangi, M., Ghalamfarsa, G., et al. (2019). S1PR1 as a Novel Promising Therapeutic Target in Cancer Therapy. *Mol. Diagn. Ther.* 23 (4), 467–487. doi:10.1007/s40291-019-00401-5

Schuler, P. J., Bendszus, M., Kuehnel, S., Wagner, S., Hoffmann, T. K., Goldbrunner, R., et al. (2012). Urokinase Plasminogen Activator, uPAR, MMP-2, and MMP-9 in the C6-Glioblastoma Rat Model. *In Vivo* 26 (4), 571–576.

Simon, T., Jackson, E., and Giamas, G. (2020). Breaking through the Glioblastoma Micro-environment via Extracellular Vesicles. *Oncogene* 39 (23), 4477–4490. doi:10.1038/s41388-020-1308-2

Snell, L. M., McGaha, T. L., and Brooks, D. G. (2017). Type I Interferon in Chronic Virus Infection and Cancer. *Trends Immunol.* 38 (8), 542–557. doi:10.1016/j.it.2017.05.005

Stockmann, C., Schadendorf, D., Klose, R., and Helfrich, I. (2014). The Impact of the Immune System on Tumor: Angiogenesis and Vascular Remodeling. *Front. Oncol.* 4, 69. doi:10.3389/fonc.2014.00069

Szklarczyk, D., Gable, A. L., Nastou, K. C., Lyon, D., Kirsch, R., Pyysalo, S., et al. (2021). The STRING Database in 2021: Customizable Protein-Protein Networks, and Functional Characterization of User-Uploaded Gene/measurement Sets. *Nucleic Acids Res.* 49, D605–D612. doi:10.1093/nar/gkaa1074

Tan, A. C., Ashley, D. M., López, G. Y., Malinzak, M., Friedman, H. S., and Khasraw, M. (2020). Management of Glioblastoma: State of the Art and Future Directions. *CA Cancer J. Clin.* 70 (4), 299–312. doi:10.3322/caac.21613

Villadangos, J. A., and Young, L. (2008). Antigen-presentation Properties of Plasmacytoid Dendritic Cells. *Immunity* 29 (3), 352–361. doi:10.1016/j.immuni.2008.09.002

Waisman, A., Lukas, D., Clausen, B. E., and Yogev, N. (2017). Dendritic Cells as Gatekeepers of Tolerance. *Semin. Immunopathol.* 39 (2), 153–163. doi:10.1007/s00281-016-0583-z

Wang, Z., Gao, L., Guo, X., Feng, C., Lian, W., Deng, K., et al. (2019). Development and Validation of a Nomogram with an Autophagy-Related Gene Signature for Predicting Survival in Patients with Glioblastoma. *Aging* 11 (24), 12246–12269. doi:10.18632/aging.102566

Wu, L., Saxena, S., and Singh, R. K. (2020). Neutrophils in the Tumor Microenvironment. *Adv. Exp. Med. Biol.* 1224, 1–20. doi:10.1007/978-3-030-35723-8_1

Xu, S., Tang, L., Li, X., Fan, F., and Liu, Z. (2020). Immunotherapy for Glioma: Current Management and Future Application. *Cancer Lett.* 476, 1–12. doi:10.1016/j.canlet.2020.02.002

Yoshihara, K., Shahmoradgoli, M., Martínez, E., Vegesna, R., Kim, H., Torres-Garcia, W., et al. (2013). Inferring Tumour Purity and Stromal and Immune Cell Admixture from Expression Data. *Nat. Commun.* 4, 2612. doi:10.1038/ncomms3612

Young, N., Pearl, D. K., and Van Brocklyn, J. R. (2009). Sphingosine-1-Phosphate Regulates Glioblastoma Cell Invasiveness through the Urokinase Plasminogen

Activator System and CCN1/Cyr61. *Mol. Cancer Res.* 7 (1), 23–32. doi:10.1158/1541-7786.mcr-08-0061

Yu, G., Wang, L.-G., Han, Y., and He, Q.-Y. (2012). clusterProfiler: an R Package for Comparing Biological Themes Among Gene Clusters. *OMICS: A J. Integr. Biol.* 16 (5), 284–287. doi:10.1089/omi.2011.0118

Zhuang, T., Chelluboina, B., Ponnala, S., Velpula, K. K., Rehman, A. A., Chetty, C., et al. (2013). Involvement of Nitric Oxide Synthase in Matrix Metalloproteinase-9- And/or Urokinase Plasminogen Activator Receptor-Mediated Glioma Cell Migration. *BMC Cancer* 13, 590. doi:10.1186/1471-2407-13-590

Conflict of Interest: The authors declare that the research was conducted in the absence of any commercial or financial relationships that could be construed as a potential conflict of interest.

Publisher's Note: All claims expressed in this article are solely those of the authors and do not necessarily represent those of their affiliated organizations, or those of the publisher, the editors, and the reviewers. Any product that may be evaluated in this article, or claim that may be made by its manufacturer, is not guaranteed or endorsed by the publisher.

frontiers | Frontiers in Oncology

ORIGINAL RESEARCH
published: 19 April 2022
doi: 10.3389/fonc.2022.830688

RNA-Binding Protein COL14A1, TNS1, NUSAP1 and YWHAE Are Valid Biomarkers to Predict Peritoneal Metastasis in Gastric Cancer

Yue Jiang[1†], Fangfang Chen[2†], Xunshan Ren[3], Yu Yang[1], Jiajun Luo[1], Jingwen Yuan[1], Jingping Yuan[2] and Qiang Tong[1*]*

[1] Department of Gastrointestinal Surgery I Section, Renmin Hospital of Wuhan University, Wuhan, China, [2] Department of Pathology, Renmin Hospital of Wuhan University, Wuhan, China, [3] Department of Orthopedics, Renmin Hospital of Wuhan University, Wuhan, China

OPEN ACCESS

Edited by:
Tao Liu,
University of New South Wales, Australia

Reviewed by:
Haruhiko Sugimura,
Hamamatsu University School of Medicine, Japan
Huaichao Luo,
Sichuan Cancer Hospital, China

***Correspondence:**
Jingping Yuan
yuanjingping@whu.edu.cn
Qiang Tong
qiangtong@whu.edu.cn

[†]These authors have contributed equally to this work

Specialty section:
This article was submitted to Molecular and Cellular Oncology, a section of the journal Frontiers in Oncology

Received: *07 December 2021*
Accepted: *25 March 2022*
Published: *19 April 2022*

Citation:
Jiang Y, Chen F, Ren X, Yang Y, Luo J, Yuan J, Yuan J and Tong Q (2022) RNA-Binding Protein COL14A1, TNS1, NUSAP1 and YWHAE Are Valid Biomarkers to Predict Peritoneal Metastasis in Gastric Cancer. Front. Oncol. 12:830688. doi: 10.3389/fonc.2022.830688

Gastric cancer (GC) is the third leading cause of tumor related mortality worldwide. Peritoneal metastasis (PM) occurs in more than half of advanced GC patients, leading to poor prognosis. Therefore, the GSE62254 cohort was used to construct a signature consisting of four RNA-binding proteins (RBP) to predict the possibility of PM in GC patients. Then, ROC curves were plotted followed by calculation of AUCs, showing that the signature had a similar predictive accuracy compared with the TNM staging system. Importantly, the capability of prediction was enhanced by combining the classifier and TNM staging. In order to validate the expression of the four RBPs in GC tissues with and without PM, immunohistochemistry was further performed on samples from 108 patients. The differential expression of COL14A1, TNS1, NUSAP1 and YWHAE was in accordance with the emergence of PM. Afterwards, we produced Kaplan–Meier curves according to the signature and differential expression of the RBPs in patients. Finally, CCK-8 assays were performed to verify the effect on cell proliferation, finding that COL14A1 and TNS1 promoted cell proliferation, while NUSAP1 and YWHAE led to suppressed cell proliferation. In conclusion, the four-RBP-based signature, combined with TNM staging, has the potential to predict risk of PM in GC.

Keywords: gastric cancer, RNA-binding protein, peritoneal metastasis, prediction model, survival analysis

INTRODUCTION

Gastric cancer (GC) is one of the most common malignant tumors as well as the third leading cause of mortality all over the world (1). The incidence of GC ranks third among all malignant tumors in China, being next to lung and hepatic cancer (2). According to a global survey, there were over one million new GC cases in 2020, with 769000 estimated deaths (3). While surgery, radiotherapy, chemotherapy and biological treatment have been adopted heretofore, the 5-year overall survival rate of GC is still poor. Nearly 50% of GC patients have unspecific gastrointestinal symptoms and debilitating features are usually present at advanced stages in most cases (4). Peritoneal metastasis (PM) occurs in about 53–66% of advanced GC patients, leading to poor prognosis (5). Regrettably,

effective treatments for peritoneal metastases are still lacking due to little understanding of the underlying mechanisms.

RNA-binding proteins (RBPs) are key players in post-transcriptional events which regulate the process of tumorigenesis, and each step leading to the initiation of malignancy may involve one or more RBPs (6). Mechanisms of RBPs regulation have been identified in cancer cells, including alternative splicing, polyadenylation, stability, subcellular localization, translation and so on (7). Several studies have provided immunohistochemical evidence that RBPs are abnormally expressed in cancers relative to adjacent normal tissues, and this expression correlates with patient prognosis (8–10). Besides, RBPs also interact with different coding or non-coding RNAs, such as microRNAs (miRNAs), long non-coding RNAs (lncRNAs) and circular RNAs (circRNAs) (11).

In consideration of the enormous influence of PM on the prognosis of GC patients, prediction of the risk has recently been a research focus. In clinical practice, miRNAs, lncRNAs, circRNAs and pathological factors including TNM staging and lymph node status have been gradually used to assess GC prognosis (12). Recently, studies have revealed that RBPs were associated with the prognosis of GC patients (13–15). Therefore, we proposed to recognize several RBPs as potential biomarkers based on transcriptome analysis to predict whether peritoneal metastasis would occur on GC patients. As a result, a 4-RBP-based classifier was constructed by use of Lasso Logistics, which could optimize the predictivity in combination with the current TNM staging system. Our results demonstrated that the 4-RBP-based classifier could be used as a reliable prognostic predictor of peritoneal metastasis in GC patients.

MATERIALS AND METHODS

Data Acquisition

Transcriptome profiling data of tumor tissues in 300 GC samples with and without peritoneal metastasis were obtained from the GSE62254 cohort. For the purpose of analyzing the correlation between gene expression signatures and the occurrence of PM in GC patients, we filtered out 79 samples whose first sites of recurrence were not peritoneal seeding or ascites. Finally, 221 patients were selected and divided into training set (n = 147) and validating set (n = 74) randomly at a 2:1 ratio for further analysis. A total of 846 genes coding for RBPs were summarized from the published literature.

Data Processing and Risk Score Calculation

737 RBPs examined in the GSE62254 cohort were subjected to Univariate Logistics analysis to select RBPs relevant to the occurrence of PM in GC patients. We selected the top 100 RBPs into Lasso Logistics analysis to acquire the coefficients. Then, four significantly correlated RBPs weighted by their coefficients were recognized to establish the prediction signature. After comparison and combination with TNM staging, a risk score formula for risk of PD in GC was constructed and demonstrated by a nomogram.

Pathway Enrichment Analysis

DAVID (version 6.7) (https://david-d.ncifcrf.gov/), an online bioinformatics analysis tool was used to perform the gene-Gene Ontology (GO) term and the Kyoto Encyclopedia of Genes and Genomes (KEGG) enrichment analysis. Metascape (https://metascape.org/gp/index.html#/main/step1) offered complementary annotation.

Patients and Tissue Samples

We went through the pathology database of Renmin Hospital of Wuhan University for GC patients with PM, finding 36 cases in the period from 2014 to 2021. Then we randomly chose 72 GC patients without PM in the year of 2016 as the control group. As a result, a total of 108 formalin-fixed, paraffin-embedded GC tissue samples were obtained. All the patients underwent surgical treatment at Renmin Hospital of Wuhan University and there were none previous chemotherapies, radiotherapies, or other treatments before surgery on these patients. The study was approved by the Ethics Committee of Renmin Hospital of Wuhan University.

Immunohistochemical (IHC)

The paraffin tissues were cut into 4 um-thick sections, dried, dewaxed in xylene, and dehydrated in ascending series of ethanol. Antigen retrieval was conducted by microwave heating with citrate buffer (pH 6.0) for 20 min. Subsequently, paraffin sections were rinsed with PBS (3×5 min) and then blocked with 3% hydrogen peroxide at room temperature for endogenous peroxidase ablation for 25 min. Then the samples were exposed to Bovine Serum Albumin (BSA) at room temperature for 30 min to decrease nonspecific antibody binding after rinsing in PBS. The tissue sections were incubated overnight at 4°C with the primary antibody (anti-COL14A1, 1:200, ThermoFisher, America; anti-TNS1, 1:200, Abcam, British; anti-NUSAP1, 1:100, Abcam, British; anti-YWHAE, 1:500, Abcam, British);. After rinsing in PBS, the tissue sections were incubated with horseradish peroxidase-labeled anti-rabbit antibodies at room temperature for 30 min. Then, the tissue sections were rinsed with PBS for 4 times and then dripped with freshly prepared 3,3-diaminobenzidine (DAB). Microscopically, the staining was terminated when the tissue sections were brown-yellow or brown. Subsequently, all the tissue sections were restrained with hematoxylin for about 3 min. Finally, the slices were dehydrated with ethanol and toluene and then sealed with neutral gum. PBS was used to replace the primary antibody as a negative control. The slides were viewed *via* Olympus BX53 (Tokyo, Japan) microscope. IHC staining was evaluated independently by two pathologists under the double-blind condition. The staining intensity was classified as four grades as follows: 0 (no staining), 1 (light yellow), 2 (brown-yellow), and 3 (dark brown). The percentage of positive cells was classified as five grades as follows: 0 (0%), 1 (≤30%), 2 (31-50%), 3 (51-80%), and 4 (≥80%). Five most representative fields of high magnification (400x) were selected to calculate the final score. The final immunohistochemical score was the product of staining intensity and extent, theoretically from 0 to 12. Scores

less than 4 were defined as low expression, and scores greater than or equal to 4 were described as high expression.

Cell Lines

AGS cell line and MGC-803 cell line were bought from American Type Culture Collection (ATCC, Manassas, USA). AGS cell line was maintained in Dulbecco's Modified Eagle Medium (DMEM)/F-12 (Servicebio, Wuhan, China) while MGC-803 cell line was maintained in DMEM-H (Servicebio, Wuhan, China), supplemented with 10% fetal bovine serum (ThermoFisher, America) and 1% antibiotics (Servicebio, Wuhan, China). Cells were maintained in a 37° C incubator with 5% CO2. All cell lines tested negative for mycoplasma.

Cell Transfection

The siRNA vectors against COL14A1 or TNS1 were utilized for knockdown of COL14A1 or TNS1 with scrambled siRNA (siNC) as negative control. Sequences of the siRNAs were as follows: siCOL14A1-1: 5′-GUGGUGGUAGAUGGAACUGUATT-3′; siCOL14A1-2: 5′-CUCAGGUUACCUGAUCCUUUATT-3′; siTNS1-1: 5′-CAGGUCUUACUCACCUUAUGATT-3′; siTNS1-2: 5′-GCAACUACCUGCUGUUCAATT-3′. For upregulation of NUSAP1 or YWHAE, the full length of NUSAP1 or YWHAE was inserted into pcDNA3.1 vectors (Invitrogen) and the empty plasmids were served as negative control.

Cells were plated in 6-well plates with DMEM/F-12 medium supplemented with 10% medium FBS for 24 h before transfection. Transfections of siRNAs and indicated plasmids were both performed using Lipofectamine 2000 (ThermoFisher, America) according to the manufacturer's instruction.

Quantitative Real-Time PCR (qRT-PCR)

Total RNA from cells was extracted by TRIzol reagent (ThermoFisher, America) following the supplier's instructions. Reverse transcription was conducted with the First Strand cDNA Synthesis Kit (Servicebio, Wuhan, China). PCR was implemented with SYBR Green qPCR Master Mix (Servicebio, Wuhan, China). The conditions for qRT-PCR were as follows: 95°C for 3 min, followed by 40 cycles of 10 s at 95°C, 10 s at 60°C, and 15 s at 70°C, followed by heating from 65°C to 95°C.

The sequences of main primers were as follows: COL14A1 (forward): 5′-AGTGGGTGAGAAGGCAATGA-3′, COL14A1 (reverse): 5′-CTCTCAGGCCTGGAAGTTCA-3′; TNS1 (forward):5'-TCAAGTGGAAGAACTTGTTTGCTT-3', TNS1 (reverse): 5′-CACGACAATATAGTGGAGGCACA-3′; NUSAP1 (forward): 5′-AGCCCATCAATAAGGGAGGG-3′, NUSAP1 (reverse): 5′-ACCTGACACCCGTTTTAGCTG-3′; YWHAE (forward): 5′-GCTGGATCCATGGATGATCGAGAGGATCTG-3′, YWHAE (reverse): 5′-GCTGAATTCTCACTGATTTTCGTCTTCCAC-3′; GAPDH (forward): 5′-CACCATTGGCAATGAGCGGTTC-3′, GAPDH (reverse): 5′-AGGTCTTTGCGGATGTCCACGT-3′; GAPDH was utilized as an endogenous control.

Cell Proliferation Assays

For Cell Counting Kit-8 (CCK-8) assay, transfected cells were inoculated at a density of 2 × 100 cells/well into 96-well plates and cultivated for 0, 24, 48 and 72 hours. After different incubation times, each well was added with 10 μL of CCK-8 reagent (Servicebio, Wuhan, China) and cultured for another hour. Then, the absorbance at 450 nm was recorded with a standard microplate reader (EnSight, Perkin Elmer, America).

Statistical Analysis

We used Chi-squared test and Fisher's exact test to measure both the difference between training and validating sets, and the difference between GC patients with and without PM. Univariable Logistics, Multivariate Logistics and Lasso Logistics analysis were performed using the R program. The Kaplan–Meier survival curves were drawn to demonstrate the relationship between the risk score and OS. The log-rank test was conducted to test the significance of all the Kaplan–Meier survival curves. ROC analysis was performed to measure prognostic accuracy. T-test was performed for statistical analyses in RT-qPCR and CCK-8 assay. All statistical tests were two-sided, and $P < 0.05$ was considered statistically significant. All analyses were performed in SPSS version 28.0.0 (SPSS Inc., Chicago, IL, United States) or R version 4.0.2 with the following packages: "heatmap", "glmnet", "gplot2" and "nsROC".

RESULTS

Data Source and Processing

Originally, we obtained 300 GC samples from the GSE62254 cohort. Then, 79 samples whose first sites of recurrence were not peritoneal seeding or ascites were excluded. Afterwards, a list of 846 coding genes known or predicted as RBPs were matched with the 20174 genes examined in the GSE62254 cohort (16). Finally, 737 RBPs were subjected to a Univariate Logistics analysis and the top 100 RBPs ranked according to p-value were retained for further study. The clinical characters of GC patients were downloaded from the GSE62254 cohort. Then we divided the cases into a training set (n = 147) and a validating set (n = 74) at a 2:1 ratio randomly. No significant differences were seen between the two sets in gender, age, pathological stage, Lauren's classification or lymphnode metastasis (**Table 1**). We eventually identified four RBPs strongly associated with the occurrence of PM in GC patients by Lasso Logistics analysis in the training set (**Figure 1**); chosen genes including Collagen Type XIV Alpha 1 Chain (COL14A1), Tensin 1 (TNS1), Nucleolar and Spindle Associated Protein 1 (NUSAP1) and Tyrosine 3-Monooxygenase/Tryptophan 5-Monooxygenase (YWHAE). Among the four genes, increased expression of COL14A1 and TNS1 was related to a higher risk of PM. Conversely, increased expression of NUSAP1 and YWHAE was associated with a lower risk of PM.

Establishment and Validation of a 4-RBP-Based Classifier to Predict the Risk for Peritoneal Metastasis in Gastric Cancer

The heatmaps revealed that COL14A1 and TNS1 were highly expressed in GC patients with PM in the training set, while NUSAP1 and YWHAE were highly expressed in the cases without PM (**Figure 2A**). Consistent results were observed in the validating set (**Figure 2B**). To assess the ability of the 4-RBP-based classifier to forecast the risk of PM in GC patients, we

TABLE 1 | Clinical features of GC patients in the training and validating sets.

Features	Training set (n=147)	Validating set (n=74)	Pearson $\chi 2$	P
Gender				
Male	96	44	0.725	0.395
Female	51	30		
Age				
<=65	64	33	0.022	0.881
>65	83	41		
Pathological Stage				
I+II	64	33	0.022	0.881
III+IV	83	41		
Lymphnode Metastasis				
Positive	92	54	1.627	0.202
Negative	42	16		
Lauren's Classification				
Intestinal	65	37	0.662	0.416
Diffuse & Mixed	82	37		

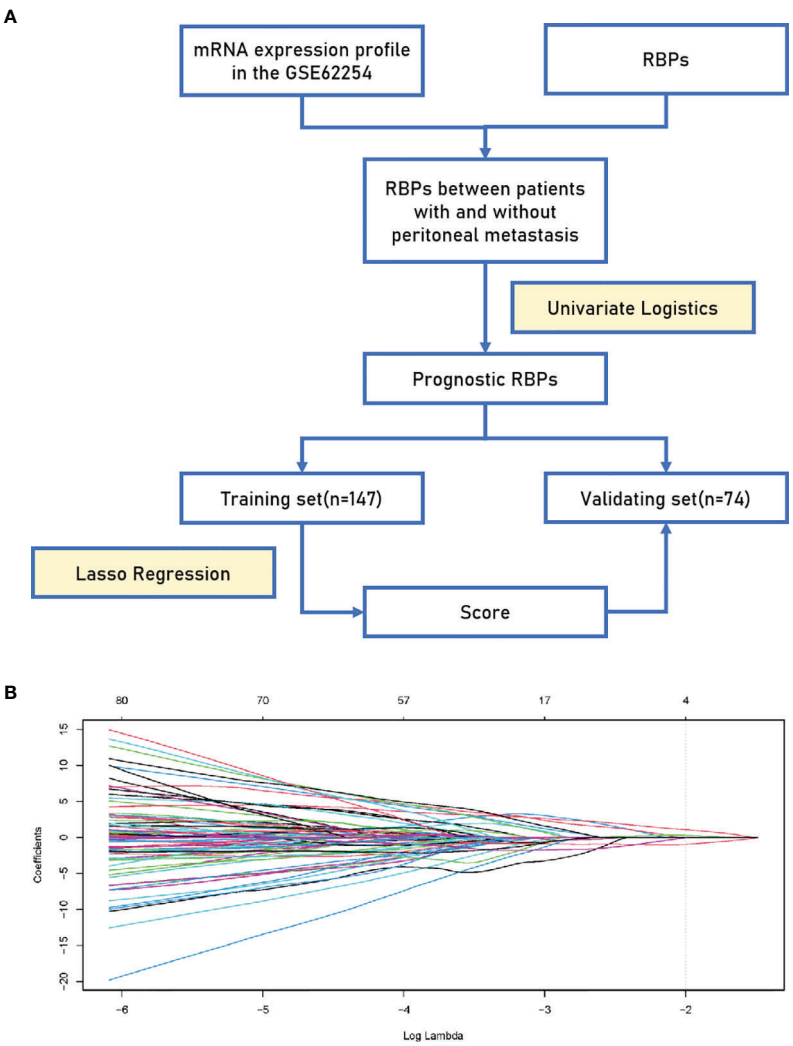

FIGURE 1 | Establishment of the 4-RBP-based signature. **(A)** A flowchart showing the process of constructing the RBP-based signature to predict the possibility of peritoneal metastasis in gastric cancer. **(B)** LASSO coefficient profiles of the 100 gastric-cancer-associated RBPs. The vertical line represents the chosen Lambda value.

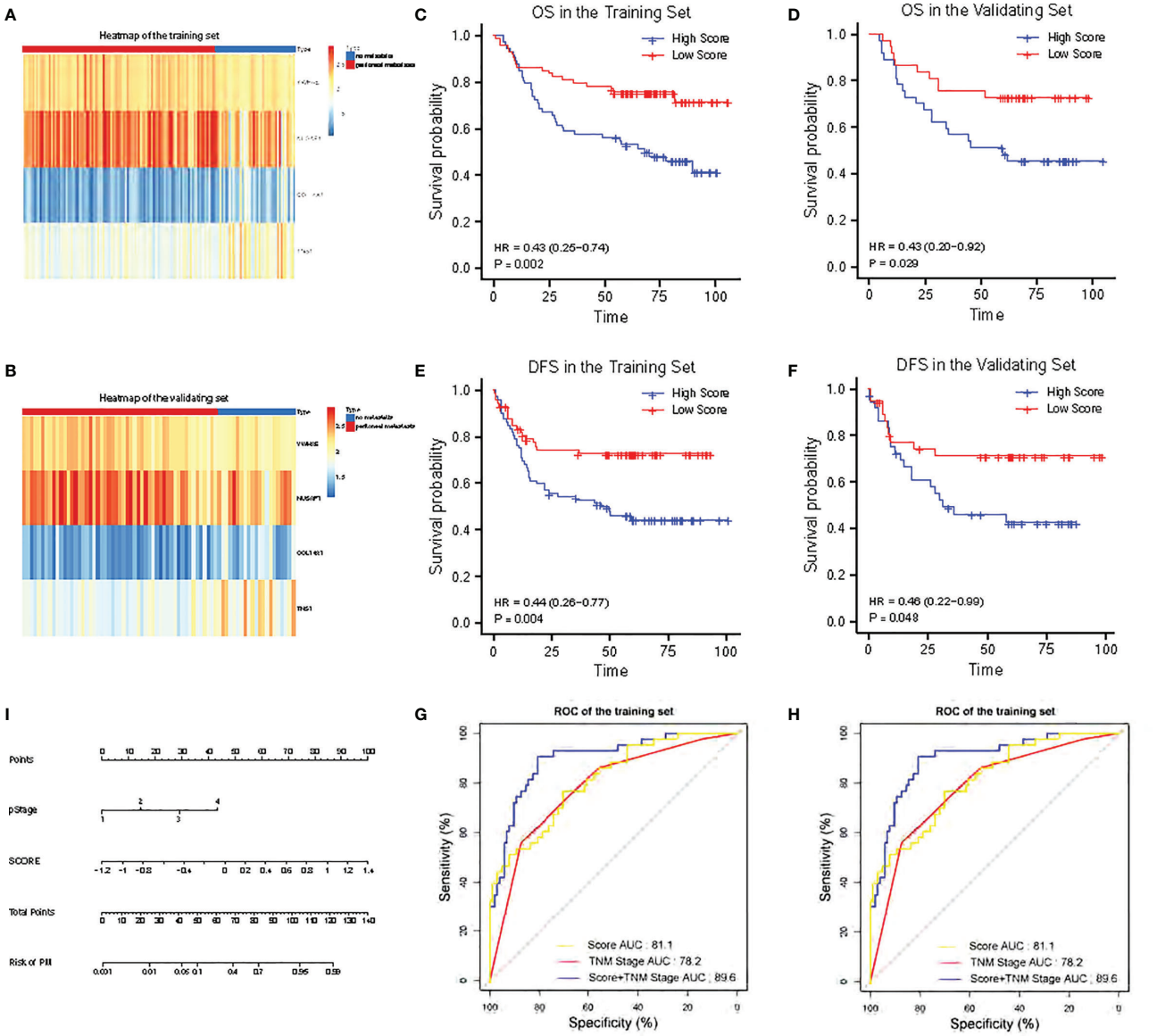

FIGURE 2 | Validation of the 4-RBP-based signature in the training set and the validating set. **(A, B)** The heatmap of the four RBPs expression profiles. **(C, D)** Kaplan–Meier analysis for overall survival (OS) of GC patients based on the risk stratification. **(E, F)** Kaplan–Meier analysis for disease-free survival (DFS) of GC patients based on the risk stratification. **(G, H)** Receiver operating characteristic (ROC) analysis for the risk of PM including the risk score, TNM stage and combination of the two. **(I)** Nomogram to predict the risk of PM in GC.

developed a risk score according to the coefficients of the four RBPs in Lasso Logistics: Risk Score = (1.08004578 * expression value of COL14A1) + (0.31114396 * expression value of TNS1) - (0.95036402 * expression value of NUSAP1) - (0.02147674 * expression value of YWHAE). The risk score formula was used to calculate the risk score in the training set, and the cases were divided into high-risk and low-risk groups owing to the cutoff of the median risk score. Kaplan–Meier curves showed that patients in the high-risk group had shorter overall survival than those in the low-risk group (p = 0.002) (**Figure 2C**); a similar result was confirmed in the validating set (p = 0.029) (**Figure 2D**). In addition, the Kaplan–Meier curves of DFS of the two sets (p = 0.004 and 0.048, respectively) were in agreement with previous results (**Figures 2E, F**).

Prognostic Value of the RBP-Based Classifier for Prediction of the Risk for Peritoneal Metastasis in Gastric Cancer

The 4-RBP-based signature, gender, and pathological stage were significantly related to peritoneal metastasis in the univariate logistics analysis. After the multivariate logistics regression analysis of the abovementioned factors, the 4-RBP-based

signature and pathological stage were retained to be dependable factors for peritoneal metastasis in the training set. Except for gender, similar results were observed in the validating set (**Table 2**). Our result showed that the 4-RBP-based signature was an independent prognostic factor for peritoneal metastasis in gastric cancer in two sets. ROC curves were then plotted to appraise the competence of the 4-RBP-based signature to successfully predict the risk of PM in GC. The AUCs, in the training set and validating set (0.811 and 0.786, respectively), showed that the RBP-based classifier had similar predictive accuracy compared with the TNM staging (AUCs were 0.782 and 0.821 respectively) (**Figures 2G, H**). However, when we combined the RBP-based risk score and TNM staging to predict the risk of PM, the predictive capability was robustly enhanced. The AUC values of this built-up prediction model were 0.896 and 0.884 respectively in the training and validating set, suggesting better predictive accuracy. Whereafter, the 4-RBP-based risk score and TNM staging were used to structure a nomogram for predicting the risk of PM in GC patients (**Figure 2I**).

Pathway Enrichment Analysis of Top 100 Correlated RBPs

To explore the possible effect of the related genes on GC, DAVID and Metascape were used to perform function enrichment analysis. The results of DAVID revealed that the top 100 related genes were primarily enriched in mRNA splicing and RNA processing in biological processes (BP) (**Figure 3A**). In assessment of cell components (CC), the genes were mainly enriched in nucleolus and nucleoplasm (**Figure 3B**). While for molecular function (MF) and KEGG, the genes were generally enriched in poly(A) RNA binding (**Figure 3C**). The results of Metascape showed that the correlated genes mainly enriched in ribonucleoprotein complex biogenesis, mRNA metabolic process, translation, Nop56p-associated pre-rRNA complex, ribonucleoprotein complex assembly and so on, suggesting that these pathways were correlative with the PM of GC with (**Figures 3D, E**).

Expression and Predictive Importance of the Four RBPs in Clinical Samples

We obtained 36 peritoneal metastatic samples of GC and 72 samples without PM. There was no significant difference between the two groups in gender, age, lymph node metastasis, HER-2, Ki67 (%), Lauren's classification or lymphatic invasion assessed by IHC staining in 108 GC patients, 36 of which with PM (**Table 3**). However, we found that COL14A1 and TNS1 were over-expressed in peritoneal metastatic lesions compared with primary tumor tissues (**Figures 4A–D**); whereas conversely, NUSAP1 and YWHAE were over-expressed in primary tumor tissues compared with peritoneal metastatic lesions (**Figures 4E–H**), which is in accordance with our findings in the bioinformatic analysis above. Kaplan–Meier curves were separately drawn due to differential expression of the four RBPs in the GC patients (**Figures 4I–L**). It revealed that patients with a high expression of COL14A1 had shorter overall survival than those with low expression ($p = 0.047$), while there was no significance in the graph divided by the expression of TNS1, NUSAP1 and YWHAE ($p = 0.855$, 0.255 and 0.053, respectively). Nevertheless, according to the Kaplan–Meier curves, patients with high expression of NUSAP1 and YWHAE tended to have longer overall survival compared to those with low expression, which was consistent with our previous findings. Later, the patients were divided into high- score and low- score groups according to their 4-RBP-based signature. Kaplan–Meier curves further revealed that patients in the high-score group had shorter overall survival than those in the low-score group ($p = 0.02$) (**Figure 4M**).

Effects of the Four RBPs in Gastric Cancer *In Vitro*

To discover the function of COL14A1 and TNS1 in gastric cancer cells directly, we performed siRNA knockdown in human AGS cell line with two different siRNA sequences. Forty-eight hours after transfecting siRNA into the cancer cells, a drastic drop in the expression level of COL14A1 and TNS1 was assessed by qRT-PCR (**Figures 5A, C**). Then we measured cell proliferation by conducting CCK-8 assays. Results showed evident decrease of proliferation in AGS cells after knockdown of COL14A1 and TNS1 (**Figures 5B, D**). Subsequently, similar experiments of NUSAP1 and YWHAE were carried out with an overexpression plasmid, producing consistent outcomes (**Figures 5E–H**). Finally, repeated experiments were conducted in the MGC-803 cell line and accordant results were achieved (**Figures 5I–P**).

TABLE 2 | Univariate and multivariate logistics analysis of the 4-RBP-based signature with peritoneal metastasis in the training set and the validating set.

Features	Univariate Logistics		Multivariate Logistics	
	HR (95% CI)	P	HR (95% CI)	P
Traning set				
Age (>65 vs. <=65)	1.786 (0.865, 3.688)	0.122	0.669 (0.230, 1.942)	0.459
Gender (Male vs. Female)	0.951 (0.915, 0.989)	**0.003**	0.989 (0.949, 1.030)	0.585
Pathological stage (I+II vs. III+IV)	3.743 (2.249, 6.231)	**<0.001**	4.169 (2.133, 8.148)	**<0.001**
4-RBP-based signature (High risk vs. Low risk)	51.419 (10.719, 246.657)	**<0.001**	37.604 (7.233, 195.503)	**<0.001**
Validating set				
Age (>65 vs. <=65)	1.139 (0.411, 3.156)	0.798	0.588 (0.138, 2.498)	0.472
Gender (Male vs. Female)	0.990 (0.952, 1.030)	0.554	0.992 (0.932, 1.055)	0.788
Pathological stage (I+II vs. III+IV)	4.855 (2.217, 10.633)	**<0.001**	4.658 (1.888, 11.488)	**<0.001**
4-RBP-based signature (High risk vs. Low risk)	16.119 (3.706, 70.105)	**<0.001**	14.411 (2.118, 98.044)	**0.006**

HR, hazard ratio; CI, confidence interval.

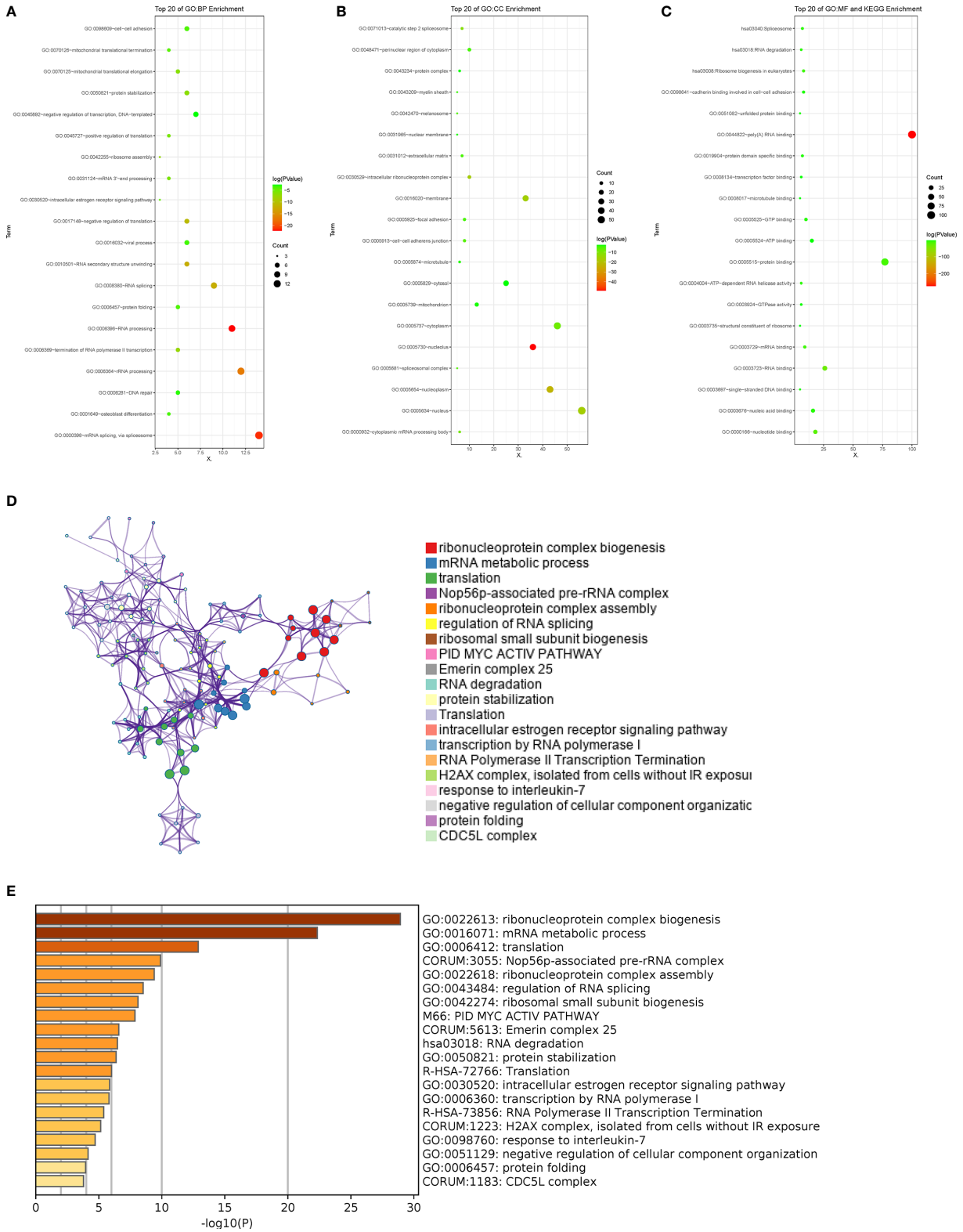

FIGURE 3 | Pathway enrichment analysis of the related RBPs. **(A-C)** GO term and KEGG enrichment analysis performed by DAVID in BP, CC, MF and KEGG. **(D, E)** Pathways associated with the related RBPs were enriched by Metascape.

TABLE 3 | Clinical features of GC patients in the non-metastasis and peritoneal metastatic sets.

Features	Non-Metastasis (n=72)	Peritoneal Metastasis (n=36)	Pearson χ^2	P
Gender				
Male	36	20	0.297	0.586
Female	36	16		
Age				
<=65	34	19	0.296	0.586
>65	38	17		
Differentiation				
Medium & High	28	17	0.686	0.408
Low	44	19		
Lymphnode Metastasis				
Positive	47	18	2.338	0.126
Negative	25	18		
Lauren's Classification				
Intestinal	35	16	0.167	0.683
Diffuse & Mixed	37	20		

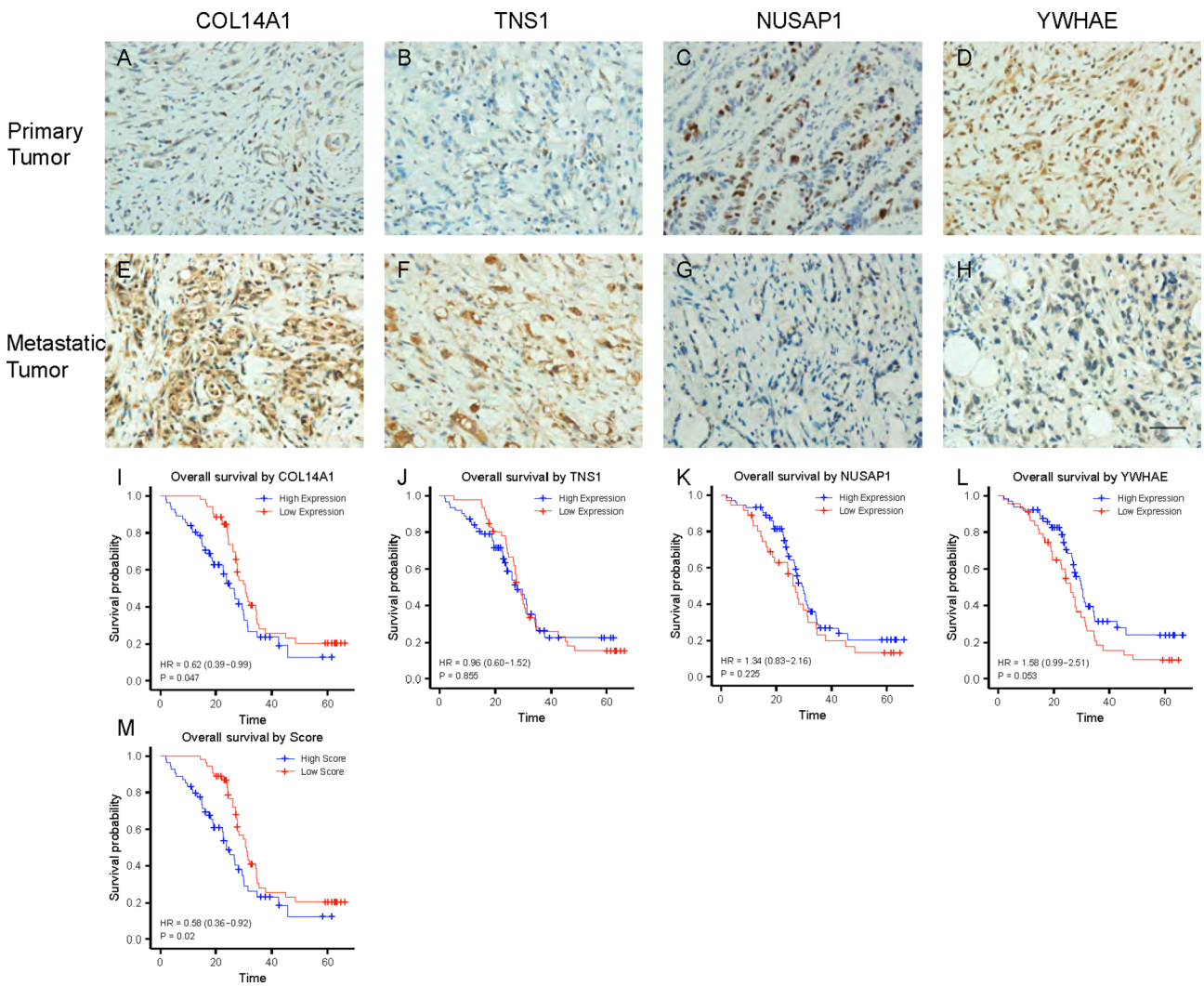

FIGURE 4 | Expression and validation of the 4 RBPs in clinical samples. **(A–D)** IHC staining of COL14A1, TNS1, NUSAP1 and YWHAE in primary GC lesions. **(E–H)** IHC staining of COL14A1, TNS1, NUSAP1 and YWHAE in peritoneal metastasis lesions. Scale bar 1000μm. **(I–L)** Kaplan–Meier analysis for overall survival (OS) of GC patients based on different expression of COL14A1, TNS1, NUSAP1 and YWHAE. **(M)** Kaplan–Meier analysis for OS based on diverse scores.

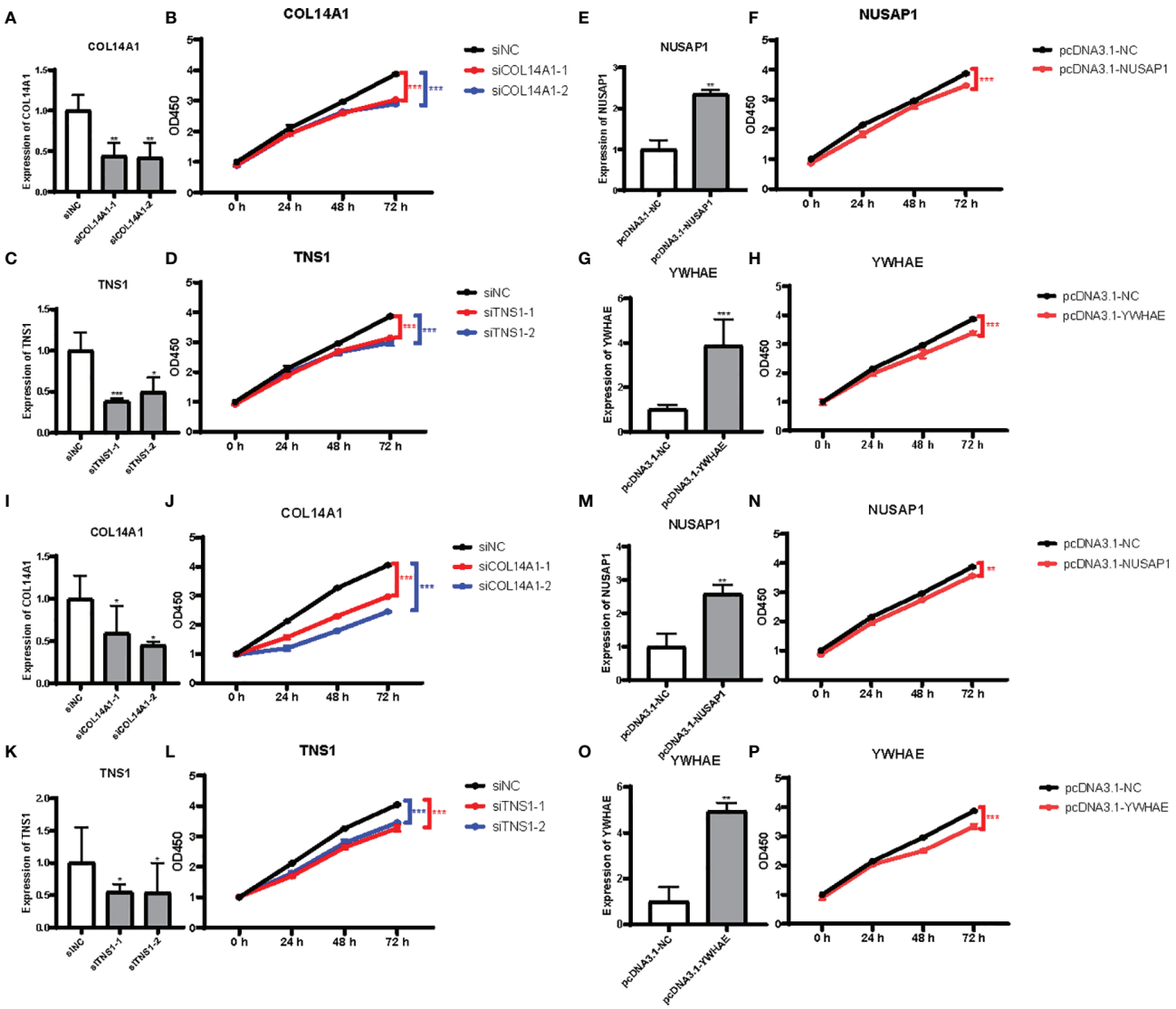

FIGURE 5 | Effects of the 4 RBPs on GC cells *in vitro*. **(A–D)** Verification of knockdown of COL14A1 and TNS1, upregulation of NUSAP1 and YWHAE in AGS cell line. **(E–H)** Results of CCK-8 assays after transfection for 48 hours. **(I–P)** The same assays as aforementioned in MGC-803 cell line (N = 3). Data are presented as the mean ± SD values. *P versus < 0.05, **P versus < 0.01, ***P versus < 0.001.

DISCUSSION

Mutations and alterations in RBP expression levels, which have been observed in many tumor tissues, are known to impact large sets of genes and contribute to tumor initiation and growth (17). Increasing literature has demonstrated that RBPs are of vital importance in the initiation, development, and recurrence of many tumors. For example, the RNA-binding protein NONO promotes breast cancer proliferation by post-transcriptional regulation of SKP2 and E2F8 (18). RBPs also play a vital role in the initiation of GC. It was reported that RBM5 downregulation was involved in GC progression, behaving as a tumor suppressor gene in GC (19). RBPs have the potential to be used as novel biomarkers as well. Musashi1 was reported to affect medulloblastoma growth *via* a network of cancer-related genes and was an indicator of poor prognosis (20). As a result, RBPs can regulate the biology of cancer and apparently possess potential as novel biomarkers.

Various models to predict the occurrence of GC have been created, including miRNA-based signatures, lncRNA-based monographs, even mixed-RNA-based classifiers (21–23). Each of them performs well at predicting the overall survival of GC. However, no RBP-based classifier for predicting the risk of PM in GC has been established yet. RBPs are a subset of molecules exhibiting different roles in regulating progression and development of malignancies. Taking the limited capability of a single RBP in prognostic prediction, we constructed a predictive model based on mRNA expression of four

RBPs by univariate Cox regression and Lasso Logistics analysis. Patients were divided into two categories based on their median-risk score. After sample analysis, it turned out that high-risk patients have a greater possibility of PM than low-risk patients, suggesting that the signature had a robust ability for prediction of PM in GC patients. The 4-RBP-based score (AUCs being 81.1 and 78.6) presented a similar capability in forecasting PM risk as TNM staging (AUCs being 78.2 and 82.1) both in the training set and the validating set. Afterwards, we combined the 4-RBP-based signature together with TNM staging to evaluate prognosis on account of the extensive application of TNM staging in the clinic. It revealed that the combinative model (AUCs being 89.6 and 88.4) was more accurate than either the 4-RBP-based score or the TNM staging model employed separately. Therefore, we plotted a nomogram for practical application.

Four prognosis-related RBPs were selected to build the classifier, including COL14A1, TNS1, NUSAP1 and YWHAE. COL14A1 has been reported to exhibit a high mutation prevalence and an unexpectedly higher incidence of nonsynonymous mutations in GC, resulting in poor outcomes (24). There have also been studies demonstrating that downregulation of NUSAP1 suppresses cell proliferation, migration, and invasion *via* inhibition of the mTORC1 signaling pathway in gastric cancer (25). In addition, YWHAE silencing induces cell proliferation, invasion and migration through the upregulation of CDC25B and MYC in gastric cancer cells (26). However, functions of TNS1 in GC have not been explored yet. These articles provide evidence that support our model's potential to assess the risk of PM in GC.

To verify the capacity of our 4-RBP-based signature, we brought 108 GC patients into our research, 36 of which were diagnosed with PM. IHC staining revealed that COL14A1 and TNS1 were over-expressed in peritoneal metastatic lesions relative to primary tumor tissues. On the contrary, NUSAP1 and YWHAE were over-expressed in primary tumor tissues compared to the peritoneal metastatic lesions, which was in accordance with our findings from bioinformatic analysis. Afterwards, the patients were divided into high- and low-score groups using the 4-RBP-based model. Kaplan–Meier curves revealed that patients in the high- score group had shorter overall survival than those in the low- score group ($p = 0.011$). Furthermore, we performed CCK-8 assays in AGS cells after knockdown of COL14A1, TNS1 and overexpression of NUSAP1, YWHAE. The results all showed decrease of proliferation.

In order to explore the biological function of the 4-RBP signature, we performed pathway enrichment analysis. Our results showed that those genes relevant to risk score were mainly enriched in cellular component organization or biogenesis, metabolic process, and positive or negative regulation of biological process, etc. Interestingly, we compared pathways predicted with annotations of these four RBPs in GeneCards6 and found that COL14A1 played an adhesive role by integrating collagen bundles, probably associated with the surface of interstitial collagen fibrils *via* COL1. Moreover, the COL2 domain may then serve as a rigid arm which sticks out from the fibril and protrudes a large N-terminal globular domain into the extracellular space, where it might interact with other matrix molecules or cell surface receptors. There was also a study characterizing the interaction of gastric cancer with peritoneal fibrosis which determined that TGF-b1 plays a key role in induction of peritoneal fibrosis, resulting from collagen formation and deposition, which in turn affected gastric cancer adhesion and metastasis *in vitro* and *in vivo* (27). It was also reported that TNS1-silenced fibroblasts exhibited a strongly reduced capacity to contract collagen gels (28), probably leading to some effects on PM of GC. Furthermore, it has been reported not long ago that YWHAE silencing induced cell proliferation, invasion, and migration through the upregulation of CDC25B and MYC in gastric cancer cells in accordance with our conclusion above. However, NUSAP1 was demonstrated to facilitate cell proliferation, migration, and invasion *via* inhibition of the mTORC1 signaling pathway in gastric cancer, which was contrary to our results (25). So far, we have found no reasonable explanation for the exact mechanisms of these RBPs, indicating that more research is required to investigate their specific roles in PM of GC.

CONCLUSION

In general, we identified four RBPs associated with risk of PM of GC. We then constructed a 4-RBP-based classifier to help predict the prognosis, ultimately providing a tremendous help in clinical decisions. Our results showed that this classifier can successfully categorize patients into high-risk and low-risk groups with large differences and promote the predictive ability of the current TNM staging system. Nevertheless, large-scale, multi-center, and prospective studies are necessary to confirm our results before the 4-RBP-based signature is applied in the clinic.

DATA AVAILABILITY STATEMENT

The datasets presented in this study can be found in online repositories. The names of the repository/repositories and accession number(s) can be found in the article/**Supplementary Material**.

ETHICS STATEMENT

The studies involving human participants were reviewed and approved by the Ethics Committee of Renmin Hospital of Wuhan University. Written informed consent for participation was not required for this study in accordance with the national legislation and the institutional requirements.

AUTHOR CONTRIBUTIONS

YJ was responsible for designing the protocol, writing the protocol and report, conducting the search, screening potentially eligible studies, extracting and analyzing data, interpreting results, updating reference lists, and creating the tables. FC was responsible for designing the protocol and screening potentially eligible studies. She contributed to writing the report, extracting and analyzing data, interpreting results. XR contributed to data extraction and provided

feedback on the report. YY, JL, and JWY contributed to arbitrating potentially eligible studies, extracting and analyzing data and interpreting results. JPY and QT provided feedback on the report. All authors contributed to the article and approved the submitted version.

FUNDING

This work was supported by the National Natural Science Foundation of China (No. 81172186) (QT), by the Natural Science Foundation of Hubei Province (No. 2018CFB504) (QT), and by the Guidance Foundation of Renmin Hospital of Wuhan University (No. RMYD2018M67) (QT).

SUPPLEMENTARY MATERIAL

The Supplementary Material for this article can be found online at: https://www.frontiersin.org/articles/10.3389/fonc.2022.830688/full#supplementary-material

REFERENCES

1. Bray F, Ferlay J, Soerjomataram I, Siegel L, Torre A, Jemal A, et al. Global Cancer Statistics 2018: GLOBOCAN Estimates of Incidence and Mortality Worldwide for 36 Cancers in 185 Countries. *CA Cancer J Clin* (2018) 68 (6):394–424. doi: 10.3322/caac.21492
2. Chen W, Zheng R, Baade D, Zhang S, Zeng H, Bray F, et al. Cancer Statistics in China, 2015. *CA Cancer J Clin* (2016) 66(2):115–32. doi: 10.3322/caac.21338
3. Sung H, Ferlay J, Siegel L, Laversanne M, Soerjomataram I, Jemal A, et al. Global Cancer Statistics 2020: GLOBOCAN Estimates of Incidence and Mortality Worldwide for 36 Cancers in 185 Countries. *CA Cancer J Clin* (2021) 71(3):209–49. doi: 10.3322/caac.21660
4. Herrero R, González P, Markowitz L. Present Status of Human Papillomavirus Vaccine Development and Implementation. *Lancet Oncol* (2015) 16(5):e206–16. doi: 10.1016/S1470-2045(14)70481-4
5. Dong D, Tang L , Li Z , Fang M , Gao J , Shan X, et al. Development and Validation of an Individualized Nomogram to Identify Occult Peritoneal Metastasis in Patients With Advanced Gastric Cancer. *Ann Oncol* (2019) 30 (3):431–8. doi: 10.1093/annonc/mdz001
6. Wu Y, Liu Y , He A , Guan B, He S, Zhang C, et al. Identification of the Six-RNA-Binding Protein Signature for Prognosis Prediction in Bladder Cancer. *Front Genet* (2020) 11:992. doi: 10.3389/fgene.2020.00992
7. Pereira B, Billaud M, Almeida R. RNA-Binding Proteins in Cancer: Old Players and New Actors. *Trends Cancer* (2017) 3(7):506–28. doi: 10.1016/j.trecan.2017.05.003
8. Velasco X, Kosti A, Guardia A, Santos C, Tegge A, Qiao M, et al. Antagonism Between the RNA-Binding Protein Musashi1 and miR-137 and Its Potential Impact on Neurogenesis and Glioblastoma Development. *RNA (New York N Y)* (2019) 25(7):768–82. doi: 10.1261/rna.069211.118
9. Busà R, Paronetto P, Farini D, Pierantozzi E, Botti F, Angelini F, et al. The RNA-Binding Protein Sam68 Contributes to Proliferation and Survival of Human Prostate Cancer Cells. *Oncogene* (2007) 26(30):4372–82. doi: 10.1038/sj.onc.1210224
10. Liang G, Meng W, Huang X, Zhu W, Yin C, Wang C, et al. miR-196b-5p-Mediated Downregulation of TSPAN12 and GATA6 Promotes Tumor Progression in Non-Small Cell Lung Cancer. *Proc Natl Acad Sci USA* (2020) 117(8):4347–57. doi: 10.1073/pnas.1917531117
11. Hudson W, Ortlund E. The Structure, Function and Evolution of Proteins That Bind DNA and RNA. *Nat Rev Mol Cell Biol* (2014) 15(11):749–60. doi: 10.1038/nrm3884
12. Serra O, Galán M, Ginesta M, Calvo M, Sala N, Salazar R. Comparison and Applicability of Molecular Classifications for Gastric Cancer. *Cancer Treat Rev* (2019) 77:29–34. doi: 10.1016/j.ctrv.2019.05.005
13. Hu C, Liu Y, Zhang H, Huang G. The RNA-Binding Protein PCBP2 Facilitates Gastric Carcinoma Growth by Targeting miR-34a. *Biochem Biophys Res Commun* (2014) 448(4):437–42. doi: 10.1016/j.bbrc.2014.04.124
14. Wang X, Hu H, Liu H. RNA Binding Protein Lin28B Confers Gastric Cancer Cells Stemness *via* Directly Binding to NRP-1. *Biomed Pharmacother* (2018) 104:383–9. doi: 10.1016/j.biopha.2018.05.064
15. Zhang J, Ding F, Jiao D, Li Q, Ma H. The Aberrant Expression of MicroRNA-125a-5p/IGF2BP3 Axis in Advanced Gastric Cancer and Its Clinical Relevance. *Technol Cancer Res Treat* (2020) 19:1533033820917332. doi: 10.1177/1533033820917332
16. Castello A, Fischer B, Eichelbaum K, Horos R, Beckmann M, Strein C, et al. Insights Into RNA Biology From an Atlas of Mammalian mRNA-Binding Proteins. *Cell* (2012) 149(6):1393–406. doi: 10.1016/j.cell.2012.04.031
17. Correa B, Araujo R, Qiao M, Burns C, Chen C, Schlegel R, et al. Functional Genomics Analyses of RNA-Binding Proteins Reveal the Splicing Regulator SNRPB as an Oncogenic Candidate in Glioblastoma. *Genome Biol* (2016) 17 (1):125. doi: 10.1186/s13059-016-0990-4
18. Iino K, Mitobe Y, Ikeda K, Takayama K, Suzuki T, Kawabata H, et al. RNA-Binding Protein NONO Promotes Breast Cancer Proliferation by Post-Transcriptional Regulation of SKP2 and E2F8. *Cancer Sci* (2020) 111 (1):148–59. doi: 10.1111/cas.14240
19. Kobayashi T, Ishida J, Shimizu Y, Kawakami H, Suda G, Muranaka T, et al. Decreased RNA-Binding Motif 5 Expression Is Associated With Tumor Progression in Gastric Cancer. *Tumour Biol* (2017) 39(3):1010428317694547. doi: 10.1177/1010428317694547
20. Vo D, Subramaniam D, Remke M, Burton L, Uren J, Gelfond A, et al. The RNA-Binding Protein Musashi1 Affects Medulloblastoma Growth *via* a Network of Cancer-Related Genes and Is an Indicator of Poor Prognosis. *Am J Pathol* (2012) 181(5):1762–72. doi: 10.1016/j.ajpath.2012.07.031
21. Kim S, Bae J, Ahn M, Heo J, Kim K, Choi W, et al. MicroRNA Signatures Associated With Lymph Node Metastasis in Intramucosal Gastric Cancer. *Mod Pathol* (2020) 34(3): 672–683. doi: 10.1038/s41379-020-00681-x
22. Chen Q, Hu L, Chen K. Construction of a Nomogram Based on a Hypoxia-Related lncRNA Signature to Improve the Prediction of Gastric Cancer Prognosis. *Front Genet* (2020) 11:570325. doi: 10.3389/fgene.2020.570325
23. Han L, Zhang X, Wang A, Ji Y, Cao X, Qin Q, et al. A Dual-Circular RNA Signature as a Non-Invasive Diagnostic Biomarker for Gastric Cancer. *Front Oncol* (2020) 10:184. doi: 10.3389/fonc.2020.00184
24. Li X, Wu K, Xing R, Wong H, Liu Y, Fang X, et al. Distinct Subtypes of Gastric Cancer Defined by Molecular Characterization Include Novel Mutational Signatures With Prognostic Capability. *Cancer Res* (2016) 76(7):1724–32. doi: 10.1158/0008-5472.CAN-15-2443
25. Ge Y, Li Q, Lin L, Jiang M, Shi L, Wang B, et al. Downregulation of NUSAP1 Suppresses Cell Proliferation, Migration, and Invasion *via* Inhibiting Mtorc1 Signalling Pathway in Gastric Cancer. *Cell Biochem Funct* (2020) 38(1):28–37. doi: 10.1002/cbf.3444
26. Leal M, Ribeiro F, Rey A, Pinto R, Smith C, Moreira-Nunes A, et al. YWHAE Silencing Induces Cell Proliferation, Invasion and Migration Through the Up-Regulation of CDC25B and MYC in Gastric Cancer Cells: New Insights About YWHAE Role in the Tumor Development and Metastasis Process. *Oncotarget* (2016) 7(51):85393–410. doi: 10.18632/oncotarget.13381
27. Lv Z, Zhao W, Jin L, Wang W, Dong Q, Li N, et al. Blocking TGF-β1 by P17 Peptides Attenuates Gastric Cancer Cell Induced Peritoneal Fibrosis and Prevents Peritoneal Dissemination *In Vitro* and *In Vivo*. *Biomed Pharmacother* (2017) 88:27–33. doi: 10.1016/j.biopha.2017.01.039
28. Saintigny G, Bernard F, Juchaux F, Pedretti N, Mahé C. Reduced Expression of the Adhesion Protein Tensin1 in Cultured Human Dermal Fibroblasts Affects Collagen Gel Contraction. *Exp Dermatol* (2008) 17(9):788–9. doi: 10.1111/j.1600-0625.2008.00707.x

Conflict of Interest: The authors declare that the research was conducted in the absence of any commercial or financial relationships that could be construed as a potential conflict of interest.

Publisher's Note: All claims expressed in this article are solely those of the authors and do not necessarily represent those of their affiliated organizations, or those of the publisher, the editors and the reviewers. Any product that may be evaluated in

this article, or claim that may be made by its manufacturer, is not guaranteed or endorsed by the publisher.

frontiers | Frontiers in Oncology

ORIGINAL RESEARCH
published: 27 April 2022
doi: 10.3389/fonc.2022.825899

Exosomal lncRNA LINC01356 Derived From Brain Metastatic Nonsmall-Cell Lung Cancer Cells Remodels the Blood–Brain Barrier

Sumin Geng[1,2*†], *Shaohua Tu*[1,2†], *Zhenwei Bai*[1,2] *and Yixiong Geng*[3]

[1] Department of Neurosurgery, Beijing Tiantan Hospital, Capital Medical University, Beijing, China, [2] China National Clinical Research Center for Neurological Diseases, Beijing, China, [3] School of Basic Medical Sciences, Capital Medical University, Beijing, China

OPEN ACCESS

Edited by:
Yin-Yuan Mo, University of Mississippi Medical Center, United States

Reviewed by:
Ravindra Deshpande, Wake Forest School of Medicine, United States
Mohd Ahmar Rauf, University of Miami Hospital, United States

***Correspondence:**
Sumin Geng
sumingeng@126.com

†*These authors have contributed equally to this work and share first authorship*

Specialty section:
This article was submitted to Molecular and Cellular Oncology, a section of the journal Frontiers in Oncology

Received: *30 November 2021*
Accepted: *22 March 2022*
Published: *27 April 2022*

Citation:
Geng S, Tu S, Bai Z and Geng Y (2022) Exosomal lncRNA LINC01356 Derived From Brain Metastatic Nonsmall-Cell Lung Cancer Cells Remodels the Blood–Brain Barrier. Front. Oncol. 12:825899. doi: 10.3389/fonc.2022.825899

Brain metastasis is a severe complication that affects the survival of lung cancer patients. However, the mechanism of brain metastasis in lung cancer remains unclear. In this study, we constructed an *in vitro* BBB model and found that cells from the high-metastatic nonsmall cell lung cancer (NSCLC) cell line H1299 showed a higher capacity to pass through the blood–brain barrier (BBB), as verified by Transwell assays, than cells from the low-metastatic NSCLC cell line A549. Brain microvascular endothelial cells (BMECs) could internalize H1299-derived exosomes, which remarkably promoted A549 cells across the BBB. The BBB-associated exosomal long noncoding RNA (lncRNA) was selected from the RNA-Seq dataset (GSE126548) and verified by real-time PCR and Transwell assays. LncRNA LINC01356 was significantly upregulated in H1299 cells and exosomes derived from these cells compared to that of A549 cells. Moreover, LINC01356 was also upregulated in serum exosomes of patients with NSCLC with brain metastasis compared with those without metastasis. In addition, BMECs treated with LINC01356-deprived exosomes expressed higher junction proteins than those treated with the control exosomes, and silencing LINC01356 in exosomes derived from H1299 cells could inhibit A549 cells from crossing the BBB. These data might indicate that the exosomal lncRNA LINC01356 derived from brain metastatic NSCLC cells plays a key role in remodeling the BBB system, thereby participating in brain metastasis in lung cancer.

Keywords: lung cancer, lncRNA LINC01356, exosome, BBB, brain metastasis

INTRODUCTION

Patients with lung cancer initially present with brain metastases in 10%–25% of cases, with up to 50% of patients developing brain metastases throughout their disease course (1). Survival of patients with brain metastasis (BM) is limited to mere weeks, extended to months upon administration of multidisciplinary treatment (2–5). The blood–brain barrier (BBB) plays an important role in BM because one of the vital steps in the complex process of BM is the migration of metastatic cells through the BBB. The BBB regulates homeostasis of the central nervous system by forming a tightly regulated neurovascular unit that includes endothelial cells (ECs), pericytes and astrocytes, which

together maintain normal brain function (6, 7). However, it is still largely unknown how cancer cells pass through the BBB to cause BM.

Long noncoding RNAs (lncRNAs) are transcripts longer than 200 nucleotides with no protein-coding capacity that drive many important cancer phenotypes through their interactions with other cellular macromolecules, including DNA, protein, and RNA (8). Some lncRNAs play critical roles in regulating the BBB and blood-tumor barrier (BTB) permeability in some brain tumors (9, 10). LncRNAs are also important during the metastasis of cancer (11–14). Extracellular vesicles, a heterogeneous group of cell-derived membranous structures comprising exosomes (30–100 nm in diameter) and microvesicles, which are continuously secreted by cells to the extracellular environment, represent a novel vehicle for cell-cell communication and are involved in multiple physiological and pathological processes (15, 16). Exosomes, of endocytic origin and that are released into the extracellular space by all cell types through the fusion of multivesicular bodies, carry proteins, RNAs (mRNAs, noncoding RNAs including microRNAs) and DNA sequences, for example, tumorassociated molecules in the case of cancer and premetastatic niche establishment (15–21). A variety of molecules carried within exosomes, such as miRNAs and lncRNAs, can be transferred from exosome-producer and recipient cells and are involved in the tumor microenvironment and metastasis (22–29). However, it remains poorly understood whether and how lung cancer cell-secreted exosomal lncRNAs regulate the BBB and are involved in brain metastases.

In this study, we investigated the roles of exosomal lncRNAs in the brain metastasis of NSCLC by using the highly metastatic NSCLC cell line H1299, the low-metastatic NSCLC cell line A549 and an *in vitro* model of BBB.

MATERIALS AND METHODS

Cell Culture

H1299 cells were cultured in RPMI 1640 medium (10-040-CVR, CORNING) supplemented with 10% heat-inactivated FBS (Invitrogen) and antibiotic–antimycotic agents at 37°C in 5% CO^2 RPMI-1640. A549 cells were cultured in DMEM/F12 medium (10-092-CVR, CORNING) supplemented with 10% heat-inactivated FBS (Invitrogen) and antibiotic–antimycotic agents at 37°C in 5% $CO^{2,}$ and human brain vascular pericytes (HBVPs) and brain capillary epithelial cells (BMECs, Procell) were cultured in ECM medium (sciencell 1001) containing 10% FBS at 37°C in an atmosphere of 5% CO^2.

Transwell Assay

Transwell assays were used to determine migration and invasive ability. Cell migration was assessed using 0.8 μm 24-well chambers (353097, Falcon), and cell invasion was assessed using BioCoat™ Matrigel® 0.8 μm 24-well chambers (354480, BioCoat). Cells 1×10^5 were plated in the top chamber. The lower chamber contained 700 μl of medium (DMEM/F12 CORNING; RPMI 1640 (CORNING) supplemented with 10% FBS (21-040-CV, CORNING). The cells were incubated for 24 h, cells in the upper chamber were removed, and cells on the lower surface were stained with 0.1 crystal violet (C0121 blue sky).

BBB *In Vitro* Model

To investigate the function of exosomes in the BBB, we established an *in vitro* BBB model as previously described (25). HBVP was plated on the lower surface of the upper chamber, and BMECs were plated in the upper chamber. Astrocytes were cultured in the lower chamber. The barrier function of the BBB model was evaluated by determining its transepithelial/transendothelial electrical resistance (TEER).

Exosome Isolation

Cancer cells were cultured, and the medium was then replaced with serum-free medium and cultured for another 48 hours. The culture was centrifuged at 300 g for 10 min. The supernatant was collected, and dead cells were removed by centrifugation at 2000×g for 10 min, followed by centrifugation at 10000×g for 30 min to remove cell debris. The supernatant was ultra centrifuged at 4°C and 100000×g for 1 h. This step was repeated. The supernatant was removed, and the exosome precipitate was added to precooled 1× phosphate-buffered saline (PBS). The exosomes were verified by transmission electron microscopy (TEM), the exosomes diameter was measured by Nanoparticle Tracking Analysis (NTA). The protein expression is verified by SDS page analysis and CD63 protein was verified through western blotting (WB).

Exosome Tracing Experiment

Exosomes were extracted from $1.5x10^6$ cells, then the exosomes were labeled with DiI dye (Blue sky#C1036) and incubated for 20 min. The cells were incubated with mouse brain microvascular endothelial cells, and exosomes were located by observing fluorescence.

Transwell Invasion Assay Using the *In Vitro* BBB Model

Cancer cell invasion was assessed in an *in vitro* BBB model. The cells were trypsinized and labeled with green fluorescent protein (GFP). Cancer cells were plated at a density of 2×10^4 cells in serum-free DMEM, and RAPM-1640 medium containing 10% serum was used as the chemoattractant in the lower chamber. After 48 h, the noninvading cells were removed, and the invading cells were labeled with GFP. All assays were performed in triplicate.

Screening for Brain Metastasis-Related lncRNAs

To explore which exosomal lnc-RNAs are involved in lung cancer BM, we used primary lung tumor RNA-Seq data (GSE126548) from patients with BM and non-metastatic NSCLC for analysis. First, we downloaded GSE126548 data, using the DeSeq package analysis of BM and transfer of NSCLC patients differentially expressed lncRNA, significance of difference threshold is set to FDR < 0.05, | log2 fold change | > 1. Then, analyzed the target lncRNA differential expression by

miRanda (http://www.microrna.org/miRanda) and RNAhybrid (https://bibiserv.cebitec.uni-bielefeld.de/rnahybrid/). The function of target Genes was predicted by Gene Ontology (GO), the Kyoto Encyclopedia of Genes and Genomes (KEGG) analyzed the signaling pathways involved in target Genes.

Real-Time PCR

The expression of lncRNAs was validated by real-time PCR. Total RNA from the exosomes and cells was extracted by TRIzol reagent (Invitrogen). The quantity and quality of the extracted RNA was determined by a NanoDrop 2000 spectrophotometer (Wilmington, DE, USA). Qualified RNA samples with an A260/280 ratio >1:9 were used for real-time PCR. A PrimeScript RT kit (Takara Bio, Dalian, China) was used to synthesize complementary DNA (cDNA). Real-time PCR was performed using a SYBR-Green PCR kit (Roche Diagnostics, Indianapolis, IN, USA). PCR was performed on an ABI QuantStudio^{TM}6 Flex System. U6 was used as the internal reference, and the primer sequences used for PCR are shown in **Table 1**. The PCR was run at 95°C for 10 min for denaturation, 45 cycles of 95°C for 15 sec, and 60°C for 60 sec and dissociation at 95°C for 10 sec, 60°C for 1 min, and 95°C for 15 sec. The data were analyzed by the 2 $-\Delta\Delta$Ct method. The PCRs were all repeated three times.

Western Blot

Proteins from exosomes and BMECs were extracted, and the concentration was determined using a BCA assay kit (Pierce Biotechnology, Inc., Rockford, IL, USA). The resolved proteins were transferred to polyvinylidene fluoride membranes (Millipore, Bedford, MA, USA). The proteins were blocked in 5% milk and incubated with primary antibodies against CD63 (1:1000, EXOAB-CD63A-1, SBI), ZO-1 (1:1000, 13663S, Cell Signaling Technology), claudin-5 (1:1000, Ab131259, Abcam), N-cadherin (1:5000, Ab76011, Abcam), Occludin (1:1000, Ab216327, Abcam) and glyceraldehyde-3-phosphate dehydrogenase (GAPDH, 60004-1-Lg, Proteintech) overnight at 4°C. The samples were then incubated with anti-rabbit or anti-mouse horseradish peroxidase-conjugated secondary antibodies. Enhanced chemiluminescence reagent (Thermo Fisher Scientific, Waltham, MA, USA) was used to show the protein bands, and optical density was assessed *via* ImageJ software.

TABLE 1 | Primer sequence.

Gene symbol	Primer sequence
SLC7A11-AS1	F 5' ACCAGACAGCAGTGCTCAAG 3'
	R 5' GAGAACTGACAGCCAGGGAA 3'
LINC01356	F 5' CTTTCCACGCGCTTGTTTCG 3'
	R 5' CCCAAGACGTAGAGCTTCCC 3'
LINC01252	F 5' AAAAGACGGCCTCTGTCTGG 3'
	R 5' TGTCCTGACACTTCTGCCAC 3'
CTD-2319I12.2	F 5' GGCTTGGAGATTTTTCGCCG 3'
	R 5' AGCCTTCCTCCTCCTGTGAT 3'
CTA-373H7.7	F 5' CACCCGAGGTCCAAAGAGAA 3'
	R 5' ATGAGTCCCCTCAGATGCAG 3'

Statistical Analysis

GraphPad Prism 8.0 and SPSS 25 were used to analyze the real-time PCR data. Two-tailed Student's t-test was used to compare the differences between two groups. The mean value ± standard deviation was used to present the experimental data. A $P < 0.05$ was considered statistically significant. Cell number was counted by ImageJ software.

RESULTS

Confirmation of Brain Metastatic Cell Lines

A previous study showed that H1299 is a highly invasive cell line and that A549 cells are minimally invasive (28). Transwell assays were used to confirm the invasion of H1299 and A549 cells. The results demonstrated that both the migration and invasion abilities of H1299 cells were significantly higher than those of A549 cells (**Figure 1**).

Establishment of an *In Vitro* BBB Model

To better investigate the invasion of lung cancer cells into the brain, we established an *in vitro* BBB model. The *in vivo* BBB commonly consists of BMECs, pericytes, and astrocytes. Therefore, we seeded BMECs on the upper part of the upper compartment. Then, the pericytes were seeded on the lower part of the upper compartment, and the astrocytes were seeded on the lower compartment (**Figure 2A**). The conjunction of the *in vitro* model was confirmed by TEER, and the TEER increased in 3-4 days and remained at a sufficiently high level (**Figure 2B**).

Identification of Exosomes Derived From NSCLC Cells

To explore the influence of exosomes on the BBB *in vitro* model, we extracted exosomes from H1299 and A549 cells, which were identified through TEM. (**Figure 2C**) and the signature protein CD63 (**Figure 2E**). The exosomes diameter was analyzed by NTA (**Figure 2D**) and the protein expression was identified by SDS page analysis (**Figure 2F**). TEM revealed that the extracted particles were 100 to 150 nm in size with a complete membrane structure, which corresponded with exosomes, while WB results showed that these particles significantly expressed the exosome marker CD63. NTA revealed that the peak diameter of particles from A549 is 128.1nm and the full width at half maxima (FWHM) is 119.3nm, while the peak diameter of particles from H1299 is 158.6nm and the FWHM is 82.4nm, which indicate that the main component of particles is exosomes.

Exosomes From H1299 Cells Can Promote Cancer Cell Invasion in an *In Vitro* BBB Model

The exosomes were labeled with DiI dye added to the *in vitro* BBB model cocultivation for 24 hours separately. The figures show that the exosomes from H1299 and A549 cells could be absorbed by BMECs (**Figure 3A**). Then, to determine whether NSCLC with low invasiveness could penetrate the BBB model treated with exosomes, we counted the A549 cells that were

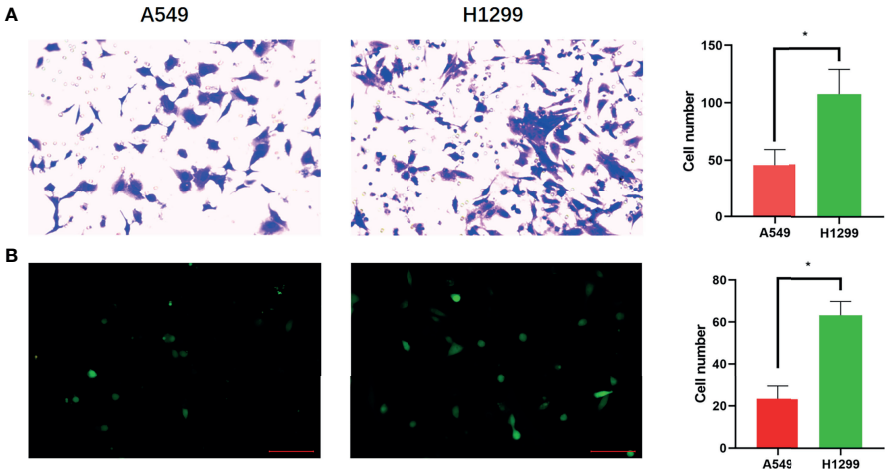

FIGURE 1 | Confirmation of brain metastatic cell lines. **(A)** Transwell assay shows the migration ability of A549 and H1299 cells and cell numbers of A549 and H1299 cells in the Transwell assay. **(B)** Transwell assay shows the invasive ability of A549 and H1299 cells and cell numbers of A549 and H1299. (N = 3, one-way ANOVA, *P < 0.05).

processed by H1299 and A549 exosomes and crossed the BBB, which were labeled with GFP (**Figure 3B**). The results demonstrated that A549 cells penetrated the *in vitro* BBB model treated with H1299 exosomes more than those treated with A549 exosomes (**Figure 3C**).

Exosomes Derived From NSCLC Cells Remodel the BBB by Carrying LINC01356

To further explore how H1299-derived exosomes promote A549 cells to cross the *in vitro* BBB model. We first analyzed the lncRNAs differentially expressed between H1299 and A549 cells from the RNA-Seq dataset GSE126548. A total of 99 differentially expressed lncRNAs were found. Compared with the exosomes of A549 low metastatic NSCLC cells, 59 lncRNAs were upregulated and 40 lncRNAs were downregulated in the exosomes of H1299 high metastatic NSCLC cells (**Figure 4A**). We screened five candidate lncRNAs, LINC01252, CTD-2319I12.2, CTA-373H7.7, LINC01356, and SLC7A11-AS1, which were stable and significantly increased in expression. Through qRT–PCR verification, we found that LINC01356 was significantly

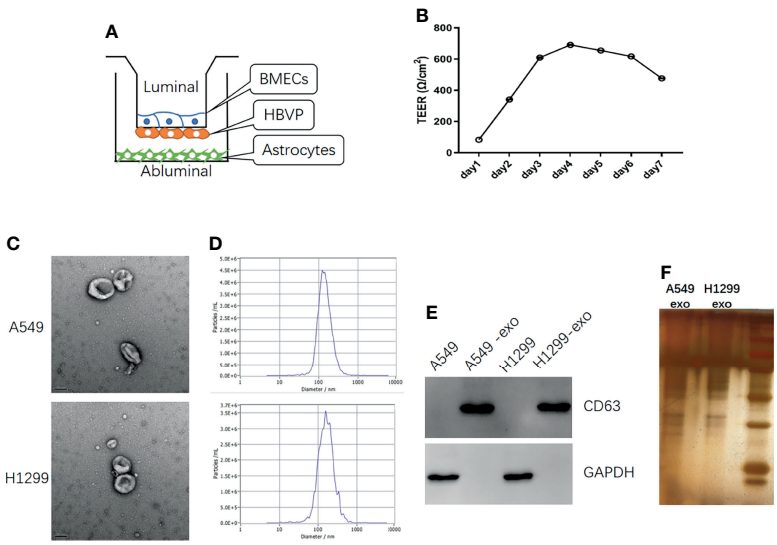

FIGURE 2 | The *in vitro* BBB model establish and identification of exosomes derived from NSCLC cells. **(A)** Schematic diagram of the *in vitro* BBB model, *in vitro* **(B)** The curve over time of TEER established in the *in vitro* BBB model. **(C)** TEM identification of exosomes from A549 and H1299 cells. **(D)** The NTA analysis of the diameter of exosomes from A549 and H1299 cells. **(E)** Western blot identification of the exosome marker CD63 in cells and exosomes. **(F)** SDS page analysis of exosomes protein expression.

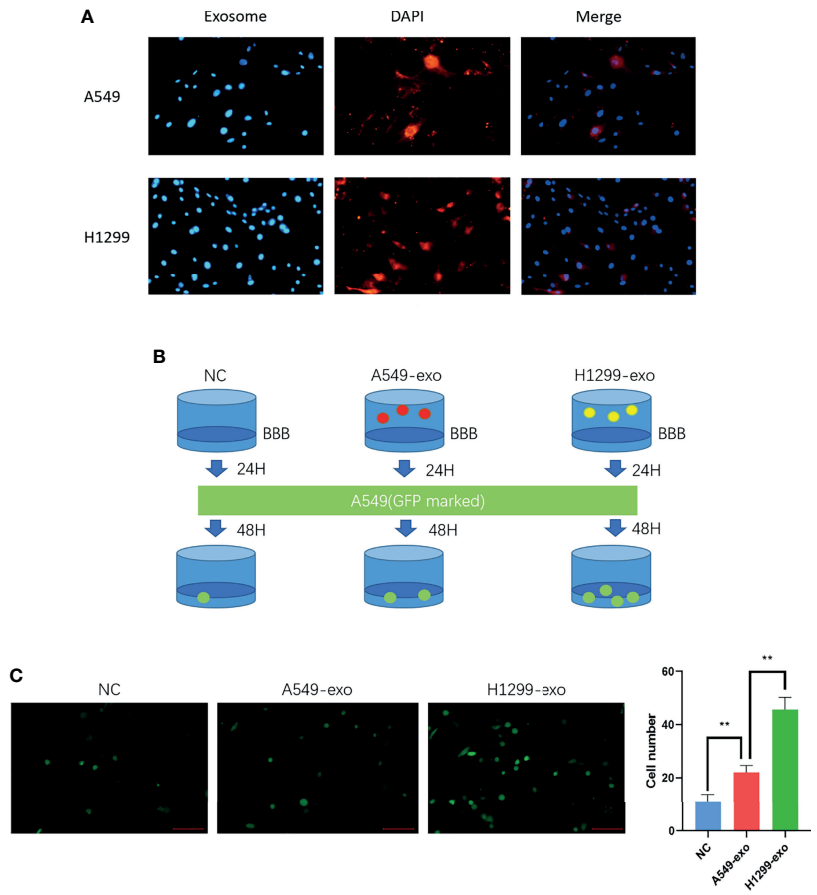

FIGURE 3 | The exosomes from a highly metastatic cell line can promote cancer cell invasion in an *in vitro* BBB model. **(A)** DiI dye tracing of exosomes from A549 and H1299 cells. BMECs internalized exosomes after 24 incubation. **(B)** Schematic diagram of the Transwell assay for cancer cell-derived exosomes promoting A549 cells to penetrate the BBB model. The *in vitro* BBB model was incubated with exosomes for 24 h, and then GFP-marked A549 cells were cultured for another 48 h. **(C)** Exosomes were added to the BBB *in vitro* model and incubated for 24 hours. Then, A549 cells were added, and the number of cells crossing was counted after 48 hours (magnification ×200, one-way ANOVA, *P < 0.05, **P < 0.01).

upregulated in both cells (**Figure 4B**) and exosomes (**Figure 4C**) in H1299 cells, and the expression level was the highest. Therefore, we further explored the effect of LINC01356 on the BBB.

First, we added exosomes from A549 and H1299 cells to BBB models *in vitro* and measured the expression level of LINC01356 in BMECs separately. The figure shows that LINC01356 is more highly expressed in exo-H1299-treated BMECs (**Figure 4D**). Then, we transfected small interfering RNAs (siRNAs) to interfere with the efficiency of LINC01356 siRNA silencing. Moreover, siRNA-1140 showed the highest interference effect and was selected for further investigation (**Figure 4E**). siRNA-1140 was then used to transfect H1299 cells to generate LINC01356-deficient silnc-Exos, and LINC01356 expression was dramatically decreased in silnc-Exos (**Figure 4F**). Finally, we compared the invasive ability of A549 cells treated with normal H1299 exosomes (NC-Exos) and LINC01356-deficient exosomes (silnc-Exos) through Transwell assays. The results showed that A549 cells treated with NC-Exos successfully crossed the *in vitro* BBB model. However, the infiltrated cell number of A549 cells treated with silnc-Exos was lower. (**Figures 4G, H**). To further study the effect of LINC01356 on cell junctions, we detected the expression of tight junction proteins in BMECs. The expression levels of ZO-1, Occludin, Claudin and N-cadherin proteins were significantly decreased in the BMECs transfected with NC exosomes compared to those transfected with siRNA exosomes (**Figures 4J, K**).

Exosomal lncRNA LINC01356 Expression Is Higher in the Serum of Patients With Brain Metastases

To further confirm whether the expression level of LINC01356 is higher in patients with brain metastases, we collected six lung cancer patient plasma samples with (n=3) or without (n=3) brain metastasis. The level of LINC01356 in exosomes was determined by qRT–PCR. The level of exosomal LINC01356 was

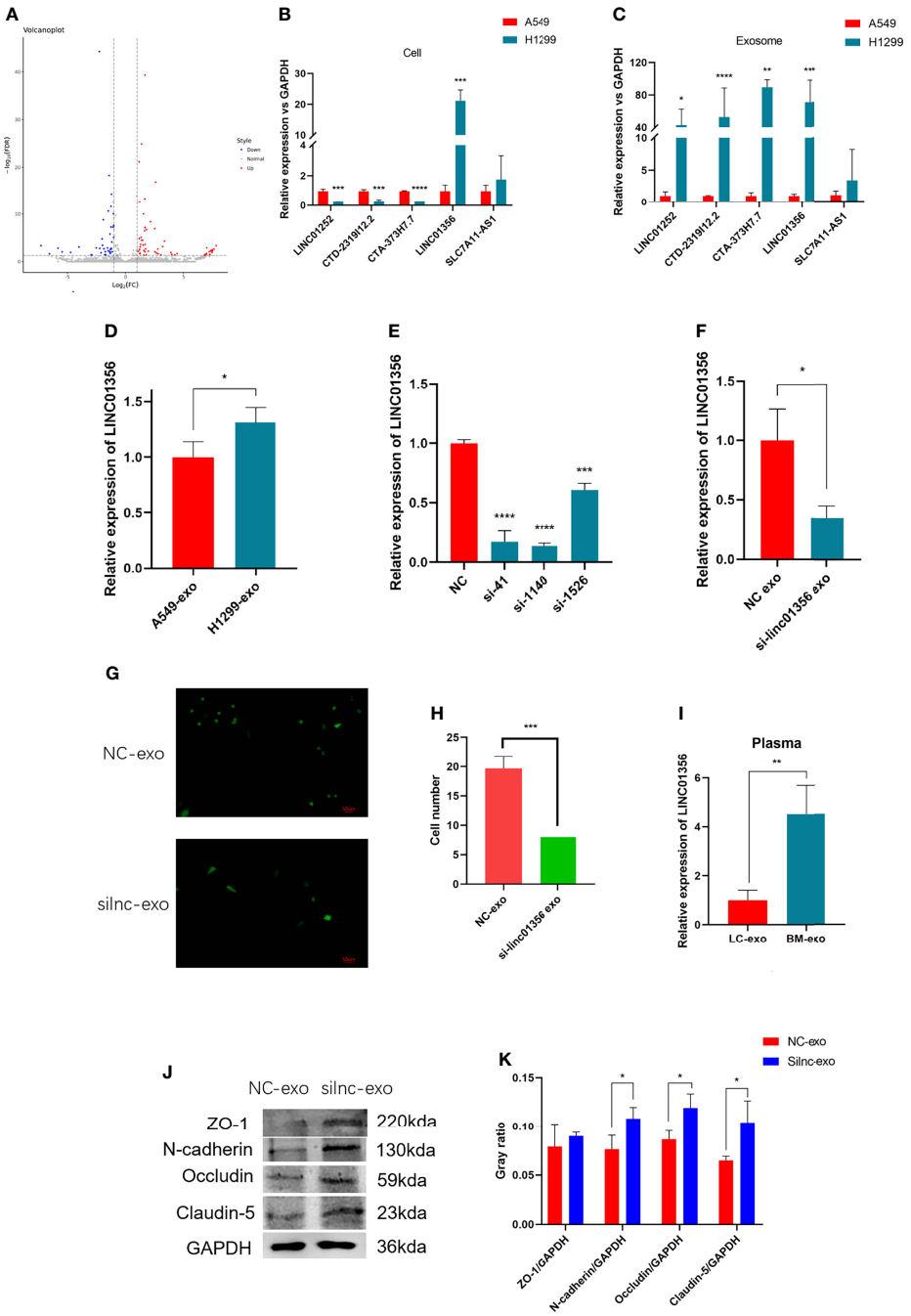

FIGURE 4 | Mechanism of exosomal LINC01356 *in vitro* BBB model remodeling and lung cancer brain metastasis. **(A)** Volcano plot of differentially expressed lncRNAs between brain metastatic and nonbrain metastatic lung cancer cells. Data were obtained from the GSE126548 database. **(B)** The top five most highly differentially expressed lncRNAs were verified by RT–PCR in A549 and H1299 cells. **(C)** The top five most highly differentially expressed lncRNAs were verified by RT–PCR in exosomes from A549 and H1299 cells. **(D)** LINC01356 expression level of BMECs incubated with exosomes from A549 and H1299 cells. **(E)** Different interference rates of siRNAs were verified by RT–PCR. **(F)** LINC01356 expression level of BMECs incubated with NC-Exos and silnc-Exos. **(G)** Immunofluorescence image and number of A549 cells crossing through the BBB *in vitro* model treated with NC-Exos and silnc-Exos. **(H)** Cell number of Fig. 3g. **(I)** Expression level of LINC01356 in LC-Exos and BM-Exos. **(J)** Western blotting was used to detect the expression of tight junction and adhesive proteins in BMECs treated with NC-Exos and silnc-Exos. **(K)** Gray ratio of western blot for junction protein. The expression levels of ZO-1, N-cadherin, Occludin and Claudin-5 protein increased when siRNA interfered with LINC01356. Among them, the expression of ZO-1 was not statistically significant. (NC-Exo= exosomes derived from H1299 cells without siRNA transfection, silnc-Exo= exosomes derived from H1299 cells treated with siRNA, LC-Exo= plasma exosomes from lung cancer patients without metastasis, BM-Exo= plasma exosomes from lung cancer patients with brain metastasis, *P < 0.05, **P < 0.01, ***P < 0.001, ****P < 0.0001).

significantly higher in the plasma of patients with brain metastasis (**Figure 4I**).

DISCUSSION

The BM of lung cancer is an important factor affecting patient survival. The mechanism of tumor metastasis to the brain is currently unclear. Fortunately, emerging evidence suggests that EVs (species of exosomes and shed microvesicles) have crucial roles in cancer development, including premetastatic niche formation and metastasis (25, 30, 31). For exosomal miRNAs derived from brain metastatic breast cancer cells, exosome-mediated transfer of cancer-secreted miR-105 destroys tight junctions and the integrity of the BBB (24), and cancer-derived EVs containing miR-181c trigger the breakdown of the BBB (25). For lncRNAs, exosomes derived from highly brain metastatic breast cancer cells might destroy the BBB system and promote the passage of cancer cells across the BBB by transferring lncRNA GS1-600G8.5 (29). These studies all indicate that EVs containing miRNAs and lncRNAs destroy the BBB and promote brain metastasis in breast cancer. However, there is a lack of relevant research on the mechanism of lung cancer brain metastasis. In this study, we first indicate that exosomal lncRNA LINC01356 derived from brain metastatic NSCLC cells remodels the BBB.

First, we compared the invasive ability between A549 and H1299 cells, and the results showed that the highly metastatic cell lineH1299 could infiltrate the *in vitro* BBB model more easily. To explore the mechanism, we investigated whether exosomes of A549 and H1299 cells play a role in this process, and the results revealed that H1299-derived exosomes can be absorbed by BMECs in an *in vitro* BBB model and improve the permeability of A549 cells, which indicated a crucial role of tumor-derived exosomes in BBB remodeling. To further explore the mechanism by which exosomes affect the *in vitro* BBB model. We analyzed the lncRNAs differentially expressed between H1299 and A549 cells in the data and validated them through qRT-PCR. The results indicated that exosome-derived LINC01356 is more highly expressed in both exosomes and H1299 cells, which may indicate that LINC01356 plays a key role in *in vitro* BBB model remodeling. Silencing LINC01356 remarkably inhibited the invasion ability of a lung cancer cell line in an *in vitro* BBB model. Finally, western blot analysis suggested that LINC01356 can affect the expression of the junction proteins Occludin, Claudin and N-cadherin. This evidence may indicate that exosomal LINC01356 can remodel the BBB in an *in vitro* model by decreasing the expression of Claudin, Occludin and N-cadherin. Most importantly, we found that plasma-derived exosomes from lung cancer patients with brain metastasis expressed significantly higher levels of LINC01356 than those from patients without brain metastasis. This finding may suggest that LINC01356 could also affect the BBB *in vivo* in lung cancer patients, and further research is needed to verify this notion.

Although exosomal LINC01356 proved to be a critical factor in lung cancer brain metastasis, the mechanism remains to be further explored. In addition, LINC01356 was higher in the plasma of lung cancer patients with brain metastasis, which means that LINC01356 could be a predictive factor of the likelihood of brain metastasis. Moreover, whether blocking exosomal LINC01356 can prevent brain metastasis in patients with lung cancer still needs to be further explored. Exosome-derived LINC01356 can change the permeability of the *in vitro* BBB model, and exosomes can carry molecules and drugs, which means that they can be used to promote the effect of drugs in the central nervous system. Therefore, exosomal LINC01356 may be a suitable candidate vehicle for drug delivery. We speculate that it may strengthen the therapeutic effect of drugs in primary central nervous system tumors or infections. Whether exosomal LINC01356 can be used in the adjuvant treatment of central nervous system diseases needs to be further explored. In conclusion, exosomal LINC01356 could be a novel predictive factor and therapeutic target for brain metastasis, and it may also be an adjuvant to drug therapy for central nervous system diseases.

CONCLUSION

In conclusion, the high-metastatic NSCLC cell line H1299 could infiltrate the *in vitro* BBB model more easily than cells from the low-metastatic NSCLC cell line A549, and H1299-derived exosomes can be absorbed by BMECs in an *in vitro* BBB model and improve the permeability of A549 cells, which indicated a crucial role of tumor-derived exosomes in BBB remodeling. Furthermore, LncRNA LINC01356 was significantly upregulated in H1299 cells and exosomes derived from these cells compared to that of A549 cells, BMECs treated with LINC01356-deprived exosomes expressed higher junction proteins than those treated with the control exosomes, and silencing LINC01356 in exosomes derived from H1299 cells could inhibit A549 cells from crossing the BBB, which may indicate that exosomal LINC01356 can remodel the BBB in an *in vitro* model. Meanwhile, exosomal LINC01356 is more highly expressed in the plasma of NSCLC patients with brain metastasis. It may promote the process of lung cancer brain metastasis through remodeled BBB by targeting cell junction proteins.

DATA AVAILABILITY STATEMENT

The original contributions presented in the study are included in the article/supplementary materials. Further inquiries can be directed to the corresponding author.

AUTHOR CONTRIBUTIONS

SG: Experiment design and manuscript revision. ST: Writing manuscript. ZB: Experiment and data acquisition. YG: Experiment and data acquisition. All authors contributed to the article and approved the submitted version.

REFERENCES

1. Ulahannan D, Khalifa J, Faivre-Finn C, Lee SM. Emerging Treatment Paradigms for Brain Metastasis in Non-Small-Cell Lung Cancer: An Overview of the Current Landscape and Challenges Ahead. *Ann Oncol* (2017) 28(12):2923–31. doi: 10.1093/annonc/mdx481
2. Singh M, Venugopal C, Tokar T, McFarlane N, Subapanditha MK, Qazi M, et al. Therapeutic Targeting of the Premetastatic Stage in Human Lung-to-Brain Metastasis. *Cancer Res* (2018) 78(17):5124–34. doi: 10.1158/0008-5472.CAN-18-1022
3. Oh Y, Taylor S, Bekele BN, Debnam JM, Allen PK, Suki D, et al. Number of Metastatic Sites Is a Strong Predictor of Survival in Patients With Nonsmall Cell Lung Cancer With or Without Brain Metastases. *Cancer* (2009) 115 (13):2930–8. doi: 10.1002/cncr.24333
4. Riihimäki M, Hemminki A, Fallah M, Thomsen H, Sundquist K, Sundquist J, et al. Metastatic Sites and Survival in Lung Cancer. *Lung Cancer* (2014) 86 (1):78–84. doi: 10.1016/j.lungcan.2014.07.020
5. Tsakonas G, De Petris L, Ekman S. Management of Brain Metastasized Non-Small Cell Lung Cancer (NSCLC) - From Local Treatment to New Systemic Therapies. *Cancer Treat Rev* (2017) 54:122–31. doi: 10.1016/j.ctrv.2017.02.004
6. Arvanitis CD, Ferraro GB, Jain RK. The Blood-Brain Barrier and Blood-Tumour Barrier in Brain Tumours and Metastases. *Nat Rev Cancer* (2020) 20 (1):26–41. doi: 10.1038/s41568-019-0205-x
7. Wilhelm I, Molnár J, Fazakas C, Haskó J. Krizbai IA.Role of the Blood-Brain Barrier in the Formation of Brain Metastases. *Int J Mol Sci* (2013) 14(1):1383–411. doi: 10.3390/ijms14011383
8. Schmitt AM, Chang HY. Long Noncoding RNAs in Cancer Pathways. *Cancer Cell* (2016) 29(4):452–63. doi: 10.1016/j.ccell.2016.03.010
9. Ma SC, Li Q, Peng JY, Zhouwen JL, Zhang DN, Zhang CB, et al. CLDN5 Affects lncRNAs Acting as ceRNA Dynamics Contributing to Regulating Blood-Brain Barrier Permeability in Tumor Brain Metastasis. *Oncol Rep* (2018) 39(3):1441–53. doi: 10.3892/or.2018.6208
10. Guo J, Shen S, Liu X, Ruan X, Zheng J, Liu Y, et al. Role of Linc00174/miR-138-5p (miR-150-5p)/FOSL2 Feedback Loop on Regulating the Blood-Tumor Barrier Permeability. *Mol Ther Nucleic Acids* (2019) 18:1072–90. doi: 10.1016/j.omtn.2019.10.031
11. Wang S, Liang K, Hu Q, Li P, Song J, Yang Y, et al. JAK2-Binding Long Noncoding RNA Promotes Breast Cancer Brain Metastasis. *J Clin Invest* (2017) 127(12):4498–515. doi: 10.1172/JCI91553
12. Tan BS, Yang MC, Singh S, Chou YC, Chen HY, Wang MY, et al. LncRNA NORAD Is Repressed by the YAP Pathway and Suppresses Lung and Breast Cancer Metastasis by Sequestering S100P. *Oncogene* (2019) 38(28):5612–26. doi: 10.1038/s41388-019-0812-8
13. Wang H, Huo X, Yang XR, He J, Cheng L, Wang N, et al. STAT3-Mediated Upregulation of lncRNA HOXD-AS1 as a ceRNA Facilitates Liver Cancer Metastasis by Regulating SOX4. *Mol Cancer* (2017) 16(1):136. doi: 10.1186/s12943-017-0680-1
14. Kim J, Piao HL, Kim BJ, Yao F, Han Z, Wang Y, et al. Long Noncoding RNA MALAT1 Suppresses Breast Cancer Metastasis. *Nat Genet* (2018) 50(12):1705–15. doi: 10.1038/s41588-018-0252-3
15. van Niel G, D'Angelo G, Raposo G. "Shedding Light on the Cell Biology of Extracellular Vesicles," Nature Reviews. *Mol Cell Biol* (2018) 19(4):213–28. doi: 10.1038/nrm.2017.125
16. Villarroya-Beltri C, Baixauli F, Gutierrez-Vazquez C, Sanchez-Madrid F, Mittelbrunn M. Sorting It Out: Regulation of Exosome Loading. *Semin Cancer Biol* (2014) 28:3–13. doi: 10.1016/j.semcancer.2014.04.009
17. Valadi H, Ekström K, Bossios A, Sjöstrand M, Lee JJ, Lötvall JO. Exosome-Mediated Transfer of mRNAs and microRNAs Is a Novel Mechanism of Genetic Exchange Between Cells. *Nat Cell Biol* (2007) 9(6):654–9. doi: 10.1038/ncb1596
18. Nolte-'t Hoen EN, Buermans HP, Waasdorp M, Stoorvogel W, Wauben MH. 'T Hoen PA.Deep Sequencing of RNA From Immune Cell-Derived Vesicles Uncovers the Selective Incorporation of Small Non-Coding RNA Biotypes With Potential Regulatory Functions. *Nucleic Acids Res* (2012) 40(18):9272–85. doi: 10.1093/nar/gks658
19. Thakur BK, Zhang H, Becker A, Matei I, Huang Y, Costa-Silva B, et al. Double-Stranded DNA in Exosomes: A Novel Biomarker in Cancer Detection. *Cell Res* (2014) 24(6):766–9. doi: 10.1038/cr.2014.44
20. Hoshino A, Costa-Silva B, Shen TL, Rodrigues G, Hashimoto A, Tesic Mark M, et al. Tumour Exosome Integrins Determine Organotropic Metastasis. *Nature* (2015) 527:329–35. doi: 10.1038/nature15756
21. Peinado H, Zhang H, Matei IR, Costa-Silva B, Hoshino A, Rodrigues G, et al. Pre-Metastatic Niches: Organ-Specific Homes for Metastases. *Nat Rev Cancer* (2017) 17:302–17. doi: 10.1038/nrc.2017.6
22. Zomer A, Maynard C, Verweij FJ, Kamermans A, Schafer R, Beerling E, et al. *In Vivo* Imaging Reveals Extracellular Vesicle-Mediated Phenocopying of Metastatic Behavior. *Cell* (2015) 161(5):1046–57. doi: 10.1016/j.cell.2015.04.042
23. Hsu YL, Hung JY, Chang WA, Lin YS, Pan YC, Tsai PH, et al. Hypoxic Lung Cancer-Secreted Exosome miR-23a Increased Angiogenesis and Vascular Permeability by Targeting Prolyl Hydroxylase and Tight Junction Protein ZO-1. *Oncogene* (2017) 36(34):4929–42. doi: 10.1038/onc.2017.105
24. Zhou W, Fong MY, Min Y, Somlo G, Liu L, Palomares MR, et al. Cancer-Secreted miR-105 Destroys Vascular Endothelial Barriers to Promote Metastasis. *Cancer Cell* (2014) 25(4):501–15. doi: 10.1016/j.ccr.2014.03.007
25. Tominaga N, Kosaka N, Ono M, Katsuda T, Yoshioka Y, Tamura K, et al. Brain Metastatic Cancer Cells Release microRNA-181c-Containing Extracellular Vesicles Capable of Destructing Blood-Brain Barrier. *Nat Commun* (2015) 6 (1):6716. doi: 10.1038/ncomms7716
26. Yousefi M, Bahrami T, Salmaninejad A, Nosrati R, Ghaffari P, Ghaffari SH. Lung Cancer-Associated Brain Metastasis: Molecular Mechanisms and Therapeutic Options. *Cell Oncol (Dordr)* (2017) 40(5):419–41. doi: 10.1007/s13402-017-0345-5
27. Zhang L, Zhang S, Yao J, Lowery FJ, Zhang Q, Huang WC, et al. Microenvironment-Induced PTEN Loss by Exosome microRNA Primes Brain Metastasis Outgrowth. *Nature* (2015) 527(7576):100–4. doi: 10.1038/nature15376
28. Zhang R, Xia Y, Wang Z, Zheng J, Chen Y, Li X, et al. Serum Long Non Coding RNA MALAT-1 Protected by Exosomes Is Up-Regulated and Promotes Cell Proliferation and Migration in Non-Small Cell Lung Cancer. *Biochem Biophys Res Commun* (2017) 490(2):406–14. doi: 10.1016/j.bbrc.2017.06.055
29. Lu Y, Chen L, Li L, Cao Y. Exosomes derived from brain metastatic breast cancer cells destroy the blood-brain barrier by carrying lncRNA GS1-600G8.5. *BioMed Res Int* (2020) 2020:7461727. doi: 10.1155/2020/7461727
30. Xu R, Rai A, Chen M, Suwakulsiri W, Greening DW, Simpson RJ. Extracellular Vesicles in Cancer - Implications for Future Improvements in Cancer Care. *Nat Rev Clin Oncol* (2018) 15(10):617–38. doi: 10.1038/s41571-018-0036-9
31. Becker A, Thakur BK, Weiss JM, Kim HS, Peinado H, Lyden D. Extracellular Vesicles in Cancer: Cell-To-Cell Mediators of Metastasis. *Cancer Cell* (2016) 30(6):836–48. doi: 10.1016/j.ccell.2016.10.009

Conflict of Interest: The authors declare that the research was conducted in the absence of any commercial or financial relationships that could be construed as a potential conflict of interest.

frontiers | Frontiers in Oncology

ORIGINAL RESEARCH
published: 05 May 2022
doi: 10.3389/fonc.2022.823377

STAT6 Upregulates NRP1 Expression in Endothelial Cells and Promotes Angiogenesis

Peng Gao[1,2†], *Guanghui Ren*[3†], *Jiangjiu Liang*[1] *and Ju Liu*[2*]

[1] Department of Gerontology, The First Affiliated Hospital of Shandong First Medical University & Shandong Provincial Qianfoshan Hospital, Jinan, China, [2] Institute of Microvascular Medicine, Medical Research Center, The First Affiliated Hospital of Shandong First Medical University & Shandong Provincial Qianfoshan Hospital, Jinan, China, [3] Shandong Provincial Key Laboratory of Animal Resistant, School of Life Sciences, Shandong Normal University, Jinan, China

OPEN ACCESS

Edited by:
Michal Amit Rahat,
Technion-Israel Institute of Technology, Israel

Reviewed by:
Jian-Hong Shi,
Affiliated Hospital of Hebei University, China
Luca Tamagnone,
Catholic University of the Sacred Heart, Rome, Italy

***Correspondence:**
Ju Liu
ju.liu@sdu.edu.cn

[†]These authors have contributed equally to this work

Specialty section:
This article was submitted to Molecular and Cellular Oncology, a section of the journal Frontiers in Oncology

Received: 27 November 2021
Accepted: 11 April 2022
Published: 05 May 2022

Citation:
Gao P, Ren G, Liang J and Liu J (2022) STAT6 Upregulates NRP1 Expression in Endothelial Cells and Promotes Angiogenesis. Front. Oncol. 12:823377. doi: 10.3389/fonc.2022.823377

The role of signal transducer and activator of transcription 6 (STAT6) in tumor growth has been widely recognized. However, its effects on the regulation of angiogenesis remain unclear. In this study, we found that STAT6 promoted angiogenesis, possibly by increasing the expression of neuropilin-1 (NRP1) in endothelial cells (ECs). Both STAT6 inhibitor (AS1517499) and STAT6 siRNA reduced EC proliferation, migration, and tube-formation, accompanied by downregulation of NRP1, an angiogenesis regulator. Furthermore, IL-13 induced activation of STAT6 and then increased NRP1 expression in ECs. IL-13-induced EC migration and tube formation were inhibited by NRP1 siRNA. Luciferase assay and chromatin immunoprecipitation assay demonstrated that STAT6 could directly bind to human NRP1 promoter and increase the promoter activity. In tumor xenograft models, inhibition of STAT6 reduced xenograft growth, tumor angiogenesis, and NRP1 expression *in vivo*. Overall, these results clarified the novel mechanism by which STAT6 regulates angiogenesis, and suggested that STAT6 may be a potential target for anti-angiogenesis therapy.

Keywords: endothelial cell, tumor angiogenesis, STAT6, neuropilin-1, transcriptional regulation

INTRODUCTION

Blood vessels, especially the capillaries, run throughout the body, providing oxygen and nutrients and exchanging cellular and tissue byproducts to maintain normal functioning of tissues (1). However, insufficient vascularization causes impaired healing of fractures and placental deficiency, whereas increased vascularization leads to atherosclerosis, hemangioma, and neoplastic

Abbreviations: EDN1, endothelin-1; KDR, kinase insert domain-containing receptor; MCP-1/CCL2, monocyte chemoattractant protein-1; MMP2, matrix metalloproteinase-2; NRP1, neuropilin-1; PTGS1/COX1, cyclooxygenase 1; SMAD5, mothers against DPP homolog 5; SPHK1, sphingosine kinase 1; VEGFA, vascular endothelial growth factor A.

development (2). Aberrant vascularization causes a variety of diseases (3) and hence, reasonable arrangement of blood vessels is a therapeutic strategy, especially for cancer treatment.

Tumor cells are not restricted by the cell cycle and grow faster than normal cells. Therefore, more nutrients are needed for tumor cell growth (4). When the diameter of a tumor is larger than 2 mm, more new vessels are needed to support tumor growth (5). Angiogenesis refers to the formation of new blood vessels from the existing vessels, which are tightly regulated by the balance between pro- and anti-angiogenic molecules. However, the balance is unsettled when existing vessels are insufficient to support tumor overgrowth. An increase of pro-angiogenic molecules' secretion induced by inflammation and hypoxia is commonly seen in the tumor microenvironment, which induces tumor angiogenesis (6). Angiogenesis provides not only nutrition for tumor growth but also a channel for tumor metastasis in tumorigenesis. Therefore, inhibition of angiogenesis has broad prospects for anti-tumor and other angiogenesis-related disease therapy.

Signal transducer and activator of transcription 6 (STAT6), a member of the STAT family, reportedly participates in inflammation and tumorigenesis by regulating the transformation between M1 and M2 macrophages (7, 8). IL-4 or IL-13 bind to IL-4Rα or IL-13Rα1 on the cell surface, and activate the STAT6 signaling pathway by phosphorylating STAT6 on Tyr-641 (9). Two phosphorylated STAT6 monomers form dimers and translocate into the nucleus to bind certain promoters with the sequence of TTCnnnGAA ("n" can be A, T, G, or C) (10–12). High expression of STAT6 has been detected in many types of cancer, including non-small-cell lung cancer and colorectal cancer (13, 14). STAT6 knockout mice have a higher tolerance to lung cancer metastasis than wild-type mice (15). The mechanism of action of STAT6 in tumorigenesis is being gradually understood, but is still unclear in with respect to tumor angiogenesis.

Transmembrane glycoprotein neuropilin-1 (NRP1), which was first found in neuronal and endothelial cells, is essential for normal embryonic development, axon guidance, and angiogenesis (16). Owing to the lack of enzyme activity, NRP1 acts as a co-receptor of VEGFR2 (kinase insert domain-containing receptor; KDR) (17). VEGF binds to NRP1, which promotes the interaction of NRP1 and KDR, and activates downstream signaling events of VEGF (17). NRP1 was initially thought to enhance VEGF binding to KDR (18). However, NRP1 still promotes tumor angiogenesis, in the absence of VEGFR (19). VEGF is widely recognized as a pro-angiogenic factor for stimulating angiogenesis and blockade of the VEGF signal pathway is an effective anti-tumor therapy (20).

In this study, we found that inhibition of STAT6 activity reduced NRP1 expression, and decreased proliferation, migration, and tube-formation of endothelial cells (ECs). Activation of STAT6 by IL-13 increased NRP1 expression and increased proliferation, migration, and tube-formation of ECs. In addition, STAT6 directly bound to the *NRP1* promoter and increased its transcription activity. In the tumor xenografts model, inhibition of STAT6 activation reduced tumor angiogenesis and NRP1 expression, suggesting the therapeutic potential of STAT6 inhibitors.

MATERIAL AND METHODS

Cell Lines and Reagents

Human umbilical vein endothelial cells (HUVEC) were purchased from PromoCell (Heidelberg, Germany), and cultured in Dulbecco's modified Eagle's medium (DMEM) (Gibco, Carlsbad, CA, USA) with 10% (v/v) fetal bovine serum (FBS) (Gibco) and antibiotics (100 IU/mL penicillin and 100 mg/mL streptomycin) (Gibco). The A549 cell line was purchased from Cell Resource Center of Life Sciences (Shanghai, China), and cultured in Roswell Park Memorial Institute 1640 medium (RPMI 1640) (Gibco) containing 10% FBS (Gibco). HUVEC were treated with recombinant human IL-13 protein (50 ng/mL) (213-ILB, R&D systems, Minneapolis, MN, USA) and STAT6 inhibitor, AS1517499 (AS) (1 mM) (HY-100614, MCE, NJ, USA).

Knockdown of STAT6 and NRP1

Small interference RNA of human STAT6 and human NRP1 were purchased from GenePharma (Shanghai, China). The sequences of siRNA are shown in **Table 1**. HUVECs (2.5×10^4) were seeded in six-well plates and cultured overnight. *NRP1* siRNA (2 and 3) (100 nM) or *STAT6* siRNA (100 nM) were transfected using Lipofectamine 2000 (Invitrogen, Carlsbad, CA, USA) according to the manufacturer's instructions. Subsequent experiments were performed after cells were incubated at 37°C in a humidified atmosphere of 5% CO_2 or 21% O_2 for 48 h.

Mouse Xenograft Assays

All experimental protocols related to animals were performed in compliance with the guidelines of the Animal Care and Use Committee of the First Affiliated Hospital of Shandong First Medical University. The mouse xenograft was performed as in a previous study (21). Briefly, 10 male BALB/c nude mice (5-6 weeks old), weighing roughly 20 g were housed in a specific pathogen-free animal facility and exposed to a 12-h light/dark cycle. A549 (5×10^6) with Matrigel (356234, BD Biosciences, Franklin Lakes, NJ, USA) mixed by volume ratio 1:1 was

TABLE 1 | Sequences of siRNA used in this study.

Primer name	Sequence (5'->3')	
Negative control S	UUCUCCGAACGUGUCACGUTT	
Negative control R	ACGUGACACGUUCGGAGAATT	
Human *NRP1* S	CCAUACCAGAGAAUUAUGATT	1
Human *NRP1* R	UCAUAAUUCUCUGGUAUGGTT	
Human *NRP1* S	CAGCCUUGAAUGCACUUAUTT	2
Human *NRP1* R	AUAAGUGCAUUCAAGGCUGTT	
Human *NRP1* S	GUAUACGGUUGCAAGAUAATT	3
Human *NRP1* R	UUAUCUUGCAACCGUAUACTT	
Human *STAT6* S	AGGAAGAACUCAAGUUUAATT	
Human *STAT6* R	UUAAACUUGAGUUCUUCCUGC	

injected into the subcutaneous region (the right flanks) of mice, and tumor sizes were determined using the formula: length × width^2×0.52. Seven days after implantation, when the tumor size reached a volume of 100 mm^3, mice were randomly divided into two groups. Administration with AS1517499 (25 mg/kg intratumorally injection, twice a week) was started and lasted for 30 days.

Correlation of STAT6 and Down-Regulated Genes in Lung Adenocarcinoma

The correlation between STAT6 and angiogenesis genes in LUAD was performed *via* Gene Expression Profiling Interactive Analysis (22) (GEPIA, Zemin Zhang' Lab, Biomedical Pioneering Innovation Center, Peking University, Beijing, China; http://gepia.cancer-pku.cn/), according to a previous report (21).

Trypan Blue Staining and Cell Counting

HUVECs were seeded in 10-cm dishes and cultured overnight. AS (1 mM) was added, and the cells were incubated at 37°C in a humidified atmosphere at 5% CO_2 or 21% O_2 for 24 h. The cells were then digested with trypsin. Then, 0.4% trypan blue (Beyotime Biotechnology, Shanghai, China) was used to assess cell viability after AS treatment. The ratio of live to dead cells was calculated by a Cell Counting Equipment (Jimbio CL, Leso Technology Co., Ltd, Shandong, China) according to the manufacturer's instructions.

MTT

HUVECs (3×10^3) were seeded in 96-well plates and cultured overnight. AS (1 mM) and/or IL-13 (50 ng/mL) were added, and the cells were incubated for 0 h, 24 h, 48 h, and 72 h at 37°C in a humidified atmosphere. After incubation, 10 μL MTT solutions (5 mg/mL) were added to each well and incubated for 4 h. The colorimetric intensity was analyzed using a 96-well plate reader at a wavelength of 490 nm.

Scratch Test

HUVECs (1×10^6) were seeded in a 35 mm^2 Petri dish and cultured overnight. Two parallel mark lines were made in the bottom of the disc using a marker pen, and cells were scratched with a 1000 μL pipette tip perpendicular to the above-mentioned lines. The culture medium was removed and the cells were washed with phosphate-buffered saline (PBS). Cells were further incubated with serum-free medium, which contained AS (1 mM) and/or IL-13 (50 ng/mL). The scratches were photographed at both 0 and 20 h.

Tube-Formation Assay

HUVECs were treated with AS (1 mM) and/or IL-13 (50 ng/mL) for 24 h.

Matrigel diluted with endothelial cell basal medium-2 (EBM-2) (lonza, Basel, Switzerland) containing 2% FBS was added to a pre-chilled 96-well plate and incubated at 37°C for 40 min, and then HUVECs (2×10^4) were seeded in 96-well plates. EBM-2 was added to the cells during the process of the assay. The 96-well plate was incubated at 37°C in a humidified atmosphere for 6 h. Tube-formation was observed using an inverted light microscope (Olympus, Tokyo, Japan). ImageJ software (National Institutes of Health, Bethesda, MD, USA) was used to measure the tube length, and tube-formation was expressed as a percentage of the control group.

Vectors

The 2000-bp fragments of the *NRP1* promoter were obtained from the Eukaryotic Promoter Database (EPD, https://epd.epfl.ch//index.php). Using the *Xho*I and *Hind*III restriction sites, the *NRP1* promoter was cloned into pGL3-basic (Promega, Madison, WI) (named *NRP1*-promoter), and pRL-TK (Promega) was used as the reference control.

Dual-Luciferase Reporter Assay

HUVECs (2×10^4) were seeded in 24-well plates and cultured overnight. *NRP1*-promoter (0.5 μg) was transfected using Lipofectamine 2000 according to the manufacturer's instructions. After 24 h of transfection, AS (1 μM) and/or IL-13 (50 ng/mL) were added to the media, and the 24-well plate was incubated at 37°C in a humidified atmosphere for an additional 24 h. HUVECs in the 24-well plates were lysed for luciferase assay. Luciferase and Renilla activities were determined by a Luciferase-Renilla assay system (E1980, Promega) on an LB960 luminometer (Berthold, Germany).

Chromatin Immunoprecipitation Assay

HUVECs were fixed with 1% formaldehyde for 10 min at room temperature, and then 1× glycine solution was used to stop fixing. HUVECs were washed twice with ice-cold PBS containing an EDTA-free protease inhibitor mixture (Roche, Basel, Switzerland) and collected by a cell scraper. Fragmentation of genomic DNA was performed by sonication. Immunoprecipitation was performed using a SimpleChIP® Enzymatic Chromatin IP Kit (Magnetic Beads) (9005, Cell Signaling Technology, Danvers, MA, USA) with antibodies for STAT6 (ab32520, Abcam, Waltham, MA) according to the manufacturer's instructions. Rabbit IgG was used as a negative control. The primer sequences used are listed in **Table 2**. The PCR products were separated on 2% agarose gel and visualized under ultraviolet light (Protein Sample, Silicon Valley CA, USA).

Angiogenesis Polymerase Chain Reaction Assay and Quantitative Real-Time PCR

HUVECs (1×10^6) were seeded in a 35-mm^2 Petri dish and cultured overnight. AS (1 μM) or IL-13 (50 ng/mL) was used

TABLE 2 | Primers used in this study.

Primer name	Sequence (5'->3')	ChIP or qRT-PCR
Human *NRP1* F1	CAGGTGATGACTTCCAGCTCA	qRT-PCR
Human *NRP1* R1	CCCAGTGGCAGAAGGTCTTG	
Human *ACTIN* F1	TTGCCGACAGGATGCAGAA	qRT-PCR
Human *ACTIN* R1	GCCGATCCACACGGAGTACT	
Human *STAT6* F1	CTTTCCGGAGCCACTACAAG	qRT-PCR
Human *STAT6* R1	AGGAAGTGGTTGGTCCCTTT	
Human *NRP1* promoter F1	CTTTCCGGAGCCACTACAAG	ChIP
Human *NRP1* promoter R1	AGGAAGTGGTTGGTCCCTTT	

to treat HUVECs for 12 h. Total RNA was extracted by using RNAiso Plus (TaKaRa, Kyoto, Japan), and cDNA was synthesized by using a PrimeScript First Strand cDNA Synthesis Kit (TaKaRa) according to the manufacturer's instructions. Angiogenesis PCR array plates (Wcgene biotech, Shanghai, China) and qRT-PCR were performed by monitoring an increase in fluorescence of SYBR green dye (Tiangen, Beijing, China) using a CFX96TM Real-Time System (Bio-Rad, Hercules, CA, USA). The relative expression of RNA was calculated using actin as an endogenous internal control. Primer sequences are presented in **Table 2**.

Western Blotting

HUVECs were washed twice with ice-cold PBS and lysed with cell lysis buffer (Beyotime Biotechnology) containing an EDTA-free protease inhibitor (Roche). Tumor tissue was incubated with ice-cold cell lysis buffer containing protease inhibitor and disrupted with Tissuelyser-24. Protein concentration was quantified using the Pierce™ BCA Protein Assay Kit (Thermo Fisher Scientific, Waltham, MA, USA). Western blotting was performed as previously described (23). Blots were incubated with Pierce ™ ECL Western Blotting Substrate (Thermo Fisher), and detected by AI 680 (General Electric Company, Boston, MA) Antibodies used for western blotting included rabbit anti-phospho-STAT6 (Tyr-641, 1:1000, Cell Signaling Technology); rabbit anti-STAT6 (1:1000, Abcam); rabbit anti-NRP1 (1:1000, Affinity); rabbit anti-NRP1 (1:1000, Abcam); and rabbit anti-Tubulin (1:5000, Proteintech). The secondary antibody was horseradish peroxidase (HRP)-conjugated goat anti-rabbit immunoglobulin G (IgG) (1:8000, Proteintech).

Immunohistochemistry Staining and Immunofluorescence Staining

Immunohistochemistry staining and immunofluorescence staining were performed as described in a previous report (24). Briefly, the tumors were stripped and fixed in 4% paraformaldehyde at room temperature for 24 h, and then embedded in paraffin for sectioning. Sections were dewaxed and dehydrated using an alcohol gradient, heated, and blocked with hydrogen peroxide at room temperature. For the immunohistochemistry staining, rabbit anti-NRP1 (1:1000, affinity) was used as the primary antibodies. After rinsing with PBS, sections were incubated with a secondary antibody from the MaxVisionTM HRP-Polymer anti-mouse/rabbit IHC Kit (Maixin, China). BX51 microscopic imaging system (Olympus) was used to observe the digitized images, and microvessel density was determined with Image J software (National Institutes of Health, Bethesda, MD, USA) by quantifying NRP1-positive pixels in the digitized images. For immunofluorescence staining, mouse anti-CD31 (1:200, Abcam) and rabbit anti-NRP1 (1:200, Abcam, ab25998) were used as the primary antibodies. Alexa Fluor 488 goat anti-rabbit (1:200; Abcam) and Alexa Fluor 594 donkey anti-mouse secondary antibody (1:200; Abcam) were used as the primary antibodies. DAPI was used to display the nucleus. The sections were photographed using an Olympus LCX100 Imaging System (Olympus).

Statistical Analyses

All values are presented as mean ± standard error of the mean (SEM). Statistical analysis was performed using GraphPad Prism 9 software (GraphPad). An unpaired Student's *t*-test was used for analyses between two groups; for three or more groups, one-way analysis of variance (ANOVA) followed by Bonferroni's *post-hoc* test was used for statistical analysis. $P<0.05$ was considered to indicate statistical significance.

RESULTS

Inhibition of STAT6 Reduces Migration, Proliferation, And Tube-Formation of ECs

To assess the effect of STAT6 on EC angiogenesis, HUVECs were incubated with different concentrations of STAT6 inhibitor, AS1517499 (AS). The expression of STAT6 was not affected by AS; however, as expected, AS reduced the phosphorylation of STAT6 in a dose-dependent manner (**Figure 1A**). Incubation with 1 μM AS significantly inhibited EC migration (**Figure 1B**), cell proliferation (**Figure 1D**), and tube-formation (**Figure 1E**). Moreover, incubation with 1 μM AS did not increase cell death as compared with the control group (**Figure 1C**). STAT6 siRNA was also used to evaluate the effect of STAT6 on EC angiogenesis. Knockdown of STAT6 significantly reduced STAT6 expression at both the protein and RNA level (**Figures S1A–C**). Proliferation, tube-formation, and migration of ECs were all inhibited by STAT6 expression blockade (**Figures S1D–H**). These results suggest that inhibition of STAT6 with AS reduces EC angiogenesis.

STAT6 Regulates the Expression of Angiogenic Genes

PCR arrays were used to analyze the expression of pro-angiogenesis genes in HUVECs incubated with 1 μM AS for 24 h. Eighty-six angiogenesis-related genes were detected *via* the qPCR array. Nine genes, *NRP1, MMP2, KDR, VEGFA, CCL2, SPHK1, SMAD5, EDN1*, and *PTGS1*, were significantly down-regulated by AS treatment (**Figure 2**). To further confirm our results, the correlation of mRNA level in LUAD between STAT6 and these genes was analyzed by GEPIA. The analysis was based on the bulk gene expression datasets in the TCGA and the Genotype-Tissue Expression (GTEx) projects. The results of the scatter plot analysis indicated a positive correlation between the mRNA levels of *STAT6* and *NRP1* (R=0.41), *STAT6* and *MMP2* (R=0.39), *STAT6* and *KDR* (R=0.29), *STAT6* and *VEGFA* (R=0.2), *STAT6* and *CCL2* (R=0.23), *STAT6* and *SPHK1* (R=0.36), *STAT6* and *SMAD5* (R=0.2), *STAT6* and *EDN1* (R=0.25), and *STAT6* and *PTGS1* (R=0.27) (**Figure S2**). These data suggest that STAT6 regulates lung tumor angiogenesis by mediating the expression of pro-angiogenic genes.

STAT6 Affects the Expression of NRP1

The correlation scores between the mRNA levels of *STAT6* and *NRP1* was the highest in these candidate genes. To further determine whether NRP1 expression was regulated by STAT6, we

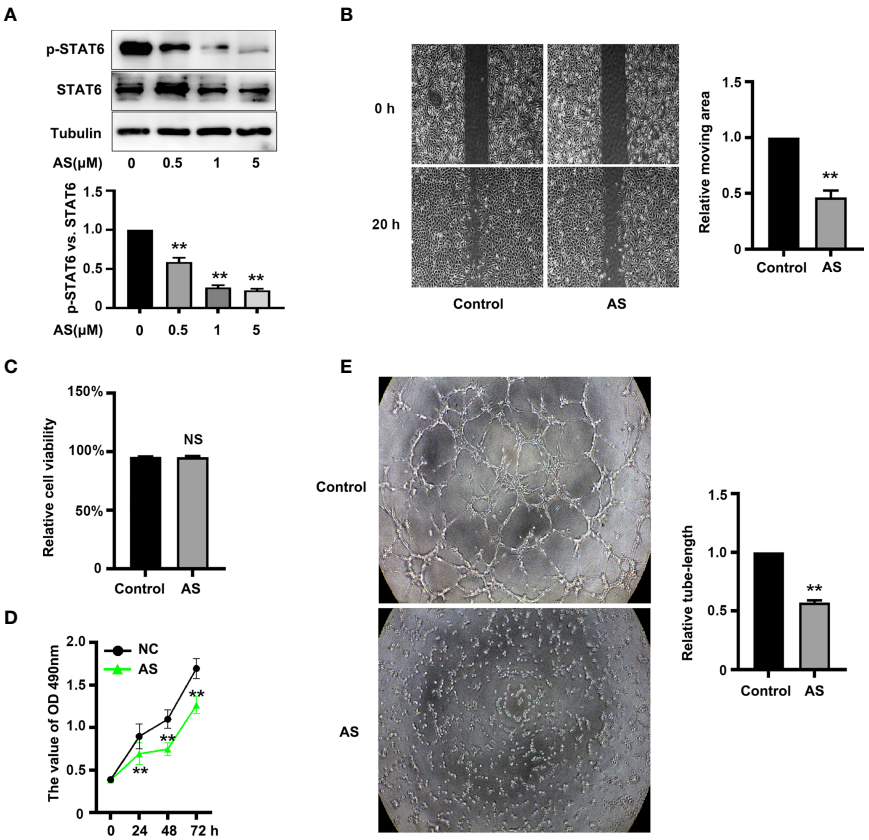

FIGURE 1 | AS treatment reduces STAT6 activity and inhibits HUVEC migration, proliferation, and tube-formation. **(A)** Phosphorylation of STAT6 was detected by western blotting in HUVECs treated with 0.5, 1, or 5 μM AS for 24 h, n=3, **P*<0.05 vs. control. **(B)** The typical images and the relative moving area of HUVECs treated with AS (1 μM) for 20 h, n=5, ***P*<0.01 vs. control. **(C)** The relative cell viability of HUVECs treated with AS (1 μM) for 24 (h.) NS denotes no significant difference, **(D)** The cell growth curve of HUVECs treated with AS (1 μM) for 0 h, 24 h, 48 h, and 72 h, n=5, ***P*<0.01 vs. control. **(E)** The typical images of STAT6 affected HUVECs tube-formation. HUVECs were treated with AS (1 μM) for 24 h, n=5, **P<0.01 vs. control.

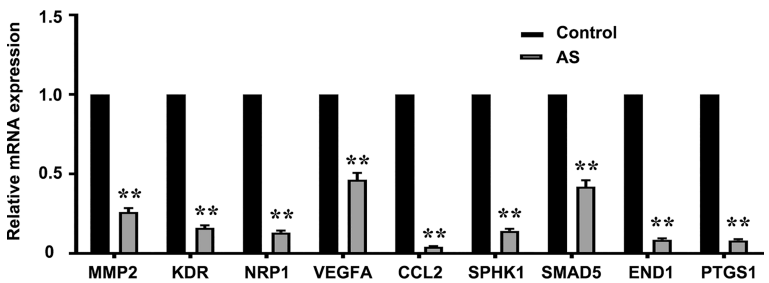

FIGURE 2 | AS treatment reduces pro-angiogenesis gene expression. Pro-angiogenesis genes were detected by PCR in HUVECs treated with an inhibitor of STAT6 (1 μM) for 24 h. ***P*<0.01 vs. control. MMP2, matrix metalloproteinase-2; KDR, kinase insert domain-containing receptor; NRP1, neuropilin-1; VEGFA, vascular endothelial growth factor A; CCL2/MCP-1, monocyte chemoattractant protein-1; SPHK1, sphingosine kinase 1; SMAD5, mothers against DPP homolog 5; EDN1, endothelin-1; PTGS1/COX1, cyclooxygenase 1.

detected NRP1 expression in the presence of STAT6 inhibitor (AS) or activator (IL-13). We found that AS treatment significantly reduced the protein and mRNA expression of NRP1 (**Figures 3A–C**). In contrast, IL-13 increased NRP1 protein and mRNA expression (**Figures 3D–F**). In addition, NRP1 expression was detected by qPCR and western blotting when HUVECs were treated with AS (1 μM), IL-13 (50 ng/mL), and AS combined with IL-13. AS reduced the phosphorylation of STAT6, which was

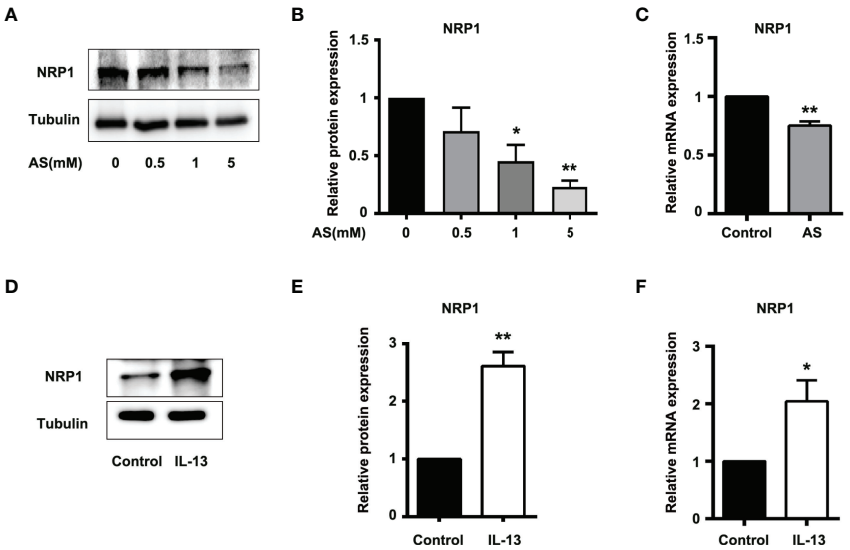

FIGURE 3 | STAT6-mediated NRP1 expression in HUVECs. **(A)** Expression of NRP1 was detected by western blotting in HUVECs treated with 0.5, 1, or 5 μM AS for 24 (h) **(B)** Relative NRP1 expression normalized with tubulin after AS treatment, n=3, **P*<0.05 vs. control, ***P*<0.01 vs. control. **(C)** Expression of *NRP1* was detected by qPCR in HUVECs treated with AS (1 μM) for 24 h, n=3, ***P*<0.01 vs. control. **(D)** Expression of NRP1 was detected by western blotting in HUVECs treated with IL-13 (50 ng/mL) for 24 (h) **(E)** Relative NRP1 expression normalized with tubulin after IL-13 treatment, n=3, **P*<0.05 vs. control, ***P*<0.01 vs. control. **(F)** Expression of NRP1 was detected by qPCR in HUVECs treated with IL-13 (50 ng/mL) for 24 h, n=3, ***P*<0.01 vs. control.

induced by IL-13 (**Figures 4A, B**). Furthermore, the increasing NRP1 was inhibited by AS treatment (**Figure 4C**). The mRNA level of NRP1 was reduced by AS treatment, and increased by IL-13 treatment. AS reduced NRP1 expression even in the presence of IL-13 (**Figure S3**). Knockdown of STAT6 by STAT6 siRNA was used to evaluate the effect of IL-13 on NRP1 expression. Western blotting showed that knockdown of STAT6 reduced NRP1 expression even in the presence of IL-13 (**Figure S4**). Taken together, these findings suggest that the STAT6 signal pathway promotes NRP1 expression.

STAT6/NRP1 Signal Pathway Regulates EC Proliferation, Migration, and Tube-Formation

To explore the role of the STAT6 signaling pathway in EC angiogenesis, we assessed the effect of AS (1 μM), IL-13 (50 ng/mL), or AS combined with IL-13 treatment on EC proliferation, migration, and tube-formation. IL-13 treatment for 24 h did not affect the proliferation of HUVECs. When the proliferation time was prolonged to 48 h, IL-13 treatment modestly increased the proliferation of HUVECs (**Figure 4D**). For the AS and IL-13 co-treatment group, AS treatment abolished the promoting effect of IL-13 on HUVEC proliferation (**Figure 4D**). Moreover, migration of HUVEC was also modestly increased by IL-13 treatment, and AS treatment abolished the promoting effect of IL-13 on HUVEC migration (**Figures 4E, F**). Tube-formation was increased by IL-13 treatment, and AS treatment abolished the promoting effect of IL-13 on HUVEC tube-formation (**Figures 4G, H**). Similar results were obtained by disrupting STAT6 expression. Knockdown of STAT6 also inhibited EC proliferation. Furthermore, knockdown of STAT6 reduced migration, and tube-formation, induced by IL-13 (**Figure S1**). In addition, knockdown of NRP1 by siRNA also reduced EC proliferation, and inhibited EC migration and tube-formation even in the presence of IL-13 (**Figures S5** and **S6**). These results suggested that the STAT6 signaling pathway promotes EC angiogenesis.

STAT6 Regulates NRP1 Expression by Binding to its Promoter

The positive role of NRP1 in angiogenesis has been wide verified (25, 26). To discover the mechanism of STAT6-regulated NRP1 expression, we first analyzed the effect of AS and IL-13 treatment on the promoter activity of *NRP1*. Luciferase assay showed that the promoter activity of *NRP1* is much higher than the promoter activity of pGL3-basic, and AS treatment significantly inhibited the promoter activity of *NRP1* when compared with non-AS treatment (**Figure 5A**). IL-13 increased the phosphorylation of STAT6, and the promoter activity of *NRP1* was enhanced by IL-13 incubation (**Figure 5B**). Compared with the control group, co-treatment with both IL-13 and AS reduced the promoter activity of *NRP1*, but there was no significant difference between the co-treatment group and AS treatment group (**Figure S7**). Taken together, these results showed that inhibition of STAT6 reduced promoter activity of *NRP1*. We further searched the binding sequences of STAT6 in the promoter region of human *NRP1* and assessed the homologous sequences of STAT6 binding sites between different species. Sequence analysis indicated that one presumptive STAT6 binding site located at the promoter regions of human *NRP1* was from -1613 to -1605. These sequences were highly homologous with *M. musculus* (-1663 to -1655), *R.*

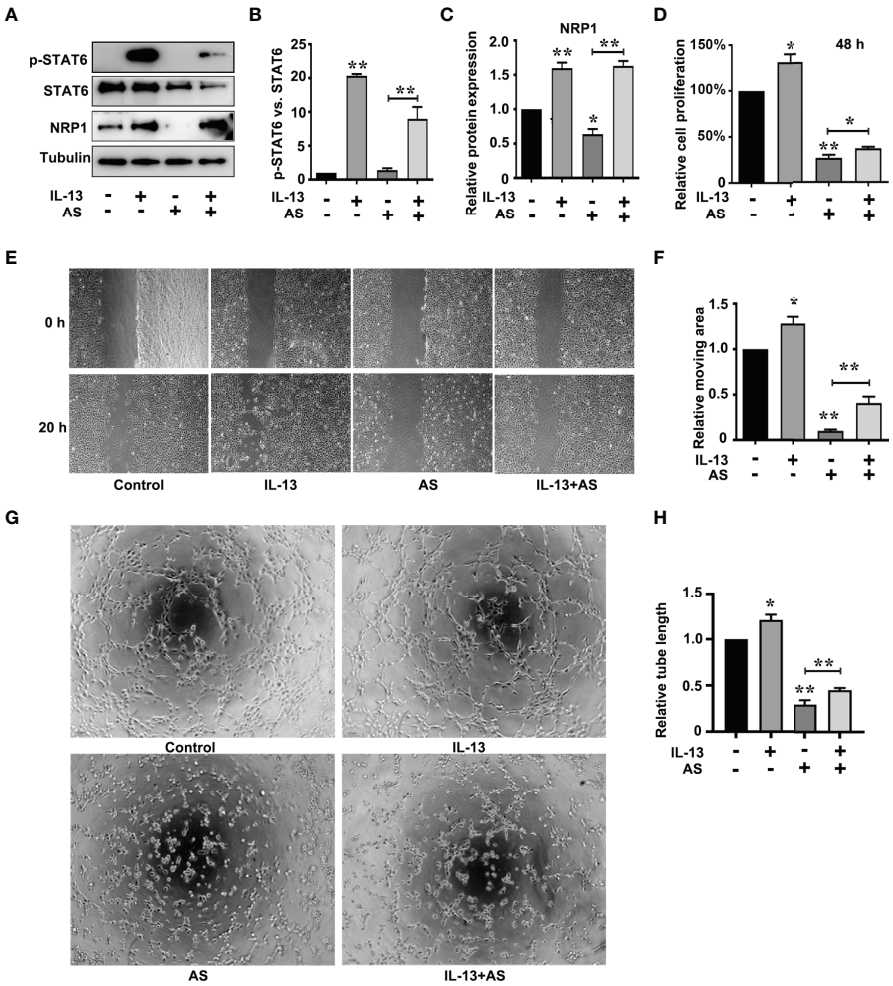

FIGURE 4 | STAT6-mediated NRP1 expression and promotes migration, proliferation, and tube-formation in HUVECs. **(A)** Phosphorylation of STAT6, STAT6, and NRP1 were detected by western blotting in HUVECs treated with AS (1 μM), IL-13 (50 ng/mL), and AS combined with IL-13 for 24 (h) **(B)** Relative STAT6 phosphorylation level was normalized with STAT6, n=3, ***P*<0.01 vs. control. **(C)** Relative NRP1 expression normalized with tubulin after AS and IL-13 treatment, n=3, **P*<0.05 vs. control, ***P*<0.01 vs. control. **(D)** The relative cell proliferation was detected by MTT in HUVECs treated with AS (1 μM), IL-13 (50 ng/mL), and AS combined with IL-13 for 48 h, n=5, **P*<0.05 vs. control, ***P*<0.01 vs. control. **(E, F)** The typical images and the relative moving area of HUVECs treated with AS (1 μM), IL-13 (50 ng/mL), and AS combined with IL-13 for 20 h, n=5, **P*<0.05 vs. control, ***P*<0.01 vs. control. **(G, H)** Typical images and relative tube length of HUVECs treated with AS (1 μM), IL-13 (50 ng/mL), and AS combined with IL-13 for 24 h, n=5, **P*<0.05 vs. control, ***P*<0.01 vs. control.

norvegicus (-1651 to -1643), *S. scrofa* (-1530 to -1522), and *B. taurus* (-1562 to -1554) (**Figure 5C**). Therefore, a ChIP primer was designed according to the regions from -1613 to -1605 of the human *NRP1* promoter. We found that enrichment of STAT6 at the *NRP1* promoter; AS treatment reduced this enrichment, and incubation with IL-13 modestly enhanced the enrichment (**Figures 5D, E**). These results suggest that STAT6 binds to the promoter region of *NRP1* and enhances NRP1 expression.

Inhibition of STAT6 Activity Suppresses Tumor Angiogenesis and NRP1 Expression *In Vivo*

Nude mice xenograft assay was performed to further evaluate the *in vivo* effect of STAT6 on angiogenesis. After being administered with AS for 30 days, we found that the bodyweight of the xenograft mice was not affected by AS treatment (**Figure 6A**), and the tumor size and tumor weight were suppressed by AS treatment (**Figures 6B–D**). These results confirmed that AS treatment inhibited the growth of tumor xenografts in nude mice. We further explored the effects of AS treatment on tumor angiogenesis. CD31 was used as an EC marker, and IHC assay found that AS administration reduced vascular density (**Figures 6E, F**). Moreover, the expression of STAT6 and NRP1 were also detected in subcutaneous tumors. As expected, the phosphorylation of STAT6 was down-regulated by AS administration, and the expression of NRP1 was also reduced (**Figures 6G–I**). *In situ* analysis of NRP1 level by immunostaining and immunofluorescence staining showed that AS treatment

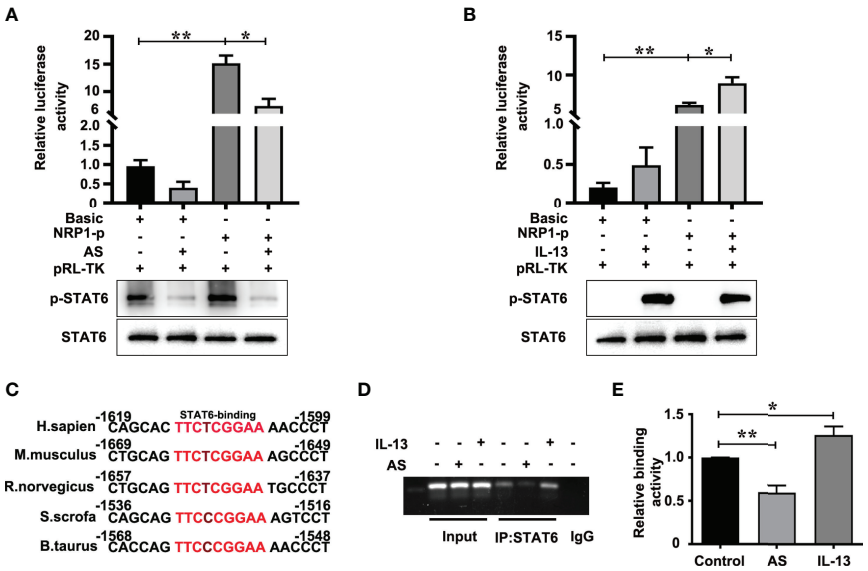

FIGURE 5 | STAT6 directly targets the *NRP1* promoter in HUVECs. **(A)** Luciferase assay in HUVECs after transfection with pGL3-Basic (Basic) or pGL3-*NRP1* prompter (*NRP1*-p) and then treated with or without AS (1 μM AS) for 24 (h) The level of phosphorylation of STAT6 and total STAT6 were also detected by western blotting, n=3, **P*<0.05, *NRP1*-p vs. *NRP1*-p treated with AS, ***P*<0.01 *NRP1*-p vs. basic. **(B)** Luciferase assay in HUVECs after transfection with pGL3-Basic (Basic) or pGL3-*NRP1* prompter (*NRP1*-p) and then treated with or without IL-13 (50 ng/mL) for 24 (h) The level of phosphorylation of STAT6 and total STAT6 were also detected by western blotting, n=3, **P*<0.05, *NRP1*-p vs. *NRP1*-p treated with IL-13, ***P*<0.01 *NRP1*-p vs. basic. **(C)** The conserved sequence of STAT6 binding sites in the *NRP1* promoter sequence were compared between different species. **(D, E)** ChIP assay was performed using anti-STAT6 antibody in HUVECs after treatment with AS (1 μM) or IL-13 (50 ng/mL) for 24 h, and then amplified by PCR, n=3, **P*<0.05 vs. control, ***P*<0.01 vs. control.

reduced the expression of NRP1 was in the entire cell type compared with control group (**Figure S8**). These results confirmed that STAT6 regulates the expression of NRP1 and affects tumor angiogenesis *in vivo*.

DISCUSSION

In 1971, Folkman reported that solid neoplasms are always accompanied by angiogenesis, and the new capillary supported tumor growth and metastasis (27). Anti-angiogenesis was then developed as a strategy for tumor treatment, and it has already been used in anti-tumor combined therapy. Apatinib, an inhibitor of VEGFR, and bevacizumab, humanized anti-VEGF monoclonal antibodies, have been used to treat non-small-cell lung cancer combined with PD-L1 antibody or chemotherapy (28). More anti-angiogenesis targets are needed for the cocktail of antibodies or inhibitors. In our study, we found that STAT6 was a potential target for anti-angiogenesis therapy. Activation of STAT6 promoted proliferation, migration, and tube-formation of HUVECs and inhibition of STAT6 reduced proliferation, migration, and tube-formation of HUVECs. We also confirmed the mechanisms of STAT6 affecting EC function by binding to the promoter of *NRP1* and increasing NRP1 expression (**Figure 7**). Thus, STAT6 is a potential therapeutic target for anti-tumor angiogenesis.

STAT6 is generally recognized as a transcription factor that promotes M2 polarization of macrophages (29). Recently, the effect of STAT6 on angiogenesis has also been reported. VEGF treatment increases the nuclear translocation of STAT6 and promotes EC migration (30). Silencing STAT6 with siRNA inhibits VEGF-induced *in vivo* angiogenesis (30). In human LUAC squamous cell carcinoma, high expression of STAT6 has been detected (31). STAT6 deficiency with siRNA inhibits carcinogen-induced lung cancer growth and improves prognosis in cancer transplantation mice model (31). Inhibitor of STAT6 (AS1517499) combined with 5-fluorouracil markedly reduce the tumor load (32). In an orthotopic 4T1 mammary carcinoma mouse model, AS1517499 treatment attenuated tumor growth and early liver metastasis (33). In our study, AS1517499 administration for both HUVECs and nude mouse xenograft showed that inhibition of STAT6 reduced proliferation, migration, and tube-formation of HUVECs and reduced tumor size and tumor angiogenesis in a mouse xenograft model. Our results are similar to previous reports.

IL-13 is an inflammatory factor that has multiple functions including regulation of tumor development (11). IL-13 activates STAT6 and promotes the M2 polarization of macrophages. The conditioned medium of IL-13-treated M2 macrophages induces tumor invasion, migration, and angiogenesis of A549 and H1299 cells (34). In our study, IL-13 was also used to incubate HUVECs, and we found that IL-13 treatment modestly promoted the proliferation and migration of HUVECs. Co-treatment with AS1517499 blocked the promotion of proliferation and migration induced by IL-13. These data suggested the target role of STAT6 for anti-angiogenesis therapy.

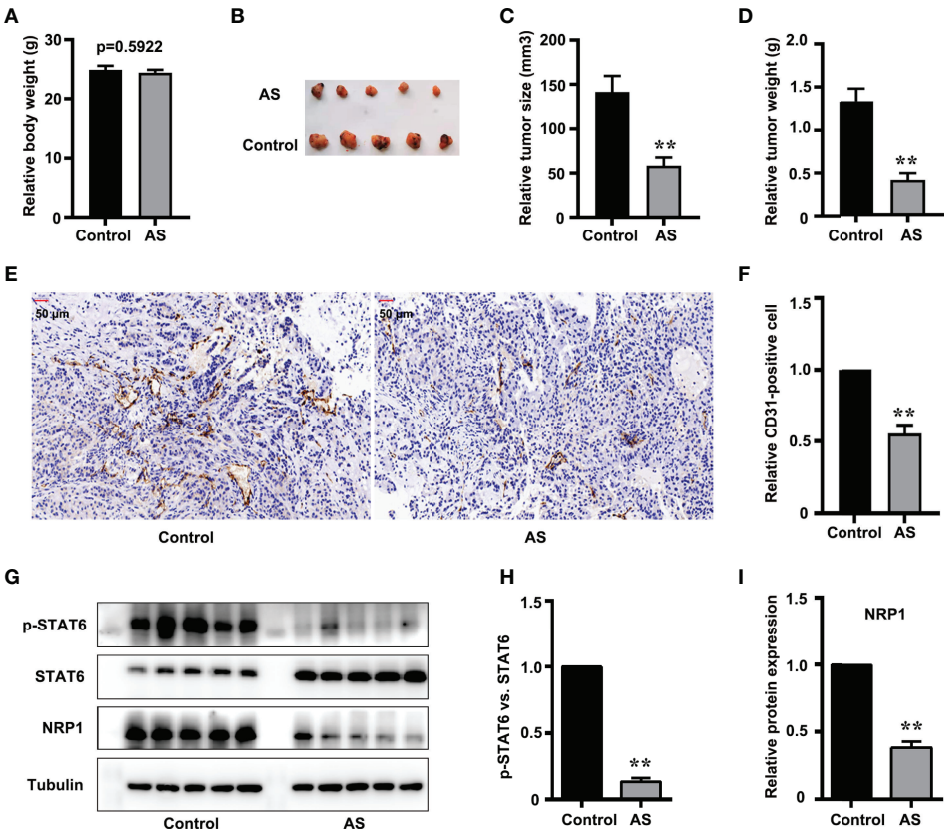

FIGURE 6 | Inhibition of STAT6 reduces xenograft growth and tumor angiogenesis *in vivo*. **(A)** Body weights were measured before all nude mice were killed. **(B)** Resected subcutaneous tumors from indicated A549 cell-injected groups in nude mice. **(C, D)** Tumor weight and tumor volume were measured, n=5, $^{**}P<0.01$ vs. control. **(E, F)** Vascular intensity by A549 cell-derived tumor treated with AS (25 mg/kg body weight) was evaluated by IHC with anti-CD31 antibody. Scale bar: 50 μm. n=5, $^{**}P<0.01$ vs. control. **(G)** Phosphorylation of STAT6, STAT6, and NRP1 were detected by western blotting in tumor tissue. **(H)** Relative STAT6 phosphorylation level normalized with STAT6, n=5, $^{**}P<0.01$ vs. control. **(I)** Relative NRP1 expression normalized with tubulin, n=5, $^{**}P<0.01$ vs. control.

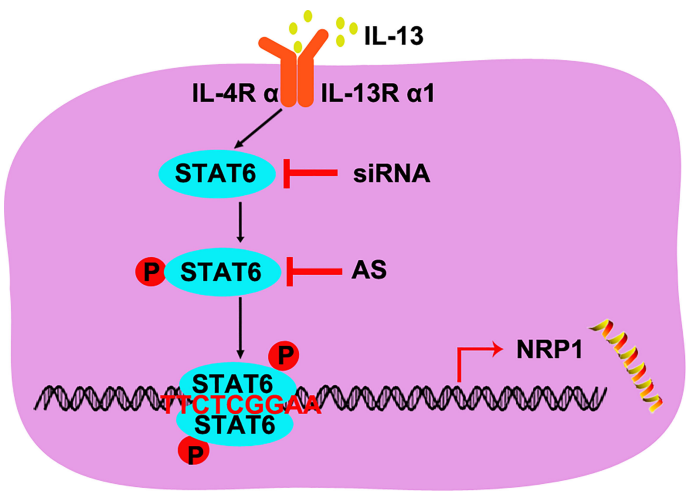

FIGURE 7 | A schematic underlying the mechanism of STAT6-promoted NRP1 expression in HUVECs.

To explore the mechanisms of STAT6-mediated angiogenesis, we further detected the expression of pro-angiogenic genes. Inhibition of STAT6 activity reduced the expression of *CCL2*, *MMP2*, *KDR*, *NRP1*, *VEGFA*, *SPHK1*, *SMAD5*, *EDN1*, and *PTGS1*. Some of these genes are reportedly regulated by STAT6. For instance, activation of STAT6 binds upstream of the VEGF promoter (from -338 to -305 bp) in mouse ECs and promotes VEGF expression (30). IL-13 selectively increases CCL2 expression and secretion through IL-4Rα and STAT6 phosphorylation in HUVECs (35). Inhibition of IL-4Rα/STAT6 signal pathway by anti IL-4Rα antibody reduces CCL2 expression (35). IL-13 also promotes EC angiogenesis by activating STAT6 and then increasing the expression of vascular cell adhesion molecule-1 (VCAM-1) and soluble VCAM-1 (36). In HT-1080 tumor cells, progesterone-induced blocking factor (PIBF) treatment increases STAT6 phosphorylation, and inhibition of PIBF with siRNA significantly reduces MMP2 expression (37). These data suggest that STAT6 regulates lung tumor angiogenesis by mediating the expression of pro-angiogenic genes.

NRP1 is identified as a receptor for VEGFA165 and class-3 semaphorins, and is crucial for mouse and zebrafish vascular development as well as pathological angiogenesis (25, 26). Although semaphorin-NRP1 signaling is not essential for vascular development in mouse embryos, semaphorin 3A (SEMA3A) participates in modulating tumor angiogenesis in mouse cancer models (38). It has been reported that SEMA 3A inhibited VEGF-mediated angiogenesis in an NRP1-dependent manner (39), and over-expression of SEMA 3A induced EC apoptosis and promoted vascular maturation by recruiting pericytes and monocytes expressing NRP1 (40, 41). Both SEMA 3A and VEGF increased vascular permeability in an NRP1-dependent manner; however, they used distinct downstream effectors (39). Another study also reported that SEMA3A could induce permeability signaling by NRP2 and VEGFR1, independent of NRP1 (42). Therefore, NRP1 is essential for transmitting both VEGF and SEMA 3A signals to regulate tumor angiogenesis. It has been reported that recombinant rat NRP-1 chimera treatment increases tubular morphogenesis and cell migration of human dermal microvascular endothelial cells (HDMECs) and HUVECs (43). In patients with non-small cell lung cancer (NSCLC), high expression of NRP1 has shorter overall survival than in patients with low expression of NRP1. Inhibition of NRP1 suppresses tumor migration and angiogenesis (44). In our study, the correlation score between the mRNA levels of *STAT6* and *NRP1* was the highest in the potential target molecules. We found that IL-13 treatment up-regulated the expression of NRP1, and AS1517499 administration reduced the expression of NRP1 in HUVECs. Interestingly, AS1517499 blocked the promotion of NRP1 expression induced by IL-13. All this evidence indicates that NRP1 is a new target for STAT6 in regulating EC angiogenesis.

We extensively explored the underlying mechanisms by which STAT6 regulates NRP1 expression. As an important component of the VEGF signal pathway, multiple regulatory elements regulate NRP1 expression in a cooperative manner. There are one AP1 element and two SP1 elements that contributed to constitutive and tumor promoter-induced promoter activity of *NRP1* in HeLa cells (45). TEA domain transcription factor (TEAD) binding motif is also present in the promoter region of *NRP1*, and the expression of NRP1 is regulated by TEAD in hepatocellular carcinoma (HCC) (46). In the present study, we found the binding site of STAT6 (TTCnnnGGA sequence) (12) in the promoter region of *NRP1*, which was conserved in many species. Luciferase assay demonstrated that activation of STAT6 by IL-13 increased the transcription activity of *NRP1* promoter, while inhibition of STAT6 activity by AS1517499 significantly reduced *NRP1* promoter transcription activity. ChIP assay demonstrated that STAT6 is directly bound to promoter region of *NRP1* in HUVECs.

The impact of STAT6 inhibition on NRP1 mRNA levels (**Figure 3C**) is modest. The involvement of other factors involved in the regulation of NRP1 expression cannot be overlooked. In fact, both SP1 and HIF-1α positively regulate NRP1 expression in tumor cells (47, 48). STAT6 interacted with SP1 and increased the expression of p21 and p27 in promoting breast cancer cell proliferation (49). In B-lymphoblastoid cell line, type I IFN-activated STAT6 could increase Sp1 and BCL6 through STAT2 and exert the anti-proliferative effects (50). In glioma cells, STAT6 negatively regulated HIF-1α expression *via* mTOR/S6K/S6 axis (51). Although the binding of STAT6 to the NRP1 promoter was detected in our study, the experimental results indicated that other mediators participated in the regulation of NRP1 expression by STAT6. This regulation could also rely on an indirect mechanism. As discussed earlier, STAT6 can influence tumor angiogenesis through factors such as VCAM-1 and MMP (36, 37), and NRP1 is not the only target molecule of STAT6.

Taken together, our results indicate that STAT6 promotes EC proliferation, migration, and tube-formation. In addition, STAT6 upregulates NRP1 expression in ECs and promotes angiogenesis. Therefore, STAT6 may be considered potential therapeutic target for anti-angiogenic therapy.

DATA AVAILABILITY STATEMENT

The raw data supporting the conclusions of this article will be made available by the authors, without undue reservation.

ETHICS STATEMENT

The animal study was reviewed and approved by Animal Care and Use Committee of the First Affiliated Hospital of Shandong First Medical University.

AUTHOR CONTRIBUTIONS

PG and JL conceived and designed the experiments. PG and GR performed the experiments. PG, GR, and JJL analyzed the data. PG, GR, and JL wrote the paper. JL reviewed and edited the paper. All authors contributed to the article and approved the submitted version.

FUNDING

This study was supported by the Natural Science Foundation of Shandong Province (ZR2019BH007), the foundation of Qianfoshan Hospital (QYPY2020NSFC0820), the Jinan City's Science and Technology Innovation Program of Clinical Medicine (202019175), the National Nature Science Foundation of China (81873473), Academic Promotion Program of Shandong First Medical University (2019QL014), and Shandong Taishan Scholarship (JL).

SUPPLEMENTARY MATERIAL

The Supplementary Material for this article can be found online at: https://www.frontiersin.org/articles/10.3389/fonc.2022.823377/full#supplementary-material

Supplementary Figure 1 | Knockdown of STAT6 inhibits HUVEC proliferation, tube-formation, and migration. **(A)** The expression of STAT6 was detected by western blotting in HUVECs after transfected with STAT6 siRNA for 48 h. **(B)** The relative STAT6 expression normalized with tubulin, n=3, **P*<0.05 vs. control. **(C)** The mRNA level of STAT6 was detected by qPCR in HUVECs after transfected with STAT6 siRNA for 48 h, n=3, ***P*<0.01 vs. control. **(D)** After transfected with STAT6 siRNA for 48 h, HUVECs were cultured for 0 h, 24 h, 48 h, and 72 h, the cell growth curve of HUVECs were detected by MTT, n=5, ***P*<0.01 vs. control. **(E, F)** After transfected with STAT6 siRNA for 48 h, The typical images and relative tube length of HUVECs were detected in the presence or absence of IL-13 (50 ng/mL), n=5, **P*<0.05 vs. control, NS, no significant difference. **(G, H)** After transfected with STAT6 siRNA for 48 h, the typical images and the relative moving area of HUVECs treated with or without IL-13 (50 ng/mL) for 20 h, n=5, ***P*<0.01 vs. control, NS denotes no significant difference.

Supplementary Figure 2 | STAT6 expression in LUAD tissues is positively correlated with *MMP2*, *KDR*, *NRP1*, *VEGFA*, *CCL2*, *SPHK1*, *SMAD5*, *EDN1*, and *PTGS1* levels. A-I, Scatter plot analysis of the correlation between mRNA levels of *STAT6* and *MMP2*, *KDR*, *NRP1*, *VEGFA*, *CCL2*, *SPHK1*, *SMAD5*, *EDN1* or *PTGS1* in LUAD of tissues.

Supplementary Figure 3 | AS treatment reduces NRP1 mRNA levels in presence of IL13 stimulation. The mRNA levels of NRP1 were detected by qPCR in HUVECs treated with AS (1 μM), IL-13 (50 ng/mL), and AS combined with IL-13 for 24 h. Relative NRP1 mRNA levels were normalized with actin, n=3, ***P*<0.01 vs. control, NS denotes no significant difference.

Supplementary Figure 4 | Knockdown of STAT6 reduces NRP1 expression in the presence of IL-13 in HUVECs. **(A)** Phosphorylation of STAT6, STAT6, and NRP1 were detected by western blotting in STAT6 knockdown of HUVECs treated with or without IL-13 (50 ng/mL). **(B)** Relative NRP1 expression was normalized with Tubulin, n=3, **P*<0.05 vs. control, NS denotes no significant difference.

Supplementary Figure 5 | Knockdown of NRP1 by NRP1 siRNA 2 inhibits HUVEC migration, proliferation, and tube-formation. **(A)** The expression of NRP1 was detected by western blotting in HUVECs after transfected with NRP1 siRNA 2 for 48 h. **(B)** The relative NRP1 expression normalized with tubulin, n=3, **P*<0.05 vs. control. **(C)** The mRNA level of NRP1 was detected by qPCR in HUVECs after transfected with NRP1 siRNA 2 for 48 h, n=3, ***P*<0.01 vs. control. **(D)**, After transfected with NRP1 siRNA 2 for 48 h, HUVECs were cultured for 0 h, 24 h, 48 h, and 72 h, the cell growth curve of HUVECs were detected by MTT, n=5, ***P*<0.01 vs. control. **(E, F)** After transfected with NRP1 siRNA 2 for 48 h, The typical images and relative tube length of HUVECs were detected in the presence or absence of IL-13 (50 ng/mL) n=5, ***P*<0.01 vs. control, NS denotes no significant difference. **(G, H)** After transfected with NRP1 siRNA 2 for 48 h, the typical images and the relative moving area of HUVECs treated with or without IL-13 (50 ng/mL) for 20 h, n=5, **P*<0.05 vs. control, NS denotes no significant difference.

Supplementary Figure 6 | Knockdown of NRP1 by NRP1 siRNA 3 inhibits HUVEC migration, proliferation, and tube-formation. **(A)** The expression of NRP1 was detected by western blotting in HUVECs after transfected with NRP1 siRNA 3 for 48 h. **(B)** The relative NRP1 expression normalized with tubulin, n=3, **P*<0.05 vs. control. **(C)** The mRNA level of NRP1 was detected by qPCR in HUVECs after transfected with NRP1 siRNA 3 for 48 h, n=3, ***P*<0.01 vs. control. **(D)**, After transfected with NRP1 siRNA 3 for 48 h, HUVECs were cultured for 0 h, 24 h, 48 h, and 72 h, the cell growth curve of HUVECs were detected by MTT, n=5, ***P*<0.01 vs. control. **(E, F)** After transfected with NRP1 siRNA 3 for 48 h, The typical images and relative tube length of HUVECs were detected in the presence or absence of IL-13 (50 ng/mL) n=5, ***P*<0.01 vs. control, NS denotes no significant difference. **(G, H)** After transfected with NRP1 siRNA 3 for 48 h, the typical images and the relative moving area of HUVECs treated with or without IL-13 (50 ng/mL) for 20 h, n=5, **P*<0.05 vs. control, NS denotes no significant difference.

Supplementary Figure 7 | Inhibition of STAT6 reduces the promoter activity of NRP1 in the presence of IL-13. Luciferase assay in HUVECs after transfection with pGL3-*NRP1* prompter (*NRP1*-p) and then treated with AS (1 μM), IL-13 (50 ng/mL), and AS combined with IL-13 for 24 h, n=5, ***P*<0.01 vs. control, NS denotes no significant difference.

Supplementary Figure 8 | Inhibition of STAT6 reduces expression of NRP1 *in vivo*. **(A)** The expression of NRP1 in A549 cell-derived tumor treated with or without AS (25 mg/kg body weight) was evaluated by IHC with anti-NRP1 antibody. Scale bar: 50 μm. **(B)** Relative NRP1 positive cell, n=5, ***P*<0.01 vs. control. **(C)** The expression of NRP1 in A549 cell-derived tumor treated with or without AS (25 mg/kg body weight) was evaluated by immunofluorescence with anti-NRP1 antibody (green) and anti-CD31 antibody (red). DAPI was used to display the nucleus. Scale bar: 50 μm.

REFERENCES

1. Goncalves RC, Banfi A, Oliveira MB, Mano JF. Strategies for Re-Vascularization and Promotion of Angiogenesis in Trauma and Disease. *Biomaterials* (2021) 269:120628. doi: 10.1016/j.biomaterials.2020.120628
2. Carmeliet P, Jain RK. Angiogenesis in Cancer and Other Diseases. *Nature* (2000) 407(6801):249–57. doi: 10.1038/35025220
3. Carmeliet P. Angiogenesis in Health and Disease. *Nat Med* (2003) 9(6):653–60. doi: 10.1038/nm0603-653
4. DeBerardinis RJ, Chandel NS. Fundamentals of Cancer Metabolism. *Sci Adv* (2016) 2(5):e1600200. doi: 10.1126/sciadv.1600200
5. Gao P, Niu N, Wei T, Tozawa H, Chen X, Zhang C, et al. The Roles of Signal Transducer and Activator of Transcription Factor 3 in Tumor Angiogenesis. *Oncotarget* (2017) 8(40):69139–61. doi: 10.18632/oncotarget.19932
6. Finger EC, Giaccia AJ. Hypoxia, Inflammation, and the Tumor Microenvironment in Metastatic Disease. *Cancer Metastasis Rev* (2010) 29 (2):285–93. doi: 10.1007/s10555-010-9224-5
7. Lin Y, Li B, Yang X, Liu T, Shi T, Deng B, et al. Non-Hematopoietic STAT6 Induces Epithelial Tight Junction Dysfunction and Promotes Intestinal Inflammation and Tumorigenesis. *Mucosal Immunol* (2019) 12(6):1304–15. doi: 10.1038/s41385-019-0204-y
8. Huang S, Dong D, Zhang Y, Chen Z, Geng J, Zhao Y. NEAT1 Regulates Th2 Cell Development by Targeting STAT6 for Degradation. *Cell Cycle* (2019) 18 (3):312–9. doi: 10.1080/15384101.2018.1562285
9. Knight JM, Mandal P, Morlacchi P, Mak G, Li E, Madison M, et al. Small Molecule Targeting of the STAT5/6 Src Homology 2 (SH2) Domains to Inhibit Allergic Airway Disease. *J Biol Chem* (2018) 293(26):10026–40. doi: 10.1074/jbc.RA117.000567
10. Stark GR, Darnell JE Jr. The JAK-STAT Pathway at Twenty. *Immunity* (2012) 36(4):503–14. doi: 10.1016/j.immuni.2012.03.013
11. Terabe M, Park JM, Berzofsky JA. Role of IL-13 in Regulation of Anti-Tumor Immunity and Tumor Growth. *Cancer Immunol Immunother* (2004) 53 (2):79–85. doi: 10.1007/s00262-003-0445-0
12. Szanto A, Balint BL, Nagy ZS, Barta E, Dezso B, Pap A, et al. STAT6 Transcription Factor Is a Facilitator of the Nuclear Receptor PPARgamma-

Regulated Gene Expression in Macrophages and Dendritic Cells. *Immunity* (2010) 33(5):699–712. doi: 10.1016/j.immuni.2010.11.009
13. Pastuszak-Lewandoska D, Domanska-Senderowska D, Antczak A, Kordiak J, Gorski P, Czarnecka KH, et al. The Expression Levels of IL-4/IL-13/STAT6 Signaling Pathway Genes and SOCS3 Could Help to Differentiate the Histopathological Subtypes of Non-Small Cell Lung Carcinoma. *Mol Diagn Ther* (2018) 22(5):621–9. doi: 10.1007/s40291-018-0355-7
14. Wang CG, Ye YJ, Yuan J, Liu FF, Zhang H, Wang S. EZH2 and STAT6 Expression Profiles Are Correlated With Colorectal Cancer Stage and Prognosis. *World J Gastroenterol* (2010) 16(19):2421–7. doi: 10.3748/wjg.v16.i19.2421
15. Ostrand-Rosenberg S, Clements VK, Terabe M, Park JM, Berzofsky JA, Dissanayake SK. Resistance to Metastatic Disease in STAT6-Deficient Mice Requires Hemopoietic and Nonhemopoietic Cells and Is IFN-Gamma Dependent. *J Immunol* (2002) 169(10):5796–804. doi: 10.4049/jimmunol.169.10.5796
16. Liu C, Somasundaram A, Manne S, Gocher AM, Szymczak-Workman AL, Vignali KM, et al. Neuropilin-1 Is a T Cell Memory Checkpoint Limiting Long-Term Antitumor Immunity. *Nat Immunol* (2020) 21(9):1010–21. doi: 10.1038/s41590-020-0733-2
17. Herzog B, Pellet-Many C, Britton G, Hartzoulakis B, Zachary IC. VEGF Binding to NRP1 Is Essential for VEGF Stimulation of Endothelial Cell Migration, Complex Formation Between NRP1 and VEGFR2, and Signaling *via* FAK Tyr407 Phosphorylation. *Mol Biol Cell* (2011) 22(15):2766–76. doi: 10.1091/mbc.E09-12-1061
18. Soker S, Miao HQ, Nomi M, Takashima S, Klagsbrun M. VEGF165 Mediates Formation of Complexes Containing VEGFR-2 and Neuropilin-1 That Enhance VEGF165-Receptor Binding. *J Cell Biochem* (2002) 85(2):357–68. doi: 10.1002/jcb.10140
19. Zachary IC. How Neuropilin-1 Regulates Receptor Tyrosine Kinase Signalling: The Knowns and Known Unknowns. *Biochem Soc Trans* (2011) 39(6):1583–91. doi: 10.1042/BST20110697
20. Holmes DI, Zachary I. The Vascular Endothelial Growth Factor (VEGF) Family: Angiogenic Factors in Health and Disease. *Genome Biol* (2005) 6 (2):209. doi: 10.1186/gb-2005-6-2-209
21. Gao P, Ren G. Identification of Potential Target Genes of Non-Small Cell Lung Cancer in Response to Resveratrol Treatment by Bioinformatics Analysis. *Aging (Albany NY)* (2021) 13(19):23245–61. doi: 10.18632/aging.203616
22. Tang Z, Li C, Kang B, Gao G, Li C, Zhang Z. GEPIA: A Web Server for Cancer and Normal Gene Expression Profiling and Interactive Analyses. *Nucleic Acids Res* (2017) 45(W1):W98–W102. doi: 10.1093/nar/gkx247
23. Gao P, Wang LL, Liu J, Dong F, Song W, Liao L, et al. Dihydroartemisinin Inhibits Endothelial Cell Tube Formation by Suppression of the STAT3 Signaling Pathway. *Life Sci* (2020) 242:117221. doi: 10.1016/j.lfs.2019.117221
24. Gao P, Tian Y, Xie Q, Zhang L, Yan Y, Xu D. Manganese Exposure Induces Permeability in Renal Glomerular Endothelial Cells *via* the Smad2/3-Snail-VE-Cadherin Axis. *Toxicol Res (Camb)* (2020) 9(5):683–92. doi: 10.1093/toxres/tfaa067
25. Kawasaki T, Kitsukawa T, Bekku Y, Matsuda Y, Sanbo M, Yagi T, et al. A Requirement for Neuropilin-1 in Embryonic Vessel Formation. *Development* (1999) 126(21):4895–902. doi: 10.1242/dev.126.21.4895
26. Jahn CL, Klobutcher LA. Genome Remodeling in Ciliated Protozoa. *Annu Rev Microbiol* (2002) 56:489–520. doi: 10.1146/annurev.micro.56.012302.160916
27. Folkman J. Tumor Angiogenesis: Therapeutic Implications. *N Engl J Med* (1971) 285(21):1182–6. doi: 10.1056/NEJM197111182852108
28. Qiao M, Jiang T, Zhou C. Shining Light on Advanced NSCLC in 2017: Combining Immune Checkpoint Inhibitors. *J Thorac Dis* (2018) 10(Suppl 13): S1534–46. doi: 10.21037/jtd.2018.04.99
29. Jetten N, Verbruggen S, Gijbels MJ, Post MJ, De Winther MP, Donners MM. Anti-Inflammatory M2, But Not Pro-Inflammatory M1 Macrophages Promote Angiogenesis *In Vivo*. *Angiogenesis* (2014) 17(1):109–18. doi: 10.1007/s10456-013-9381-6
30. Tang X, Yang Y, Yuan H, You J, Burkatovskaya M, Amar S. Novel Transcriptional Regulation of VEGF in Inflammatory Processes. *J Cell Mol Med* (2013) 17(3):386–97. doi: 10.1111/jcmm.12020
31. Fu C, Jiang L, Hao S, Liu Z, Ding S, Zhang W, et al. Activation of the IL-4/STAT6 Signaling Pathway Promotes Lung Cancer Progression by Increasing M2 Myeloid Cells. *Front Immunol* (2019) 10:2638. doi: 10.3389/fimmu.2019.02638
32. Mendoza-Rodriguez MG, Sanchez-Barrera CA, Callejas BE, Garcia-Castillo V, Beristain-Terrazas DL, Delgado-Buenrostro NL, et al. Use of STAT6 Phosphorylation Inhibitor and Trimethylglycine as New Adjuvant Therapies for 5-Fluorouracil in Colitis-Associated Tumorigenesis. *Int J Mol Sci* (2020) 21(6):2130. doi: 10.3390/ijms21062130
33. Binnemars-Postma K, Bansal R, Storm G, Prakash J. Targeting the Stat6 Pathway in Tumor-Associated Macrophages Reduces Tumor Growth and Metastatic Niche Formation in Breast Cancer. *FASEB J* (2018) 32(2):969–78. doi: 10.1096/fj.201700629R
34. Xu F, Cui WQ, Wei Y, Cui J, Qiu J, Hu LL, et al. Astragaloside IV Inhibits Lung Cancer Progression and Metastasis by Modulating Macrophage Polarization Through AMPK Signaling. *J Exp Clin Cancer Res* (2018) 37 (1):207. doi: 10.1186/s13046-018-0878-0
35. Goebeler M, Schnarr B, Toksoy A, Kunz M, Brocker EB, Duschl A, et al. Interleukin-13 Selectively Induces Monocyte Chemoattractant Protein-1 Synthesis and Secretion by Human Endothelial Cells. Involvement of IL-4R Alpha and Stat6 Phosphorylation. *Immunology* (1997) 91(3):450–7. doi: 10.1046/j.1365-2567.1997.00263.x
36. Fukushi J, Ono M, Morikawa W, Iwamoto Y, Kuwano M. The Activity of Soluble VCAM-1 in Angiogenesis Stimulated by IL-4 and IL-13. *J Immunol* (2000) 165(5):2818–23. doi: 10.4049/jimmunol.165.5.2818
37. Halasz M, Polgar B, Berta G, Czimbalek L, Szekeres-Bartho J. Progesterone-Induced Blocking Factor Differentially Regulates Trophoblast and Tumor Invasion by Altering Matrix Metalloproteinase Activity. *Cell Mol Life Sci* (2013) 70(23):4617–30. doi: 10.1007/s00018-013-1404-3
38. Yang J, Hirata T, Liu YS, Guo XY, Gao XD, Kinoshita T, et al. Human SND2 Mediates ER Targeting of GPI-Anchored Proteins With Low Hydrophobic GPI Attachment Signals. *FEBS Lett* (2021) 595(11):1542–58. doi: 10.1002/1873-3468.14083
39. Acevedo LM, Barillas S, Weis SM, Gothert JR, Cheresh DA. Semaphorin 3A Suppresses VEGF-Mediated Angiogenesis Yet Acts as a Vascular Permeability Factor. *Blood* (2008) 111(5):2674–80. doi: 10.1182/blood-2007-08-110205
40. Koh HM, Lee HJ, Kim DC. Usefulness of CD109 Expression as a Prognostic Biomarker in Patients With Cancer: A Systematic Review and Meta-Analysis. *Med (Baltimore)* (2021) 100(11):e25006. doi: 10.1097/MD.0000000000025006
41. Hagiwara S, Sasaki E, Hasegawa Y, Suzuki H, Nishikawa D, Beppu S, et al. Serum CD109 Levels Reflect the Node Metastasis Status in Head and Neck Squamous Cell Carcinoma. *Cancer Med* (2021) 10(4):1335–46. doi: 10.1002/cam4.3737
42. Lee KY, Kuo TC, Chou CM, Hsu WJ, Lee WC, Dai JZ, et al. Upregulation of CD109 Promotes the Epithelial-To-Mesenchymal Transition and Stemness Properties of Lung Adenocarcinomas *via* Activation of the Hippo-YAP Signaling. *Cells* (2020) 10(1):28. doi: 10.3390/cells10010028
43. Uniewicz KA, Cross MJ, Fernig DG. Exogenous Recombinant Dimeric Neuropilin-1 Is Sufficient to Drive Angiogenesis. *J Biol Chem* (2011) 286 (1):12–23. doi: 10.1074/jbc.M110.190801
44. Hong TM, Chen YL, Wu YY, Yuan A, Chao YC, Chung YC, et al. Targeting Neuropilin 1 as an Antitumor Strategy in Lung Cancer. *Clin Cancer Res* (2007) 13(16):4759–68. doi: 10.1158/1078-0432.CCR-07-0001
45. Rossignol M, Pouyssegur J, Klagsbrun M. Characterization of the Neuropilin-1 Promoter; Gene Expression Is Mediated by the Transcription Factor Sp1. *J Cell Biochem* (2003) 88(4):744–57. doi: 10.1002/jcb.10384
46. Lin J, Zhang Y, Wu J, Li L, Chen N, Ni P, et al. Neuropilin 1 (NRP1) Is a Novel Tumor Marker in Hepatocellular Carcinoma. *Clin Chim Acta* (2018) 485:158–65. doi: 10.1016/j.cca.2018.06.046
47. Yu DC, Waby JS, Chirakkal H, Staton CA, Corfe BM. Butyrate Suppresses Expression of Neuropilin I in Colorectal Cell Lines Through Inhibition of Sp1 Transactivation. *Mol Cancer* (2010) 9:276. doi: 10.1186/1476-4598-9-276
48. Fu R, Du W, Ding Z, Wang Y, Li Y, Zhu J, et al. HIF-1alpha Promoted Vasculogenic Mimicry Formation in Lung Adenocarcinoma Through NRP1 Upregulation in the Hypoxic Tumor Microenvironment. *Cell Death Dis* (2021) 12(4):394. doi: 10.1038/s41419-021-03682-z
49. Wei M, Liu B, Gu Q, Su L, Yu Y, Zhu Z. Stat6 Cooperates With Sp1 in Controlling Breast Cancer Cell Proliferation by Modulating the Expression of P21(Cip1/WAF1) and P27 (Kip1). *Cell Oncol (Dordr)* (2013) 36(1):79–93. doi: 10.1007/s13402-012-0115-3

50. Hsu YA, Huang CC, Kung YJ, Lin HJ, Chang CY, Lee KR, et al. The Anti-Proliferative Effects of Type I IFN Involve STAT6-Mediated Regulation of SP1 and BCL6. *Cancer Lett* (2016) 375(2):303–12. doi: 10.1016/j.canlet.2016.02.047
51. Park SJ, Kim H, Kim SH, Joe EH, Jou I. Epigenetic Downregulation of STAT6 Increases HIF-1alpha Expression *via* mTOR/S6K/S6, Leading to Enhanced Hypoxic Viability of Glioma Cells. *Acta Neuropathol Commun* (2019) 7 (1):149. doi: 10.1186/s40478-019-0798-z

Conflict of Interest: The authors declare that the research was conducted in the absence of any commercial or financial relationships that could be construed as a potential conflict of interest.

Publisher's Note: All claims expressed in this article are solely those of the authors and do not necessarily represent those of their affiliated organizations, or those of the publisher, the editors and the reviewers. Any product that may be evaluated in this article, or claim that may be made by its manufacturer, is not guaranteed or endorsed by the publisher.

frontiers | Frontiers in Oncology

TYPE Original Research
PUBLISHED 09 August 2022
DOI 10.3389/fonc.2022.837781

OPEN ACCESS

EDITED BY
Shiwei Duan,
Zhejiang University City College, China

REVIEWED BY
Lubor Borsig,
University of Zurich, Switzerland
Hong Shen,
Xiangya Hospital, Central South University, China

*CORRESPONDENCE
Qin Han
hanqin@ibms.pumc.edu.cn
Chunmei Bai
baichunmei1964@163.com
Robert Chunhua Zhao
zhaochunhua@ibms.pumc.edu.cn

†These authors share first authorship

SPECIALTY SECTION
This article was submitted to Molecular and Cellular Oncology, a section of the journal Frontiers in Oncology

RECEIVED 17 December 2021
ACCEPTED 28 June 2022
PUBLISHED 09 August 2022

CITATION
Xue C, Gao Y, Sun Z, Li X, Zhang M, Yang Y, Han Q, Bai C and Zhao RC (2022) Mesenchymal stem cells derived from adipose tissue accelerate the progression of colon cancer by inducing a MTCAF phenotype *via* ICAM1/STAT3/AKT axis. *Front. Oncol.* 12:837781. doi: 10.3389/fonc.2022.837781

Mesenchymal stem cells derived from adipose tissue accelerate the progression of colon cancer by inducing a MTCAF phenotype *via* ICAM1/STAT3/AKT axis

Chunling Xue[1†], Yang Gao[2†], Zhao Sun[2], Xuechun Li[1], Mingjia Zhang[1], Ying Yang[2], Qin Han[1*], Chunmei Bai[2*] and Robert Chunhua Zhao[1*]

[1]Beijing Key Laboratory, Institute of Basic Medical Sciences Chinese Academy of Medical Sciences, School of Basic Medicine Peking Union Medical College, Center of Excellence in Tissue Engineering Chinese Academy of Medical Sciences, Peking Union Medical College Hospital, Beijing, China, [2]Department of oncology, Peking Union Medical College Hospital, Chinese Academy of Medical Science and Peking Union Medical College, Beijing, China

Previous studies have shown that the risk of colon cancer is greatly increased in people with obesity, and fat content in colorectal cancer tissue is increased in people with obesity. As an important part of tumor microenvironment, adipose-derived mesenchymal stem cells (MSCs) are also another important source of cancer-associated fibroblasts (CAFs), which may be one of the important mechanisms of affecting tumor progression. However, the mechanism is poorly defined. In the present study, CAFs were transformed from MSCs [MSC-transformed CAFs (MTCAFs)] by co-culturing with HCT116 cells. Bioinformatics and Western blotting analysis indicated a positive correlation between intercellular adhesion molecule-1(ICAM-1) and the progression of colon cancer. In clinical colon cancer specimens, we found that ICAM-1 was highly expressed and related to shorter disease-free survival, which might act as an indication for the progression of clinical colon cancer. Our data showed that ICAM-1 secreted from MTCAFs could positively promote

Abbreviations: MSCs, mesenchymal stem cells; hADSCs, human adipose-derived mesenchymal stem cells; CAFs, cancer-associated fibroblasts; MTCAF, MSC-transformed CAF; α-SMA, alpha–smooth muscle actin; FAPA, fibroblast activation protein alpha; CRC, colorectal cancer; TME, tumor microenvironment; IL-6, interleukin-6; CCL2, CC-chemokine ligand 2; SDF-1/CXCL-12, stromal cell-derived factor 1; ICAM-1, Intercellular adhesion molecule-1; LFA-1, leukocyte-function associated antigen-1; DMEM, Dulbecco's Modified Eagle Medium; TEM, transmission electron microscopy; IHC, immunohistochemistry; IF, immunofluorescence.

the proliferation, migration, and invasion of colon cancer cells by activating signal transducer and activator of transcription 3 (STAT3) and Serine/threonine-protein kinase (AKT) signaling and that blocking ICAM-1 in MTCAFs reversed these effects. We further verified that ICAM-1 secreted from MTCAFs promoted tumor progression *in vivo*. Taken together, ICAM-1 plays a critical role in regulating tumor growth and metastasis, which could be a potential therapeutic target in colon cancer.

KEYWORDS

ICAM-1, progression, survival, cell trafficking, AKT and STAT3 signaling

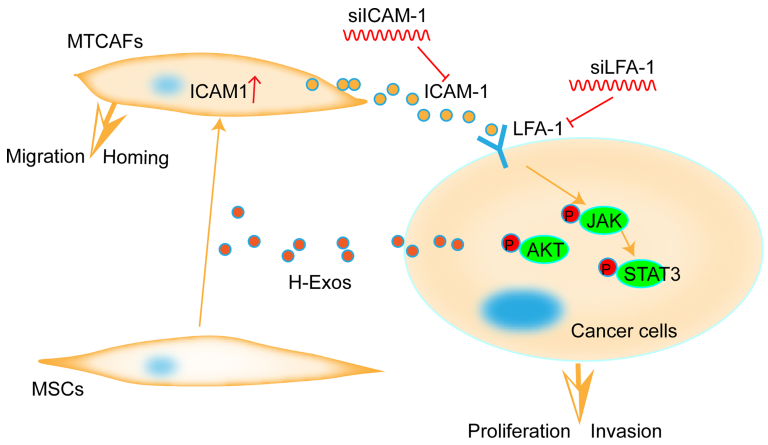

GRAPHICAL ABSTRACT
Parsimony diagram for the progression of cancer by MTCAF-derived ICAM1. ICAM-1 secreted from MTCAFs enhances the migration and invasion ability of colorectal cancer cells by activating the AKT and STAT3 pathway in cancer cells.

Introduction

Mesenchymal stem cells (MSCs) are an important component of the tumor microenvironment (TME). MSCs are also referred to as "mesenchymal stromal cells", which implies that MSCs have characteristics associated with stem cells. Importantly, MSCs are a population of adult multipotent cells that have the capacity of self-renewal and can differentiate into osteoblasts, chondrocytes, and adipocytes (1, 2). In addition, MSCs can be obtained from different tissues including the bone marrow, adipose tissues, placenta, or umbilical cord (1, 3). Several studies have demonstrated that MSCs possess multilineage differentiation potential (4) and can differentiate into cancer-associated fibroblasts (CAFs) *via* co-culturing with cancer cells that can secrete cytokines, growth factors, and CAF-specific proteins (5, 6).

Colorectal cancer is one of the most common malignancies globally, with about 1.2 million new cases and 600,000 deaths per year, accounting for the third highest incidence and the fourth leading cancer-related morbidity (7, 8). Recent studies have shown that cancer progression and metastasis are not only associated with the properties of tumor cells but also depend on the TME (9). The stroma of colon cancer forms a complex ecosystem containing immune cells, endothelial cells, and CAFs, with the latter characterized by overexpression of marker proteins, including alpha–smooth muscle actin (α-SMA) and fibroblast-activated protein (FAP) (10, 11); these provide a niche for cancer cells to modulate tumor invasion and growth (12, 13). Recent studies show that CAFs are actively involved in tumorigenesis, and it can be anticipated that the molecular characteristics of CAFs have an impact on the clinical behavior of a tumor (14–16).

Intercellular adhesion molecule-1 (ICAM-1) is a 90-kDa cell surface glycoprotein of the immunoglobulin superfamily, which has been shown to be responsible for cancer metastasis (17, 18). ICAM-1 is the most important ligand of leukocyte function–associated antigen-1 (LFA-1), which is an αLβ2 chain integrin expressed on the surface of endothelial cells and modulates the behavior of leukocytes by mediating their adhesion to other cells through its interaction with cell-surface ligands (19). In addition, the interaction between LFA-1 and ICAM-1 is involved in inflammatory responses, inflammatory pathologies,

autoimmune diseases, and many cancer processes (19). ICAM-1 expression is positively related with the activation of IL-6/AKT/STAT3/NF-κB signaling pathways (20). However, the effect of knocking down ICAM-1 on tumorigenesis is unknown. STAT3 is a well-known and significant mediator of malignant progression in colorectal cancer, which is mainly activated by IL-6 (21). IL-6 binds to soluble or membrane-bound IL-6 receptor (IL-6Rα) polypeptides, which stimulates the activation of Janus kinases (JAKs), and the downstream effectors, STAT3, Shp-2-Ras, and phosphatidylinositol 3′ kinase (PI3K)–Akt (22, 23). CAFs within the TME actively contribute to sustained STAT3 activation in colorectal cancer (21). In addition, activation of IL-6-STAT3 signaling contributes fibroblasts to their conversion into CAFs in normal gastric fibroblasts (21, 24), and IL-6 enhances the proliferation of human colon carcinoma cells *in vitro* (25, 26).

Here, we sought to better understand the mechanism by which CAFs promote cell migration and invasion in colorectal cancer so as to implicate it as a potential target that could be explored further for its clinical relevance in the treatment of colorectal cancer.

Materials and methods

Cell culture

HCT116 cells were obtained from the Cell Resource Center, Peking Union Medical College (which is the headquarters of the National Infrastructure of Cell Line Resource, NSTI), which were cultured in Dulbecco's Modified Eagle Medium (DMEM)/high glucose (11965092, Gibco, USA) supplemented with 10% fetal bovine serum (FBS; 16140071, Gibco, USA) and penicillin (100 IU)/streptomycin (100 μg/ml) at 37°C in a 5% CO_2 incubator. Cells are available within 15 generations. The extraction and culture methods of MSC refer to previous studies.

Isolation and culture of human adipose-derived MSCs

We collected adult fat samples from plastic surgery hospitals after obtaining informed consent from the donors. Using D-Hanks' buffer, the adipose tissue was washed twice with two antibiotics (penicillin and streptomycin) and centrifuged at 800*g* for 3 min. The upper layer was transferred to a new 50-ml centrifuge tube. Then, 0.2% collagenase P (Life Technologies Corporation) was added to the tubes containing the pelleted tissue for enzymatic digestion followed by incubation at 37°C for 30 min. Subsequently, the digested adipose tissue was filtered with a 100-μm cell strainer. The sample was centrifuged at 1,500*g* for 10 min. Next, 2×10^6 cells were seeded in T75 flasks and incubated at 37°C and 5% CO_2 in a cell incubator.

Extraction of exosomes secreted by HCT116 cells

DMEM (Life Technologies Corporation) was replaced with human adipose-derived MSC (hAD-MSC) culture medium without FBS, 36–48 h before exosome extraction. Supernatants were harvested after culture and centrifuged at 3,000*g* for 10 min to remove dead cells and cell debris. The sample was transferred to the ultrafiltration apparatus (Life Technologies Corporation) with a 100,000-kDa–molecular weight ultrafiltration membrane. Exosomes were resuspended in D-Hanks' buffer, and the suspension was filtered with a 0.2-μm microporous membrane filter, dispensed in 1.5-ml sterile microcentrifuge tubes, and preserved at −80°C.

Identification of exosomes using transmission electron microscopy

The purified exosomes were diluted and dropped onto a copper mesh for 5 min for precipitation. Then, filter paper was used to absorb excess liquid, and the sample was air dried. Subsequently, 3% phosphotungstic acid in water was used to counterstain the sample for 2 min. Finally, exosomes were observed using a transmission electron microscope (Olympus, Japan) and photographed.

Exosome uptake

1,1-Dioctadecyl-3,3,3,3-tetramethylindotricarbocyaine iodide (DiR; 1 μM) (Life Technologies Corporation) is a lipophilic carbon cyanine dye that can bind lipoproteins in a manner similar to phospholipids and is embedded in the membrane of the biomass and oriented within the membrane. Diffusion movement can be used to observe cell-bound or endocytic lipoproteins under a fluorescence microscope, and this allows for semi-quantitative analysis (27). Purified exosomes were exposed to 1 μM DiR for 10 min. After incubating with MSCs for 10 h, the cells were washed with PBS three times, and the nuclei were stained with Hoechst 33342 (10 μg/ml) for 15 min at room temperature and washed with Phosphate Buffered Saline (PBS) three times. The cells were observed under a fluorescence microscope (OLYMPUS) and photographed.

Cell–cell co-culture

A Transwell® chamber (0.4 μm) (Corning) was used to co-culture the HCT116 cells with the hAD-MSCs at 1:1 ratio. The cells were passaged when cell density is 90%. Cell–cell co-culturing samples were collected at days 0, 3, 5, 7, and 9.

siRNAs infection

Small interfering RNA (siRNAs) were used to knockdown ICAM-1 mRNA and synthesized by GenePharma company (China). The sequence of knocking down ICAM-1 is GGCTGGAGCTGTTTGAGAACA. Specific operation of virus infection was described as previous report (28).

Western blotting analysis

Proteins were extracted from cells using IP lysis buffer (87787, Thermo Fisher Scientific) with a cocktail (4693116001, Roche, Basel, Switzerland) and PhosSTOP (4906845001, Roche). The proteins were denatured in SDS (Sigma-Aldrich) with loading buffer and boiled for 10 min at 100°C. Sodium dodecyl sulfate polyacrylamide gel electrophoresis (SDS-PAGE) was used to separate the proteins followed by the transfer of protein bands onto polyvinylidene fluoride (PVDF) membranes (Merck Millipore, Billerica, MA, USA). The membranes were then blocked with 5% milk in Tris-buffered saline–Tween 20 followed by overnight incubation at 4°C with primary antibodies. They were then washed and incubated with appropriate secondary antibodies for 1 h at room temperature, and bands were visualized using the enhanced chemiluminescence detection kit Life Technologies Corporation. The ICAM-1 (5915, 1:1,000), IL-6 (12912, 1:1,000), AKT (9272,1:1,000), Extracellularr regulated protein kinases (ERK) (4695, 1:1,000), p-ERK1/2 (4370, 1:1,000), p-JNK (9251, 1:1,000), anti-rabbit Horseradish Peroxidase labeled Anti-mouse IgG (IgG-HRP) (14708,1:2,000), Phospho-Stat3 (Tyr705, 9145, 1:1,000), Stat3 (D3Z2G, 12640, 1:1,000), Jak2 (D2E12, 3230, 1:1,000), Phospho-Jak2 (Tyr1007, 3771, 1:1,000), and anti-mouse IgG-HRP (14709, 1:2,000) antibodies were obtained from Cell Signaling Technology (Danvers, MA, USA); IL-8 (500-M08, 1:1,000) and p-Akt (ser473, 66444-1-IG, 1:2,000) antibodies were purchased from ProteinTech (Chicago, IL, USA).

Real-time quantitative polymerase chain reaction

RNA was extracted from cell samples using TRIzol (Thermo Fisher Scientific). RNA was thawed in 30 μl of RNA free water (Applygen) and reverse-transcribed (60 μl) according to the protocol recommended for the TaKaRa M-MLV reverse transcriptase (Takara). Amplification of the gene fragment was performed. To amplify the ICMA1, IL-6, IL-8, and Glyceraldehyde-3-phosphate dehydrogenase (GAPDH) genes, one-step real-time quantitative polymerase chain reaction (RT-PCR) was performed as follows: 95°C for 5 min, 95°C for 10 s, 60°C for 40 s, 40 cycles. Reactions were performed in triplicate, and independent experiments were repeated three times. The RT-PCR data were analyzed using StepOne Software 2.1, and primers are presented in **Table 1**.

Enzyme-linked immunosorbent assay

The levels of soluble IL-6/8/TNFα in the supernatant of primary MTCAFs and the supernatant were measured using an enzyme-linked immunosorbent assay (ELISA) kit (Jiangsu Meimian industrial Co., Ltd., TNFα: MM-0132M1, IL-6: MM-0163M1, and IL-8:MM-0123M1), according to the manufacturer's instructions. The absorbance (450 nm) of each sample was detected on a standard automatic microplate reader (BioTek, USA).

Cell invasion and migration assay

Colorectal cancer cell migration and invasion assay was conducted using 24-well Matrigel-coated Transwell inserts (BD Biosciences, San Diego, CA, USA). Approximately 2×10^5 cells were seeded in serum-free medium in the upper chamber. Next,

TABLE 1 Sequences for primers.

Items	Direction	Sequence
IL6 primer	sense	ACTCACCTCTTCAGAACGAATTG
	reverse	CCATCTTTGGAAGGTTCAGGTTG
IL8 primer	sense	ACTCCAAACCTTTCCACCCC
	reverse	TTCTCAGCCCTCTTCAAAAACTTC
GAPDH primer	forward	GGTCACCAGGGCTGCTTTTA
	reverse	GGATCTCGCTCCTGGAAGATG
ICAM1 primer	forward	ACGTTGGATGAGCACTCAAGGGGAGGTCAC
	reverse	ACGTTGGATGGCTACCACAGTGATGATGAC

DMEM with FBS was added to the lower chamber, and after incubation at 37°C with 5% CO_2 for 24–48 h, the non-filtered cells were removed using a cotton swab and the migratory cells were stained with 0.1% crystal violet solution. The invasive cells attached to the bottom surface of the filter were quantified under a light microscope (200×). The data are presented as the average number of cells from randomly chosen fields. Each treatment condition was assayed using triplicate filters, and all filters were counted in five areas.

Wound healing

Using marker pen is to marker the 6-well plate with the ruler, which draw horizontal lines evenly (0.5-1cm). Each hole have to pass through at least 3 lines. Cell density is about 5*105 cells/pole. Next day, holding the head of the spear against the ruler and trying to keep it to the horizontal line in order to scratch. Wash the cells three times with PBS, remove the suspending cells, and add serum-free medium. Putting it into an incubator at 37°C with 5%CO2. Sampling at different hours and taking photos.

Patients and samples

This is a retrospective cohort study. Colorectal cancers were obtained with informed consent from patients in Peking Union Medical College Hospital (Beijing, China) during January 2014 to December 2016. All specimens were collected using the protocols approved by the Ethics Committee of Peking Union Medical College Hospital. All patients were R0 resected and pathologically diagnosed with CRC.

Immunohistochemistry

The resected tissue samples were fixed with formaldehyde, embedded in paraffin, and prepared into 4-m-thick sections. The slides were then dewaxed and hydrated. Next, we decreased the peroxidase activity by treating with 3% H_2O_2. The sections were blocked by using 10% normal goat serum and incubated with appropriate primary antibody overnight at 4°C. Then, PBS diluted secondary antibody at 1:100 was added followed by incubation at room temperature for 2 h. All immunostained sections were then lightly restained with hematoxylin. The results of immunohistochemistry (IHC) were evaluated by two pathologists independently. If the results were inconsistent, the final result would be judged by the third pathologist. The membrane staining of cells >5% was defined as ICAM-1 positive.

Agilent expression profiling gene chip

The total RNA of the sample was quantified by NanoDrop ND-2000 (Thermo Scientific), and then, the RNA integrity was checked by Agilent Bioanalyzer 2100 (Agilent Technologies). After passing the RNA quality inspection, the labeling of the sample, the hybridization of the chip, and the elution refer to the standard process of the chip. First, total RNA is reverse-transcribed into double-stranded cDNA and then cRNA labeled with Cyanine-3-CTP (Cy3) is synthesized. The labeled cRNA is hybridized with the chip, and the original image is obtained by scanning with Agilent Scanner G2505C (Agilent Technologies) after elution.

Animal experiments

All mice were maintained and manipulated according to the guidelines established by the Medical Research Animal Ethics Committee of Peking Union Medical University. The samples were randomly assigned. A mixture of 5×10^6 HCT116 cells were re-suspended with 1×10^6 cells or PBS (5:1) in 100 µl of PBS and subcutaneously injected into 6-week-old female athymic nude mice (BALB/C). Tumor formation was examined after 7 days. We detected the tumor size every three days, recorded the data, and finally calculated the volume (1/2 *the long side*the short side squared). When tumor volume reached 1–1.5 cm, the animals were sacrificed. Tissues were collected and sectioned followed by some sections being fixed with 10% buffered formalin for IHC analysis, whereas the others were preserved at −80°C for Western blotting.

Writing statement

Participants have provided written informed consent to take part in the study.

Statistical analysis

All data are expressed as means ± SD from at least three independent experiments. The statistics were analyzed by SPSS 25.0 statistical software (IBM, Armonk, USA). The relationship between the expression of ICAM-1 and disease-free survival (DFS) was evaluated by the Kaplan–Meier method. DFS was defined as the time from complete resection of tumor to disease recurrence. Statistical analysis was performed using two-tailed t-tests and one-way ANOVA. $P < 0.05$ was considered statistically significant. Each experiment was repeated at least three times to obtain a P-value and to control for systematic errors.

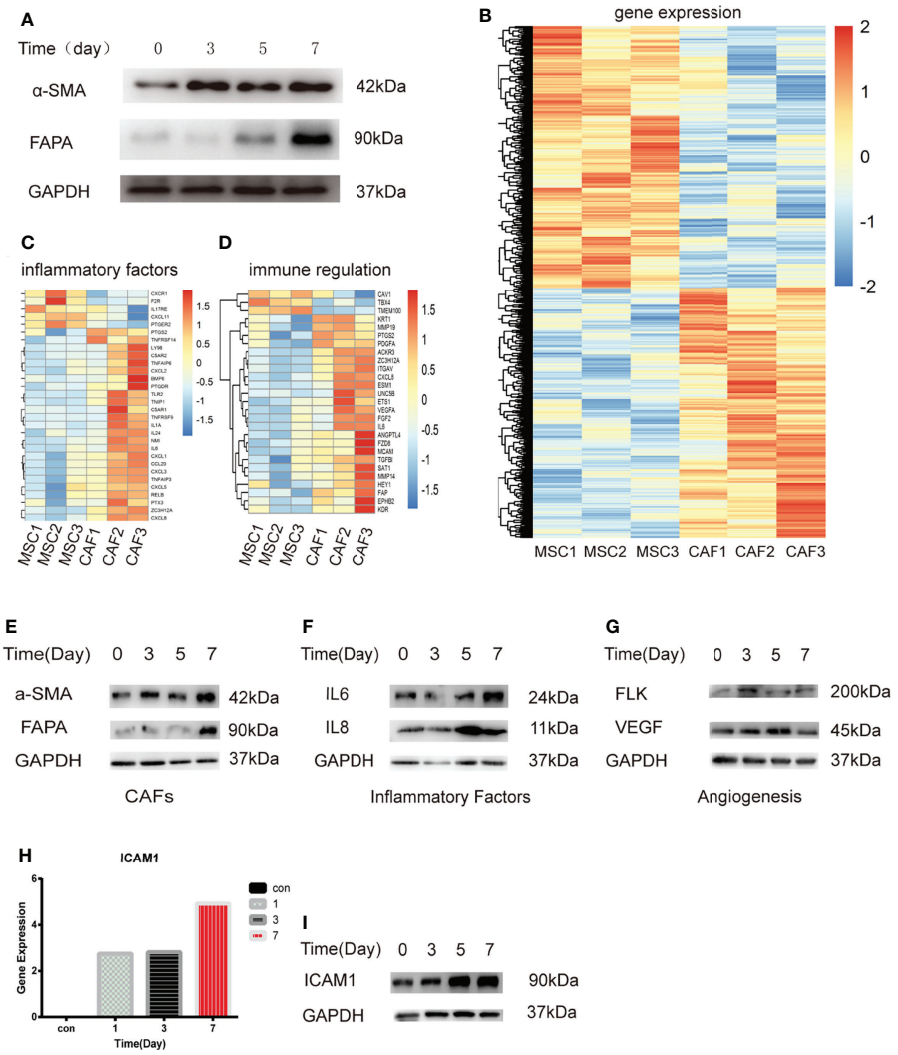

FIGURE 1
Transcriptome analysis of MSCs treated with H-Exos. **(A)** Detection of genes associated with MTCAF using Western blotting with the situation of MSCs with H-Exos at days 0, 3, 5, and 7. **(B)** Heat map showing the differentially expressed genes (DEGs) in HCT116-exos–treated MSCs (CAF1-3) and control MSCs (MSC1-3). **(C)** DEGs associated with inflammatory factors. **(D)** DEGs associated with immune regulation. **(E)** Detection of genes associated with MTCAF using Western blotting with the situation of co-culturing with HCT116 cells and MSCs at days 0, 3, 5, and 7. **(F)** Detection of genes associated with inflammatory factors using Western blotting. **(G)** Detection of genes associated with angiogenesis using Western blotting. **(H)** The expression of ICAM-1 was measured at days 0, 1, 3, and 7 by expression profiling gene chip **(I)** The expression of ICAM-1 using Western blotting at days 0, 1, 3, and 7.

Results

Exosomes derived from HCT116 (H-Exos) induce the differentiation of MSCs into MTCAFs

Previous studies have shown that MSCs can differentiate into CAFs (4, 29). First, we applied H-Exos to induce MSCs differentiate into CAFs, which is named MTCAFs, and we found that MTCAFs have the higher CAF-specific gene expression (α-SMA and FAPA) (**Figure 1A**). The characteristics of H-Exos are presented in **Supplementary Figure 1**. Next, we evaluated the transcriptomic alterations and identified activated proteins in MTCAFs compared with MSCs; MTCAFs was kept into a transcriptionally active state, which was demonstrated by an increased number of upregulated genes (**Figure 1B**). Meanwhile, clustering identified upregulation of gene markers related to cell secreted inflammatory factors and immune regulation in MTCAFs compared with MSCs (**Figures 1C, D**). To be similar to the physiologic al conditions, we applied the co-culturing system, and we found that the co-culturing effect with HCT116 cells and MSCs is the same as that in exosomes secreted from HCT116 cells with MSCs (**Figure 1E**). Western blotting

analysis showed an increase in the inflammatory and angiogenesis proteins from transcriptome analysis results (**Figures 1F, G**). In addition, the Agilent expression profiling gene chip results showed that ICAM-1 expression increased gradually during MSCs differentiation, and Western blotting analysis showed the same effect (**Figures 1H, I**). In conclusion, HCT116 cells can promote the differentiation of MSCs into MTCAFs and screen key gene ICAM-1 during the differentiation process.

ICAM-1 might act as an indication for the progression of clinical colon cancer

To explore the correlations between ICAM-1 expression and progression and prognosis of patients with colon cancer, we collected patients samples with colon cancer from Oncomine Database, which includes paracarcinoma tissue and colorectal cancer tissue. The Oncomine analysis showed that α-SMA, ICAM-1, and LFA-1 exhibited a higher expression in colorectal cancer compared with colon tissue (**Figures 2A–C**), and ICAM-1 was positively correlated with α-SMA and LFA-1 (**Figures 2D, E**). To further clarify the function of these genes, we used clinical specimens for further analysis. The expression of ICAM-1 and α-SMA in tumor tissue of patients with stage I, II, and III CRC were obtained by using immunofluorescent staining. The result showed that ICAM-1 and α-SMA were co-expressed in clinical samples (**Figure 2F**). Next, we enrolled 72 patients (n = 72), 38 samples showed ICAM-1 positive, and 34 samples showed ICAM-1 negative (**Figure 2G**). On basis of this, we analyze the relationship between ICAM-1 expression and patient survival, and the result showed that the DFS of patients with positive ICAM-1 expression was significantly shorter than that of ICAM-1–negative patients [(28.06 ± 1.47) months *vs.* (38.87 ± 3.35) months, P = 0.013] (**Figure 2H**). These results suggest that ICAM-1 is inversely associated with survival in patients with colorectal cancer.

ICAM-1 is critical for the migration and homing abilities of MTCAFs

To further validate the function of ICAM-1 in the process of MSC differentiating into MTCAFs, we detected the invasion and migration abilities of MTCAFs, and the results showed that MTCAFs with ICAM-1 knockdown presented with significantly decreased abilities of migration (**Figures 3A, B**) and invasion (**Figures 3C, D**) compared with MTCAFs, which means that the ICAM-1 may play an important role in the MTCAFs. To further understand the situation of MTCAF homing, we built a nude mouse xenograft tumor model (mice, n = 10). HCT116 cells were subcutaneously co-implanted with MSCs (S1), MSCs with ICAM-1 knockdown (S2) and PBS (NC) at a ratio of 5:1. We next detected the abilities of distant migration by *in vivo* fluorescence image, and we found that homing to the lungs in S1 group was more stronger than that in S2 group (**Figure 3E**). To determine which cells migrate to the lungs, we next detected the CAF-specific marker genes (α-SMA and FAPA) by immunofluorescence staining, and the results showed that MTCAFs migrate to the lung in the S1 group compared with the other two groups (**Figure 3F**). These results show that the ICAM-1 gene mediates the movement of MTCAFs, which may influence the progression of colon cancer cells.

ICAM-1 regulates the inflammatory secretion of MTCAFs and mediates the inflammatory microenvironment

In our study, the transcriptomic analysis indicated that H-Exos activated different signals including TNFα and IL6 signaling pathways in MTCAFs (**Figure 4A**). Among the inflammatory factors, Western blotting analysis revealed that the expression of IL-6 and IL-8 was decreased, whereas MTCAFs were knocked down by ICAM-1 (**Figure 4B**). This result was further verified by ELISA to detect ICAM-1, IL-6, and IL-8 concentration of serum on day 7 (**Figure 4C**). In addition, by accessing immune cell infiltration *in vivo*, we showed that the number of F4/80 macrophages was lower in tumors in S2 group compared with S1 group (**Figures 4D, E**). Some studies suggest that the inflammatory factors, IL-6, IL-8, and TNFα, are major regulators of tumor stroma interaction in the cancer microenvironment (32–35). We examined their expression levels in mice serum by ELISA (n = 5) and found increased levels of IL-6 and IL-8 (**Figures 4F, G**). In conclusion, MTCAFs with ICAM-1 are able to mediates the inflammatory microenvironment.

MTCAFs regulate colon cancer cell invasion and migration *via* secreting ICAM-1

In our study, we further explored the effect of MTCAF-derived ICAM-1 on the HCT116 cells, and we found that migration abilities (**Figures 5A, B**) and invasion abilities (**Figures 5C, D**) of HCT116 cells were obviously weakened at day 7 when MTCAFs were knocked down. We next analyzed whether MTCAFs with ICAM-1 knockdown affected the tumor progression and immune environment by using a nude mouse xenograft tumor model (mice, n = 10). HCT116 cells were subcutaneously co-implanted with MSCs (S1), ICAM-1 knockdown MSCs (S2), or PBS (NC) at a ratio of 5:1. Mice in S1 group promoted the growth of tumor compared with the other two groups *in vivo* (**Figures 5E, F**). Next, we assessed the tumor weight by excising the tumor from mice, and the results were similar to those observed for tumor growth (**Figures 5G,**

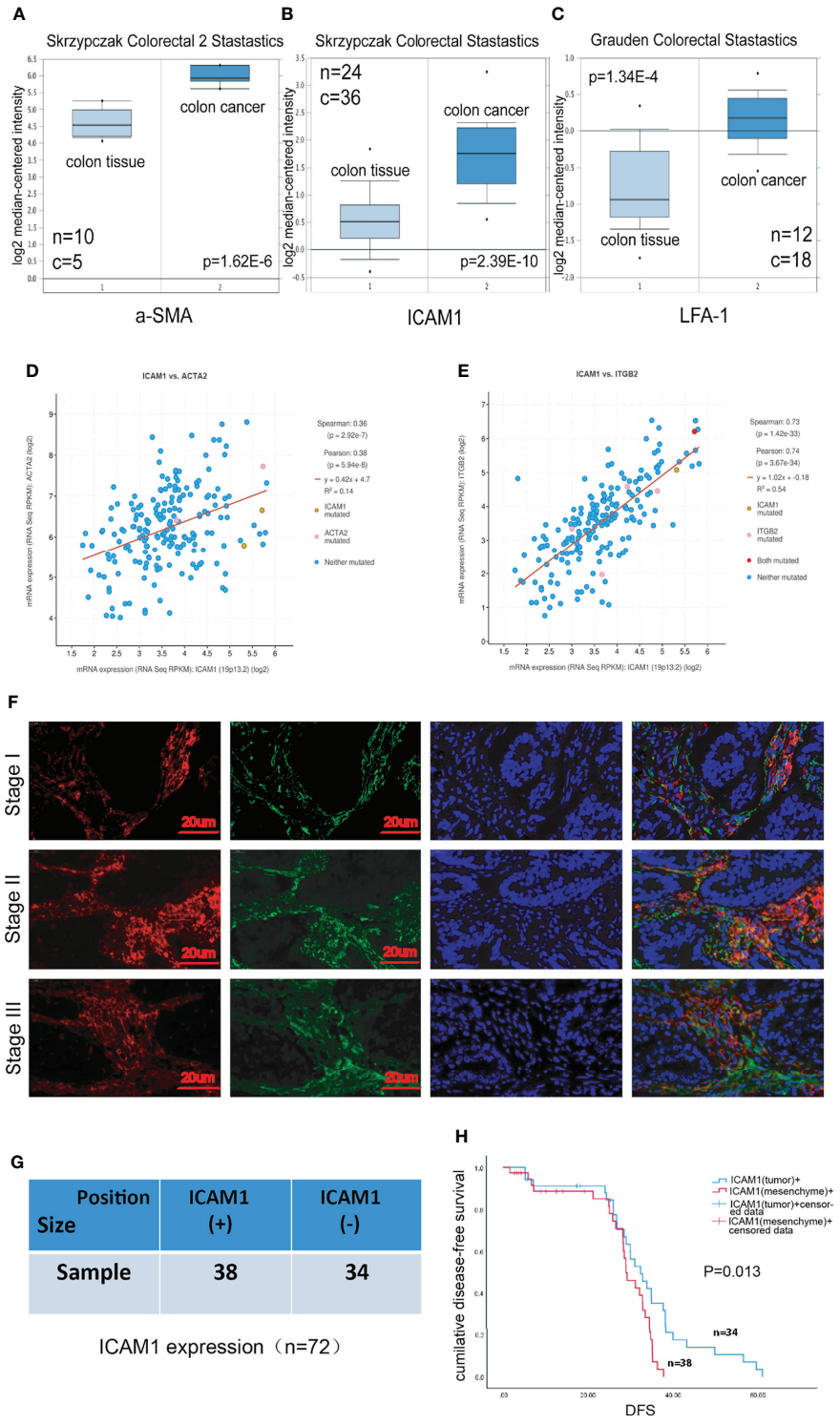

FIGURE 2
ICAM-1 expression has a poor prognosis in patients. **(A–C)** The expression analysis in relation to ICAM-1, α-SMA, and LFA-1 from Oncomine Database, respectively. **(D, E)** cBioPortal Database indicated the correlation between ICAM-1 and α-SMA or LFA-1. **(F)** Colon cancer tissues specimens consisting of patients with stage I, II, and III CRC were immunofluorescent staining with antibody against ICAM-1 (red), α-SMA (green), and nucleus (blue). **(G)** The enrolled 72 patients were divided into two groups including only mesenchymal ICAM-1 positive (30) and mesenchymal ICAM1 negative (31). **(H)** Kaplan–Meier curves for DFS of mesenchymal ICAM-1 expression. *$p < 0.05$, **$p < 0.01$, and ***$p < 0.001$.

10.3389/fonc.2022.837781

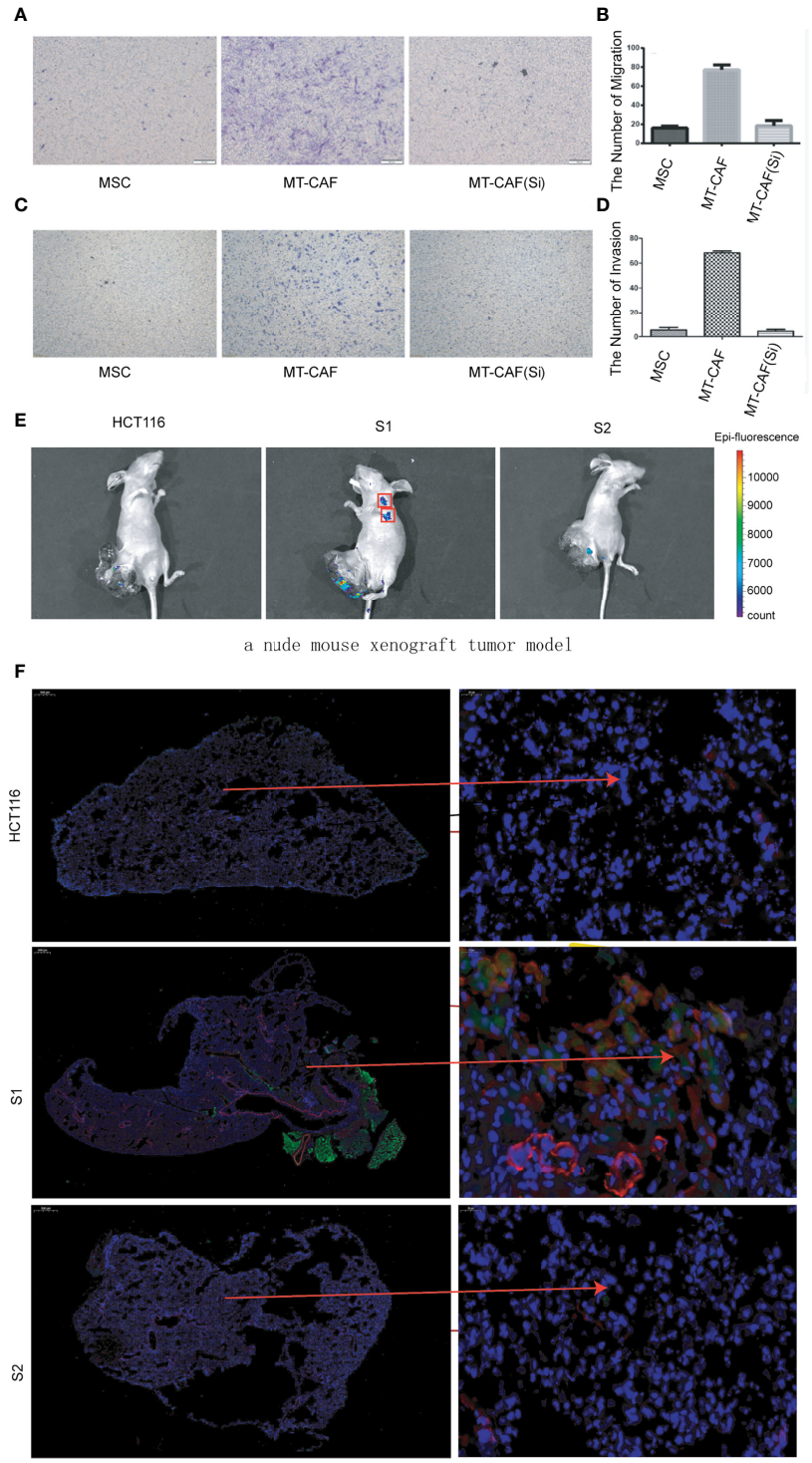

FIGURE 3
Knockdown ICAM-1 in MTCAFs attenuates their migration and homing abilities. **(A, B)** Transwell migration assays to evaluate the MTCAF migratory capacity were performed and are represented. The left side shows a representative microscopic image of the crystal violet staining. The right shows the quantitative results. **(C, D)** Transwell migration assays to evaluate the MTCAF invasion capacity were also performed and are represented. The left side shows a representative microscopic image of the crystal violet staining. The right shows the quantitative results. **(E)** *In vivo* fluorescence image showing the effect of combined MSC transplantation on tumor metastasis. Three groups of mice were transplanted with HCT-116 5 × 10^6 cells, HCT-116 5 × 10^6 cells + MSC 1 × 10^6 cells, and HCT-116 5 × 10^6 cells + MSC with ICAM1 knocking down 1 × 10^6 cells. The MSC cell lines carried GFP. **(F)** MTCAF density was measured using immunofluorescence staining in mice lung tissues by staining α-SMA and GFP transfected in MSCs.

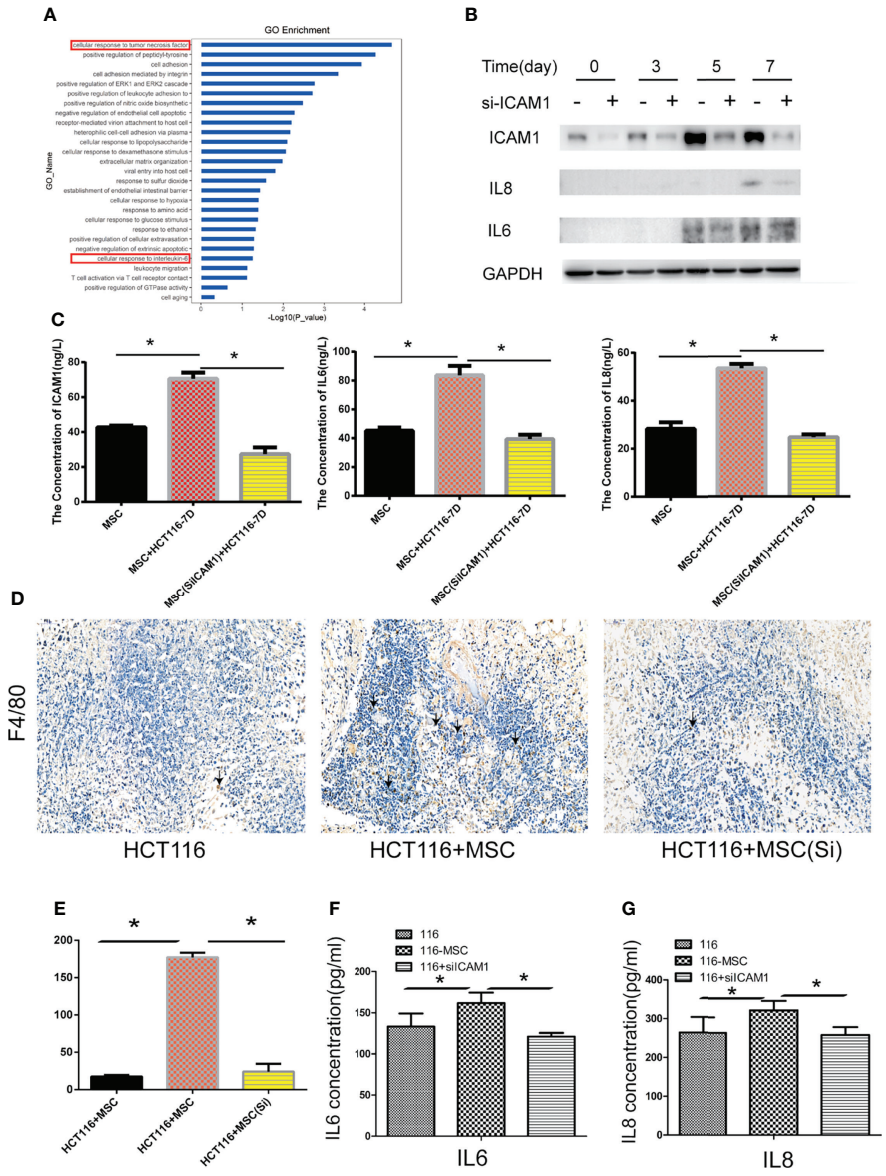

FIGURE 4
ICAM-1 mediates the inflammatory microenvironment. **(A)** Go enrichment analysis showed that inflammatory signaling pathways in MTCAF were significantly activated with the situation of H-Exos stimulation. **(B)** The expression of IL6 and IL8 was detected by Western blotting (WB) in MTCAFs or MTCAFs with knocking down ICAM1 at days 0, 3, 5, and 7. **(C)** ELISA detection detected the ICAM1, IL6, and IL8 expression from cellular supernatant with ICAM1 or without ICAM1. **(D, E)** Macrophage infiltration into tumor tissues was examined using immunohistochemistry for the detection of the F4/80. Representative images of F4/80 stainings for each group are shown (magnification, × 400). Panel **(E)** shows the quantitative results. **(F, G)** IL-6 and IL-8 from mice serum levels were evaluated using ELISA in the three different groups (n = 5). *$p < 0.05$, **$p < 0.01$, and ***$p < 0.001$.

H). Meanwhile, Ki67 staining was performed, and the results showed that the proliferation capacity of the S1 group was significantly higher than NC group, whereas knocking down ICAM-1 significantly decreased the ability of proliferation (Figures 5I, J). We found that HCT116 cells can also migrate into the lungs in S1 group but not in S2 group and NC group (Figure 5K). These results show that ICAM-1 mediates progression of colon cancer cells.

ICAM-1 secreted from MTCAFs mediates the STAT3 and AKT signaling pathway in colon cancer cells

LFA-1 has been reported to be the most important ICAM-1 receptor (31). In our study, wound healing assay confirmed that ICAM-1 secreted by MTCAFs regulates migration of HCT116 cells by interacting with LFA-1 expressed on HCT116 cells (Figure 6A).

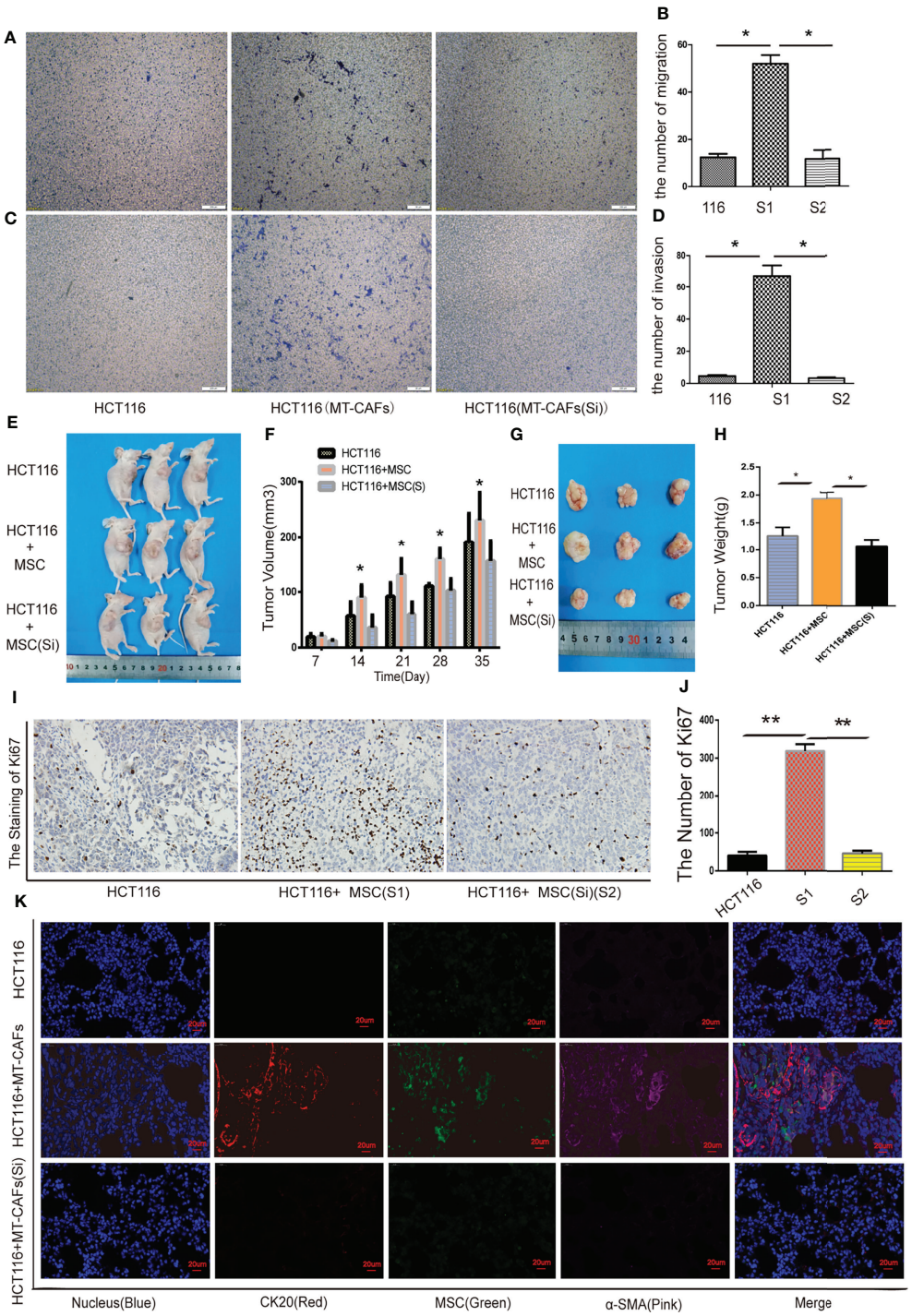

FIGURE 5
ICAM-1 from MTCAFs influences the progression of colon cancer cells. **(A, B)** Transwell migration assays to evaluate the HCT116 cells migration capacity were also performed. Panel **(A)** indicates a representative microscopic image of the crystal violet staining. Panel **(B)** shows the quantitative results. **(C, D)** Transwell assays to evaluate the HCT116 cells invasion capacity were also performed. Panel **(C)** indicates a representative microscopic image of the crystal violet staining. Panel **(D)** shows the quantitative results. **(E)** Representative photographs of HCT116 tumors generated in nude mice eco-implanted with MSCs (S1), MSCs after ICAM-1 silencing (S2), or PBS (NC) at a ratio of 5:1. **(F)** The quantitative data referent to **(E)**. **(G)** The weight (g) of tumors were discorded. **(H)** The quantitative data referent to **(G)**. **(I, J)** The expression of Ki67 in tumor tissue of mice in S1, S2, and NC groups was detected by immunohistochemistry. **(J)** The quantitative data. **(K)** MSCs and HCT116 density were measured using immunofluorescence staining in mice lung tissue (CK20, red, represents colorectal cancer cells; α-SMA, pink, represents MTCAFs; green, fluorescent protein carried by MSCs; and Hoechst3342, blue, represents the nucleus. *$p < 0.05$, **$p < 0.01$, and ***$p < 0.001$.

10.3389/fonc.2022.837781

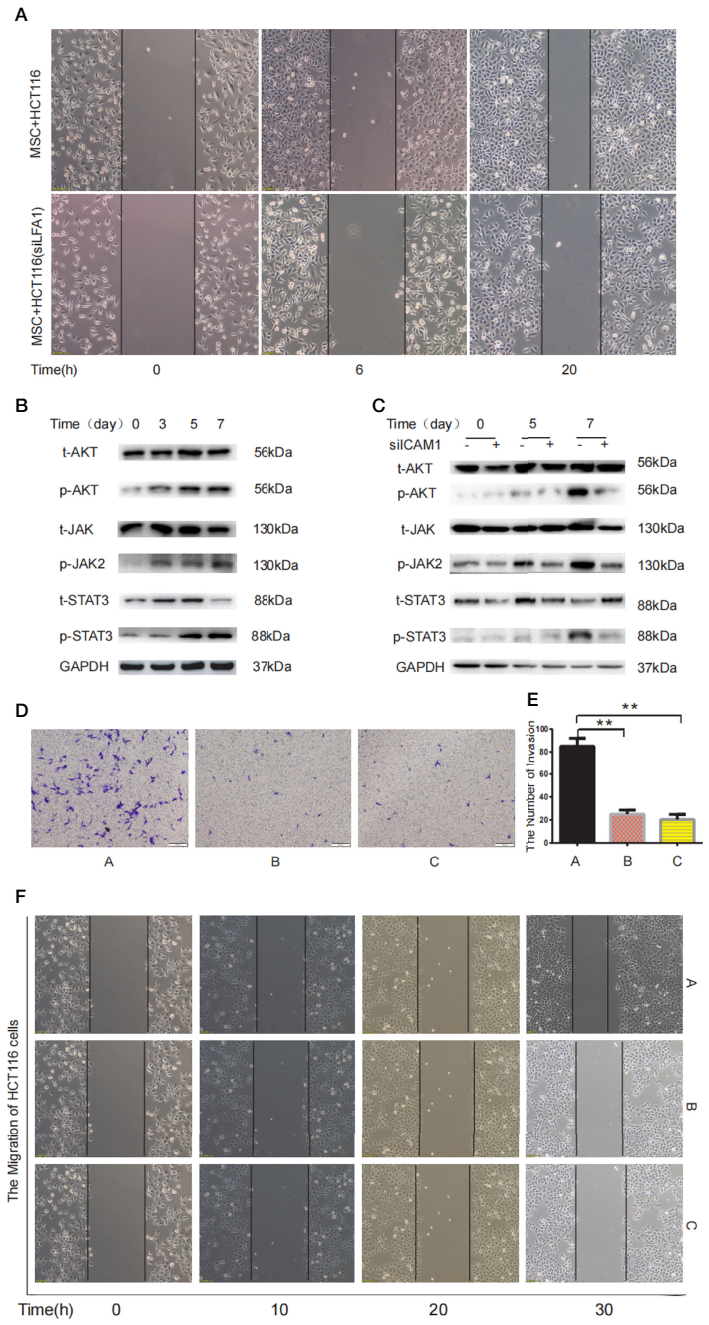

FIGURE 6
MTCAF-derived ICAM-1 mediates STAT3 and Akt signaling pathways in colon cancer cells. **(A)** The migration ability of HCT116 cells was detected by wound healing in two different treatment groups including MSC co-culturing with HCT116 cells or HCT116 cells with LFA inhibitor (44 nM) groups. **(B)** Western blotting assay was used to detect the phosphorylation of AKT and STAT3 in HCT116 cells when HCT116 cells and MSCs were co-cultured at days 0, 3, 5, and 7. GAPDH was used as the control group. **(C)** Western blotting was used to detect AKT and STAT3 signaling pathway in HCT116 cells with co-culturing with MSCs or MSCs knocking down ICAM-1. GAPDH was used as the control group. **(D)** Invasive ability of HCT116 cells was measured using the Transwell assay. The left shows the microscopic image of the crystal violet staining [group A represents the HCT116 and MSC co-culture group, group B represents the HCT116 and MSC co-culture group with AKT inhibitor (10 10 μM) group, and group C represents the HCT116 and MSC co-culture group with STAT3 inhibitor (2.14 μM) group). **(E)** The microscopic image of the crystal violet staining. **(F)** The wound healing was used to detect migration ability of HCT116 cells at different time (group A represents the HCT116 and MSC co-culture group, group B represents the HCT116 and MSC co-culture group with AKT inhibitor group, and group C represents the HCT116 and MSC co-culture group with STAT3 inhibitor group). $^{**}p < 0.01$ and $^{***}p < 0.001$.

Western blotting results showed that JAK, STAT3, and AKT were also activated in HCT116 cells co-cultured with MTCAFs after day 3 (**Figure 6B**), whereas MTCAFs were knocked down by ICAM-1, and the phosphorylation of JAK, STAT3, and AKT in HCT116 cells was significantly decreased (**Figure 6C**). Next, we detected the migration and invasion ability of HCT116 cells in different treatment groups, including HCT116 and MSC co-culture group (group A), HCT116 and MSC co-culture plus STAT3 inhibitor group (group B), and HCT116 and MSC co-culture plus AKT inhibitor group (group C). Transwell results showed that HCT116 cell invasion was significantly reduced in groups B and C compared with group A (**Figures 6D, E**). Wound healing test results showed that the migration ability of HCT116 cells in groups B and C was significantly weakened compared with group A (**Figure 6F**). Finally, immunohistochemistry demonstrated that MTCAFs can activate AKT and STAT3 signaling pathways in tumor tissues in nude xenograft tumor models (**Supplementary Figure 2**). These results suggest that MTCAF-derived ICAM-1 promotes the progression of colon cancer cells by binding LFA-1 to activate STAT3 and AKT signaling pathways.

Discussion

It has been well established that CAFs promotes various tumor progression, and CAFs originate in a variety of cells including MSCs, endotheliocyte, and epithelial cell (36). In our study, we mainly use MSC-derived CAFs (MTCAFs).

Mechanistically, this mainly contributed to the matrix deposition and remodeling, interactions with cancer cells *via* extensive reciprocal signaling, and crosstalk with infiltrating immune cells (30, 37–39). Although recent studies have found that CAFs attribute to the progression of colon cancer (40, 41), the origin and role of CAFs incolon cancer and its mechanism have needed to be fully elucidated. Here, we confirm that MSC-derived CAFs promote the growth, migration, and invasion of colon cancer cells and testify the critical role of CAFs in the microenvironment of colon cancer.

Recent reports have shown that CAFs can secrete various cytokines such as growth factor, inflammatory factors, and chemokine, which can stimulate diverse signaling pathways and biological functions of different cancers (10). Previous studies have shown that several cytokines in CAFs were increased, which contribute to the progression of various cancer including IL8, IL6, and TGF-β1 (10, 42–44). In our work, we identified a novel cytokine, ICAM-1, which is a transmembrane molecule stabilizing cell–cell and cell-extracellular matrix interactions and facilitating transendothelial transmigration (45, 46). MTCAF-derived ICAM-1 has double roles: It not only regulates the growth and migration of MTCAFs by mediating the expression of IL6 and IL8 in MTCAFs but also can promote the proliferation and invasion of cancer cells. Previous study has shown that the prognosis of the patients with ICAM-1–negative tumors was significantly poorer than that of those with ICAM-1–positive tumors (47). This result is not contradictory with our result. We consider that this difference between our results and the previous reports may be due to ICAM-1 derived from MTCAFs. Our results further verified this hypothesis. We found that ICAM-1 expression was high in fibroblasts (i.e., mesenchymal cells of tumor tissue) of tumor tissue in patients with different clinical stages, which negatively correlated with patient survival, consistent with our results *in vivo* and *in vitro*.

One of the critical problems is the molecular mechanism of ICAM-1 derived from MTCAFs action on colon cancer cells in our study. It has been found that CAFs can be activated by some cytokines in TME, such as IL6, IL8, and Fibroblast growth factor 2 (FGF2) (43, 48), which further activates various pathways including IL6-STAT3 and AKT signaling pathways (43, 49). Interestingly, these pathways have been also shown to regulate ICAM-1 expression (20). Therefore, we found that MTCAF-derived ICAM-1 promotes the progression by activating the STAT3 and AKT signaling in colon cancer cells. However, this specific question needs further study.

Most studies have demonstrated that ICAM-1 regulates cancer metastasis *via* the binding receptor, LFA-1, which can activate numerous pathways (50–52). ICAM-1–induced tumor COX-2 impaired the antitumor activity *via* binding LFA-1 during hepatic metastasis (52). The expression of inflammatory cytokines, such as IL-1β, TNFα, IL-6, and IFN-γ, tightly regulates ICAM-1 expression (53, 54). In addition, the ICAM-1/LFA-1 pathway regulates important cell–cell interactions including leukocyte adhesion and migration, especially the killing of tumor cells by natural killer cells and cytotoxic T lymphocytes (CTLs) (55, 56). At present, various tumor cells have been shown to highly express ICAM-1 that is known to be a potent ligand for LFA-1 on CTLs. Most studies have revealed that ICAM-1 plays an important role in the progress and metastasis of many cancers (21, 57–59). However, the function of ICAM-1 in CAFs has not been revealed in the TME of colorectal cancer. In our study, we found that ICAM-1 derived from MTCAFs promotes the migration and invasion of colorectal cancer cells by binding LFA-1 receptor of colon cancer, subsequently activating AKT and STAT3 in HCT116 cells. The possible mechanism is that MTCAFs activate the AKT and STAT3 signaling pathways in colon cancer cells *via* the ICAM-1/LFA-1axis.

Although we confirmed the important role of MTCAF-derived ICAM-1 in colorectal cancer, there are still many limitations, such as stage IV patients were not included in our study. One reason for lacking of stage IV patients was that those patients rarely underwent surgery in the past years. We can enroll larger sample capacity to further explore the correlation between ICAM-1 and clinical features in this should be the future.

Conclusion

In summary, we found that ICAM-1 secreted from CAFs enhances the migration and invasion ability of colorectal cancer cells by activating the AKT and STAT3 pathway in cancer cells (Figure 6). Our results provide a better cognition of how CAFs work in the TME in colorectal cancer. MTCAF-derived ICAM-1 may play an important role in promoting cancer metastasis and can serve as a predictive and prognostic biomarker in colorectal cancer.

Data availability statement

The datasets presented in this study can be found in online repositories. The names of the repository/repositories and accession number(s) can be found in the article/Supplementary Material.

Ethics statement

The studies involving human participants were reviewed and approved by This is a retrospective cohort study. Colorectal cancers were obtained with informed consent from patients in Peking Union Medical College Hospital (Beijing, China) during January 2014 to December 2016. All specimens were collected using the protocols approved by the Ethics Committee of Peking Union Medical College Hospital. All patients were R0 resected and pathologically diagnosed with CRC. The patients/participants provided their written informed consent to participate in this study.

The animal study was reviewed and approved by the Ethics Committee at the Chinese Academy of Medical Sciences and Peking Union Medical College.

Author contributions

The study was designed by QH, ZS, CB, and RZ. CX carried out the experiments, performed the statistical analyses, and wrote the manuscript. YG and XL contributed to the statistical analyses. MZ and YY helped do some experiments. All authors have read and approved the final manuscript. All authors contributed to the article and approved the submitted version.

Funding

This work was supported by the National Key Research and Development Program of China (2016YFA0101000, 2016YFA0101003, and 2018YFA0109800), CAMS Innovation Fund for Medical Sciences (2017-I2M-3-007), the 111 Project (B18007), and National Natural Science Foundation of China (81672313 and 81700782).

Conflict of interest

The authors declare that the research was conducted in the absence of any commercial or financial relationships that could be construed as a potential conflict of interest.

Publisher's note

All claims expressed in this article are solely those of the authors and do not necessarily represent those of their affiliated organizations, or those of the publisher, the editors and the reviewers. Any product that may be evaluated in this article, or claim that may be made by its manufacturer, is not guaranteed or endorsed by the publisher.

Supplementary material

The Supplementary Material for this article can be found online at: https://www.frontiersin.org/articles/10.3389/fonc.2022.837781/full#supplementary-material

SUPPLEMENTARY FIGURE 1
Characterisation of exosomes derived from HCT116 cells (HCT116-exos) and *in vitro* uptake assay results. **(A)** The morphology of HCT116-exos was assessed using electron microscopy. **(B)** HSP70, HSP90, and CD63 expression in HCT116cells and HCT116-exos was analyzed using Western blotting. **(C)** HCT116-exos size distribution was evaluated by NTA analysis. **(D)** Uptake of DiR-labelled HCT116-exos by MSCs was also evaluated after 10h.

SUPPLEMENTARY FIGURE 2
Knocking down ICAM-1 from MTCAFs attenuates STAT3 and AKT signaling *in vivo*. (E) (A/B)AKT and STAT3 signaling pathways were measured using immunohistochemical staining in mice tumor tissues.

References

1. Whiteside TL. Exosome and mesenchymal stem cell cross–talk in the tumor microenvironment. *Semin Immunol* (2018) 35:69–79. doi: 10.1016/j.smim.2017.12.003

2. Lazennec G, Jorgensen C. Concise review: adult multipotent stromal cells and cancer: risk or benefit? *Stem Cells (Dayton Ohio)* (2008) 26(6):1387–94. doi: 10.1634/stemcells.2007–1006

3. Zhou H, Guo M, Bian C, Sun Z, Yang Z, Zeng Y, et al. Efficacy of bone marrow–derived mesenchymal stem cells in the treatment of sclerodermatous chronic graft–versus–host disease: clinical report. *Biol Blood Marrow Transplant J Am Soc Blood Marrow Transplant* (2010) 16(3):403–12. doi: 10.1016/j.bbmt.2009.11.006

4. Keating A. Mesenchymal stromal cells: new directions. *Cell Stem Cell* (2012) 10(6):709–16. doi: 10.1016/j.stem.2012.05.015

5. Yang X, Li Y, Zou L, Zhu Z. Role of exosomes in crosstalk between cancer–associated fibroblasts and cancer cells. *Front Oncol* (2019) 9:356. doi: 10.3389/fonc.2019.00356

6. Gascard P, Tlsty TD. Carcinoma–associated fibroblasts: orchestrating the composition of malignancy. *Genes Dev* (2016) 30(9):1002–19. doi: 10.1101/gad.279737.116

7. Brenner H, Kloor M, Pox CP. Colorectal cancer. *Lancet (London England)* (2014) 383(9927):1490–502. doi: 10.1016/s0140–6736(13)61649–9

8. Richman DM, Tirumani SH, Hornick JL, Fuchs CS, Howard S, Krajewski K, et al. Beyond gastric adenocarcinoma: Multimodality assessment of common and uncommon gastric neoplasms. *Abdominal Radiol (New York)* (2017) 42(1):124–40. doi: 10.1007/s00261–016–0901–x

9. Quail DF, Joyce JA. Microenvironmental regulation of tumor progression and metastasis. *Nat Med* (2013) 19(11):1423–37. doi: 10.1038/nm.3394

10. Zhou Z, Zhou Q, Wu X, Xu S, Hu X, Tao X, et al. VCAM–1 secreted from cancer–associated fibroblasts enhances the growth and invasion of lung cancer cells through AKT and MAPK signaling. *Cancer Lett* (2020) 473:62–73. doi: 10.1016/j.canlet.2019.12.039

11. Marsh T, Pietras K, McAllister SS. Fibroblasts as architects of cancer pathogenesis. *Biochim Biophys Acta* (2013) 1832(7):1070–8. doi: 10.1016/j.bbadis.2012.10.013

12. Ligorio M, Sil S, Malagon–Lopez J, Nieman LT, Misale S, Di Pilato M, et al. Stromal microenvironment shapes the intratumoral architecture of pancreatic cancer. *Cell* (2019) 178(1):160–75.e27. doi: 10.1016/j.cell.2019.05.012

13. Huynh J, Chand A. Therapeutically exploiting STAT3 activity in cancer – using tissue repair as a road map. *Nat Rev Cancer* (2019) 19(2):82–96. doi: 10.1038/s41568–018–0090–8

14. Paulsson J, Micke P. Prognostic relevance of cancer–associated fibroblasts in human cancer. *Semin Cancer Biol* (2014) 25:61–8. doi: 10.1016/j.semcancer.2014.02.006

15. Chang HY, Sneddon JB, Alizadeh AA, Sood R, West RB, Montgomery K, et al. Gene expression signature of fibroblast serum response predicts human cancer progression: similarities between tumors and wounds. *PloS Biol* (2004) 2(2):E7. doi: 10.1371/journal.pbio.0020007

16. Berdiel–Acer M, Sanz–Pamplona R, Calon A, Cuadras D, Berenguer A, Sanjuan X, et al. Differences between CAFs and their paired NCF from adjacent colonic mucosa reveal functional heterogeneity of CAFs, providing prognostic information. *Mol Oncol* (2014) 8(7):1290–305. doi: 10.1016/j.molonc.2014.04.006

17. Liu S, Li N, Yu X, Xiao X, Cheng K, Hu J, et al. Expression of intercellular adhesion molecule 1 by hepatocellular carcinoma stem cells and circulating tumor cells. *Gastroenterology* (2013) 144(5):1031–41.e10. doi: 10.1053/j.gastro.2013.01.046

18. van der Saag PT, Caldenhoven E, van de Stolpe A. Molecular mechanisms of steroid action: a novel type of cross–talk between glucocorticoids and NF–kappa b transcription factors. *Eur Respir J Suppl* (1996) 22:146s–53s.

19. Zimmerman T, Blanco FJ. Inhibitors targeting the LFA–1/ICAM–1 cell–adhesion interaction: design and mechanism of action. *Curr Pharm Des* (2008) 14(22):2128–39. doi: 10.2174/138161208785740225

20. Liu CW, Lee TL, Chen YC, Liang CJ, Wang SH, Lue JH, et al. PM2.5–induced oxidative stress increases intercellular adhesion molecule–1 expression in lung epithelial cells through the IL–6/AKT/STAT3/NF–kappaB–dependent pathway. *Part Fibre Toxicol* (2018) 15(1):4. doi: 10.1186/s12989–018–0240–x

21. Sanchez–Lopez E, Flashner–Abramson E, Shalapour S, Zhong Z, Taniguchi K, Levitzki A, et al. Targeting colorectal cancer *via* its microenvironment by inhibiting IGF–1 receptor–insulin receptor substrate and STAT3 signaling. *Oncogene* (2016) 35(20):2634–44. doi: 10.1038/onc.2015.326

22. Grivennikov S, Karin E, Terzic J, Mucida D, Yu GY, Vallabhapurapu S, et al. IL–6 and Stat3 are required for survival of intestinal epithelial cells and development of colitis–associated cancer. *Cancer Cell* (2009) 15(2):103–13. doi: 10.1016/j.ccr.2009.01.001

23. Kishimoto T. Interleukin–6: from basic science to medicine–40 years in immunology. *Annu Rev Immunol* (2005) 23:1–21. doi: 10.1146/annurev.immunol.23.021704.115806

24. Lee KW, Yeo SY, Sung CO, Kim SH. Twist1 is a key regulator of cancer–associated fibroblasts. *Cancer Res* (2015) 75(1):73–85. doi: 10.1158/0008–5472.can–14–0350

25. Becker C, Fantini MC, Schramm C, Lehr HA, Wirtz S, Nikolaev A, et al. TGF–beta suppresses tumor progression in colon cancer by inhibition of IL–6 trans–signaling. *Immunity* (2004) 21(4):491–501. doi: 10.1016/j.immuni.2004.07.020

26. Becker C, Fantini MC, Wirtz S, Nikolaev A, Lehr HA, Galle PR, et al. IL–6 signaling promotes tumor growth in colorectal cancer. *Cell Cycle (Georgetown Tex)* (2005) 4(2):217–20.

27. Shen Y, Xue C, Li X, Ba L, Gu J, Sun Z, et al. Effects of gastric cancer cell–derived exosomes on the immune regulation of mesenchymal stem cells by the NF–kB signaling pathway. *Stem Cells Dev* (2019) 28(7):464–76. doi: 10.1089/scd.2018.0125

28. Li J, Li N, Chen Y, Hui S, Fan J, Ye B, et al. SPRY4 is responsible for pathogenesis of adolescent idiopathic scoliosis by contributing to osteogenic differentiation and melatonin response of bone marrow–derived mesenchymal stem cells. *Cell Death Dis* (2019) 10(11):805. doi: 10.1038/s41419–019–1949–7

29. Yang Y, Gu J, Li X, Xue C, Ba L, Gao Y, et al. HIF–1α promotes the migration and invasion of cancer–associated fibroblasts by miR–210. *Aging Dis* (2021) 12(7):1794–807. doi: 10.14336/ad.2021.0315

30. Strell C, Paulsson J, Jin SB, Tobin NP, Mezheyeuski A, Roswall P, et al. Impact of epithelial–stromal interactions on peritumoral fibroblasts in ductal carcinoma in situ. *J Natl Cancer Inst* (2019) 111(9):983–95. doi: 10.1093/jnci/djy234

31. Gadek TR, Burdick DJ, McDowell RS, Stanley MS, Marsters JCJr., Paris KJ, et al. Generation of an LFA–1 antagonist by the transfer of the ICAM–1 immunoregulatory epitope to a small molecule. *Sci (New York NY)* (2002) 295(5557):1086–9. doi: 10.1126/science.295.5557.1086

32. Wang S, Xu M, Li X, Su X, Xiao X, Keating A, et al. Exosomes released by hepatocarcinoma cells endow adipocytes with tumor–promoting properties. *J Hematol Oncol* (2018) 11(1):82. doi: 10.1186/s13045–018–0625–1

33. Xie G, Yao Q, Liu Y, Du S, Liu A, Guo Z, et al. IL–6–induced epithelial–mesenchymal transition promotes the generation of breast cancer stem–like cells analogous to mammosphere cultures. *Int J Oncol* (2012) 40(4):1171–9. doi: 10.3892/ijo.2011.1275

34. Kaverina N, Borovjagin AV, Kadagidze Z. Astrocytes promote progression of breast cancer metastases to the brain via a KISS1–mediated autophagy. *Autophagy* (2017) 13(11):1905–23. doi: 10.1080/15548627.2017.1360466

35. Yan J, Xiang J, Lin Y, Ma J, Zhang J, Zhang H, et al. Inactivation of BAD by IKK inhibits TNFalpha–induced apoptosis independently of NF–kappaB activation. *Cell* (2013) 152(1–2):304–15. doi: 10.1016/j.cell.2012.12.021

36. Chen X, Song E. Turning foes to friends: targeting cancer–associated fibroblasts. *Nat Rev Drug Discov* (2019) 18(2):99–115. doi: 10.1038/s41573–018–0004–1

37. Sahai E, Astsaturov I. A framework for advancing our understanding of cancer–associated fibroblasts. *Nat Rev Cancer* (2020) 20(3):174–86. doi: 10.1038/s41568–019–0238–1

38. Lo A, Wang LS, Scholler J, Monslow J, Avery D, Newick K, et al. Tumor–promoting desmoplasia is disrupted by depleting FAP–expressing stromal cells. *Cancer Res* (2015) 75(14):2800–10. doi: 10.1158/0008–5472.Can–14–3041

39. Kraman M, Bambrough PJ, Arnold JN, Roberts EW, Magiera L, Jones JO, et al. Suppression of antitumor immunity by stromal cells expressing fibroblast activation protein–alpha. *Sci (New York NY)* (2010) 330(6005):827–30. doi: 10.1126/science.1195300

40. Unterleuthner D, Neuhold P, Schwarz K, Janker L, Neuditschko B, Nivarthi H, et al. Cancer–associated fibroblast–derived WNT2 increases tumor angiogenesis in colon cancer. *Angiogenesis* (2020) 23(2):159–77. doi: 10.1007/s10456–019–09688–8

41. Hu JL, Wang W, Lan XL, Zeng ZC, Liang YS, Yan YR, et al. CAFs secreted exosomes promote metastasis and chemotherapy resistance by enhancing cell stemness and epithelial–mesenchymal transition in colorectal cancer. *Mol Cancer* (2019) 18(1):91. doi: 10.1186/s12943–019–1019–x

42. Yuen KC, Liu LF, Gupta V, Madireddi S, Keerthivasan S, Li C, et al. High systemic and tumor–associated IL–8 correlates with reduced clinical benefit of PD–L1 blockade. *Nat Med* (2020) 26(5):693–8. doi: 10.1038/s41591–020–0860–1

43. Cheng Y, Li H, Deng Y, Tai Y, Zeng K, Zhang Y, et al. Cancer–associated fibroblasts induce PDL1+ neutrophils through the IL6–STAT3 pathway that foster immune suppression in hepatocellular carcinoma. *Cell Death Dis* (2018) 9(4):422. doi: 10.1038/s41419–018–0458–4

44. Nii T, Makino K, Tabata Y. A cancer invasion model of cancer–associated fibroblasts aggregates combined with TGF–β1 release system. *Regen Ther* (2020) 14:196–204. doi: 10.1016/j.reth.2020.02.003

45. Huang C, Li N, Li Z, Chang A, Chen Y, Zhao T, et al. Tumour–derived interleukin 35 promotes pancreatic ductal adenocarcinoma cell extravasation and metastasis by inducing ICAM1 expression. *Nat Commun* (2017) 8:14035. doi: 10.1038/ncomms14035

46. Millan J, Hewlett L, Glyn M, Toomre D, Clark P, Ridley AJ. Lymphocyte transcellular migration occurs through recruitment of endothelial ICAM–1 to caveola– and f–actin–rich domains. *Nat Cell Biol* (2006) 8(2):113–23. doi: 10.1038/ncb1356

47. Maeda K, Kang SM, Sawada T, Nishiguchi Y, Yashiro M, Ogawa Y, et al. Expression of intercellular adhesion molecule–1 and prognosis in colorectal cancer. *Oncol Rep* (2002) 9(3):511–4.

48. Czubayko F, Liaudet–Coopman ED, Aigner A, Tuveson AT, Berchem GJ, Wellstein A. A secreted FGF–binding protein can serve as the angiogenic switch in human cancer. *Nat Med* (1997) 3(10):1137–40. doi: 10.1038/nm1097–1137

49. Ji K, Liang H, Ren M, Ge X, Mi H, Pan L, et al. The immunoreaction and antioxidant capacity of juvenile blunt snout bream (Megalobrama amblycephala) involves the PI3K/Akt/Nrf2 and NF–κB signal pathways in response to dietary methionine levels. *Fish Shellfish Immunol* (2020) 105:126–34. doi: 10.1016/j.fsi.2020.07.005

50. Ell B, Mercatali L, Ibrahim T, Campbell N, Schwarzenbach H, Pantel K, et al. Tumor–induced osteoclast miRNA changes as regulators and biomarkers of osteolytic bone metastasis. *Cancer Cell* (2013) 24(4):542–56. doi: 10.1016/j.ccr.2013.09.008

51. Soto MS, O'Brien ER, Andreou K, Scrace SF, Zakaria R, Jenkinson MD, et al. Disruption of tumour–host communication by downregulation of LFA–1 reduces COX–2 and e–NOS expression and inhibits brain metastasis growth. *Oncotarget* (2016) 7(32):52375–91. doi: 10.18632/oncotarget.10737

52. Arteta B, Lasuen N, Lopategi A, Sveinbjornsson B, Smedsrod B, Vidal–Vanaclocha F. Colon carcinoma cell interaction with liver sinusoidal endothelium inhibits organ–specific antitumor immunity through interleukin–1–induced mannose receptor in mice. *Hepatol (Baltimore Md)* (2010) 51(6):2172–82. doi: 10.1002/hep.23590

53. Sallusto F, Lanzavecchia A. Efficient presentation of soluble antigen by cultured human dendritic cells is maintained by granulocyte/macrophage colony–stimulating factor plus interleukin 4 and downregulated by tumor necrosis factor alpha. *J Exp Med* (1994) 179(4):1109–18. doi: 10.1084/jem.179.4.1109

54. Shen J, Devery JM, King NJ. Adherence status regulates the primary cellular activation responses to the flavivirus West Nile. *Immunology* (1995) 84(2):254–64.

55. Dustin ML, Springer TA. T–Cell receptor cross–linking transiently stimulates adhesiveness through LFA–1. *Nature* (1989) 341(6243):619–24. doi: 10.1038/341619a0

56. Mukai S, Kagamu H, Shu S, Plautz GE. Critical role of CD11a (LFA–1) in therapeutic efficacy of systemically transferred antitumor effector T cells. *Cell Immunol* (1999) 192(2):122–32. doi: 10.1006/cimm.1998.1439

57. Feng H, Stachura DL, White RM, Gutierrez A, Zhang L, Sanda T, et al. T–Lymphoblastic lymphoma cells express high levels of BCL2, S1P1, and ICAM1, leading to a blockade of tumor cell intravasation. *Cancer Cell* (2010) 18(4):353–66. doi: 10.1016/j.ccr.2010.09.009

58. Ferrara N. Natural killer cells, adhesion and tumor angiogenesis. *Nat Med* (1996) 2(9):971–2. doi: 10.1038/nm0996–971

59. Reina M, Espel E. Role of LFA–1 and ICAM–1 in cancer. *Cancers* (2017) 9 (11). doi: 10.3390/cancers9110153

Frontiers in Oncology

Advances knowledge of carcinogenesis and tumor progression for better treatment and management

The third most-cited oncology journal, which highlights research in carcinogenesis and tumor progression, bridging the gap between basic research and applications to imrpove diagnosis, therapeutics and management strategies.

Discover the latest Research Topics

See more →

Frontiers

Avenue du Tribunal-Fédéral 34
1005 Lausanne, Switzerland
frontiersin.org

Contact us

+41 (0)21 510 17 00
frontiersin.org/about/contact